

# 1994

## Solid-State Sensors, Actuators, and Microsystems Workshop

Greeting from the Chair

Committees

Table of Contents

Author Index

Keyword Index

Copyright

[www.hh1994.org](http://www.hh1994.org)



Sponsored by the  
Transducer Research Foundation, Inc.  
Additional support provided:  
Defense Advanced Research Projects Agency

Hilton Head Workshop  
June 12 - 16, 1994 • Hilton Head, South Carolina  
Editors: David S. Eddy & Roger T. Howe

TRF Catalog Number: 94TRF-0001  
Library of Congress Control Number: 94-60019  
ISBN Number: 0-9640024-0-X  
ISSN 1539-2058 (Print) • ISSN: 1539-204X (Electronic)  
DOI 10.31438/trf.hh1994.0

# 1994

## Solid-State Sensors, Actuators, and Microsystems Workshop

Hilton Head Island, South Carolina • June 12 - 16, 1994

All opinions expressed in this digest are those of the authors and are not binding on Transducer Research Foundation, Inc.

Copies of available volumes of this digest may be obtained from the Transducer Research Foundation, Inc., c/o 307 Laurel Street, San Diego, California 92101-1630 USA (+1-619-232-9499)

Copyright and Reprint Permission: Abstracting is permitted with credit to the source. Libraries are permitted to photocopy beyond the limit of U.S. copyright law for private use of patrons those articles in this volume that carry a code at the bottom of the first page, provided the per-copy fee indicated in the code is paid through Copyright Clearance Center, 222 Rosewood Drive, Danvers, MA 01923. For other copying, reprint or republication permission, contact Transducer Research Foundation, Inc., c/o 307 Laurel Street, San Diego, California 92101-1630 USA, info@transducer-research-foundation.org. All rights reserved. Copyright ©1994 by the Transducer Research Foundation, Inc. Personal use of this material is permitted. However, permission to reprint/republish this material for advertising or promotional purposes or for creating new collective works for resale or redistribution to servers or lists, or to reuse any copyrighted component of this work in other works must be obtained from the Transducer Research Foundation, Inc.

TRF Catalog Number: 94TRF-0001

Library of Congress Control Number: 94-60019

ISBN Number: 0-9640024-0-X

ISSN 1539-2058 (Print) • ISSN: 1539-204X (Electronic)

DOI 10.31438/trf.hh1994.0

This product contains Adobe Acrobat software. Copying this product's instructions and/or designs for use on future CD-ROMs or digital products is prohibited without written permission from The Printing House and Adobe Systems Incorporated. The Printing House or its suppliers are not liable for any direct, indirect, special, incidental, or consequential damages to your hardware or other software arising out of the use—or the inability to use—the material on this CD-ROM. This includes, but is not limited to, the loss of data or loss of profit. Adobe, Acrobat and the Acrobat logo are trademarks of Adobe Systems Incorporated or its subsidiaries and may be registered in certain jurisdictions.

If you have questions regarding the installation, please contact:



The Printing House

Phone: +1-608-873-4500

Hours: Monday through Friday, 8 am - 5 pm CST

E-mail: graphics@printinghouseinc.com

## 1994 Solid-State Sensor and Actuator Workshop

On behalf of the entire organizing committee, I am pleased to welcome you to Hilton Head Island for the sixth Solid-State Sensor and Actuator Workshop. This year we celebrate our tenth anniversary and many of us fondly remember our past experiences in the previous "Hilton Head Workshop" meetings. If you are attending your first Hilton Head Workshop, I hope that you will share in this enthusiasm for Hilton Head's rich tradition by week's end.

The Hilton Head Workshop is one of the regional meetings held in North America, Europe, and Asia during the even-numbered years, alternating with the much larger international TRANSDUCERS conferences held in odd-numbered years. TRANSDUCERS '93 was held in Yokohama, Japan, and TRANSDUCERS '95 will take place in Stockholm, Sweden.

The format of the Workshop is intentionally designed to provide a highly interactive forum for US and Canadian workers to meet and discuss recent advances in emerging technologies for sensing and actuation devices and systems for physical, chemical, and biological applications. It is a single session meeting, with ample time allotted for discussion of each paper, and with blocks of unscheduled time to encourage informal interactions among participants. From the very first meeting in 1984, graduate students have been encouraged to attend and participate in the Workshop. Many of the active professionals in attendance at this Workshop gave their first student papers here at Hilton Head.

The serious work of putting the formal technical program in place started last summer with the call for papers. The Program Committee reviewed all the papers that were submitted last winter and considered a number of options for invited papers to make up the formal technical program. Because of the outstanding response in submitted papers, the Program Committee expanded the technical program to sixty papers and extended the length of the Workshop to four full days. All of the papers which make up the formal technical program are printed in this Technical Digest. In order to provide a forum for the presentation of recent results, a "Late News" Poster Session will be held on Wednesday evening before the Rump Session. As in the past, the Rump Session will be devoted to a discussion topic of major importance to the field. In keeping with past Workshops, Tuesday afternoon is left open for sharing leisure activities with your colleagues. I encourage each of you to take full advantage of the various opportunities that the Workshop offers.

With the magnitude of effort needed to organize this Workshop, we were fortunate to have the support of a number of organizations and individuals. This year's Workshop is sponsored by the non-profit Transducers Research Foundation which provided the business infrastructure for the meeting. Special thanks is due to the National Science Foundation and Linton Salmon for the provision of travel assistance grants for graduate students presenting papers, and to Richard Muller for his diligence in obtaining and distributing this support on behalf of the Workshop.

In closing, I thank the entire Organizing Committee -- with special thanks to Tom Poteat for his arrangements of this fine meeting site, to Joe Giachino for looking after the important financial matters, and to the Program Committee chaired by Roger Howe for its work in arranging the technical program. Finally, I thank the authors for providing the essential contributions of their work to the Workshop, and to all the participants for being here and taking part to the fullest.

Enjoy your Workshop!



David S. Eddy  
General Chairman

# 1994 Solid-State Sensor and Actuator Workshop

## Organizing Committee

General Chairman and Publications	David S. Eddy General Motors Corporation
Technical Program Chairman	Roger T. Howe University of California - Berkeley
Treasurer	Joseph M. Giachino Ford Motor Company
Local Arrangements	Tom Poteat Sandia National Laboratories
Assistant Local Arrangements	Mark G. Allen Georgia Institute of Technology
Program Meeting Arrangements	Robert Huber University of Utah
University Grants	Richard S. Muller University of California - Berkeley

## Technical Program Committee

Luc Bousse Molecular Devices Corporation	Mehran Mehregany Case Western Reserve University
David W. Burns Honeywell, Inc.	Khalil Najafi University of Michigan
Clifford D. Fung The Foxboro Company	Kurt E. Petersen NovaSensor, Inc.
D. Jed Harrison University of Alberta	Antonio J. Ricco Sandia National Laboratories
James H. Logsdon Delco Electronics Corporation	Martin A. Schmidt Massachusetts Institute of Technology

**1994 Solid-State Sensor and Actuator Workshop  
June 13-16, 1994  
Crystal Sands Resort, Hilton Head Island, South Carolina**

**PROGRAM**

**Sunday, June 12:**

**7:00 - 9:00 pm WELCOME RECEPTION with no-host bar**

**Monday, June 13: Session 1**

**7:15 am Breakfast**

**7:45 am Welcome and Introduction (D. S. Eddy)**

	<b>Silicon Microstructure Applications (R. T. Howe)</b>	<b>Page</b>
<b>8:15 am</b>	<b>Deformable Grating Light Valves for High Resolution Displays</b> R. B. Apte, F. S. A. Sandejas, W. C. Banyai, and D. M. Bloom Stanford University (Invited)	<b>1</b>
<b>9:00</b>	<b>512 X 512 Infrared Scene Projector Array for Low-Background Simulations</b> B. H. Cole, C.-J. Han, R. E. Higashi, J. Ridley, J. Holmen, <i>et al</i> , Honeywell Technology Center	<b>7</b>
<b>9:25</b>	<b>A High-Density Tactile Imager for Reading Embossed Characters</b> R. J. DeSouza and K. D. Wise, University of Michigan	<b>13</b>
<b>9:50</b>	<b>Micromechanical Data Storage with Ultra Low-Mass Cantilevers</b> H. J. Mamin, L. S. Fan, S. Hoen, and D. Rugar, IBM Almaden Research Center	<b>17</b>
<b>10:15</b>	<b>Coffee Break</b>	

## Monday, June 13: Session 2

### Chemical Microinstruments (A. J. Ricco)

<b>10:40 am</b>	<b>Integrated Electrophoresis Systems for Biochemical Analysis</b> D. J. Harrison, Z. Fan, K. Fluri, and K. Seiler University of Alberta	<b>21</b>
<b>11:05</b>	<b>A Simple Packaging Process for Chemical Sensors</b> M. E. Poplawski, R. W. Hower, and R. B. Brown University of Michigan	<b>25</b>
<b>11:30</b>	<b>Chip-Level Encapsulation of Implantable CMOS Microelectronic Arrays</b> J. L. Lund and K. D. Wise, University of Michigan	<b>29</b>
<b>11:55 am</b>	<b>Lunch</b>	

## Monday, June 13: Session 3

### Microactuators - I (M. Mehregany)

<b>1:15 pm</b>	<b>Piezoelectric Cantilever Microphone and Microspeaker</b> S. S. Lee, R. P. Ried, and R. M. White University of California at Berkeley	<b>33</b>
<b>1:40</b>	<b>Batch-Fabricated Area-Efficient Milli-Actuators</b> L.-S. Fan, S. J. Woodman, R. C. Moore, L. Crawforth, T. C. Reiley, and M. A. Moser, IBM Almaden Research Center	<b>38</b>
<b>2:05</b>	<b>Magnetic Microactuation of Polysilicon Flexure Structures</b> J. W. Judy, R. S. Muller, and H. H. Zappe University of California at Berkeley	<b>43</b>
<b>2:30</b>	<b>Laterally Driven Electromagnetic Actuators</b> H. Guckel, T. R. Christenson, T. Earles, and J. Klein University of Wisconsin - Madison J. D. Zook and T. Ohnstein, Honeywell Technology Center M. Karnowski, Sandia National Laboratory, Albuquerque	<b>49</b>

**Monday 3:05 - 5:30: Contributed Poster Session**

<b>Area</b>	<b>Title, Authors, and Affiliation</b>	<b>Page</b>
<b>Chem Sensor</b>	<b>Micro-hotplate Gas Sensor</b> R. E. Cavicchi, J. S. Suehle, P. Chaparala, K. G. Kreider, M. Gaitan, and S. Semancik, National Institute of Standards and Technology	<b>53</b>
<b>Chem Sensor</b>	<b>Response of the Sandia Robust Wide Range Hydrogen Sensor to H<sub>2</sub>O<sub>2</sub> Mixtures</b> R. C. Hughés, D. J. Moreno, M. W. Jenkins, and J. L. Rodriguez Sandia National Laboratories	<b>57</b>
<b>Chem Sensor/System</b>	<b>Microfabricated Electrochemical Detector for Capillary Electrophoresis</b> R. J. Reay, R. Dadoo, C. W. Storment, R. N. Zare, and G. T. A. Kovacs Stanford University	<b>61</b>
<b>Chem Sensor/System</b>	<b>Electrically Driven Separations on a Microchip</b> S. C. Jacobsen, R. Hergenroeder, A. W. Moore, and J. M. Ramsey Oak Ridge National Laboratory	<b>65</b>
<b>Physical Sensor</b>	<b>Navigation Grade Silicon Accelerometers with Sacrificially Etched SIMOX and BESOI Structure</b> K. Warren, Litton Guidance & Control Systems	<b>69</b>
<b>Physical Sensor</b>	<b>Advanced Micromachined Condenser Hydrophone</b> J. Bernstein and M. Weinberg, C. S. Draper Laboratory, and E. McLaughlin, J. Powers, and F. Tito, Naval Undersea Warfare Cen.	<b>73</b>
<b>Physical Sensor</b>	<b>Burstproof, Thermal Pressure Sensor for Gases</b> U. Bonne and D. Kubisiak Honeywell Technology Center	<b>78</b>
<b>Process Tech</b>	<b>Using Electron Cyclotron Resonance (ECR) Source to Etch Polyimide Molds for Fabrication of Electroplated Microstructures</b> W. H. Juan, S. W. Pang, A. Selvakumar, M. W. Putty*, and K. Najafi University of Michigan and *General Motors Research Laboratories	<b>82</b>
<b>Process Tech</b>	<b>Silicon-on-Insulator (SOI) by Zone-Melting-Recrystallization (ZMR) as a Micromechanical Material</b> P. D. Aquilino and P. M. Zavracky Northeastern University	<b>86</b>
<b>Process Tech</b>	<b>Uses of Electroplated Aluminum in Micromachining Applications</b> A. B. Frazier and M. G. Allen Georgia Institute of Technology	<b>90</b>

**Monday, June 13: Contributed Poster Session (Cont.)**

<b>Area</b>	<b>Title, Authors, and Affiliation</b>	<b>Page</b>
<b>Process Tech</b>	<b>Dry-Released Process for Aluminum Electrostatic Actuators</b> C. W. Storment, D. A. Borkholder, V. A. Westerlind, J. W. Suh, N. I. Maluf, and G. T. A. Kovacs Stanford University	<b>95</b>
<b>Process Tech</b>	<b>Surface Micromachined Multiple Level Tungsten Microactuators</b> L.-Y. Chen and N. C. MacDonald Cornell University	<b>99</b>
<b>Process Tech</b>	<b>Studies on the Sealing of Surface Micromachined Cavities Using Chemical Vapor Deposited Materials</b> C. Liu and Y.-C. Tai California Institute of Technology	<b>103</b>
<b>Process Tech</b>	<b>Microfabrication of Tweezers with Large Gripping Forces and a Large Range of Motion</b> W.-H. Chu and M. Mehregany Case Western Reserve University	<b>107</b>
<b>Process Tech</b>	<b>Wafer-Bonding Technology for Microfabricated Shear-Stress Sensors with Backside Contacts</b> H. D. Goldberg, K. S. Breuer, and M. A. Schmidt Massachusetts Institute of Technology	<b>111</b>
<b>Process Tech</b>	<b>A Compact Passive Strain Sensor with a Bent Beam Deformation Multiplier and a Complementary Motion Vernier</b> Y. B. Gianchandani and K. Najafi University of Michigan	<b>116</b>
<b>Relia- bility</b>	<b>Reliability Study of Polysilicon Based Microhotplates</b> N. R. Swart and A. Nathan University of Waterloo	<b>119</b>
<b>CAD</b>	<b>A Heuristic Approach to the Electromechanical Modeling of MEMS Beams</b> M. R. Boyd, S. B. Crary, and M. D. Giles University of Michigan	<b>123</b>

## Tuesday, June 14: Session 4

**7:45 am Breakfast**

	<b>Micromachining Processes (M. G. Allen)</b>	<b>Page</b>
<b>8:15 am</b>	<b>Silicon Wafer Bonding for Micromechanical Devices</b> M. A. Schmidt, Massachusetts Institute of Technology (Invited)	<b>127</b>
<b>9:00</b>	<b>Milli-Scale Polysilicon Structures</b> C. Keller and M. Ferrari, University of California at Berkeley	<b>132</b>
<b>9:25</b>	<b>High-Density Vertical Comb Array Microactuators Fabricated Using a Novel Bulk/Poly-Silicon Trench Refill Technology</b> A. Selvakumar and K. Najafi, University of Michigan	<b>138</b>
<b>9:50</b>	<b>Laser Stereo Micromachining at One-Half Million Cubic Micrometers Per Second</b> T. M. Bloomstein and D. J. Ehrlich Lincoln Laboratory, Massachusetts Institute of Technology	<b>142</b>
<b>10:15</b>	<b>Coffee Break</b>	

## Tuesday, June 14: Session 5

	<b>Microaccelerometers (D. W. Burns)</b>	<b>Page</b>
<b>10:40 am</b>	<b>Integrated Test-bed for Multi-Mode Digital Control of Suspended Microstructures</b> G. K. Fedder and R. T. Howe, University of California at Berkeley	<b>145</b>
<b>11:05</b>	<b>Micromachined Structures Fabricated Using a Wafer-Bonded Sealed Cavity Process</b> C. H. Hsu and M. A. Schmidt, Massachusetts Institute of Technology	<b>151</b>
<b>11:30</b>	<b>Surface Micromachined Shock Sensor for Impact Detection</b> P. F. Man and C. H. Mastrangelo, University of Michigan	<b>156</b>
<b>11:55</b>	<b>A Bulk-Silicon Capacitive Microaccelerometer with Built-In Overrange and Force Feedback Electrodes</b> K. J. Ma, N. Yazdi, and K. Najafi, University of Michigan	<b>160</b>
<b>12:20 pm</b>	<b>Lunch</b>	
	<b>Afternoon free</b>	
<b>6:00 pm</b>	<b>Banquet</b>	

### Wednesday, June 15: Session 6

**7:45 am Breakfast**

	<b>Chemical Sensors (L. Bousse)</b>	<b>Page</b>
<b>8:15 am</b>	<b>Compatibility and Incompatibility of Chemical Microsensors and Analytical Equipment with Micromachining</b> M. Madou, Microfabrication Applications (Invited)	<b>164</b>
<b>9:00</b>	<b>Diamond Film Based Structures for Gas Sensing Applications</b> W. P. Kang, Y. Gurbuz, J. L. Davidson, and D. V. Kerns Vanderbilt University	<b>172</b>
<b>9:25</b>	<b>Fabrication and Properties of a Si-Based High Sensitivity Microcalorimetric Gas Sensor</b> M. Zanini, J. H. Visser, L. Rimai, <i>et al</i> , Ford Research Laboratory U. Bonne, Honeywell Technology Center, L. Brewer, O. W. Bynum, and M. A. Richard, Advanced Sensor Devices	<b>176</b>
<b>9:50</b>	<b>New Materials and Multidimensional Cluster Analysis for SAW Chemical Sensor Arrays</b> A. J. Ricco, G. C. Osbourn, and J. W. Bartholomew, Sandia National Laboratories, R. M. Crook and C. Xu, Texas A&M University, and R. E. Allred, Adherent Technologies	<b>180</b>
<b>10:15</b>	<b>Coffee Break</b>	

### Wednesday, June 15: Session 7

	<b>Computer-Aided Design (R. Huber)</b>	<b>Page</b>
<b>10:40 am</b>	<b>A Quantitative Model for the Measurement of Residual Stress Using Electrostatic Pull-In of Beams</b> P. M. Osterberg, R. K. Gupta, J. R. Gilbert, and S.D. Senturia Massachusetts Institute of Technology	<b>184</b>
<b>11:05</b>	<b>A Methodical Approach to the Design of Compliant Micromechanisms</b> G. K. Ananthasuresh, S. Kota, and Y. Gianchandani, Univ. of Mich.	<b>189</b>
<b>11:30</b>	<b>Clustering-Based Pattern Recognition Applied to Chemical Recognition Using SAW Array Signals</b> G. C. Osbourne, J. W. Bartholomew, G. C. Frye, and A. J. Ricco Sandia National Laboratories	<b>193</b>
<b>11:55</b>	<b>Lunch</b>	

**Wednesday, June 15: Session 8**

	<b>Physical Sensors (M. A. Schmidt)</b>	<b>Page</b>
<b>1:15 pm</b>	<b>Nongimbaled Solid-State Compass</b> G. J. Olson, R. B. Smith, G. F. Rouse, H. B. French, and J. E. Lenz Honeywell Technology Center	<b>197</b>
<b>1:40</b>	<b>Bulk-Silicon Tunneling-Based Pressure Sensor</b> C. Yeh and K. Najafi, University of Michigan	<b>201</b>
<b>2:05</b>	<b>An Ultra-Sensitive Capacitive Pressure Sensor with a Bossed Dielectric Diaphragm</b> Y. Zhang and K. D. Wise, University of Michigan	<b>205</b>
<b>2:30</b>	<b>Fabrication of Ultrasensitive Force Detectors</b> S. Hoen, O. Zueger, C. S. Yannoni, H. J. Mamim, K. Wago, and D. Rugar, IBM Almaden Research Center	<b>209</b>
<b>2:55 pm</b>	<b>Adjourn -- afternoon free</b>	
<b>7:00 - 8:00</b>	<b>Late News Poster Session</b>	
<b>8:00 -</b>	<b>Rump Session</b>	

**Thursday, June 16: Session 9**

<b>7:45 am</b>	<b>Breakfast</b>	
	<b>Resonant Microsensors (K. E. Petersen)</b>	<b>Page</b>
<b>8:15 am</b>	<b>A Micromachined Vibrating Ring Gyroscope</b> M. W. Putty and K. Najafi* (invited) General Motors R & D Center and *University of Michigan	<b>213</b>
<b>9:00</b>	<b>A Digital Pressure Sensor Based on Microbeams</b> D. W. Burns, J. D. Zook, R. D. Horning, and W. R. Herb Honeywell Technology Center and H. Guckel, University of Wisconsin - Madison	<b>221</b>
<b>9:25</b>	<b>Piezoelectrically Activated Resonant Microbridge Accelerometer</b> D. B. Hicks, S.-C. Chang, M. W. Putty, and D. S. Eddy General Motors Research and Development Center	<b>225</b>
<b>9:50</b>	<b>Microtextured Resonators for Measuring Liquid Properties</b> S. J. Martin, G. C. Frye, and R. W. Cernosek Sandia National Laboratories and S. D. Senturia, Massachusetts Institute of Technology	<b>229</b>
<b>10:15</b>	<b>Coffee Break</b>	

**Thursday, June 16: Session 10**

	<b>Microactuators II (C. Fung)</b>	<b>Page</b>
<b>10:40 am</b>	<b>The Development of Polysilicon Micromotors for Optical Scanner Applications</b> K. Deng, H. Miyajima, V. H. Dhuler, M. Mehregany, S. W. Smith, F. L. Merit, and S. Furukawa, Case Western Reserve University	<b>234</b>
<b>11:05</b>	<b>Microchopper-Modulated IR Microlamp</b> P. Y. Chen and R. S. Muller, University of California at Berkeley	<b>239</b>
<b>11:30</b>	<b>Micromachined Jets for Manipulation of Macro Flows</b> D. J. Coe, M. G. Allen, M. A. Trautman, and A. Glezer Georgia Institute of Technology	<b>243</b>
<b>11:55</b>	<b>Lunch</b>	

**Thursday, June 16: Session 11**

	<b>Microflow Components and Systems (K. E. Petersen)</b>	<b>Page</b>
<b>1:15 pm</b>	<b>A Robust Normally Closed Silicon Microvalve</b> P. W. Barth, C. C. Beatty, L. A. Field, J. W. Baker, and G. B. Gordon Hewlett-Packard Company	<b>248</b>
<b>1:40</b>	<b>Thermopneumatically Actuated Microvalves and Integrated Electro-fluidic Circuits</b> M. J. Zdeblick, R. Anderson, J. Jankowski, B. Kline-Schoder, L. Christel, R. Miles, and W. Weber Redwood Microsystems	<b>251</b>
<b>2:05</b>	<b>A Multichannel Neural Probe for Selective Chemical Delivery at the Cellular Level</b> J. Chen and K. D. Wise, University of Michigan	<b>256</b>
<b>2:30</b>	<b>Microfabricated Fused Silica Chambers for Flow Cytometry</b> D. Sobek, S. D. Senturia, and M. L. Gray Massachusetts Inst. of Technology	<b>260</b>
<b>2:55</b>	<b>A Micromachined Polysilicon Hot-Wire Anemometer</b> F. Jiang, Y.-C. Tai, C.-H. Ho*, and W. J. Li*, California Institute of Technology *University of California, Los Angeles	<b>264</b>
<b>3:20</b>	<b>Adjourn</b>	

**ERRATA: A HEURISTIC APPROACH TO THE ELECTROMECHANICAL  
MODELING OF MEMS BEAMS (pp. 123-126)**

*Michael R. Boyd, Selden B. Crary, and Martin D. Giles*

All references to "mutual capacitance" should be replaced by "capacitance."  
The first paragraph of the last page should be replaced with the following:

We have also made comparisons in Figure 1 with the MSA results of Reitan [4] that used a 6×6 discretization and with the approximate equation of Love that is valid for  $g/w \ll 1$ . Finally, we made comparisons of MSA with calculations using FASTCAP [5] for single plates and parallel plate capacitors of various sizes. The results were in agreement to better than 0.5%.

# **TECHNICAL PAPERS**

## **Solid-State Sensors, Actuators, and Microsystems Workshop**

**1994**

**Hilton Head Island, South Carolina  
June 12 - 16**



# DEFORMABLE GRATING LIGHT VALVES FOR HIGH RESOLUTION DISPLAYS

Raj B. Apte, Francisco S. A. Sandejas,  
William C. Banyai, and David M. Bloom

Ginzton Laboratory  
Stanford University  
Stanford, CA 94305-4085

## Abstract:

The Grating Light Valve (GLV) is a micromechanical phase grating that can be used for black&white or color display applications. Operation is based on electrically controlling the mechanical positions of the grating elements to modulate the diffraction efficiency. Proper choice of the grating dimensions allows the structure to operate as a digital optical device.

Since the grating is inherently dispersive, the GLV can be used for color displays. In addition, the devices are bistable and may be able to operate with a passive matrix of contacts and still achieve the performance of an active matrix light valve. Eight bits of gray scale are possible using time division multiplexing and the fast (20 ns) switching speed of the GLV. The contrast ratio of the device is very sensitive to processing errors; to date, a ratio of 20:1 has been measured. With better processing, a color contrast of 200:1 should be achieved for a monochrome pixel.

Stiction of the micromachined grating elements to the substrate during the final wet processing step and during operation remains a problem. However, our current approach uses rough (150 Å-RMS) polysilicon films to reduce the area of contact. When doped, the polysilicon can be patterned to function as a bottom electrode for two-dimensional array applications. Although this structure suffers from some of the difficulties of a non-planar process, it was used to demonstrate two-dimensional arrays of devices with switching voltages as low as 11V.

## Introduction:

The basic principle of operation for the GLV is illustrated in figure 1. The structure is a reflection phase grating consisting of aluminum overcoated silicon nitride microbridges. With no voltage applied, the total path length difference between light reflected from the microbridges and the substrate equals the wavelength of incoming light. These reflections add in phase and the grating reflects light as a flat mirror. When a voltage is applied between the microbridges and the substrate, the electrostatic force pulls the microbridges down.

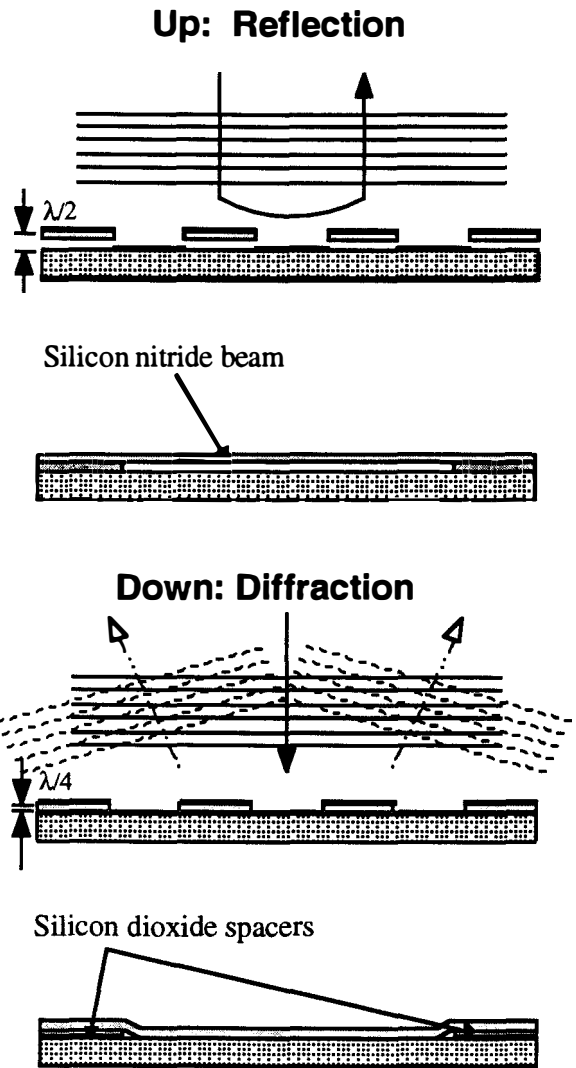


Figure 1: Operational principle of GLV.

Now the total path length difference between light reflected from the microbridges and the substrate is one-half wavelength, and the reflections interfere destructively causing light to be diffracted. For example, when a pixel consisting of 10 one-micron line-pairs in the *down* state is illuminated with normally incident white light, the  $\pm$ first-order diffraction beams have an angular bandwidth of approximately  $4^\circ$  about  $\pm 14^\circ$ . Also, 42% of the light is diffracted into each of the first-order beams, so that an overall efficiency of 84% is possible when both beams are collected. Light in higher-order modes is diffracted at large angles and is not collected by the optical system.

## Optical Design:

An example of a basic optical system for realizing a display is shown in figure 2. It contains

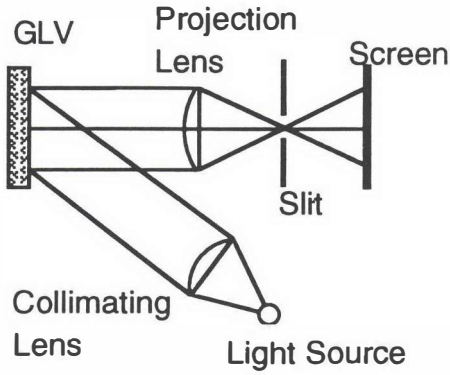


Figure 2: GLV Optical System.

a simple imaging system with unity magnification: the object plane containing the GLV array and the image plane containing the viewing screen are both  $2F$  from the lens, where  $F$  is the focal length. The GLV array is illuminated by a collimated light source and there is a spatial filter in the Fourier plane, i.e. one focal length in front of the lens. The GLV array is made up of individual pixels. Figure 3 is a micrograph of a  $25\ \mu\text{m}$  by  $25\ \mu\text{m}$  pixel consisting of 12 one-micron linepairs (a linepair is a one-micron microbridge and a one-micron space). The critical parameters in the system design are the number of linepairs defining a pixel, the degree of source collimation, and the width of the slit. Note that a slit is used because light is only diffracted in the plane perpendicular to both the microbridges and the plane of the pixel. The best way to understand the operation of the GLV system is to work through the three cases for realizing monochrome, black&white, and color imaging.

For monochrome operation, we consider a point source of spectrally pure light, in this case green light at  $\lambda_p=530\text{nm}$ , that is collimated by a lens. With the GLV in the down state, the incident light is diffracted into the +first-order according to diffraction grating equation

$$\sin \theta_i - \sin \theta_d = \lambda / p, \quad (1)$$

where  $\theta_i$  is the incident angle,  $\theta_d$  is the diffraction angle,  $\lambda$  is the wavelength, and  $p$  is the spacing between the microbridges. The diffracted light is collected by the imaging lens and brought to a focus in the focal plane of the lens, since the diffracted light from the grating remains collimated, before continuing to the image plane where it interferes to form an image<sup>1</sup>. The distance from optical axis in the focal (Fourier) plane where the light comes to a focus is given by the ray tracing equation

$$\partial X \cong \partial \theta \cdot F, \quad (2)$$

where  $F$  is the focal length of the lens. If we choose the microbridge spacing  $p=2.25\ \mu\text{m}$ , the incident angle of collimated light  $\theta_i=13.6^\circ$  with respect to the optical axis, and  $\lambda_g=530\text{nm}$ , then the angle of the diffracted light is zero with respect to

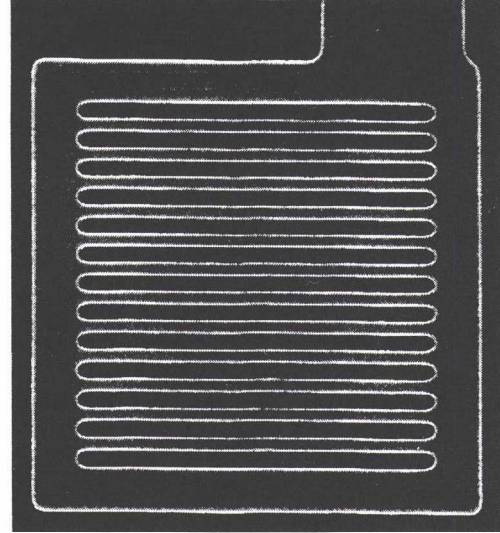


Figure 3: GLV  $25\ \mu\text{m}$  x  $25\ \mu\text{m}$  pixel.

the optical axis. Therefore, all green light is brought to focus at the on-axis focal point of the imaging lens. We have assumed that all diffracted light is in the  $\pm$ first-order, however, in reality, a small amount of light is diffracted into the second and third orders. When the GLV is in the up state there is no diffraction and the light is specularly reflected at an angle  $-13.6^\circ$  with respect to the optical axis, which will come to a focus  $12\ \text{mm}$  from the optical axis in the focal plane, according to equation (2). Now, the angular width of the diffracted light is given by <sup>2</sup>

$$\partial \theta \cong \lambda / D, \quad (3)$$

where  $D$  is the width of pixel. If we require the half-angular width of the diffracted light to be less than  $13.6^\circ/2$  then  $D \geq 2.23\ \text{mm}$ . Therefore, if we use one 1.125mm linepairs ( $D=2.25\ \text{mm}$ ), then, using equation (3) to calculate the angular extent of the first-order beam and equation (2) to calculate its spatial extent in the focal plane of the lens, we find that a slit width of  $11.8\ \text{mm}$  will pass the diffracted light but block the reflected light. Notice that only a single linepair will function as an effective light valve. The contrast ratio, when measured as light through the slit when the microbridges are down to

when they are up, will be unrealistically large due to our assumption of a spectrally-pure point source. In fact, the finite width of the source translates to angular error in the collimated incident light via equation (2). This error must be taken into account when calculating  $D$ , resulting in an increase in  $D$ , or number of linepairs. The finite extent of the source will have a considerable effect on the color operation described below.

For the second case of black&white operation, we consider a whitelight point source. Two refinements are required in this case since the diffraction angle will be slightly different for the red and blue components and the GLV is perfectly reflecting in the up state only for the center green wavelength. The red components will be offset slightly to one side while the blue components are offset slightly to the other side of the green light in the focal plane. The offset can be calculated by differentiating equation (1) with respect to  $l$ , such that

$$\partial\theta_d = -\partial\lambda / d \cos\theta_d. \quad (4)$$

Equation (4) can be used to calculate  $\delta\theta$  and that value plugged into equation (2) to calculate  $\delta X$ . For the system described above, the offset for blue light at 465 nm is  $\delta X_b=1.4$  mm while the offset for red light at 625 nm is  $\delta X_r=2.1$  mm. The offset means that the number of linepairs must be increased to keep the spatial extent of the light in the focal plane to less than 11.8mm. Recalculating the pixel width by requiring the spatial extent of the red light to be less than  $2 \times (11.8/2 - 2.1)$ mm means that  $D=4.1\mu\text{m}$ . This means that a minimum of two linepairs is required for black&white operation of a GLV system. In fact, we only considered the center wavelengths of the red and blue light but should have considered the full bandwidth of the source used, usually from 400-700nm. The second consideration for black and white operation is the thickness of the microbridge and spacer. Our assumption was that the diffracted light turns on and off when the bridge move from down to up. In reality, this condition only holds at a single wavelength. In figure 4, we see that when the microbridges are in the down position most of the light is diffracted into the first order with some of the light diffracted into the second and third orders. When the microbridges are up, then most of the light is in the specular mode and the first order is nulled. However, when the diffraction into the first-order is replotted in terms of wavelength about

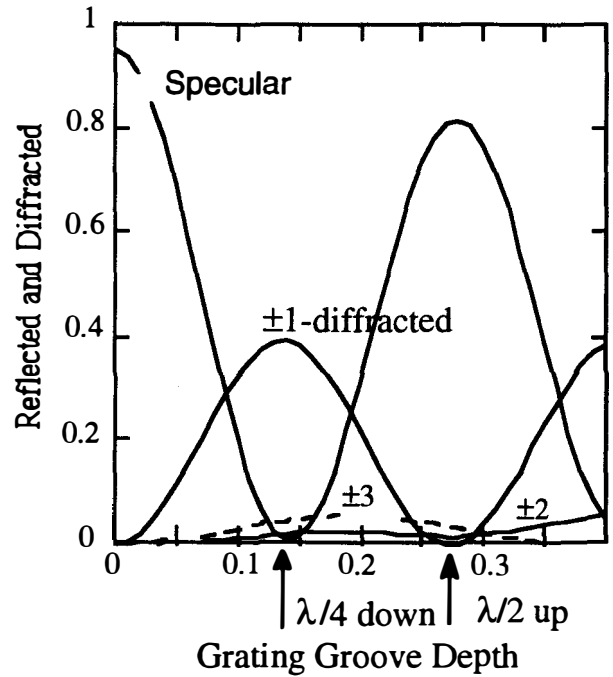


Figure 4: Diffraction efficiency<sup>3</sup> for several orders of an aluminum reflection phase grating with 2.00  $\mu\text{m}$  period, illuminated at normal incidence at 550 nm. Note the finite reflectivity of aluminum limits the specular reflection with no grooves to 92-94%. [Gaither 1988; Veldkamp 1989]

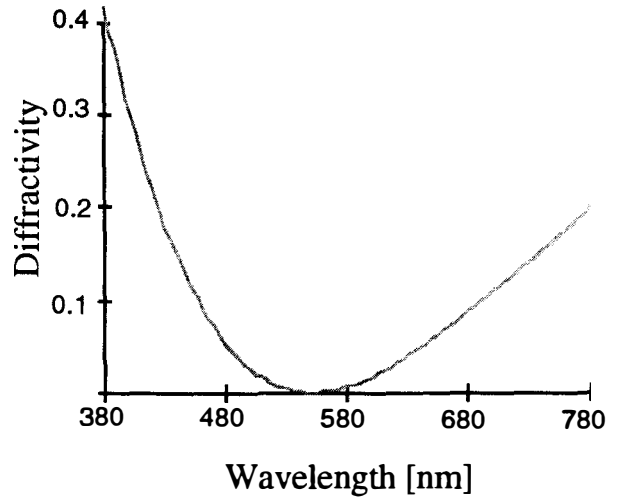


Figure 5: Diffractivity of the first order as a function of wavelength for a " up " pixel with a 550nm design wavelength.

the  $\lambda/2$  groove depth, as in figure 5, we see that some light is diffracted into the first order due to the finite bandwidth of the light source. The effect of

this leakage is to limit the achievable contrast ratio to 82:1 for a whitelight source.

The third case to consider is when the GLV system is configured for color operation. In the previous examples it was shown that the angles at which the various colors are diffracted are determined solely by the grating period as indicated in equation (1). The movement of the microbridges only changes the amount of light diffracted but not the direction of diffraction. For the pixel described above with a period of  $2.25\mu\text{m}$ , the green light is diffracted normal to the GLV plane. We can now make similar pixels for the red and blue wavelengths by requiring  $\theta_d=0$  for  $\theta_i=13.6$ . Using equation (1), we calculate  $p_r=2.66\mu\text{m}$  and  $p_b=1.97\mu\text{m}$ . For the display shown in figure 1, we now replace each green pixel with a red-green-blue triad, as shown in figure 6. Color is then realized

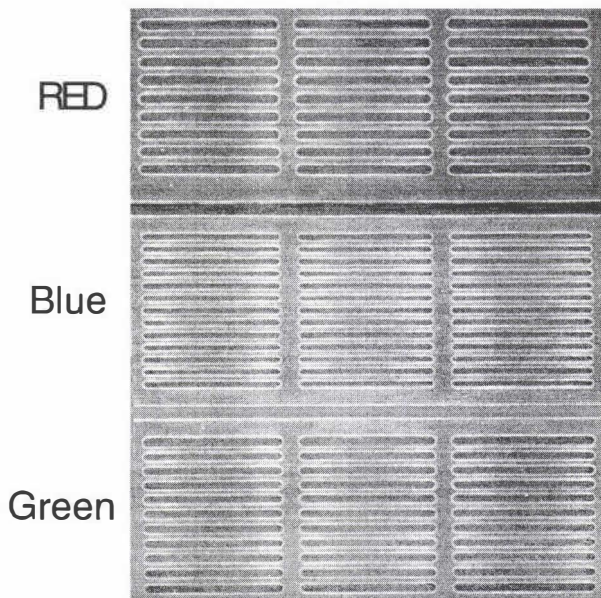


Figure 6: Red, blue and green pixels.

by reducing the slit width to only allow a limited bandwidth about each of the primary colors, as illustrated in figure 7. The slit width can be calculated by assuming a bandwidth, 80nm for example, and using the above equations. The slit width for color operation of the above system is only 2mm. The number of linepairs also has to be recalculated to limit the angular extent of each color, as shown in figure 7. Or, to put it another way, so that all of the light from the center wavelength passes through the slit. From the above equations,  $D=530\text{nm}\times 50\text{mm}/2\text{mm}=13\mu\text{m}$ , or about 6 linepairs. This is the minimum number required. Using more linepairs translates to purer colors, which is why our designs tend to use 10-12 linepairs. There is also a tighter constraint on the spatial extent of the

point source, since deviations from collimation allow unwanted color through the slit, reducing the color purity. An upper bound on the spatial extent of the source can be determined by assuming that the deviation in the focal plane due to collimation error is less than one-half the slit width. It turns out that when the focal lengths of the collimation lens and the imaging lens are equal the constraint translates directly to the source, so the source is limited to 1mm. The final consideration for color operation is the contrast ratio. With a triad of pixels the contrast ratio is degraded due to all three pixels sharing the same thickness of microbridge. For example, when the green pixel is off the red and blue pixels still diffract light, according to figure 5. The red-green-blue contrast ratios change from the monochrome values of 20, 341, and 22 to triad values of 36, 59, and 6. The red improves slightly due to the narrower slit used in the color GLV system.

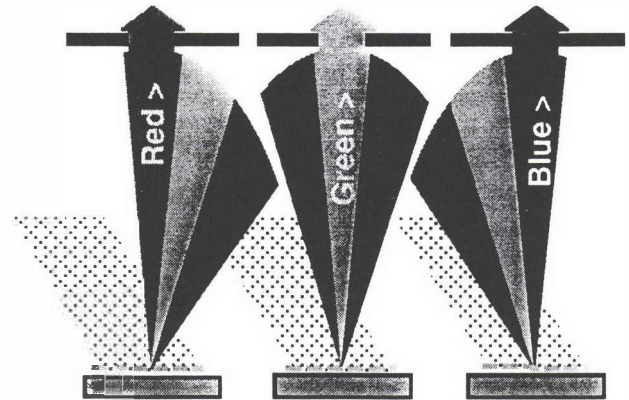


Figure 7: Color display approach: changing the grating period for a constant incident angle adjusts which color is diffracted normal to the surface.

#### Beam Mechanics:

The most striking feature of the mechanical operation of the GLV is the hysteresis of the deflection of the microbridges as a function of applied voltage. The reason for the hysteresis is that the electrostatic attraction between the top and bottom electrodes is a nonlinear function of the deflection while the restoring force caused by the stiffness and tension is linear, as illustrated in figure 8. The hysteresis curve for a single pixel is shown in figure 9. To generate this curve, the light diffracted into the +first-order was measured as a function of applied voltage. The switching voltage is approximately 20V and is largely determined by the stress in the nitride microbridge as well as its length. In our earlier discussion, we calculated the number of linepairs which determined the width of the pixel, however, we did not discuss the reason

for the length of the microbridge. It is determined by the desired usable surface area on the microbridge for diffraction when in the deflected state and the stiffness required for providing the restoring force. In fact, a longer structure requires more film stress to keep the restoring force for equal. Figure 10 illustrates the trend in switching voltages for two different length pixels. Low switching voltages (5V range) are possible with 25  $\mu\text{m}$  long microbridges, but at the expense of the restoring force used to overcome stiction.

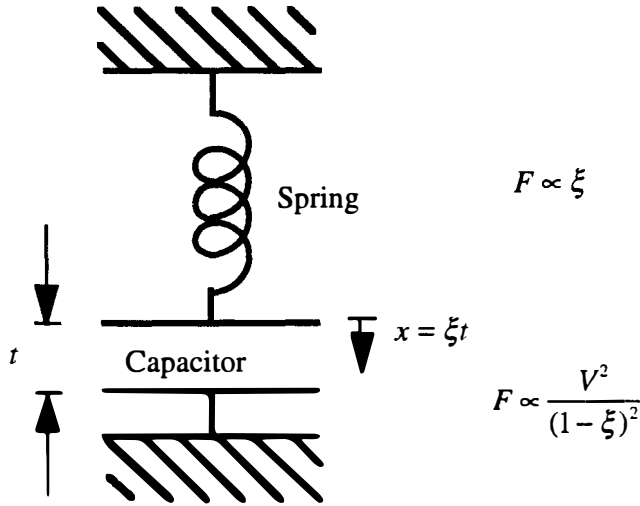


Figure 8: The basic model for the GLV beam mechanics. The spring represents the restoring force caused by the beam stiffness and tension. The capacitor represents the electrostatic attraction between the electrodes.

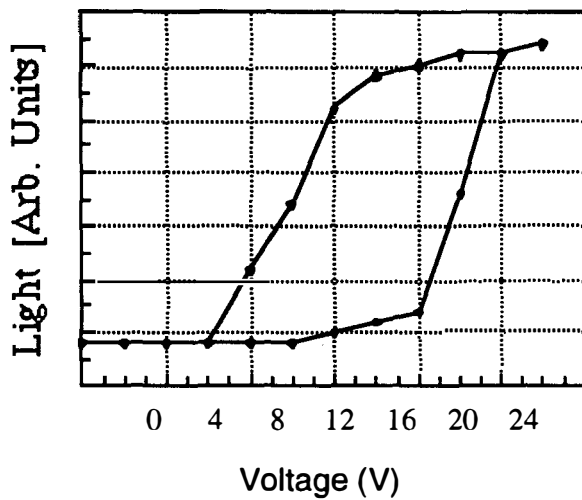


Figure 9: Hysteresis curve for pixel with 25  $\mu\text{m}$  long microbridges under 800 MPa of tension.

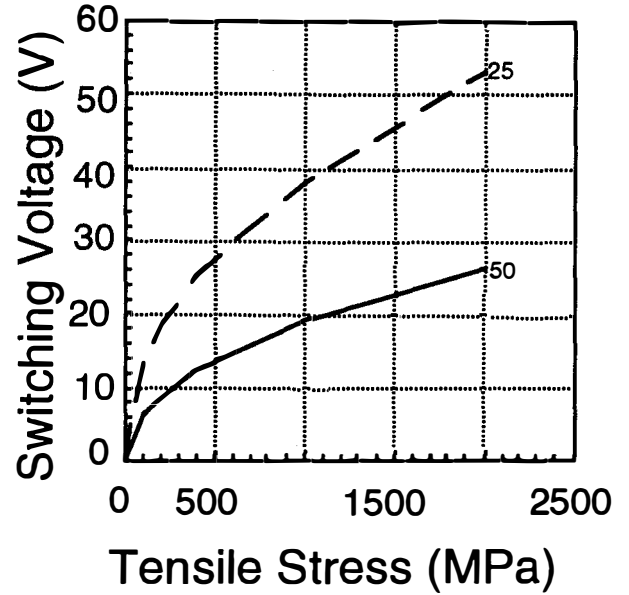


Figure 10: Switching voltage versus microbridge tension for two different lengths.

The other mechanical property of importance is the resonant frequency of the microbridge. When under tensile stress<sup>4</sup>,

$$f_{res}^{stress} = \frac{1}{2\pi L} \sqrt{10 \frac{\sigma}{\rho}}, \quad (5)$$

where  $\rho$  is the density of the silicon nitride,  $s$  is the stress, and  $L$  is the length. This can be compared to the resonant frequency under low or no stress,

$$f_{res}^{nonstress} = \frac{h}{2\pi L^2} \sqrt{10 \frac{E}{\rho}} \quad (6)$$

where  $E$  is Young's modulus. The ratio of these two resonant frequencies is

$$\frac{f_{res}^{stress}}{f_{res}^{nonstress}} = \frac{L}{h} \sqrt{\frac{\sigma}{E}} \quad (7)$$

For example with a stress of  $\sigma = 200 \text{ MPa}$ , the resonant frequency increases by a factor of 3 over the nonstressed case to a value of 5.1 MHz. This fast response is important to the operation of the GLV since grayscale modulation can be implemented by pulsewidth modulation. However, from the preceding discussion, we note that there is a tradeoff between switching voltage and stress: the devices with the highest stress will be the fastest but will also suffer from large switching voltages. Our

fastest measured switching time to date has been 20ns switching times for pixels with 20  $\mu\text{m}$  long microbridges under 800 MPa of tension.

#### Fabrication:

The first step in fabrication of the device illustrated in figure 1 was to deposit on an I-Prime wafer 1325  $\text{\AA}$  of silicon dioxide and 1325  $\text{\AA}$  of silicon nitride. The nitride was patterned to form the frame and beams of the device. Then an isotropic, selective etch was used to undercut the oxide from beneath the beams. In order to free the beams, at least 0.75  $\mu\text{m}$  of undercut was needed. This was not enough, however, to completely remove the oxide from beneath the frame. In this way the frame remained supported by the oxide, and the beams were supported by the frame. Lastly, 400  $\text{\AA}$  of aluminum was evaporated onto the top of the structure to form the top electrode and reflector. These devices suffer from the effects of stiction when released and operated, unless short (15 $\mu\text{m}$ ) microbridges and high tension nitride were used, requiring drive voltages as high as 40V.

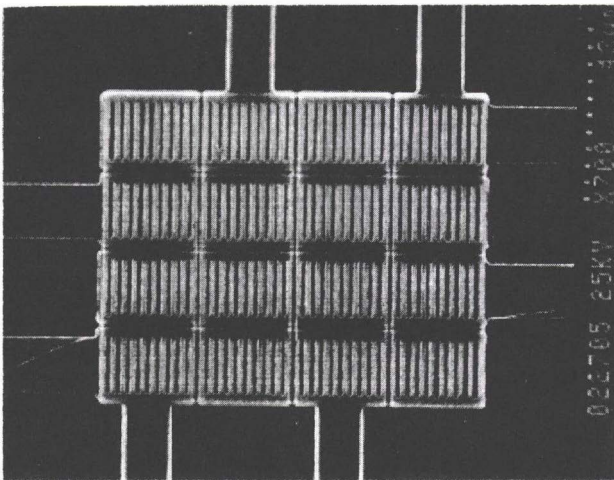


Figure 11: 4x4 array with polysilicon bottom electrodes.

Our more recent approach utilizes rough polysilicon films to overcome the sticking problem. This was successfully applied to the two dimensional array illustrated in figure 11. Processing begins with a 5000  $\text{\AA}$  oxide isolation layer being grown on a bare silicon substrate. On top of this layer a 3000-6000  $\text{\AA}$  undoped polysilicon layer was grown. The layer was probably amorphous initially, but it crystallizes during subsequent high temperature processing (the reflow step). The polysilicon was diffusion doped with phosphorous, cleaned, and patterned into the bottom interconnect layer. 1325  $\text{\AA}$  of low temperature LPCVD oxide were deposited on top of

the nonplanar bottom electrode traces. This oxide was doped with 8% phosphorous to reduce the reflow temperature. The oxide was steam reflowed at 1000  $^{\circ}\text{C}$  for 20 minutes. 1325  $\text{\AA}$  of LPCVD nitride was deposited next, then patterned and dry etched. The wafer was then cleaned to remove all traces of photoresist and then released. The oxide spacer was removed from under the beams. In addition, oxide was removed from under the edges of the frames and the bottom electrode traces. The overhanging polysilicon and nitride provide the isolation. These devices switched at 11V and did not exhibit stiction problems.

#### Conclusion:

We have given a general overview of the design of the GLV system with an emphasis on the critical optical constraints, namely, the number of linepairs required per pixel for optimum contrast ratio, the slit width and the source width. The salient feature of the GLV system is its inherent ability to be configured for color operation, at the expense of contrast ratio and loss of two-thirds of the optical power. Also, the basic microbridge mechanics were discussed to illustrate hysteresis and high-speed operation. Finally, two-dimensional array fabrication was described.

#### Acknowledgments:

This research was supported by grants from ARPA/ARO DAAL03-92-G-0232 and ARPA/AFOSR F49620-93-I-0609.

#### References:

1. For a more detailed explanation see Abbe's theory of image formation in *Principles of Optics*, Born, M and E. Wolfe, Pergamon Press, New York, 1959.
2. See pages 61-63 in *Introduction to Fowler Optics*, Goodman, J. W., McGraw-Hill Book Company, San Francisco, 1968.
3. Gaither, S. A. , "Two-Dimensional Diffraction from a Surface-Relief Grating," Computer Program, Vers. 26 May 1988, courtesy of W. Veldkamp, MIT Lincoln Laboratory; Veldkamp, W. B., G. J. Swanson, S. A. Gaither, C.-L. Chen, and T. R. Osborne, "Binary Optics: A Diffraction Analysis," MIT Lincoln Laboratory, Aug. 23, 1989. ODT-20.
4. Solgaard, O., "Integrated Semiconductor Light Modulators for Fiber-Optic and Display Applications", Ph.D. Thesis, Stanford U , 1992.

# 512x512 INFRARED SCENE PROJECTOR ARRAY FOR LOW-BACKGROUND SIMULATIONS

B.E. Cole, C.-J. Han, R.E. Higashi, J. Ridley, J. Holmen, J. Anderson, D. Nielsen, H. Marsh, K. Newstrom, C. Zins, P. Wilson, K. Beaudoin  
Honeywell Technology Center  
10701 Lyndale Ave S., Bloomington, Minnesota 55420

## Abstract

Resistor arrays are one popular approach to obtaining an IR scene projector capable of wide dynamic range. This paper describes the application of the Honeywell microstructure technology to the fabrication of infrared scene projector arrays with resistively heated emitters. The excellent thermal isolation achieved with Honeywell's microbridge structure has reduced the power requirement by two orders of magnitude compared with competing polysilicon or metal film microbridge resistor devices. Average thermal conductance of the Honeywell microbridge has been measured at  $1 \times 10^{-6}$  W/°C. Cooling requirements are greatly simplified because of the low power requirement. Display nonuniformity caused by voltage drops across the buslines also is significantly reduced. The two-level microbridge structure integrates the emitters with the addressing electronics and allows a very large (82%) fill factor in a 3.5-mil pitch design. The microbridge structures are monolithically integrated on top of cryogenic CMOS electronics. TiNx is used as the resistor element because of its resistivity and its low thermal coefficient of resistance. This thin-film resistor is sandwiched between two silicon nitride layers to provide the mechanical strength for supporting the large-area microbridge structure and for passivation of the resistor film during fabrication. The array operates at 20 K for low-radiance background simulations. Each element can be heated to 600 K to simulate targets.

## Array Description

### Pixel Properties

The major challenge in IR projector array technology is to produce a high-emittance structure that still requires low power. Fig. 1 is a schematic representation of the Honeywell structure used to achieve these goals. The key factors that contribute to high emittance are high fill factor, high emittance, and high-temperature operation. High fill factor is achieved with a two level structure that maximizes the radiating area by placing the pixel drive and addressing electronics directly under the emitting structure. High radiance is achieved by fabricating the pixel with thin absorbing films that have enhanced emittance when a reflector is placed at the substrate level.

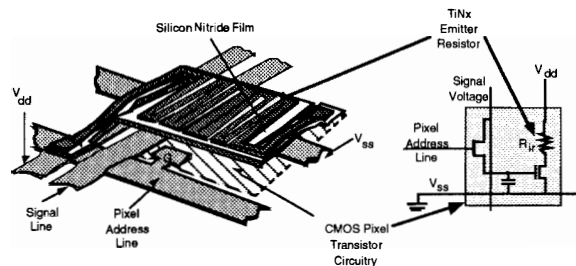


Fig. 1: Schematic of array and substrate pixel cell electronics showing the two-level approach to achieving high-radiance pixels.

The key to low power in the Honeywell design is the use of low-thermal-conductance materials, most notably  $\text{Si}_3\text{N}_4$ , that are patterned into well-defined shapes, which leads to well-defined thermal conductance paths to the substrate. The low thermal conductance would normally lead to long time constants if not for the fact that the pixel thin films contribute negligible thermal mass. As a typical example, the pixel thermal mass,  $C$ , is on the order of  $10^{-9}$  J/K for a 2-mil pixel. The thermal conductance,  $G$ , depending on temperature is typically in the range of  $3 \times 10^{-5}$  W- $\mu\text{m}/\text{K}$ . Thus a pair of 30- $\mu\text{m}$ -long legs will have a thermal conductance of about  $10^{-6}$  W/K. The thermal time constant is given by

$$\tau = C/G$$

A 2-mil pixel with 30- $\mu\text{m}$  legs will have a time constant in the range of 1 ms. The radiance, depending somewhat on wavelength, reaches 90% of the final level within a few thermal time constants. The frame rate of the scenes being projected should be compatible with this pixel thermal time constant.

### Array Pixel Cell Electronics

An important aspect of the array design is the substrate electronics. The substrate electronics at the pixel perform two main functions. The electronics select the proper pixel using the address lines and then ensure that the analog temperature value written to the pixel maintains the desired emitter temperature between address frames. The latter function ensures that the pixels are flicker free. To achieve this, row and column address voltages select a pass transistor that transmits the analog temperature signal to the gate of a power FET, which controls the current flowing to the pixel resistor. The size of the FET determines the amount of current through the pixel and, in combination with the pixel thermal conductance, defines the maximum pixel temperature difference between the substrate and the emitter. The emitter resistor is in contact with the substrate with two vias, one that contacts the  $V_{dd}$  line, and the other that contacts the drive FET. Because of the high pixel heating efficiency, a 10- $\mu\text{m}$  by 5- $\mu\text{m}$  FET gate dimension is sufficient to achieve temperature rises of many hundreds of degrees. All the cell electronics are easily contained within the pixel cell, which has been as small as 2 mils. The address voltage is strobed to the gate of the power FET through an address line contact, which selects the proper row.

The electronics under each pixel include a sample-and-hold and a drive transistor. Digital decoders and analog buffer drivers are attached to the edges of the array to reduce input lines. The array is organized into groups of eight columns each. Eight analog lines enter the array and are multiplexed through the array. Nine digital lines control the row address and six digital lines control the column address. The entire array may be addressed at 30 frames per second. This gives each pixel 1  $\mu\text{s}$  to read in the analog signal and store the value in the sample-and-hold circuit. The array die size is 1.9 in.  $\times$  1.9 in. and fits on a 4-in. wafer. A 512x512 array has been successfully fabricated. Despite the large array size, the current uniformity is within  $\pm 2.5\%$ , and fewer than 0.7% of the pixels are dead.

The gate voltage on the drive FET determines the pixel current and temperature. This analog signal voltage containing the temperature information is maintained on the gate of the drive FET with a pixel hold capacitor. We have found that at cryogenic temperatures, the hold capacitor stores the charge sufficiently long to produce less than a 1% temperature droop over a period of many minutes. One source of unwanted pixel temperature change arises when current-induced voltage changes at the bottom plate of the hold capacitor change the gate voltage from the value originally written to the pixel. This is most significant when the array is carrying large currents, which occurs when large regions of the array are running at high temperatures. To minimize this effect, we have maximized the conductance of the return lines by having the  $V_{ss}$  return line in both first metal and second metal. Vias connect the two layers. This design modification distributes the current return paths in a two-dimensional sheet. This has been significant in reducing scene-dependent temperature variations and maintaining array temperature uniformity.

### Performance Modeling

Performance of the array has been modeled using a spreadsheet calculation that takes account of the temperature-dependent properties of the array, specific heat, thermal conductance, resistance, and FET current. This model calculates both steady-state conditions and dynamic array performance. For most array designs,

the major goal is to achieve the desired maximum radiance, which is a function of pixel temperature, detector wavelength band, and pixel fill factor at the desired response speed. Array temporal requirements range from below video to 1-kHz frame rates. Radiance ranges range from low background radiance levels near cryogenic temperatures to very high radiance temperatures in the range of 1000 deg. Another common variable in the design is the temperature distribution of the pixels in the array at any one condition. All of these factors, not to mention the optical system in which the array is located, significantly affect the pixel design. The main goal in the design of the array is to achieve the desired specification with the minimal power dissipation.

The following plots are typical performance goals for a given arbitrary array consisting of 50% fill factor pixels with a 40-kΩ resistor designed to achieve 1000 K temperatures. This is achieved with a FET of 5-μm × 5-μm gate dimensions operating at 77 K with a 160-μA maximum current through a pixel with two legs of approximately 25-μm length with a conductance of 4e-7 W/K. Fig. 2 shows the modeled thermal properties obtained by extrapolating amorphous SiO<sub>2</sub> data to thin-film SiN thermal properties. The thermal properties vary significantly when operating at cryogenic temperatures. The thermal conductance is the average of the hot and cold thermal conductance, which is approximately half of the high-temperature conductance since the end pinned at the substrate temperature has a much lower value.

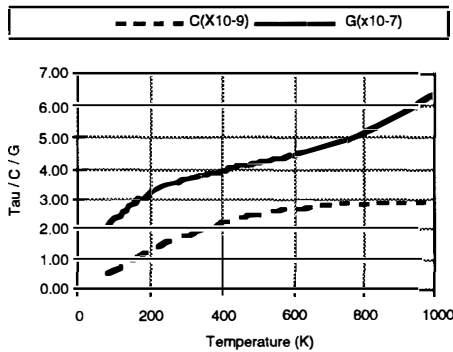


Fig. 2: Approximate pixel thermal properties for large temperature gradients as used in modeling performance.

Fig. 3 shows the locus of operating points for this pixel/FET combination. A straight line would be caused by a resistor with zero TCR. The TiN<sub>x</sub> resistors used in our array have resistance change of about a factor of two between cryogenic temperatures of 77 K and 1000 K peak temperature. Approximate temperature-dependent resistances have been obtained by measuring films at cryogenic temperatures and measuring heated pixels at higher temperatures. FET I/V measurements have been made at 77 K, 40 K, and 20 K. In general, the FET gate voltage threshold changes from 1.0 to 1.5 V and the electrical conductance doubles at cryogenic temperatures. The optimum operating point providing reduced power without temperature saturation is achieved by having the locus of points reach the linear/saturation transition region of the FET.

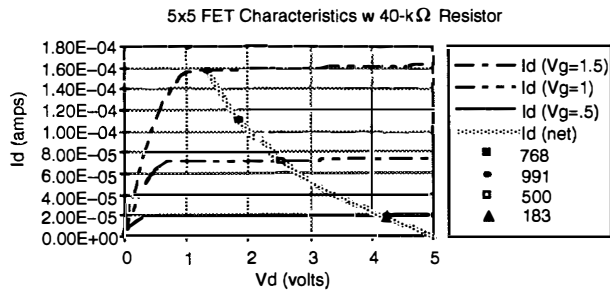


Fig. 3: Calculated pixel/FET operating characteristics.

The gate voltage addressed to the power FET controls the current to the pixel and, in combination with the pixel thermal conductance,

determines the steady-state temperature. Fig. 4 shows the current and temperature achieved with a 40 K resistor in series with the FET operating at 77 K.

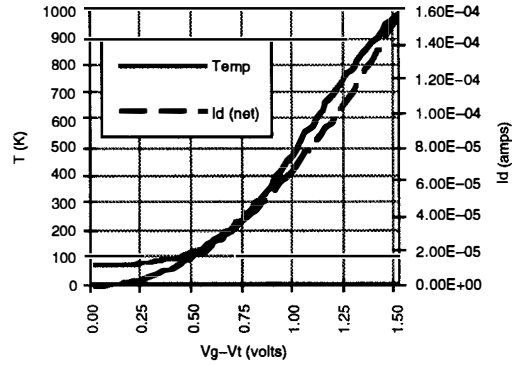


Fig. 4: Calculated pixel current and temperature.

The main reason for cryogenic array operation is to achieve low backgrounds and high dynamic range. Fig. 5 shows the IR radiance of the pixel in two bands, MWIR and LWIR. The maximum radiance as a function of FET gate voltage is respectively 1000 and 10 times greater than blackbody room temperature radiance. The dynamic performance is much greater at the short wavelengths, but the maximum intensity of the two band is comparable at the maximum signal voltage. By operating at cryogenic temperatures, dynamic ranges of up to 12 orders of magnitude in the MWIR bands can be achieved for testing very sensitive detectors.

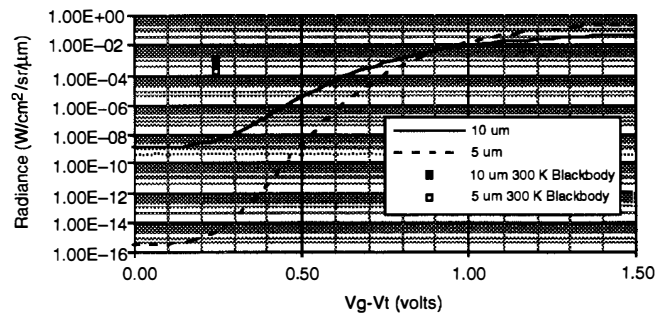


Fig. 5: Calculated pixel radiance.

The temporal performance of the pixel is also very important. In general, the array should operate significantly faster than the camera or seeker under test. Fig. 6 shows a plot of dynamic temperature and 5- and 10-μm IR radiance changes as a function of the final steady-state level for a pixel going from 77 K to 1000 K. Note that the temperature leads the radiation in heating but lags in cooling. This pixel design with a thermal time constant of 8.5 ms reaches within 90% of the final radiance level in 15 ms on heating and less than 10 ms on cooling. With this particular design, frame rates as high as 30–60 Hz can be achieved. Higher frame rates of similar brightness require faster pixels, achieved by increasing conductance and using larger FETs to compensate for the increased pixel heat loss.

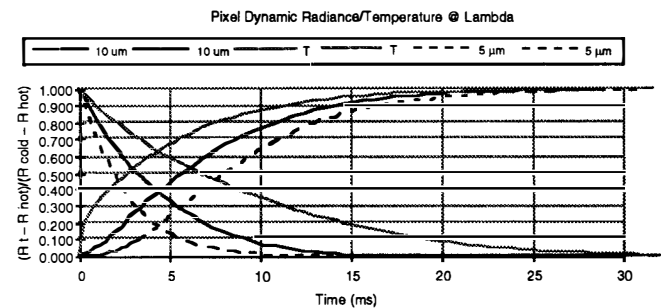


Fig. 6: Calculated dynamic properties of pixel.

An optimal design minimizes current and power dissipation. Fig. 7 shows the power for a worst-case condition where all 512x512 pixels are heated to a specified temperature. The power is dissipated in the resistor as well as in the FET. Reducing the FET power dissipation can be minimized by FET design but always entails some dissipation to ensure that the maximum temperature can be reached. To heat 250,000 pixels to 1000 K requires 200 W. Although this is a fair amount of power, most scenes involving all pixels at maximum temperature require only short millisecond durations and thus only a few joules of energy. Heat sinking with liquid nitrogen cryogen provides at worst a substrate temperature rise of a few degrees.

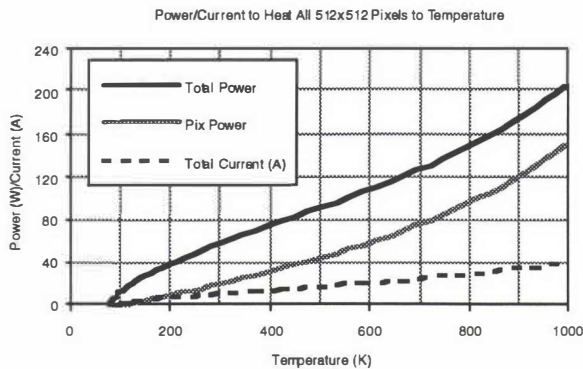


Fig. 7: Calculated full array power and current

### Cryogenic Design Considerations

Control of radiance by the pixel drive FET has been measured at room temperature and at 77 K. Several competing factors produce very similar performance between cryogenic and room temperatures. At cryogenic temperatures, the thermal conductance is about half that of room temperature. The thermal mass is also lower so that the time constant remains approximately temperature independent for small temperature excursions. However, the lower thermal conductance makes the maximum power dissipation, and hence the maximum temperature difference in the emitter, twice as great at cryogenic temperatures. In general, the FET electrical conductance for a given gate voltage over threshold is approximately two times greater at cryogenic temperatures, but the gate threshold increase from 1.0 to 1.5 V reduces the gate voltage range. All these factors must be considered in the design of the substrate electronics to achieve the desired temperature range. In general, contrary to intuition, cryogenic operation produces somewhat hotter pixels than room temperature operation. Fig. 8 shows the measured effective IR blackbody temperature achieved with a pixel from a 128x128 array operated at 77 K and designed for a maximum radiance equivalent to a 400 K temperature. Fig. 9 shows the IR temperature of a higher conductance pixel operated at room temperature.

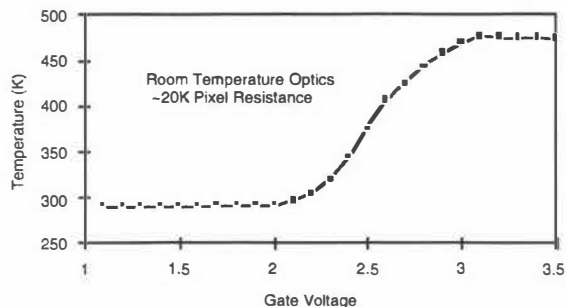


Fig. 8: Effective pixel blackbody temperature measured using an 8- to 12- $\mu\text{m}$  IR camera as a function of the analog signal voltage in a section of the 128x128 array. The array pixel is operated at 77 K and starts to draw current at 1.5 V, but because of warm temperature optics, radiation intensity is not above background levels until the pixel temperature reaches about 300 K. The pixels in this array have a leg length of 60  $\mu\text{m}$ .

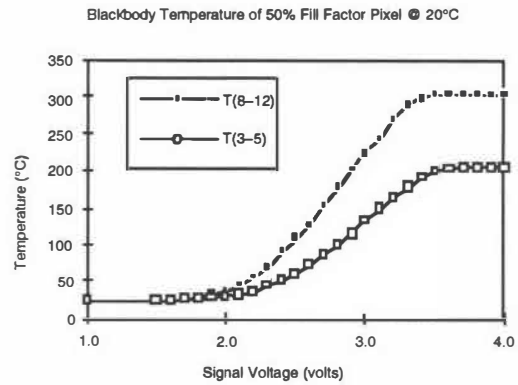


Fig. 9: Somewhat similar array operated at room temperature and measured with two calibrated cameras in the MWIR and LWIR bands. The pixels in this array are the same fill factor as those of Fig. 2 but have a 30- $\mu\text{m}$  leg length, which gives them comparable thermal conductance when operated at room temperature. The FET conductance per unit voltage is lower at room temperature, but the increased range combined with the higher room temperature starting point produces fairly comparable radiance levels.

## Device Fabrication and Measurements

### Pixel Design Variations

Arrays can be fabricated with a wide range of pixel sizes and pitches to meet the requirements of a specific optical system. To date, we have fabricated two types of arrays for cryogenic operation. A 512x512 array containing pixels on a 3.5-mil pitch has been fabricated to project distant target patterns for a large collimating system at up to video frame rates. A 128x128 array of pixels on a 2-mil pitch has been fabricated to achieve performance over the 8- to 12- $\mu\text{m}$  band in a smaller cryogenic system in which scene projection at high frame speed is important. This 128x128 array is the first step in the development of a 512x512 array and has been used to demonstrate the capability of the technology for frame rates above 200 Hz. Fig. 10 shows two different 2-mil pixel designs: a 65% fill factor design capable of 30-Hz frame rates and a 15% fill factor design capable of 200 Hz frame rates, each with the same conductance. The 65% fill factor design has a leg length of 8  $\mu\text{m}$ , while the 15% design has a leg length of 30  $\mu\text{m}$ . The pixels are arranged in a pseudohexagonal geometry for improved spatial resolution and have one shared electrical contact to the substrate  $V_{dd}$  line. The substrate is located approximately 1-2  $\mu\text{m}$  below the microbridge and contains the metal lines. The pixels are flat to within a few tenths of a micron. This is important for maintenance of pixel optical properties and ensures that the pixels are not in thermal contact with the substrate. Pixel flatness is maintained by paying great attention to thin-film stress during the fabrication process.

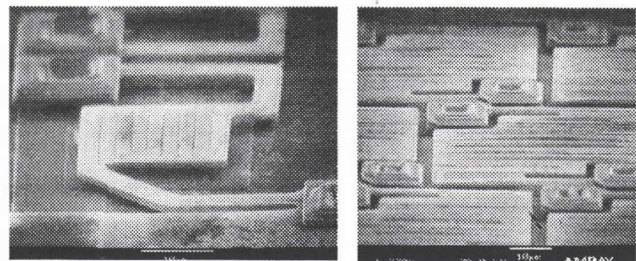


Fig. 10. Photomicrographs of 65% fill factor and 15% fill factor 2-mil pixels.

### Emitter Fabrication Process

The majority of the emitter structure consists of  $\text{Si}_3\text{N}_4$  film. Films of  $\text{Si}_3\text{N}_4$  also forms the bulk of the leg material that makes the thermal contact between the substrate and the emitter. A serpentine resistor material is embedded in the  $\text{Si}_3\text{N}_4$  film. For cryogenic operation we

require a resistor material which has a low TCR, is resistant to the sacrificial etch material, and has a sheet resistance on the order of a few hundred ohms/square. Sputtered TiN<sub>x</sub> films meet this criteria. The film compositions can be varied over narrow limits by changing the nitrogen content during deposition and the post deposition annealing.

The basic fabrication process, depicted in Fig. 11, consists of depositing and patterning a sacrificial layer on a substrate containing the electronics. The silicon nitride films and resistor films are deposited and patterned over the sacrificial layer. The TiN<sub>x</sub> resistor makes contact with the substrate metals. The final process step is to remove the sacrificial layer with an etchant and form a free-standing bridge.

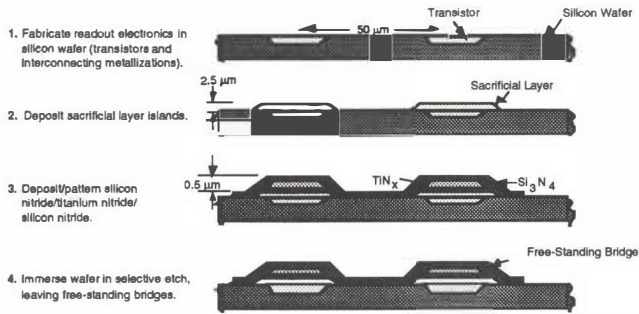


Fig. 11: Summary of microemitter array fabrication process.

### Die Processing Status

We have fabricated arrays of 128×128 pixels on a 2-mil pitch and arrays with 512×512 elements on a 3.5-mil pitch. We have recently processed two wafer runs. The 128×128 run of four wafers contains approximately 60 die on each 4-in. wafer. The 512×512 run of six wafers has only one 2-in. x 2-in. die on each 4-in. wafer. After fabrication, the die are probed at the wafer level before being diced up, mounted in packages, and exercised in a cryogenic dewar. The probing at wafer level is accomplished by addressing each pixel one at a time and measuring the current drawn by the array as that pixel is turned on and then off. A map and current histogram are obtained for each die. Because the measurement is taken with the FET in the saturation region, the map is principally a measure of dead pixels and FET current uniformity.

A major issue relative to the performance of the array is dead-pixel count. One of the main causes of dead pixels are shorts between the x and y substrate metallization lines that provide the current to the pixels. These shorts can effectively make every column pixel defective. A second cause of dead pixels is the inability of the current to reach the emitter resistor. The primary causes of this defect are an open resistor being attacked during etch or poor electrical contact between the resistor and the substrate.

### Electrical Measurements: Array FET Uniformity and Pixel Outage Measurements

The best two wafers from the 128×128 run, which was made with an improved Si<sub>3</sub>N<sub>4</sub> procedure to reduce etch attack, had only about five die out of 100 with row and column outages. A good measure of array quality is the count of those pixels that have a current outside the average current by more than 20%. The best die had only two pixels outside this range, and 55% of the die (~30/54) from the best wafer had less than 1% (163/16384) of the pixels outside this range. Four of the die had only one dead pixel. The standard deviation in pixel current for most of the die is in the range of 3% to 5%.

The best 512×512 wafer had a similar high degree uniformity in pixel current. Figs. 12 and 13 are a current map and a histogram for the best 512×512 array. The average current flow is 147 μA with a 3% standard deviation. Of the 262,144 pixels, 1919, or only 0.7%, are outside the 3-σ range and 895 of those, or 0.3% of the total, are dead. The remaining dead pixels are contained in one column and

two rows. Since this array will be used in an application in which individual pixels cannot be resolved, this low level of pixel outage should be more than sufficient to produce the desired imagery.

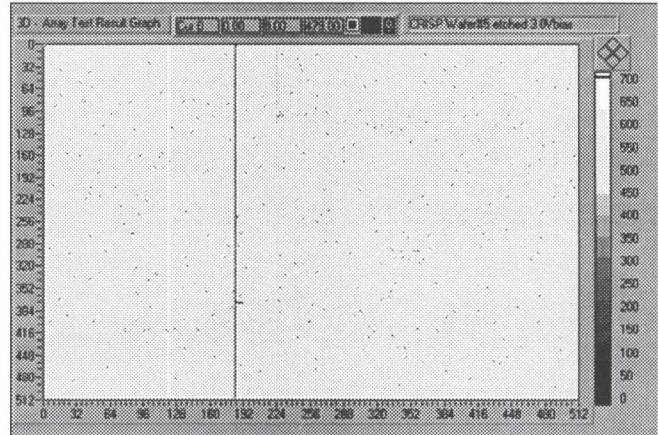


Fig. 12: Current map of 512×512 array uniformity.

### Electrical Measurements: Pixel Resistance Uniformity

Another measure of pixel uniformity is the pixel resistance variation. Placed on the wafers containing 128×128 die with substrate electronics are 8×8 arrays of individual pixels without FETs that are wired out for resistance mapping. The pixels cover the real estate that would normally be occupied by the central 64×64 portion of a 128×128 array. Fig. 13 shows that the pixels have a uniformity in resistance on the order of 1%. This resistance uniformity combined with the FET uniformity of ~3% provides an high degree of pixel-to-pixel uniformity throughout the array.

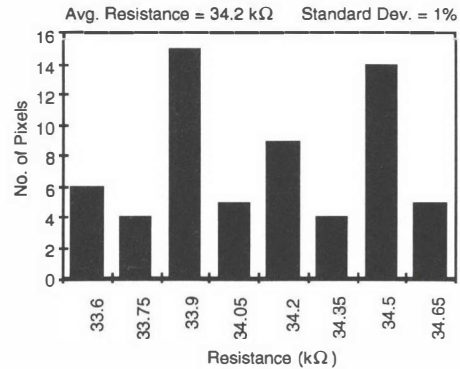


Fig. 13. Resistance histogram of 8×8 pixel array showing high degree of TiN<sub>x</sub> resistance uniformity.

### Time Constant Measurements

In the design of the pixels, a tradeoff occurs between speed and brightness. For slow-response pixels, high fill factors are typically preferred. Larger fill factor pixels have greater brightness for a given temperature but because of the larger pixel mass require higher conductance to achieve the desired response speed. For pixels capable of high speed, smaller pixels with less than optimal fill factors may be desired. The pixels require higher temperatures to achieve the desired radiance goal but require less power and lower currents despite the higher temperature. Fig. 14 shows the calculated temperature (400 K) required to achieve a specific blackbody radiance for LWIR and MWIR bands. Because of the highly nonlinear radiance in the MWIR band, a much lower temperature is required to overcome the loss of fill factor than for the LWIR band. The excellent low-power operation is achieved primarily because of the low pixel thermal mass. A good general figure of merit for pixel power requirements is the power required to achieve a specific radiance. The power scales linearly with temperature difference between the pixel and the substrate, and inversely with pixel thermal

time constant determined by the leg length. It can be expressed in terms of  $\mu\text{W}\cdot\text{ms}$  per unit pixel area, as shown in Fig. 15. Smaller pixels with lower fill factor require less power but require a higher temperature. The 2-mil pixel arrays, in particular, take advantage of these tradeoffs to achieve the desired performance goals of high speed and low power.

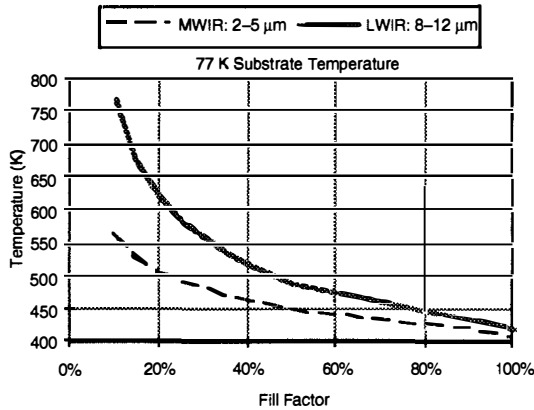


Fig. 14: Calculation of pixel temperature required to achieve 400 K blackbody temperatures assuming 80% emittance.

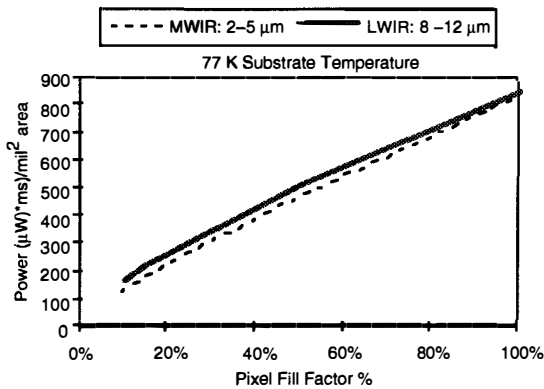


Fig. 15: Power required to achieve desired radiance as a function of pixel fill factor for a given thermal time constant.

A comparison of the two array types we have fabricated is instructive for understanding the range of properties:

Property	128x128 - 2 mil	512x512 - 3.5 mil
Active array area	0.25 in. x 25 in.	1.75 in. x 1.75 in.
Pixel fill factor	15% and 50%	90%
Leg length	30 mm	8 mm
Thermal time constant	2-5 ms	30 ms
Operating temperature	40 K	20 K
FET gate size	5 mm x 5 mm	5 mm x 10 mm

Measurements of pixel thermal time constants shown in Fig. 16 have been taken on 15% and 50% fill factor pixels with the same 30- $\mu\text{m}$  leg length and a 3.5-mil pixel with a 8- $\mu\text{m}$  leg length. These measurements were taken by applying a heating pulse of varying duration to a 128x128 array of pixels wired together. The radiation measured as blackbody temperature was viewed with a 3-5- $\mu\text{m}$  radiometric camera through a KCl window in a room-temperature vacuum chamber. The arrays are maintained in a vacuum below 25 mtorr for optimal operation since in air the pixel thermal conductance would be dominated by air conduction. The vacuum requirements are totally compatible with cryogenic operation. Room-temperature operation can also be achieved by mounting the arrays in standard vacuum packages containing IR windows.

A pulse repetition frequency of 32 Hz was selected so that the camera was nearly in phase with the temperature change so that

changes in a millisecond time period could be seen. The data was fit to a standard rolloff function of the form:

$$dT = T_{\text{max}} / (1 + \tau^2 / t^2)^{1/2}$$

The conductance of the 30- $\mu\text{m}$  legs for the 15% and 50% pixels is comparable, but the resistor on the pixel had a different number of squares, which gives rise to a different temperature maximum. From the fit to the data, it can be seen that the 15% fill factor pixel has a significantly faster response time, 2.5 ms, than the 50% fill factor pixel response time of 6 ms. The 3.5-mil pixel has a leg length of only 8  $\mu\text{m}$  and a higher conductance, but the increased thermal mass more than offsets the increased conductance to yield a longer thermal time constant on the order of 15 ms.

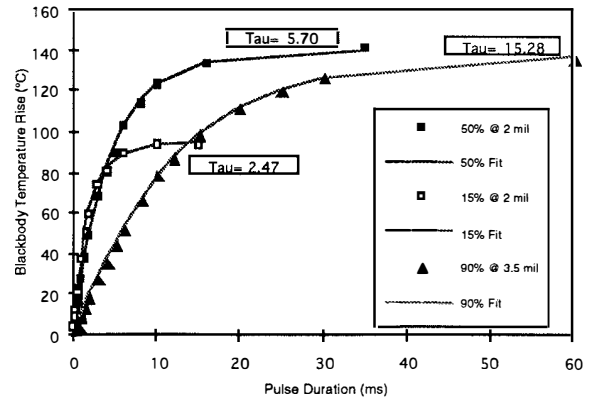


Fig. 16: Time constant measurement obtained by measuring the temperature rise as a function of pulse duration. The measurements were obtained with a 3-5- $\mu\text{m}$  camera for three different pixel designs, two 2-mil pixels with the same leg length but different fill factors, and a 3.5-mil pixel of greater area but with a shorter leg length and thus greater conductivity.

### Optical Performance and Measurements

One benefit of this thermal structure design is that the radiating region of the pixel is maintained at a uniform temperature largely independent of pixel fill factor. Fig. 17 show a finite-difference calculation of the temperature gradient across the emitting region for a 30% fill factor pixel. The analysis shows that over 90% of the pixel area remains at a temperature within 2% of the maximum. By concentrating the temperature drop to the small leg region, we are able to maximize the pixel area temperature uniformity and hence achieve a high radiance for a specific maximum temperature.

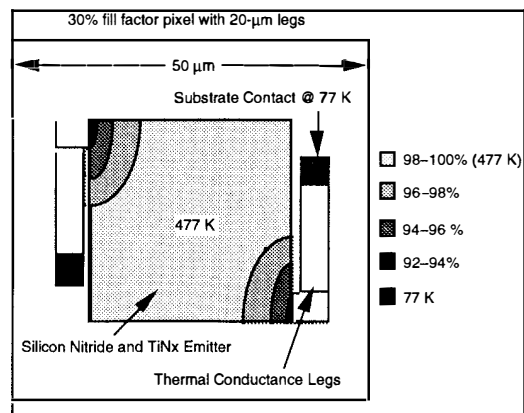


Fig. 17: Calculated temperature uniformity of 30% fill factor emitter region on 2-mil pitch pixel.

The optical performance is optimized by using thin metal films of approximately 300  $\Omega/\text{square}$  sheet resistance. In addition to providing the proper pixel resistance of about 30 k $\Omega$  with a 100-square serpentine to minimize pixel current, this sheet resistance

also contributes to the optical properties to achieve high emittance. In addition, by using a reflecting film at the substrate level and maintaining a vacuum spacing between the reflector and the emitter on the order of  $1.5\ \mu\text{m}$ , we produce a resonant emitter. For optimal performance in a narrow IR band, the gap dimension obtained by choice of sacrificial layer thickness can be selected to optimize that resonance at a specific wavelength. For wider band performance, the emittance can be detuned by placing a thin metal film of comparable absorptance on the underside of the emitter. The resistor sheet resistance combined with the optical properties of  $\text{Si}_3\text{N}_4$ , a reflector at the substrate levels contribute to the overall high emittance of the structure. Calculations of the optical properties shown in Fig. 18 are confirmed by measurements at  $3\text{--}5\ \mu\text{m}$  and  $8\text{--}12\ \mu\text{m}$  with IR cameras that indicate that the effective radiance in these bands corresponds to a high emittance level. IR spectral radiance measurements taken on an array with wideband design is shown in Fig. 19. As shown, the measured spectra closely approximates a blackbody spectra.

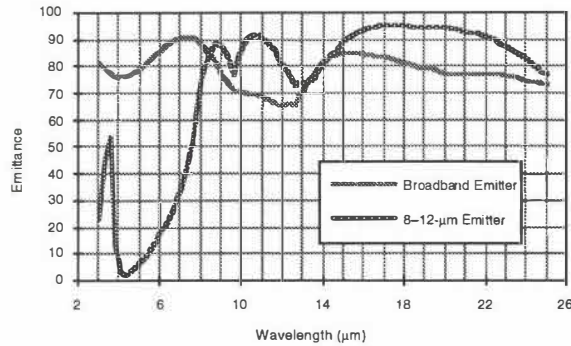


Fig. 18: Comparison of calculated IR emittance for two different emitter designs.

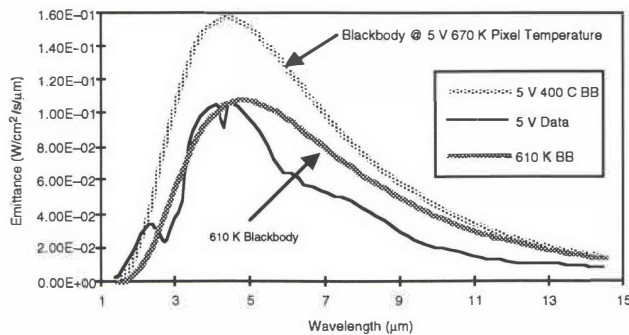


Fig. 19: Measured spectral radiance for a CRISP array compared to a blackbody at the 670 K pixel temperature and a slightly lower 610 K temperature that closely matches the spectrum.

## 2.7 Imagery

Imagery has been generated with a  $128\times 128$  array from a previous run. Fig. 20 is one video frame from a visible Desert Storm scene played to the array and viewed with an  $3\text{--}5\text{-}\mu\text{m}$  IR camera. The array was operated at 77 K temperatures. This array from the first run had a much higher pixel outage, on the order of 10% randomly distributed, which was corrected by processing and design changes in the recently completed second run. Although the drive systems being developed will have pixel correction algorithms, the present video was taken by having the camera provide the pixel correction. This was achieved by calibrating the camera to the array by observing the array at two different temperatures. Although not seen

in this frame, the thermal time constant of the array ensures that there is no carryover of information from scene to scene. Imagery using the  $512\times 512$  array and new  $128\times 128$  arrays is planned for the near future.

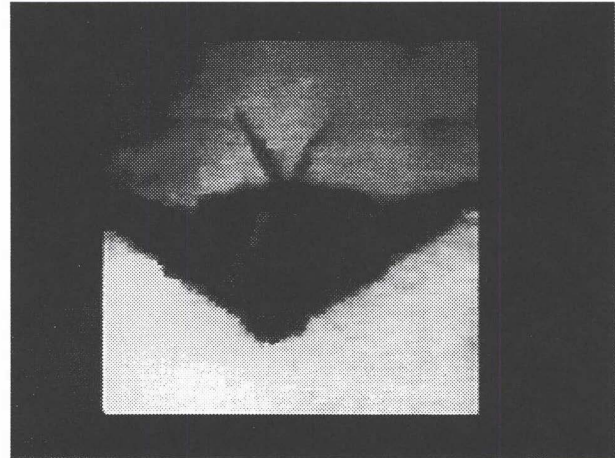


Fig. 20: IR Frame of Desert Storm tape projected by scene projector and viewed in  $3\text{--}5\text{-}\mu\text{m}$  IR band with InSb camera.

## CONCLUSIONS

Arrays up to  $512\times 512$  dimension have been fabricated. These arrays have millisecond time constants and address speeds, making them capable of projecting high-frame-rate scenes for IR simulations. In addition, the cryogenic operating temperatures combined with the high pixel emitter temperatures make these arrays capable of projecting scenes of very high dynamic range.

## ACKNOWLEDGMENTS

We wish to acknowledge the support of Defense Nuclear Agency under contract DNA001-92-C-0041 (NODDS) and Wright Laboratory, Eglin AFB, FL, through contract F08630-92-C-0016 (CRISP). We acknowledge the measurements performed by George C. Goldsmith II of Guided Weapons Evaluation Directorate at Eglin AFB; Bob Stockbridge of the Seeker Technology Evaluation Branch at Wright Laboratory, Eglin AFB; Lawrence Jones of Science Application International Corp., Shalimar, FL; and D. Pritchett, B. Sawyer, and T. Old of Mission Research Corporation, Santa Barbara, CA.

## REFERENCES

- Wood, R.A.; Han, C.-J.; and Kruse, P.W., "Integrated Uncooled Infrared Detector Imaging Array," IEEE Solid-State Sensor and Actuator Workshop, Hilton Head Island, SC, 1992, pp. 132-135.
- Cole, B.; Han, C.-J.; Higashi, R.; Werner, T.; Sawyer, B.; Ludington, B.; and Old, T., "Ultra-low Power Scene Projector for Targets Against Space Backgrounds," SPIE, Vol. 1967, 1993, Orlando, FL, pp. 39-50.
- Williams, O., and Reeves, G., "Thermal Comparison of Emissive Infrared Projector Devices," SPIE, Vol. 1967, 1993, Orlando, FL, pp. 2-14.
- Lake, S.P.; Pritchard, A.; Sturland, I.M.; Murray, A.R.; Prescott, A.J.; and Gough, D.W., "Description and Performance of a  $256\times 256$  Electrically Heated Pixel IR Scene Generator," SPIE, Vol. 1486, Orlando, FL, 1991.

# A HIGH-DENSITY TACTILE IMAGER FOR READING EMBOSSSED CHARACTERS

Richard J. DeSouza and Kensall D. Wise

*Center for Integrated Sensors and Circuits*  
Department of Electrical Engineering and Computer Science  
The University of Michigan, Ann Arbor, MI 48109-2122

## ABSTRACT

This paper describes a high-density high-compliance tactile imager suitable for reading embossed characters on credit cards. The sensor has 16 flexible silicon shanks arranged in a single row. Each shank is 6mm long, 100 $\mu$ m wide and 10 $\mu$ m thick. Piezoresistive strain gauges incorporated on the shanks give a high-sensitivity analog readout as the tips of the shanks deflect over characters on the scanned card surface. Fabrication is accomplished using a five-mask single-sided bulk-micromachined dissolved-wafer process. The devices have a sensitivity of 10mV/mm at 5V and a minimum resolution of 1 $\mu$ m. The fabrication process is compatible with the realization of shanks on 50 $\mu$ m centers and allows a high degree of design flexibility in setting device performance for a variety of surface profilometry applications.

## INTRODUCTION

Magnetic strips are currently employed worldwide to carry information on credit cards for use in financial transactions. However, it is not uncommon for the strips to fail, and a backup system is badly needed. It is widely believed that a tactile imaging system can provide a low cost alternative to allow the card number and perhaps other information to be read automatically when the magnetic strip is no longer functional. As more and more financial dealings are implemented using credit cards and other card-access systems, the need for such imagers is becoming increasingly evident. However, the devices must be low-cost and capable of working reliably over hundreds of thousands to millions of scan operations in environmental conditions that can include large temperature variations and high humidity.

Over the past decade, there have been a variety of semiconductor-based approaches to the realization of high-resolution tactile imagers [1-4]. Among the more promising recent devices are those based on x-y organized capacitive arrays, either bulk- or surface-micromachined [5,6]. For the work reported here, a bulk-micromachined capacitive-cell approach [5] was first explored. This device used a 500 $\mu$ m pixel spacing with a split-boss arrangement capable of producing an effective spatial resolution of 250 $\mu$ m. The doubly-supported capacitive bridge cell exhibited low noise, high sensitivity, and high resolution. However, profilometer scans of typical cards show height irregularities in the embossed characters of 50 $\mu$ m or more. This is a serious problem with most previously reported solid-state imaging arrays since their total vertical compliance is typically limited to a few microns. Vertical compliance can be increased using a deformable pad overlay, but with degraded spatial resolution. As a result, we altered our approach to a high-density multishank linear piezoresistive array based on a modification of the neural probes we have been developing for a number of years [7,8]. This "microbrush" array is scanned across the card surface to read the characters. This approach overcomes the vertical compliance problems of planar arrays and has been designed to read the entire credit-card account number in a single scan.

## DESIGN CONSIDERATIONS

The design of the new device was governed by the specifications on the dimensions and position of the account number on credit cards set by the American National Services Institute for financial services [9]. The number field on the credit card is about 5mm x 68mm in size with the height of the embossed characters being typically 500 $\mu$ m above the front surface of the card. The width of the lines that form the numbers is 0.51mm, and this decides the maximum allowable pitch between consecutive shanks to achieve sufficient resolution. Although theoretically either side of the card could be used for the scans, labels sometimes obscure portions of the back side, making the front side a more appropriate target surface.

A top view and cross-section of the tactile imager structure is shown in Fig. 1. For the present 16-shank prototype arrays, each shank is 6mm long, 100 $\mu$ m wide, and 10 $\mu$ m thick. The shanks have a center-to-center spacing of 400 $\mu$ m, resulting in a scan line 6.4mm wide. This gives sufficient resolution as well as some tolerance for any misalignment during a scan. In the future, a 64-shank imager will be implemented to increase the present resolution by another factor of four. Two polysilicon resistors are provided per shank, arranged in a half-bridge configuration so that ambient temperature sensitivity due to the TCR of the resistors is suppressed. One resistor is located at the base of the shank, where maximum stress is developed. It acts as piezoresistive strain gauge and gives a high-sensitivity analog readout. The other resistor is located on the rear of the substrate and is used as the reference. The shank tips deflect as they go over the embossed characters, and the corresponding change in strain results in an electrical output signal.

The strength of each shank can be analyzed by considering it to be a cantilever beam [10]. The fracture stress is a weak function of the shank thickness and is over an order of magnitude higher than the maximum levels expected in use. This is important since the brush must be able to reverse direction against the scanned characters without damage. Shanks can be elastically bent through angles of more than 90° (corresponding to radii of <400 $\mu$ m) without damage.

## FABRICATION

Fabrication begins with standard p-type <100> silicon wafers that are first oxidized and patterned to define the intended tactile sensor areas. The patterned areas are subjected to a deep boron diffusion that forms the base of the sensor, acting as an etch stop for the final EDP etch. An optional shallow boron diffusion can also be used to define a thinner area of the probe shank to concentrate bending under the strain gauge and optimize its sensitivity. Next, LPCVD dielectric layers consisting of an oxide-nitride-oxide combination are deposited. Then polysilicon is deposited and patterned to form the strain gauges. Upper dielectric layers which are similar to the lower dielectrics are deposited and contact openings are patterned and etched.

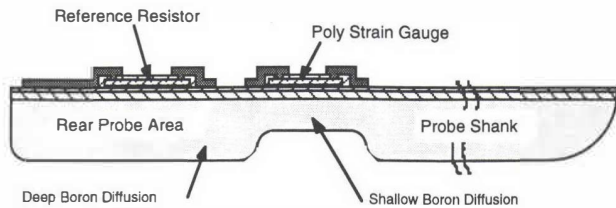
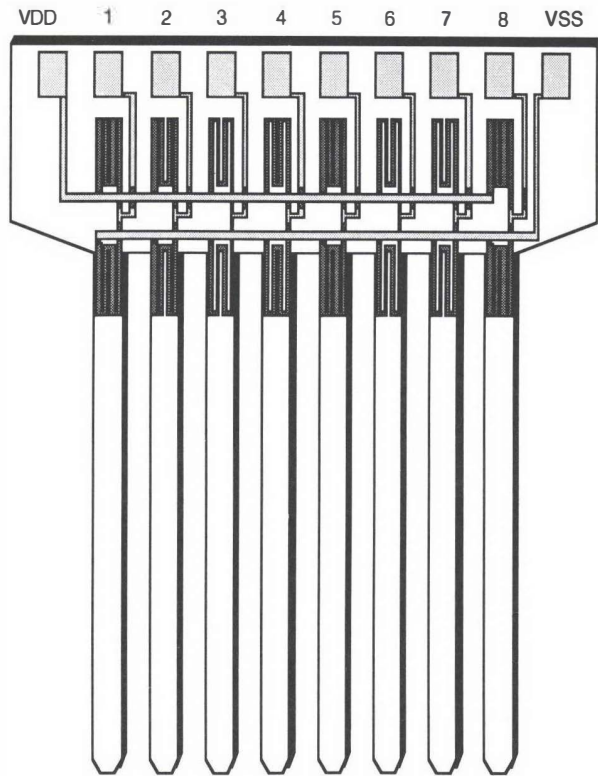


Fig. 1: Top view and cross-section of a bulk-micromachined tactile imager. Independent shanks, each containing an integrated strain gauge, brush over the substrate, creating an electrical image of the surface topography.

A 500Å-Cr/3000Å-Au metallization layer is sputtered onto the wafers, and a lift-off process is used to define the metal interconnects and bonding sites. The dielectrics are now etched from the field areas. Finally, the wafers are thinned from the back-side to a thickness of about 150µm in an isotropic etch (10% HF, 90% nitric acid) and are then subjected to an unmasked etch in ethylene diamine pyrocatechol (EDP), which dissolves the lightly-doped silicon substrate but does not significantly attack silicon doped with boron in concentrations higher than about  $7 \times 10^{19} \text{ cm}^{-3}$  or any of the other exposed materials. The overall fabrication process is single-sided on wafers of standard thickness and requires only five masks. The process is also compatible with a standard CMOS process [8], making it straightforward to incorporate on-chip circuitry in the future. Such circuitry will be important in providing the first-level amplification and multiplexing necessary to ensure high signal-to-noise ratios and environmental immunity on arrays involving higher numbers of channels. It is also important to note that the neural probes, which have a structure similar to these imagers, are known to be compatible with long-term use in saline.

Hence, the imager structure should offer ample environmental immunity for credit card applications. Figure 2 shows two views of a completed 16-shank device, while Fig. 3 shows a SEM view of the tip of a shank. Figure 4 shows the strain-gauge area at the base of a shank.

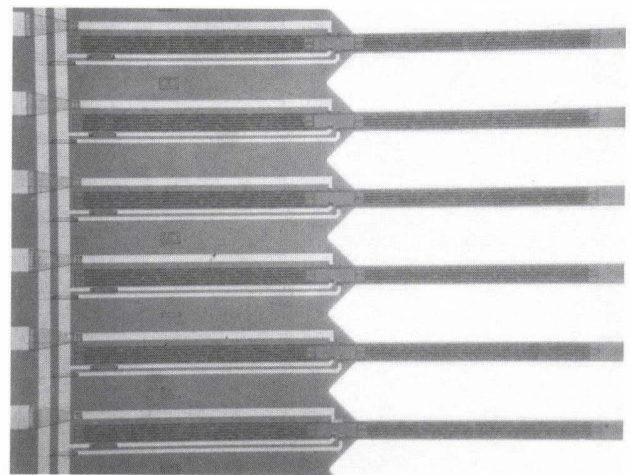
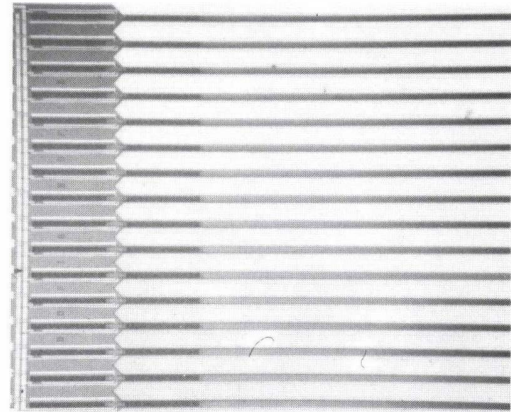


Fig. 2: Top views of a 16-shank tactile line imager showing the overall device (above) and a detail of the strain gauges at the rear of the substrate. The shanks are on 400µm centers.

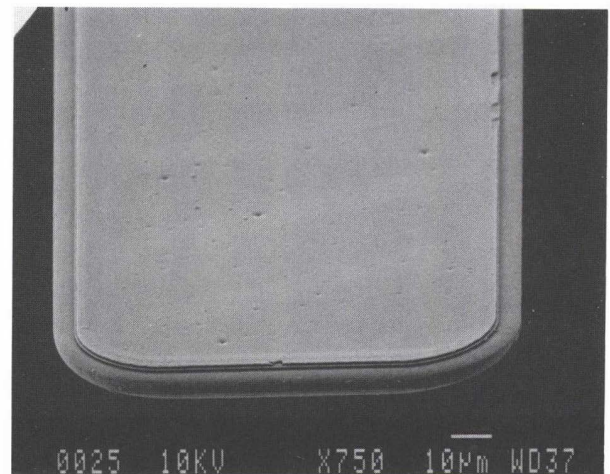


Fig. 3: SEM view of the tip of a microbrush shank.

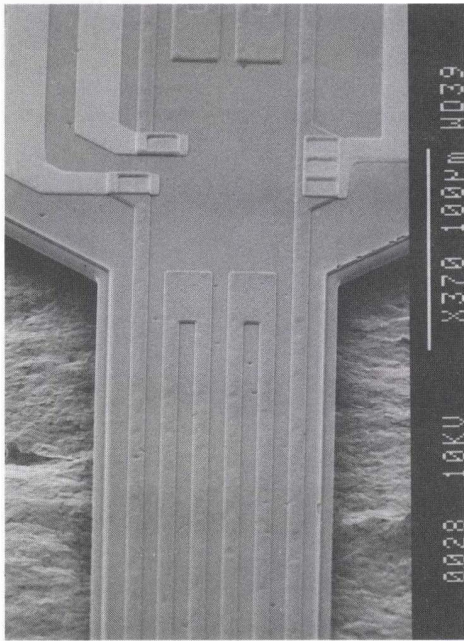


Fig. 4: SEM view of the strain gauge at the rear of a microbrush shank. The shank width is 100µm.

#### DEVICE PERFORMANCE

Tests conducted on typical devices have shown that the strain gauges have a sensitivity of 10mV/mm when operating from a 5V supply. This corresponds to a gauge factor of 19 (Fig. 5), which matches previously published data [10] as well as theoretical calculations. Because the height of the embossed characters is about 500µm, an output signal of at least 5mV is obtained, resulting in an excellent signal-to-noise ratio. Assuming an electrical noise level of 10µV, the minimum resolution is 1µm.

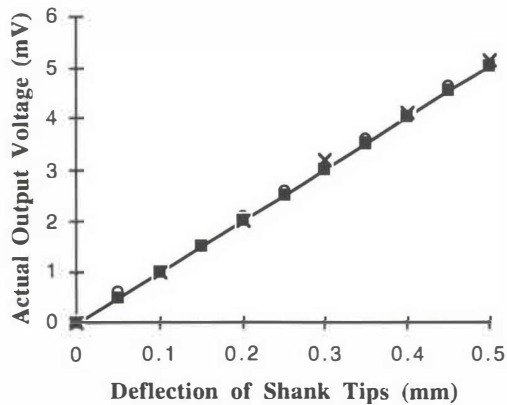
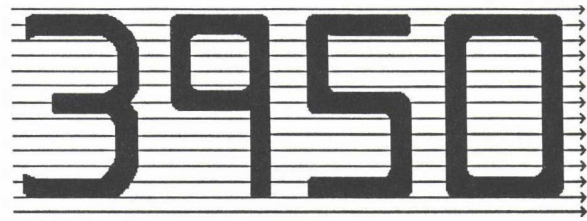


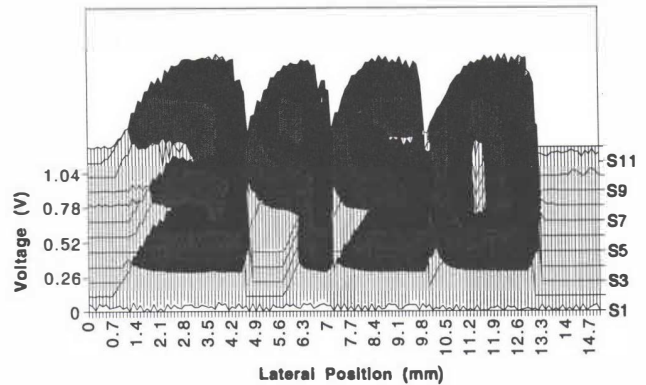
Fig. 5: Output characteristic of the tactile sensor with offset correction for several sets of data. The supply voltage is 5V.

Scans have been made on several different credit cards with the microbrush brought in contact perpendicular to the front surface of the cards. A z-micropositioner was used to accurately set an

initial deflection on the tines so that they always touch the card surface even when not over a character. The output from each channel is amplified using a difference amplifier and fed to a computer through a data acquisition board. A reading taken with only the initial deflection determines the offset correction values. A sample scan is shown in Fig. 6 with the output being displayed as a 3-D surface plot using Microsoft Excel. No other image processing was performed. Figure 6(a) shows the credit-card numbers and the tracks along which the microbrush shanks contacted the card surface. Figure 6(b) shows the resulting analog outputs with the image of the numbers clearly recognizable. The scan speed was 15mm/sec and the scan interval was 6.67msec, giving a 100µm lateral resolution. The sampling frequency between successive channels was 100kHz, resulting in a skew of less than 2.4µm per scan interval. Using an optical encoder to keep track of lateral distance during a scan makes it possible to have scan speeds of 50mm/sec or more so that the entire account number can be read in less than two seconds.



(a)



(b)

Fig. 6: Sample scan of the embossed characters "3950" on a credit card (above) and the corresponding output plot represented as 3-D surface (below).

#### CONCLUSIONS

A high-density high-compliance tactile imager for reading embossed characters has been reported. The present 16-shank line imager has shanks that are 6mm long, 100µm wide and 10µm thick with a 400µm pitch. It is scanned across the front surface of the credit-card, permitting the entire account number to be read in a single scan. Polysilicon strain gauges give a readout sensitivity of 10mV/mm and a vertical resolution of about 1µm. Fabrication is accomplished using a well-developed five-mask single-sided dissolved-wafer process that is capable of producing imagers having a lateral resolution as small as 50µm. The devices are immune to

most environmental conditions, and the process technology is CMOS compatible, making it possible to incorporate on-chip circuitry on such arrays in the future. This high-compliance tactile sensor can easily be optimized for use in a variety of surface profilometry applications requiring vertical resolution in the range from one micron to several thousand microns. The microbrush is being built into a feedback system to automatically control device positioning and perform dynamic compensation for offsets during a scan.

### REFERENCES

1. R. A. Boie, "Capacitive Impedance Readout Tactile Image Sensor," *Proc. Int. Conf. on Robotics*, Atlanta, pp. 370-378, March 1984.
2. M. H. Raibert, "An All-Digital VLSI Tactile Array Sensor," *Proc. Int. Conf. on Robotics*, Atlanta, pp. 314-319, March 1984.
3. S. Sugiyama, K. Kawahata, M. Yoneda, and I. Igarashi, "Tactile Image Detection using a 1k-Element Silicon Pressure Sensor Array," *Sensors and Actuators, A21-A23*, pp. 397-400, 1990.
4. K. Chun and K. D. Wise, "A High-Performance Silicon Tactile Imager based on a Capacitive Cell," *IEEE Trans. Electron Devices*, 32, pp. 1196-1201, July 1985.
5. K. Suzuki, K. Najafi, and K. D. Wise, "A 1024-Element High Performance Silicon Tactile Imager," *IEEE Trans. Electron Devices*, 37, pp. 1852-1860, Aug. 1990.
6. M. R. Wolffenbuttel, *Surface Micromachined Capacitive Tactile Image Sensor*. Ph.D. Thesis, Delft University of Technology, Delft, The Netherlands, April 1994.
7. K. Najafi, K. D. Wise, and T. Mochizuki, "A High-Yield IC-Compatible Multichannel Recording Array," *IEEE Trans. Electron Devices*, 32, pp. 1206-1211, July 1985.
8. S. J. Tanghe, and K. D. Wise, "A 16-Channel CMOS Neural Stimulation Array," *IEEE J. of Solid-State Circuits*, 27, pp.1819-1825, December 1992.
9. American National Standards for Financial Services - Financial Transaction Cards, *American National Standards Institute Inc*, New York, 1983.
10. K. Najafi, and J. F. Hetke, "Strength Characterization Of Silicon Microprobes In Neurophysiological Tissues," *IEEE Trans. Biomed. Eng.*, 37, pp. 474-481, May 1990.

# MICROMECHANICAL DATA STORAGE WITH ULTRA LOW-MASS CANTILEVERS

H.J. Mamin, L.S. Fan, S. Hoen, and D. Rugar

IBM Research Division, Almaden Research Center, 650 Harry Road, San Jose, California  
95120-6099

## Abstract

We describe a micromechanical approach to data storage based on the atomic force microscope. For this purpose, we have fabricated  $\text{Si}_3\text{N}_4$  cantilevers which have 30 times less mass than the smallest commercially available cantilevers. With these cantilevers, we have demonstrated reading real data at rates exceeding 1 Mbit/s.

## Introduction

Scanning probe microscopy has long been seen as a possible basis for an ultrahigh density data storage device.[1] Both the scanning tunneling microscope (STM) and the atomic force microscope (AFM) have demonstrated the ability to write and detect surface features on the nanometer scale.[2] One of the keys difficulties in making this approach practical is the extremely low data rates typically achieved with these techniques. Recently, however, we have developed a new micromechanical approach based on the AFM that combines high density with more reasonable data rates.[3] Using commercially available cantilevers,[4] we demonstrated reading and writing at frequencies up to 100 kHz.

In this technique, the tip of an AFM cantilever is placed in contact with a rotating surface, as shown in Fig. 1. The substrate material is polycarbonate, and the writing is done by heating the tip with a pulsed infrared laser. With the tip in contact, the heated tip softens the polymer surface, and the pressure from the tip creates a small pit. Typical pulse parameters are 20 mW and 1  $\mu\text{s}$  pulses, with a loading force on the tip of roughly  $10^{-7}$  N. Pits as small as 100 nm across and 10 nm deep have been written in this way.[3]

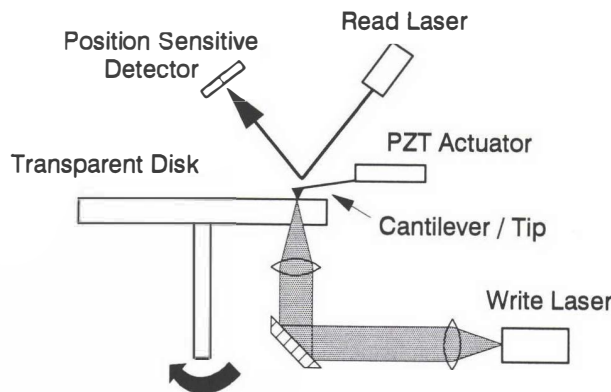


Fig. 1. Experimental setup. Focused laser beam propagates through transparent polycarbonate sample and heats the optically absorbing AFM tip. The heated tip softens the substrate, and the local tip pressure creates an indentation. The sample is placed on a precision air-bearing spindle to allow for sample rotation. The PZT actuator is used to maintain generally constant loading force.

In Fig. 2. we show an AFM micrograph of a pattern written into a test sample in this manner. The sample, which was a section of a grooved optical disk, was raster-scanned under the tip using piezoelectric scanners, and pits were written by pulsing the laser at the desired locations. This pattern represents a density of about 25 Gbit/in<sup>2</sup>, a more than 20 $\times$  increase in areal density compared to conventional optical recording.

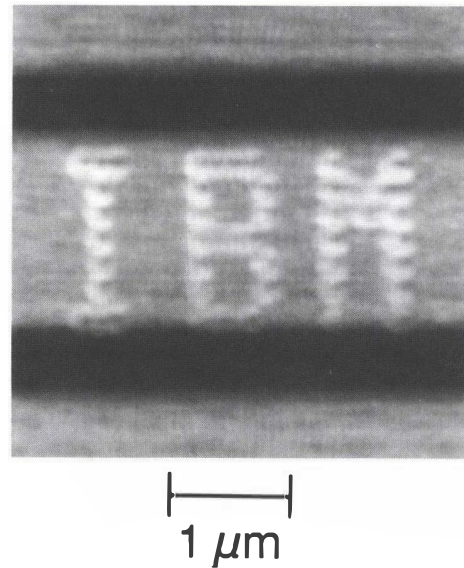


Fig. 2. "IBM" written between the grooves of an optical disk. Each letter would nearly fit inside a typical CD ROM mark.

We detect the marks on the rotating sample with mechanical readback. As the tip rides over the surface of the sample, a topographic feature such as a pit causes a deflection of the cantilever. This deflection is then detected using a standard optical sensor, as shown in Fig. 1. The data rate in this mechanical scheme is related to  $f_{\text{max}}$ , the maximum frequency at which the tip can track the surface. For a rectangular beam, a simple model which neglects higher order modes gives

$$f_{\text{max}} = f_0 \left( \frac{2z_L}{h} \right)^{1/2} = 0.46 \left( \frac{F_L}{mh} \right)^{1/2}$$

where  $f_0$  is the resonant frequency,  $h$  is the pit depth,  $z_L$  is the load displacement of the cantilever,  $F_L$  is the loading force, and  $m$  is the mass of the cantilever.[3] Because of wear and signal-to-noise considerations, the loading force and pit depth cannot be varied arbitrarily. Thus the primary means to improve performance is to reduce the cantilever mass. This is easily understood, as it is the

acceleration imparted to the tip that determines the response. Our efforts have therefore been to fabricate smaller cantilevers as a means to improve data rate.

### Fabrication

Our cantilevers were made from silicon nitride and had integrated pyramidal tips, following the process of Albrecht *etal.*[5] We made both triangular and rectangular levers. The lateral dimensions were chosen so as to make the cantilevers straightforward to fabricate and reasonable to work with in our setup. The thickness was then chosen to give spring constants on the order of 1 N/m. Using these criteria, we chose to make a series of cantilevers with lengths 20-30  $\mu\text{m}$  and thickness 0.35  $\mu\text{m}$ . The resulting mass ranged from 0.3-0.6 ng, depending on geometry. For comparison, commercial silicon nitride cantilevers have a mass of at least 10 ng. Figure 3 shows an optical micrograph of our cantilevers. A rectangular and an open triangular cantilever are shown; closed triangular levers were also fabricated. A scanning electron micrograph is also shown of the pyramidal tip on a triangular cantilever. Tip radii well under 100 nm have been obtained.

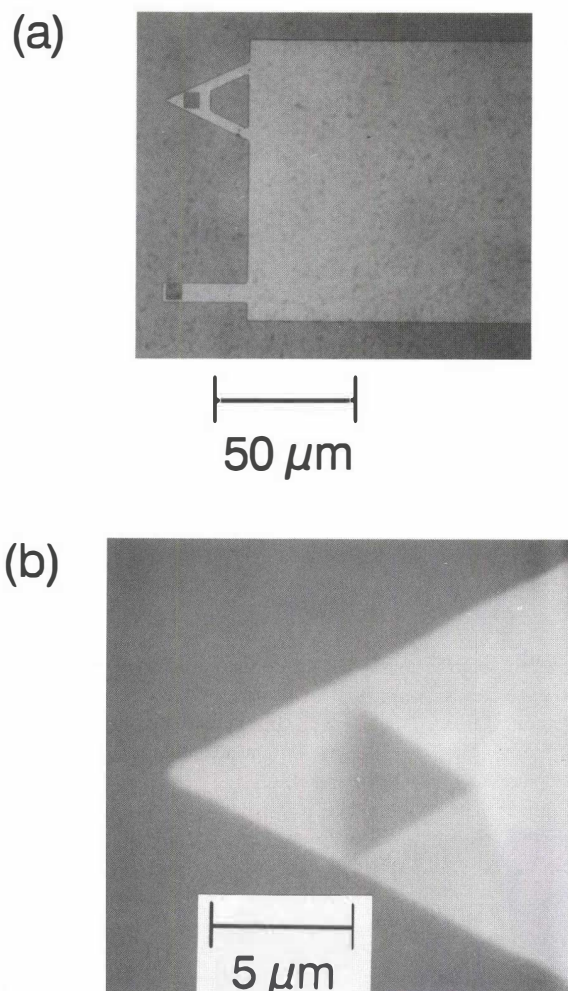


Fig.3.(a) Optical micrograph of cantilevers on the plated Cu support. (b) Scanning electron micrograph of pyramidal tip.

One of the difficulties in making cantilevers with pyramidal tips is that the tips end up on the wrong side; that is, they point toward the silicon support, which interferes with sample access. In commercial cantilevers, this problem is solved by anodically bonding the nitride layer to a glass substrate, then etching away the silicon support.[5] We have used a fairly straightforward alternative, in which we plated a thick film of copper onto the nitride at the base of the cantilevers, as shown in Fig. 4. This film then provided a suitably rigid support after the removal of the silicon.

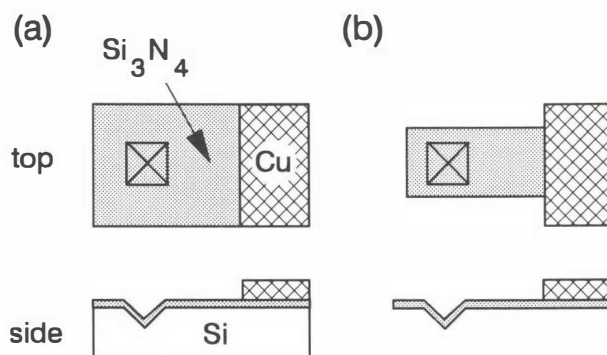


Fig. 4. (a) Formation of  $\text{Si}_3\text{N}_4$  structure. The tip is formed by depositing onto a (111) etch pit in Si(100). A Cu backing layer is plated before removal of the Si. (b) A freestanding cantilever is formed upon removal of the Si. The 12  $\mu\text{m}$  thick Cu film provides rigid support over its 0.5mm dimensions.

The vibrational noise spectrum of a weak cantilever shows a distinct peak at its resonant frequency due to its thermally-driven noise.[6, 7] On a closed triangular cantilever, we observed this peak at 1.3 MHz, in excellent agreement with the value of 1.35 MHz calculated for a cantilever without a tip. (We took the modulus  $E$  to be  $1.6 \times 10^{11} \text{N/m}^2$  and density  $\rho$  to be  $3300 \text{kg/m}^3$ .[5]) The spring constant  $k$  was calculated from the geometry to be 2 N/m. This can also be estimated from the amplitude and width of the thermal noise peak, using the fact that the integrated noise energy is of order  $k_B T$ .[6] With this method we obtained 3 N/m, in reasonable agreement. The rectangular cantilevers had calculated spring constants closer to the design point of 1 N/m, with frequencies at about 600 kHz. For comparison, the resonant frequency of a commercial cantilever is typically about 90 kHz with a spring constant of roughly 0.4 N/m.

### Results and Discussion

The new cantilevers gave significantly enhanced performance, as shown in Fig. 5. A grooved glass disk was used as a test sample, where the groove width was 0.8  $\mu\text{m}$ . In the upper trace, taken with the commercial cantilever, the basic groove periodicity was seen, along with some unwanted ringing, corresponding to higher order cantilever modes. With the new cantilevers, however, the tip cleanly tracked the surface without ringing, as shown in the lower trace.

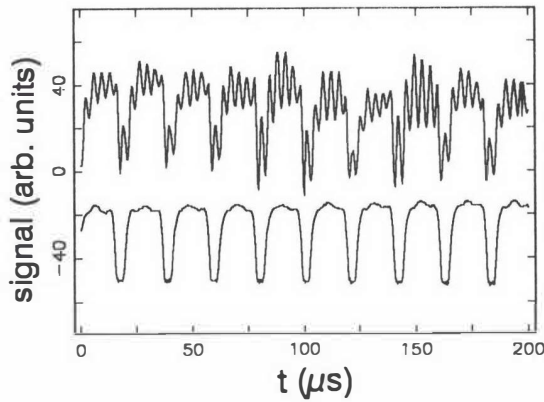


Fig. 5. Readback signal on a grooved glass test structure. Upper curve, obtained using a commercial cantilever, shows unwanted ringing, degrading signal-to-noise. Lower curve was obtained with a new low-mass cantilever, and gives an accurate representation of the surface topography.

To measure the data rate, we first wrote a series of tracks containing known data patterns. The data are represented by the spacing between the pits, which varies as shown in Fig. 6. This data pattern was a pseudorandom 127 bit sequence of 1's and 0's which repeated. The writing was performed at a rate of about 200 kbit/s; its speed was limited by the thermal response time of the tip, currently about 5  $\mu$ s.

The readback signal from a triangular cantilever on such a track is shown in Fig. 7, along with the corresponding data pattern. A 1 is seen above every peak in the waveform. The data rate from this waveform corresponds to 830 kbit/s. This is nearly an order of magnitude higher rate than was previously possible.

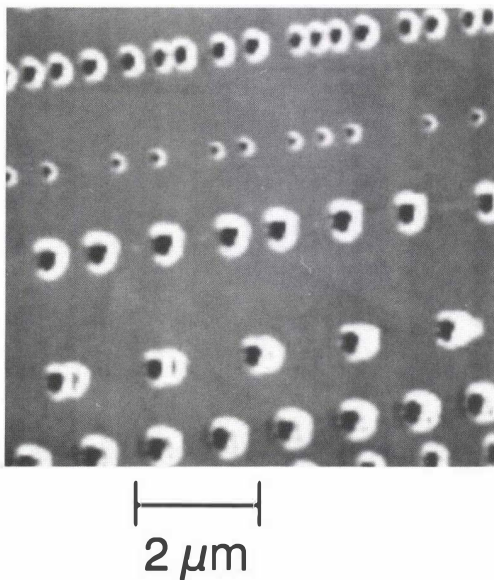


Fig. 6. AFM micrograph of tracks written thermomechanically on the rotating sample. Data are encoded by the spacing between the pits. Data are encoded using a (2,7) run-length limited code, meaning that there are between 2 and 7 0's between every 1.

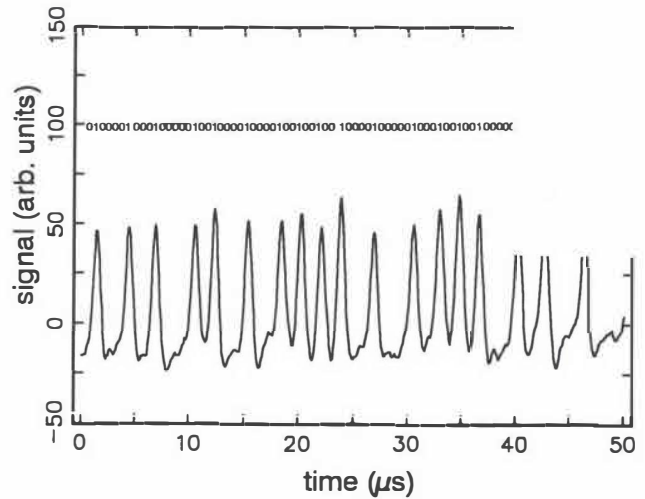


Fig. 7. Readback signal on data tracks shown above. The corresponding data pattern is shown above the waveform. The clock period is 0.6  $\mu$ s, which with a rate 1/2 (2,7) code corresponds to a data rate of 830 kbit/s (Ref. 8) This data rate is nearly an order of magnitude higher than achieved with conventional cantilevers.

We can use standard algorithms to detect the location of the peaks, and then characterize the readback in a number of ways. First, we can simply decode the peaks to get back to our original data, and compare to look for errors. We found that we typically got about 1-3 errors per 1000 bits, for a raw error rate of the order of  $10^{-3}$ . This value is high by data storage standards, but is excellent for a scanning probe technique, and can be brought lower using standard error correction schemes.[8] We can also analyze how accurately the peaks are located in time or space to determine the jitter. Figure 8 shows a histogram of peak spacings for data read at 1.2 Mbit/s. Distinct histograms are observed at the expected spacings, with quite narrow widths, suggesting that somewhat higher density recording is possible. We note that the above data rate is equivalent to original CD-ROM rates.

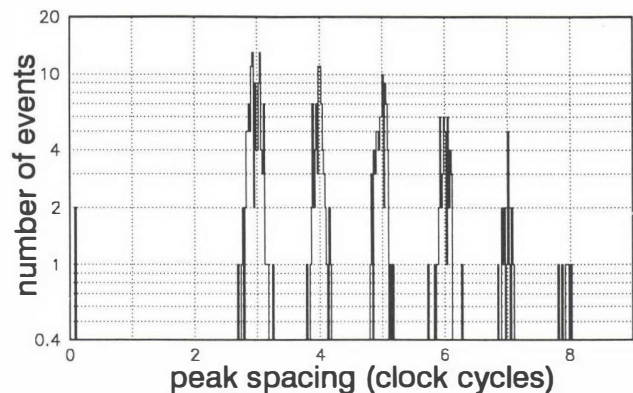


Fig. 8. Histogram of peak spacings for data read at 1.2 Mbit/s. The histograms are non-overlapping, indicating low timing jitter. One clock cycle corresponds to 0.6  $\mu$ s.

## Conclusion

We have shown that megahertz operation of a scanning-probe-based device is possible. We have furthermore used our device to store kilobytes of real data with few errors. Reducing the mass of the cantilevers was key to achieving these data rates, and further reduction in size will be needed to reach even higher data rates. Because we have not pushed the limits of micromachining, we expect that improvements of another order of magnitude may be possible. Beyond that, it is also possible in principle to fabricate arrays of levers to operate in parallel for higher data rate.

## Acknowledgement

The authors gratefully acknowledge the use of the Berkeley Microfabrication Laboratory.

## References

1. C.F. Quate, U.S. Patent Number 4,575,822, (1986).
2. See, for example, review articles by U. Staufer in *Scanning Tunneling Microscopy II*, R. Weisendanger and H.-J. Güntherodt, Eds. (Springer, Berlin), p. 273, and C.F. Quate in *Highlights in Condensed Matter Physics and Future Prospects*, L. Esaki, ed. (Plenum, New York), p. 573.
3. H.J. Mamin and D. Rugar, *Appl. Phys. Lett.* **61**, 1003 [1992].
4. obtained from Park Scientific Instruments and Digital Instruments.
5. T.R. Albrecht, S. Akamine, T.E. Carver, and C.F. Quate, *J. Vac. Sci. Technol. A* **8**, 3386 [1990].
6. Y. Martin, C.C. Williams, and H.K. Wickramasinghe, *J. Appl. Phys.* **61**, 4723 [1987].
7. G.M. McClelland, R. Erlandsson, and S. Chiang in *Review of Progress in Quantitative Nondestructive Evaluation*, D.O. Thompson and D.E. Chimenti, ed. (Plenum, New York, 1987) p. 307.
8. C.D. Mee and E.D. Daniel, *Magnetic Recording* (McGraw-Hill Book Co., New York, 1987).

# Integrated Electrophoresis Systems for Biochemical Analyses

D.J. Harrison, Z. Fan, K. Fluri, K. Seiler  
Dept. of Chemistry, University of Alberta, Edmonton,  
AB, Canada T6G 2G2

## Abstract

Microfluidic systems have been micromachined in glass chips for systems intended for chemical analysis or sensing. Using electroosmotic pumping, voltages control the direction of fluid flow without the need for valves. Mixing of reagent solutions, chemical reactions and separation of compounds in mixtures can be achieved.

## Introduction

Microflow systems can be prepared in glass substrates using silicon micromachining techniques. These systems can offer advantages in performance relative to stand-alone sensors, as has been demonstrated for ISFET-based analyzers [1,2]. We have etched systems composed of complex networks of intersecting capillaries, in which chemical reactions, sample injection and separation of individual components of a sample can be achieved [3,4]. The systems use electroosmotic effects for fluid pumping at velocities up to about 1 cm/s in 20  $\mu\text{m}$  capillaries. Electroosmotic pumping also allows control of the direction of fluid flow at the intersection of capillaries, without a need for valves or other moving parts. Separations are achieved using electrophoretic effects, i.e. the differing mobilities of ions within an electric field result in different migration rates and this leads to separation. The separations are as efficient as in conventional capillary electrophoresis systems, and can be an order of magnitude faster, owing to the short distances involved. We have shown we can separate and detect mixtures of amino acids within 3 to 14 sec [4] and even more rapid separations have been reported by Effenhauser et al. [5]. The potential applications of such systems include miniaturized analytical systems that could compete with bench-top instruments or chemical sensors in terms of performance, analysis time or durability [3-7].

To practically realize the use of electroosmotic pumping in a complex manifold of channels it is necessary to develop an understanding of the factors that control flow within such systems, particularly at the intersection of two channels containing different solutions. One of the best ways to achieve this is to visually image the flow process within the channels [4]. In addition, the quantitative study of flow rates and study of the ability to control the direction of solvent flow using applied fields is required. In this report we present both images and quantitative studies of diffusional and convective mixing of solutions at channel intersections.

The applications of micromachined devices could be quite varied if the chips can be made versatile. Performing chemical reactions on-chip is a key aspect of extending the versatility of these devices. To this end we have demonstrated that a variety of device layouts can be used for mixing reagents on-chip, the first step in inducing a chemical reaction, and reaction of amino acids with a fluorescent label is presented.

## Results and Discussion

### Electrical Characteristics.

A device referred to as COCE was prepared, consisting of three channels intersecting at a T-shaped junction, and this was used to study the application of potential to all three solvent reservoirs simultaneously. The device geometry and the labeling scheme we have used for the channel reservoirs, lengths and resistances are shown in Figure 1. As a first step the impedance characteristics of the network were determined. The dc electrical impedance of the intersecting capillaries was modelled as a network of resistors, as is shown in Figure 1b, and the validity of the model was examined.

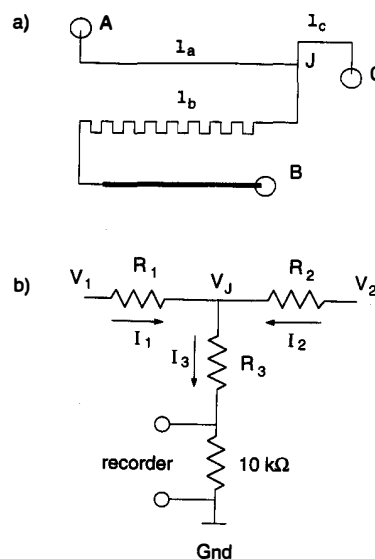


Figure 1. a) Device COCE layout with reservoir labels and channel lengths,  $l_x$ , indicated. Overall dimensions were 2.8 by 7.0 cm. b) Equivalent circuit for device COCE. Subscripts refer generally to the resistances of the 3 channels of the device in a).

Table 1 gives the measured lengths and resistances between the reservoirs and the intersection point, and the ratios of these values to those for the channel length  $l_a$ . Channel length  $l_b$  consisted of both a 23 mm length that was 220  $\mu\text{m}$  wide and a longer 30  $\mu\text{m}$  wide segment. The wider segment length was expressed in terms of an equivalent length of 30  $\mu\text{m}$  wide channel, specifically 3.1 mm, for the calculations. The data show that the resistances  $R_a$ ,  $R_b$ , and  $R_c$  are indeed proportional to the channel lengths within experimental error, as would be expected providing there is no defect in the bonding of the glass cover plate to the etched piece.

Table I. Lengths and Resistances for COCE Device.

	A	B	C
Length (mm)	45	93.3	8
Resistance $G\Omega$	$0.32 \pm 0.02$	$0.72 \pm 0.02$	$0.079 \pm 0.008$
$L/L_a$	1	$2.07 \pm 0.03$	$0.18 \pm 0.01$
$R/R_a$	1	$2.3 \pm 0.2$	$0.25 \pm 0.08$

A,B,C refer to the lengths shown in Figure 1. Error in the lengths is about 0.5 mm. Ratios of lengths relative to  $L_a$ , and resistances relative to  $R_a$  are given.

With two voltage sources and a near ground potential connected to the channels, as illustrated in Figure 1b, the current in each channel and the potential at the intersection are readily expressed using Kirchhoff's Rules where the assumed directions of the currents  $I_1$ ,  $I_2$  and  $I_3$  are shown in Figure 1b. The 10 k $\Omega$  resistor has been omitted, as it is much smaller than  $R_3$ . Solving for  $V_j$  and  $I_3$  gives equations 1 and 2,

$$V_j = (V_1 R_2 R_3 + V_2 R_1 R_3) / (R_1 R_2 + R_2 R_3 + R_1 R_3) \quad (1)$$

$$I_3 = [V_1 R_2 + V_2 R_1] / (R_1 R_2 + R_2 R_3 + R_1 R_3) \quad (2)$$

While in general the potentials  $V_1$  and  $V_2$  can have any polarity, in this study  $V_1$  was always positive and  $V_2$  was always negative. Equation 2 shows that a plot of  $I_3$  versus  $V_1$  will be linear when  $V_2$  is held constant, however  $I_3$  may be positive or negative depending on the potentials applied and the resistance of each channel.

The behavior of the device with potentials applied to all three channels was evaluated according to the scheme indicated in the inset of Figure 2. The current was measured from the potential drop across a 10 k $\Omega$  resistor between ground and reservoir C, with  $V_1$  and  $V_2$  applied to reservoirs A and B, respectively. In this configuration the resistances for eq 1 and 2 were  $R_1 = R_a$ ,  $R_2 = R_b$ , and  $R_3 = R_c$ . The current was indeed linear in  $V_1$  when  $V_2$  was held constant. Figure 2 shows the data obtained for three different values of  $V_2$ . It was possible to calculate the current using eq 2 and the measured channel resistances given in Table 1, and the calculated response is shown as the solid lines in Figure 2. The very good agreement illustrated between theory and experiment shows that the model is accurate. It can be used to determine potentials and currents within a complex network of capillaries when several voltage sources are applied simultaneously.

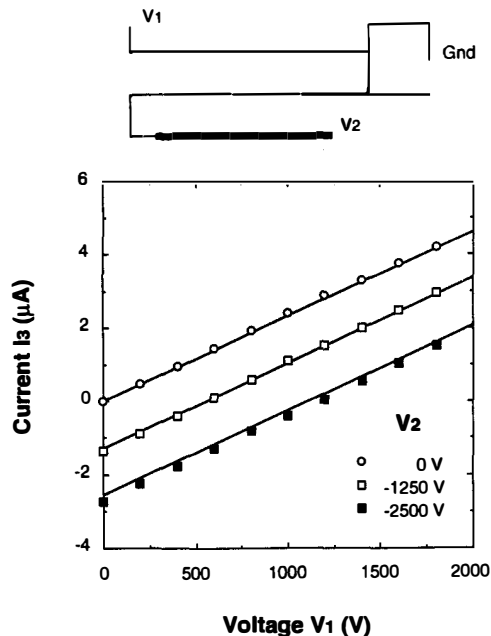


Figure 2. Current as a function of  $V_1$  applied to reservoir A, with the indicated values of  $V_2$  applied to reservoir B. Symbols are for experimental data, solid lines are for current calculated from equation 2 using the data in Table 1. The inset shows the applied potential scheme.

### Leakage Control

We have previously discussed leakage effects at the intersection of channels [3-6]. In particular, if a side channel is left floating while a potential is applied to cause flow in the main channel there will be leakage of solution from the side channel, contaminating the main channel. We have indirectly shown that both convective and diffusion effects contribute to this mixing, or leakage effect at the intersection [3,4]. In previously studied devices with various layouts, the concentration of sample leaking into the main channel was about 3% of that in the sample channel. We show here that these effects can be controlled by applying voltages to several channels simultaneously.

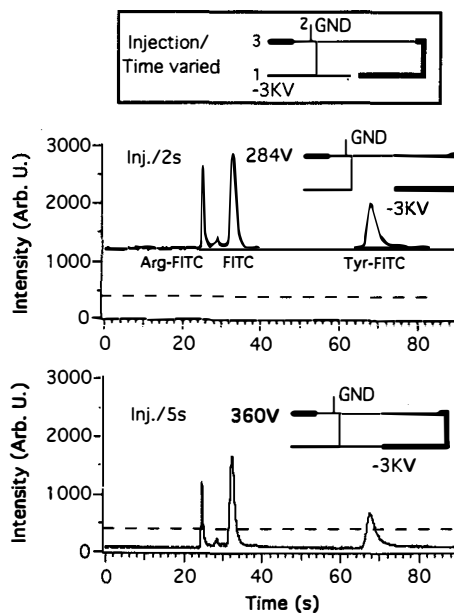


Figure 3. Separation of 20  $\mu$ M Arg-FITC and 40  $\mu$ M Tyr-FITC in 0.054 M carbonate buffer, pH 9.1, with potentials applied to three reservoirs of device Jet-1. The dashed line indicates the background level when the sample channel was instead left floating during separation.

Figure 3 shows data obtained in another device, Jet-1, with the layout indicated in the figure. The resistances of each of the channels of this device were determined as described above. The separation of fluorescein isothiocyanate (FITC) labelled arginine (arg) and tyrosine (tyr) is shown. For these experiments sample solution was present in reservoir 2, which was held at ground. As shown in the diagram at the top, samples were injected across a "double T" injector towards reservoir 1, which was at -3 kV. This injector creates a sample plug in the separation channel about 150  $\mu$ m in length.

To evaluate the ability to control leakage during a separation we applied potentials to reservoirs 2, 3 and 4 simultaneously, as shown in the insets of Figure 3. In the first electropherogram of Figure 3, 284 V was applied to reservoir 3 during the separation. The background fluorescence level was high compared to the background seen when the sample channel was instead left floating (dashed line). From the

measured resistances of the channels the calculated potential at the intersection of the sample and separation channels should be  $-17 \pm 12$  V with 284 V on reservoir 3 and -3 kV on reservoir 4. With the sample channel at ground there should be a net flow out of the sample channel resulting in an increased background, as was observed. When the potential at reservoir 3 increases, the potential at the injection point will eventually become positive, which should electroosmotically push sample solution back towards reservoir 2. As shown in Figure 3, 360 V at reservoir 3 lowered the background fluorescence below the level observed when the sample channel was left floating. The decrease in background showed that the flow in the sample channel was reversed, and establishes that leakage effects can be controlled using applied potentials.

#### Mixing of Solutions Using Voltage Control

When electroosmotic flow is present in a capillary the linear flow velocity,  $v$ , is given by eq 3,

$$v = (\mu_{eo} + \mu_{ep})E \quad (3)$$

where  $\mu_{eo}$  and  $\mu_{ep}$  are the electroosmotic and electrophoretic mobilities, respectively, and  $E$  is the electric field applied.<sup>14</sup>

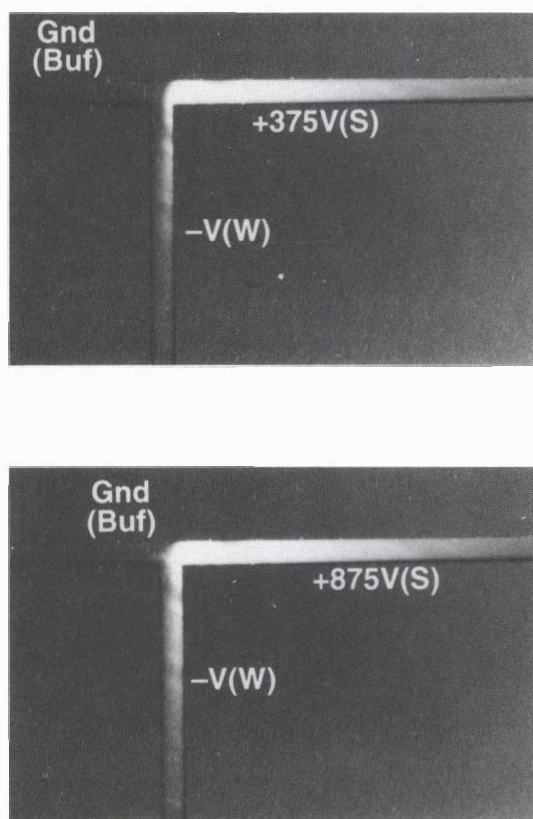


Figure 4. Photomicrographs showing controlled mixing of 10 mM carbonate buffer, pH 9.1, and 100  $\mu$ M fluorescein. Channels are 30  $\mu$ m wide. Flow direction was from the two horizontal channels into the vertical channel.

The overall mobility,  $\mu$ , is the vector sum of these two mobilities, and  $\mu_{eo}$  is generally larger than  $\mu_{ep}$  in absolute terms. The velocity of species  $i$  in each of the channels is given by equations 4-6,

$$v_{i,1} = \mu_i (V_1 - V_J) / l_1 \quad (4)$$

$$v_{i,2} = \mu_i (V_2 - V_J) / l_2 \quad (5)$$

$$v_{i,3} = \mu_i V_J / l_3 \quad (6)$$

where  $V_J$  is given by eq 2, and the various  $v_i$  refer to the velocity of species  $i$  in each channel of length  $l$ . The subscripts 1, 2 and 3 refer to the velocity and channel length associated with the potential sources  $V_1$ ,  $V_2$  and ground, respectively. It is assumed the ionic strength (resistivity) and pH in each channel is the same. These expressions indicate that controlled mixing of solutions should be possible at the intersection of the three channels by adjustment of the potentials  $V_1$  and  $V_2$ .

The COCE device was mounted under a microscope equipped with a camera and the region near the intersection was illuminated with 488 nm light. Any striations visible in the fluorescent dye stream seen in Figure 4 and later photos are due to non-uniformity in the illumination or collection efficiencies, as is the tendency of the intensity to fade at the edges of the photos. Potentials were applied to the three reservoirs with the polarities indicated in Figure 4. Sample (S) was driven towards the waste reservoir (W), while buffer (Buf) was also driven towards waste by the applied potentials. The two solutions mixed downstream of the intersection. The data establish that increasing the potential on the sample reservoir increased the amount of dye relative to buffer downstream of the intersection.

#### Mixing chamber

Figure 5 shows the layout of a device called Jet-3, which has a mixing chamber incorporated. All channels of single line width are 30  $\mu$ m wide, whereas the blackened bulky lines are 300  $\mu$ m wide. The large box between in the figure was used as a mixing chamber. The chamber was 4.5 mm long and 170  $\mu$ m wide. The volume of the chamber, excluding the islands, was about  $3.6 \times 10^{-3}$  mm<sup>3</sup>. The offset between the side channels connected to reservoirs 3 and 4 was 220  $\mu$ m.

Samples were introduced through reservoirs 1 and 2, while the other reservoirs and channels were filled with a buffer. To drive two different sample solutions through the chamber for mixing, a positive potential was applied to reservoir 1, with another applied to 2. Reservoir 3 was at ground. It is likely that diffusion served as the main driving force for mixing once the solutions were within the chamber, but this was not studied in detail. After a fixed time the potentials were switched off. Then the mixture in the chamber was injected through the double T injector. Application of a voltage between reservoirs 4 and 5 then caused the separation.

An example of mixing two solutions followed by their separation is shown in Figure 5. One solution contained fluorescein, while the other contained two labelled amino acids arginine and tyrosine. The bottom of the figure shows that all three components were observed when the sample plug was then separated. As a comparison, an electrophrogram without mixing is also shown in the top of Figure 5. In this case only the amino acid mixture was driven into the mixing chamber and the injector, so the final separation of the sample solution shows there is no fluorescein present.

#### On-column Reaction

Many chemicals are not detected using a fluorescence detection scheme unless they are chemically derivatized with

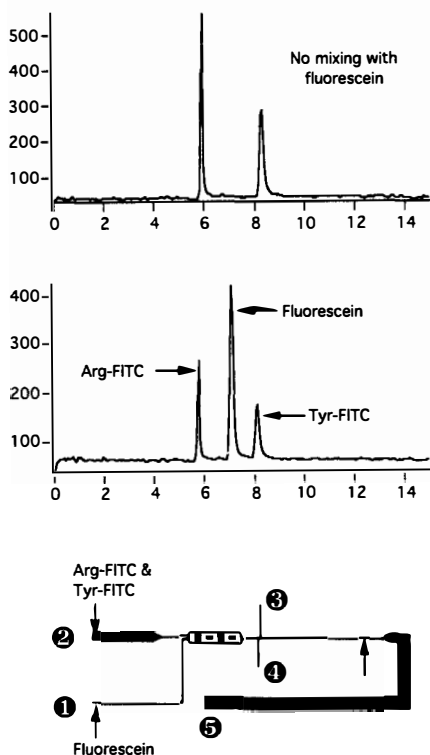


Figure 5. Layout of mixing chamber device. Top shows separation of amino acids, bottom shows separation of fluorescein from amino acids after mixing in chamber.

a fluorescent label. This reaction can be done before a separation is performed, but there are advantages if it is done after the separation. In chromatography this is known as post-column derivatization, in electrophoresis it may be called a post-capillary reaction. This is a chemical reaction performed "on-the-fly" in the sample stream as it moves towards a detector, and it creates a fluorescent product when a sample is present. The most common reagent used for post-column derivatization is *o*-phthalaldehyde (OPA), which reacts with primary amines to create a fluorescent product. It can be used to detect primary amines including amino acids.

We have performed some preliminary experiments with post-capillary reaction within a chip. The OPA reagent stream was delivered into the main separation channel from a side channel under potential control. The reaction was monitored a short distance downstream with a fluorescence detector, fluorescence being excited with a 325 nm laser. Pyrex glass has a fluorescent background at this excitation wavelength, so that the signal to noise performance is limited. Quartz or fused silica will be needed as the device substrate to improve this. Figure 6 shows the detection of an amino acid following reaction with OPA. The efficiency of the electrophoretic separation was degraded by the following OPA reaction, and some noise in the base line is apparent. It appears that these effects are due to the efficiency of mixing at the 90° intersection used in this device. Modifications in the mixer design have been made that are hoped will improve the efficiency and performance. Nevertheless, these results demonstrate that it is possible to perform chemical reactions within the chip that can be used to facilitate a chemical analysis.

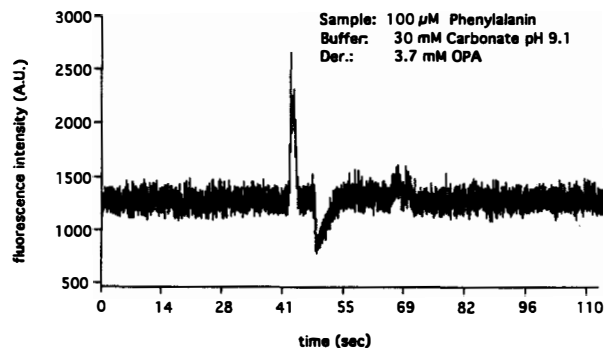


Figure 6. Post-capillary reaction of OPA with phenylalanine, evidenced by fluorescence detection.

## Conclusions

This study has demonstrated the feasibility of using electroosmotic pumping to control flow in a manifold of flow channels without the use of valves. The fluidic control that can be achieved within these valveless devices allows for control of solution mixing, and enables us to effect reactions within the flowing streams. Biologically important molecules such as amino acids can be separated, allowed to react, and then detected, all within the confines of the chip, and within a few seconds. A number of different mixers can be designed to perform these reactions, providing increased flexibility in terms of decreased problems from leakage at intersections and increased reaction times.

## Acknowledgments

We thank Ciba-Geigy and NSERC of Canada for support. Z.F. thanks the Alberta Microelectronic Centre for a graduate fellowship and use of their facilities.

## References

1. W. Olthuis, B.H. van der Schoot, P. Bergveld *Sens. Actuat.* **17**, 279 (1989).
2. S. Shoji, M. Esashi, T. Matsuo *Sens. Actuat.* **14**, 101 (1988).
3. K. Seiler, D.J. Harrison, A. Manz *Anal. Chem.* **65** (1993) 1481.
4. D.J. Harrison, K. Fluri, K. Seiler, Z. Fan, C.S. Effenhauser, A. Manz *Science* **261** (1993) 895.
5. Effenhauser, C. S.; Manz, A.; Widmer, H. M. *Anal. Chem.* **1993**, *65*, 2637-2642.
6. Harrison, D. J.; Manz, A.; Fan, Z.; Lüdi, H.; Widmer, H. M. *Anal. Chem.* **1992**, *64*, 1926-1932.
7. R.J. Gale, K. Ghowsi, in *Biosensor Technology, Fundamentals and Applications*, R.P. Buck, W.E. Hatfield, M. Umana, E.F. Bowder, Eds., Marcel Dekker, New York, **1990**, pp 55-62.

# A Simple Packaging Process for Chemical Sensors

M.E. Poplawski, R. W. Hower, and R.B. Brown  
Department of Electrical Engineering and Computer Science  
Center for Integrated Sensors and Circuits  
The University of Michigan, Ann Arbor, Michigan 48109-2122

## Abstract

A new packaging process for silicon-based chemical sensor arrays has been developed using semiconductor, thick film, and flip-chip technologies. Passive sensors are fabricated on silicon in a semiconductor process compatible with the incorporation of on-chip electronics. Sensor-specific polymer membranes are screen-printed directly onto individual electrode sites. Substrates with flow channels are made from glass using semiconductor process technology. Sensor chips are mounted onto the substrate using a flip-chip approach in which the fluid channels are sealed with a polymer gasket. Electrical contacts between the chip and substrate are made through conductive epoxy bumps. Conductors are brought out to the edge of the substrate, where they are accessible to the next level of system interconnect through a standard board-edge connector.

## Introduction

Among the most promising approaches for reducing the cost of chemical sensing instruments is the use of semiconductor processing technology to mass produce microsensors. This technology has proven capable of producing many types of functional solid-state chemical sensors [1,2,3]. Arrays of such sensors are valuable because they can provide multicomponent analysis, interference compensation, redundancy, and extended dynamic range. Disposable sensor arrays will be at the heart of many future biomedical and industrial chemical analysis instruments. Truly cost-effective arrays, however, require both inexpensive sensors and inexpensive (batch-fabricated) packaging. Ideally, these packages should also protect the sensors during handling, allow simple replacement of the sensor array, and have adequate input/output density. For chemical analysis applications, the packaging scheme must include a fluid channel. As the size of this channel is reduced, the required sample size and cost of calibration are reduced.

## Packaging Issues for Sensors

Sensors fabricated on silicon have many advantages, including reproducibility provided by semiconductor process technology, low cost associated with batch fabrication, process support by the electronics industry, and the capability (in theory) of forming integrated sensors. The integration of such sensors with signal conditioning electronics, micromachined chambers or flow channels, or other types of sensors, however, has historically been hindered by the lack of simple and effective encapsulation, interconnection, and packaging technologies.

Sensor system partitioning can be approached in many ways; in choosing a specific level and method of integration, consideration must be given to application demands, process compatibility issues, and final system cost. An alluring approach for silicon sensors is the combination of sensors and electronics on monolithic chips. Such devices are conceptually capable of improved performance, efficiency, and reliability as compared to equivalent systems assembled from multiple components. Unfortunately, successful incarnations require great developmental efforts, and may suffer from problems associated with the inherent loss of modularity, the virtues of which have been convincingly presented elsewhere [4]. An alternative that has recently received much attention is the adaptation of commercial multichip modules (MCMs) for sensor integration [5]. MCMs interconnect chips through metal lines that have been patterned by thick- or thin-film

methods on a suitable substrate, such as ceramic or silicon. The interconnection between chips and the substrate has been achieved by wire bonding, tape automated bonding, thin metal film, and flip-chip methods.

Conventionally, silicon-based sensors are passivated and tested prior to separating them into individual dice. Sensor chips are attached individually or in groups onto a suitable substrate, such as a printed circuit board or header, and wire bonded to the same to provide electrical I/O connections between the chip and the next level of interconnection. In addition, the substrate serves as a package for the sensor by providing it with mechanical and environmental protection and a path for dissipating heat. Among the many techniques available for chip-to-package attachment are epoxy bonding, anodic bonding, electrostatic bonding, eutectic bonding, low-temperature glass bonding, thermocompression metallic bonding, ultrasonic welding, and laser welding. Chip-to-package interconnect is achieved using the same technologies described previously for realizing chip-to-substrate connections in MCMs.

The packaging requirements for chemical, biological, and biomedical sensors are more complex, since their sensing elements must be in direct contact with the measuring environment, which from an electronic point of view is hostile. This places inordinate demands on the device encapsulation, the final technology needed to package a sensor. Furthermore, most of the processes for chip-to-package attachment are incompatible with chemical sensors. The high temperatures and fields required by these techniques are detrimental to thin film electrode materials, ionophores, and biological layers. The fabrication of these sensors must be partitioned so that all processing which follows the formation of these sensitive elements is low temperature (typically below 50 C). Of the attachment possibilities listed previously, epoxy bonding offers the lowest process temperature and the least thermally induced stress [6].

## A Simple Packaging Process

Successful sensor design calls for the sensor and its packaging be conceived at the same time [4]. The process presented here packages silicon-based chemical sensor arrays with substrates containing flow channels. The package assembly can be fully automated, and the sensor and substrate are manufactured exclusively with batch fabrication technologies.

### *Advances in Flip-Chip Interconnect Technology*

The concept of flipping or inverting chips for mounting offers some distinct advantages for integrated circuits in general. Shorter interconnect distances result in lower inductance and faster signal response. Thermal performance is enhanced in two ways: the conductive bumps provide excellent thermal pathways, and the backside of the chip remains accessible for heat sinking. Array bond pad configurations can be used to increase I/O capacity and to provide uniform power and heat distribution. Because all bonds are formed simultaneously, assembly is quick and efficient. This last point is most important to solid-state sensors. Automated assembly can give sensors packaged in this manner an important economic advantage over those packaged in a more time-consuming and costly process.

As developed nearly 20 years ago, flip-chip interconnect technology has traditionally connected dice to a substrate through raised metallic bumps fabricated on the chip pads or on matching

**Table 1: Semiconductor Process Specifications**

General Features	CMOS Compatible
Interconnect	Polysilicon
Encapsulation	LPCVD Dielectrics
Sensor Site Metals	Gold, Silver, Platinum
Sensor Site Coatings	Platinum Black, Silver Chloride

pads on the substrate. While these solder bumps provide the lowest inductance and resistance path available between chip and substrate, their formation requires special metallurgy and high temperature processes. A chip is placed face down, aligned to the substrate, and the solder bumps are reflowed at a temperature in the range of 300 °C to join the two pads. As mentioned previously, high temperatures are not compatible with many of the polymeric or biological components required by chemical sensors. In addition, due to the chip-face-down feature of this approach, its application to sensor interconnection has been limited. This has been true for chemical sensors in particular, as exposure of the sensing elements to a measuring environment has been difficult to achieve.

Recent advances in the materials used for flip-chip interconnect, however, have made this technology available for chemical sensor design. It is now possible to replace the traditional solder bumps with a conductive polymer, or epoxy. The epoxy can be cured at low temperature, and unlike solder it does not flow when the chip is mated to the substrate, thereby making possible a finer pitch. The advent of precision screen-printing equipment has made deposition of such materials quick, easy, and cost-effective. This simple advance makes obsolete the complex and costly solder bump process without sacrificing electrical performance [7]. The polymer flip chip is an efficient, practical, high-volume production method. With conductive polymer interconnect, flip-chip technology can be part of the solution to the packaging challenges of chemical sensor arrays.

The following process uses the flip-chip approach to electrically connect and physically attach a silicon sensor chip and package substrate. A polymer is used to form a seal to contain solution within the channel and protect the rest of the package. Low temperature curing polymers have been used previously [8] to encapsulate silicon sensors and bond them to glass. Generally, polymers are not capable of providing a hermetic seal because they exhibit a finite permeability to moisture. Attempts at using polymers for encapsulation [9] have shown that, in most cases, poor adhesion to the substrate, rather than polymer permeability, leads to encapsulation failure; one notable exception to this rule is silicone rubber, which has excellent adhesion properties but eventually fails due to interface modification caused by moisture penetration. Nevertheless, for many applications, polymer attachment will yield acceptable lifetimes.

#### Silicon Processing

Sensors are fabricated in silicon using a sequence of CMOS-compatible semiconductor process steps and thick film technology, allowing for the future incorporation of on-chip signal conditioning electronics [10, 11]. The semiconductor process features are

**Table 2: Thick Film Technology for Chemical Sensors**

Structure	Material	Thickness
ISE Contact Layer	Silver Epoxy	50 μm
Ion-Selective Membranes	PVC, Silicone Rubber	150 μm
Enzyme Immobilization	PVA, Hydrogel	75 μm
Flip-Chip Bond Pads	Silver Epoxy	25 μm
Channel Sealant	Silicone	75 μm

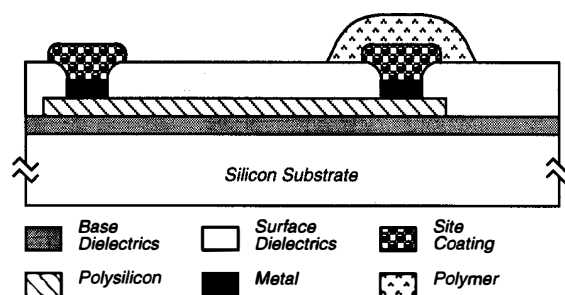


**Fig. 1:** A schematic cross-section of a generic solid-state electrode. The site coating may be either silver epoxy or an electroplated material.

summarized in Table 1. The basic structure of a solid state electrode, as shown in Fig. 1, is quite simple. Polysilicon leads connect the sensors to silver output pads. Sensors are realized by the formation of various metal sites using a lift-off process. Coatings may be applied to selected sensor sites by a wafer-scale electroplating process using a grid, such as the one shown in Fig. 2. Following completion of the semiconductor process sequence, all remaining structures are formed using thick-film technology [12]. Precision screen printing is used to deposit sensor-specific polymer structures, silver epoxy flip-chip interconnect bumps, and the channel sealant, as summarized in Table 2. This example of technology partitioning during sensor fabrication carries over to the proposed package structure. The electrically conductive silver epoxy used to make interconnect bumps and to provide a stable connection between the site metal and membrane material was obtained from Epoxy Technology (Billerica, MA). This material (EPO-TEK® H20E-PFC) is a component in the company's recently patented polymer flip chip (PFC™) process [13], which is capable of stenciling 50 micron high bumps with a 12 mil pitch, as well as 25 micron high bumps with a 8 mil pitch. The epoxy has excellent electrical and thermal conductivity, a suitable viscosity for stencil or screen printing, curing temperatures as low as 50 C, and a pot life of three days.

#### Substrate Processing

Substrates were made from both soda lime and Pyrex (Dow Corning #7740) glass wafers, 100mm in diameter and 62 mils in thickness, obtained from Mooney Precision Glass (Huntington, WV). Soda lime was chosen for its low cost, while Pyrex is a well characterized micromachinable material, and its low temperature coefficient of expansion makes it desirable for applications in which the test solution needs to be heated or maintained at an elevated temperature. Glass substrate fabrication, as shown in Fig. 3, requires just two photolithography steps, followed by a single

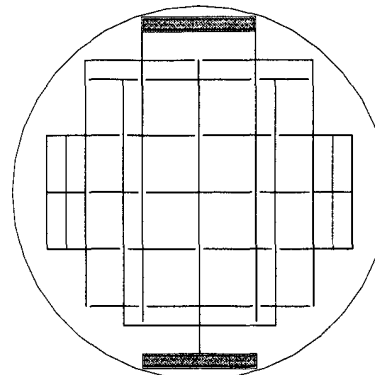


**Fig. 2:** A two-tier wafer-level grid which contacts selected sensor sites for electroplating and supports chip sizes of 5 x 15, 10 x 15, and 15 x 15 mm.



(i.) A clean glass wafer (of thickness compatible with a selected board-edge connector) is first sputter-coated with silver to protect the backside, and photoresist patterned for the flow channel.



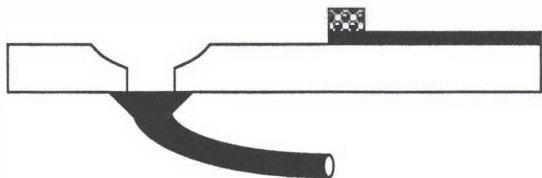
(ii.) The surface is then sputter-coated with silver, which will serve as both a channel mask, and provide substrate interconnect.



(iii.) Following removal of the silver over the flow channel by lift-off, the wafer is patterned for interconnect.



(iv.) With the photoresist left intact to protect the surface of the interconnect metal, the flow channel is etched into the glass using the exposed silver as a mask.



(v.) Finally, all excess silver is etched, thereby defining the interconnect, and the photoresist is removed. Silver epoxy is screen printed at the bond pad points. Holes drilled into the channel serve as fluid ports, to which tubing is attached.

Fig. 3: Process sequence for glass substrate fabrication.

screen printing step. Following semiconductor processing, holes are drilled into each end of the flow channel for fluid ports, and the substrates are partially cut with a wafer saw. Silver epoxy is printed to form the other half of the flip-chip interconnect bond, and the substrates are separated from each other. The substrates have arrays of metal leads, each of which is brought out to the substrate edge in a configuration compatible with standard board-edge connectors.

The two glass materials used etch quite differently, as seen in Fig. 4. The sidewall profile for the Pyrex is straight, at an angle of about  $35^\circ$ , while the soda lime glass profile is rounded. In addition, the etched surface of the soda lime glass channel is uniformly rough, while the floor of the Pyrex channel is almost perfectly smooth. The Pyrex sidewalls, however, do have well-defined erosion marks. Etching processes and mechanisms for these two materials are still being investigated, along with the suitability of their characteristics for various applications.

While glass was successfully used as the substrate material, it is not the only nor perhaps even the most desirable material available. Glass is a good choice for research applications, however, because it is relatively inexpensive, can be etched or drilled, is mechanically stable, has good thermal conductivity, and

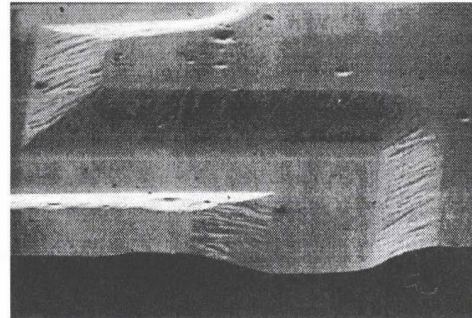
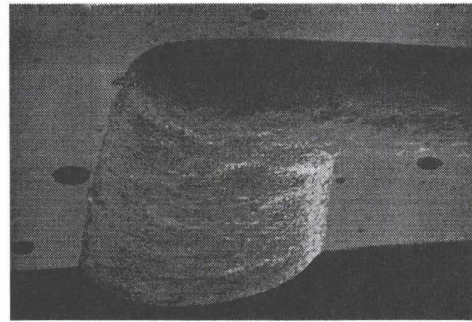


Fig. 4: Flow channels etched in (top) soda lime and (bottom) Pyrex glass.

has very low absorption of gasses. For volume production, substrates made from injection-molded plastic will be more cost-effective. Our packaging process can easily be made compatible with injection-molded substrates by screen-printing the substrate interconnect.

### Packaged Sensor Assembly

Following fabrication of both the sensor chip and glass substrate, the package is ready for assembly, which may be achieved by either of two methods. In both cases, the silicon chip is inverted over the substrate and mounted over the flow channel, as shown in Fig. 5. A polymer which is screen-printed around the perimeter of the sensor array seals the channel by acting as a gasket at the silicon-substrate interface.

In one method, the silicon is embedded within a recess in another (smaller) piece of glass, shown in Fig. 5 as the top mounting plate. The channel sealant and conductive polymer are printed and cured prior to assembly. The top mounting plate is

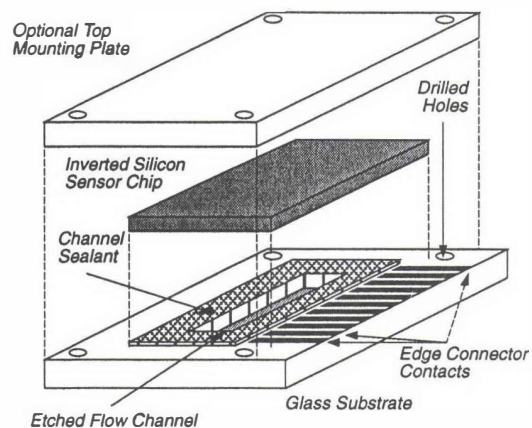
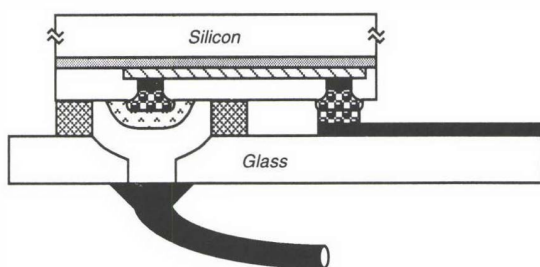


Fig. 5: A schematic of each of the package components and the assembly process (not drawn to scale). The channel sealant is shown on the glass substrate to aid in defining the area it covers; it is actually printed on the silicon chip.



**Fig. 6:** A schematic depiction (not to scale) of the electrical connection and seal between the silicon sensor chip and the glass substrate.

aligned and secured to the glass substrate by small fasteners which slide through pre-drilled holes in both pieces of glass. This structure allows for separation of the chip from the substrate following testing, allowing either piece to be examined or replaced. The clamping force of the fasteners gives this method the advantage of a longer package lifetime during use. The fasteners also simplify alignment of the chip to the substrate.

In an alternative method, the entire package is disposable. The channel sealant and conductive polymer are applied just prior to assembly. After the conductive polymer bumps on both surfaces are aligned through the glass and contacted, the entire package is processed to cure the polymers. For additional protection, the chip may be coated with a moisture resistant encapsulant.

This flip-mounting procedure for assembly both establishes electrical contact between the silicon and the substrate through the conductive polymer bumps, and aligns the sensing sites inside the flow channel, as shown in Fig. 6. The packaged sensor is made ready for use following the attachment of tubing over the ports on the back side of the substrate.

## Results

The process has been successfully applied to the packaging of multi-sensor arrays of solid-state potentiometric, amperometric, and conductimetric sensors fabricated on silicon chips measuring 15 mm x 15 mm. The glass substrates used contain 1-mm wide by 0.25-mm deep flow channels. A finished package is shown in Fig. 7. It interfaces to a standard 20-pin board-edge connector with 100-mil spaced contacts and shielded ribbon cable interconnect.

Ongoing work is focused on studies of the seal integrity and lifetime in both the disposable and reusable versions of the package. Scaling limitations for the sensor structures and the flow channel will also be determined as a function of detection limit and flow rate.

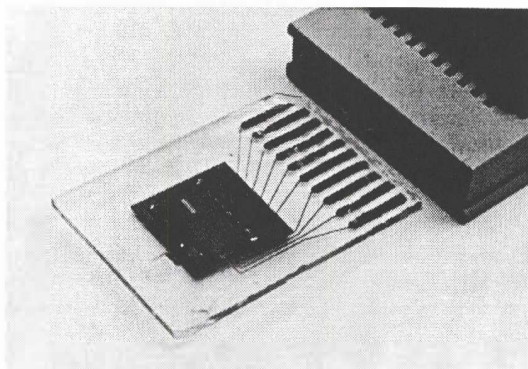


**Fig. 7:** A packaged silicon-based sensor chip, assembled without the top mounting plate. The substrate measures 28 mm x 40 mm and has two flow channels.

## Summary

Chemical sensors have unique packaging, interconnect, and encapsulation requirements. Successful commercialization of these devices will come only when all the design demands are simultaneously and cost-effectively met. System-level partitioning for chemical sensors calls for the integration of a sensing structure which may incorporate delicate polymeric or biological materials, some signal conditioning circuitry for most applications, and packaging that protects the devices without interfering with their operation. The method presented here for achieving this final criterion involves the incorporation of a micromachined channel within the package. By incorporating this element into the packaging design, and using flip-chip technology to seal the channel and electrically connect the sensor to output leads on the package, one can realize devices which meet the needs of both prototype and disposable chemical sensors.

## Acknowledgments

The authors would like to thank Mr. Wayne Bear for technical assistance.

## References

- [1] H. D. Goldberg, G. S. Cha, R. W. Hower, and R. B. Brown, "Batch Fabrication of Solid-State Ion-Selective Sensors," *Technical Digest of The Third International Meeting on Chemical Sensors*, Cleveland, OH, pp. 31-32, September 1990.
- [2] M. E. Poplawski, H. C. Cantor, A. R. Midgley, and R. B. Brown, "Microfabricated Amperometric Biosensors," *Technical Digest of the 6th International Conference on Solid-State Sensors and Actuators*, San Francisco, CA, pp. S1-S3, June 1991.
- [3] P. Jacobs, J. Suls, and W. Sansen, "Design and Performance of a Planar Differential Conductivity Sensor for Urea," *Technical Digest of the 7th International Conference on Solid-State Sensors and Actuators*, Yokohama, Japan, pp. 518-521, June 1993.
- [4] S. D. Senturia and R. L. Smith, "Microsensor Packaging and System Partitioning," *Sensors and Actuators*, vol. 15, pp. 221-234, 1988.
- [5] A. S. Laskar and S. Blythe, "Epoxy Multichip Modules: A Solution to the Problem of Packaging and Interconnection of Sensors and Signal-Processing Chips," *Sensors and Actuators A*, vol. 36, pp. 1-27, 1993.
- [6] H. Reichl, "Packaging and Interconnection of Sensors," *Sensors and Actuators A*, vol. 25-27, pp. 63-71, 1991.
- [7] R. Estes and F. Kulesza (Epoxy Technology, Inc.); P. Delivoria; D. Buczek and G. Riley (HyComp Inc.), "Environmental and Reliability Testing of Conductive Polymer Flip Chip Assemblies," *Presented as the 1993 International Electronics Packaging Conference*.
- [8] R. L. Smith and S. D. Collins, "Micromachined Packaging for Chemical Microsensors," *IEEE Transactions on Electron Devices*, Vol. 35, pp. 787-792, 1988.
- [9] A. Grisel, C. Francis, E. Verney, and G. Mondin, "Packaging Technology for Integrated Electrochemical Sensors," *Sensors and Actuators*, vol. 17, pp. 285-295, 1989.
- [10] W. Sansen, M. Lambrechts, and J. Suls, "Fabrication of Voltametric Sensors with Planar Techniques," *Technical Digest of the 3rd International Conference on Solid-State Sensors and Actuators*, Philadelphia, PA, pp. 334-337, June 1985.
- [11] W. Sansen, D. DeWachter, L. Callewaert, M. Lambrechts, and A. Claes, "A Smart Sensor for the Voltametric Measurement of Oxygen and Glucose Concentrations," *Sensors and Actuators B1*, pp. 298-302, 1990.
- [12] H. D. Goldberg, D. P. Liu, R. W. Hower, M. E. Poplawski, and R. B. Brown, "Screen Printing: A Technology for Partitioning Integrated Microsensor Processing," *Technical Digest of the 1992 Solid-State Sensor and Actuator Workshop*, Hilton Head Island, SC, pp. 140-143, June 1992.
- [13] U. S. Patent #5,074,947; December 1991. "Flip Chip Technology using Electrically Conductive Polymers & Dielectrics".

# CHIP-LEVEL ENCAPSULATION OF IMPLANTABLE CMOS MICROELECTRODE ARRAYS

Jennifer L. Lund and Kensall D. Wise

*Center for Integrated Sensors and Circuits*  
The University of Michigan  
Ann Arbor, MI 48109-2122

## ABSTRACT

This paper discusses the development of chip-level encapsulation for implantable multichannel microelectrode arrays which incorporate CMOS circuitry. The coatings must be capable of protecting the circuitry in-vivo for periods of years while maintaining selective access to recording sites having impedance levels in the megohm range. Stress-compensated, 0.75 $\mu\text{m}$ -thick LPCVD dielectrics provide protection over polysilicon interconnects on the electrode shanks, while 1 $\mu\text{m}$  of planarizing low temperature (420 $^{\circ}\text{C}$ ) oxide (LTO) is used over aluminum interconnect in the circuit areas. Additional layers of PECVD nitride, metal, and silicone can be added as desired over the circuit area for enhanced chemical, electrical, and optical protection. A two-step, self-aligned technique is used to define the recording sites and bonding pad areas. The resulting process allows batch fabrication of the sensors with very high yield and permits operation of both the transducers and circuitry in a challenging environment.

## INTRODUCTION

An important challenge in the integration of sensors with on-chip signal processing circuitry has been providing adequate encapsulation of those circuits against the environment while providing the selective access needed between that environment and the on-chip transducers. For example, chemical sensors must typically be immersed in the analyte, and gas sensors may be required to function in the presence of corrosive gases. Implantable biosensors must operate immersed in salt water at 37 $^{\circ}\text{C}$ , yet must remain robust for years since they cannot be easily replaced once implanted. One possible solution is to separate the sensors physically from the electronics; however this necessitates finding a suitable interconnect (with similar encapsulation requirements), and often results in increased packaging cost and complexity, increased size, added noise, or signal losses. Thus, it is critically important to develop chip-level packaging approaches that permit long-term circuit operation while allowing environmental access for the transducers.

An application for which such encapsulation is particularly important is the development of microelectrode arrays for recording the extracellular potentials generated by individual neurons in the central nervous system [1,2]. Such arrays are important both in studying the information processing techniques employed in biological neural networks and in the development of next-generation neural prostheses such as those for the hearing impaired. Passive recording arrays (without on-chip circuitry) have been successfully applied in many physiological studies [3,4] in both acute and chronic situations. Over 1200 of the probes developed at the University of Michigan have been supplied for such studies, and chronic implants have remained functional for periods of more than one

year. These passive arrays have typically employed from 5 to 24 recording sites, but there is a growing need to integrate much larger numbers of sites into two- and three-dimensional arrays. The use of large numbers of electrodes is primarily important in allowing the user to select sites that are positioned near active neurons. Large arrays demand active electronics on the probe to allow dynamic site selection and provide signal conditioning.

Recently, thin-film recording arrays have been successfully integrated with CMOS circuitry for electronic recording site positioning, amplification of the neural signals, reduction of channel output impedances, and multiplexing of the recordings from selected sites onto a smaller number of output leads [5]. Figure 1 shows a schematic view of such an active probe. The probe substrate is defined by a region of heavily boron-diffused silicon, while the signal processing electronics are fabricated in an undoped well at the base of the probe shank. Thirty-two recording electrodes are connected to the circuitry by 3 $\mu\text{m}$ -pitch polysilicon interconnect lines. A photograph of a completed CMOS recording probe is shown in Fig. 2. A typical probe is 15 $\mu\text{m}$  thick with a shank width from 25-75 $\mu\text{m}$ , depending on the number of electrodes required. Shank lengths vary with the application, but are typically in the 3-4mm range.

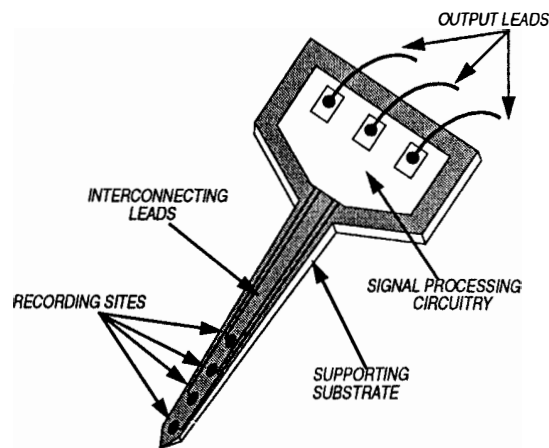


Fig. 1: Schematic drawing of a multi-site multiplexed microelectrode array.

While details of the circuit design and its measured performance have been presented previously [5,6], use of these active probes in-vivo has been limited due to low yield in producing them, which in turn has been related to difficulties in adequately encapsulating them against both the ethylenediamine-pyrocatechol (EDP) etch used to free the probes from the substrate and the saline environment of the body. This paper presents a solution to this problem which is useful for active neural probes and which may be much more broadly applicable to integrated sensors generally.

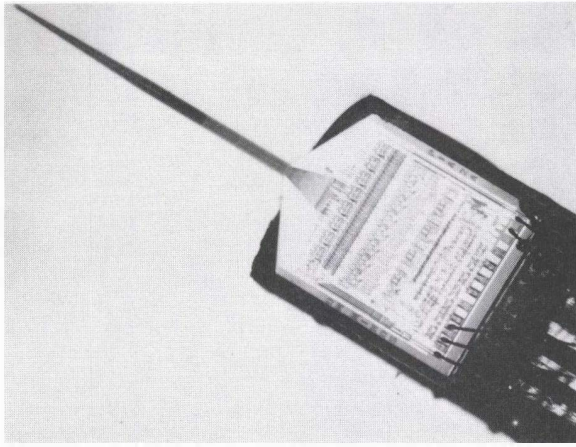


Fig. 2: Photograph of a completed 32-site micromachined CMOS recording probe.

### FABRICATION TECHNIQUES

Active recording microelectrode arrays are fabricated by merging a  $3\mu\text{m}$ , p-well, double-polysilicon/single-metal CMOS process with boron etch-stopped micromachining techniques [5]. First, the wafer is masked for a selective boron diffusion which defines shape of the probe substrate. Then a standard CMOS process sequence is used for the formation of the circuitry and the interconnect to the sites. Finally, the recording sites and bonding pads are defined and the probes are etched free of the substrate. A schematic cross-section of a completed microprobe is shown in Fig. 3.

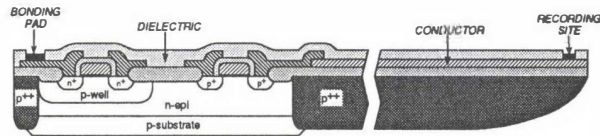


Fig. 3: Schematic cross-section of a neural probe fabricated via the merged CMOS/boron etch-stopped micromachining process.

In order to implement chip-level encapsulation for this structure, a metal-upper dielectric system is required which permits ohmic contact to the circuitry, is metallurgically stable, and yields passivation capable of protecting the sensor under bias in saline over periods of years while allowing selective access to the recording sites. We have investigated three different approaches for creating such a system: i) modification of the circuit metal to permit the use of high-temperature, low-pressure chemical vapor deposited (LPCVD) dielectrics over the entire structure prior to the final etch; ii) encapsulation with LPCVD dielectrics prior to circuit metallization, followed by the use of a noble metal for interconnect and passivation with a polymer after the final etch; and iii) use of standard aluminum circuit metallization combined with lower-temperature dielectric materials.

#### Refractory Metals and Silicides

LPCVD dielectrics have proven very effective in the encapsulation of passive probe structures. Such materials have permitted successful long term implants in-vivo and have maintained sub-picoampere leakage at  $\pm 5\text{V}$  in saline soak tests for more than three years [7]. However, their application over active circuitry demands the use of an interconnect material other than aluminum. The requirements for a circuit metal in a

CMOS process are fairly rigorous: it must have very low sheet resistance and low contact resistance to both  $p^+$  and  $n^+$  silicon and polysilicon; it must be easy to deposit and pattern; it must have good adhesion to the encapsulating dielectrics and must have a compatible thermal expansion coefficient, and it must be able to withstand with any post-deposition chemical cleaning processes or high temperature steps. The most likely candidates for such a material are the refractory metals and their silicides, including  $\text{TiSi}_2$ ,  $\text{MoSi}_2$ ,  $\text{WSi}_2$ , and  $\text{TiN/W}$ . However, previously-reported approaches such as that presented in [8] have not proven feasible in this case. The finite etch rates of  $\text{SiO}_2$  and  $\text{Si}_3\text{N}_4$  in EDP, the need for a diffusion barrier against electrolyte penetration, the need to minimize capacitive coupling to the tissue, and the lack of circuit planarity all mandate the use of a relatively thick ( $>1\mu\text{m}$ ) passivation layer. Additionally, it is essential that the probe shanks be flat to ease penetration and minimize tissue damage; hence, stress-balanced layers of both oxide and nitride are required over the electrode conductors. Therefore, the interconnect used must be able to withstand temperatures up to  $920^\circ\text{C}$  for periods of about three hours. Co-sputtered  $\text{Ti/W}$  and  $\text{WSi}_2$  films were found to crack and peel after 20-40 minutes at these temperatures, despite the use of rapid thermal annealing (RTA) to relieve stress. Even at the minimum temperatures required for the deposition of LPCVD nitride (about  $820^\circ\text{C}$ ) the sheet resistance of  $\text{TiSi}_2$  films escalated rapidly from  $2\Omega/\text{square}$  to over  $4.5\Omega/\text{square}$ , making these films unsuitable for use in CMOS circuitry.

#### "Unpassivated" Metal Approach

The motivation behind the second method was the idea that if the vulnerable parts of the circuit (i.e. the silicon) could be protected from the final EDP etch with high quality dielectrics, then all that would be needed was a circuit metal which was not attacked in EDP. The circuits could then be encapsulated before implantation with a biocompatible polymer such as Dow-Corning Silastic<sup>®</sup> MDX4-4210. There are many metal combinations that are compatible with EDP, including  $\text{Cr/Au}$ ,  $\text{Ti/Pt/Au}$ , and  $\text{Ti/Ir}$ . We have used all of these successfully in other applications; however, we felt this approach to be less reliable than the use of an inorganic thin film, since the sole protection for the circuitry would come from the polymer layer. This method also does not allow for the deposition of a conductive optical shield which could be grounded to the probe substrate. Accordingly, while this option could probably work successfully, we elected to pursue the method described below.

#### Low Temperature Dielectrics

A low stress ( $<100\text{MPa}$ , tensile),  $350^\circ\text{C}$  plasma-enhanced chemical vapor deposited (PECVD) nitride was developed for use over aluminum metallization; however this approach was unsuccessful due to high defect densities and inadequate step coverage in these films. In PECVD, the reaction is catalyzed in the gas phase by the plasma and there is little mobility of the reacted species once they have settled due to the low surface temperature of the wafer. We found that PECVD films were subject to minute seams around contact and metal edges (Fig. 4) which allowed EDP to attack the underlying silicon (Fig. 5). In order to obtain acceptable step coverage, it was necessary to perform several successive depositions and planarizing etch-backs. This process was both time and labor intensive and still resulted in poor yield. While PECVD films may make good inter-metal dielectrics and encapsulants for other applications, we were unable to apply them successfully to the probes, where both 1.5 hour EDP etches and long-term exposure to salt water under bias tend to reveal such problems very quickly.

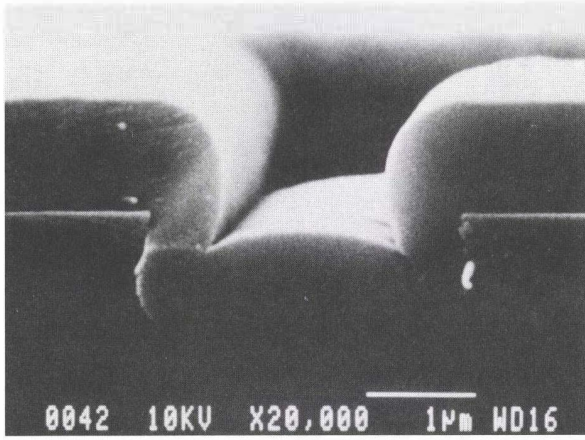


Fig. 4: Seam formed at the edge of a  $1\mu\text{m}$  step by a thick PECVD nitride film.

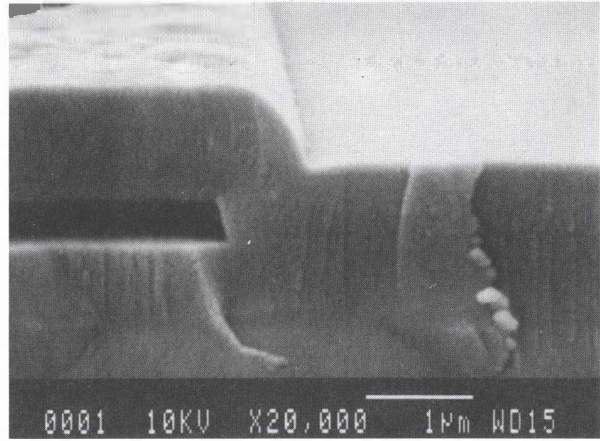


Fig. 6: Low temperature oxide (LTO) passivation of an aluminum interconnect line.

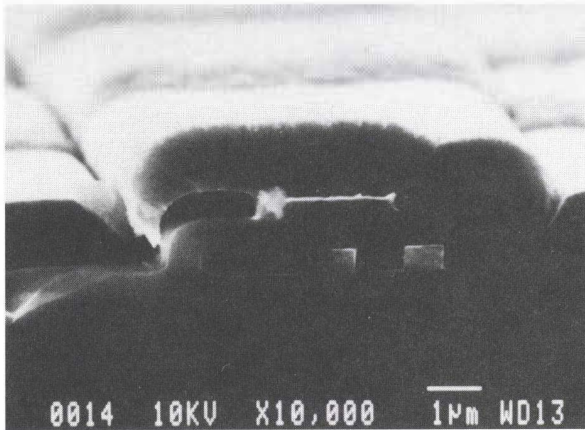


Fig. 5: Attack of the silicon substrate due to inadequate step coverage of PECVD films.

The final option investigated was the use of low temperature oxide (LTO) deposited at  $420^\circ\text{C}$ . Initial experiments showed that it exhibited low stress and etch rates below  $500\text{\AA}/\text{hr}$  in EDP while providing excellent coverage over step heights of  $1\mu\text{m}$  as indicated by the SEM photograph in Fig. 6. A comparison of the relevant properties of LPCVD, PECVD, and LTO films is cataloged in Table 1. Several active probe wafers have been passivated with LTO and etched in EDP with no significant attack of the circuit areas.

### REVISED PROCESS FLOW

Some revision of the overall probe process flow was necessary in order to incorporate LTO encapsulation. In the new process flow, electrode conductors are routed in polysilicon (instead of metal), which is deposited and patterned at the same time as the gate material so that the leads can be encapsulated by LPCVD  $\text{SiO}_2$  and  $\text{Si}_3\text{N}_4$ . The higher resistance of the electrode conductors is not of concern here since they are connected directly to MOS inputs and draw no current. Prior to metallization, the entire probe is passivated with the LPCVD oxide/nitride combination; then contacts to the circuitry are opened. The electrode sites are opened at the same time. This is followed by deposition and patterning of aluminum metallization; however no metal is retained over the electrode sites. A thick blanket ( $1\mu\text{m}$ ) of LTO is deposited, and then

Film Type	Temp. [ $^\circ\text{C}$ ]	$N_f$	Stress [MPa]	BHF Etch Rate [ $\text{\AA}/\text{min}$ ]	EDP Etch Rate [ $\text{\AA}/\text{hr}$ ]
LPCVD $\text{SiO}_2$	920	1.460	-320	1570	300
LPCVD $\text{Si}_3\text{N}_4$	820	2.010	1440	<50	400
PECVD $\text{SiO}_x$	300	1.463	-220	3125	N/A
PECVD $\text{Si}_x\text{N}_y$	350	1.890	-100	280	550
LTO	420	1.455	-130	4070	485

Table 1: Comparison of measured properties of various dielectric films.

approximately  $7500\text{\AA}$  are selectively removed over the shanks and bonding pad areas. Another mask is used to remove the remaining  $2500\text{\AA}$  of LTO and inlay a noble metal (gold or iridium) in the bonding pads and sites. This two-step, self-aligned process allows contact to be made to two different materials (aluminum and polysilicon) which have two different upper dielectric structures (LPCVD + LTO or just LTO) with the same mask. Details are shown in Figs. 7 and 8. Also, PECVD nitride is frequently used on top of the LTO for additional low-temperature passivation as desired. Finally, a gold shield is placed over the circuit areas for use as an additional chemical barrier and an electrical and optical shield.

### TEST RESULTS

Figure 9 shows the in-vitro response of one of the eight preamplifiers as well as the multiplexed output signal from all eight channels of one of the 32-site active probes realized with the above process. Reference "frame marks" are inserted in the 9<sup>th</sup> window of each cycle to allow external regeneration of the on-chip clock and demultiplexing of the neural signals. The probe circuitry is fully functional with high yield. Figure 10 shows single unit potentials recorded with the device in rat cerebral cortex.

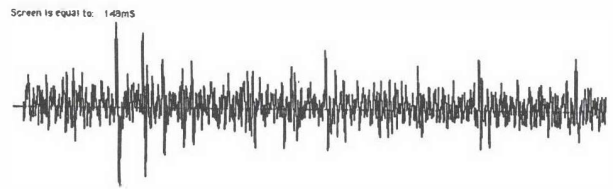


Fig. 10: Spontaneous neural activity recorded from rat cerebral cortex using a 32-site active electrode array.

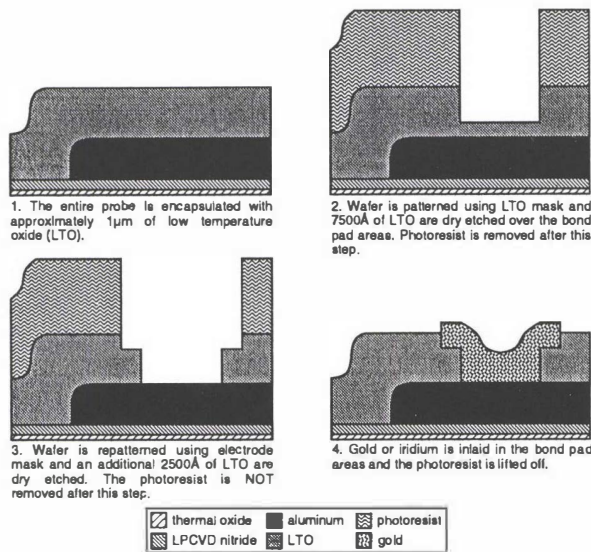


Fig. 7: Formation of bonding pads.

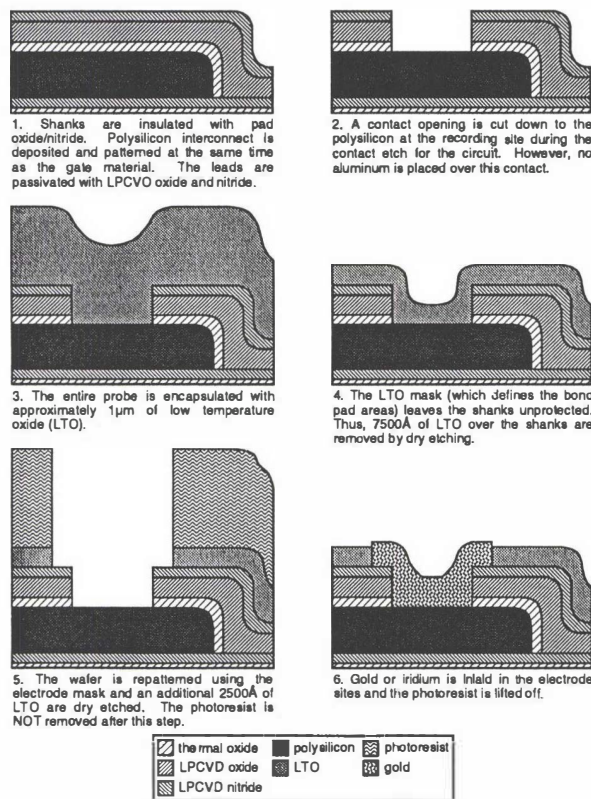


Fig. 8: Formation of recording sites.

In addition to ongoing in-vivo studies of cell localization and migration with the active probes, other in-vitro tests of this encapsulation scheme are underway. Special passive structures, similar to passive ribbon cable interconnects currently under soak, have been fabricated. These designs use aluminum interconnect and varied combinations of LTO, PECVD nitride, and gold for encapsulation. These structures are being tested for comparison of the efficacy of these films under bias in solution versus the LPCVD dielectrics used over the shanks and on passive probes.

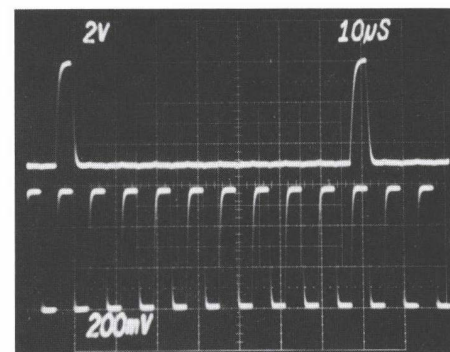
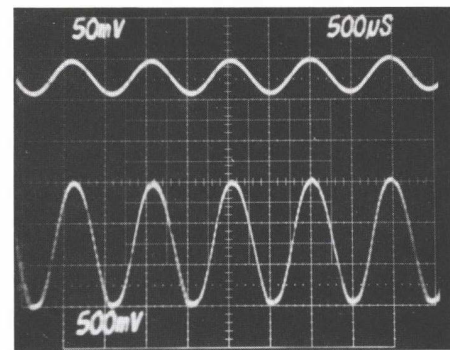


Fig. 9: Preamplifier output (top) and multiplexed data channel (bottom) from an active probe fabricated using the modified process flow.

### Acknowledgments

The authors wish to acknowledge the support of the Neural Prosthesis Program, National Institutes of Health (NINDS), under contract NIH-NINCDS-NO1-NS-4-2303, as well as the support of the AT&T Foundation Ph.D. Scholars Program. The assistance of Mr. Michael Putty of the GM Research Laboratories in LTO deposition is also very much appreciated.

### REFERENCES

- [1] K. Drake, K. Wise, J. Farraye, D. Anderson, and S. BeMent, "Performance of Planar Multisite Microprobes in Recording Extracellular Single-Unit Intracortical Activity," *IEEE Trans. Biomed. Engr.*, 35, pp. 719-732, September 1988.
- [2] K. Najafi, K. Wise, and T. Mochizuki, "A High-Yield IC-Compatible Multichannel Recording Array," *IEEE Trans. Electron Devices*, 32, pp. 1206-1211, July 1985.
- [3] R. Carter and J. Houk, "Multiple Single-Unit Recordings from the CNS Using Thin-Film Electrode Arrays," *IEEE Trans. Rehab. Engr.*, to be published.
- [4] G. Buzsaki, Z. Horvath, R. Urioste, J. Hetke, and K. Wise, "High-Frequency Network Oscillation in the Hippocampus," *Science*, vol. 256, pp. 1025-1027, May 1992.
- [5] J. Ji and K. Wise, "An Implantable CMOS Analog Signal Processor for Multiplexed Microelectrode Recording Arrays," *Digest Solid State Sensor and Actuator Workshop*, pp. 107-110, June 1990.
- [6] J. Ji and K. Wise, "An Implantable CMOS Circuit Interface for Multiplexed Microelectrode Recording Arrays," *IEEE J. Solid-State Circuits*, SC-26, pp. 433-443, March 1992.
- [7] J. Hetke, J. Lund, K. Najafi, K. Wise, and D. Anderson, "Silicon Ribbon Cables for Chronically-Implantable Microelectrode Arrays," *IEEE Trans. Biomed. Engr.*, to be published April 1994.
- [8] W. Yun, R. Howe, and P. Gray, "Surface Micromachined, Digitally Force-Balanced Accelerometer with Integrated CMOS Detection Circuitry," *Digest Solid State Sensor and Actuator Workshop*, pp. 126-131, June 1992.

# Piezoelectric Cantilever Microphone and Microspeaker

Seung S. Lee<sup>†</sup>, R.P. Ried<sup>\*</sup>, and Richard M. White<sup>\*</sup>

Berkeley Sensor & Actuator Center  
An NSF/Industry/University Cooperative Research Center  
<sup>†</sup>Department of Mechanical Engineering  
<sup>\*</sup>Department of Electrical Engineering and Computer Sciences  
University of California, Berkeley, CA 94720

## Abstract

A micromachined piezoelectric cantilever transducer, which works both as a microphone and as a microspeaker, has been fabricated and tested. The  $2000 \times 2000 \times 3 \mu\text{m}^3$  cantilever has a zinc oxide (ZnO) piezoelectric thin film on a supporting layer of low-pressure chemical-vapor-deposited (LPCVD) low-stress silicon nitride. A highlight of the fabrication process which may also be relevant for other micromachined structures is the technique for producing a flat, multilayer cantilever. The measured microphone sensitivity is fairly constant at  $2 \text{ mV}/\mu\text{bar}$  in the low frequency range and rises to  $20 \text{ mV}/\mu\text{bar}$  at the lowest resonant frequency of 890 Hz. The  $2 \text{ mV}/\mu\text{bar}$  sensitivity is the highest reported to date for a microphone with a micromachined diaphragm. When measured into a  $2 \text{ cm}^3$  coupler with 4 V (zero-peak) drive, the microspeaker output sound pressure level (SPL) is 75 dB at 890 Hz. It increases to approximately 100 dB SPL at 4.8 kHz with 6 V (zero-peak) drive. The measured microphone frequency response agrees well with the results of an ABAQUS simulation.

## Introduction

There is growing interest in the micromachining of acoustic transducers, chiefly microphones [1,2,3]. Among the advantages of micromachining over conventional fabrication are improved dimensional control, extreme miniaturization, the ability to integrate with on-chip circuitry, and potential low-cost as a result of batch processing.

Microphones are basically pressure sensors that detect airborne sound pressures that are ten orders of magnitude lower than ambient pressure. Hence, a microphone needs an extremely compliant diaphragm to have an acceptable sensitivity [4].

In this article, we present a piezoelectric transducer built on a micromachined *cantilever*. Earlier micromachined microphones had diaphragms that were clamped on all four edges. In comparison, the cantilever dia-

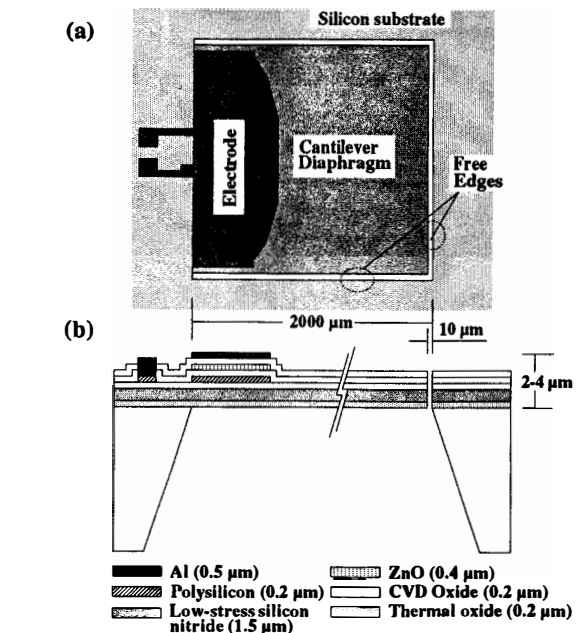


Figure 1. (a) Top view and (b) cross section of the piezoelectric cantilever microphone and microspeaker.

phragms are much more compliant. The cantilever is free from the tension found in clamped-clamped diaphragms, which decreases the transducer response [5]. Use of the cantilever produces a microphone with a sensitivity greater than all previously reported microphones with micromachined diaphragms [6,7]. In addition, when the device is driven electrically as an output transducer (microspeaker), the relatively large deflections of the free end produce significant acoustic output.

## The Device and Its Fabrication

Figure 1 shows a top view and a cross-section of the cantilever transducer. Figure 2 shows the process flow which has three main parts: diaphragm formation (steps 1-4), frontside processing (steps 5-11), and releasing the free edges of the cantilever (steps 12-14). The chief processing challenge is to fabricate a *flat* thin multilayer cantilever diaphragm. For this we need a cantilever having a

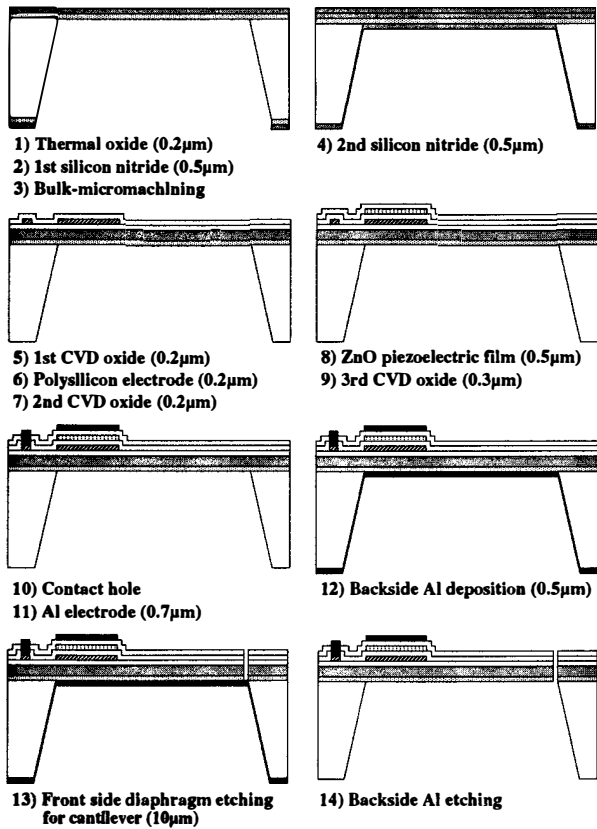


Figure 2. Microfabrication process flow.

controlled distribution of residual stress. This is achieved through a two-step silicon nitride deposition for reasons that are explained in the next section.

The fabrication starts with 4-inch silicon wafers covered with a 0.2- $\mu\text{m}$ -thick thermal oxide. The first 0.5- $\mu\text{m}$ -thick LPCVD low-stress silicon nitride layer is deposited at 835 °C and 300 mTorr from a vapor having a 6:1 volume ratio of dichlorosilane ( $\text{SiH}_2\text{Cl}_2$ ) to ammonia ( $\text{NH}_3$ ). An orientation-dependent etchant (KOH or EDP) is used to release the silicon nitride diaphragm by etching the silicon wafer from the backside. A second 0.5- $\mu\text{m}$ -thick silicon nitride layer is deposited on both sides of the diaphragm (reactant gas ratio 4:1).

The 0.2- $\mu\text{m}$ -thick LPCVD polysilicon electrodes are then formed on the diaphragm over a 0.2- $\mu\text{m}$ -thick low-temperature oxide (LTO) layer. A 0.5- $\mu\text{m}$ -thick layer of ZnO is then RF-magnetron sputtered onto a second, 0.2- $\mu\text{m}$ -thick LTO layer. The wafers are annealed for 25 minutes at 950 °C after the polysilicon and LTO depositions. After a 0.3- $\mu\text{m}$ -thick LTO layer is laid down to encapsulate the ZnO and contact windows have been opened, aluminum (Al) is sputter-deposited and patterned to form the top electrode [8].

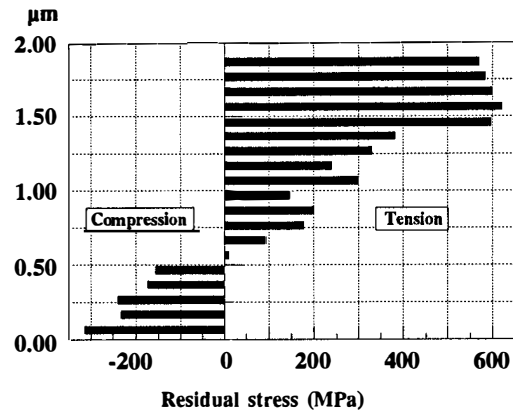


Figure 3. Residual stress vs. distance from the bottom of low-stress silicon nitride layer (835 °C and 4:1 volume ratio of reactant gas).

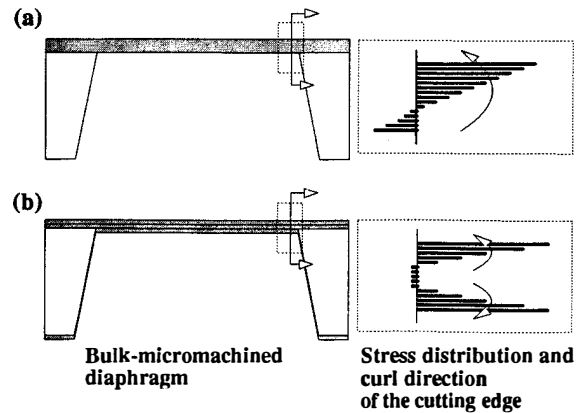
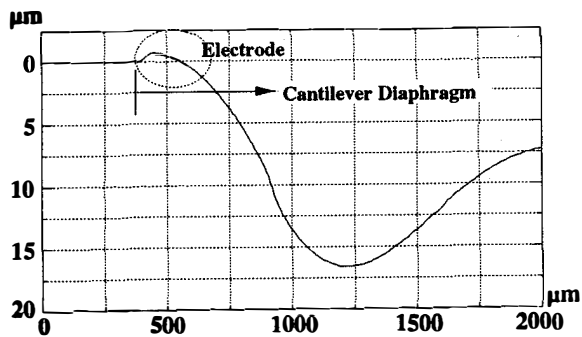


Figure 4. Stress distribution and curl direction of the cut edges (indicated by the arrows) of (a) the conventional silicon nitride diaphragm, and (b) the modified silicon nitride diaphragm.

A 0.5- $\mu\text{m}$ -thick Al film is sputter-deposited on the backside of the diaphragm in order to support the diaphragm during the frontside cutting process that produces the cantilever. The thickness of the backside Al is restricted to a value that depends on the stresses of the multilayer diaphragm, since Al has its own residual tensile stress. Thicker Al layers (roughly 1.5  $\mu\text{m}$  or more) are found to break the diaphragm because of their high tensile stress, and thinner Al layers are found not to support the diaphragm during the frontside cutting process.

The cantilever is released by using an LTO wet etch and silicon nitride dry etch ( $\text{SF}_6/\text{He}$ ) of the frontside multilayer diaphragm, followed by a wet etch ( $\text{K}_3\text{Fe}(\text{CN})_6/\text{KOH}$ ) of the underlying, supporting Al layer.



**Figure 5.** Profile of a completed transducer as measured by a profilometer.

The wafers are diced with a diamond saw, and individual microphones are glued and wire-bonded to ceramic packages which have a 3 mm-diameter ventilation hole formed by a diamond drill. The ventilation hole can be left open during testing or sealed to form a 15 mm<sup>3</sup> back-cavity volume.

### Fabricating Flat Transducers

Transducers fabricated with designs prior to that shown in Fig. 2 were significantly curled upward or downward. This is undesirable because it decreases the effective device area upon which the sound wave impinges (microphone) or which launches the sound wave (microspeaker).

The downward curl is due to the high residual compressive stress of the ZnO layer. It was found that the curl is considerably reduced by patterning the ZnO so that it is not contiguous to the silicon-support portion of the cantilever.

The upward curl arises because of the *gradient* of residual stress of the silicon nitride layer, which is illustrated in Fig. 3. The stress profile of Fig. 3 has been obtained by successively removing thin layers of the film and measuring wafer curvature [9]. The stress distribution in the silicon nitride seems to be related to annealing during the deposition at 835 °C. The earlier a layer is deposited, the longer this layer is annealed. The gradient in the residual stress generates a moment that causes the upward curl, as illustrated in Fig. 4(a)

Figure 4(b) shows the solution used in the process flow of Fig. 2 in order to produce a cantilever with a symmetric stress distribution in the silicon nitride. The initial 0.5- $\mu\text{m}$ -thick silicon nitride layer is deposited with a 6:1 reactant gas ratio to form the diaphragm prior to bulk-micromachining. The low (50 MPa) residual tensile stress of the thin, initial diaphragm makes it more resistant to rupture [10].

After bulk-micromachining, the second 0.5- $\mu\text{m}$ -thick low-stress silicon nitride is deposited with a 4:1 gas ratio. The larger tensile stress (250 MPa) of the second layer is used to maintain diaphragm flatness during subsequent processing steps. Since the second silicon nitride deposition occurs on both sides of the original diaphragm, the stress gradients become symmetric. The first silicon nitride layer is also annealed during the second layer deposition and its stress distribution becomes negligible. The result is a relatively flat cantilever. This technique of producing a flat cantilever despite the stress gradient in the component films may have applications to other micro-machined structures.

Figure 5 shows the profile of a completed transducer as measured by a Tencor Alphastep 200 profilometer. The out-of-plane deflection of the transducer is less than 20  $\mu\text{m}$ . We have verified with non-contact optical measurements that the profile of Fig. 5 is accurate to within experimental error of 3  $\mu\text{m}$ . Across a given wafer, the majority of the transducers had out-of-plane deflections below 35  $\mu\text{m}$ .

### **Design and Simulation**

In order to understand the device characteristics and process of designing for specific desired responses, we need a reliable model of the device. We use a combination of finite-element simulations and analytical modeling to calculate the microphone output voltage as a function of the frequency of the acoustic excitation.

Using ABAQUS, we have determined the strains developed in the cantilever at different excitation frequencies and integrated the strain across the electrode area. Since we have not yet modeled the acoustical damping of the microphone, we chose a damping factor for ABAQUS such that the simulated and measured quality factor  $Q$ s of the lowest resonant peaks would be identical.

The microphone output voltage at a particular frequency is proportional to the integral of the strains generated across the assumed electrode area. In this electrode design process, the equivalent circuit model is also considered, which includes the effects of capacitive loading [8]. Through the design iterations, the electrode pattern shown in Fig. 1(a) was found to produce the best low-frequency response. Figure 6 shows the simulated microphone frequency response (curve A) of the transducer with a low-frequency sensitivity of 3.8 mV/ $\mu\text{bar}$ .

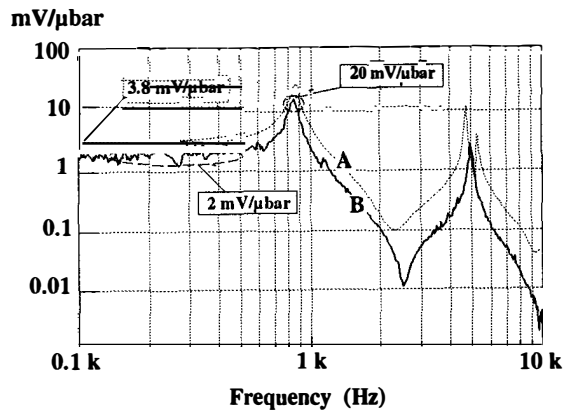


**Figure 6.** Measured microphone frequency response (curve B) of the transducer compared with the ABAQUS simulation result (curve A) from 100 Hz to 10 kHz.

### Experimental Results

#### Microphone Testing

The microphone frequency response has been measured in an electrically-shielded anechoic chamber containing a calibrated microphone (B&K 4135). The test and reference microphones are placed at the same distance from the source of acoustic signals, which is the end of a 6.5 mm diameter tube that leads into the chamber from an external conventional loudspeaker.

Figure 6 shows the typical measured microphone sensitivity (curve B) of the cantilever device when tested without backing. The microphone sensitivity is fairly constant at 2 mV/μbar in the low frequency range and rises to 20 mV/μbar at the lowest resonant frequency of 890 Hz. The 2 mV/μbar is the highest reported for a microphone with a micromachined diaphragm. The low-frequency sensitivity and the resonant frequencies are in good agreement with the simulation result. Independent testing shows that backing with a 15 mm<sup>3</sup> cavity will reduce the low-frequency sensitivity by about 8 dB, to around 0.8 mV/μbar.

#### Microspeaker Testing

We measured the acoustic output of the cantilever device into a 2 cm<sup>3</sup> coupler with a calibrated B&K microphone. Figure 7 shows the microspeaker output in the 100 Hz to 10 kHz frequency range with 4 V(zero-peak) input drive. The resonant frequencies coincide with those of the microphone response at 890 Hz and 4.8 kHz, as we expect. Figure 8 shows the sound pressure level produced by the microspeaker in the 1 kHz to 50 kHz frequency range. Figure 9 shows that the output pressure is propor-

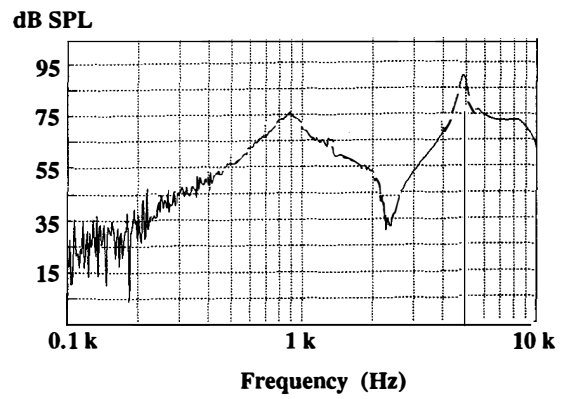


**Figure 7.** Microspeaker output pressure into a 2 cm<sup>3</sup> coupler in the 100 Hz to 10 kHz range with 4 V(zero-peak) drive.

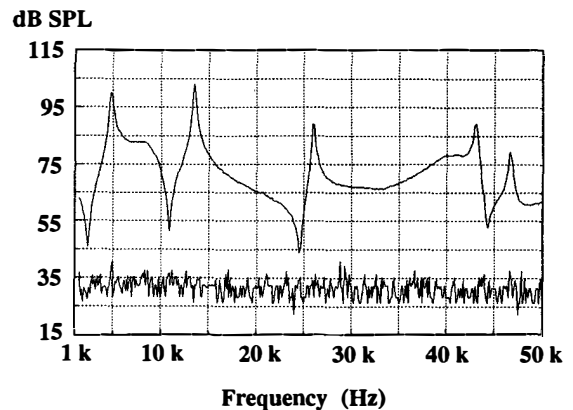


**Figure 8.** Microspeaker output pressure into a 2 cm<sup>3</sup> coupler in the 1 kHz to 50 kHz range with 4 V(zero-peak) drive. The lower trace is the noise level of the B&K 4135 reference microphone.

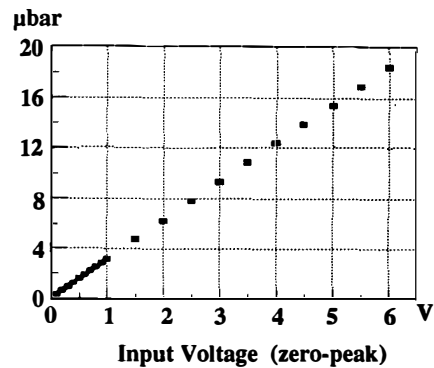


**Figure 9.** Microspeaker output pressure vs. input voltage measured at 4.8 kHz.

tional to the input drive voltage from 0.1 to 6 V(zero-peak) at 4.8 kHz. The highest output pressure corresponds to approximately 100 dB SPL.

## Conclusions

A piezoelectric micromachined cantilever microphone and microspeaker has been fabricated and tested. By controlling the distribution of residual stress, we were able to make 2000  $\mu\text{m}$ -long cantilevers whose maximum out-of-plane deflections were typically no more than 35  $\mu\text{m}$ . The microspeaker output is proportional to the input drive, and rises to approximately 100 dB SPL at 4.8 kHz and 6 V (zero-peak) drive. The microphone sensitivity is fairly constant at 2 mV/ $\mu\text{bar}$  in the low frequency range, and is 20 mV/ $\mu\text{bar}$  at the lowest resonant frequency of 890 Hz. The high microphone sensitivity and the high microspeaker output are due to the high compliance of the cantilever diaphragm. Future work will include modelling of acoustic leakage around the perimeter of the cantilever into the back cavity volume.

## Acknowledgment

The authors thank K. Voros, B. Hamilton, and the staff in the Microfabrication Lab at the University of California, Berkeley for their assistance on the fabrication process. Portions of this work were performed as part of the Program on Advanced Technology for the Highway (PATH) of the University of California, in cooperation with the State of California, Business and Transportation Agency, Department Transportation, and the United States Department of Transportation, Federal Highway Administration.

## References

1. G.M. Sessler, "Acoustic Sensors," *Sensors and Actuators*, A25-A27, pp. 323-330, 1991.
2. J. Bergqvist and F. Rudolf, "A New Condenser Microphone in Silicon," *Sensors and Actuators*, A21-A23, pp. 123-125, 1990.
3. E.S. Kim, J.R. Kim, and R.S. Muller, "Improved IC-compatible Piezoelectric Microphone and CMOS Process," *International Conference on Solid-State Sensors and Actuators, Transducers '91*, San Francisco, California, pp. 270-273, June, 1991.
4. W. Kuhnel and G. Hess, "Micromachined Subminiature Condenser Microphones in Silicon," *Sensors and Actuators*, A32, pp. 560-564, 1992.
5. R.P. Ried, E.S. Kim, D.M. Hong, and R.S. Muller, "Residual-Stress Compensation in Clamped-Clamped Micromachined Plates," *Micromechanical Systems, ASME Winter Annual Mtg.*, Anaheim, California, pp. 23-32, Nov., 1992.
6. E. Graf, W. Kronast, S. Duhring, B. Muller, and A. Stoffel, "Silicon Membrane Condenser Microphone with Integrated Field-Effect Transistor," *Sensors and Actuators*, A37-A38, pp. 708-711, 1993.
7. T. Bourouina, S. Spirkovitch, F. Ballieu, and C. Vauge, "A New Condenser Microphone with a p+ Silicon Membrane," *Sensors and Actuators*, A31, pp. 149-152, 1992.
8. E.S. Kim, "Integrated Microphone with CMOS Circuits on a Single Chip," *Ph.D Thesis*, EECS Dept., University of California, Berkeley, May, 1990.
9. P. Krulevitch, G.C. Johnson, and R.T. Howe, "Stress and Microstructure in Phosphorous Doped Polycrystalline Silicon," *Mat. Res. Soc. Symp. Proc.*, vol. 276, pp. 79-84, 1991.
10. Misao Sekimoto, Hideo Yoshihara, and Takashi Ohkubo, "Silicon Nitride Single-layer X-ray Mask," *J. Vac. Sci. Technol.*, vol 21(4), pp. 1017-1021, 1982.

## Batch-Fabricated Area-Efficient Milli-Actuators

L.-S. Fan, S. J. Woodman, R. C. Moore, L. Crawforth, T. C. Reiley,  
M. A. Moser

IBM Research Division  
Almaden Research Center  
650 Harry Road, San Jose, CA 95120-6099

### Abstract

We report here a one-mm-sized microfabricated actuator with linearized output capability of 0.2 mN when driven at 60 Volts. This is achieved through an area-efficient design, a high-aspect ratio microfabrication process, and a large signal linearization scheme. The area-efficient design allows full utilization of the chip area for energy conversion. The high-aspect ratio microfabrication process allows the generation of structures an order of magnitude larger than conventional structures in all three dimensions, while still retaining the minimum in-plane features. The large signal linearization scheme permits linearized force output with driving voltages as large as the biasing voltage. This increased output force enables the batch-fabricated microactuators to be used in many new, practical applications in which the microactuators are required to move an additional load, as well as their own mass.

### Introduction

Many practical applications, such as attaching microactuators on the back of magnetic recording sliders for improved tracking performance, require that the microactuator move milligram loads at 10's of G's of acceleration. For dynamic performance, it is also important that any nonlinearity in the device be minor to permit the closing of a high bandwidth feedback loop. Achieving this goal requires a linearized driving force of a few hundreds  $\mu\text{N}$  generated in a mm-sized area. This requirement on the linearized force output from the microactuator is four orders of magnitude larger than the conventional force output from a typical polysilicon device. Here, we will show how one can achieve the goal through an area-efficient design, a high-aspect ratio microfabrication process, and a large signal linearization scheme.

### Area-efficient Electrostatic Microactuators

In addition to the achievable energy density, the effectiveness of an actuator will depend on how efficiently the device utilizes the chip area for energy conversion, along with other constraints such as position independent output, stroke range etc.. Constant in-plane force in the mN range, with a few  $\mu\text{m}$  of stroke can be generated in a microfabricated electrostatic structure assuming full utilization of the available area such as the electrical tree structure [1-2] shown in Fig. 1. In this approach, energy conversion cells populate the whole area and efficiently convert electrical energy into force or torque. The electrodes in Fig. 1 are grouped into three sets, each with three levels of hierarchy: trunk, branch, leaf. Each level branches out from a higher level, and the scheme

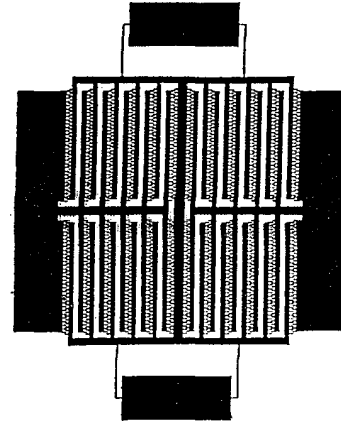


Figure 1. Top View of an area-efficient electrode tree structure with the air gaps between electrodes being less than 2  $\mu\text{m}$ .

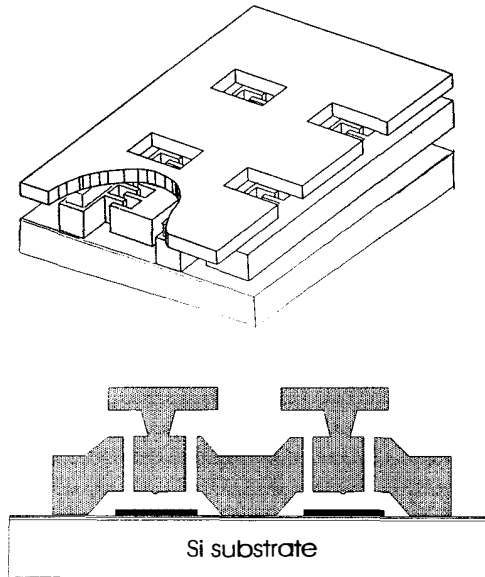


Figure 2. Perspective and cross sectional view of the area efficient actuator with a bonding platform connecting all of the movable electrodes on top.

can be recursively extended if needed. The electrodes are layout such that only one masking level is needed to define the electrode sets that can generate position-independent electrostatic force in both direction. A bonding platform covering most of the area is formed on top of the electrode. It is used to connect all the movable electrodes and also acts as the platform for payload attachment. A stud layer is used to elevate the bonding platform to a certain height above the stator electrodes; this height depends on the vertical electrical field component and spring stiffness. Figure 2 shows the perspective view and cross section of an area-efficient actuator.

### Device Processing

The force output of the interdigitated microactuator is proportional to the height-to-width aspect ratio of the gaps between fingers, and this requires a high-aspect-ratio fabrication process. [4-7] To achieve this and to maximize the stiffness/mechanical bandwidth aspect of the device, we reported earlier [2] a process capable of fabricating 20  $\mu\text{m}$  thick microminiature metal structures with minimum features sizes less than 2  $\mu\text{m}$ . This added structure height and associated rigidity has enabled us to fabricate structures with in-plane dimensions of a few millimeters using a low-stress, plated copper. The structures have dimensions an order of magnitude larger than conventional micromechanical structures in all three dimensions, while still retaining the minimum in-plane features. This is achieved by using a combination of very low-stress plating, photoresist and a projection optical system. Here, we have extended the process to allow the microfabrication of an area-efficient electrode tree structure as proposed in [1], based on a flexure

type of actuator [3]. For the electrostatic devices, copper is used, which is compatible with the PSG (phosphor-silicate glass)-HF sacrificial layer system, thereby minimizing the process changes of the conventional silicon-based surface micromachining. Since plating is a low temperature process, this silicon-based technology could potentially be merged with on-chip silicon control and sensing circuitry. Fig. 3 outlines the fabrication sequence of the device. The Si wafer is first oxidized at 1050° C, and followed by deposition of LPCVD silicon nitride as a passivation layer. An LPCVD polysilicon shield layer is deposited and patterned by  $\text{CCl}_4$  plasma etching. An LPCVD PSG sacrificial layer is deposited at 450° C and patterned by wet etch in BHF. Recessed holes are time-etched into the PSG layer to form molds for dimples. A full-film chromium and copper composite layer (Cr 100 Å and Cu 900 Å thick) is sputtered onto wafers as a plating seed layer. A plating stencil is formed by a patterned 22- $\mu\text{m}$ -thick photoresist layer. The edges of the wafers are exposed to UV to form a contact ring of seed layer which is then contacted to the plating electrode during the Cu plating. The plated copper is twenty  $\mu\text{m}$  thick, and a 2- $\mu\text{m}$  margin on the photoresist is left for the plating nonuniformity to avoid plating mushroom over the photoresist. This is necessary to avoid shunting of the interdigitated electrodes which are only 2  $\mu\text{m}$  apart. The intrinsic stress level of the plated copper layer is as low as 20 MPa. A copper bonding platform connecting all of the movable electrodes on top is formed in two other similar plating steps for structural rigidity and payload attachment, and the actuators are finally released in an HF based etchant. A supercritical  $\text{CO}_2$  drying release process [8] is used. The final

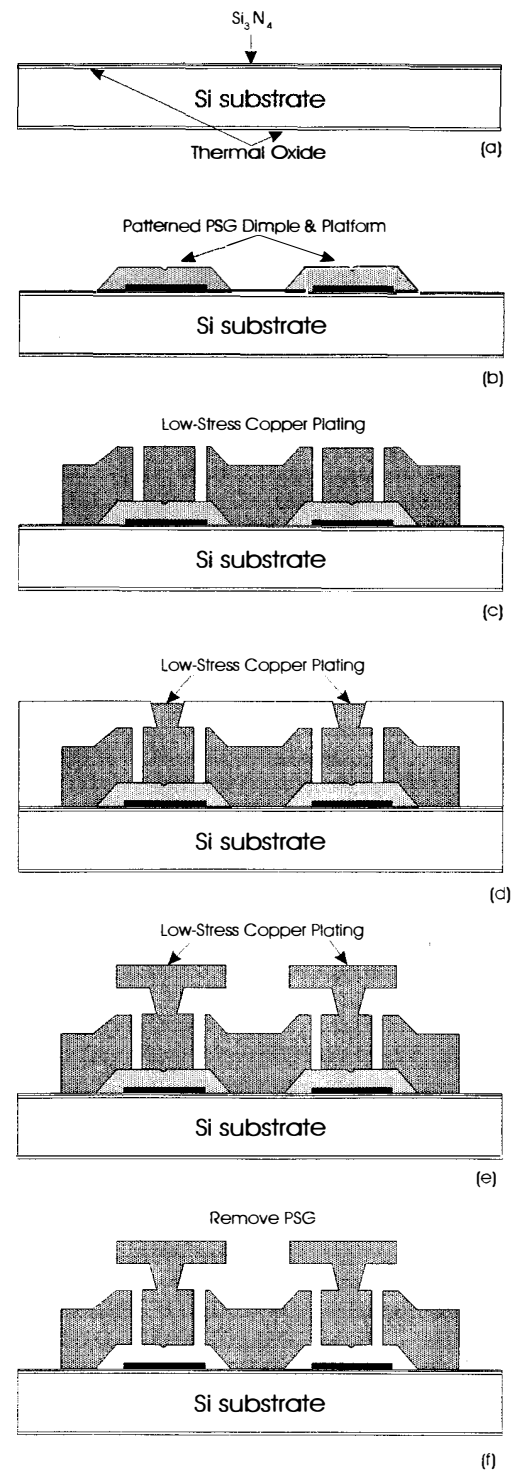


Figure 3. Outline of device fabrication sequence. (a) substrate is isolated (b) first conducting layer and sacrificial layer are patterned (c) high-aspect-ratio stencil plating (d) pedestal plating (e) bonding platform plating (e) release process.

released structures are shown in the SEM micrographs in Fig. 4 and Fig. 5 with and without the bonding platform.

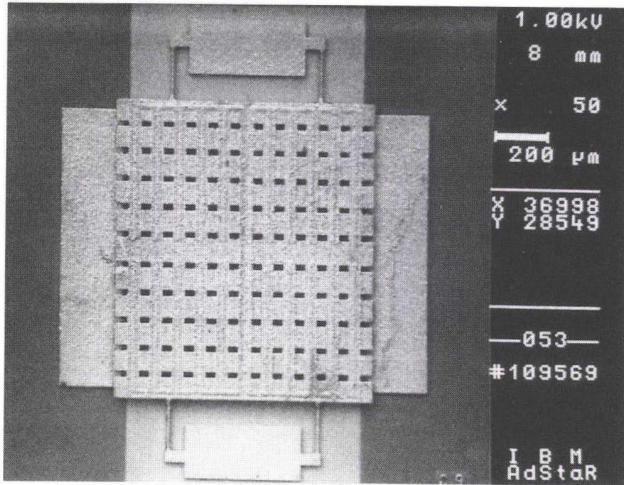


Figure 4. SEM micrograph of a released area-efficient microactuator.

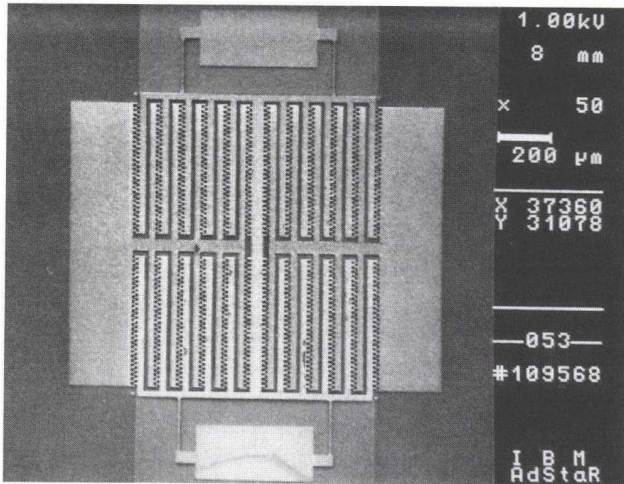


Figure 5. SEM micrograph of an area-efficient actuator with the bonding platform removed to expose the electrode tree structure.

### Large signal linearization

Electrostatic actuators are square law devices. Although the force is independent of position within the designed stroke range for interdigitated electrode configurations, the force/acceleration is proportional to the square of the applied voltage between the moving electrode and stator electrode. Linearization becomes an important issue for this category of electrostatic actuator control. A typical linearization scheme is to sum a small control voltage to a large DC biasing voltage, and the quadratic nonlinearity in the control signal can be ignored for large bias voltages [2],[4]. Although the electrical driving force is linearized in the scheme,

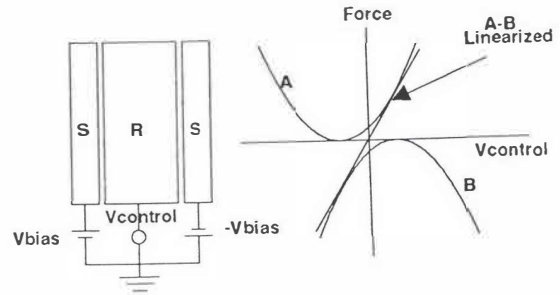


Figure 6. (a) Large signal linearization scheme with an anti-symmetrical bias on the stators (b) Nonlinearity is cancelled out, and the output is linearized with driving voltages as large as the biasing voltage.

the spring stiffness becomes asymmetric if the DC bias causes large initial displacement. Finally, the linearity scheme breaks down when the “small signal” voltage is nearly as large as the DC bias voltage. In practical servo applications, one would need the actuator to generate as large a force or torque as possible by putting in the maximum allowable signal while still maintaining system linearity. In order to drive the device in a large signal linearized mode, a new linearization bias configuration is used as shown in Fig. 6(a). The force/input relation becomes

$$F_{el} = \alpha_1(V_{bias} + V_{control})^2 - \alpha_2(V_{bias} - V_{control})^2$$

$$= 4\alpha V_{bias}V_{control}$$

where  $\alpha_1$  and  $\alpha_2$  are force constants of the two sides, here set equal to  $\alpha$ .

The amplitude of the control signal can be equal to or even larger than the large DC bias and still maintain the linear relation in this configuration, and the optimum bias and maximum control signal should both be one half of the maximum allowable voltage for the system. Fig. 6(b) shows how two segments of the transfer curves are put together for a linearized curve. Also, there is no initial displacement and the initial spring stiffness is symmetric in this case. Certainly, this scheme depends on good process tolerance control and the symmetry of this particular device in order to satisfy the condition that  $\alpha_1$  equals  $\alpha_2$ .

### Microactuator Characteristics

A Laser Doppler Velocimeter (LDV) was used to measure the in-plane motion. The frequency response function is measured on the system using the control voltage as an excitation and the LDV displacement as a response. The dominant resonance is at 9 kHz as shown in Fig. 7. Fig. 7 also shows the phase response with a clean 180 degrees transition after first resonance. We showed in earlier paper [2] that a significant reduction in the peaking amplitude response can be achieved in this kind of actuator using a PI controller [9].

The output force of microactuators can be obtained from the measured amplitude of acceleration when sinusoidal excitations at frequencies significantly higher than the first resonance are used. Fig. 8 shows the acceleration per volt

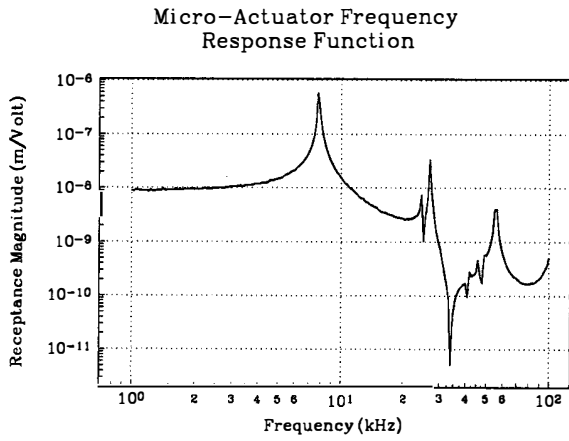


Figure 7. Amplitude and phase of microactuator frequency response function up to 100kHz.

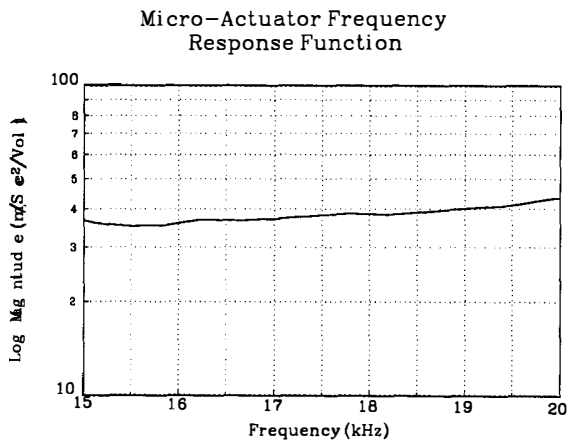
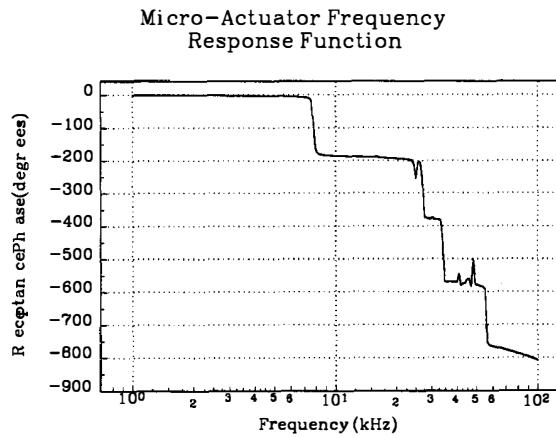


Figure 8. Acceleration per volt of a sinusoidal driving voltage for an area-efficient actuator biased at 30 volts.

of a sinusoidal driving voltage from 15 to 20 kHz for an actuator biased at 30 Volts. Given a movable electrode mass of  $45 \mu\text{g}$ , a force output of  $6 \times 10^{-8} \text{N/V}^2$  is obtained; i.e., a linearized force output of 0.2 mN can be obtained from this one-mm-sized microactuator at 60 Volts, which is a feasible voltage generated on a modified CMOS chip.

To verify the linearity, the actuator was driven with a sinusoidal excitation well below the first resonant frequency to ensure a zero phase shift. Fig. 9 shows the actuator displacement in the time domain, while driven by a large signal sinusoidal wave at 5 KHz, which is below the resonant frequency. It shows that the actuator tracks the input signal. The input amplitude is 20 V in this case, and the displacement versus input curve is plotted in Fig. 10. Good linearity is obtained and no hysteresis is observed, compared to typical piezoelectric or magnetic approaches where the linearity will greatly depend on the material characteristics used for transduction in addition to possible flexure nonlinearity.

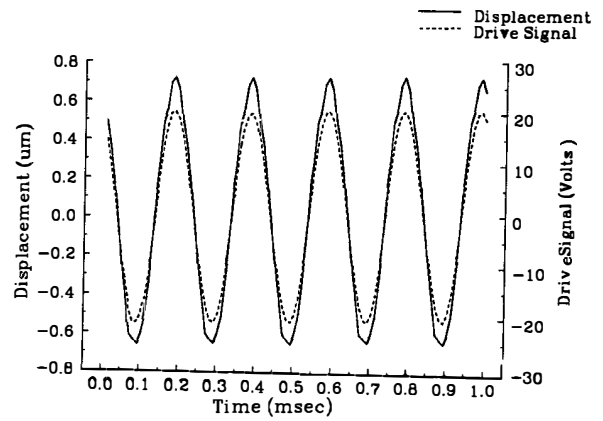


Figure 9. Actuator displacement driven by a 5 kHz sinusoidal excitation shows the actuator output tracks the input signal.

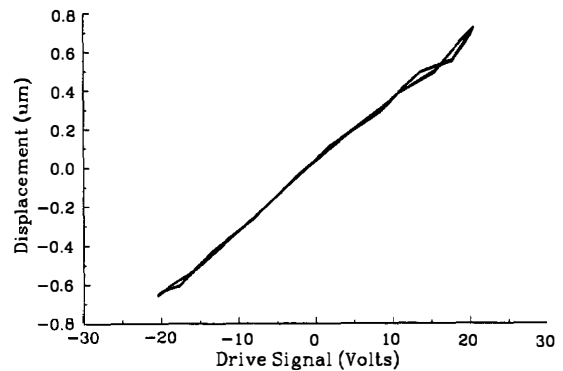


Figure 10. Displacement vs. input curve using the large signal linearization scheme.

## Area-Efficient Rotary Microactuators

A consideration with the in-plane linear microactuators is that the force generated does not necessarily pass through the center of mass (C.M.) of the combined mass of payload and movable electrode. Thus, one needs to take the cross-axis torque into consideration in a practical system design. A rotary version of the area-efficient actuator such as shown in Fig. 11 (with upper bonding plate not shown) will reduce this complication. Since the rotational axis passes through the center of mass of the movable electrode in this symmetric design, a centered payload will make the combined system C.M. on the axis of rotation.

Another consideration with linear microactuators is that shock loads applied in the direction of motion lead to displacements of the actuator. The displacement may be sufficient to disrupt successful operation during high G shocks. A rotary version of the area-efficient actuator will also greatly reduce the shock sensitivity. The same area-efficient process described above is used to fabricate such a device. Fig. 11 shows an SEM photograph of a microfabricated area-efficient rotary microactuator. The springs are designed such that they provide a sufficiently low torsional spring constant to allow rapid in-plane rotation under the electrostatic forces available, and sufficiently high load bearing capability to accommodate shock loads. One handy way to achieve low rotational stiffness while maintaining the same out-of-plane stiffness is to split a spring into several ones as shown in Figure 12. This is because the vertical stiffness is linearly proportional to the width of the spring, but the in-plane bending stiffness is proportional to the cube of the thickness in the bending direction. For certain applications a rotary version of area-efficient design may have advantageous shock resistance and reduced cross-axis mechanical coupling.

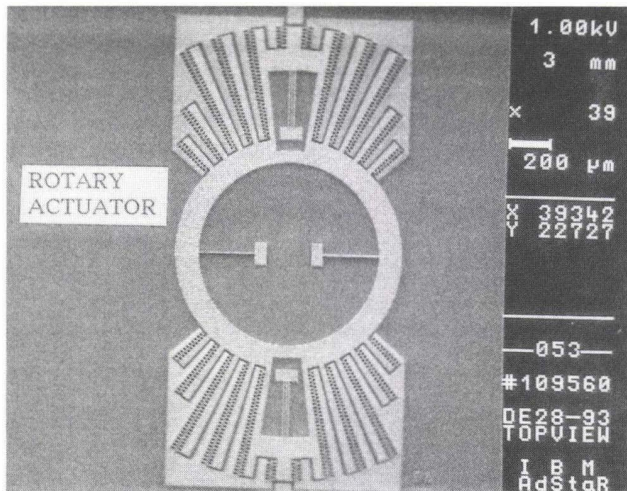


Figure 11. SEM micrograph of an area-efficient rotary actuator. (without the bonding platform)

## Summary

We have described the design, process and characteristics of area-efficient microfabricated actuators. Through an area-efficient design, a high-aspect ratio microfabrication process, and a large signal linearization scheme, we have shown that a one-mm-sized microfabricated actuator is capable of linearized output of 0.2 mN when driven at 60 Volts. The compactness, the linearity and the increased output force/torque may enable the batch-fabricated microactuators to be used in many practical and new applications such as slider tracking in magnetic recording, optical tracking, non-resonant mode scanning/chopping, optical frequency domain demultiplexing with a tunable external Fabry-Perot cavity etc.. A design for a rotary microactuator was shown, and some of its potential advantages given.

## Acknowledgment

The authors want to acknowledge L. H. Lane, S. Hoen, D. D. Tang, H. Santini, H. Levinson for valuable inputs and support.

## References

- [1] L. S. Fan, "Towards mN electro-and magneto-static microactuators." Proceedings of the Workshop on Microtechnologies and Applications to Space Systems, NASA, 191-192 (June 1993)
- [2] L.-S. Fan, L. H. Lane, N. Robertson, L. Crawforth, M. A. Moser, T. C. Reiley, W. Imano, "Batch-fabricated milli-actuators", Proceedings of IEEE ASME Micro Electro Mechanical System, 179-183 (Feb. 1993)
- [3] W. C. Tang, T. C. H. Nguyen, R. T. Howe, "Laterally driven polysilicon resonant microstructures", Sensors and Actuators, Vol. 20 25-32 (1989)
- [4] W. Becker, W. Ehrfeld, P. Haggmann, A. Maner and D. Munchmeyer, "Fabrication of microstructures with high aspect ratios and great structural heights by synchrotron radiation lithography, galvanofarming, and plastic moulding (LIGA process)", Microelectronic Engineering 4 (1986) 35-56.
- [5] H. Guckel, T. R. Christenson, K. J. Skrobis, D. D. Denton, B. Choi, E. G. Lovell, J. W. Lee, S. S. Bajikar and T. W. Chapman, "Deep X-Ray and UV lithographies for micromechanics", Proc. of the IEEE Solid-State Sensor and Actuator Workshop, Hilton Head, SC, (1990) 118-122.
- [6] A. B. Frazier, M. G. Allen, "High aspect ratio electroplated microstructures using a photosensitive polyimide process", Proc. IEEE MEMS'92 workshop, Travemunde, Germany (1992) 97-102
- [7] G. Engelmann, O. Ehrmann, J. Simon, H. Reichl, "Fabrication of high depth-to-width aspect ratio microstructures", Proc. IEEE MEMS'92 workshop, Travemunde, Germany (1992)
- [8] G. T. Mulhern, D. S. Soane, R. T. Howe, "Supercritical carbon dioxide drying of microstructures", Digest of Technical Papers, International Conference on Solid-State Sensors and Actuators, 296-298, Yokohama, Japan, (1993)
- [9] R. C. Dorf, Modern Control Systems, Third Edition, Addison-Wesley Publishing Co., Reading, MA, 1980.

# Magnetic Microactuation of Polysilicon Flexure Structures

Jack W. Judy, Richard S. Muller, and Hans H. Zappe

Berkeley Sensor & Actuator Center (BSAC)  
Department of EECS, University of California  
Berkeley, California 94709

**Abstract**—A novel microactuator technology that combines magnetic thin films with polysilicon flexural structures is described. Devices are constructed in a batch-fabrication process which combines electroplating with conventional lithography, materials, and equipment. A microactuator consisting of a  $400 \times (47\text{--}40) \times 7 \mu\text{m}^3$  rectangular plate of NiFe attached to a  $400 \times (0.9\text{--}1.4) \times 2.25 \mu\text{m}^3$  polysilicon beam has been displaced over 1.2 mm, rotated over  $180^\circ$ , and actuated with over 0.185 nNm of torque. Theoretical expressions for the displacement and torque are developed and compared to experimental results.

## I. INTRODUCTION

**M**AGNETIC microactuation has recently been

demonstrated by several research groups [1-5]. In most cases magnetic-microactuator fabrication is not accomplished in a continuous batch process, but rather with the addition of steps such as manual assembly. The cantilever actuator described by Ahn and Allen is an exception [3]. In our paper, we describe batch-fabricated magnetic microactuators which are made in a relatively simple process. This process combines electroplated NiFe films with surface-micromachined polycrystalline silicon. This combination of materials provides new opportunities for actuated-structure designs. Specifically, forces and displacements that are larger than those generated with electrostatic microactuators are readily obtained. An important feature of this technology is provided by the ability to control the actuators via a remote source for the magnetic field. This type of control can achieve significant actuation both in and out of the plane of the wafer. These advantages of magnetic drive can accelerate and broaden the already impressive results obtained with actuated polysilicon microflexural elements [6-8]. Full integration of magnetically actuated elements into microsystems can be expected to have significant impact. There appears to be no major obstacle to the merger of electrical, mechanical, and magnetic microfabrication technologies.

## II. TECHNOLOGY

The new microactuators are produced by adding fabrication steps to a process developed at BSAC to produce polysilicon surface-parallel microresonant systems [9]. All steps are added near the end of the fabrication sequence, just prior to the micromechanical-device "release" step. This processing sequence avoids contamination by the magnetic material during the conventional microelectronic and micromechanical fabrication steps.

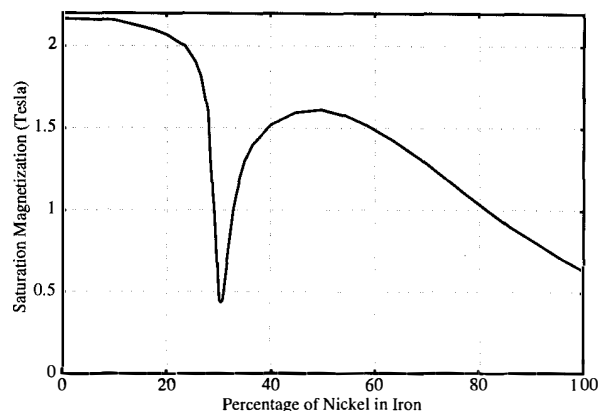


Fig. 1. The saturation magnetization of a NiFe film as a function of composition. (Based on Bozorth [10])

Furthermore, no additional step adds significantly to the thermal budget for the wafer.

The micromechanical flexures are constructed with phosphorus-doped LPCVD polysilicon. An electroplated nickel-iron alloy is used as the magnetic material because of its relatively high saturation magnetization. In addition, the magnetic properties of NiFe have been well-documented because of its very widespread commercial use. The NiFe is electroplated by using a variation of a procedure described by Ahn, Kim, and Allen [4]. For magnetic thin-film heads, one normally seeks to control the film composition at 81% Ni, 19% Fe in order to eliminate stress-induced magnetic anisotropy. Plating control to achieve a given composition is challenging, however, and our films turned out to be rich in nickel -- roughly 95% Ni and 5% Fe as measured by an energy-dispersive, x-ray microanalysis system mounted in a scanning-electron microscope [11]. On the other hand, to maximize actuation performance the saturation magnetization should be maximized. For a NiFe film this occurs at a composition of 100% Fe. Unfortunately, iron corrodes easily and thus it is beneficial to add nickel which is much more corrosion resistant. A composition of 50% nickel provides improved corrosion resistance and corresponds to a local maximum of the saturation magnetization (Figure 1). A nickel-iron alloy with 50% nickel and 50% iron has historically been referred to as 50 Permalloy [12]. A design concern for non-released structures made with 50 Permalloy is that the magnetostriction is much higher at 50% nickel ( $\sim 2.6 \times 10^{-5}$ ) than at 81% nickel ( $\sim 0$ ). Thus, unless the stress in the magnetic film can be relaxed (for example, in this work in which the magnetic element can move freely) there may be significant mechanical effects on the magnetic properties.

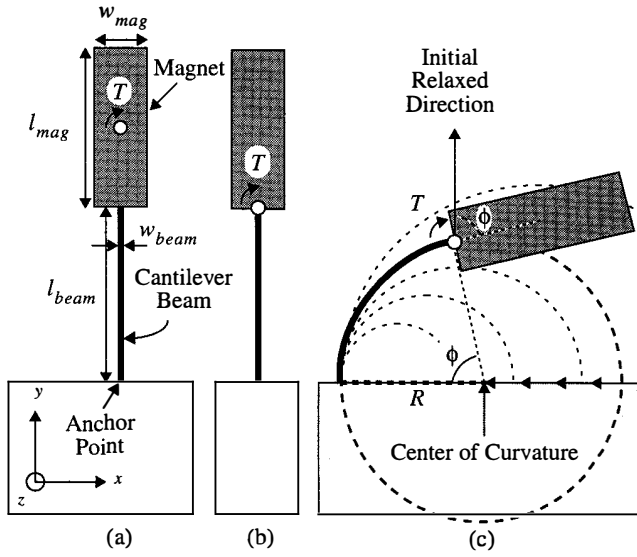


Fig. 2. (a) Mechanical structure of the microactuator. (b) Reduction of the mechanical system. (c) Circular beam bending. The arrows indicate the motion of the center of curvature as  $T$  is increased from zero.

### III. MECHANICAL ANALYSIS

For a first microactuated element, we built and studied the structure shown in Fig. 2a. It consists of a narrow cantilever beam made of polysilicon which is anchored to the substrate at one end and attached to a wide plate of magnetic material at the other end. When the long and thin magnetic plate is placed in a uniform magnetic field it experiences only a pure moment and not a translational force. Since the magnetic material is much wider, thicker, and stiffer than the cantilever beam, the magnetic material can be assumed to be mechanically rigid. To simplify the analysis, we recognize that a pure moment applied to a rigid body can be translated to any position on the rigid body. Therefore, the resulting mechanical model becomes that of a simple cantilever beam which is fixed at one end and has a concentrated moment or torque  $T$  applied to the other end (Fig. 2b).

If we assume that the cantilever beam has a uniform cross section, the application of a torque results in pure bending. Thus, increasing the magnetic field  $H$  configures the beam along the path of a circular arc, whose center translates in from infinity along the anchoring surface (Fig. 2c). In terms of the torque  $T$  on the plate, the radius of curvature  $R$  of the cantilever beam is given by

$$R = \frac{l_{beam}}{\phi} = \frac{E_y I}{T} \quad (1)$$

with cantilever-beam length  $l_{beam}$ , elastic modulus  $E_y$ , and moment-of-inertia  $I$  [13]. The angle  $\phi$  is the angular mechanical deflection from the initial relaxed direction.

The fabrication process that forms the polysilicon beam produces a trapezoidal cross section. Using the moment-of-inertia of a beam with a trapezoidal cross section [14], the angular deflection in Eq. (1) can be expressed as

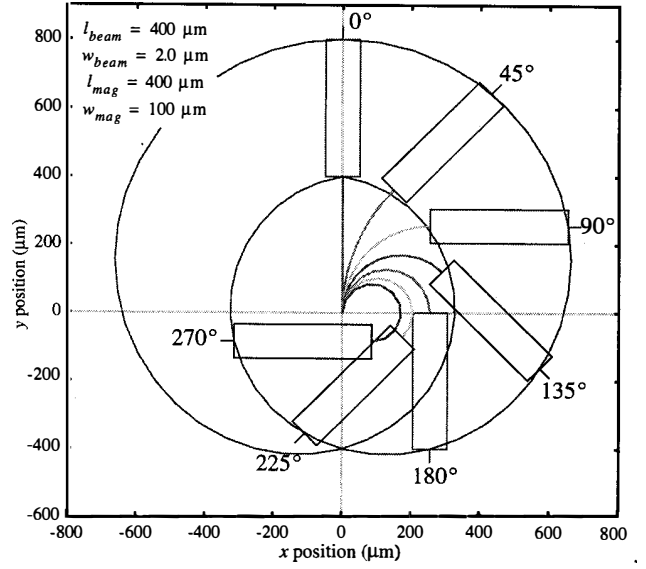


Fig. 3. Plot of the deflection of the end of the microactuator. The cardioid traces out the position of the tip as the angular deflection of the plate  $\phi$  is increased by increasing the torque  $T$ . The resulting deformed shape is shown for angular deflections of  $\phi = 0, 45, 90, 135, 180, 225$  and  $270^\circ$ .

$$\phi = \frac{48 T l_{beam}}{E_y h (a+b) (a^2 + b^2)} = \frac{T}{k_\phi} \quad (2)$$

with beam thickness  $h$ , upper-beam width  $a$ , and lower-beam width  $b$ . Equation (2) is useful for determining the torque  $T$  from observation of the angular mechanical deflection  $\phi$ . The angular spring constant  $k_\phi$  of this mechanical structure is given by

$$k_\phi = \frac{E_y h (a+b) (a^2 + b^2)}{48 l_{beam}} \quad (3)$$

Equations (1) to (3) assume Hooke's-law behavior for the cantilever material.

#### A. Description of Motion

Coordinates for the position of the tip of the actuated cantilever can be obtained from a straightforward geometrical analysis. The results, given in Eqns. (4) and (5), are plotted in Fig. 3.

$$x_{tip} = \frac{l_{beam}}{\phi} (1 - \cos \phi) + l_{mag} \sin \phi \quad (4)$$

$$y_{tip} = \frac{l_{beam}}{\phi} \sin \phi + l_{mag} \cos \phi \quad (5)$$

Figure 3 is a plot of the path traced out by the tip of a microactuator with a cantilever beam of length  $l_{beam} = 400 \mu\text{m}$  and a rigid magnetic plate of length  $l_{mag} = 400 \mu\text{m}$ . To achieve these large deflections the moment is increased by varying the magnetic-field intensity and direction. The largest  $x$ -translation of the tip is

$$x_{max} \approx \pm \left( \frac{2}{\pi} l_{beam} + l_{mag} \right) = \pm 654 \mu\text{m} \quad (6)$$

and the largest  $y$ -translation of the tip is

$$y_{max} \approx -(2l_{mag} + l_{beam}) = -1200 \mu\text{m} \quad (7)$$

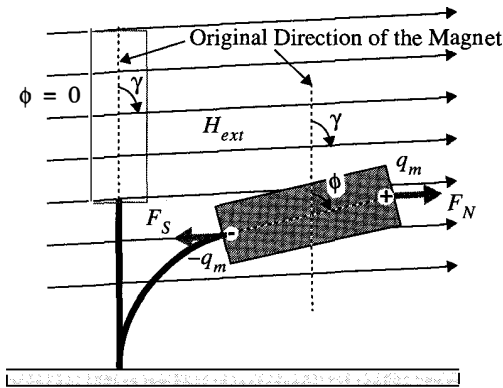


Fig. 4. Positions of the effective magnetic “charges” and directions of the forces that they generate. The angular mechanical deflection  $\phi$  and the angle between the magnetic field and the original direction of the cantilever structure  $\gamma$  are also labeled.

#### IV. MAGNETIC ANALYSIS

The behavior of long and narrow magnets in a magnetic field can be modeled using the concept of “effective magnetic charges.” Although no magnetic monopoles exist, these effective magnetic charges are formed in pairs and they are mathematically identical to electrical charges. To generate a useful picture of the magnetic-field pattern, one can postulate that positive magnetic charges reside on the magnetic north pole and negative magnetic charges reside on the magnetic south pole. In Fig. 4, we use this concept to introduce magnetic charges  $q_m$  and  $-q_m$  to the cantilever actuator.

Since, to first order, we assume the magnetic material is uniformly magnetized, the magnetic charges exist only on the very ends of the magnet. The charges, which are separated by the length of the magnet, experience the forces  $F_N = q_m H_{ext}$  and  $F_S = -q_m H_{ext}$ . These forces line up with the external field lines (Fig. 4). The angle between the original direction of the magnet and the direction of the magnetic field is  $\gamma$ . To deflect the structure by an angle  $\phi$ , the magnetic-field direction is held constant while its intensity is increased from zero to  $H_{ext}$ . The forces  $F_N$  and  $F_S$  act on the length of the magnet to generate a torque

$$T_{mag} = q_m H_{ext} l_{mag} \sin(\gamma - \phi) \quad (8)$$

The magnetic charge is given by  $q_m = M A_{mag}$  with magnetization  $M$  and magnet cross-sectional area  $A_{mag}$ . Equation (8) thus reduces to

$$T_{mag} = V_{mag} M H_{ext} \sin(\gamma - \phi) \quad (9)$$

where  $V_{mag}$  is the volume of the magnet.

As is familiar for a compass needle, an unrestrained magnetic element will rotate until it is aligned with the magnetic field ( $\phi = \gamma$ ). However, if the rotation of the magnet is restrained by a mechanical spring, the magnetic torque  $T_{mag}$  causes the magnet to rotate until the mechanical restoring torque of the spring

$$T_{mech} = k_\phi \phi \quad (10)$$

compensates for  $T_{mag}$  and an equilibrium angle is attained. The mechanical restoring torque that achieves

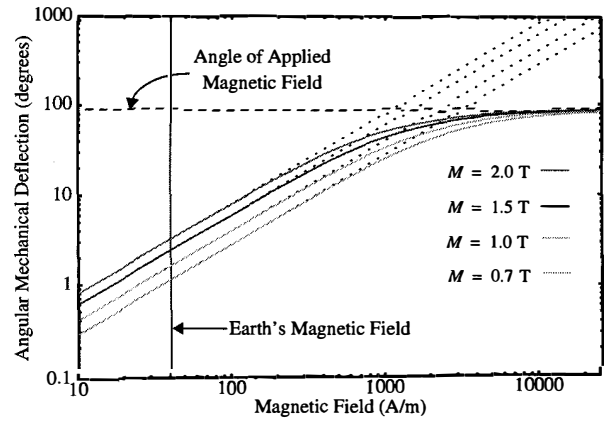


Fig. 5. Plot of the theoretical angular mechanical deflection  $\phi$  as a function of magnetic-field intensity  $H_{ext}$ . The magnetization  $M$  is varied (0.7, 1.0, 1.5, and 2.0 T). The magnetic field is applied at a constant angle  $\gamma = 90^\circ$ . The beam is made of polysilicon with an elastic modulus  $E_\gamma = 170$  GPa and dimensions  $2 \times 2 \times 400 \mu\text{m}^3$  ( $k_\phi = 567$  pNm). The magnet has dimensions  $10 \times 100 \times 400 \mu\text{m}^3$ .

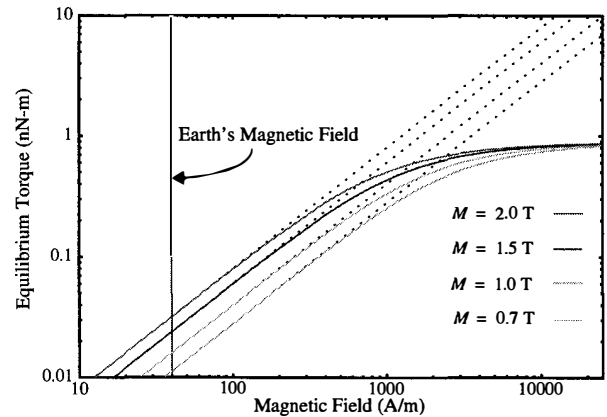


Fig. 6. Plot of the theoretical equilibrium torque for the same conditions used in Fig. 5.

equilibrium is referred to as the equilibrium torque  $T_{equil}$ . By equating Eqns. (9) and (10), the angular mechanical deflection of the cantilever structure is found

$$\phi = \left( \frac{V_{mag} M H_{ext}}{k_\phi} \right) \sin(\gamma - \phi) \quad (11)$$

Eq. (11) is a transcendental equation that can be solved numerically. Plots of the angular mechanical deflection  $\phi$  and the equilibrium torque  $T_{equil}$ , as functions of magnetic-field intensity  $H_{ext}$ , are given in Figs. 5 and 6, respectively. In both plots, the lines reach asymptotic values defined by the choice for the direction of the stationary magnetic field ( $\gamma = 90^\circ$ ). If the relative angular difference between the magnet and the magnetic field is maintained at  $\gamma - \phi = 90^\circ$ , the magnetic torque given in Eq. (9) is maximized. The extrapolated lines illustrate the maximum angular deflection and equilibrium torque possible for a given magnetic field. This occurs when the angle of the magnetic field is allowed to rotate with the moving magnet. The magnetic material was formed into rectangular and elliptical shapes to investigate the effects of shape on device performance. An ellipsoid is a special geometry for a magnetic material because an ellipsoid can

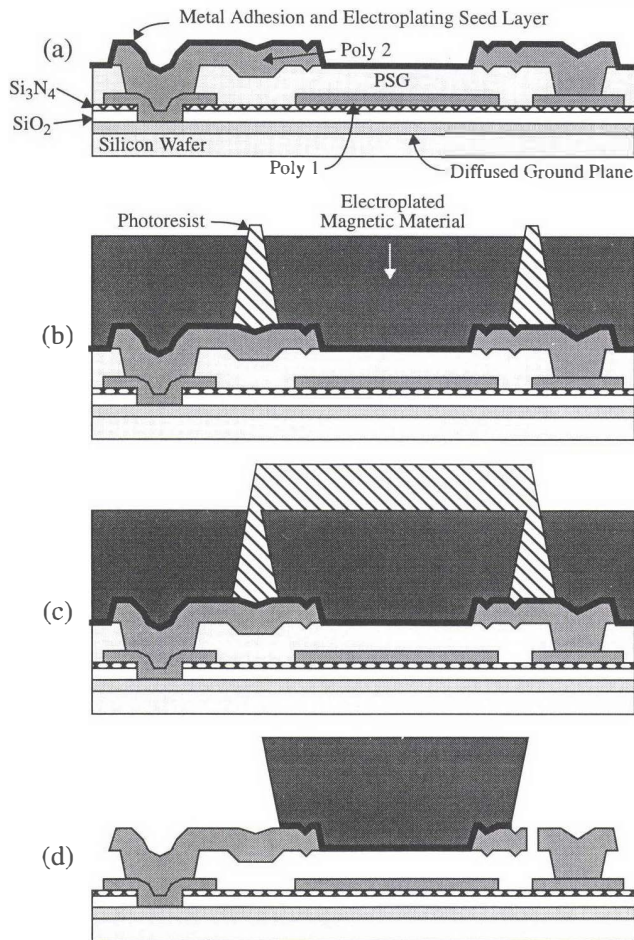


Fig. 7. (a) Metallic adhesion and seed-layer deposition. (b) Photoresist frame definition and magnetic-material electrodeposition. (c) Protective photoresist definition prior to magnetic-material etch. (d) Sacrificial material removal and fuse breaking to release the device.

be magnetized *uniformly* and the effect of its shape can be calculated analytically [15]. However, the magnetic theory described above is not appropriate for ellipsoids or rectangles that have aspect ratios (length/width) of less than  $\sim 4$ . This is because the magnetization vector inside the magnetic material can rotate away from the easy axis and thus the material no longer acts like a permanent magnet. All experimental data reported in this paper were obtained from actuators that had rectangular pieces of magnetic material with an aspect ratio of 10.

## V. FABRICATION

As stated in Section II, magnetic elements were fabricated in steps added at the end of a process that had been developed to produce polysilicon resonant structures. With only the final “release” step for mechanical structures remaining, an adhesion layer (10 nm of Cr) and an electroplating seed layer (100 nm Cu) are deposited by evaporation on top of the polysilicon flexure (Fig. 7a).

Next, four layers of a common I-line photoresist (Olin Hunt 6512) are spun onto the wafer which aggregates to a total resist thickness of roughly  $10\ \mu\text{m}$ . The wafer is then exposed in an optical (10:1 reduction) wafer stepper

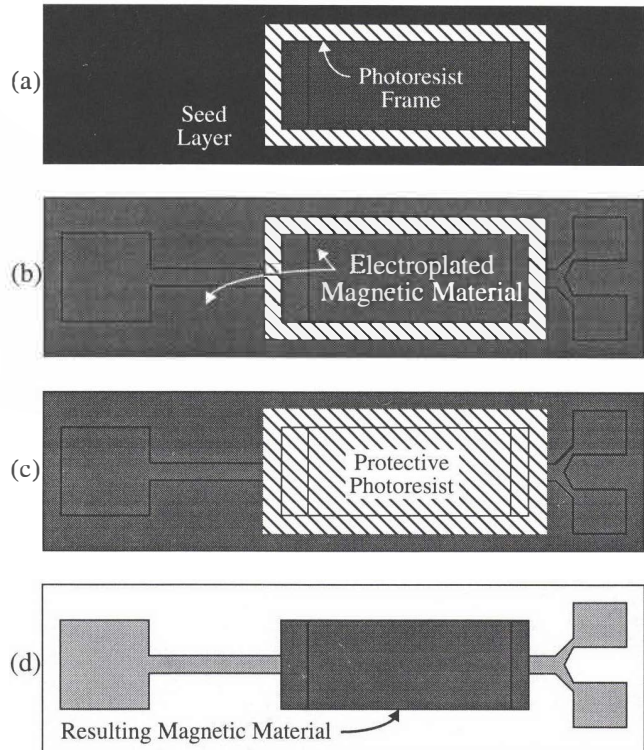


Fig. 8. Top view of the fabrication process which illustrates the frame plating technique. (a) Definition of a photoresist frame on top of the adhesion and seed layers. (b) Electrodeposition of the magnetic material. (c) Definition of the protective photoresist. (d) Removal of excess NiFe and protective photoresist.

(GCA) for 5.25 s per die. After developing the resulting photoresist, the sidewall slope is quite low ( $45$  to  $60^\circ$ ). Fortunately, abrupt vertical slopes on the resist are not important for these devices. This is because actuation by an external magnetic field does not require surface-to-surface interactions such as those found in linear and rotary variable-capacitance and variable-reluctance microactuators.

In the next step, the magnetic material is electroplated to a thickness of  $7.0\ \mu\text{m}$  (Fig. 7b). Because of the slope of the photoresist, the magnetic material has an inverted trapezoidal cross sectional. Except for the omission of a saccharin additive, the plating solution was the same as that described in reference [4]. To assure a uniform deposition rate and a uniform composition, a frame-plating technique is employed (Fig. 8b) [16]. After the thick resist is removed, a new layer is deposited and patterned over the regions of magnetic material that are to be preserved (Fig. 7c and Fig. 8c). The unprotected NiFe and the Cu beneath it are then removed. After the photoresist is stripped, the Cr adhesion layer is etched away in a dilute Cr etch (Fig. 8d). Unfortunately this etch results in a yield loss since the Cu is etched faster than the Cr and thus the NiFe becomes undercut. To improve yield a better method of removing the excess electroplating seed layer is needed. At this time, sputter etching and ion milling are being considered as alternatives. The devices are then released in a concentrated HF etch (Fig. 7d). Due to the

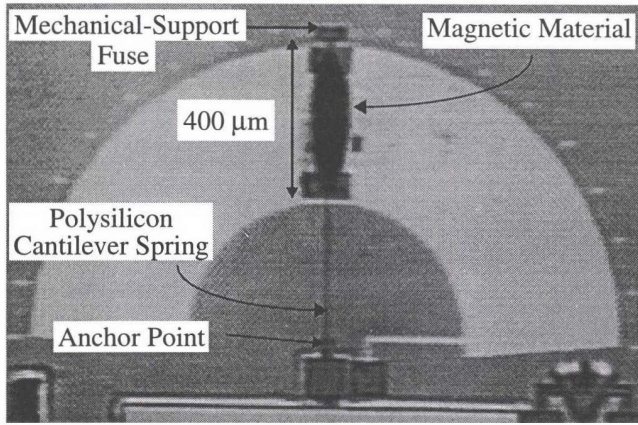


Fig. 9. Optical photograph of a microactuator with no applied magnetic field. This actuator consists of an elliptical piece of magnetic material with dimensions  $400 \times (107-100) \times 7 \mu\text{m}^3$  and a polysilicon beam with dimensions  $400 \times (0.9-1.4) \times 2.25 \mu\text{m}^3$ .

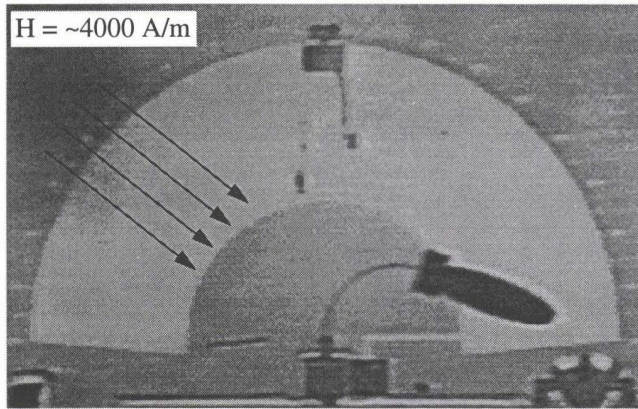


Fig. 10. Optical photograph of the microactuator with a large magnetic field applied at an angle  $\gamma$  greater than  $90^\circ$ .

large size and compliance of these devices, polysilicon fuses were used to help them survive the release etch and rinse [17].

## VI. EXPERIMENTAL RESULTS

Figure 9 shows an optical photograph of one of the batch-fabricated magnetic microactuators when not under the influence of a magnetic field. Figure 10 shows the microactuator after it has been deflected by an applied magnetic field. For the purpose of illustration, the angle  $\gamma$  was allowed to increase beyond the nominal  $90^\circ$  to investigate the maximum deflection of these devices. A deflection greater than  $180^\circ$  was observed before the beam fractured.

Before we knew the composition of the NiFe film we had expected the material to demagnetize by breaking up into closure domains when the magnetic field was removed. Instead, it remained magnetized and hence acted like a permanent micromagnet. Since our films were nickel rich, such a permanent-magnet behavior is not surprising. The remanent magnetization can be overcome by applying a magnetic field that is larger than the coercive field. When the magnetization switches, the mechanical structure abruptly changes directions so that it points in a

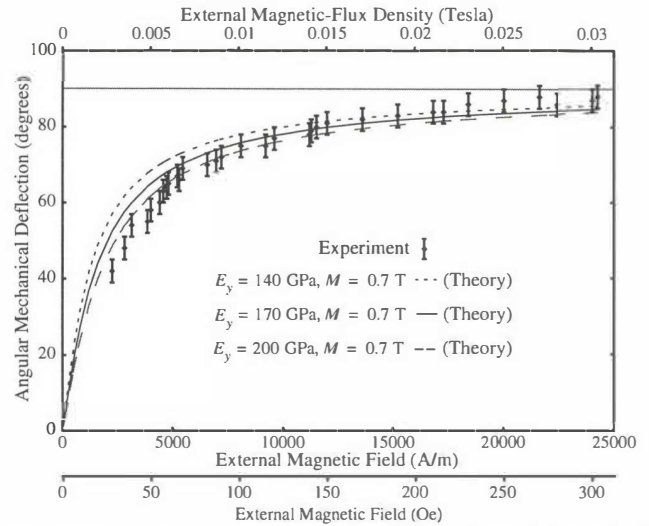


Fig. 11. Comparison of experimental deflection data and theoretical calculations for an actuator consisting of a rectangular piece of magnetic material with dimensions  $400 \times (47-40) \times 7 \mu\text{m}^3$  and a polysilicon beam with dimensions  $400 \times (0.9-1.4) \times 2.25 \mu\text{m}^3$ .

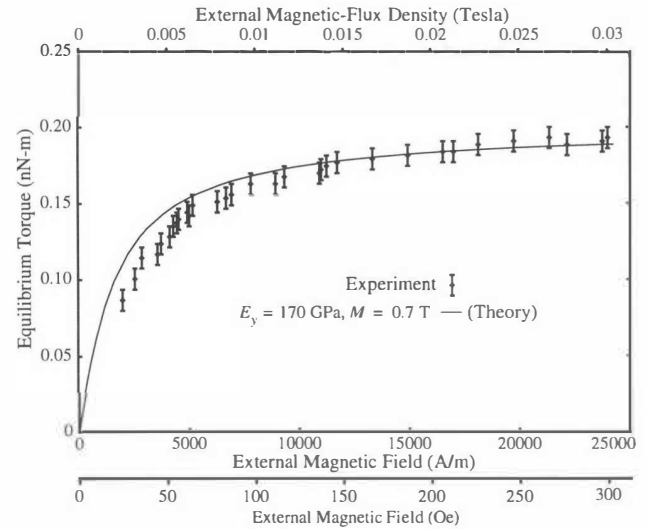


Fig. 12. Comparison of experimental torque data with theoretical calculations ( $k_\phi = 127 \text{ pNm}$ ).

new equilibrium direction. Because of this observed permanent-magnet behavior, a more complex soft-magnetic material analysis is not required for these geometries [18].

The actuators were placed in a magnetic field created by an off-chip electromagnet. The magnetic field, which was varied from 0 to 24,000 A/m (300 Oe or 0.03 T), was maintained at a constant direction  $\gamma = 90^\circ$  with respect to the original cantilever direction. The angular deflection of the device was measured optically. The measured angular deflections are compared with theory in Fig. 11. The theoretical curves give approximate bounds for variations of the elastic modulus  $E_y$  of polysilicon. Using Eq. (2) the measured angular deflection is converted into an experimental torque which is then compared to the theoretical calculations obtained with  $E_y = 170 \text{ GPa}$  (Fig. 12). The experimental results agree well with the theoretical curves especially at higher magnetic fields.

There are two explanations for the over estimate at low magnetic fields. First, the magnetization  $M$ , which is assumed to be constant, is actually a hysteretic function of the applied magnetic field. The magnetization at low magnetic fields is lower than the magnetization at high fields. Second, the effective magnetic charges are assumed to be located at the very ends of the magnet. In practice the magnetic charges are distributed in a volume located near the ends of the magnet. The distance between the charge distributions is less than the physical length of the magnetic material. Therefore, the effective length of the magnet is shortened and the magnetic torque given by Eq. (8) is reduced.

The amount of mechanical force that can be applied by this microactuator is limited by the stiffness of the mechanical flexure. If the flexure is very compliant, then large deflections are possible. However, attempts to push a heavy object cause the beam to bend away from the object instead of transferring the force. If the mechanical flexure is made stiffer, the actuator is able to apply larger forces to an object, but the maximum displacement is reduced. Thus, for a given application, the desired torques, forces, and displacements determine the mechanical-flexure geometry, the magnetic-material geometry (volume and length-to-width aspect ratio), and the required magnetic field.

## VII. CONCLUSIONS

This research has demonstrated that magnetic films can be integrated into surface micromachining with polysilicon microflexures. The tip of an 800  $\mu\text{m}$  long cantilever has been deflected over a distance of 1.2 mm and rotated through an angle of  $>180^\circ$  under an imposed torque of greater than 0.185 nNm. Actuation both in and out of the plane of the wafer is easily achieved. Similarly fabricated magnetically actuated microstructures might be applied to micromanipulators, microgrippers, magnetometers or microphotonic systems. Magnetic force is also of interest for studies of fundamental properties like yield and fracture strain as well as for crack propagation in polysilicon microstructures. Increasing the concentration of Fe from 5 to 50% should theoretically increase the magnetic torque at a given field by a factor of 2.0.

## ACKNOWLEDGMENTS

The authors thank the staff of the Berkeley Microfabrication Laboratory for excellent support and service. We are grateful for helpful discussions with Prof. Jack H. Judy concerning magnetism and magnetic materials. In addition, the following members of the Recording Heads Department, Almaden Research Center, IBM Research Division were valuable resources of practical magnetic-materials-processing knowledge and advice: Long-Sheng Fan, Robert Fontana, Linda Lane, Tim Reiley, Neil Robertson, and Ching Tsang. Partial graduate-student research support was provided by an IBM Fellowship and by the State of California CALTRANS PATH project.

## REFERENCES

- [1] B. Wagner, W. Benecke, G. Engelmann, and J. Simon, "Microactuators with moving magnets for linear, torsional, or multiaxial motion," *Sensors and Actuators A (Physical)*, Vol. A32, no. 1-3, pp. 598-603, 1992.
- [2] H. Guckel, K. J. Skrobis, T. R. Christenson, J. Klein, S. Han, B. Choi, E. G. Lovell, and T. W. Chapman, "Fabrication and testing of the planar magnetic micromotor," *J. Micromech. Microeng.*, vol. 1, no. 3, pp. 135-138, 1991.
- [3] C. H. Ahn and M. G. Allen, "A fully integrated micromagnetic actuator with a multilevel meander magnetic core," *Tech. Dig. IEEE Solid-State Sensor and Actuator Workshop*, Hilton Head Island, South Carolina, June 22-25, 1992, pp. 14-18.
- [4] C. H. Ahn, Y. J. Kim, and M. G. Allen, "A planar variable reluctance magnetic micromotor with fully integrated stator and wrapped coils," *Proc. IEEE Micro Electro Mechanical Syst.*, Fort Lauderdale, Florida, February 7-10, 1993, pp. 1-6.
- [5] H. Guckel, T. R. Christenson, H. J. Skrobis, T. S. Jung, J. Klein, K. V. Hartojo, and I. Widjaja, "A first functional current excited planar rotational magnetic micromotor," *Proc. IEEE Micro Electro Mechanical Syst.*, Fort Lauderdale, Florida, February 7-10, 1993, pp. 7-11.
- [6] R. Brennen, A. P. Pisano, and W. C. Tang, "Multiple mode micromechanical resonators," *Proc. IEEE Micro Electro Mechanical Syst.*, Napa Valley, California, February 11-14, 1990, pp. 9-14.
- [7] M. W. Judy and R. T. Howe, "Highly compliant suspensions using sidewall beams," *7th Int. Conf. Solid-State Sensors and Actuators Dig. of Tech. Papers*, Yokohama, Japan, June 7-10, 1993, pp. 54-57.
- [8] N. Takeshima, K. J. Gabriel, M. Ozaki, J. Takahashi, H. Horiguchi, and H. Fujita, "Electrostatic parallelogram actuators," *7th Int. Conf. Solid-State Sensors and Actuators Dig. of Tech. Papers*, Yokohama, Japan, June 7-10, 1993, pp. 63-66.
- [9] W. C. Tang, T.-C.H. Nguyen, M. W. Judy, and R. T. Howe, "Electrostatic-comb drive of lateral polysilicon resonators," *Sensors and Actuators A (Physical)*, vol. A21, no. 1-3, pp. 328-331, 1990.
- [10] R. Bozorth, *Ferromagnetism*, New York, D. Van Nostrand Company Inc., 1951. (Reprinted 1978 AT&T, New Jersey)
- [11] *Energy-Dispersive X-Ray Microanalysis: An Introduction*, Kevex Corporation, Foster City, California 94404, 1983.
- [12] B. D. Cullity, *Introduction to Magnetic Materials*, Reading, Massachusetts, Addison-Wesley Pub. Co., 1972, p. 527.
- [13] E. P. Popov, *Engineering Mechanics of Solids*, Englewood Cliffs, New Jersey, Prentice Hall, 1990.
- [14] R. J. Roark, *Roark's Formulas for Stress and Strain*, Warren C. Young, Editor, New York, McGraw-Hill, 1989.
- [15] J. A. Osborn, "Demagnetizing factors of the general ellipsoid," *Phys. Rev.*, vol. 67, no. 11 & 12, pp. 351-357, 1945.
- [16] S. Liao, "Electrodeposition of magnetic materials for thin-film heads," *IEEE Transactions on Magnetics*, vol. 26, no. 1, pp. 328-332, 1990.
- [17] G. K. Fedder, J. C. Chang, and R. T. Howe, "Thermal assembly of polysilicon microstructures with narrow-gap electrostatic comb drive," *Tech. Dig. IEEE Solid-State Sensor and Actuator Workshop*, Hilton Head Island, South Carolina, June 22-25, 1992, pp. 63-68.
- [18] J. W. Judy, "Magnetic microactuators with polysilicon flexures," *Masters Report*, Department of Electrical Engineering and Computer Sciences, University of California, Berkeley, 1994.

# LATERALLY DRIVEN ELECTROMAGNETIC ACTUATORS

*H. Guckel, T.R. Christenson, T. Earles, J. Klein,  
J.D. Zook<sup>†</sup>, T. Ohnstein<sup>†</sup>, M. Karnowski<sup>‡</sup>*

*Department of Electrical and Computer Engineering  
University of Wisconsin, Madison, WI 53706*

*<sup>†</sup>Sensor and System Development Center  
Honeywell Inc., Bloomington, MN 55420*

*<sup>‡</sup>Sandia National Laboratories  
Albuquerque, NM 87185*

## ABSTRACT

Linear actuators are potentially useful devices if output forces near or above 10 milliNewton can be produced with total travel in the 250  $\mu\text{m}$  range. These two goals, when combined with required positional accuracies and packaging considerations, can be achieved for magnetic actuators which are fabricated by LIGA-like processing tools.

Preliminary actuator design and fabrication has centered on permalloy structures with 100  $\mu\text{m}$  height. Twenty turn current to flux converters with 10 ampere-turn capability are used to drive a ferromagnetic, spring supported slider into a coil gap. Total travel of 250  $\mu\text{m}$  with 0.28 milliNewton of force has been achieved with 1 Newton/meter spring constants. Since the structure can be extended easily to 3000  $\mu\text{m}$ , the design goal is within reach.

The manufacturing technique has anticipated optical excitation by photodiode inclusion. These devices in shuttered and un-shuttered form can meet the drive current needs and may produce self resonant behavior when excited by unmodulated light.

## INTRODUCTION

The commercial viability of micro electro mechanical systems, MEMS, requires that at least three major issues are addressed. The first one of these involves the potential market. MEM systems based on linear actuators fit well into a variety of applications. Micro relays, especially surge protection devices, have a large market potential if contact resistance and high voltage isolation problems can be overcome. This implies that relay closure forces should be in the 1 gram or 10 milliNewton range and that relay throw must exceed 100 micrometer. Similar output force requirements with even larger throws are needed for micro pump and micro valve applications. Output force and throw requirements increase even more for optical applications and normally add positioning requirements as additional complications.

A second problem area comes from the interplay between system requirements and components which fit into a system. Packaging issues need to be resolved early and so will compatibility questions with drive and control circuitry. Packaging difficulties reduce as the impedance level of the MEM components decrease and gain additionally from low rather than high voltage requirements.

Microelectronic compatibility issues are very complicated and are mostly cost driven. However, the need to sense some actuator function normally requires that electronic devices are co-fabricated with the MEM structures.

Finally there is the manufacturing tool problem. Cost effectiveness is a major issue and becomes very troublesome if the system is a replacement for an existing system rather than a MEM system with unique attributes. The required three dimensionality in the tool and tight tolerance requirements with multi material capability produce major challenges not only to tool selection but also tool development. The required tool attributes clarify somewhat if one assumes that the selected manufacturing technique is based on a photoresist technology. This results in prismatic geometries and results in actuator output forces of the form

$$F_{\text{OUT}} = \rho_E V_A \quad (1)$$

where  $\rho_E$  is the energy density; i.e.  $\frac{1}{2} \mathbf{D} \cdot \mathbf{E}$  or  $\frac{1}{2} \mathbf{B} \cdot \mathbf{H}$  for electrostatics and magnetostatics respectively; and  $V_A$  is the active volume of the actuator in which  $\rho_E$  is stored. This volume may be written as

$$V_A = \alpha V_{\text{PH}} = \alpha H A_{\text{PH}} \quad (2)$$

where  $\alpha$  is the filling fraction or the effectiveness with which the physical volume  $V_{\text{PH}}$  with area  $A_{\text{PH}}$  and height  $H$  was used. This notation leads to

$$\frac{F_{\text{OUT}}}{A_{\text{PH}}} = \rho_E \alpha H \quad (3)$$

as a primitive figure of merit for the actuator and/or the processing tool.

Equation (3) suggests that photoresist processes with large structural height lead to better actuators. If these processes also are characterized by high geometric resolution the filling fraction,  $\alpha$ , will increase which improves the figure of merit. The energy density should be as large as possible which favors magnetics slightly. However, as stated earlier, anticipated packaging, reliability and compatibility issues shift the actuator mechanism significantly toward magnetics.

## LINEAR ACTUATOR CONSTRUCTION

The linear actuator which is of interest here is aimed at the markets which have already been mentioned. The technical goals are for output forces in the 1 milliNewton range with throws, total travel, of 250  $\mu\text{m}$ . The device is generic in the sense that it solves several needs. The device is mildly specialized by a specific application which involves an optical grating which is re-configured by the actuator. This is best done with a device which produces an output force which is constant with displacements. Furthermore, since the grating can serve as a spring, the actuator type involves a spring return design.

The actuator mechanism which has been selected here involves magnetics. The material of choice for the magnetic portion of the actuator is permalloy with a composition of 78% Ni and 22% Fe. The alloy is produced by electroplating and behaves as a soft ferromagnetic material with as plated coercivity of less than 0.3 Oersted, saturation flux density of 10,000 gauss and permeability of 2000. The maximum energy density for this alloy is  $4(10)^5$  Newton/m<sup>2</sup>.

The actuator consists of three main sections: the electric current to magnetic field conversion structure; an electromagnet with an air gap, and the ferromagnetic slider which moves into the gap and the spring constraint. There are at least two major technical problems: the construction of the electromagnet with enveloping coils and the spring design and manufacturing issue. Both difficulties benefited from previous experiences. Thus, the magnet design is based on earlier experiences with similar issues for rotational machines [1] and very much improved magnetic material processing. The design of the springs and their support is based on unsuccessful actuator design with sliding friction. Therefore, the linear actuator which is reported on here was designed without sliding surfaces. This is possible if the slider-spring combination is rigidly locked to the substrate at two or more supports and elevated above the substrate in all other regions. Vertical magnetic forces in the gap can be used to produce the desired levitation. This behavior of magnetic actuators is very desirable and is not available in electrostatics due to pull-down forces between the slider and the substrate. The remaining major issue is that of a suitable spring material. This problem was solved more or less by accident. The magnetic behavior of the permalloy is consistent with material which is nearly amorphous. This type of crystallinity has been used in polysilicon for excellent, long term stable mechanical flexures[2]. The same results have been obtained with the permalloy which is used here where spring designs with maximum strain levels of 0.5% have produced excellent results and are considered to be conservative.

There are two unusual aspects of the actuator which have been incorporated in the design. One of these recognizes the fact that photodiodes are devices which operate well as current supplies for low impedance loads. They can be designed to drive the device from unmodulated light and, in a slightly more complicated situation, can produce self-resonances. Since quality factors of several hundred can be anticipated resonant applications are particularly attractive for low power operation. The limitations which this imposes on the actuator is that of fixed frequency operation. This can be overcome in a push-pull design where the effective spring constant can be controlled electronically which in effect tunes the resonant frequency. Both attributes have been incorporated into the current design and will be reported on separately.

## CONSTRUCTION TECHNIQUE

The construction tool which has been used to produce experimental actuators is that of x-ray assisted processing based on LIGA[3]. The modifications and extensions which have been used to improve the processing tool fall into two categories: photoresist processing and assembly[4].

In typical LIGA processing, the x-ray sensitive photoresist is applied by casting and in-situ polymerization. The polymer shrinkage and confinement by the substrate surface combine to produce a highly strained photoresist layer which is difficult to anneal. This mechanical strain limits the resolution of the process and reduces the yield significantly. The problem has been removed by using cell cast sheets of optimized polymethylmethacrylate, PMMA, machining it to size and solvent bonding the strain free material to the substrate of choice. Typical PMMA thicknesses are in the few millimeter range. The desired photoresist thickness is achieved by milling the polymer layer to the desired value, mild annealing to remove tool strain, and if so desired, mechanical polishing. This technique has been used to produce photoresist thicknesses from 50  $\mu\text{m}$  to several centimeters.

Exposure of these extreme photoresist thicknesses is possible if proper x-ray photon energies are used. Thus, at 3000 eV the absorption length in PMMA is roughly 100  $\mu\text{m}$  which would imply maximum, reasonable exposure depths to, say, 500  $\mu\text{m}$ . On the other hand, 20,000 eV photons have absorption lengths of 1 cm in PMMA and have been used to expose to 10 cm depths[5].

Assembly enhances the three-dimensionality of high aspect ratio processing[6]. It can and has been used to produce submicron tolerances in assembled structures for x-ray exposed devices because LIGA-like processing produces vertical pattern variation of less than 0.1  $\mu\text{m}$  per 100  $\mu\text{m}$  of structural height. The thick photoresist processing which is being used here has maintained this highly desirable attribute and if anything has produced better sidewall finishes as Fig. 1 illustrates.

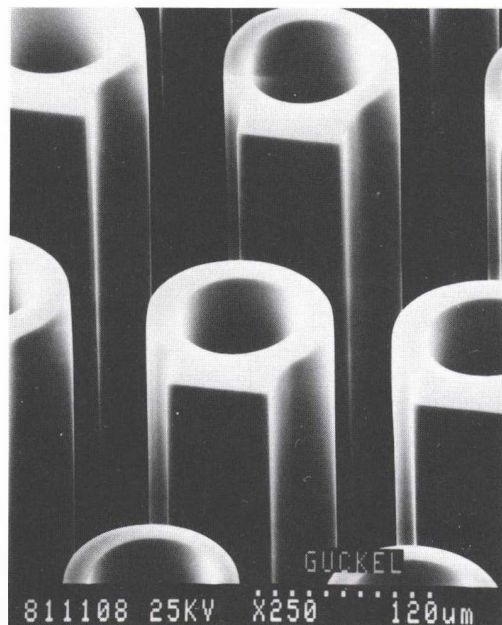


Fig. 1 3.2 mm high PMMA posts after developing.

## ACTUATOR RESULTS

The physical layout of the linear actuator is shown in Fig. 2. The electromagnet uses 20 turns. It is designed in such a way that flux saturation occurs for air gaps of  $10\ \mu\text{m}$  with a fully closed slider at  $100\ \mu\text{m}$  of structural height. Maximum allowed terminal current is  $500\ \text{mA}$  which produces an mmf of up to 10 ampere-turns. The details of the construction technique for the magnet are given in reference [1]. The magnet design has been verified by two and three-dimensional numerical calculations. Output forces of  $280\ \mu\text{N}$  at  $100\ \mu\text{m}$  structural height indicate that the design goal of  $1000\ \mu\text{N}$  can be reached easily at  $500\ \mu\text{m}$  height. The instability which a displacement of the slider in the gap can cause is prevented by spring design and four posts which prevent the slider from contact with the magnet pole faces.

Figure 2 employs three photodiodes. The two large ones are for DC-biasing. A shuttered photodiode under the slider acts as a position sensor and can also be used in connection with a simple phase shifting network to attempt self-resonant excitation with unmodulated light. The spring-slider combination to accomplish this is shown in Fig. 3.

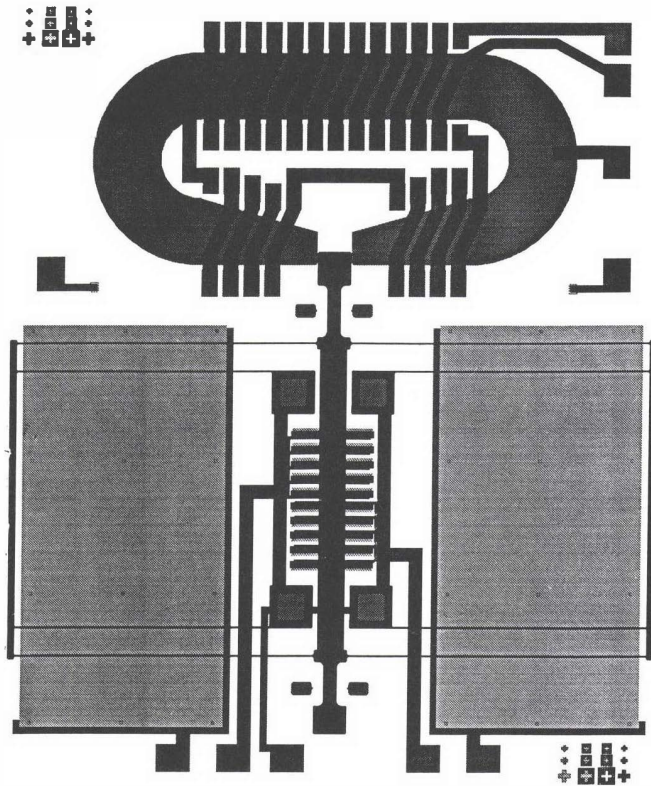


Fig. 2 Layout for single sided linear actuator with photodiodes

The spring design involves spring constants of roughly 1 Newton/meter with  $250\ \mu\text{m}$  of total travel. Since the spring is very tall the system becomes very stiff in the substrate direction. Assembly of the spring to square posts has proven to be quite simple and has produced rigid supports for the slider. Fig. 4 illustrates the structure just before wire bonding. The device which is shown in Fig. 4 is the push-pull version of the actuator.

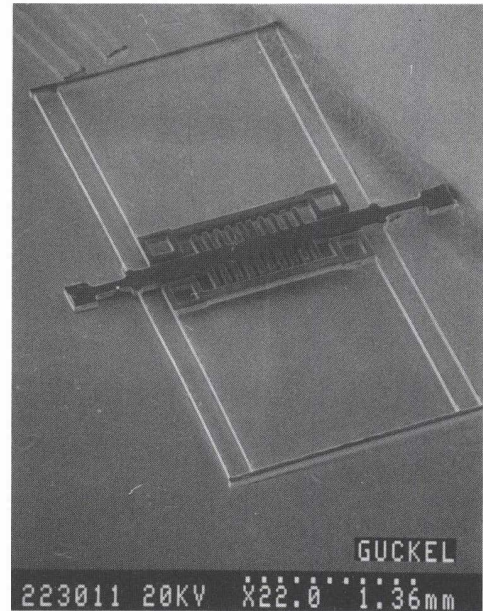


Fig. 3 Shutter-slider with springs prior to assembly.

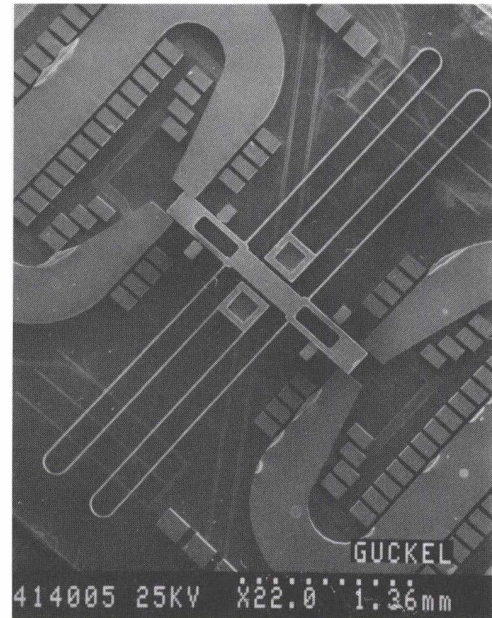


Fig. 4 Assembled double-sided actuator.

The DC-displacement of the actuator is very close to predicted values. Thus, 300 mA of DC-current into 5 ohms produces 200  $\mu\text{m}$  of travel. Further improvements will occur with better coil construction techniques.

The fundamental resonance of this type of actuator is low because the total slider mass approaches 1 milligram. This produces typical resonances near 230 cps with quality factors of 40 in air. Oscillation amplitudes of 120  $\mu\text{m}$  peak-to-peak with 5mA of excitation have been obtained and involve power dissipation in the 100  $\mu\text{Watt}$  range.

### CONCLUSION

The results which have been achieved so far indicate that linear actuators with sufficient force output and travel are feasible. The preliminary structures will improve with better coil fabrication techniques. Very much reduced device areas will result from modified LIGA-like processing sequences which emphasize three-dimensionality. The availability of permanent magnets is anticipated and will do much to reduce power dissipation in the devices.

### ACKNOWLEDGMENTS

This work was supported in part by the National Science Foundation under grant #ECS-9116566. Additional financial support via ARPA-DALP Contract ONR N00014-93-1-0911 is acknowledged. The cooperation of Dr. E. Johnson and Dr. D.P. Siddons of Brookhaven National Laboratory is gratefully acknowledged. Mr. T. Martin's (Quantum Devices Inc.) assistance with wire bonding is greatly appreciated. We acknowledge the support of the staffs of the Center for X-ray Lithography, F. Cerrina, Director, and the Synchrotron Radiation Center for their help and the use of their facilities. The Center for X-ray

Lithography is supported by SEMATECH Center of Excellence SRC Grant No. 88-MC-507 and the Department of Defense Naval Research Laboratory Grant No. N00014-91-J-1876. The Synchrotron Radiation Center, D. Huber, Director, is supported by the National Science Foundation Grant No. DMR-88-21625.

### REFERENCES

- [1] H. Guckel, T.R. Christenson, K.J. Skrobis, J. Klein, M. Karnowsky, "Design and Testing of Planar Magnetic Micromotor Fabricated by Deep X-ray Lithography and Electroplating," *Transducers '93 Conference, Yokohama, Japan, 7-10 June 1993*, pp. 76-79.
- [2] H. Guckel, D. W. Burns, C. C. G. Visser, H. A. C. Tilmans, D. DeRoo, "Fine Grained Polysilicon Films with Built-in Tensile Strain," *IEEE Trans. on Elect. Devices*, Vol. 35, No. 6, June 1988, pp. 800-801.
- [3] E.W. Becker, W. Ehrfeld, P. Hagmann, A. Maner, D. M $\ddot{u}$ nchmeyer, "Fabrication of Microstructures with High Aspect Ratios and Great Structural Heights by Synchrotron Radiation Lithography, Galvanofarming, and Plastic Moulding (LIGA Process)," *Microelectronic Engineering*, 4, pp. 35-56, 1986.
- [4] H. Guckel, "Micromechanics via X-Ray Assisted Processing," *American Vacuum Society 40th National Symposium, Orlando, FL, 15-17 November 1993*, to be published in *Journal of Vacuum Science and Technology*.
- [5] D.P. Siddons, E.D. Johnson, and H. Guckel, "Precision Machining using Hard X-rays," *Synchrotron Radiation News*, Vol. 7, No. 2, 1994, pp. 16-18.
- [6] H. Guckel, K. Skrobis, T. R. Christenson, J. Klein, S. Han, B. Choi, E.G. Lovell, "Fabrication of Assembled Micromechanical Components via Deep X-ray Lithography," *Proc. of IEEE Micro Electro Mechanical Systems, Nara, Japan, Jan. 1991*, pp. 74-79.

## Micro-hotplate Gas Sensor

R. E. Cavicchi\*, J. S. Suehle, P. Chaparala<sup>o</sup>, K. G. Kreider,  
M. Gaitan, and S. Semancik

National Institute of Standards and Technology, Gaithersburg, MD 20899

### Abstract

Micro-hotplates have been fabricated on a silicon wafer using CMOS technology. These micro-machined devices offer a wide range of temperature control, from 20 °C -550 °C or 1000 °C, depending on design materials, and a fast thermal response of about 1 ms. They may be fabricated in arrays with electrical circuitry on the same chip. To make sensors from CMOS chips or wafers requires a new technology for processing, which include anisotropic etching of Si, lithography, and film deposition. All process steps must be compatible with existing CMOS components and structures and must take into account the geometry and stability of micromachined structures. For gas sensors that use semiconducting oxides, the challenge is to make ohmic contacts that use a very small contact area and are rugged against thermal cycling. The micro-hotplate array can serve as a mini-laboratory for efficient process optimization using parallel experiments. The elements of a micro-hotplate array can be programmed with different temperature schedules through the process steps, and subsequently analyzed in one test/characterization cycle. An example of a film growth study is shown in which array elements are set to different temperatures during sputter deposition of tin oxide. The rapid thermal time constant of these structures offers opportunities for new modes of sensor operation which can reduce the power consumption and improve the selectivity of oxide sensors. Techniques that uses temperature pulses are demonstrated for low power sensing of H<sub>2</sub> in air and for distinguishing ethanol from methanol vapor.

### Introduction

The development of gas sensors based on micromachined structures is a rapidly growing area of research. Potential advantages include low power consumption, lower cost and higher reliability via batch fabrication, improved selectivity through the use of arrays, and the development of "smart sensors" that incorporate on-chip electronics for data acquisition and signal processing. A key element for many applications is temperature-control. We have developed micromachined "micro-hotplate" arrays in which each element in the array performs the function of a conventional "hotplate" on a microscopic scale. The micro-hotplates may be used for heating during fabrication of the sensing films, for producing fixed temperature matrices and also fast temperature modulation during sensor operation, and for reconditioning of the active sensing films.

Figure 1 shows one design configuration of a micro-hotplate<sup>1</sup>. This device consists of a micromachined bridge which supports the following successive layers separated by insulation: 1) a polysilicon heater; 2) an aluminum hotplate with electrical connections for 4-point temperature measurement; and 3) open aluminum contact pads to make electrical contact to a deposited overlayer. This device has a temperature range from 20 to 550°C (limited by thermal migration of the aluminum), thermal time constant of 1 ms, and a temperature/power coefficient of 8 °C/mW. Other designs which use only polysilicon and no aluminum have temperature ranges to 1000 °C.

The basic micro-hotplates are fabricated using a combination of CMOS device fabrication and post-CMOS processing steps. The use of CMOS chips offers the advantages of high reliability, low-cost,

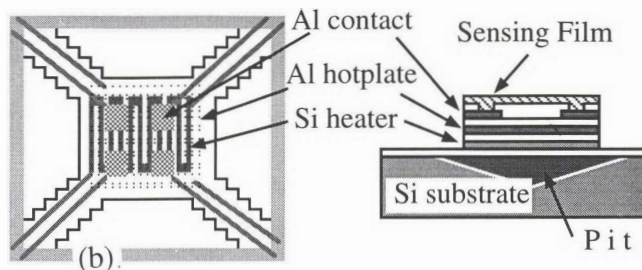
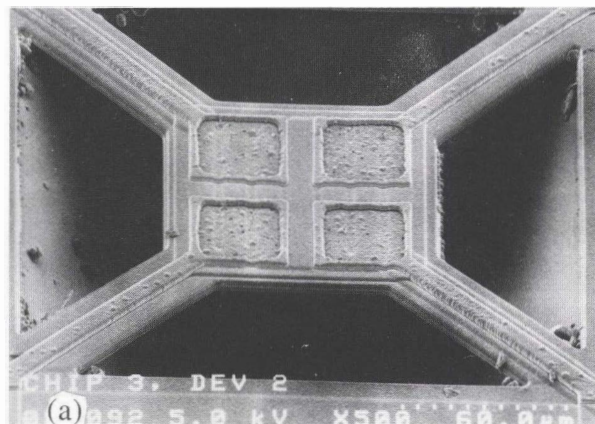


Figure 1. (a) SEM micrograph of suspended micro-hotplate structure with SnO<sub>2</sub> film coating. (b) Schematic illustrating the various layers comprising the structure.

and simple integration of on-chip electronics for multiplexing and signal processing. Chips received from the foundry are etched to realize the microbridge structures. Additional post-CMOS processing is required to optimize the electrical contacts to the sensing film, and to deposit selective sensor coatings on the individual micro-hotplates.

Development of these processing steps is an area where there remains much applied research to be done. Example technological issues are the ability of post-CMOS layers to withstand the harsh anisotropic etch, lift-off of photolithographically defined layers on micro-machined structures, surface cleaning procedures, formation of ohmic contacts to sensing films, the choice of top-side or bottom side contacts, calibration of temperature and the achievement of a uniform temperature distribution over the hotplate, and the thermal and mechanical stability of thin films and interfaces over small (10-100 $\mu\text{m}$ ) length scales at the elevated temperatures and rapid thermal cycles that will be used during micro-hotplate device operation.

Gas sensors based on the conductance change of semiconducting oxides at elevated temperatures are traditionally operated at a fixed temperature in the range 300  $^{\circ}\text{C}$  to 700  $^{\circ}\text{C}$ . In this operating mode, many gases can give rise to a conductance change in the sensor, and the ability to determine the composition of the sensed gas is limited. Partial selectivity to a specific gas is obtained through the use of catalytic additives to the sensing film. Because of the rapid thermal time constants for micro-hotplate based sensors, other modes of sensing are possible. These modes will use the dynamic response at specific temperatures to characterize surface chemical reactions that are producing a sensing response. An example of one operating mode is a repetitive temperature pulse train in which the conductance is measured between pulses. The characteristic response to this pulse train can be analyzed using pattern recognition algorithms which can be incorporated into the CMOS electronics on the sensor chip. In principle, the device can use additional alternative pulse trains to further refine the compositional analysis.

### Microscopic Thermal Processing of Materials

Solid state gas sensors commonly use catalyst-doped tin oxide as the active sensing medium. Sensing properties depend on the film microstructure, which in turn depends on the growth and subsequent thermal processing of the film. We use the micro-hotplate array to simultaneously set temperature process schedules

for the individual micro-hotplates during tin oxide deposition. Experiments were done using both 36 and 4-element arrays. Using in-situ electrical measurements, and ex-situ scanning electron microscopy images (Figure 2), we were able to quantify the increase in electrical conductance and film microcrystal size with growth temperature. This technique has also been used in conjunction with chemical vapor deposition as a self-lithography. In

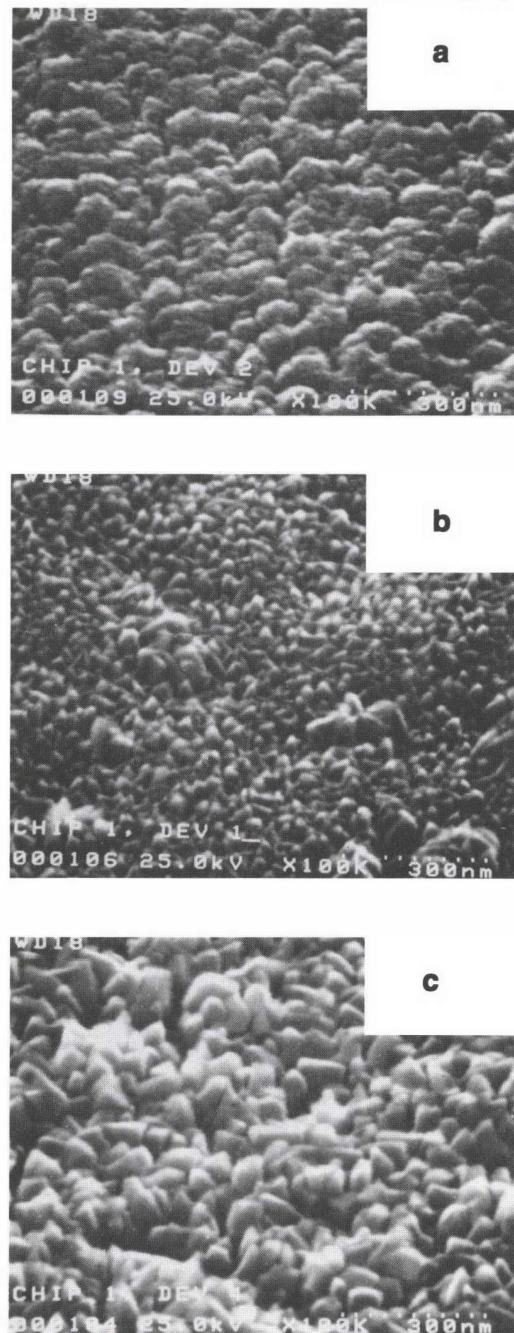


Figure 2. SEM micrographs of  $\text{SnO}_2$  films grown on three micro-hotplates on the same chip. Each micro-hotplate was set to a different temperature during the growth as follows: (a) 25  $^{\circ}\text{C}$ , (b) 300  $^{\circ}\text{C}$ , (c) 500  $^{\circ}\text{C}$ .

this case, a film grows only on the hotplates that are heated to the deposition temperature required by a given chemical vapor. Such temperature-processing of sensing films can also be used to periodically recondition an operating sensor, for example, to eliminate the buildup of contamination during operation.

### Temperature Pulsing for Sensor Operation

The very fast thermal response of micro-hotplates offers new opportunities for sensor operation. For reasons of lower cost and portability, sensors with reduced power requirements are desirable. Micro-hotplates used in our experiments require 47 mW to maintain 400°C, about ten times less power than a conventional Figaro sensor. Operation of sensors at much lower power levels is possible using temperature pulsing. As a demonstration, we have measured the response of SnO<sub>2</sub> to 0.1 % H<sub>2</sub> in air using 400°C, 10 ms temperature pulses every 1 s as shown in Figure 3. The power consumption of the device is only 470 μW. A sensor operating at this power level would run for nearly a year on an alkaline 9 V battery.

Transient phenomena can also be used for sensing. A tin oxide-coated micro-hotplate was subjected to a constant dose of water vapor (important for humidity effects on sensors). In Figure 4 is shown the electrical response to 500°C 10 ms desorption pulses and subsequent re-adsorption of H<sub>2</sub>O. The data is shown for a dose at 1.3 Pa. The response amplitudes and transient characteristics have been measured at different pulse amplitudes, base temperature, and pulse durations to obtain

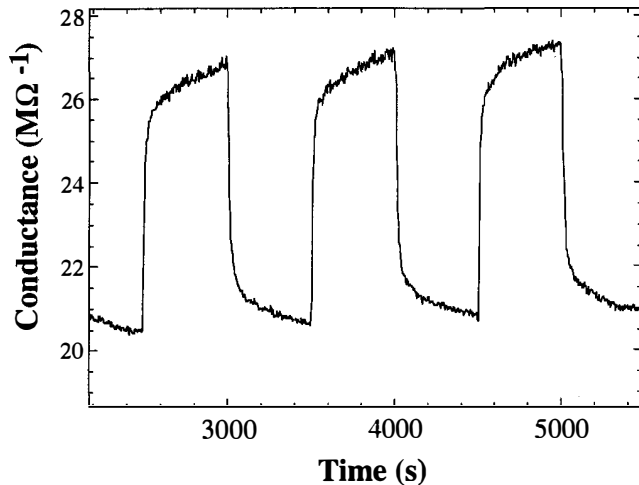


Figure 3. Response to exposure cycles of air injected with 0.1 % hydrogen every 500 s. Sample is operated using 10 ms pulses to 400 °C every 1.0 s. Conductance is measured at room temperature, between the pulses.

adsorption/desorption kinetic parameters--a signature of the H<sub>2</sub>O response. Response is easily detectable at 0.01Pa. Measurement of low partial pressures of water vapor in vacuum deposition environments is a critical issue that micro-hotplate technology may be able to address. Response at very low pressures may be obtainable using polymer films that are highly sensitive to water.

These sensors can also be operated in temperature-pulsed modes in which the amplitude of the temperature pulse is varied. Figure 5 shows an operating mode in which a series of increasing temperature pulses is applied, with a constant temperature increment. The conductance is measured between the pulses, while the micro-hotplate is at room temperature. The pulse cycle is repeated continuously. The response to admission of methanol and ethanol to air is shown in Figure 6. Both gases cause an increase in the tin oxide conductance. Conventional oxide sensors, operating at a fixed temperature would have difficulty in distinguishing the two gases, as both would give rise to a conductance increase. The patterns of response to the pulse sequence as shown in Figure 6 (b), a portion of the data in Figure 6 (a), reveals clear differences between the kinetic behavior of the two gases. A sensor operating with pattern recognition circuitry would be able to select which gas was being sensed. Pulse sequences in which the pulse width or duty cycle are also varied would provide additional selectivity enhancements.

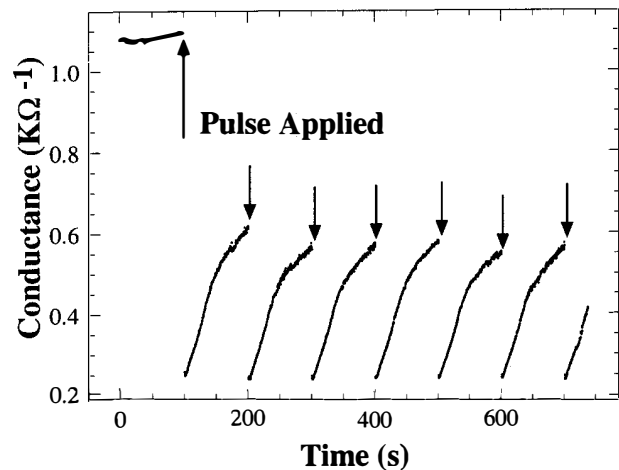


Figure 4. Pulsed desorption - adsorption sequence for H<sub>2</sub>O on SnO<sub>2</sub> on a micro-hotplate. While dosing at 1.3Pa (10mT), and with a base temperature of 20°C, the sample was pulsed to 500°C for 10 ms, every 100 s.

## Conclusions

Micro-hotplates have been fabricated from CMOS integrated circuit chips. The devices have a wide temperature range and fast thermal response. Processing CMOS-fabricated chips into smart sensors presents new challenges for process technology. The ability to thermally process materials on an array of devices allows for efficient optimization of some of these processes. The rapid thermal response of micro-hotplate based sensors offers new avenues for achieving selectivity to specific gases. Temperature-pulsed operating modes have been used to demonstrate the ability to distinguish two gases.

## Acknowledgement

We would like to acknowledge Samuel Jones for the SEM images in this report.

\*R. E. Cavicchi, Bldg 221 A303, NIST, Gaithersburg MD 20899  
E-MAIL: dcav@enh.nist.gov

◊NIST Graduate Research Fellow at the Center for Reliability Engineering, Univ. MD.

1.) J. S. Suehle, R. E. Cavicchi, M. Gaitan, and S. Semancik, IEEE Electron Device Lett., Vol. 14, no. 3, pp. 118-120, 1993.

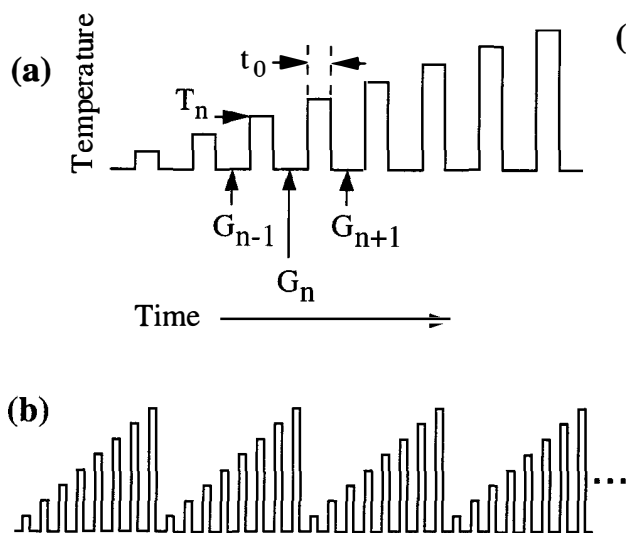


Figure 5. (a) Temperature pulse train applied to the micro-hotplate during sensor operation. Pulse width is  $t_0$ . Conductance  $G$  is measured between pulses, while the sample is at 30 °C. This pulse train is repeated as shown in (b).

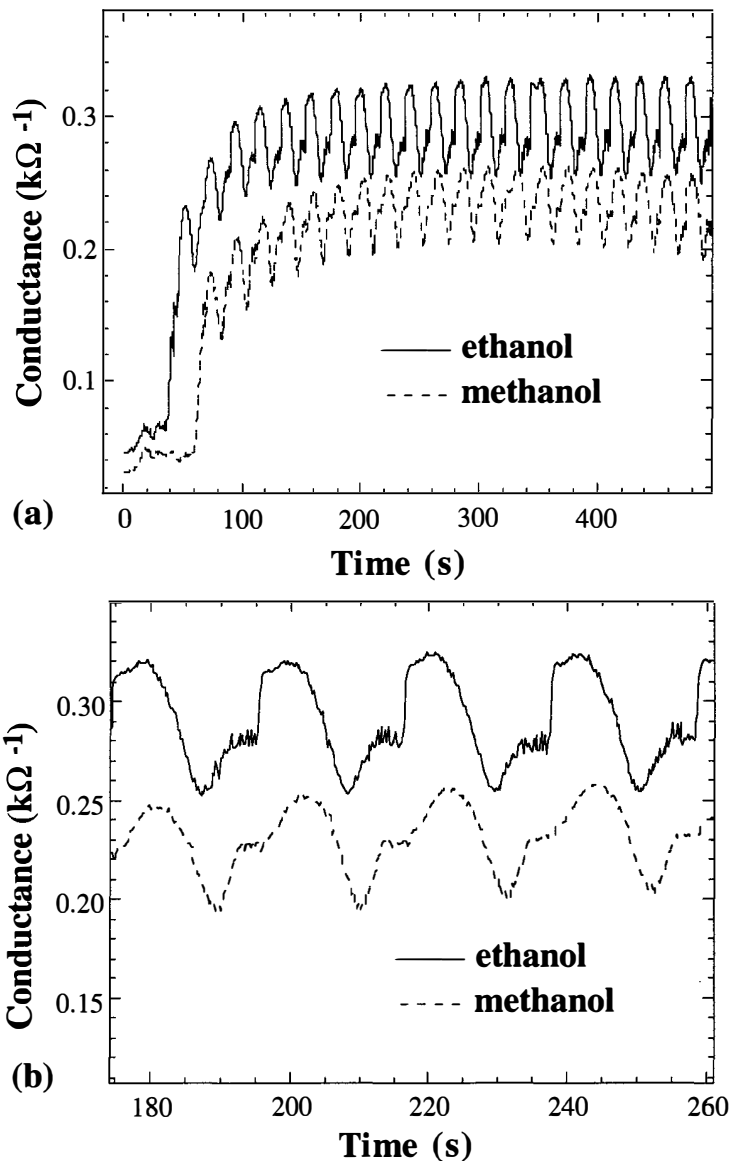


Figure 6. Response of a gas sensor using the repetitive sequence of temperature pulses as described in Figure 5. The sample is a SnO<sub>2</sub> film on a micro-hotplate. The pulse temperature ranged from 30 to 450 °C in 5 °C steps. Pulse width was 100 ms. Conductance is measured between the pulses. (a) Response to the admission of ethanol or methanol vapor. (b) Detail from the data in (a), showing the response to four cycles of the temperature pulse sequence. The sample pulse is at 30 °C at 174 s and 450 °C at 194 s.

# THE RESPONSE OF THE SANDIA ROBUST WIDE RANGE HYDROGEN SENSOR TO H<sub>2</sub>-O<sub>2</sub> MIXTURES

R.C. Hughes, D. J. Moreno, M. W. Jenkins, and J. L. Rodriguez  
Sandia National Laboratories  
Albuquerque, New Mexico, 87185

## ABSTRACT

The Sandia Robust Hydrogen (SRH) sensor can detect partial pressures of H<sub>2</sub> over a wide range (~1 ppm to pure H<sub>2</sub>) because it employs two different kinds of catalytic metal sensors. A Field Effect Transistor (FET) with a catalytic gate detects low H<sub>2</sub> concentrations and a resistor of the same metal is accurate for the higher concentrations. The use of Pd alloys with Ni preserves sensor reversibility by preventing the hydride phase transition under normal operating conditions. Mixing O<sub>2</sub> with H<sub>2</sub> does change the sensor signal under some conditions and comparison of the behavior of a pure Pd device with a Pd/Ni device is given. The H<sub>2</sub> concentration in flammable mixtures can be obtained, but an additional sensor is needed to measure the concentration of oxidant.

## INTRODUCTION

The Sandia Robust Hydrogen (SRH) sensor was designed to solve a wide variety of hydrogen sensing problems in the military, space and commercial arenas. Batch fabrication can lead to large numbers of inexpensive, nearly identical sensors. This makes it feasible to deploy many point sensors in complex systems like rocket motors, semiconductor processing lines and petrochemical plants for safety and process control. The details of the design and fabrication in a standard CMOS silicon line have been reported [1]. This platform improves on the numerous other implementations in Si of Lundström's original field effect sensor concept [2] in two important ways: 1) a field effect transistor (FET) and resistor using the same thin film catalytic metal are on the same chip, along with the heater and temperature measuring p/n junction. 2) A series of Pd alloys with Ni have been developed that allow study of high H<sub>2</sub> partial pressures (pH<sub>2</sub>'s), up to pure H<sub>2</sub>. One of the beneficial aspects of the Ni alloy is that the hydride phase transition requires much higher pH<sub>2</sub>'s; sensor reversibility depends on not going through the phase transition [3]. In this paper we will present the first reports of the data from SRH sensors comparing pure Pd with Pd/Ni metallizations for sensing mixtures of H<sub>2</sub> and O<sub>2</sub>.

Over the years there have been a number of reports on the response of catalytic gate field effect devices to mixtures of H<sub>2</sub> and O<sub>2</sub> in both ultra high vacuum and laboratory air. Some of these studies have been reviewed by Lundström, et al. [2,4] and it has been found that the sensor response is a complicated function of the partial pressures of both H<sub>2</sub> and O<sub>2</sub>. No single model predicts the behavior of all the experimental sensors, and there is a wide variation in the ratio of response to a given pH<sub>2</sub> with and without O<sub>2</sub> present among more or less "identical" sensors. In general the presence of high pO<sub>2</sub> causes the signal from a given pH<sub>2</sub> to become smaller.

The models all assume that H<sub>2</sub> molecules must dissociate into adsorbed hydrogen atoms (H<sub>a</sub>) on the outer surface of the catalytic thin film. Dissociation is always the slow step in the response of the sensor to steps in pH<sub>2</sub>. The H<sub>a</sub> quickly comes into equilibrium with H in the bulk of the film and the field effect sensing sites on the inner metal/insulator interface. The isotherms for the bulk and interface are very different [3] so that the FET has a large response for low pH<sub>2</sub> and the resistor gives accurate values for high pH<sub>2</sub>, notably in the range for explosive mixtures of H<sub>2</sub> (30 Torr).

When no O<sub>2</sub> is present, the gas phase pH<sub>2</sub> is in thermodynamic equilibrium with the surface, bulk and interface. However, the presence of O<sub>2</sub> leads to the water forming reaction on the catalyst surface. At low pH<sub>2</sub> and high pO<sub>2</sub> the chemical reaction causes

both the FET and the resistor to give a reading indicating lower pH<sub>2</sub>'s. At pH<sub>2</sub>'s above about 6 Torr, our Pd/Ni sensors show little effect from a pO<sub>2</sub> of 140 Torr (the pure Pd devices are destroyed by these pH<sub>2</sub>'s, so no data is available). It is beyond the scope of this paper to validate a particular detailed model of H<sub>2</sub>-O<sub>2</sub> reactions on Pd and Pd/Ni thin films. Rather we show the practical results of both kinds of catalytic sensor in laboratory environments. The response of the Pd/Ni sensor at the higher levels of pH<sub>2</sub> and pO<sub>2</sub> is given special attention.

## EXPERIMENT

A photograph of the SRH sensor is seen in Fig. 1. The die size is approximately 270 by 120 mils. The large Al metallizations at both ends are power MOSFETs for heating the chip. The use of MOSFETs allows lower power consumption in the control circuits than resistive heaters. There are nine diodes for use as temperature sensors and ESD (electrostatic discharge) protection circuitry. The 6 pairs of catalytic gated FET's are in the center of the die. In practice only one FET is bonded out and no significant performance differences were observed with the different FET designs. The meander line H<sub>2</sub> sensing resistor can be seen in the lower middle of the chip. The catalytic gates and resistors are deposited in a sputtering process as the last step in the wafer fabrication. The sputter target for the Pd/Ni sensors has 9% (atomic) Ni. For both the Pd and Pd/Ni sensors the metallizations are 0.1 microns thick and the 20 micron wide meander line gives the Pd/Ni resistor about 1000 ohms base resistance. More fabrication details are given in Ref. [1].

A printed circuit board with the analog control circuit and signal processing is used for each sensor. The analog signals from the sensor read-out circuits are digitized and sampled by a LabVIEW

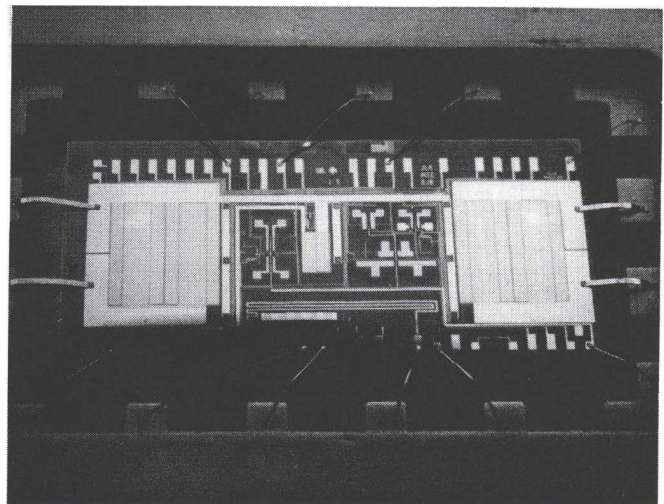


Fig. 1. A photograph of the SRH sensor mounted in a 16 pin DIP package. The die size is approximately 270 by 120 mils. The large Al metallizations at both ends are power MOSFETs for heating the chip. The 6 pairs of catalytic gated FET's are in the center of the die. The meander line H<sub>2</sub> sensing resistor can be seen in the lower middle of the chip.

program. The data was obtained with a previously described Gas Sensor Test Bed [3], using a manifold that has fixtures for separate sensors in series with the flow of the mixtures. These experiments had one Pd SRH and one Pd/Ni(9%) SRH along with a commercial fuel cell oxygen sensor (Nyad, Inc., Concord, CA, model OS-2) in series. The flow rate for the data shown in this paper was held at one Standard Liter per Minute (SLM). Using a flow rate a factor of five lower did not change the signals for mixtures of H<sub>2</sub> and O<sub>2</sub>. The atmospheric pressure in the laboratory is about 630 Torr; the back pressure due to the flow is only a few Torr, less than daily variations in pressure. The partial pressures given in this paper are either in % (because of common usage) or Torr.

## RESULTS

Fig. 2a and 2b show typical data for one of the sensors, the Pd/Ni metallized device. In this case the device operating temperature was 80°C and the test protocol requires a 140°C anneal in synthetic air for 15 minutes in order to zero the FET before each series of test mixture pulses. The signal processing circuit [1] for reading the threshold voltage of the FET allows the analog output voltage to be zeroed with a potentiometer. Therefore the signal is proportional to the FET threshold voltage but is offset from the actual voltage. Each pulse of a gas mixture is followed by a "purge" or anneal in synthetic air.

Fig. 2a shows the FET results for two sets of pH<sub>2</sub> concentrations, 0.05% (500 ppm) and 4%, for a series of increasing pO<sub>2</sub>'s, 5%, 10%, and 20%. The last mixture is at the Lower Explosive Limit (LEL) for H<sub>2</sub>-O<sub>2</sub> mixtures. Each data point is 10 seconds apart. The FET threshold voltage goes in a negative direction when exposed to H<sub>2</sub>. It can be seen that the air purge at 80°C does not return the sensor reading to zero in the few minutes allotted in these experiments. That is the reason that the voltage at time zero is also not zero; there were other sets of pulses before the selected ones shown. There are some deeply adsorbed H<sub>a</sub>'s that require a longer or higher temperature purge for removal. For the pulses with 4% pH<sub>2</sub> the small effect of pO<sub>2</sub> mentioned above can be seen.

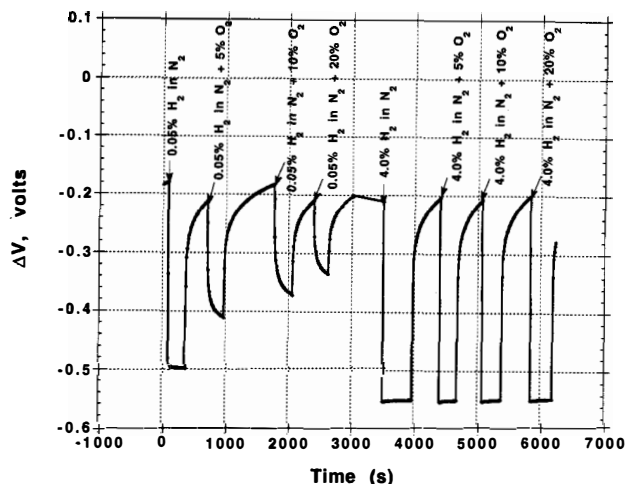


Fig. 2a. Pd/Ni FET operating at 80°C and exposed to several pulses of H<sub>2</sub>-O<sub>2</sub> mixtures. The zero is defined as the FET threshold voltage after a 140°C anneal in air. H<sub>2</sub> causes the threshold voltage to move in the negative direction. Each pulse labeled in the Fig. is followed by a dry air purge before the next mixture is selected. Data points are 10 sec apart. The last pulse, with 4% pH<sub>2</sub> (25 Torr) and 20% O<sub>2</sub> (130 Torr), is at the lower explosive limit (LEL) for H<sub>2</sub>-O<sub>2</sub> mixtures.

Fig. 2b shows the signal from the resistor on the same chip taken at the same time. The zero for the resistor was also set after the 140°C anneal and the pulses of H<sub>2</sub> before the sets shown have established a new baseline at a slightly negative value. This is a repeatable phenomenon for these resistor sensors. H dissolved in the bulk of the metal film increases the resistance because of increased electron scattering. The 0.05% (500 ppm) pH<sub>2</sub> pulse gives a very small signal, about 0.3 in units of % change in resistance over base resistance. Adding pO<sub>2</sub> reduces the signal to close to zero. The isotherm for the bulk concentration of H follows a  $\sim(\text{pH}_2)^{0.5}$  relation [3] and so the signal for 4% pH<sub>2</sub> is much larger. The result of adding a pO<sub>2</sub> of 20% (120 Torr) is a small reduction in signal. The fact that this mixture is at the lower explosive limit has little effect on the trend of the data; the temperature of the sensor is too low to support true combustion. The "error" in reading the pH<sub>2</sub> level without knowledge of the pO<sub>2</sub> level in this case is about 20% (i.e. the signal for the last pulse would correspond to 20 Torr instead of 25 Torr pH<sub>2</sub>). Data taken with a higher pH<sub>2</sub>, 252 Torr, shows no difference between pO<sub>2</sub>=0 and 120 Torr.

The Nyad O<sub>2</sub> sensor gives accurate readings of the pO<sub>2</sub> even in the presence of H<sub>2</sub>. Data has been taken up to 252 Torr pH<sub>2</sub> for 130 Torr of pO<sub>2</sub>.

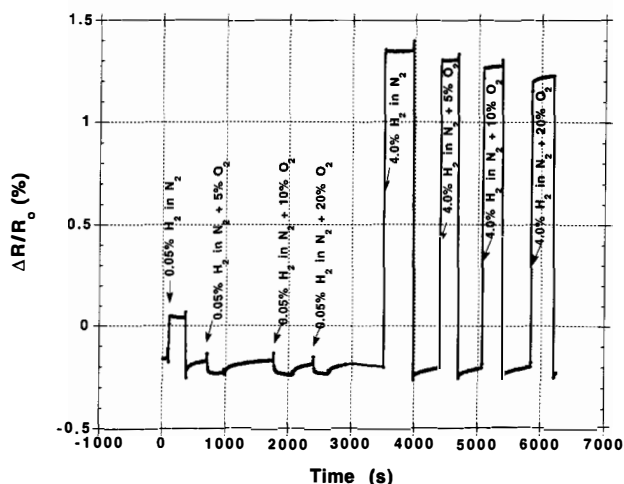


Fig. 2b. The Pd/Ni resistor data on the same sensor as for Fig. 2a taken at the same time. The value of zero is defined after the 140°C anneal and several H<sub>2</sub> exposures prior to the data shown here establish a new "zero" value for the resistor.

Figs. 3 and 4 show the steady state signals from both the Pd and Pd/Ni SRH FET sensors including the data from Fig. 2. The threshold voltage shifts,  $\Delta V$ , in Figs. 3 and 4 were computed using the zero annealed value and the sign was changed to give consistent positive signals. The data for three temperatures is given for both pO<sub>2</sub> equal to zero and 20%. These data emphasize the fact that the ratio of the signals with and without O<sub>2</sub> are remarkably independent of temperature. The lines connecting the data points are guides to the eye. The thick dashed line in Fig. 3 is from a model described in the Discussion section.

Figs. 5 and 6 show the steady state signals from both the Pd and Pd/Ni resistor sensors including the data from Fig 2b. The signal is measured from the purge value in air to the steady state value. The resistance changes at a given pH<sub>2</sub> are quite temperature dependent because the solubility of H in the films decreases with increasing temperature. In order to show the temperature dependence of the O<sub>2</sub> effect, the data without O<sub>2</sub> at 80°C and 110°C have been normalized to the 50°C data by the following solubility constants: 1.5 times all

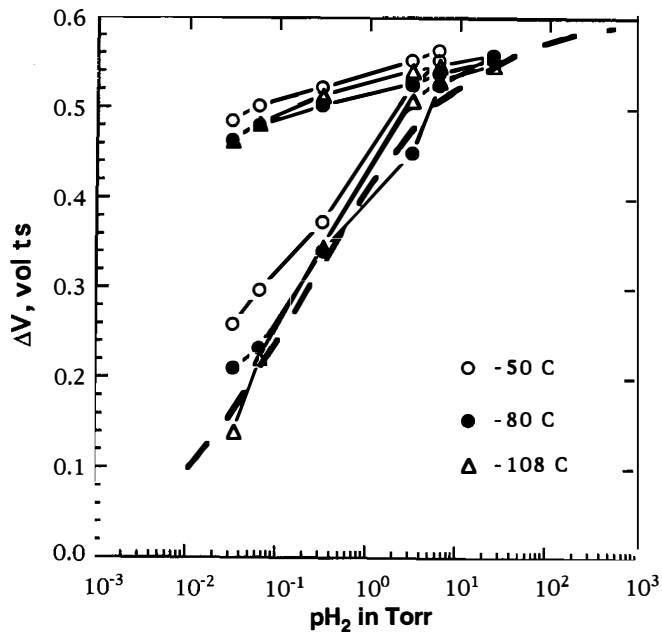


Fig. 3. The Pd/Ni FET threshold voltage shifts at the three indicated temperatures. The top three sets are the isotherms in  $N_2$ , while the lower curves are in 20%  $O_2$ . The zero value is defined after a purge in air at  $140^\circ C$ .

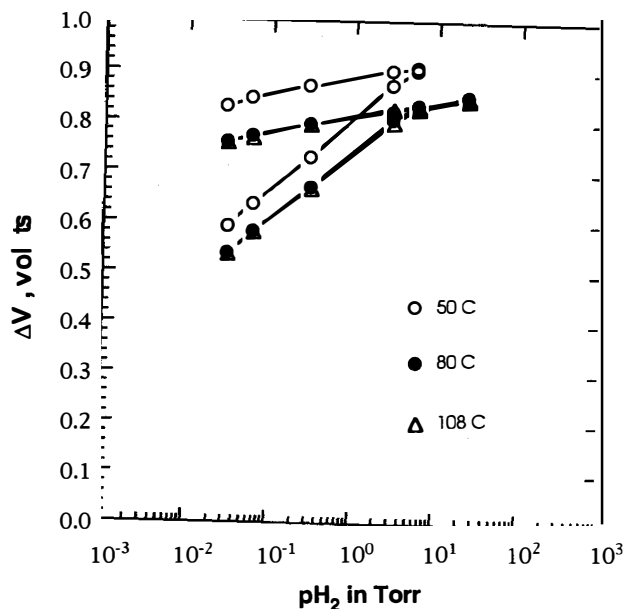


Fig. 4. Pd FET data at three temperatures. The top three sets are the isotherms in  $N_2$ , while the lower curves have 20%  $O_2$ . The zero value is defined after a purge in air at  $140^\circ C$ .

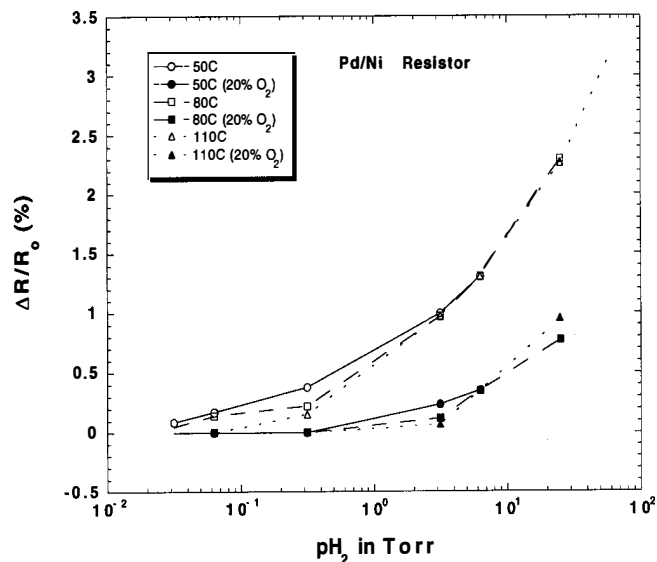


Fig. 5. The signals from the Pd/Ni resistor taken at the same time and on the same chip as Fig. 3. Examples of some of the data are seen in Fig. 2b. The temperature dependence due to  $H$  solubility has been normalized to show the lack of temperature dependence of the mixture signals. The lower data are for the mixtures with 20%  $O_2$ .

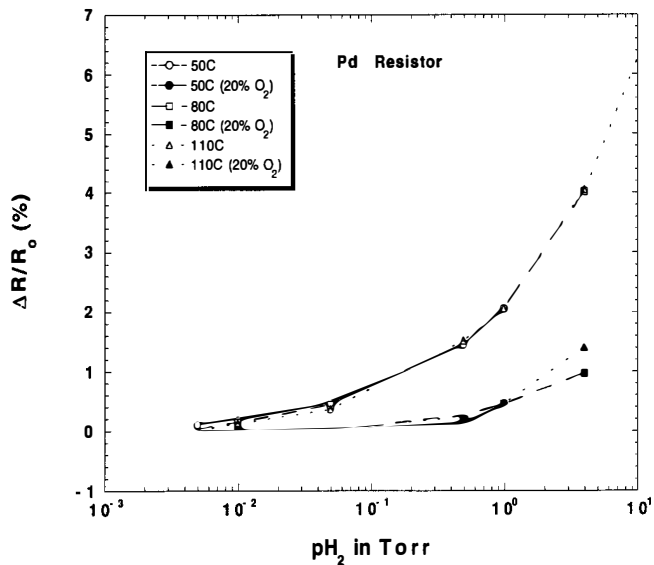


Fig. 6. The signals from the Pd resistor taken at the same time and on the same chip as Fig. 4. The temperature dependence due to  $H$  solubility has been normalized to show the lack of temperature dependence of the mixture signals. The lower data are for the mixtures with 20%  $O_2$ .

the  $80^\circ C$  data and 2 times all the  $110^\circ C$  data. All the steady state signal data with 20%  $O_2$  were normalized to the  $110^\circ C$  data for clarity. The intent of plotting the data in this fashion is to emphasize that the same lack of temperature dependence of the  $pO_2$  effect shows up in both the FET data and the resistor data.

## DISCUSSION

The models for the effect of  $pO_2$  on the signal from a given  $pH_2$  mostly differ in assumptions about chemical reaction rate constants between species adsorbed on the catalyst surface. Since there are many possible species and values for the rate constants which are difficult to measure, it has been hard to "prove" one model over another. A particularly simple model given by Lundström [4] assumes that  $O_2$  reacts directly with  $H_a$  and a steady state solution to the kinetic equations gives:

$$\Delta V / (\Delta V_0 - \Delta V) = A/B (pH_2/pO_2)^{0.5}$$

where  $\Delta V$  is the measured FET threshold voltage shift,  $\Delta V_0$  is the maximum shift seen at very high  $pH_2$ ,  $A$  is a rate constant for  $H_2$  dissociation and  $B$  is a rate constant for the  $O_2$  reaction. The data in Figs. 3 and 4 with  $pO_2$  can be fit fairly well with this equation. The dashed thick line in Fig. 3 shows one theory curve for a value of  $A/B$ . On a semilog plot like this different values of the  $A/B$  ratio simply translate the theory curve along the x axis. The lack of temperature dependence in the data can be rationalized by assuming that the rate constants  $A$  and  $B$  both have the same activation energy.

For  $pH_2$ 's lower than about 1 Torr, there is an obvious difference in the  $pO_2$  effect between Pd and Pd/Ni in Figs. 3 and 4. This difference can be used in a pattern recognition scheme to obtain values for unknown  $pH_2$  and  $pO_2$  values. One such scheme was given in Ref. [5] using Pd/Ag and Pd tunnel diode sensors. So far this procedure has not proven to be very reliable because different sensors, which should be close to identical, give different  $A/B$  ratios depending on the cleanliness of the catalytic surface and other undefined conditions [4].

In addition, all the pattern recognition schemes fail for high  $pH_2$  where there is no effect on the sensor signal from  $pO_2$ . The Nyad  $O_2$  sensor was shown to provide accurate  $pO_2$  values even in the presence of high  $pH_2$ , up to 252 Torr. There are many potential users who wish to know the  $pH_2$  as accurately as possible in order to know if an explosive mixture exists. Combining an SRH and fuel cell  $pO_2$  sensor is one way to solve the problem, although other oxidizing gases, like  $N_2O$ , will also form explosive mixtures with  $H_2$ . Another solution would be to use a combustible gas sensor of the pellistor type to diagnose explosive mixtures. A silicon micromachined pellistor filament could be integrated with the SRH sensor, and although the pellistor technology is notoriously difficult to maintain in calibration, useful information about potentially flammable mixtures could be obtained.

In summary, we have shown that both the Pd and Pd/Ni gated SRH-FET structures respond to  $H_2$ - $O_2$  mixtures in a similar fashion to other field effect Pd devices reported in the literature [2,4]. The FETs can sense the presence of  $H_2$  reliably down to about 10 ppm (~10 milli Torr) in air, but the exact concentration will be undetermined unless the  $pO_2$  is known from other measurements (or if the sensor is outdoors and it can be assumed that  $pO_2$  ~20%). The Pd/Ni FET gives reversible measurements of  $pH_2$  up to pure  $H_2$  as long as the sensor chip temperature is  $>50^\circ C$ .

The resistor sensors do not give reliable readings for less than about 1 Torr  $pH_2$  in air, although for  $pO_2=0$ , they can sense  $pH_2$  to quite low levels. This behavior can be easily understood if it is assumed that the bulk concentration of H follows the same equilibrium relationship to  $H_a$  with or without  $O_2$  present. The Pd/Ni resistor gives accurate readings of  $pH_2$  above ~10 Torr, in particular around the LEL for  $H_2$  of 30 Torr. We are investigating other alloys of Pd with the intent of finding one that is so sensitive to  $pO_2$  that pattern recognition can be used to determine both  $pH_2$  and  $pO_2$  at high  $pO_2$  levels.

## ACKNOWLEDGMENTS

We would like to thank Paul McWhorter and the Sandia colleagues and support staff in the Sandia Microelectronics Development Lab (MDL) for their work on the design, fabrication and testing of the SRH sensor chip. Special thanks to D. Peterson, G. Bailey and B. Tafoya.

This work was performed at Sandia National Laboratories and was supported by the U.S. Department of Energy under Contract No. DE-AC04-76DP00789.

## REFERENCES

1. J. L. Rodriguez, R. C. Hughes, W. T. Corbett, and P. J. McWhorter, "Robust, Wide Range Hydrogen Sensor", in IEDM Tech Digest, IEEE cat. # 92CH3211-0, San Francisco, CA, Dec. 13-16, 1992, pp. 521-524.
2. I. Lundström, C. Svensson, A. Spetz, H. Sungren and F. Winquist, "From Hydrogen Sensors to Olfactory Images—twenty years with catalytic field-effect devices", Sensors and Act., **B13**, 16, (1993).
3. R. C. Hughes and W. K. Schubert, "Thin Films of Pd/Ni alloys for detection of high hydrogen concentrations", J. Appl. Phys., **71**, 542 (1992).
4. I. Lundström, "Hydrogen Sensitive MOS-Structures Part 1: Principles and Applications", Sensors and Actuators, **1**, 403, (1981).
5. R.C. Hughes, W. K. Schubert, T. E. Zipperian, J. L. Rodriguez and T. A. Plut, "Thin-film Pd and Ag alloys and layers for metal-insulator-semiconductor sensors" J. Appl. Phys. **62**, 1074 (1987).

# MICROFABRICATED ELECTROCHEMICAL DETECTOR FOR CAPILLARY ELECTROPHORESIS

Richard J. Reay, Rajeev Dadoo, Christopher W. Storment,  
Richard N. Zare, and Gregory T. A. Kovacs\*

\* To whom correspondence should be addressed. G. T. A. Kovacs, Department of Electrical Engineering, Stanford University, Room CIS 130, Stanford, CA 94305-4070, email: kovacs@glacier.stanford.edu

R. J. Reay, C. W. Storment and G. T. A. Kovacs are with the Department of Electrical Engineering, Stanford University. R. Dadoo and R. N. Zare are with the Department of Chemistry, Stanford University.

## ABSTRACT

A microfabricated electrochemical detector, suitable for retrofitting existing capillary electrophoresis (CE) systems and providing them with improved analytical capabilities has been demonstrated. This approach provides the advantages of electrochemical detection and overcomes previous limitations caused by manual fabrication. Deep channels were plasma etched into a silicon substrate to form coupling channels for conventional CE capillaries. Platinum detection electrodes were lithographically patterned on a glass wafer that was aligned and anodically bonded to the silicon, sealing the capillary channels. After dicing, bond wires were attached to exposed bond pads and capillaries were epoxied into the two coupling channels of each detector. Amorphous ("black") platinum was then electrodeposited onto the detection electrodes, completing the device. When used with custom-built conductivity measurement circuitry,  $\text{Li}^+$  and  $\text{K}^+$  ions were detected at a concentration limit of 0.7  $\mu\text{molar}$ .

## INTRODUCTION

Capillary electrophoresis (CE) is a powerful analytical separation technique for the analysis of complex mixtures. In CE, an unknown sample is introduced at the inlet of a capillary channel filled with a buffer solution, and a high voltage is applied across the length of the capillary. Different constituents of the sample migrate through the capillary at different rates depending on their electrophoretic mobilities. Mobility is a complex function of a particle's charge, mass, and shape in solution. A difference in mobilities allows separation of the sample into its components. By detecting the chemicals passing through the outlet of the capillary as a function of time, and knowing the mobilities of the possible constituents, the chemical composition of the sample can be determined.

Substantial work has already been done in the area of fabricating integrated CE systems. Our origi-

nal efforts in this area were based on fabricating the entire CE column on a silicon wafer using plasma etching, subsequent growth of a dielectric, and sealing with an anodically bonded glass cover. Successful separations resulted, but without undue efforts to increase the deposited dielectric thicknesses, the high breakdown voltages desired could not be achieved. Other groups have made similar efforts [1, 2, 3] including the use of glass as a substrate to avoid breakdown problems due to thin dielectrics on conductive silicon substrates [4, 5]. We decided to pursue a different approach in which we construct the detector from silicon and use a conventional capillary. This strategy avoids breakdown problems and preserves the capability to take advantage of silicon micromachining and, potentially, on-chip circuitry.

Several detectors for CE have been developed including absorbance, fluorescence, mass-spectrometric, and electrochemical methods. Electrochemi-

cal detection has certain advantages including sensitivity and selectivity for individual species [6]. In addition, the required electrodes can readily be implemented in a micromachined device. Several different types of electrochemical detection can be used, including conductivity measurement, impedance spectroscopy, amperometry, and voltammetry. Two key problems with electrochemical detection that need to be overcome are isolation of the detection apparatus from the 1 to 30 kV potentials present, and rejection of power supply noise. If the electrodes are not precisely perpendicular to the fluid flow, a large noise signal is coupled into the electrodes from the high voltage power supply. Another difficulty with previous electrochemical detectors is the irreproducible construction and inaccurate placement of the electrodes inside the separation column [7]. This paper describes a batch-fabricated, micromachined electrochemical detector that overcomes these problems.

## MATERIALS AND METHODS

The electrochemical detector discussed herein is a micromachined channel that is inserted into the flow path of a conventional polyimide-coated silica capillary. The detector consists of a deep plasma-etched trench in a 10 mm x 4 mm silicon die that is sealed with anodically bonded glass. The trench in the silicon has two widths. One region matches the 150  $\mu\text{m}$  outer diameter of the external capillary and provides structural support; the other region matches the 50  $\mu\text{m}$  inner diameter of the capillary and acts as part of the flow channel. Platinum microelectrodes patterned on the glass are aligned to the trench to allow electrochemical sensing in the channel (Figure 1). Standard CE capillaries are inserted into the channel and sealed with epoxy, placing the detector into the flow path (Figure 2).

The silicon trenches were etched using a  $\text{SF}_6/\text{C}_2\text{ClF}_5$  plasma to a depth of 150  $\mu\text{m}$  using a two-layer AZP4620 photoresist mask. A 0.5  $\mu\text{m}$  silicon dioxide layer was then thermally grown to electrically isolate the silicon substrate. Platinum electrodes and bond-pads were patterned using lift-off onto a Tempax™ glass wafer. The glass was then aligned and anodically bonded to the silicon wafer at 350°C and 2000 V at atmospheric pressure. For access to the bond pads, trenches were etched below the bond

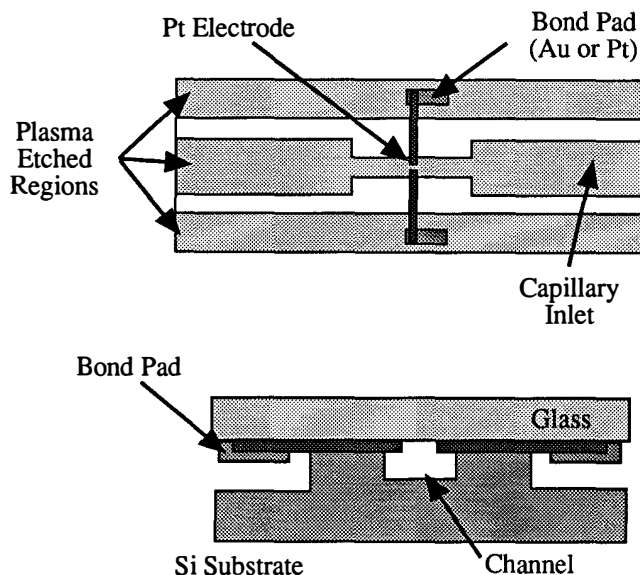


Figure 1: Illustration of the structure of the micromachined capillary electrophoresis detector. The upper view shows the device as seen through the top glass cover. The lower view is a cross-section in the electrode region. (Not to scale.)

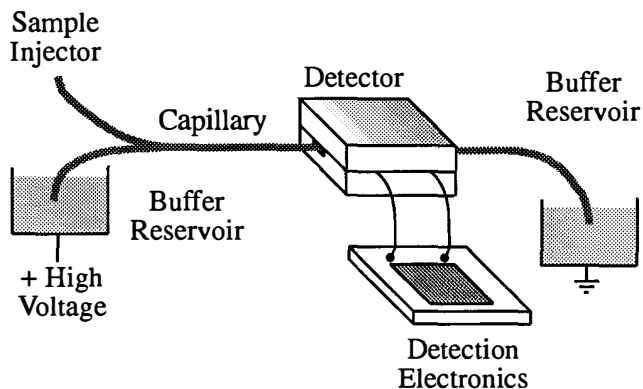


Figure 2: Diagram illustrating the use of the micromachined detector in a typical CE system.

pads during the capillary trench etch step. The resulting overhanging silicon covering the bond pads was removed during dicing. Gold bond wires were therm-sonically bonded to the platinum pads and onto matching copper traces on a glass supporting substrate. To improve the sensitivity of conductivity measurements, amorphous (“black”) platinum was electrodeposited on the platinum electrodes [8]. This lowered the total electrode impedance by more than an order of magnitude. Photographs of the resulting structure are shown in Figures 3 and 4.

The electrochemical detection instrumentation has been realized with a precision battery-powered circuit. A.C. conductivity was measured with a custom designed analog lock-in amplifier and 18-bit A/D converter (Figure 5). A microcontroller chip controls the analysis and transmits the resulting data over an infrared serial link to a personal computer running custom analysis software. Floating the instrumentation at the capillary potential allows high voltage isolation and improves power supply noise rejection.

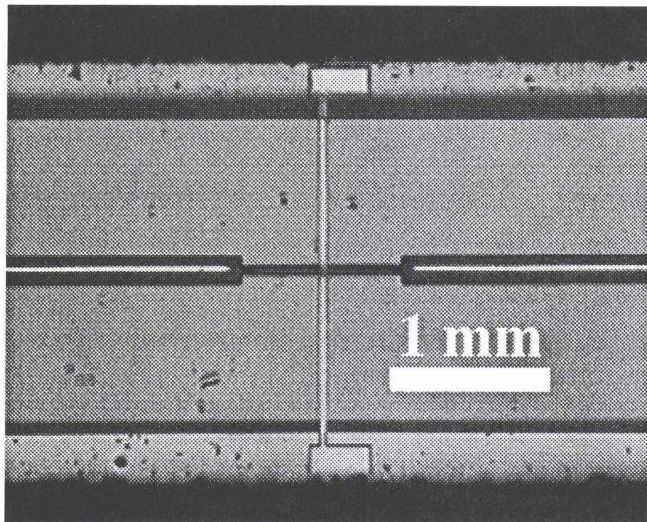


Figure 3: Optical micrograph of a completed detector, viewed through the top glass.

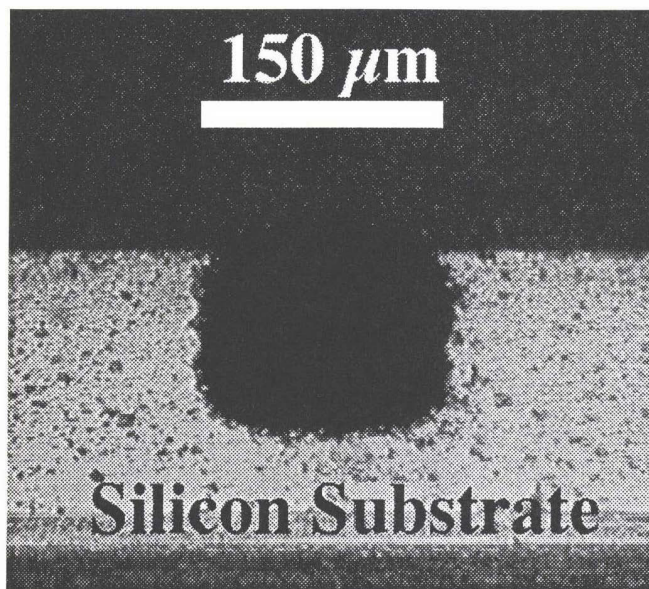


Figure 4: Cross-sectional view of the inlet of a detector.

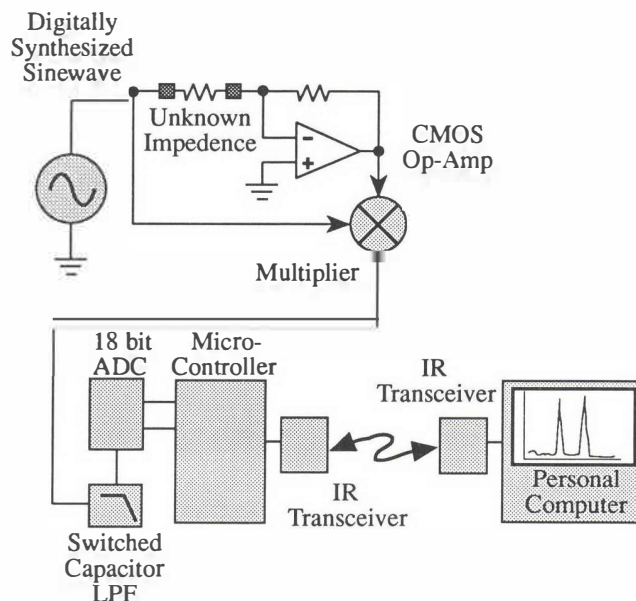


Figure 5: Block diagram of experimental conductivity-based, optically-isolated CE detection system.

## EXPERIMENTAL RESULTS

Preliminary electrophoresis experiments performed with the system show clear separation of peaks and a good signal-to-noise ratio. An analysis of a solution containing  $K^+$ ,  $Na^+$  and  $Li^+$  ions is shown in Figure 5. The detection limit for these ions is better than  $7 \times 10^{-7}$  M, which is comparable to the best reported detection limits for conductivity measurement [7]. Improvement of the sensitivity is expected by using lower conductivity buffer solutions.

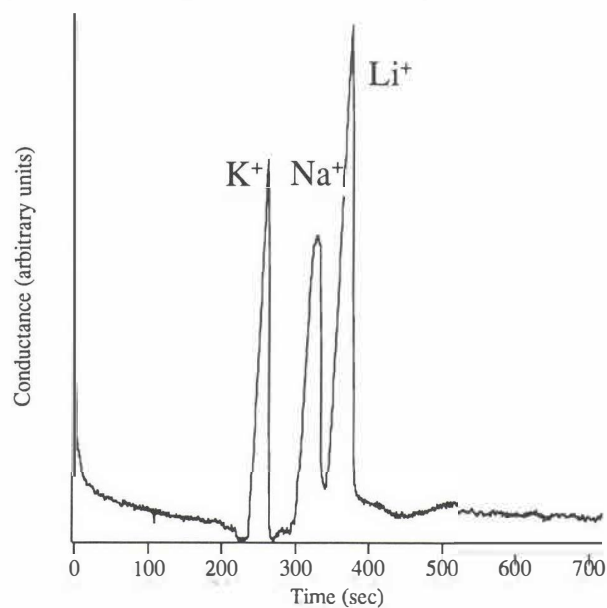


Figure 6: Typical detection results using 4 kV applied voltage and 0.7 millimolar concentrations of  $K^+$ ,  $Na^+$  and  $Li^+$ . The capillary used in this case was 20 cm in length.

## CONCLUSION

A microfabricated electrochemical CE detector system has been developed. This process allows accurate, reproducible construction of a detector that is compatible with existing electrophoresis systems. Improved detection electronics have reduced the noise that is common in electrochemical CE detection. The overall system performance was comparable to the best reported conductivity detection systems for CE.

## ACKNOWLEDGMENTS

R. Reay is supported under a National Science Foundation Graduate Fellowship. This work was supported by a Stanford University Office of Technology Licensing Research Incentive Grant.

## REFERENCES

- [1] S. J. Pace, "Silicon Semiconducting Wafer for Analyzing Micronic Biological Samples," United States Patent No. 4,908,112, Mar. 13, 1990.
- [2] R. S. Sethi, J. Brettle, C. Lowe, "Chromatographic Separation Device," U.K. Patent No. 2,191,110A, Dec. 9, 1987.
- [3] D. J. Harrison, P.G. Glavina, A. Manz, "Toward miniaturized electrophoresis and chemical analysis systems on silicon: an alternative to chemical sensors," *Sensors and Actuators B*, vol. 10, 1993, pp.107-116.
- [4] D. J. Harrison, Z. Fan, K. Seiler and K. Flurri, "Miniaturized Chemical Analysis Systems Based on Electrophoretic Separations and Electroosmotic Pumping," *Proceedings of the 7th International Conference on Solid-State Sensors and Actuators*, June 7 - 10, 1993, Yokohama, Japan, pp. 403 - 406.
- [5] N. Burggraf, A. Manz, E. Verpoorte, N. de Rooij, H. M. Widmer, "Synchronized Cyclic Capillary Electrophoresis. A Novel Approach to Ion Separations in Solution," *Proceedings of the 7th International Conference on Solid-State Sensors and Actuators*, June 7 - 10, 1993, Yokohama, Japan, pp. 399-402.
- [6] X. Huang, R. N. Zare, "Improved End-Column Conductivity Detector for Capillary Zone Electrophoresis," *Anal. Chem.*, vol. 63, 1991, pp. 2193-2196.
- [7] X. Huang, T.J. Pang, M.J. Gordon, R.N. Zare, "On-Column Conductivity Detector for Capillary Zone Electrophoresis," *Anal. Chem.*, vol. 59, 1987, pp. 2747-2749.
- [8] C. Marrese, "Preparation of Strongly Adherent Platinum Black Coatings," *Anal. Chem.*, vol. 59 (1), Jan. 1987, pp. 217-218.

# Electrically Driven Separations on a Microchip

Stephen C. Jacobson, Roland Hergenröder,  
Alvin W. Moore and J. Michael Ramsey

Chemical and Analytical Sciences Division  
Oak Ridge National Laboratory  
PO Box 2008, Bldg. 4500S, MS 6142  
Oak Ridge, Tennessee 37831-6142

## Summary

We have fabricated glass microchips using standard photolithographic, etching and deposition techniques. Following the fabrication of the channels, a direct bonding technique is used to join the substrate and cover plate to form a network of closed channels used in the experiments. Control of the electroosmotically driven flow of the buffer, analyte and reagent makes possible the precise control of the fluids within the channel manifold. The microchip can be operated under a continuous or discrete sampling mode, and analyte plugs can be injected onto the column independent of time, with no analyte bias and high reproducibility. Several microchip column geometries for capillary electrophoresis and open channel electrochromatography have been produced and studied using laser induced fluorescence. Also, chemical reactions for pre- and post-column derivatization have been performed on-microchip.

## Introduction

The microfabrication of analytical instrumentation will potentially enable the laboratory to be transported to the samples rather than vice versa. The concepts of miniaturization can be based on conventional laboratory approaches to chemical measurement problems and would benefit from this large, well-established knowledge base. In addition, micromachined chemical instruments as opposed to single analyte chemical sensors would be able to identify and quantify the individual members of the desired class of compounds using a single device.

Microinstrumentation could well derive benefits similar to microelectronics, i.e., low cost, compact size, high speed, integration of several functions and highly parallel analyses. The approach taken is to micromachine a monolithic device and on this microchip implement chemical separation techniques, e.g. capillary electrophoresis<sup>1,2,3,4,5,6</sup> and open channel electrochromatography<sup>7</sup>. Also, on-microchip pre- and post-separation derivatization<sup>8,9</sup> have been coupled to capillary electrophoresis separations.

## Experimental

The microchips were fabricated using standard photolithographic, wet chemical etching, and bonding techniques. A photomask was fabricated by sputtering chrome (50 nm) onto a glass slide and ablating the column design into the chrome film using a CAD/CAM laser machining system (Resonetics, Inc.). The column design was then transferred onto the substrates using a positive photoresist (Shipley 1811). The channels were etched into the substrate in a dilute HF/NH<sub>4</sub>F bath. To form the separation column, a coverplate was bonded to the substrate over the etched channels using a direct bonding technique. Cylindrical glass reservoirs were affixed on the substrate using RTV silicone (General Electric). Platinum electrodes provided electrical contact from the power supply (Spellman CZE1000R) to the solutions in the reservoirs.

Column performance and separations were monitored on-microchip via laser induced fluorescence (LIF) using an argon ion laser (514.5 nm for sulforhodamine B, dichlorofluorescein, and fluorescein, 20 mW; 351.1 nm for amino acid/OPA products, 15 mW; Coherent Innova 90) for excitation. The fluorescence signal was collected with a photomultiplier tube (PMT; Oriel 77340) for point detection. The data acquisition/ voltage switching apparatus is computer controlled using programs written in-house in Labview 3.0 (National Instruments). The compounds

used for the experiments were sulforhodamine B, disodium fluorescein and dichlorofluorescein (Exciton Chemical Co., Inc.), arginine, phenylalanine, glycine, and o-phthaldialdehyde (Sigma Chemical Co.).

### Results and Discussion

Capillary electrophoresis appears to be the most promising separation technique because of the experimental simplicity. However, microchips have a limited surface area on which to fabricate a device. One approach is to design and construct a column geometry such as a serpentine which enables a long separation column to be fabricated in a compact area. The schematic in Figure 1 shows the microchip with the serpentine separation column which is 165 mm long in an 8 mm by 8 mm area.

The sample is loaded into the injection cross via a frontal electropherogram travelling from the analyte reservoir to the analyte waste reservoirs. Once the front of the slowest analyte passes through the injection cross, the sample is ready to be injected. The analyte plug is confined to the injection cross by flows from the buffer and waste reservoirs, thereby pinching the plug at the injection cross. The size of the sample plug can be controlled by the relative potentials applied to the buffer, analyte, and waste reservoirs. Here, the relative potentials applied to the reservoirs for the sample loading mode at the buffer, analyte, analyte waste, and waste reservoirs are 0.6, 0.8, 0.0, and 1.0, respectively. To inject the sample into the separation column, the potentials applied to the reservoirs are reconfigured. The primary flow path for the separation is from the buffer reservoir to the waste reservoir. To prevent bleeding of excess analyte into the separation column, the analyte and analyte reservoirs are maintained at a fraction of the potential applied to buffer reservoir. The relative potentials for the separation mode at the buffer, analyte, analyte waste, and waste reservoirs are 1.0, 0.5, 0.5,

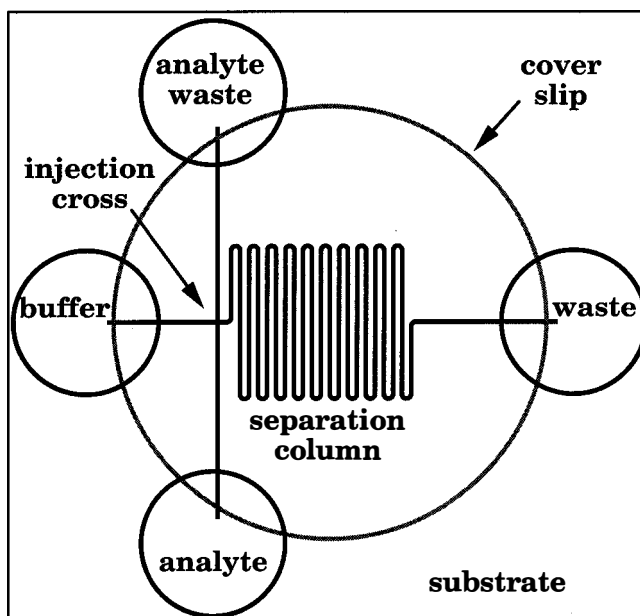


Figure 1. Schematic of the microchip with serpentine channel geometry. Reservoirs are affixed at the terminus of each channel and are labeled by the solution present. The separation column is 165 mm long. The channels are 80  $\mu\text{m}$  wide and 5  $\mu\text{m}$  deep.

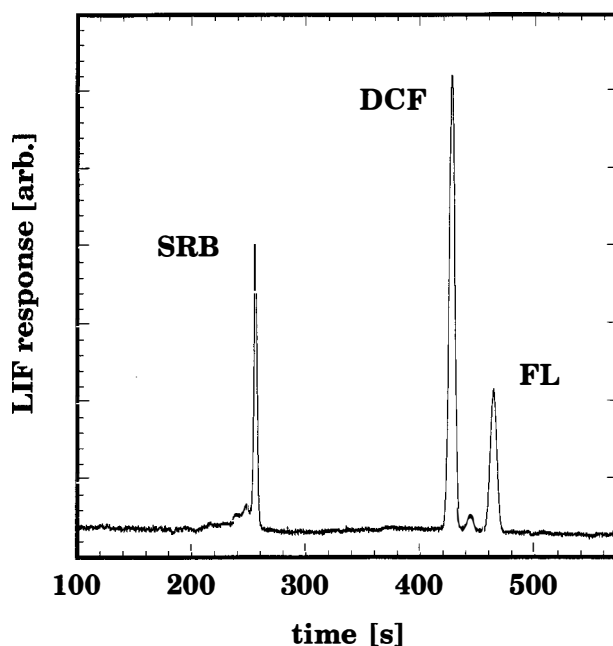


Figure 2: Electropherogram of sulforhodamine B (SRB), dichlorofluorescein (DCF), and fluorescein (FL) separated on the serpentine microchip with  $E_{\text{sep}} = 160 \text{ V/cm}$  and  $L_{\text{sep}} = 165 \text{ mm}$ .

and 0.0, respectively.

The electropherogram in Figure 2 demonstrates a separation detected at the end of the serpentine geometry. The efficiencies for sulforhodamine B, dichlorofluorescein, and fluorescein are 42400, 34600, and 31400 plates, respectively. The primary contributions toward band broadening on this microchip are from axial diffusion<sup>10</sup>, injection plug length, detector observation length<sup>11</sup>, and column geometry<sup>5</sup>. The contribution of the column geometry to the total plate height is:

$$(1) \quad H_{\text{geo}} = n (w \theta)^2 / (12 L_{\text{sep}})$$

where  $n$ ,  $w$ ,  $\theta$ , and  $L_{\text{sep}}$  are the number of turns, the width of the turns, the angle of the turns, and the separation length, respectively. For this microchip,  $H_{\text{geo}}$  equals  $0.85 \mu\text{m}$  for twenty  $180^\circ$  turns, one  $90^\circ$  turn and a 165 mm separation length. In the case of sulforhodamine B,  $H_{\text{geo}}$  constitutes 22% of the total band dispersion.

Another device that has been fabricated on a microchip is a pre-column reactor coupled to capillary electrophoresis for analysis. The reaction studied is o-phthaldialdehyde (OPA) with amino acids in the presence of a reducing agent, 2-mercaptoethanol<sup>12</sup>. The reaction is moderately fast (typical half-time of reaction with amino acids of 4 s<sup>13</sup>), yet for several amino acids the fluorescent product is short lived,  $\approx 10$  minutes<sup>14</sup>. A microchip with a pre-column reactor addresses both problems by having sufficient time for the reaction and the continuous preparation of new product. In Figure 3 the schematic for the microchip with a pre-column reactor is shown.

The microchip was operated in a continuous reacting/ separation mode. The sample and reagent are continuously pumped in a volumetric ratio of  $\approx 1:1$  through the reaction chamber toward the analyte waste reservoir. Buffer was simultaneously pumped from the buffer reservoir toward the waste and analyte waste reservoirs. The buffer stream prevents the analyte from leaking into the

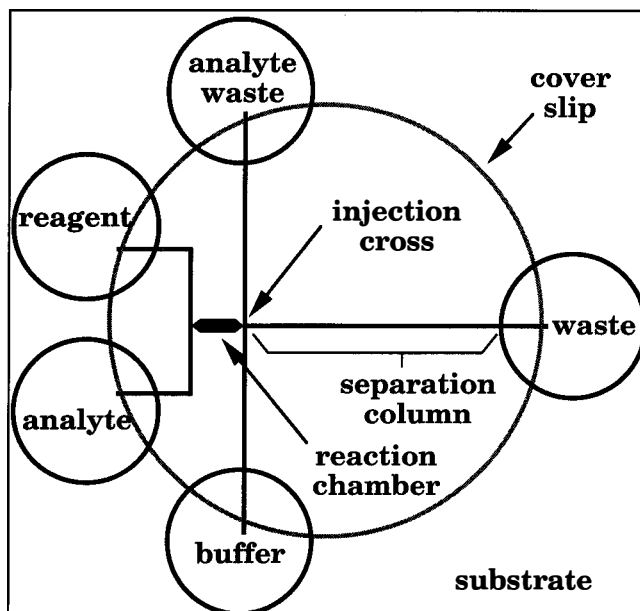


Figure 3. Schematic of the microchip with pre-column reactor. Reservoirs are affixed at the terminus of each channel and are labeled by the solution present. The reaction chamber and separation column are 2 and 15.5 mm long, respectively. The channel in the reaction chamber is  $96 \mu\text{m}$  wide and  $6 \mu\text{m}$  deep. The channel in the separation column is  $31 \mu\text{m}$  wide and  $6 \mu\text{m}$  deep.

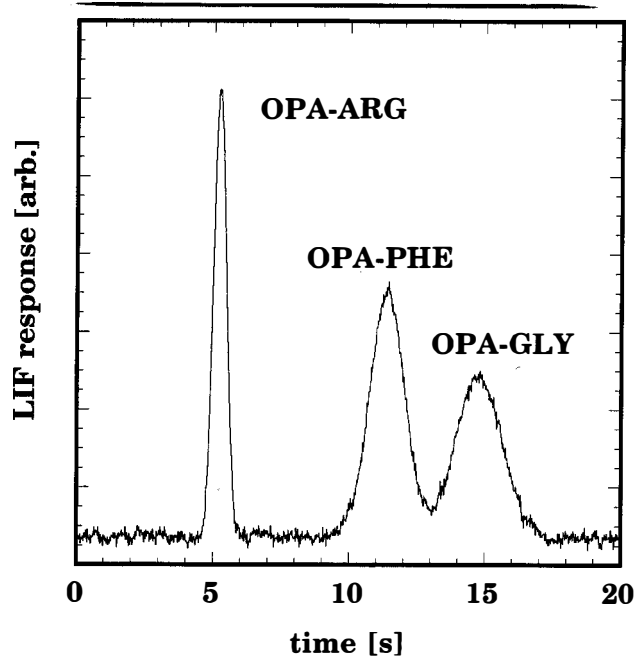


Figure 4. Electropherogram of arginine (ARG), phenylalanine (PHE) and glycine (GLY) using pre-column derivatization with o-phthaldialdehyde (OPA) with  $E_{\text{sep}} = 800 \text{ V/cm}$  and  $L_{\text{sep}} = 10 \text{ mm}$ .

separation column. To make an injection of the reaction chamber effluent, the potential at the buffer reservoir was simply floated for a brief period of time (0.1 to 1.0 s), which allowed sample to migrate into the separation column as in an electrokinetic injection<sup>15</sup>. To break off the injection plug, the potential at the buffer reservoir is reapplied. The length of the injection plug is a function of the time of the injection and the electric field strength in the column. To obtain these flow patterns, one configuration for the relative potentials at the buffer, analyte, reagent, analyte waste, and waste reservoirs is 1.0, 0.5, 0.5, 0.2 and 0.0, respectively.

Figure 4 shows an electrophoretic separation of arginine, phenylalanine and glycine after on-microchip pre-column derivatization with OPA. The microchip used here offers the unique capability of reacting a continuously flowing stream of the analyte and a reagent of choice prior to analysis. Because the flow patterns are controlled using potentials applied to the reservoirs, the field strengths in the reaction chamber and separation column are interconnected. To have a long reaction time for the derivatization, the field strength in the reaction chamber should be minimized, but for capillary electrophoresis, the resolution between compounds increases with increasing electric field strength. With the current design, a compromise must be reached so that the OPA has a sufficient time to react without destroying the quality of the separation. The ideal arrangement would be to have an electrode placed at the intersection to control the potentials in the reaction chamber and separation column independently.

## Conclusion

Microfabrication of electrically driven separations has many advantages. The small dimensions of the microchips enables the use of relatively high electric field strengths which corresponds to faster analysis times. Electroosmotically driven flow enables buffer,

analyte and reagent streams to be controlled precisely without valves or pumps. Well-defined plugs of sample can be reproducibly injected onto the separation column. Low dead volume connections between channels can be easily fabricated allowing pre- and post-separation reactions to be incorporated on-microchip.

## Acknowledgements

Research sponsored by U.S. Department of Energy, Office of Research and Development. Oak Ridge National Laboratory is managed by Martin Marietta Energy Systems, Inc. for the U.S. Department of Energy under contract DE-AC05-84OR21400.

## Literature Cited

- [1] D.J. Harrison, A. Manz, Z. Fan, H. Lüdi, H.M. Widmer, *Anal. Chem.* **1992**, *64*, 1926.
- [2] Manz, A.; Harrison, J.; Verpoorte, E.M.J.; Fettingner, J.C.; Paulus, A.; Lüdi, H.; Widmer, H.M. *J. Chromatogr.*, **1992**, *593*, 253.
- [3] Seiler, K.; Harrison, D.J.; Manz, A. *Anal. Chem.* **1993**, *65*, 1481.
- [4] Harrison, D.J.; Fluri, K.; Seiler, K.; Fan, Z.; Effenhauser, C.S.; Manz, A. *Science*, **1993**, *261*, 895.
- [5] S.C. Jacobson, R. Hergenröder, L.B. Koutny, R.J. Warmack, J.M. Ramsey, *Anal. Chem.*, **1994**, *66*, 1107.
- [6] S.C. Jacobson, R. Hergenröder, L.B. Koutny, J.M. Ramsey, *Anal. Chem.*, **1994**, *66*, 1114.
- [7] S.C. Jacobson, R. Hergenröder, L.B. Koutny, J.M. Ramsey, *Anal. Chem.*, in press.
- [8] S.C. Jacobson, R. Hergenröder, A.W. Moore, Jr., J.M. Ramsey, *Anal. Chem.*, submitted.
- [9] S.C. Jacobson, L.B. Koutny, R. Hergenröder, A.W. Moore, Jr., J.M. Ramsey, *Anal. Chem.*, submitted.
- [10] Giddings, J.C. *Dynamics of Chromatography, Part I: Principles and Theory*, Marcel Dekker, New York, **1965**, Ch. 2.
- [11] Sternberg, J.C., *Adv. Chromatogr.* **1966**, *2*, 205.
- [12] Roth, M. *Anal. Chem.* **1971**, *43*, 880.
- [13] Butchner, E.C.; Lowry, O.H. *Anal. Biochem.* **1976**, *76*, 502.
- [14] Lindroth, P.; Mopper, K. *Anal. Chem.* **1979**, *51*, 1667.
- [15] Jorgenson, J.W.; Lukacs, K.D. *Anal. Chem.* **1981**, *53*, 1298.

# Navigation Grade Silicon Accelerometers With Sacrificially Etched SIMOX and BESOI Structure

Keith Warren

Litton Guidance & Control Systems  
5500 Canoga Ave. MS 87  
Woodland Hills, CA 91367-6698

## ABSTRACT

This paper reports progress toward an all silicon, batch processed accelerometer designed to provide navigation grade performance ( $<50\mu\text{g}$  bias and  $<50\text{ppm}$  scale factor stability) and having a full scale range in excess of 100 g, or  $10^8$  dynamic range.

The fabrication process employs silicon on insulator (SOI) and silicon fusion bonding to make symmetrical, all Si, small gap ( $0.5\mu\text{m} - 1\mu\text{m}$ ) electrostatically force balanced devices that are rugged during fabrication and released after bonding by sacrificial etch of the buried oxide layers.

## INTRODUCTION

The aim of this work is the development of an all silicon high g range, navigation grade accelerometer with improved manufacturability over traditional bulk micromachined structures. In previous approaches [1], [2], a wafer of fragile cantilevered proofmasses capped on top and bottom by bonding to silicon or pyrex wafers with thin film electrodes presents difficulties during cleaning, handling, bond fixturing and alignment. Distortion of wafers during bonding causes difficulty in achieving electrostatic servoing gaps smaller than  $2\mu\text{m}$  with this approach. Small gaps are needed for high g, force rebalanced operation with low voltage.

Surface micromachined structures also have not met the challenges of high g, high accuracy performance, being burdened by very low mass proofmass structures. Error forces resulting from environmentally induced changes in the electronic feedback loop offset cause the proofmass to be rebalanced against the electrostatic negative spring. The forces scaled by the small mass times acceleration forces from a low mass proofmass result in significant g errors.

Many surface micromachined accelerometers do not have symmetrical damping, mechanical suspension and electric fields in the direction normal to the wafer surface. These factors make the devices subject to vibropendulous rectification (a DC bias shift due to off axis vibration).

## APPROACH

The performance and manufacturing goals reflected in the design are:

- All silicon – no dissimilar materials
- Low voltage, low power (5V)
- Highly symmetrical structure
- High motional to stray capacitance ratio
- 2 layer final alignment – more manufacturable

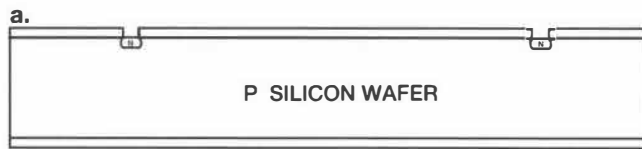
These design features are incorporated into two SOI process technologies, SIMOX and BESOI. Both designs are similar in size ( $5.2 \times 4.6\text{mm}$ ) and layout except that the SIMOX approach requires undercut diaphragms and flexures and are accordingly slotted to permit rapid undercutting. Both SOI silicon accelerometers are designed to be used in a force rebalanced mode with voltage controlled or charge controlled forcing [3]. The proofmass serves as the center node of a 3 terminal differential capacitor. The differential capacitance is used to sense the position between the proofmass and the other substrate, with these same surfaces also serving as rebalance electrodes.

## SIMOX ACCELEROMETER

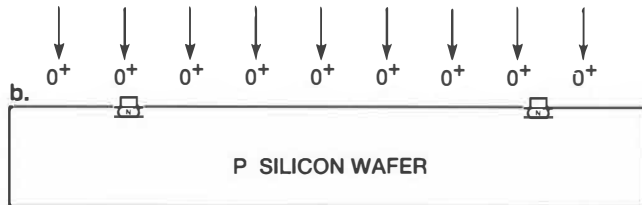
Each array of devices is fabricated from one 100mm diameter silicon wafer, ion implanted with oxygen through a mask to form a patterned buried oxide (SIMOX) followed by silicon epitaxy and dopant selective electrochemical etching to define flexures and proofmass.

The wafer is cut in half and folded on itself using silicon fusion bonding. After the two halves are aligned and bonded, access vias are anisotropically etched from the top outer surface terminating on the buried oxide. The buried oxide is etched away, forming an electrostatic forcing gap and providing freedom for the proofmass to move. Novel electrostatic guard structures have also been developed to reduce top to bottom electrode stray capacitance.

The process sequence is diagrammed in Figure 1 a–e. First, phosphorus dopant is used to produce n-type isolation regions in a p-type double-sided polished wafer.



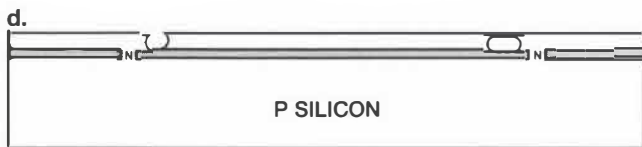
Pattern oxide for N-diffusion & backside alignment marks



Strip oxide and deposit new oxide  
Pattern oxide  
Masked oxygen ion implantation

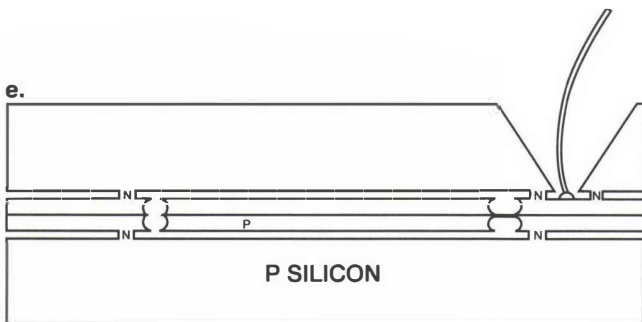


Anneal to form buried oxide



Grow epitaxial Silicon  
Grow diffusion mask oxide  
N-diffusion for flexures and protected areas

Electrochemical etch flexures and proofmass trenches  
Blanket P diffusion surfaces and flexures



Saw wafer in half  
Hydrate surfaces  
Align & fusion bond

Anisotropic etch - wire bond vias  
Etch oxide to form gap  
Metal deposition

Figure 1a-e. Simox Accelerometer Processing Sequence

Next, the phosphorous masking oxide is removed and a new 800nm thick oxide is patterned over the n-type regions to mask the 200keV,  $1E18/cm^2$  oxygen ion implantation.

Substrate temperature is maintained above 600°C during implant to prevent surface amorphization. The wafer is then post implant annealed at over 1300°C to form a buried oxide 500nm thick beneath a single crystal silicon layer 160nm thick.

After buried oxide formation and masking oxide removal a 35µm thick, p-type silicon epitaxial layer is deposited. An n-type diffusion is patterned in regions that will later be the proofmass edges, flexure and guard structure, and grooves are KOH etched through the proofmass, stopping on the buried oxide, to control squeeze film damping.

Dopant selective electrochemical etching [4] is used to form 2µm thick undercut flexures and guard structures. The presence of a buried oxide allows overetching to eliminate the cusps that form under protected structures during this type of etching. P to N selectivities of 70-100 can be obtained if etching is carried out in darkness. Figure 2 is an SEM image of an electrochemically etched flexure. Voltage contrast highlights the n-type diffused regions.

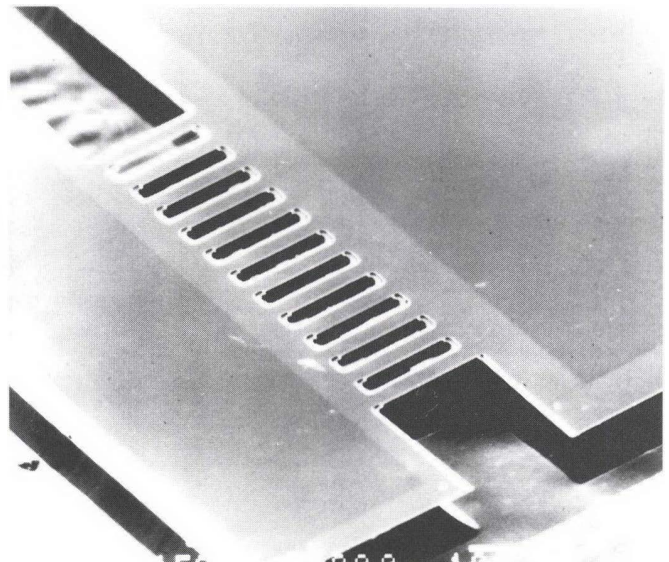


Figure 2. Electrochemically Etched Flexure

Upon completion of the electrochemical etch, the wafer is sawn in half and surfaces are cleaned and prepared for bonding with a  $NH_4OH-H_2O_2-H_2O$  solution. Infrared alignment allows the two halves to be accurately aligned and contacted. The wafer pair is annealed at 1100°C to form a strong void free bond. Topside wirebond access to all internal nodes including bottom electrode plate, guard ring, and proofmass anchor, is made through KOH etched vias etched into the top electrode plate and illustrated in cross

section in Figure 1e. The device can be released by introducing HF into these vias or as presently being done during developmental work, by dicing the wafer and performing the sacrificial etch experimentally on individual die.

The time required to sacrificially etch the buried oxide beneath the  $3000\mu\text{m} \times 3000\mu\text{m}$  proofmass has been experimentally measured to be 36 hours for a planar structure without damping grooves. The addition of damping slots should significantly shorten the undercut time but this has yet to be verified.

Single crystal silicon posts formed by the masked oxygen implant serve as the link between the outer electrode plates and the inner epitaxial silicon proofmass and guard ring frame. The single crystal posts survive long HF oxide etch times undamaged. Figure 3 is a cleaved cross section of a single crystal post bridging a 500nm gap after the buried oxide has been etched away.

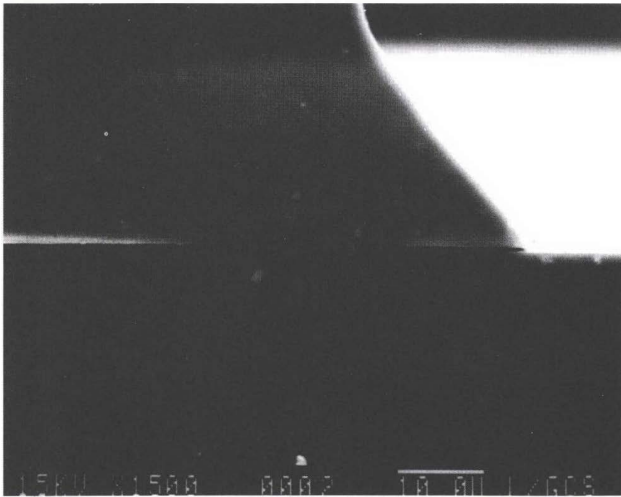


Figure 3. 500nm Gap With Silicon Post

### BESOI ACCELEROMETER

Bond and etch back techniques can be used to prepare SOI wafers with another degree of flexibility. Starting with a  $35\mu\text{m}$  thick silicon on insulator layer, both sides of the  $35\mu\text{m}$  EPI layer can be patterned since the support substrate, or handle wafer, is background and etched away after bonding, thereby exposing the previously buried oxide as the new surface. The original SOI wafer surface is patterned with shallow damping control grooves, followed by a KOH etch outlining the proofmass and terminating on the buried oxide. Flexures are patterned while the surface topology is still flat, delayed by a protective oxide while the proofmass trench is given a head start greater than the desired flexure thickness. The gap setting sacrificial oxide is initially on the surface of another wafer and can be thermal oxide, or a faster etching CVD phosphosilicate glass. Flexure formation is simpler than the electrochemical etch

used in the SIMOX case, but excellent flexure thickness uniformity (variations of a few tenths of a micron) is obtained since bulk wafer TTV does not affect flexure thickness and the epi thickness uniformity across the wafer is very good. Figure 4 is a photograph of the devices on the left and right halves of a wafer after KOH etching is completed and just prior to bonding to the sacrificial oxide wafer.

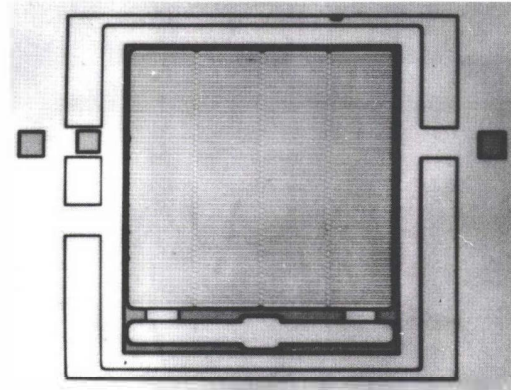


Figure 4a. Left Half of BESOI Accelerometer

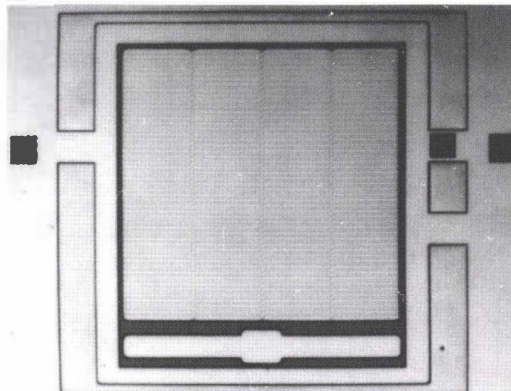


Figure 4b. Right Half of BESOI Accelerometer

After bonding these two wafers together and etchback of the handle wafer using the buried oxide as an etch stop, anchor vias are etched on the new epi surface, and bridging between the silicon epi and new substrate is accomplished with selective epitaxy. The wafer now resembles the SIMOX wafer on Figure 1d. Figure 5 is a SEM image of a cleaved BESOI wafer after the epi layer transfer. Damping control grooves are visible under the proofmass and a flexure is visible on the surface. The diaphragm visible in cross-section serves to reduce the capacitance between the substrate and guard ring.

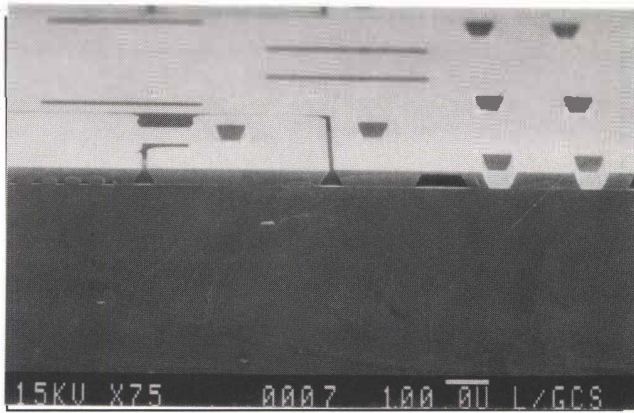


Figure 5. SEM Image of Cleaved BESOI Wafer

## SUMMARY

The design and processing of symmetrical, high-g, navigation grade accelerometers presented here overcomes several performance and manufacturing limitations of prior approaches.

This new technology combining silicon fusion bonding and SOI wafers to produce sacrificially released single crystal epitaxial structures is likely to be increasingly important for fabrication of future high performance sensors and actuators, especially as the price and availability of SOI wafers continues to improve.

## REFERENCES

- [1] K. Warren, "Electrostatically Force-Balanced Silicon Accelerometer", Navigation, vol. 38, No. 1, pp. 91-99, Spring 1991.
- [2] S. Suzuki, et.al., "Semiconductor Capacitive - Type Accelerometer with PWM Electrostatic Servo Technique", Sensors and Actuators, A21-A23, pp. 316-319, 1990.
- [3] R. Stewart and K. Warren, "Force Balanced Instrument with Electrostatic Charge Control", U.S. Patent No. 5,142,921.
- [4] C.J.M. Eijkel, et.al., "A New Technology for Micromachining of Silicon: Dopant Selective HF Anodic Etching for the Realization of Low Doped Monocrystalline Silicon Structures", IEEE Electron Device Letters, Vol. 11, No. 12, December 1990.

# Advanced Micromachined Condenser Hydrophone

J. Bernstein and M. Weinberg  
C.S. Draper Laboratory, Cambridge MA 02139

E. McLaughlin, J. Powers, and F. Tito  
NUWC New London Detachment, New London CT 06320

## Abstract

This research has resulted in small micromachined hydrophones using capacitive detection (condenser hydrophones). These hydrophones are fluid-filled variable capacitors fabricated on a 3 mm silicon chip. Theory indicates that high sensitivity (-180 dB ref. 1V/ $\mu$ Pa) can be attained using this technology. Underwater test data taken at NRL-USRD reported here for the first time have shown sensitivity of 1.6 mV/Pa (-176 dB ref. 1V/ $\mu$ Pa), 70 Hz to 6 kHz. This is approximately 20 dB higher sensitivity than is available from conventional ceramic hydrophones, the predominant underwater acoustic sensor technology. Self-noise is within 2 dB of Sea State 0. This sensitivity is an improvement of 47 dB over previously reported work. Test data on sensitivity vs. pressure shows less than 2 dB change in sensitivity from ambient pressure to 520 psi, due to the fill-fluid which confers practically unlimited depth capability on these sensors.

## Introduction

Current undersea hydrophones are almost exclusively made from ferroelectric ceramics and polymers such as PZT and PVDF. Fiber optic and magnetic hydrophones have been the subject of much research, but in general are larger or less efficient than the ferroelectrics. Micromachining offers both high sensitivity as well as on-chip electronics, potentially allowing size reduction or multi-sensing in a small package.

Previous work on condenser hydrophones goes back to at least 1946 [1], where high sensitivity was achieved. More recently work on MHz ultrasonic condenser transducers has been reported [2,3]. These transducers were air-backed, and therefore required a system of pressure compensation to allow use at depth. In the work reported

here, the transducer is completely fluid-filled, and passive pressure compensation is achieved by the use of pressure equalization slots through the diaphragm. These act as a low pass filter so that the sensitive diaphragm is not required to withstand large static pressures.

High quality condenser, electret and piezoelectric microphones can be micromachined, hence, this is an active area of research. Converting a microphone to a hydrophone requires filling the device with a fluid, and re-optimizing for the increased viscosity, bulk modulus and radiation mass that the fluid entails. The first generation "proof of concept" devices were reported in 1992 [4]. Since that time, the mechanical and electrical designs as well as the packaging have been improved, yielding an increase of 47 dB in sensitivity.

A drawing of an MCH (Micromechanical Condenser Hydrophone) chip is shown in Fig. 1. The variable capacitor is formed between a spring-supported silicon electrode and a stationary, perforated electroformed gold

electrode. Acoustic pressure causes motion of the silicon spring-supported electrode, creating a change in capacitance and a measured output voltage which is buffered by an on-chip JFET (Junction Field Effect Transistor) source follower. A large (15 G $\Omega$ ) on-chip resistor is used to set the DC bias on the gate node with minimum injection of current noise.

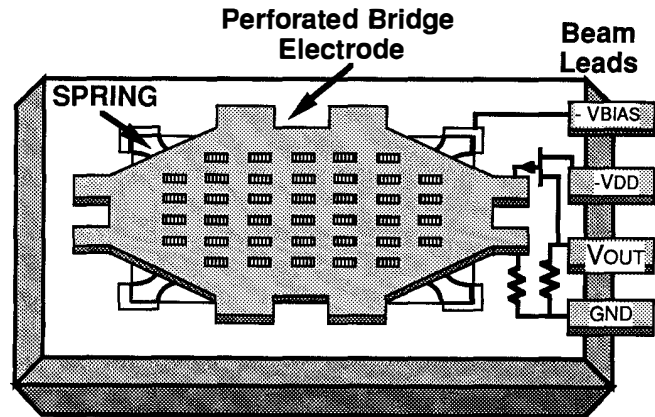


Fig. 1 Micromechanical Condenser Hydrophone chip with on-chip electronics and beam lead interconnects.

Table 1. Summary of Hydrophone Parameters

Parameter	Units	Value
Sensitivity ( $M_0$ )	dB // V/ $\mu$ Pa	-176 to -180
Sense Capacitance	pF	4
Bias Voltage	V	20 V
Diaphragm Diameter	mm	1.0
Package Cavity Volume	mm <sup>3</sup>	330
Cavity Compliance	m <sup>3</sup> / Pa	3.7 X 10 <sup>-16</sup>
Transducer Self-Noise	dB	SS 0 + 2 dB

Table 1 lists key parameters for the MCH's. Fill fluid used was Dow Corning DC 200-5 or DC 200-10 silicone oil.

Small chip size implies several sensors can go in the same package, leading to compact multi-sensors. For example, pressure (depth), sound, acceleration, tilt, electric field and magnetic sensors could all be put in a single compact package. Since both the sensors and electronics are silicon chips, the packaging is potentially simplified, and a single interconnect scheme such as wire-bonding, bump bonding, or beam leads can be used throughout.

## Theory

The condenser hydrophone is modeled using an electroacoustic analogy in which pressure (Pa) is the dual of voltage, and fluid flow (m<sup>3</sup>/s) is the dual of current. The equivalent circuit is shown in Fig. 2. In addition to the standard electrostatic reciprocal transducer circuit, the mass  $L_{CE}$  and compliance  $C_{CE}$  of the perforated counter-

electrode are included. The mass and compliance of the diaphragm (moving) electrode are designated by  $L_M$  and  $C_{SP}$  respectively. The theory is well developed elsewhere [4,8], hence only a summary is given here.

The package cavity volume has a compliance  $C_{CAV}$ . Radiation impedance, both resistance ( $R_R$ ) and the radiation mass  $L_R$  are included. In a liquid environment the radiation mass is much larger than the mass of the diaphragm electrode, and controls the resonant frequency. Both the diaphragm electrode and the bridge electrode have a compliance; the reduced spring constant is  $k_{sp,par}$ .

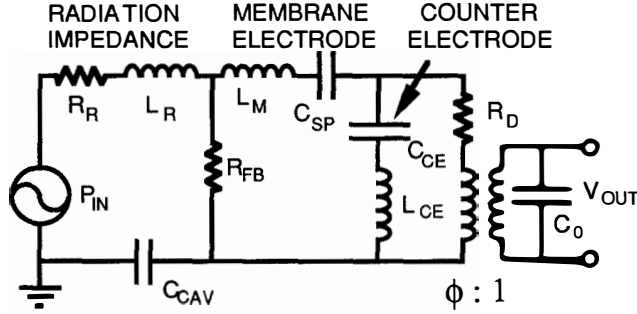


Fig. 2. Equivalent circuit of the condenser hydrophone.

The membrane electrode, of area  $S$ , has an average spring constant  $k_{sp}$  (N/m), and is separated from the perforated counter electrode by a gap  $x$ . The output capacitance is  $C_0 = \frac{\epsilon S_{CE}}{x}$ , where  $S_{CE}$  is the area of the counter electrode. A transformer of turns ratio  $\phi$  ( $\phi = C_0 V_{bias} / S x$ ) links the acoustic and electrical sides of the equivalent circuit. In acoustic units ( $m^3/Pa$ ), the compliance seen by the acoustic wave is the parallel combination  $C_{par}$  of the membrane and cavity compliance  $C_{CAV}$ , defined by

$$1. \quad C_{PAR} = \frac{C_{CAV} C_{SP}}{C_{CAV} + C_{SP}}$$

In our hydrophones the membrane is over damped due to the flow resistance through the counter electrode  $R_D$ , hence the upper frequency corner is at

$$2. \quad f_{RC} = \frac{1}{2\pi R_D C_{PAR}}$$

The snap-down voltage is given by

$$3. \quad V_{sd}^2 = \frac{8k_{sp,par} x_0^3}{27\epsilon_r \epsilon_0 S_{ce}}$$

Transducer sensitivity increases as the bias voltage is increased. For the purpose of this analysis, the transducer bias voltage is assumed to be operated at some safe fraction (58%) of the snap-down voltage.

The mid-frequency open circuit sensitivity  $M_0$  (V/Pa) of the transducer is given by

$$4. \quad M_0 = \frac{S_{ce} V_0 C_{par}}{x_0 S^2}$$

Using the simplifying assumptions that  $k_{sp,par} = k_{sp}$  (very stiff counter electrode), bias voltage =  $0.58 V_{SD}$ , and  $C_{SP} = C_{cav}$  (matched spring and cavity compliances), we derive

$$5. \quad M_0 = \sqrt{\frac{S_{ce} x_0}{40 \epsilon_r \epsilon_0 k_{sp}}}$$

## On-Chip and Hybrid Electronics

The goal of the on-chip electronics was to create an optimal JFET source follower buffer amplifier and large value bias resistor, to be manufactured with the hydrophone. The JFET source follower circuit shown in Fig. 3 is the classic circuit used in condenser microphones. Although no voltage gain is achieved, the close to unity gain output can be used to bootstrap the stray capacitances on the chip, improving gain and linearity. Due to its simplicity, the source follower can have a lower noise floor than a charge amplifier using a JFET input op-amp.

Fig. 3 shows the parasitic diode  $D_{PAR}$  between the diaphragm diffusion and the N-type substrate, as well as the parasitic capacitance  $C_{FOOT}$  under the bridge footings. The acoustically induced voltage is represented by an AC source  $V_1$ .

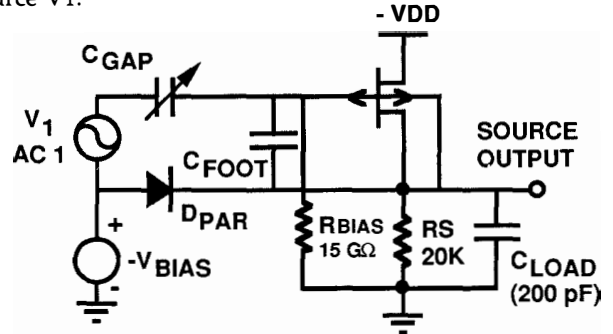


Fig. 3. On-chip JFET source follower circuit.

The first and only (to date) lot of wafers processed through the merged (mechanical plus electrical) process were unsuccessful in making working JFETs due to the gate implant being done on the wafer backs. The chips from this fabrication lot contain the large value resistors (15 GΩ), which were used in a charge amplifier circuit. The only disadvantage of the charge amp circuit is a higher noise floor compared to the intended single FET source follower.

The hybrid charge amplifier used throughout this program is shown in Fig. 4. An on-chip feedback resistor of 15 GΩ and a feedback capacitance of 4.5 pF were used to give approximately unity gain (hydrophone gap capacitance equals feedback capacitance). An RC network is used to filter noise from the bias voltage and protect against over voltages.

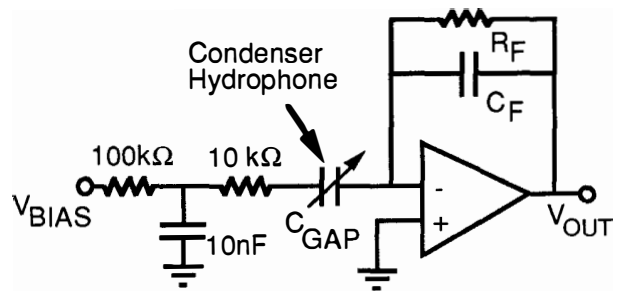


Fig. 4. Charge amplifier circuit used with hydrophones.

## Fabrication

Hydrophones were fabricated on 3" double side polished silicon wafers using standard micromachining techniques. The fabrication process used is a combination of both bulk micromachining (the boron doped silicon etch-stop), surface micromachining (the gold bridges), and microelectronics (the resistors and JFET's). A boron-doped P<sup>+</sup> etch stop, combined with an anisotropic EDP (Ethylene-Diamine Pyrocatechol) etch solution is used to form the membrane electrode, springs, and a through-hole beneath each transducer. An infra-red mask aligner is used to perform a front-to-back alignment for the through holes. V-groove slots are also cut between chips during etch, which allows the chips to be snapped apart after etching. This eliminates the sawing operation and could potentially save cost in a manufacturing operation. Perforated gold bridge electrodes (the counter electrodes) are electroplated through a photoresist mask on top of a temporary photoresist spacer layer.

The bridge electrodes are dielectrically isolated by layers of SiO<sub>2</sub> both thermally grown and deposited by chemical vapor deposition. Dielectric isolation is preferable to P-N junction isolation, since leakage currents are virtually eliminated and there are no constraints on allowable bias voltages. All fabrication steps were carried out at Draper Lab's in-house micro-fabrication facility, with the exception of ion implantation which was carried out at a vendor.

To make the process more manufacturable, several steps in the JFET process are merged with the hydrophone process. This includes the boron source/drain diffusions, which are used as P<sup>++</sup> thin structural members, and the contact and metal one masks. The gate implant is also used to make contact to the N type substrate. The addition of the on chip JFET and resistors adds only 3 photomasks to the hydrophone process, for a total of 11 masks.

Fig. 5 shows a Phase 1 "1 mm radial" springs device, with an octagonal moving plate supported by four radial single crystal silicon springs. This is the device on which test results were obtained. An SEM of the perforated electrode, a spring, and a bias resistor is shown in Fig. 6.

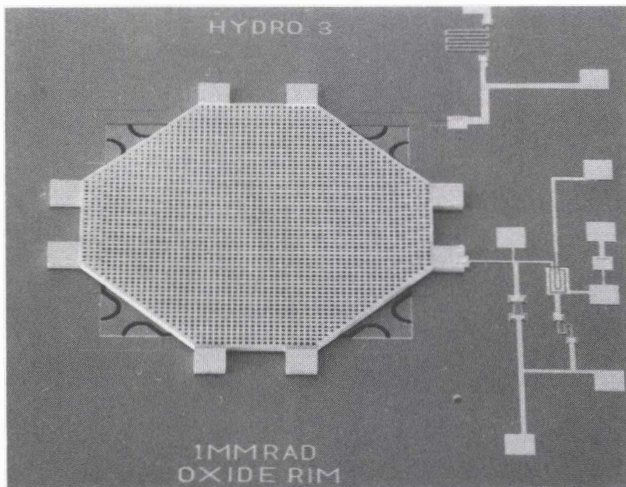


Fig. 5. SEM of Micromachined Hydrophone. 1mm diaphragm is supported by 4 radial springs

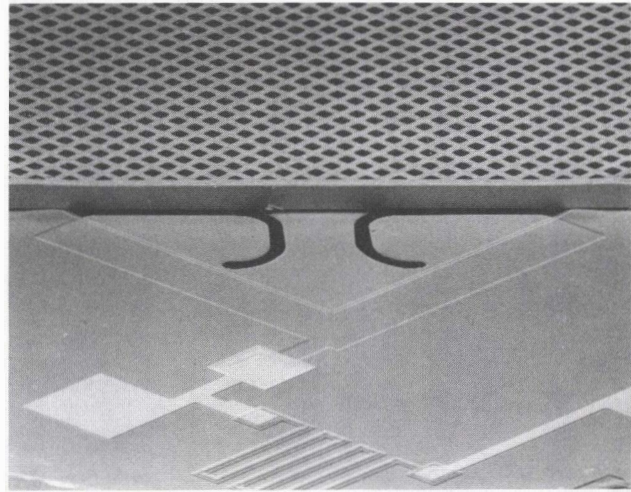


Fig. 6. SEM of spring and perforated bridge electrode.

Using the same fabrication process used to make the metal bridges, it is possible to form metal bumps or beam leads at the edge of the chip. Although conventional wirebonding was used throughout the program, beam leads would allow easy interconnect to off-chip circuitry without wire-bonds.

Tensile stress is desirable in the membrane and counter electrode to maintain flatness. Test structures similar to those previously reported [5-7] were used to measure tensile stress in the silicon and plated metal layers. Tensile stress at 50 - 60 MPa was measured in the silicon and the plated gold.

## Packaging

A thick walled Kovar flat-pack (Fig. 7) was used to house the hydrophone chip and fill fluid. The package has five glass insulated leads on one side, an OFHC copper fill tube opposite the leads, and an acoustic window machined on a third side. The package measures 14 mm X 16 mm X 10 mm, and could be made much smaller. The useful internal cavity volume of the package is approx. 0.3 cc.

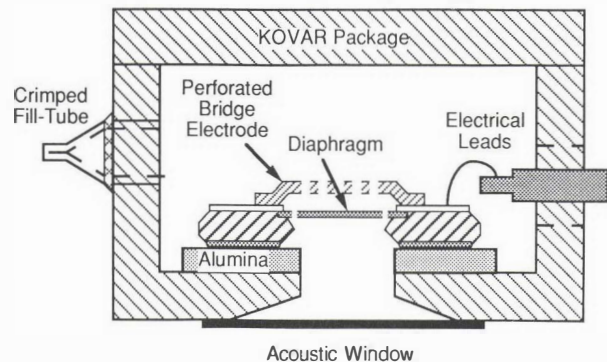


Fig. 7. Thick wall Kovar package with acoustic window.

For many applications such as towed arrays, a small cylindrical package would be preferred. An MCH chip would be placed at one or both ends of the cylindrical package, with a protective cap and a rubber boot to keep the internal fluid (silicone oil) separate from the external fluids. Acceleration insensitivity could be gained by adding the outputs of the opposing chips which share a common acoustic cavity.

Packages were fluid filled by first pumping out the air, then back-filling with silicone oil. Both sides of the chip are filled completely with fluid, leaving no voids or air-bubbles which would cause resonances. The acoustic window shown in Fig. 7 is made of Viton rubber. The window must be large enough to allow for expansion and contraction of the fill-fluid with temperature.

### Experimental Results

Micromachined hydrophones were tested at NUWC and at NRL-USRD (Naval Research Laboratory, Underwater Sound Reference Detachment). Sensitivity vs frequency was measured at 16 kPa and 3585 kPa, 22°C and 3°C. Variation of sensitivity with pressure was less than 2 dB over this pressure range. Typical frequency response is shown in Fig. 8 for four hydrophones.

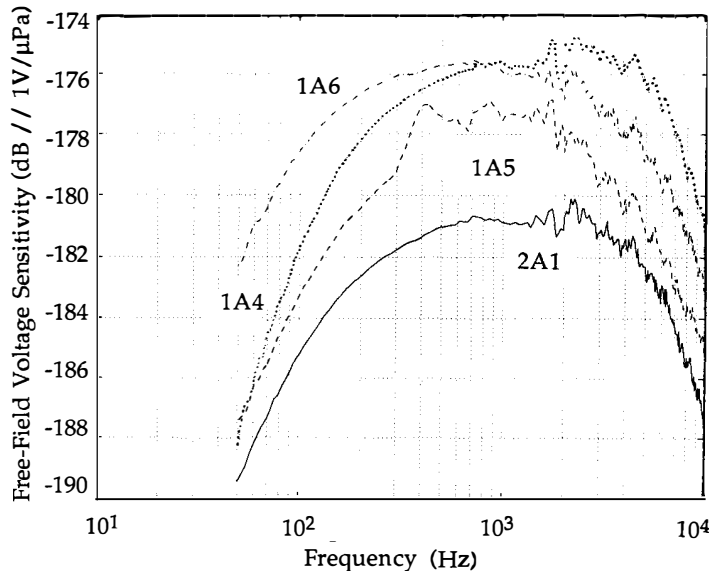


Fig. 8. Free-Field voltage sensitivity for four hydrophones  
Temperature = 22°C, Pressure = 3585 kPa

The high frequency response of these hydrophones is limited by the viscosity of the fluid. At low temperatures, the viscosity increases, causing the upper 3 dB frequency to decrease. The high frequency response could be extended by using a fluid with lower viscosity, or by further optimization of the perforated electrode.

As part of the chip-level screening, capacitance-voltage testing is carried out on each chip in air and the intended fill-fluid. Leakage currents and the snap-down voltage are also measured at that time. Fig. 9 shows C-V scans using air, castor oil, and a liquid crystal compound on a 0.5 mm "proof of concept" chip. The liquid crystal compound shows molecular alignment with the applied field, and a change in dielectric constant with applied voltage.

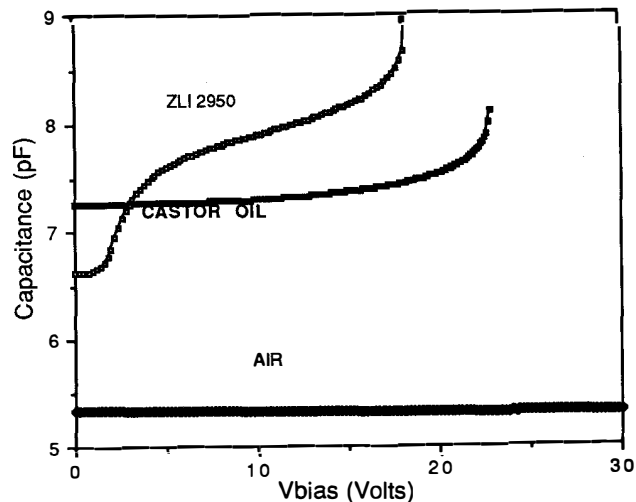


Fig. 9. C-V test of 0.5 mm hydrophone chip using air, castor oil, and liquid crystal fluid.

As part of the in-process quality control, air-acoustic testing is carried out on each hydrophone before fluid filling. These hydrophone chips make highly sensitive microphones, with sensitivity over 20 mV/Pa in a 20 kHz bandwidth. Due to their optimization for silicone oil, they are under-damped with a Q of 100 in air. Chips optimized for microphones would have fewer holes in the bridge electrode. Typical sensitivity data for a 1mm diaphragm is shown in Fig. 10.

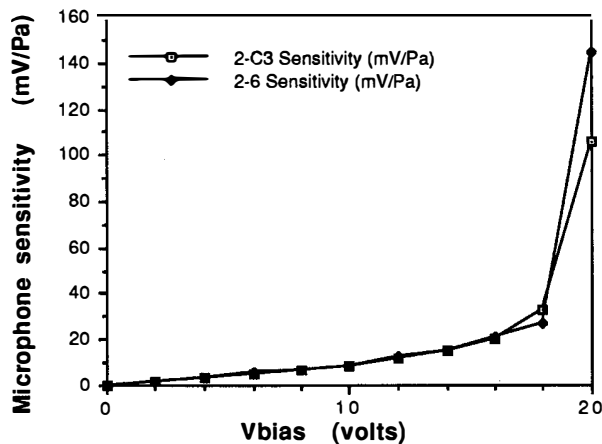


Fig. 10. Microphone sensitivity vs. bias at 1kHz  
1 mm microphone resonance at 17 kHz

### Conclusions

A micromachined condenser hydrophone on a monolithic silicon chip has demonstrated high sensitivity of 1.6 mV/Pa (-176 dB ref. 1V/μPa) and low noise (Sea State 0 + 2 dB) using an off-chip charge amplifier. Expected noise levels with an on-chip amplifier is Sea State 0 - 10 dB. This sensitivity is about 20 dB better than comparably sized ceramic hydrophones. The small size of the chip makes it useful where multiple underwater sensors are needed in one package.

## Acknowledgments

The authors would like to acknowledge the generous support of the Program Executive Office for Undersea Warfare, Advanced Systems and Technology Office (PEO-USW-ASTO). Draper Laboratory support for the proof of concept phase, package development and fill-fluid research is also gratefully acknowledged. Fabrication was carried out by Draper's team of micro-fab technicians: Connie Cardoso, Brenda Coletti, Jim Cousens and Michele Lind. Package design and hybrid fabrication were carried out by F. Petkunas and P. Chiacchi. The fluid filling station and procedure were designed, built and operated by N. Fasano. Thanks are also due to S. Finberg, who assisted with circuit design and hybrid layout. F. Miller, W. Stewart, J. Campbell J. Jackson and K. Williams assisted with data collection and testing.

## References

1. R.J. Bobber, *Underwater Electroacoustic Measurements*, Peninsula Publishing, Los Altos, 1988, p.58.
2. J.H. Cantrell Jr., J.S. Heyman, W.T. Yost, M.A. Torbett, and M.A. Breazeale, "Broadband Electrostatic Acoustic Transducer for Ultrasonic Measurement in Liquids," *Rev. Sci. Instrum.*, 50(1), Jan. 1979, pp.31-33.
3. W.T. Yost and J.H. Cantrell, "Liquid-Membrane Coupling Response of a Submersible Electrostatic Transducer," 1987 IEEE Ultrasonics Symposium, pp. 693-696.
4. J.J. Bernstein, "A Micromachined Condenser Hydrophone," Solid State Sensor and Actuator Workshop, Hilton Head Island, June 1992.
5. L. B. Wilner, "Strain and Strain Relief in Highly Doped Silicon", IEEE Solid State Sensor and Actuator Workshop, Technical Digest, June 22-25, 1992, pp. 76-77.
6. C.J. Kim, R.S. Muller, and A.P. Pisano, "Residual Strain Measurement of Thin Films Using Micro-fabricated Vernier Gauges", *Sensors and Materials*, 4,6, pp. 291-304, 1993.
7. X. Ding, W.H. Ko, and J.M. Mansour, "Residual Stress and Mechanical Properties of Boron Doped P+ Silicon Films," *Sensors and Actuators*, A21 (1990), p. 866.
8. L.E. Kinsler, A.R. Frey, A.B. Coppens, and J.V. Sanders, "Fundamentals of Acoustics", 3<sup>d</sup> edn., (J. Wiley and Sons, New York, 1982), pp. 349-351, 378-379.

# BURSTPROOF, THERMAL PRESSURE SENSOR FOR GASES

Ulrich Bonne and Dave Kubisiak

Honeywell Technology Center, 10701 Lyndale Ave.S., Bloomington, MN 55420  
Voice/fax/e-mail: (612)956-4477/956-4517/bonne\_ulrich@htc.honeywell.com  
Voice/fax/e-mail: (612)956-4072/956-4517/dkubisiak@p01.mn09.honeywell.com

## ABSTRACT

We have extended the operating range of thermal conductivity-based pressure sensors (Pirani gauges) to above 200 bar, corrected for the influence of changes in gas composition and temperature, and demonstrated repeatabilities comparable to state-of-the-art precision ( $\pm 0.1\%$ ) industrial pressure sensors.

This paper describes how such on-line corrections can be made via thermal measurements with two microbridge sensors of different dimensions, so that the effect of absolute thermal conductivity changes are sensed and effectively eliminated. The required measurements include temperature, heater conditions, and steady-state and transient heat transfer. For measuring high pressures, we took advantage of the nonideal gas changes in thermal conductivity. All the above (thermal-only) measurements were performed with single, 1.7 x 1.7-mm, Si chip sensors machined from single Si wafers.

## INTRODUCTION

This paper describes improvements of the Pirani-type or thermal conductivity-based, absolute pressure microsensors. Despite of their attractive overpressure-proof feature, they have suffered from three major disadvantages: limitation to gaseous fluids, sensitivity to gas composition changes and operation limited to pressures below atmospheric. We describe here means to eliminate the last two by introducing an approach to compensate for composition changes and by extending the useful operating range to above 150 bar. The goal is to be able to fabricate low-cost, fully compensated (temperature, composition and pressure) gas flow sensors, for metering of domestic and compressed natural gas.

The microsensor structure is very similar to those used and reported earlier[1-3], although the conductor films are of Pt and not of NiFe[1] or polysilicon[2,3].

The challenge we faced was to derive an on-line, thermal pressure sensing means, while eliminating the influence of an unknown gas composition (and temperature), without giving up the burstproof feature, low-cost, low-power and the self-contained nature of the sensor. We first pursued a compensation that was based on sensing the volumetric, isobaric specific heat,  $c_{pv} = c_p \rho$ , which is closely proportional to pressure[4,5], to which a measurement of thermal conductivity,  $k$ , would be added for composition correction[5]. But we found that the compensated pressure signal was so sensitive to prime sensor signal noise as to be useless. That is when we turned to the use of two microbridge (MB) structures of different geometry, to take advantage of expected differences in pressure- (or mean-free-path-) dependent heat loss[6], as will be described below.

## EXPERIMENTAL

The silicon-based, micromachined sensor chip, besides supporting the basic, narrow MB structure shown in Figs.1 and 2, also supported Wheatstone bridge reference resistors to provide for a first-order temperature compensation[7], and a wide MB structure, as used for flow measurements[7]. The bridge width and gap dimensions were about 3  $\mu\text{m}$  for the former and over 100  $\mu\text{m}$  for the latter. One complete chip layout is shown in Fig.3. To achieve a combination of the desired level of ruggedness and sufficient resistance with the narrow MB structure, its 10 segments of self-supported films were anchored to the substrate at intervals of about 60  $\mu\text{m}$ , as shown[1]. All heater serpentine consisted of 0.1- $\mu\text{m}$

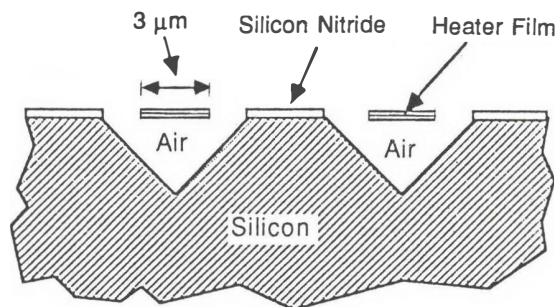


Fig. 1. Cross section of pressure microsensor[1].

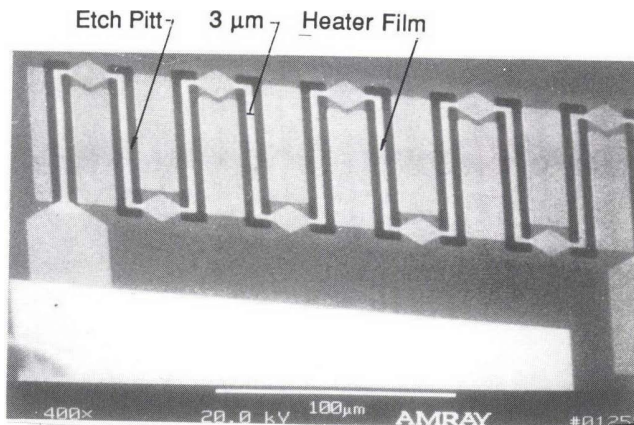


Fig. 2. SEM micrograph of thermal pressure sensor, showing narrow microbridge and gap of 3  $\mu\text{m}$ .

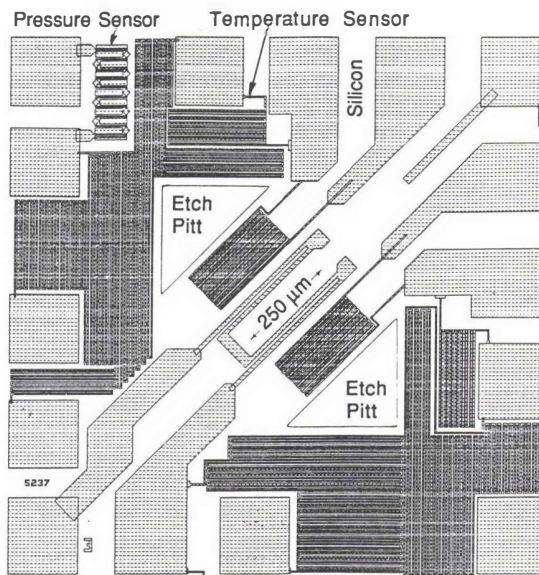


Fig. 3. Microsensor chip layout.

films of Pt, embedded in stress-reduced Si<sub>3</sub>N<sub>4</sub> films of about 1- $\mu$ m total thickness. The square Si chip measured 1.7  $\mu$ m on the side and was mounted and Au-wire bonded to standard TO5 headers. These headers could then be fastened and doubly sealed (via a metal-metal seal and a 0.5-mm-thick O-ring) to the test chamber.

The measurement circuit of the basic pressure microsensors simply consisted of a DC Wheatstone bridge. It served to maintain the heated MB structure at a constant temperature, set between 85 and 100°C, by varying the applied potential to keep the bridge in balance, and to determine its dissipated power by sensing the heater current and voltage drop. These were then digitized and multiplied.

Mean free paths were determined via published values of effective molecular collision cross sections according to the expression[8]:

$$L = RT/(N\sqrt{2}\pi\sigma_m^2) \quad (1)$$

where R = 80.206 atm-cm<sup>3</sup>/(Kmol), Universal Gas Constant; T = absolute temperature in K; N = 6.023·10<sup>23</sup>/mol, Avogadro Number; and  $\pi\sigma_m^2$  = molecular collision cross section, ( $\sigma$ -values in Å, as derived from Lennard-Jones potentials, are: 3.65 for air, 3.82 for CH<sub>4</sub>, 3.40 for Ar and 1.9 for He[8]; better fits were obtained with 3.6 for CH<sub>4</sub>, 3.8 for Ar and 1.45 for He and are within the range of values listed in ref.[8] for alternative methods for deriving  $\sigma$ -values). These cross-section data were used initially only, for evaluation of experimental data, before the use of microbridges of different geometry was adopted.

The on-line determination of k and c<sub>pV</sub> was accomplished with the wide heater elements on the chip, as described earlier[4]. This method consists of processing measurements of gas temperature and both transient and steady-state sensor temperature rise caused by heat transfer from an adjacent, intermittently heated thin-film element. Calibration of this k, c<sub>pV</sub> and pressure sensor was accomplished with an automated system, which would expose the sensor to three gases, six temperatures and six pressures, and record the measured environmental conditions, the above wide MB sensor outputs and the wide and narrow MB heater conditions. This process took about 8-10 hours and could be completed overnight.

For pressure measurements above 2 bar, the above sensor package was sealed to a  $\leq 3$ -cm<sup>3</sup> stainless steel chamber that could be connected directly to the  $\leq 200$ -bar gas pressure of a steel gas tank.

## RESULTS AND DISCUSSION

Examples of the measured pressure dependences for both wide and narrow MBs are shown in Figs.4-6. Note that the steep rise in heat loss is well on its way at 10<sup>-2</sup> bar in Figs.4 and 5 (wide MB) but not in Fig.6 (narrow MB), indicating the expected shift toward higher pressures, i.e. smaller mean free paths, as the MB dimensions are reduced. We verified that the plotted heat loss data at high pressures were directly proportional to k and that mean free path, L, and pressure, p, were "interchangeable"; i.e. that by choosing dry air as reference gas, correcting the heat loss data points according to the transformation  $Q_{corr} = (Q - Q_{vac})k_{air}/k_i + Q_{vac}$ , and shifting the pressure points from p to pL<sub>air</sub>/L, the data of all gases collapsed into the set measured for air, see Fig.5. In other words, the experimental heat loss data at low pressure could be represented by points of heuristic eq.(2) plotted by using either (1) a L/L<sub>air</sub> pressure scale shift and setting all L<sub>i</sub>  $\equiv$  L<sub>air</sub>, or (2) no pressure scale shift and letting L<sub>i</sub> represent individual mean free paths. In both cases, the k<sub>i</sub> represent the k-values of gases "i":

$$Q = Q_{vac} + k_i/k_{air}\{A_1\exp(-A_2/p/L_i) + A_3\exp(-[A_4/p/L_i]^{0.5})\} \quad (2)$$

with the constants Q<sub>vac</sub> = 0.33 mW is the measured residual heat loss in vacuum, k<sub>air</sub> = 68.255  $\mu$ cal/(cmKs), A<sub>1</sub> = 0.64998, A<sub>2</sub> = 1.291638·10<sup>-6</sup> psi-cm, A<sub>3</sub> = 0.65996, and A<sub>4</sub> = 2.741976·10<sup>-7</sup> psi-cm. The only variables are k<sub>i</sub> = thermal conductivity of gas "i" in  $\mu$ cal/(cmKs), L<sub>i</sub> = its mean free path in cm and p = pressure in

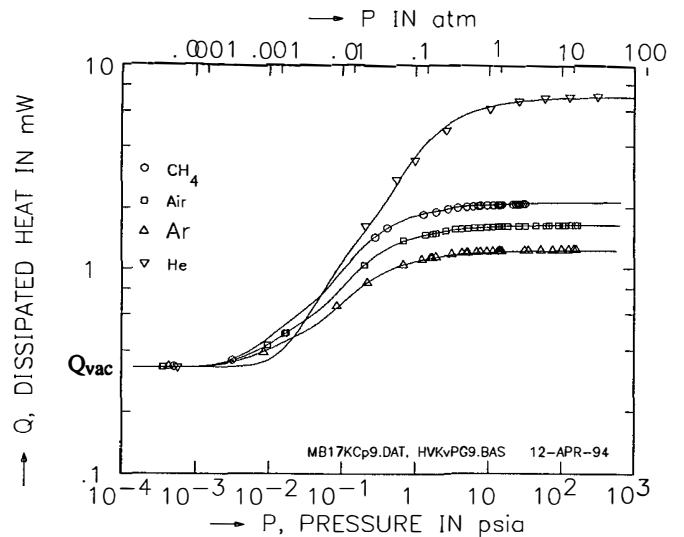


Fig. 4. Heat dissipated by a wide MB pressure sensor heater, for four gases. Data without composition correction. The fitted functions are of the form:  $Q = Q_{vac} + k_i/k_{air}\{A_1\exp(-A_2/p/L_i) + A_3\exp(-[A_4/p/L_i]^{0.5})\}$

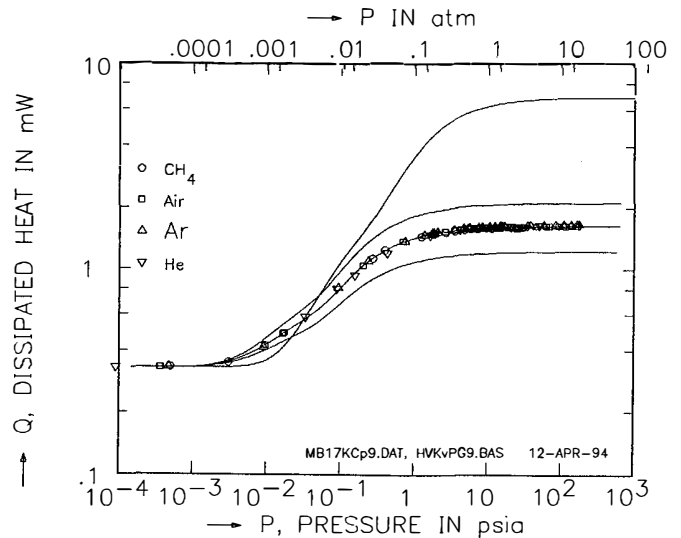


Fig. 5. Heat dissipated by a wide MB pressure sensor heater, for four gases. Data after composition correction.

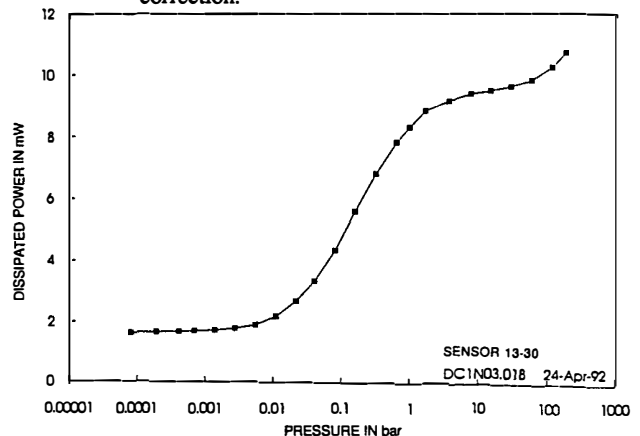


Fig. 6. Heat dissipated by a Pirani-type, narrow MB pressure sensor, up to high pressures. Sensor 13-30 before linearization, in nitrogen.

psia. In eq.(2) the  $k_i$  thus define the heat loss at high pressure and the  $L_i$  the transition region from the  $Q_{vac}$ . The second exponential term was needed to improve the quality of the curve fits, which was not deemed surprising in view of the odd geometry of the narrow MB.

The determination of effective  $L(\sigma)$ -values that led to the best fits of  $Q(p)$ , as described in the Experimental section, is offered as a (possibly new?) tool for probing into the combined influences of molecular cross section and thermal accommodation at gas-solid interfaces, involving transfer of kinetic, rotational and/or vibrational energy[9]. However, in spite of the encouragement provided by the gained physical understanding, we still needed a method for on-line, self-contained determination of mean free path, if this pressure sensing approach was to be practical. But rather than search for a method to determine  $L$ , in view of the range of uncertainty presented for its values in ref.[8], we decided to first lump all available data into one fitted expression for pressure,  $p$ , and then interpret the physics of the findings later, if warranted. The chosen expression has the form of a polynomial:

$$p = f(k, c_{pv}, I_H, V_H, I_h, V_h, T) \quad (3)$$

where  $I$  and  $V$  = heater current and voltage, respectively, and the subscripts  $H$  and  $h$  refer to the wide and narrow MBs[6]. No effort was made at the time to determine if all the listed independent variables were needed, an effort that may indeed improve the quality of the fit.

Figs.7 and 8 show examples of results obtained with this method. They were plotted after a calibration run, as described in the Experimental section, and show that the composition-dependence can be eliminated, while achieving pressure measurements to within an uncertainty of less than  $\pm 1\%$ , see Fig.7. A near-term repeatability of better than  $\pm 0.2\%$  is shown in Fig.8. In both figures the thermal pressure sensor is compared with an industrial-grade, precision, Si-piezoresistive pressure sensor (Honeywell ST3000). Fig.8 also shows that the single largest contribution to pressure signal error is the noise of the  $c_{pv}$  signal; to avoid small (0.1-0.5%) but systematic errors due to thermal convection effects, we recommend that the sensor not be used in orientations different from the one set during calibration, or that means be provided to compensate for the effect of such convective flows.

Regarding operation at high pressures, Fig.6 shows that the chosen narrow MB geometry has shifted the end of the mean free path-dependent heat loss rise to pressures that are high enough to allow the observation and utilization of the beginning of the increase in  $k$ -values due to the increasingly non-linear behaviour of gases. For example, Figs. 9 and 10 show the effects of nonideal (i.e.pressure-dependent) behavior of methane[4], which give the appearance of steadily increasing values of  $k$  and  $c_p$  above 10 bar. That is reflected in the renewed rise in heat loss above that pressure in Fig.6.

A remaining challenge is to extend the composition (and temperature) correction to those higher pressures, as illustrated in Fig.11 for  $CH_4$ ,  $C_2H_6$  and  $N_2$ , for 300 and 350 K, using simple thermal conductivity functions of the type

$$k(T,p) = a_1 + a_2 T^{n1} + a_3 T^{n2} p^{n3} \quad (4)$$

which were also used to represent the property data by Vargaftik[10] plotted in Figs.9 and 10. Note that the data plotted in Fig.9-11 did not take mean-free-path effects into account, but that Fig.9 shows that eq.(3) successfully compensated for the influences of both  $L$  and  $T$ ; the magnitude of the approx.  $k \sim T^{0.7}$  influence is illustrated in Fig.11 by plotting curve sets for both 300 and 350 K. Another challenge is to demonstrate satisfactory stability and service life, especially at the elevated temperatures many applications require[11,12].

## CONCLUSIONS AND RECOMMENDATIONS

We have demonstrated, to our knowledge for the first time, that the

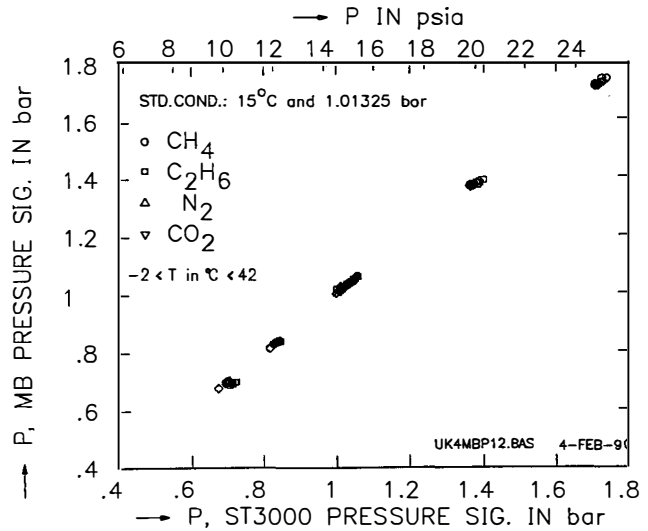


Fig. 7. Comparison between a narrow MB thermal sensor and a precision, Si-piezoresistive, industrial-grade pressure sensor.

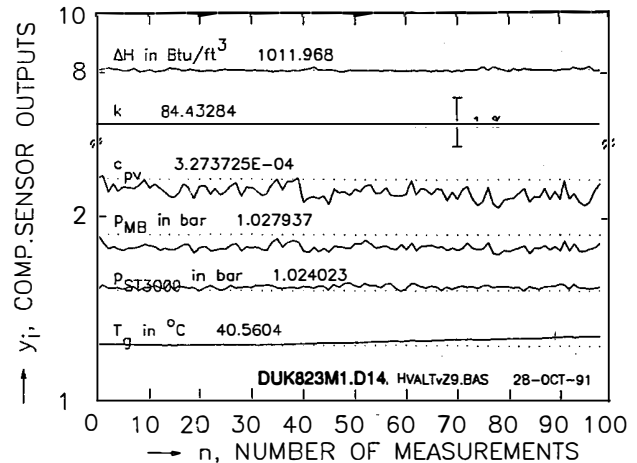


Fig. 8. Short-term repeatability of thermal pressure sensor measurements, including its compensated output, compared to a Si-piezoresistive sensor and to additional MB outputs, for methane; y-scale: 20x.

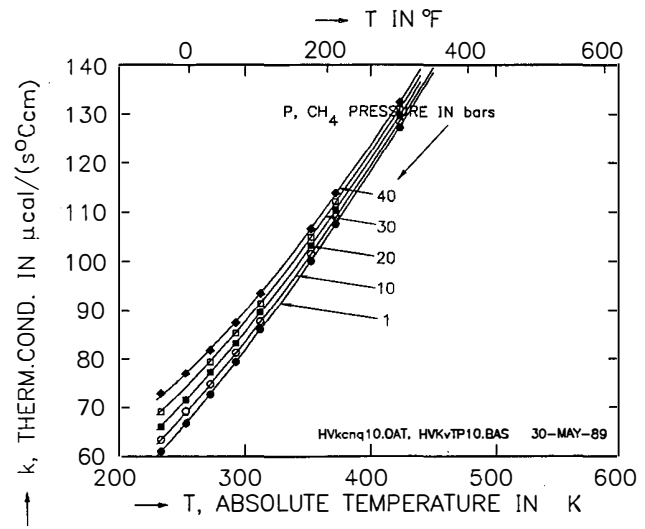


Fig. 9. Thermal conductivity of methane vs. temperature and pressure.

signals of Pirani pressure sensors can be compensated for changes in gas composition and gas temperature and that such on-line corrections can be made via measurements with two microbridge sensors of different dimensions, so that the effects of absolute thermal conductivity changes are sensed and effectively eliminated, provided that temperature and the characteristics of both heaters are also sensed.

Furthermore, increases in thermal conductivity because of the increasingly nonideal behavior of gases above atmospheric pressure were shown to provide a vehicle to extend the useful gas pressure sensing range to 200 bar and beyond.

All the above thermal-only, primary and corrective measurements were performed with single, 1.7 x 1.7-mm sensor chips machined from single Si wafers.

Future work will focus on overall signal noise reduction, reliability and service life improvements, searching for analytical replacements of the fitted, eq.(2)-type functions, and composition correction methods for use at high pressures.

### ACKNOWLEDGEMENTS

We thank J.Ridley, R.Higashi, E.Satren and K.Nguyen of HTC for their help with the microsensors fabrication, evaluation and calibration, and E.Swiatkiewicz with the experimental setup. S.James generated some of the early MB heat loss data[13].

### REFERENCES

1. S.D.James, R.G.Johnson and R.E.Higashi, "A Broad-Range, Absolute Pressure Microsensor," IEEE Solid-State Sensor and Actuator Workshop, Hilton Head, SC, 6-9 June 1988, Book of Abstracts, p.107
2. C.H.Mastrangelo and R.S.Muller, " $\mu$ -Pirani Pressure Gauge with Digital Readout," IEEE Transducers '91, Int'l Conf. on Solid-State Sensors and Actuators, San Francisco, CA, 24-27 June 1991, Proceedings, p.245
3. Priti Pal S.Juneja and Glenn H.Chapman, "A Wide-Range Vacuum Sensor Employing Phase-Sensitive Detection," Canadian Conf. on VLSI (CCVLSI), Banff, Alberta, Canada, 14-16 Nov.1993, Proceedings, p.3A7
4. U.Bonne, "Fully Compensated Flow Microsensor for Electronic Gas Metering," 1992 Int'l.Gas Research Conf., Orlando, FL, 16-19 Nov.1992, Proceedings, Vol.III, p.859
5. U.Bonne, "Versatile, Overpressure Proof, Absolute Pressure Sensor," U.S. Pat. 5,187,674, 16 Feb.1993, assigned to Honeywell
6. U.Bonne, "Absolute Pressure Sensor and Method," US Pat. 5,303,167, 12 April 1994, assigned to Honeywell.
7. P.J.Bohrer, R.E.Higashi, G.B.Hocker and R.G.Johnson, "A Microtransducer for Air Flow and Differential Pressure Sensing Applications," Workshop on Micromachining and Micropackaging of Transducers, Case Western Reserve University, Cleveland, OH, 7-9 Nov. 1984, Proceedings
8. J.O.Hirschfelder, C.F.Curtiss and R.B.Bird, "Molecular Theory of Gases and Liquids," J.Wiley & Sons, Inc., 3rd Ed., (1966) pp. 10 and 552-561
9. W.A.Wakeham, Imperial College Thermophysical Properties Data Center, London, UK, Private Communication, Apr.1994
10. N.B.Vargaftik, "Handbook of Physical Properties of Liquids and Gases," Hemisphere Publ. Co., 1975
11. U.Bonne, "Thermal Microsensors for Environmental and Industrial Controls," (invited paper) NIST Workshop on Gas Sensors: Strategies for Future Technology, Gaithersburg, MD, 8-9 September 1993, Proceedings, to be published
12. U.Bonne and D.Kubisiak, "Determination of Compressibility Factor and Critical Compression Ratio with Si-Based Microstructure Sensors," 7th IGT Symposium on Natural Gas Quality, Chicago, IL, 12-14 July 1993, Proceedings
13. U.Bonne and S.James, "Method and Apparatus for Measuring the Density of Fluids," U.S. Pat. 4,956,793, 11 Sep. 1990, assigned to Honeywell  
PBSSA94.W01'15Apr/Pressure .76%

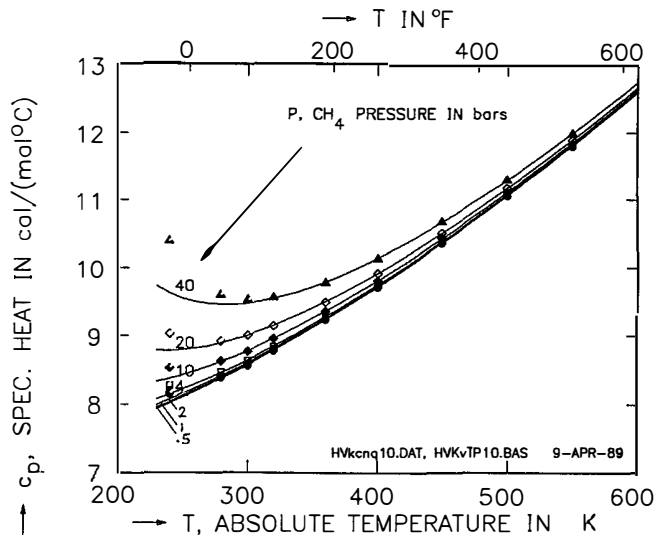


Fig.10. Specific heat of methane vs. temperature and pressure.

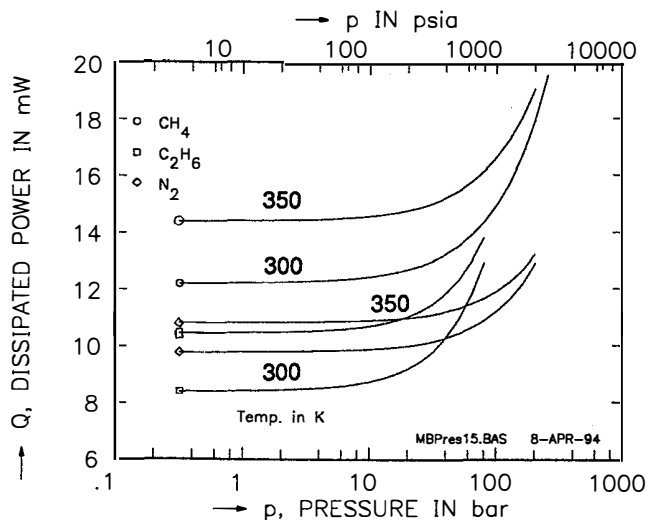


Fig.11. Calculated heat loss from a narrow MB sensor, at high pressures, for the shown gases and temperatures.

# Using Electron Cyclotron Resonance (ECR) Source to Etch Polyimide Molds For Fabrication Of Electroplated Microstructures

W. H. Juan, S. W. Pang, A. Selvakumar, M. W. Putty\*, and K. Najafi

Center for Integrated Sensors and Circuits  
Department of Electrical Engineering and Computer Science  
The University of Michigan  
Ann Arbor, MI 48109-2122

\*General Motors Research and Development Center  
Warren, MI 48090

## Abstract

Dry etching of polyimide with an electron cyclotron resonance (ECR) source and Ni electroplating were applied to fabricate laterally driven resonant microsensors. With the ECR source, the generation of reactive species and the self-induced dc bias voltage can be independently controlled to provide fast polyimide etch rate (0.91  $\mu\text{m}/\text{min}$ ) and high selectivity (3150:1) over Ti etch mask. The etch anisotropy was found to improve at higher rf power and lower pressure. Compared to conventional reactive ion etching, etching with ECR source can typically provide 10x faster etch rate and 6x higher selectivity. Resonant elements in polyimide that are 32  $\mu\text{m}$  high and 1  $\mu\text{m}$  wide have been fabricated by etching in an  $\text{O}_2$  plasma generated using the ECR source. In addition, high aspect ratio microstructures in Ni were formed by electroplating through the polyimide mold.

## I. Introduction

Resonant-based microsensors and microactuators have the advantages of high sensitivity, linear response, and better design flexibility [1-3]. In order to increase the sensitivity of these sensors, the interdigitated resonant elements should be thick but the separation between elements should be small. This requires pattern transfer technology that is capable of fabricating high aspect ratio microstructures.

Electroplating of metal through polymeric molds has been developed to fabricate thick, high aspect ratio microelectromechanical devices [4-6]. The first major application of this technology was demonstrated by the Lithographie, Galvanoformung, Abformung (LIGA) process [4] in which high energy synchrotron X-ray was required to expose the thick polymethyl methacrylate (PMMA) resist. Although this technology is unsurpassed in its capability to fabricate thick high aspect ratio microstructures, it is limited because of the need for X-ray sources, facilities, and masks. To overcome this problem, deep UV lithography has been used to expose photosensitive polymers and create the required mold [5,6]. This is a very attractive technique because it is readily available; however, it has shortcomings in that the aspect ratio is limited to  $\sim 8$ . Dry etching of a polymeric mold using reactive ion etching (RIE) has also been demonstrated [7,8], and has the same shortcomings as deep UV due to the slow etch rate and low etch selectivity.

In this work, an electron cyclotron resonance (ECR) source is used to etch thick polyimide molds with small gaps between resonant elements to create high aspect ratio microstructures. Patterns in polyimide were etched in an  $\text{O}_2$  plasma generated by the ECR source because it has many advantages over conventional RIE. With the combination of magnetic confinement and microwave power, the ECR source provides dissociation efficiency that is typically more than an order of magnitude higher than RIE [9,10]. The high efficiency allows high throughput since etching of deep microstructures up to 50  $\mu\text{m}$  thick are needed [11]. With the magnetic confinement, plasma can be maintained at much lower pressure with the ECR source. This reduces scattering of reactive species and promotes vertical profiles and smooth surface morphology. The reduced scattering at low pressure is crucial for high aspect ratio structures since even a slight divergence of the reactive ions can cause

substantial degradation in etch profile. In addition, the plasma system has a temperature controlled stage that can be cooled down to  $-130^\circ\text{C}$ . This helps to maintain vertical etch profile by suppressing the spontaneous chemical reactions [12]. The independent control of the ion energy by a rf-powered stage and the ion flux by the microwave power provides the flexibility needed to optimize the etching with high etch rate (by high ion flux) and high etch selectivity to the mask (by low ion energy). High etch selectivity is important since a thin etch mask has to hold up throughout the etching of the deep structures.

Using the ECR source, resonant elements that were 32  $\mu\text{m}$  thick with 1  $\mu\text{m}$  gap have been fabricated in polyimide. The etch conditions were optimized to provide fast etching with high selectivity, vertical profile, and smooth morphology. By electroplating Ni through the polyimide molds, resonant accelerometers were formed with aspect ratio of 11:1.

## II. Experimental

### A. Plasma System with the ECR Source

The plasma etching system with an ECR source and a rf powered electrode has been previously described [10-12]. Microwave power at 2.45 GHz is coupled into the ECR cavity by a tunable input probe and a sliding short. Twelve permanent magnets are spaced evenly around the quartz disk to provide magnetic field at 875 G for the ECR excitation. The sample stage is connected to a rf power supply at 13.56 MHz. A self induced dc bias voltage ( $V_{\text{dc}}$ ) is developed and it controls the ion energy.

Chamber pressure is controlled by the throttle valve and gas flow rate is adjusted by the mass flow controller.  $\text{O}_2$  is introduced into the base of the ECR source through an annular gas ring. A 1500 l/s turbomolecular pump is used to maintain low pressure during etching. The stage position can be adjusted from 8 to 27 cm below the ECR source. The temperature of stage can be varied from  $-130$  to  $400^\circ\text{C}$  by a combination of resistive heating and liquid  $\text{N}_2$  cooling. In order to provide good thermal conductivity, wafer is clamped down and He is flown at the backside of the wafer.

### B. Device Fabrication

Electrostatic comb-drive accelerometers with Ni plated resonant elements were fabricated. Stress-compensated  $\text{SiO}_2/\text{Si}_3\text{N}_4/\text{SiO}_2$  dielectric layers with thicknesses of 300/150/300 nm were deposited on (100) p-Si ( $\rho = 3\text{-}10 \Omega\text{-cm}$ ) by low pressure chemical vapor deposition. 2- $\mu\text{m}$ -thick Al was evaporated on top of the dielectric films as the sacrificial layer so that the resonant elements can be released from the substrate after Ni plating. The anchor areas were defined by wet etching of Al. A plating base which consisted of Cr/Au/Cr (50/300/100 nm) was evaporated over the entire wafer. Polyimide (Dupont Pyralin® PI-2611) was then spun on the wafer and multiple coatings were used for thicker layer. The polyimide was cured at  $380^\circ\text{C}$  for 60 min. 200-nm-thick Ti was evaporated as the etch mask and patterned by RIE. Patterns in polyimide were etched in an  $\text{O}_2$  plasma generated by the ECR source. After Ni was electroplated through the polyimide, the polymer was removed by a high pressure  $\text{O}_2$

plasma. Finally the sacrificial Al layer was removed by wet etching, leaving free standing resonant elements in Ni.

### III. Results and Discussion

For the etching of thick polyimide with high aspect ratio features, it is important to have high etch rate and selectivity. Figure 1 shows a comparison of etch rate and selectivity (ratio of polyimide over Ti mask etch rate) between a conventional RIE process and etching with the ECR source. For RIE, as rf power was increased from 50 to 300 W, the etch rate increased from 38 to 147 nm/min, but selectivity decreased from 528 to 115. When polyimide was etched with the ECR source, the etch rate was more than 6x higher and was 908 nm/min at 300 W. The increased etch rate is due to the higher ion flux generated by the microwave power. In addition, selectivity was 3150:1 at 50 W, much higher than RIE. Since the ECR source can generate high ion density in the discharge,  $|V_{dc}|$  is lower compared to RIE when the same rf power is applied. At 300 W rf power,  $|V_{dc}|$  was 530 V for RIE and 284 V for etching with the ECR source. The reduced  $|V_{dc}|$  provides a higher selectivity since the Ti etch mask is mainly removed by physical sputtering. The results shows that the ECR source has the advantages of achieving fast etch rate and high selectivity due to its high ion flux and low ion energy.

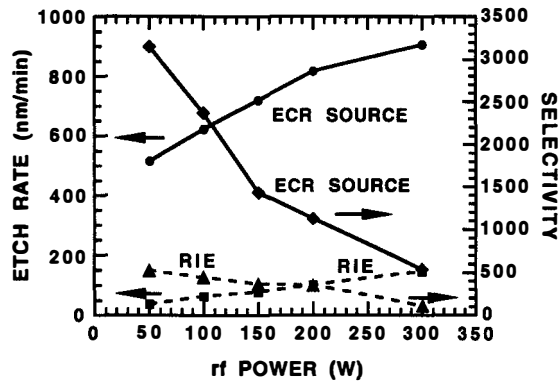


Fig. 1. Etch rate and etch selectivity comparisons between etching with an ECR source and RIE. For etching using the ECR source, microwave power was 750 W, rf power was 300 W, and  $O_2$  flow rate was 20 sccm at 0.5 mTorr and 10 cm below the source. For RIE, the  $O_2$  flow rate was 20 sccm and pressure was 3 mTorr.

The rf power not only controls the etch rate, it also has strong influence on the etch profile. The etch anisotropy was found to increase with rf power as shown in Fig. 2. At higher ion energy, the directionality of the ions has a weaker dependence on surface charge or field distribution across the wafer. The more directional ions impinging on the samples result in more vertical etch profile. The etch profile and surface morphology also depend on the pressure used during etching. More vertical etch profile and smoother surface morphology were obtained at lower pressure. This is related to the longer mean free path and reduced scattering at lower pressure. Since low pressure plasma down to 0.3 mTorr can be maintained with the ECR source, it is most suitable of generating vertical etch profile for high aspect ratio resonant elements.

Etching of thick polyimide film requires a high etch selectivity between the polyimide and the etch mask. Among the different metal etch masks investigated, Ti was found to provide the highest selectivity as shown in Fig. 3. At 50 W rf power, the selectivity for Ti was 3150:1, followed by 790:1 for Cr and 570:1 for Al. Typically, metal mask is oxidized during polyimide etching in the  $O_2$  plasma and it provides higher selectivity than  $SiO_2$  mask. Compared to Cr and Al, Ti mask provides higher etch resistance because  $TiO_x$  has the lowest sputtering yield [13]. As rf power was increased from 50 to 300 W, the selectivity between polyimide and Ti mask decreased from 3150 to 536.

Despite the lower selectivity at higher rf power, 300-nm-thick Ti mask can still hold up for the etching of 50  $\mu m$  thick polyimide.

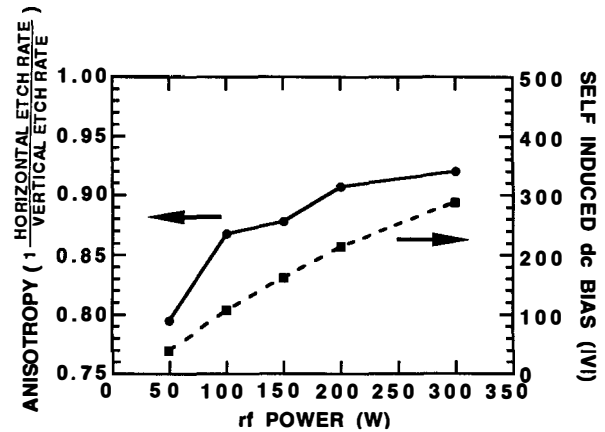


Fig. 2. Effects of rf power on polyimide etch anisotropy and self-induced dc bias. Oxygen was flown at 20 sccm with 750 W microwave power at 0.5 mTorr and 10 cm below the source.

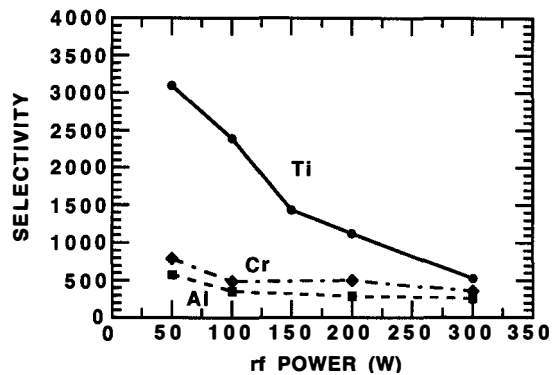


Fig. 3. Etch selectivity between polyimide and Ti, Cr, and Al masks in an  $O_2$  plasma. Flow rate was 20 sccm at 0.5 mTorr with 750 W microwave power and 10 cm below the ECR source.

Since there are features with various sizes on the microsensors, it is important to study the influence of feature size on etch rate when thick polyimide is etched. Figure 4 shows the decreased polyimide etch rate with reduced spacing between elements. The polyimide was etched down to a depth of 24  $\mu m$ . The etch rate was normalized to the etch rate of 30  $\mu m$  wide spacing. Both rf power and pressure can change the feature size dependent etch rate. At 0.5 mTorr and 300 W rf power, the normalized etch rate varies from 0.91 to 1.0 for spacing ranging from 4 to 30  $\mu m$ . When the rf power was reduced to 50 W, the normalized etch rate decreased significantly from 0.61 to 1.0 for the same range of spacing. The reduced etch rate for smaller features at lower rf power could be attributed to the less directional ions impinging on the samples. When the ion energy is lower, it is easier for the ions to be deflected by any perturbing electric field, resulting in lower ion flux at the bottom of high aspect ratio trenches. At higher pressure, the etch rate reduction for narrower spacing was more significant. The normalized etch rate for 4  $\mu m$  spacing was 0.84 at 3 mTorr and 0.91 at 0.5 mTorr. The stronger dependence of etch rate on feature size is probably due to the additional scattering at higher pressure. The increased scattering makes it more difficult for the reactive radicals and the product species to enter or exit the high aspect ratio trenches [14]. Therefore, high rf power and low pressure are desirable to provide more directional reactive species to maintain constant etch rate.

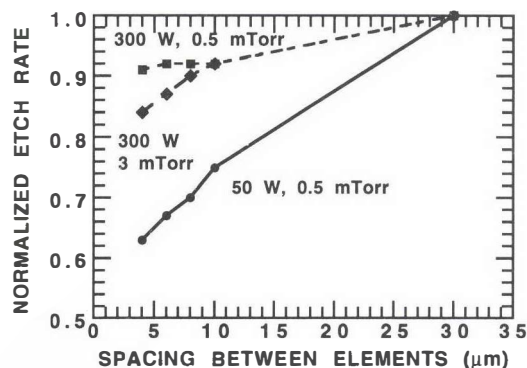


Fig. 4. Influence of feature size on polyimide etch rate.  $O_2$  flow rate was 20 sccm and the source distance was 10 cm with microwave power at 750 W and rf power at 50 and 300 W.

Since Ti etch mask was oxidized during etching of polyimide in the  $O_2$  plasma, it cannot be efficiently removed by wet etching in HF. Ar ion beam etching (IBE) was applied to remove the oxide layer before Ni electroplating. The Ti etch mask was 250 nm thick and was oxidized in the  $O_2$  plasma for 45 min, the time needed to etch 16  $\mu\text{m}$  thick polyimide. Without oxidation, the Ti etch rate in 1:10 HF:H $_2$ O solution was found to be 47 nm/sec. As shown in Fig. 5, not much oxidized Ti was etched in the diluted HF solution after 20 s. Up to 60 s of etching was needed to remove all the Ti. The removal of the oxidized Ti etch mask is more controllable by IBE with Ar ions at 500 V and 1.2 mA/cm $^2$ . The etch rate for the oxidized Ti was 10 nm/min. After removing the top 50 nm of oxidized Ti by 5 min of IBE in Ar, the rest of the etch mask can be completely removed in only 5 s by wet etching. The results indicate that IBE is very efficient in removing the TiO $_x$  and the oxidized layer has a thickness of 25-50 nm.

Figure 6 shows the high aspect ratio (32:1) resonant elements in polyimide that were etched with the ECR source. The polyimide shown in Fig. 6(a) is 32  $\mu\text{m}$  deep with 1  $\mu\text{m}$  spacing between elements. Figure 6(b) shows the higher magnification of the resonant elements in polyimide. The surface is smooth without any residue and the etch profile is vertical. After electroplating Ni through the polyimide mold, accelerometers with interdigitated resonant elements were formed as shown in Fig. 7. The gap between the Ni elements is 1.3  $\mu\text{m}$  and the Ni is 14  $\mu\text{m}$  thick. With the small spacing, high sensitivity is expected for the accelerometer.

These results demonstrate that high aspect ratio resonant elements for microsensors can be fabricated by etching polyimide in an  $O_2$  plasma generated using the ECR source. By optimizing the etch conditions, fast etch rate, high selectivity, vertical profile, and smooth surface morphology can be obtained.

#### IV. Conclusion

A plasma system with an ECR source was applied to etch high aspect ratio features in polyimide for the fabrication of electroplated Ni microsensors. Using the ECR source, polyimide was etched with fast etch rate, high selectivity, vertical etch profile, and smooth surface morphology. The high density and low energy ions generated by the ECR source provide polyimide etch rate of 0.91  $\mu\text{m}/\text{min}$  and selectivity up to 3150. The low pressure plasma allows etching of polyimide with vertical profile and smooth surface. Ti was found to have the highest etch selectivity over polyimide in the  $O_2$  plasma. After etching, the thickness of the oxidized Ti was <50 nm and it can be removed efficiently by Ar IBE. Microstructures that are 32  $\mu\text{m}$  deep and 1  $\mu\text{m}$  wide in polyimide have been fabricated. Electroplated Ni resonant elements that are 14  $\mu\text{m}$  high with 1.3  $\mu\text{m}$  spacing between elements have also been made. Plasma etching with an ECR source has been demonstrated to have the capability of generating high aspect ratio resonant elements with small spacing for highly sensitive microsensors.

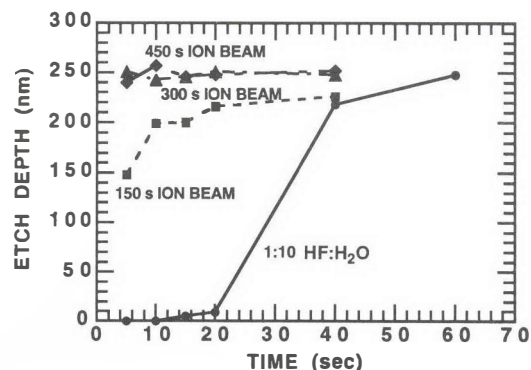
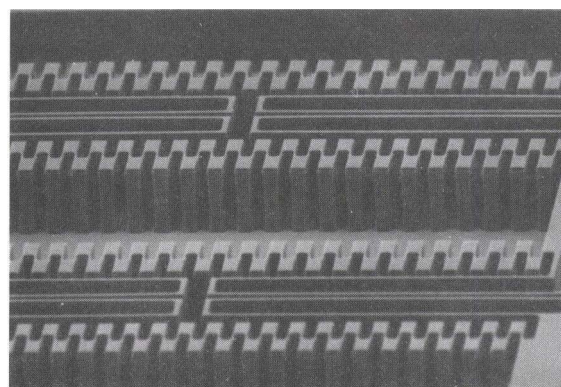
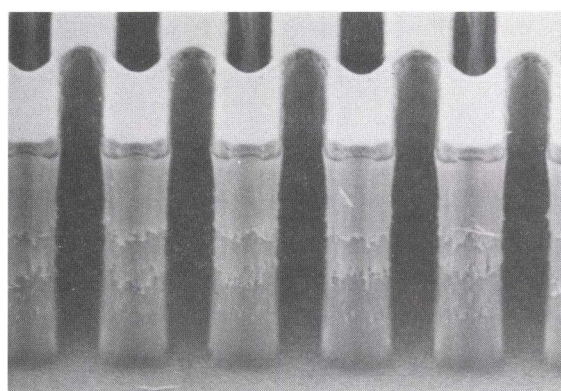


Fig. 5. The effects of Ar ion beam etching on oxidized Ti mask removal. The wet etch solution was HF:H $_2$ O = 1:10. The ion beam etching was carried out using 500 V Ar $^+$  with 1.2 mA/cm $^2$  at  $1.5 \times 10^{-4}$  Torr.

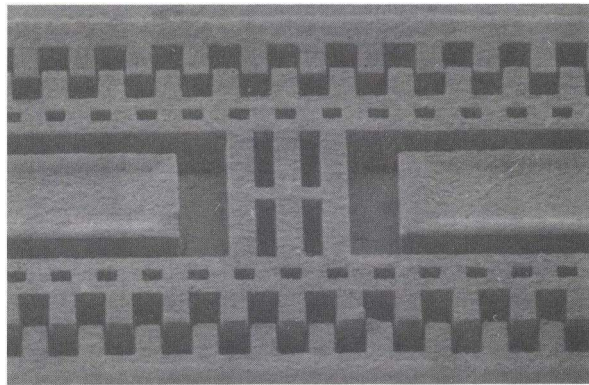


H  
10  $\mu\text{m}$   
(a)

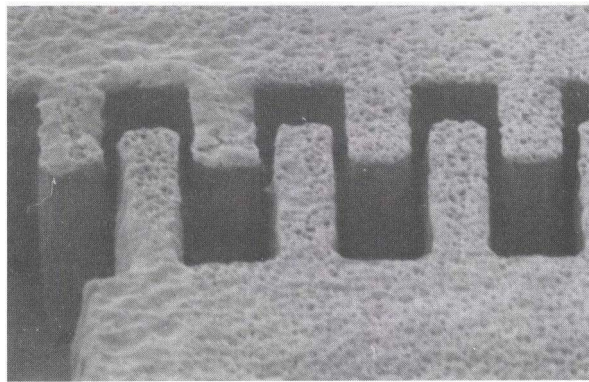


10  $\mu\text{m}$   
(b)

Fig. 6. High aspect ratio microstructures in polyimide. Etching was carried out with 750 W microwave power at 0.3 mTorr, 12.5 sccm  $O_2$ , -300 V, and 10 cm source distance. The polyimide etch depth was 32  $\mu\text{m}$  with 1  $\mu\text{m}$  spacing between resonant elements.



H  
10  $\mu\text{m}$   
(a)



10  $\mu\text{m}$   
(b)

Fig. 7. Electroplated Ni resonant elements with aspect ratio of 11:1. The Ni was plated with current density of 5 mA/cm<sup>2</sup> at 50°C.

#### Acknowledgments

The authors would like to thank Dr. S. C. Chang of GM Research and Development Center and Y. Gianchandani for many valuable discussions. This work is supported by Advanced Research Project Agency under the Contract No. J-FBI-92-149.

#### References

1. Y. Gianchandani and K. Najafi, "Micro-sized, High Aspect Ratio Bulk Silicon Micromechanical Devices," MEMS '92, Travemünde, Germany, pp. 208-213.
2. W. C. Tang, T. C. H. Nguyen, and R. T. Howe, "Laterally Driven Polysilicon Resonant Microstructures," *Sensors and Actuators*, **20**, pp. 25-32, 1989.
3. W. C. Tang, T. C. H. Nguyen, M. W. Judy, and R. T. Howe, "Electrostatic-comb Drive of Lateral Polysilicon Resonators," *Sensors and Actuators*, **A21-23**, pp. 328-331, 1990.
4. W. Ehrfeld, P. Bley, F. Gotz, P. Hagmann, A. Manar, J. Mohr, H. Moser, D. Munchmeyer, W. Schelb, D. Schmidt, and E. W. Becker, "Fabrication of Micro-structures Using the LIGA Process," *Proc., IEEE Micro Robots and Tele. Workshop*, Hyannis, MA, pp. 53-63, 1987.

5. A. B. Frazier and M. G. Allen, "High Electroplated Microstructures Using A Polyimide Process," MEMS'92, Travemünde 87-92.
6. G. Engelmann, O. Ehrmann, J. Simon, "Fabrication of High Depth-to-Width Microstructures," MEMS'92, Travemünde 93-98.
7. A. Furuya, F. Shimokawa, T. Matsuura "Micro-Grid Fabrication of Fluorinated Polyimide by Using Magnetically Controlled Reactive Ion Etching (MCRIE)," MEMS'93, Fort Lauderdale, FL, pp. 59-64.
8. K. Murakami, Y. Wakabayashi, K. Minami, M. Esashi, "Cryogenic Dry Etching for High Aspect Ratio Microstructures," MEMS'93, Fort Lauderdale, FL, pp. 65-70.
9. F. C. Sze, D. K. Reinhard, B. Musson, J. Asmussen, and M. Dahimene, "Experimental Performance of a Large-diameter Multipolar Microwave Plasma Disk Reactor," *J. Vac. Sci. Technol.* **B8**, pp. 1759-1762, 1990.
10. K. T. Sung, W. H. Juan, S. W. Pang, and M. Dahimene, "Dependence of Etch Characteristics on Charge Particles as Measured by Langmuir Probe in a Multipolar Electron Cyclotron Resonance Source," *J. Vac. Sci. Technol.* **A12**, pp. 69-74, 1994.
11. W. H. Juan and S. W. Pang, "High Aspect Ratio Polyimide Etching Using an Oxygen Plasma Generated by Electron Cyclotron Resonance Source," *J. Vac. Sci. Technol.* **B12**, pp. 422-426, 1994.
12. K. T. Sung, W. H. Juan, S. W. Pang, and M. W. Horn, "Low Temperature Etching of Silylated Resist in an Oxygen Plasma Generated by an Electron Cyclotron Resonance Source," *J. Electrochem. Soc.* **140**, pp. 3620-3623, 1993.
13. M. Cantagrel, "Comparison of the Properties of Different Materials Used as Masks for Ion-Beam Etching," *J. Vac. Sci. Technol.* **12**, pp. 1340-1343, 1975.
14. R. A. Gottscho, C. W. Jurgensen, and D. J. Vitkavage, "Microscopic Uniformity in Plasma Etching," *J. Vac. Sci. Technol.* **B10**, pp. 2133-2147, 1992.

# Silicon-on-Insulator (SOI) by Zone-Melting-Recrystallization (ZMR) as a Micromechanical Material

Paul D. Aquilino and Paul M. Zavracky

*Northeastern University  
360 Huntington Avenue  
Boston, Massachusetts 02115*

## Abstract

Silicon-on-Insulator (SOI) wafers produced by the Zone-Melting-Recrystallization (ZMR) method are an attractive candidate for use in micromachining applications. Mechanical measurements indicate an orientation dependent tensile strain in the epitaxial silicon layer on the order of  $3 \times 10^{-4}$ . This is suitable for applications such as pressure sensors. In this paper we describe a method for surface micromachining of ZMR, the measurement of strain in the epitaxial silicon layer and a surface micromachined pressure sensor process.

## Introduction

SOI wafers consist of a thin layer of single crystalline silicon separated from a bulk silicon substrate by an insulating layer. Typically the insulator is silicon dioxide. Electronic and mechanical devices can be fabricated in the thin epitaxial layer<sup>1</sup>. Active matrix LCD displays, gate arrays, and 256K static RAMs are examples of circuits being fabricated. Pressure sensors and accelerometers are examples of mechanical structures. The isolation of the silicon devices from the bulk silicon substrate offers certain performance advantages over bulk silicon technology. High temperature operation, higher speed, and greater packing density are some of these advantages. The principal advantage of SOI in microelectromechanical systems (MEMS) applications is its compatibility with high temperature electronics.

Over the past several years, a new microstructure fabrication technique known as surface micromachining has been developed<sup>2,3,4</sup>. In this process, the mechanical structure is created from thin films deposited on the front side of the wafer. SOI wafers can be used as the starting material for surface micromachined devices<sup>5,6</sup>. Using surface micromachining technology, pressure sensors with diaphragm sizes of a few mils or less are easily fabricated. These offer a significant size reduction when compared to bulk micromachined sensors. Another very important advantage of surface micromachining is that microsensors can be integrated with microelectronics<sup>7</sup>. Using a single technology to fabricate both mechanical and electrical devices allows them to be integrated together. With integral electronics, measurement noise can be significantly reduced, thereby improving the performance of surface micromachined capacitive sensors.

## The ZMR SOI Process

The ZMR SOI process begins by first growing a thermal oxide on a bulk silicon wafer. This oxide becomes the buried insulator in the SOI structure. A thin polycrystalline silicon film is deposited next and capped with a CVD oxide. The wafer is then placed in a system which consists of a lower substrate platen/heater and an upper scanning wire heater. The substrate temperature is raised to about 1200°C and the upper wire is heated and scanned such that only the thin polycrystalline silicon film melts and recrystallizes. The capping CVD oxide is subsequently removed and the wafer is complete.

One of the advantages of the ZMR SOI process for MEMS fabrication is its flexibility with respect to the buried insulator and the silicon layer. Buried insulators other than oxide can be used and insulator interfaces are clean and abrupt. The thin silicon layer thickness can be specified within the range from 0.1 micron to 1.0 micron with a thickness uniformity on the order of  $\pm 0.015$  micron as compared to 0.1 micron for bonded wafer SOI. The resulting SOI structure provides an excellent starting point for MEMS applications such as pressure sensors.

## Surface Micromachining of ZMR

In surface micromachining of ZMR SOI, the silicon film can be used to create a variety of mechanical structures. The underlying oxide layer can be used as a temporary, sacrificial support structure during processing or as the permanent support pedestal. Examples of surface micromachined structures include diagnostic devices used in analyzing film strain. On our strain diagnostic mask we have incorporated structures previously reported by H. Guckel and D. Burns at the University of Wisconsin<sup>8,9,10</sup> which include the doubly supported beams used for compressive strain measurement and ring/beam structures used for analysis of tensile strain. Spiral structures reported by the University of California, Berkeley<sup>11</sup> for the evaluation of strain non-uniformity with film thickness were also incorporated.

To measure orientation dependent tensile strain, a new surface micromachined test structure was designed at Northeastern University<sup>12</sup>. Two support posts were used to

anchor a set of long thin angled beams with vernier position measuring features at their center. With the device oriented as in Figure 1 the operation of the structure is described as follows. The angled beams release tensile strain by bending when etched free of the underlying oxide. This bending acts to reduce the angle of the beams and increases the separation between the vernier comb features. The amount of movement can be determined by observing the alignment of the comb features. Taking each comb individually, subsequent prongs are 2 microns longer than their neighbor to the left. The difference in length between neighboring prongs of the top and bottom combs is 1 micron. The overlap between left-most prongs in the unstrained condition is 2 microns. An increase in strain causing the ends of the left most prongs to come into alignment would indicate a motion of 1 micron for each comb. A further increase in strain causes subsequent combs to align. This vernier arrangement allows the relative motion of the combs to be measured to within 1 micron. Six orders of magnitude of tensile strain can be covered with three of these structures.

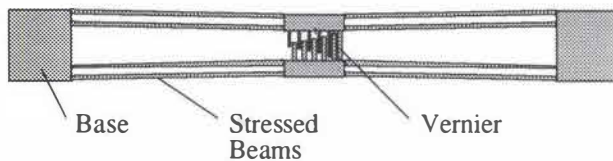


**Figure 1.** Schematic view of a tensile strain measurement structure.

In each of these structures, the silicon film is patterned in the required shape and size, leaving a large base at the support. The silicon is then etched using the underlying oxide as an etch stop. An isotropic etch of the oxide layer is used to undercut and release the structures from the substrate. The oversized support base serves to preserve the oxide under it and provide the required support pedestal.

Work being performed at Northeastern University on pressure sensors is yet another example of surface micromachining in ZMR. In a pressure sensor structure, the silicon film forms the diaphragm of the device. The oxide layer is used as a sacrificial support structure while a clamp made of polysilicon or silicon nitride is formed. Removal of this layer by an isotropic wet etch is facilitated by including etch ports in the clamp structure or by back etching through the substrate. A capacitive sensor with integral electronics shows promise for low noise, high temperature operation and is a potential application for ZMR SOI.

### Strain Measurements of ZMR<sup>11</sup>

Strain measurements were performed on the ZMR SOI film by surface micromachining a variety of diagnostic structures included in our strain diagnostic test die. The ZMR wafers used for these studies had both a silicon film and oxide thickness of 1 micron. The wafers were first patterned with an array of identical test die and the silicon film was etched in a custom built RIE using an  $SF_6/O_2$  mixture. After etching, the resist was stripped and the underlying oxide etched in 49% HF to release the test structures. The wafers were then rinsed thoroughly in DI water. Due to the delicate nature of the structures, care was taken during this rinsing step so as not to damage them.

The wafers were placed in a petri dish filled with DI water and the structures observed under a microscope. The water was subsequently displaced with isopropyl alcohol. Observation of the structures in alcohol produced results equivalent to those obtained after DI rinsing alone. To dry the

wafers, a unique hot plate drying technique was used. No significant differences were observed between the center and edge clamped spirals. This suggests that the strain in the ZMR material is uniform throughout its thickness.

In initial tests, five three inch wafers with a single flat on the (110) were evaluated from two separate lots. The tensile strain structures indicated the presence of a slight tensile strain. Measurements were made at five locations around the wafer, the center and four orthogonal perimeter locations. At each location four devices were sampled and the average reading was recorded. An asymmetry between the readings on devices perpendicular to the flat and devices parallel to the flat was observed. This was consistently observed on both the ring/beam structures and the vernier devices. For the ring/beam structures, an average strain between  $2.16 \times 10^{-5}$  and  $8.66 \times 10^{-5}$  was indicated with the bar perpendicular to the flat and between  $1.54 \times 10^{-5}$  and  $6.16 \times 10^{-5}$  parallel to the flat. The vernier structures indicated an average strain of  $1.5 \times 10^{-4}$  perpendicular to the flat and  $1.11 \times 10^{-4}$  parallel to the flat.

In the ZMR process, the wafer is scanned at  $45^\circ$  to the flat, or in a 100 direction. In a second experiment, alignment of the test die to the flat was indexed in three steps starting at 0, then  $45^\circ$  and finally  $90^\circ$  on three separate wafers. The first and last steps should yield the same results if all other conditions are equal. An anisotropy in the strain in the epitaxial silicon layer was found. No measurable strain was found in the direction of the scan and a strain of  $3.08 \times 10^{-4}$  was found in the direction perpendicular to the scan.

### A Capacitive Pressure Sensor in ZMR

One of the surface micromachined devices we are developing is a capacitive pressure sensor. This device uses a port etched into the substrate to allow differential pressure measurements and serve as an access to the sacrificial oxide layer under the diaphragm. Twenty six sensors of varying sizes are included on a die, one half of which are square and the remainder are circular. The square sensors range in size from 50 microns to 2000 microns on a side providing a maximum pressure of 265 psi to  $1 \times 10^{-4}$  psi. The circular sensors range in size from 27 microns to 1000 microns in radius providing a maximum pressure of 250 psi to  $1.3 \times 10^{-4}$  psi. Included with each sensor is a reference capacitor surrounding the device. Figure 2 shows an optical micrograph of the device.

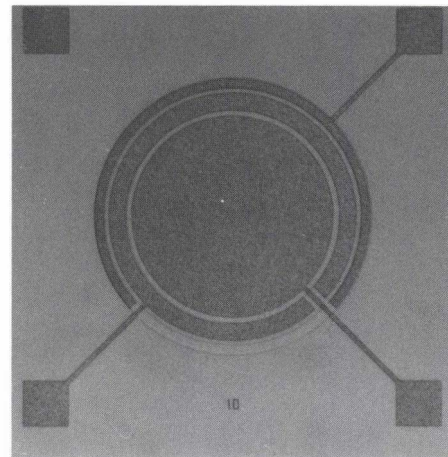


**Figure 2.** An optical micrograph of a capacitive pressure sensor fabricated in ZMR SOI with a nitride clamp.

The sensor process begins with a 3" (100) oriented ZMR SOI wafer with a 1 micron epitaxial silicon film and a 1 micron buried oxide. The wafer is nominally 25 mils thick but is backlapped and polished to 22 mils in preparation for backside processing. The silicon layer is patterned and etched by Reactive Ion Etching (RIE) in a  $\text{SF}_6/\text{O}_2$  mixture. As before, the underlying oxide layer acts as an etch stop in this etch. The oxide layer is isotropically etched in HF to remove the exposed oxide down to the substrate and to slightly undercut the silicon structures. A thin silicon nitride layer is deposited to act as a mask for the backside port etch. The backside is then patterned in an infrared aligner by aligning to front-side marks. This pattern defines the square port openings centered under each device. The nitride layer is etched in the RIE using a  $\text{O}_2/\text{CHF}_3$  mixture. The ports are then etched in an anisotropic KOH etch until they form a point. A TMAH etchant with a lower degree of anisotropy is now used to break through to the oxide under the devices and complete the ports. The thin mask nitride is removed and a thick (1 micron) silicon nitride layer is deposited to act as the diaphragm clamp structure. The silicon nitride is oxidized and the front and back are patterned. These patterning steps expose the silicon diaphragms and reference capacitors on the front and clear the ports on the backside. The wafer is dipped in BOE to clear the oxide over these features, the PR stripped and the nitride etched in phosphoric acid. A chrome-gold layer is deposited on the front-side of the wafer and coated with PR. The PR is exposed with the contact metal pattern but not developed at this point. The wafer is immersed in HF to etch the sacrificial oxide under the silicon diaphragms and free them from the substrate. After a thorough rinse in DI water, the wafer is placed in developer to develop the metal pattern. At this point the wafer is rinsed in DI water, then alcohol, and finally dried in an oven to prevent the diaphragms from collapsing to the substrate. A SEM photograph showing a detail of the clamp structure is shown in Figure 3.

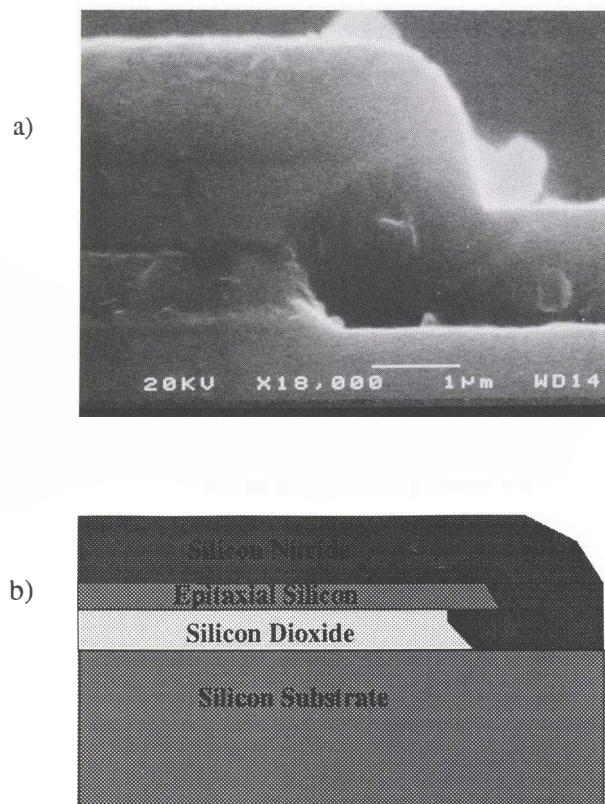


**Figure 3.** a) An SEM micrograph of a cross-sectioned sensor showing the substrate, buried oxide, epitaxial silicon and nitride layers. b) Schematic diagram of the same cross-section.

## Conclusions

ZMR SOI wafers offer a number of advantages when used as a starting material for surface micromachining. The structure of SOI provides three basic structures that can be used for surface micromachined devices; a silicon substrate, a high quality sacrificial layer, and a high quality silicon thin film. The interfaces between the silicon and insulator films are very clean, pure and abrupt. The silicon film can be specified in a range from 0.1 micron to 1.0 micron with a thickness uniformity of 0.015 microns. Strain in the silicon film is uniform throughout its thickness and while a tensile strain is present, it is observed at a maximum level of  $3 \times 10^{-4}$ .

Surface micromachined pressure sensors have been fabricated in ZMR SOI. The devices range in size from 50 microns to 2 mm across and offer a pressure range from 250 psi to  $1 \times 10^{-4}$  psi. These devices demonstrate how ZMR can be used for the fabrication of mechanical structures and offer great promise if combined with integral electronics. ZMR SOI promises small, low noise, high temperature sensing devices.

## Acknowledgments

The authors would like to express our appreciation to Kopin Corporation for their support both in terms of the donated wafers used in this study and their funding of our research program. We would also like to acknowledge the help of D.P. Vu and Mike Batty both of Kopin Corporation. In addition we would like to thank Keith Warner of Northeastern University without whose support this work could not have been accomplished.

## References

- 1 P. M. Zavracky, "ISE Technology: A Flexible SOI Solution", The 177th Meeting of the Electrochemical Society, Montreal, Quebec, May 1990.
- 2 H. Guckel and D. W. Burns, "Fabrication techniques for integrated sensor microstructures", IEEE Int. Electron Devices Meeting, pp. 176-179, 1986.
- 3 R. T. Howe, "Surface micromachining for microsensors and microactuators", J. Vac. Sci. Technol. B, Vol 6, No. 6, pp. 1809-1813, Nov/Dec 1988.
- 4 M. A. Schmidt, R. T. Howe, S. D. Senturia, "Surface Micromachining of Polyimide/Metal Composites for a Shear-Stress Sensor," IEEE Micro Robots and Teleoperators Workshop, 1987.
- 5 O. Tabata, R. Asahi, N. Fujitsuka, M. Kimura and S. Sugiyama, "Electrostatic driven optical chopper using SOI wafer", The 7th Int. Conf. on Solid-State Sensors and Actuators Digest, pp. 124-127, June 7-10, 1993.
- 6 B. Diem, M. T. Delaye, F. Michel, S. Renard, G. Delapierre, "SOI (SIMOX) as a substrate for surface micromachining of single crystalline silicon sensors and actuators", The 7th Int. Conf. on Solid-State Sensors and Actuators Digest, pp 233 - 236, June 7-10, 1993.
- 7 R. S. Payne and K. A. Dinsmore, "Surface Micromachined Accelerometer", SAE, Detroit, MI, pp. 127-135, February 25-March 1, 1991.

- 8 H. Guckel, T. Randazzo, and D. W. Burns, "A simple technique for the determination of mechanical strain in thin films with applications to polysilicon", *J. Appl. Physics*, Vol. 57, No. 5, pp. 1671-1675, 1 March 1985.
- 9 H. Guckel, D. Burns, C. Rutigliano, E. Lovell and B. Choi, "Diagnostic microstructures for the measurement of intrinsic strain in thin films", *J. Micromech. Microeng.* Vol. 2, No. 2, pp. 86-95, 1992.
- 10 D. W. Burns, "Micromechanical Integrated Sensors and the Planar Processed Pressure Transducer", Ph.D. dissertation, University of Wisconsin, Madison, WI, May 1988.
- 11 Long-Sheng Fan, R. S. Muller, W. Yun, and Roger T. Howe, and J. Huang, "Spiral microstructures for the measurement of average strain gradients in thin films", *Proc. IEEE Micro Electro Mechanical Systems*, pp. 177-181, 1990.
- 12 P. M. Zavracky and P. D. Aquilino, "Strain Analysis of Silicon-on-Insulator Films produced by Zone Melting Recrystallization", Submitted to the *IEEE/ASME MEMS Journal*.

# Uses of Electroplated Aluminum in Micromachining Applications

A. Bruno Frazier\* and Mark G. Allen  
School of Electrical Engineering  
Georgia Institute of Technology  
Atlanta, Georgia 30332-0250

\*School of Electrical Engineering  
Louisiana Tech University  
Ruston, LA 71272

## Abstract

In this paper, electroplated aluminum is explored as both a material for the fabrication of microstructures and for use in the development of micromachining processes. First, a method for the fabrication of aluminum microstructures is presented. Second, an extension of the basic photosensitive polyimide process is demonstrated for use in the fabrication of high aspect ratio microstructures. Third, electroplated aluminum is used as a sacrificial layer material in the development of a process for creation of controllable small gaps between metallic microstructural components.

## Introduction

There are many uses of aluminum for the fabrication of microdevices and for generic micromachining technology. One important application of aluminum microstructures is in the fabrication of integrated circuits. Since aluminum is the predominant material used to define electrical conductors in integrated circuit technology, microstructures such as high aspect ratio current carrying traces and micro heat sinks fabricated from aluminum would be completely compatible with the technology without the problems associated with intermetallic alloys at junctions between dissimilar metals. In addition to the use of aluminum as a material for the fabrication of microstructures, it can also be used as a processing tool to develop fabrication technologies. Two examples of the use of aluminum as a processing tool which are explored in this work include the use of electroplated aluminum as a means of producing high aspect ratio metallic microstructures and for producing controllable small gaps in metallic microdevices.

Metallic microstructures have been under study for micromachining applications for many years. Some of the more prominent applications of metal-based microstructures have been as current conductors in both magnetically [1-6] and electrostatically [7,8] driven devices. In addition, there has been applications for metallic structures with selected mechanical properties [9,10]. Several different fabrication technologies have been developed to address the needs associated with the differing applications. Among the processes that have been developed for fabrication of metallic microstructures are the LIGA process [2,3,5,8-10,11], the photosensitive polyimide process (PSPI) [1,4,7,12-14], UV-based positive and negative photoresist processes [6,15,16], and stenciling [17-19] as well as others [20-23]. Electroplated microstructures of several different elemental metals and metal alloys have been demonstrated including gold, silver, copper, nickel, and nickel alloys. To this point, electroplated aluminum microstructures have not been investigated for use in micromachining technology.

The purpose of this research is to introduce the use of electroplated aluminum as a material for the fabrication of microstructures and micromachining processes. Since the majority of the electrolytic solutions used to electroplate aluminum are based on organic solvents, one of the major problems with implementing this technology is finding a non-compatible molding material for the process. First, the issue of a compatible molding material for the aluminum electroplating process is addressed, and aluminum microstructures are demonstrated. Second, the basic PSPI process is extended to using the aluminum microstructures as electroplated molds for the fabrication of high aspect ratio metallic microstructures from metals other than aluminum. Third, electroplated aluminum is used as a sacrificial layer material in the development of a controlled small gap process for metallic microstructures.

## Aluminum Microstructures

By utilizing the material properties of aluminum such as the high thermal conductivity, high corrosion resistance, low neutron absorption, electrochemical nobility, stable mechanical properties at cryogenic temperatures, and non-sparking characteristic, many micromachining applications can be envisioned including nuclear applications, and low temperature devices. Historically, the electrodeposition of aluminum has been investigated for use in coating steel strip [24,25], in electrorefining [26], in electroforming [27-30], and in the cladding of uranium [31,32]. Limited commercial applications of aluminum plating have been reported [29, 33]. Aluminum, because it is much more chemically active than hydrogen, probably cannot be electrodeposited from solutions that contain water or any other compound with an acidic hydrogen, for example, acids, alcohols, ammonia, and primary and secondary amines [34]. It can be electrodeposited from inorganic and organic fused salt mixtures and from solutions of aluminum compounds in certain organic solvents. The fused salt baths have proven unsuitable for electroforming because of inherent thermal distortion of the deposit due to residual stresses in the films [28]. Many other fused salt baths were found to yield only thin or mechanically inferior deposits, and were highly flammable, poisonous, and inconveniently moisture-sensitive. [28] For the case of aluminum compounds in organic solvent, the aluminum chloride-lithium aluminum hydride-etheral solution, originally developed by [35,36], yielded satisfactory, low stress deposits. Low volatility, nonflammable derivatives of the aluminum chloride-lithium aluminum hydride-etheral bath have been developed by replacing part of the ether with a quaternary ammonium salt such as 2-ethoxyethyl trimethylammonium chloride [24].

Of the several electrodeposition processes that have had some commercial success, only the National Bureau of Standards hydride process has achieved a modest degree of use. Aluminum electroplating has similar commercial applications to conventional electroplated metals such as copper and nickel, but due to the higher cost of the electrolyte (ether vs. water) and the higher initial facility cost (inert atmosphere and safety requirements), it can only compete with conventional processes where the material properties of aluminum are required.

The aluminum electroplating solution composition is shown in Table 1. Additives can be introduced to the basic solution to reduce grain size and treeing, particularly in thicker deposits. Since the bath contains strong reducing agents and is anhydrous, the electroplating must be carried out in an inert atmosphere. In this work, electroplating is carried out in a sealed glove box with dry nitrogen as the ambient gas. To mix the bath, aluminum chloride is slowly added to diethyl ether in order to avoid localized overheating of the solution. The reaction of the aluminum chloride with the ether is exothermic, producing 580 calories per gram of heat. For large scale aluminum electroplating, external cooling is required during mixing of the solution. After the addition of the aluminum chloride, the lithium aluminum hydride is slowly added to prevent excessive gas evolution. As reported in literature [28,29], the bath remains operational with no change in plating quality for baths utilized in excess of four weeks. A typical current density used for electroplating is 10 - 15 mA/cm<sup>2</sup> resulting in an electroplating rate of 0.4 μm/min to 0.8 μm/min.

In the hydride bath, diethyl ether is used as the solvent. For this reason, photoresist electroplating mold processes cannot be utilized for the fabrication of aluminum microstructures. The ether results in swelling and/or decomposition of the polymers used in photoresist systems. In this work, the photosensitive polyimide process (PSPI) is used as a basis to form the electroplated

Table I. Composition of the aluminum electroplating solution (g/l refers to grams of substituent added per liter of final plating solution). The solvent-based electrolytic solution is based on diethyl ether.

Component	Quantity (g/l)
AlCl <sub>3</sub> , Aluminum Chloride	400
LiAlH <sub>4</sub> , Lithium Aluminum Hydride	15

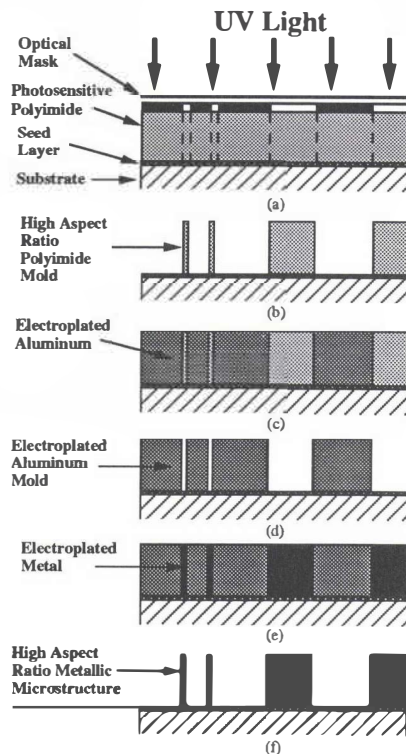


Figure 1. The extended PSPI process for the fabrication of high aspect ratio metallic microstructures. Fabrication steps 1a - 1d are required for the basic PSPI process. Steps 1e - 1f utilize electroplated aluminum as a molding material to form high aspect ratio structures.

aluminum microstructures [14]. The basic PSPI fabrication procedure, is shown in Figure 1a-1d. After the electroplating is complete, the substrate is rinsed in alcohol to remove residues from the plating bath and the polyimide mold is removed as in the basic process.

Various seed layers were investigated as seed layers for aluminum electroplated microstructures. Among the metallic seed layers investigated were gold, copper, nickel, chromium and aluminum. With the exception of chromium, all the seed metals chosen proved to be adequate as electroplating bases if the metals were protected from oxidation and contamination prior to the electrodeposition process. Electroplating using both aluminum and nickel seed layers were exceptionally sensitive to effects of oxidation.

Figure 2 shows an electroplated aluminum gear fabricated using the above process and electroplating bath. The aluminum gear has a thickness of 45  $\mu\text{m}$ , an outer diameter of 300  $\mu\text{m}$ , an inner diameter of 50  $\mu\text{m}$ , and a tooth width of 40  $\mu\text{m}$ . The surface of the microstructure is representative of the grain sizes obtained using the basic aluminum electroplating solution without the addition of additives at a plating rate of 0.4  $\mu\text{m}/\text{min}$ .

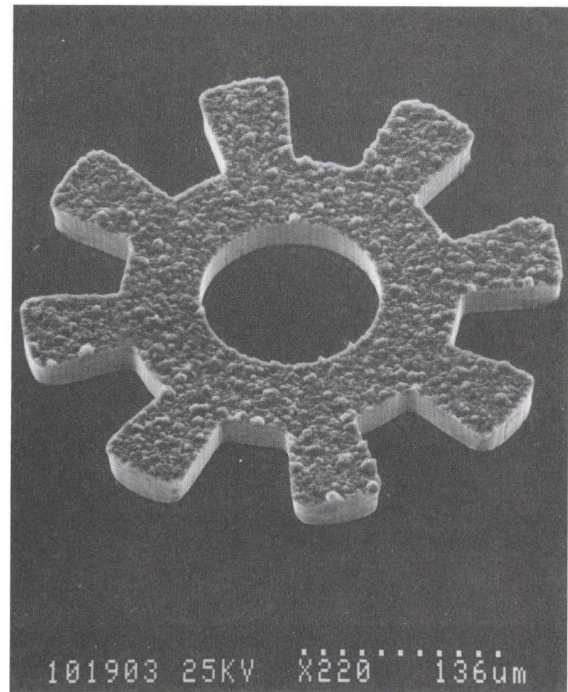


Figure 2. An electroplated aluminum gear with a thickness of 45  $\mu\text{m}$ , an inner / outer diameter of 50  $\mu\text{m}$  / 300  $\mu\text{m}$ , and a tooth width of 40  $\mu\text{m}$ .

#### High Aspect Ratio Microstructures Using Electroplated Aluminum Molds

High aspect ratio metallic microstructures have been a subject of interest for many years. As mentioned above, several processes have been demonstrated for the fabrication of high aspect ratio metallic microstructures. Of these techniques, electroplating of metals through polymer micromolds is the primary method of forming the structures. Using micromolding technologies, maximum aspects ratios of beam structures have been limited to approximately 4:1 (height:width) by non x-ray based technologies.

In this section, metallic microstructures with aspect ratios as large as 20:1 are demonstrated using an extension of the basic PSPI process [14]. This process differs from other available techniques in that electroplated aluminum micromolds have been used to form the metallic microstructures instead of polymer molding materials. The necessary extension of the PSPI process is shown in Figure 1d-1e. The process could be referred to as an inversion process in which the final metallic microstructures are of the same dimensions as the polyimide used as the initial molding material in the process. High aspect ratio microstructures have been achieved by utilizing the inversion characteristic of the process and the fact that high aspect ratio polyimide microstructures are simpler to fabricate than high aspect ratio trenches using the PSPI process. To outline the extended PSPI process, fabrication began with the basic process using photosensitive polyimide as the molding material through which aluminum was electroplated. For this study, the electroplating metal system consisted of a 300  $\text{\AA}$  titanium adhesion layer between the silicon (or ceramic) substrate and the electroplating seed layer, 1000  $\text{\AA}$  of either gold or copper as the electroplating seed layer, and an overlying layer of 1000  $\text{\AA}$  chromium to protect the electroplating seed layer during processes leading up to the electroplating step. The polyimide material used in the molding process was spun on at the desired thickness and photolithographically defined into the pattern required for the final metallic microstructure. After the aluminum has been electroplated to the top of the polyimide molds, the polyimide is removed leaving free standing aluminum microstructures (or micromolds in this case). The polyimide can be removed by several standard techniques. After removal of the polyimide, the chromium protective layer of the metal system is removed using reactive ion etching with a gas mixture consisting of 25 sccm O<sub>2</sub> and 25 sccm CHF<sub>3</sub> at a pressure of 50 mtorr and 300 watts of power

(approximate etch rate: 55 A/min). At this point in the process, the seed layer is exposed in the regions initially covered by polyimide in the basic PSPI process and the electroplated aluminum can be used as a mold for further electrodeposition of other metals including copper and nickel.

Figure 3 demonstrates the use of electroplated aluminum molds for the deposition of formed copper structures. For the case shown, the aluminum gear is formed initially using the process

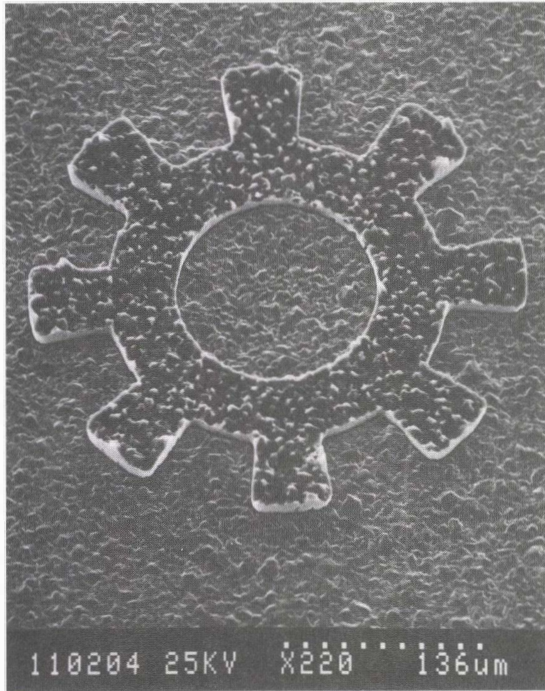


Figure 3. Electroplated aluminum gear with a thickness of 45  $\mu\text{m}$  serving as a mold for the electrodeposition of copper in the field.

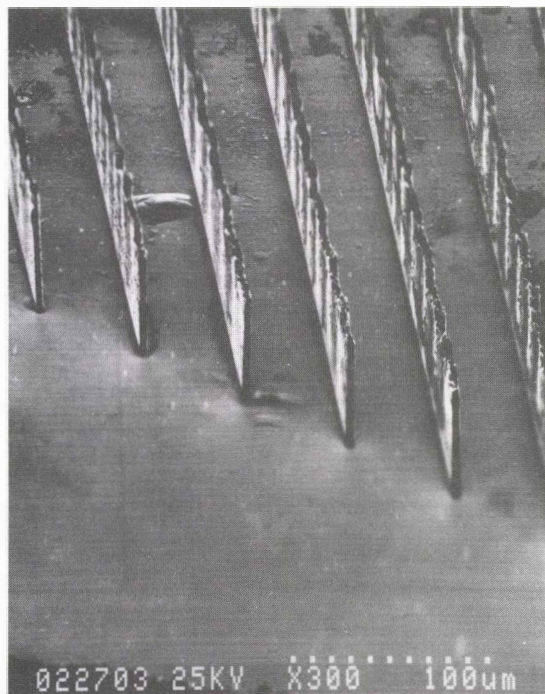


Figure 4. An array of high aspect ratio copper beams fabricated using the extended PSPI process. The beams have a height of 42  $\mu\text{m}$  and a width of 2  $\mu\text{m}$  for an aspect ratio of 21:1.

described in the previous section, followed by the deposition of copper in the pin and field area. The aluminum gear is approximately 60  $\mu\text{m}$  in thickness with a tooth width of 40  $\mu\text{m}$ , an outer diameter of 300  $\mu\text{m}$ , and an inner diameter of 50  $\mu\text{m}$ .

The use of this extended process for the realization of high aspect ratio metallic microstructures is shown in Figure 4. In this case, beams of electroplated copper are formed using aluminum molds. The beams are 42  $\mu\text{m}$  in height and have a width of 2  $\mu\text{m}$  for an aspect ratio of 21:1. Figure 5 is a close-up of a copper beam showing the smooth sidewall of the microstructure.

Other advantages of this process include the ability to fabricate metallic bimorphs for high current carrying applications, as well as using the electroplated aluminum as a thick sacrificial release layer for surface micromachining applications.

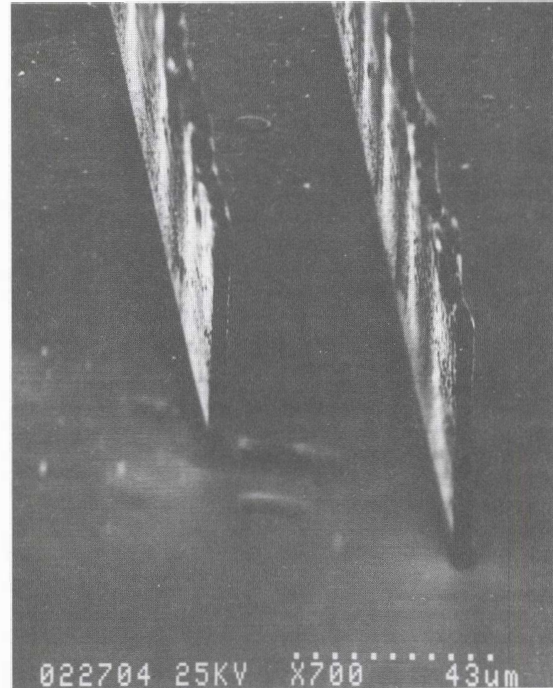


Figure 5. Close-up of the copper beam revealing the smooth sidewalls obtained with the process.

#### Small Gap Process for Metallic Microstructures

In addition to using aluminum as a processing tool for the fabrication of high aspect ratio metallic microstructures, it can also be used as a sacrificial layer in the development of a controllable small gap process for metallic microstructures. Development of a silicon based process for obtaining small gaps has already been reported [37]. In this process, metallic microstructures (other than aluminum) are fabricated using the basic PSPI process. The free standing microstructures are then conformally electroplated with aluminum, thus covering the entire microstructure with a thin layer of aluminum. The thickness of the aluminum "shell" is controlled by the electroplating current density and time duration of the electroplating cycle. The aluminum plating is followed by a second electroplating cycle in which a metal other than aluminum is deposited in the regions surrounding the existing structure. The second electroplating step uses the original seed layer as an electroplating base, and as in the case of the process for the fabrication of high aspect ratio microstructures, the metal deposited during the second cycle does not plate onto the aluminum encompassing the initial microstructure. The second metal is deposited to the desired height with respect to the initial microstructure.

Figure 6 demonstrated the use of aluminum in the controllable gap process. In this figure, the initial microstructures of copper with the thin film of electroplated aluminum are shown on either side of the metal (copper) deposited second. In the next step the

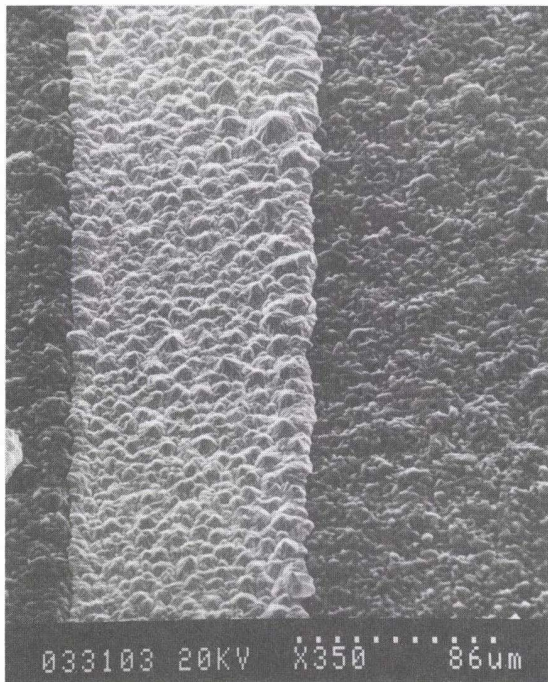


Figure 6. Demonstration of the use of electroplated aluminum as a sacrificial layer material for producing controllable small gaps between metallic microstructures.

aluminum is removed using a 1 vol% HF solution, leaving a small gap between the copper microstructures. Figure 7 shows a gap of 2  $\mu\text{m}$  between copper structures which are 60  $\mu\text{m}$  and 55  $\mu\text{m}$  in height for a gap aspect ratio of 27.5:1. Figure 8 shows a cross section of the gap and the sidewalls obtained using this process. In Figure 8, the microstructures are 55  $\mu\text{m}$  in height and the gap is 5  $\mu\text{m}$ .

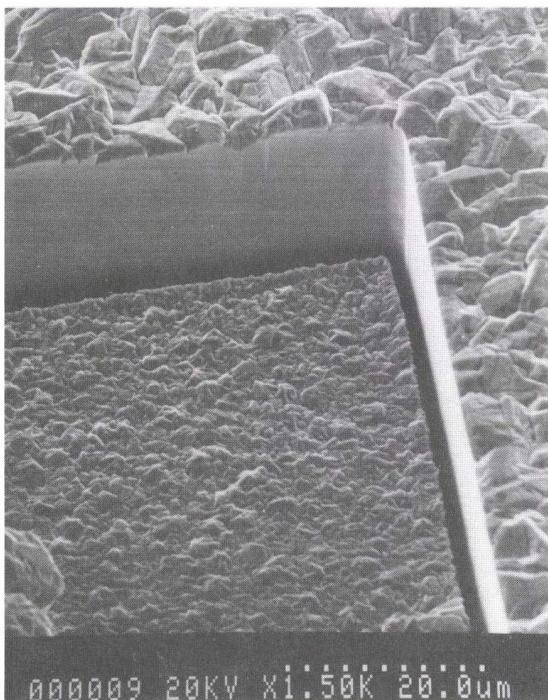


Figure 7. A high aspect ratio gap produced using the small gap process. The gap is 2  $\mu\text{m}$  and the structural heights are 60 and 55  $\mu\text{m}$ .

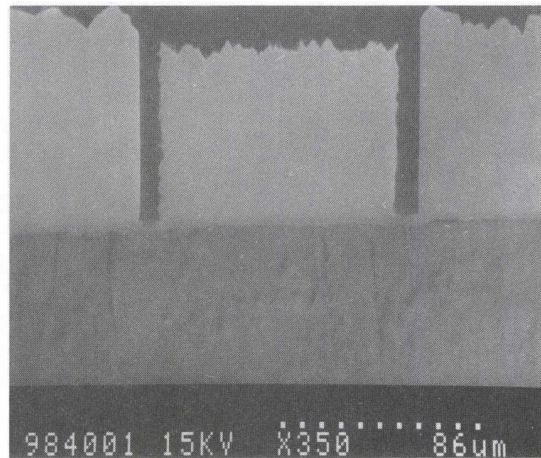


Figure 8. A cross section of two copper microstructures to study the sidewall characteristics of the process. The microstructures are 55  $\mu\text{m}$  in height and the gap is 5  $\mu\text{m}$ .

## Conclusion

Electroplated aluminum has been demonstrated to be of use in both the realization of microstructures and as a processing tool for micromachining processes. Electroplated aluminum microstructures have been demonstrated using a slightly modified version of the PSPI process. The use of aluminum as a processing tool for the fabrication of high aspect ratio metallic microstructures was demonstrated. Also, electroplated aluminum has been used as a sacrificial layer in the development of a fabrication technique for obtaining controllable small gaps between metallic microstructural components.

## Acknowledgments

We gratefully acknowledge the support of this work by Ford Motor Company, National Science Foundation of the United States under grant ECS-9117074, and OCG Microelectronic Materials.

## References

1. C.H. Ahn, Y.J. Kim, and M.G. Allen, "A Planar Variable Reluctance Magnetic Micromotor with Integrated Stator and Wrapped Coils", 1993 IEEE Micro Electro Mechanical Systems Conference, Fort Lauderdale, FL: IEEE Robotics and Automation Society & ASME Dynamic Systems and Control Division, February 7-10, 1993, pp. 1-6.
2. H. Guckel, T.R. Christenson, K.J. Scrobis, T. S. Jung, J. Klein, K.V. Hartojo, and L. Widjaja, "A First Functional Current Excited Planar Rotational Magnetic Micromotor", 1993 IEEE Micro Electro Mechanical Systems Conference, Fort Lauderdale, FL: IEEE Robotics and Automation Society & ASME Dynamic Systems and Control Division, February 7-10, 1993, pp. 7-11.
3. H. Guckel, J. Klein, T. Christenson, K. Skrobis, M. Laudon, and E.G. Lovell, "Thermo-Magnetic Metal Flexure Actuators", 1992 IEEE Solid-State Sensor and Actuator Workshop, Hilton Head, SC: IEEE Electron Devices Society, June 22-25, 1992, pp. 73-75.
4. C.H. Ahn, Y.J. Kim, and M.G. Allen, "A Fully Integrated Micromachined Toroidal Inductor with a Nickel-Iron Magnetic Core (The Switched DC/DC Boost Converter Application)", The 7th International Conference on Solid-State Sensors and Actuators, Yokohama, Japan: IEEE of Japan & Japan Science Foundation, June 7-10, 1993, pp. 70-75.
5. H. Guckel, T.R. Christenson, K.J. Skrobis and J. Klein, "Design and Testing of Planar Magnetic Micromotors Fabricated by Deep X-ray Lithography and Electroplating", The 7th International Conference on Solid-State Sensors and Actuators, Yokohama, Japan: IEEE of Japan & Japan Science Foundation, June 7-10, 1993, pp. 76-79.

6. T. Hirano and T. Furuhashi, "Dry Released Nickel Micromotors and Their Friction Characteristics", The 7th International Conference on Solid-State Sensors and Actuators, Yokohama, Japan: IEEE of Japan & Japan Science Foundation, June 7-10, 1993, pp. 80-83.
7. A.B. Frazier, J.W. Babb, M.G. Allen and D.G. Taylor, "Design and Fabrication of Electroplated Micromotor Structures," Proceedings of the ASME Winter Annual Meeting, Atlanta, GA: American Society of Mechanical Engineer, December, 1991, pp. DSC135-DSC146.
8. U. Wallrabe, P. Bley, B. Krevet, W. Menz, and J. Mohr, "Theoretical and Experimental Results of an Electrostatic Micro Motor with Large Gear Ratio Fabricated by the LIGA Process", 1992 IEEE Micro Electro Mechanical Systems Conference, Travemunde, Germany: IEEE Robotics and Automation Society & German IEEE Section, February 4-7, 1992, pp. 139-140.
9. R. Rapp, P. Bley, W. Menz, and W.K. Schomburg, "Micropump Fabricated with the LIGA Process", 1993 IEEE Micro Electro Mechanical Systems Conference, Fort Lauderdale, FL: IEEE Robotics and Automation Society & ASME Dynamic Systems and Control Division, February 7-10, 1993, p. 123.
10. A.B. Frazier, D.P. O'Brien, and M.G. Allen, "Two Dimensional Metallic Microelectrode Arrays for Extracellular Stimulation and Recording of Neurons," 1993 IEEE Micro Electro Mechanical Systems Conference, Fort Lauderdale, FL: IEEE Robotics and Automation Society & ASME Dynamic Systems and Control Division, February 7-10, 1993, p. 195-200.
11. M. Harmening, W. Bacher, P. Bley, A. El-Kholi, H. Kalb, B. Kowanz, W. Menz, A. Michel, and J. Mohr, "Molding of Three Dimensional Microstructures by the LIGA Process", 1992 IEEE Micro Electro Mechanical Systems Conference, Travemunde, Germany: IEEE Robotics and Automation Society & German IEEE Section, February 4-7, 1992, pp. 202-207.
12. A.B. Frazier and M.G. Allen, "High Aspect Ratio Electroplated Microstructures using a Photosensitive Polyimide Process", 1992 IEEE Micro Electro Mechanical Systems Conference, Travemunde, Germany: IEEE Robotics and Automation Society & German IEEE Section, February 4-7, 1992, pp. 87-92.
13. M. G. Allen, "Polyimide-Based Processes for the Fabrication of Thick Electroplated Microstructures", The 7th International Conference on Solid-State Sensors and Actuators, Yokohama, Japan: IEEE of Japan & Japan Science Foundation, June 7-10, 1993, pp. 60-65.
14. A.B. Frazier and M.G. Allen, "Metallic Microstructures Fabricated Using Photosensitive Polyimide Electroplating Molds", Journal of Microelectromechanical Systems, (2) 87-94 (1993).
15. S. G. Mearing, "Thick Liquid Photoresist for Improving Image and Plating Resolution," Solid State Technology, September, 1986.
16. T. Hirano, T. Furuhashi, and H. Fujita, "Dry Releasing of Electroplated Rotational and Overhang Structures", 1993 IEEE Micro Electro Mechanical Systems Conference, Fort Lauderdale, FL: IEEE Robotics and Automation Society & ASME Dynamic Systems and Control Division, February 7-10, 1993, p. 278-283.
17. H. Snakenborg, "A New Development in Electroformed Nickel Screens," Proceedings of the Symposium on Electroforming/Deposition Forming, American Electroplaters Society, March, 1983.
18. W.L. Guthrie, W.J. Patrick, E. Levine, H.C. Jones, E.A. Mehter, T.F. Houghton, G.T. Chiu, M.A. Fury, "A Four-level VLSI Bipolar Metallization Design with Chemical-Mechanical Planarization," IBM J. Res. Develop., vol. 36, no. 5, 1992, pp. 845-857.
19. H.D. Goldberg, D.P. Liu, R.W. Hower, M.E. Poplawski, and R. B. Brown, "Screen Printing: A Technology for Partitioning Integrated Microsensor Processing", 1992 IEEE Solid-State Sensor and Actuator Workshop, Hilton Head, SC: IEEE Electron Devices Society, June 22-25, 1992, pp. 140-143.
20. K. Ikuta and K. Hirowatari, "Real Three Dimensional Micro Fabrication using Stereo Lithography and Metal Molding", 1993 IEEE Micro Electro Mechanical Systems Conference, Fort Lauderdale, FL: IEEE Robotics and Automation Society & ASME Dynamic Systems and Control Division, February 7-10, 1993, pp. 42-47.
21. M. Boman, H. Westberg, S. Johansson, and J.-A. Schweitz, "Helical Microstructures Grown by Laser Assisted Chemical Vapour Deposition", 1992 IEEE Micro Electro Mechanical Systems Conference, Travemunde, Germany: IEEE Robotics and Automation Society & German IEEE Section, February 4-7, 1992, pp. 162-167.
22. W.H. Brunger and K.T. Kohlmann, "E-beam Induced Fabrication of Microstructures", 1992 IEEE Micro Electro Mechanical Systems Conference, Travemunde, Germany: IEEE Robotics and Automation Society & German IEEE Section, February 4-7, 1992, pp. 168-170.
23. C.C. Liu, "Electroless Plating of Metals for Micromechanical Structures", The 7th International Conference on Solid-State Sensors and Actuators, Yokohama, Japan: IEEE of Japan & Japan Science Foundation, June 7-10, 1993, pp. 66-69.
24. J.G. Beach, L.D. McGraw, and C.L. Faust, "A Low-Volatility Nonflammable Bath for Electrodepositing Aluminum", Plating, 55 (1968) 936-940.
25. B.O. Holland, "The Electrodeposition of Aluminum Upon Steel Strip from some Organic Solutions", J. Aust. Inst. Met., 6 (1961) 212-219.
26. V.K. Ziegler and H.Lemkuhl, "Die Elektrolitische Abscheidung von Aluminum aus Organischen Komplexverbindungen", Zeitschrift fuer Anorganische und Allgemeine Chemie, 283 (1956) 414-424.
27. F.J. Schmidt and I.J. Hess, "Electroforming Aluminum for Solar Energy Concentrators", NASA Rep. CR-197, April 1965.
28. F.J. Schmidt and I.J. Hess, 'Properties of Electroformed Aluminum', Plating, 53 (1966) 229-235.
29. A.G. Buschow and C.H. Esola, "Commercial Applications of the Aluminum Electroplating Process", Plating, 55 (1968) 931-940.
30. F.J. Schmidt, I.J. Hess, C.H. Esola, and A.G. Buschow, "Electroforming of Aluminum Composite Structures by Codeposition of High-Strength, High Modulus Fibers", in the 15th National SAMPE Symposium and Exposition, Los Angeles, CA, April 29 - May 1, 1969, pp. 117-124.
31. G.V. Alm and M.J. Binstock, "Aluminum Electrocladding Studies for Proposed OMR Fuel Elements", U.S.Dept. of Commerce Rep. NAA-SR-274, October 1, 1958.
32. J.G. Beach and C.L. Faust, Journal of the Electrochemical Society, 106 (1959) 654-662.
33. I.J. Hess and J.F. Betz, Metal Finishing, 69 (1971) 38-51.
34. W.B. Harding, 'Aluminum', Modern Electroplating, ed. F.A. Lowenheim, Plainfield, N.J., 1974, pp. 63-70.
35. D.E. Couch and A. Brenner, "A Hydride Bath for the Electrodeposition of Aluminum", Journal of the Electrochemical Society, 96 (1952) 234-44.
36. J.H. Connor and A. Brenner, "Electrodeposition of Metals from Organic Solutions", Journal of the Electrochemical Society, 103 (1958) 657-62.
37. T. Furuhashi, T. Hirano, K.J. Gabriel, H. Fujita, "Sub-micron Gaps without Sub-micron Etching", Proceedings of the IEEE Micro Electro Mechanical Systems Conference, Nara, Japan, Jan.30, 1991, pp. 57-62.

# DRY-RELEASED PROCESS FOR ALUMINUM ELECTROSTATIC ACTUATORS

Christopher W. Storment, David A. Borkholder, Victor A. Westerlind,  
John W. Suh, Nadim I. Maluf, and Gregory T. A. Kovacs\*

\* To whom correspondence should be addressed. G. T. A. Kovacs, Department of Electrical Engineering, Stanford University, Room CIS 130, Stanford, CA 94305-4070, email: kovacs@glacier.stanford.edu

C. W. Storment, D. A. Borkholder, V. A. Westerlind, N. I. Maluf and G. T. A. Kovacs are with the Department of Electrical Engineering, Stanford University. J. W. Suh is with the Department of Mechanical Engineering, Stanford University.

## ABSTRACT

An all-aluminum MEMS process (Al-MEMS) for the fabrication of large-gap electrostatic actuators is presented. The process is purely additive above the substrate and thereby permits a high degree of design freedom. All process steps are compatible with the future addition of underlying CMOS control circuits. Multilayer aluminum metallization is used with organic sacrificial layers to build up the actuator structures. Oxygen-based dry etching is used to remove the sacrificial layers. While this approach has been previously used by other investigators to fabricate optical modulators and displays, the specific process presented herein has been optimized for driving mechanical actuators with relatively large travels and/or out-of-plane attachments such as electroplated "digits." The gap height between the actuator and the underlying electrode(s) can be set using an adjustable polyimide sacrificial layer and aluminum "post" deposition step. Several Al-MEMS electrostatic actuators designed for use as mechanical actuators are presented.

## INTRODUCTION

The goal of this work is to develop a versatile process for the fabrication of electrostatic actuators for mechanical transducers. An all-aluminum process, using organic sacrificial layers was developed along the lines of the process of Hornbeck, et al., at Texas Instruments [1]. They have demonstrated torsionally-actuated optical modulators (and complete displays built from them) and other devices using such a technology. While polysilicon-based actuators have been successfully integrated with CMOS processes [2], the use of silicon dioxide sacrificial layers limits the maximum vertical gap to a few microns at most.

The devices described herein are intended to be used as drivers for out-of-plane actuators based on the addition of vertical extensions, or "digits" (by electroplating or other methods). For these applications, as well as large angular motion optical modulators, we require a larger gap for deflection, few

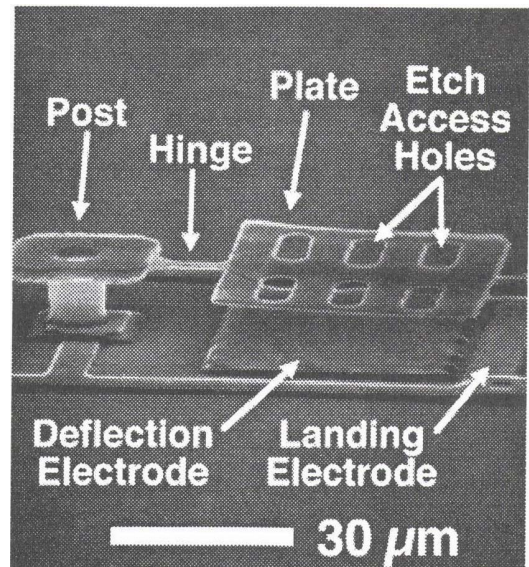


Figure 1: Scanning electron micrograph (SEM) view illustrating the basic structure of an Al-MEMS cantilever actuator, showing the interconnects, deflection and landing electrodes, post, hinge, plate and etching access holes through the plate.

constraints on geometry, and compatibility with CMOS processes for ultimately adding control circuits. In addition, we have less stringent requirements for the surface reflectivities or fill factors achievable.

Thin metal hinges and thicker plate regions are used to form the mechanical elements (shown in Figure 1), suspended above the substrate by aluminum “posts” and released by the dry etch removal of an organic sacrificial layer. The Al-MEMS process is described below, as well as some test results on the resulting actuators.

## MATERIALS AND METHODS

As stated above, the overall process is a multi-level aluminum, organic sacrificial layer sequence, illustrated in Figure 2. The following summarizes the process, and a more complete description can be found in [3]. On 100 mm diameter, p- silicon wafers, a wet thermal silicon dioxide is grown to a thick-

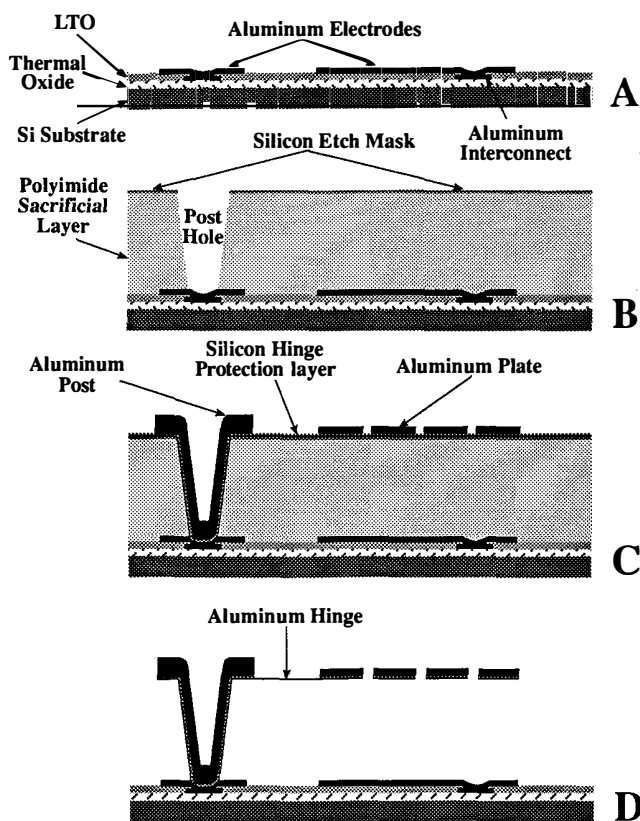


Figure 2: Diagram illustrating Al-MEMS process flow (not to scale). At stage A, the interconnects and deflection electrodes have been fabricated on the silicon. At stage B, the sacrificial polyimide layer has been deposited and patterned using a silicon etch mask layer. Stage C shows a completed actuator, prior to patterning of the silicon and hinge aluminum layers. Stage D shows a released actuator.

ness of  $0.5 \mu\text{m}$ . The first and second aluminum metallization layers for interconnects, electrodes and bond pads are deposited in a DC magnetron sputtering system, with film thicknesses for each layer of  $0.25 \mu\text{m}$ . The metal patterns are defined by coating with photoresist, exposure and wet etching.

Between the first two Al layers, an insulating low temperature oxide (LTO) is deposited in an LPCVD furnace. To make electrical contact between the two layers, via holes are etched through the oxide to expose the first layer metal using RIE etching with  $\text{O}_2$  and  $\text{CHF}_3$  reactant gases. After resist removal, the second metal layer is deposited. The top metal layer is then patterned with a photoresist mask and wet etched as for the first layer. At this point, the processing has progressed to the stage illustrated in Figure 2A.

In order to define the deflection gap at a desired value between 1 and  $20 \mu\text{m}$  Ultradel 4212 spin-on polyimide (Amoco Chemical Co., Chicago, IL) is used as the organic sacrificial spacer layer. Using the unmodified product it is possible to control thickness from 5-15  $\mu\text{m}$ . For smaller gaps the polymer can be diluted 1:1 with the appropriate thinner from Amoco and for thicker films two layers can be applied with a bake cycle between applications.

The polyimide is spun on to a thickness of 10  $\mu\text{m}$  and cured in a nitrogen purged oven. Since the subsequent layers used to form the moving parts of the actuators are opaque, physical alignment marks must be formed in the top surface of the polyimide. The polyimide is coated with thick photoresist, patterned and oxygen plasma etched to form 1  $\mu\text{m}$  deep alignment marks in the exposed polyimide. The masking photoresist is then stripped off in acetone and isopropyl alcohol, rather than dry etching, to maintain a smooth surface on the polyimide (critical for the deposition of suitable Al films above it).

After a bake to remove any adsorbed moisture and solvents,  $0.25 \mu\text{m}$  of Si is DC magnetron sputter deposited as a masking layer for the oxygen RIE to form the post holes. The silicon masking layer is patterned using photoresist over the post holes and plasma etched using  $\text{SF}_6$  and  $\text{C}_2\text{ClF}_5$  reactant gases. The post holes (approximately 10  $\mu\text{m}$  in diameter) are then formed by oxygen RIE for 1-3 hours (depending on the thickness of the polyimide). The Si etch mask is left in place to maintain a smooth surface onto which the thin hinge layers can be depos-

ited. This stage of the processing is illustrated in Figure 2B.

After etching the post holes into the polyimide, three low stress layers of Al, Si and Al are DC magnetron sputter deposited without breaking vacuum. It was verified that the stress in the Al films could be kept below 75 MPa (compressive), corresponding to films of Al that were extremely smooth to optical and electron microscopic examination. The first layer of Al is deposited to a thickness between 0.1 and 0.3  $\mu\text{m}$  to form the thin hinge structures. Next, 0.2  $\mu\text{m}$  of Si is deposited to act as a wet etch mask for the hinges. Finally, a 1 - 2  $\mu\text{m}$  layer of Al is deposited to form mechanically stable posts to which the hinges and moving parts are connected. A thick layer of photoresist is applied, patterned and used to pattern the thick upper Al layer using wet etching down to the Si hinge protection layer. The photoresist is stripped by oxygen plasma etching followed by another application and patterning of photoresist and plasma patterning of the silicon protective layer ( $\text{SF}_6$  and  $\text{C}_2\text{ClF}_5$  reactant gases) into the final hinge shapes. Following oxygen plasma stripping of the photoresist, 0.5  $\mu\text{m}$  of low stress Al is sputtered as before to form the movable upper electrode plates. As for the previous metallization steps, this layer is coated with photoresist and patterned using wet etching to define the plates and the hinges (which are already masked by the etched silicon protective layer). This stage of the processing is illustrated in Figure 2C.

Having thus completed the fabrication sequence, the wafers are coated with photoresist to protect against particulates and damage from the water jet during dicing. Following dicing and removal of particulates, the individual dice are oxygen plasma etched to remove the protective photoresist,  $\text{SF}_6$  and  $\text{C}_2\text{ClF}_5$  plasma etched to remove the protective Si layer on the hinges and then oxygen plasma etched to remove the sacrificial polyimide layer. Finally, the Si remaining on the underside of the hinges (from the post-hole mask) is removed using a  $\text{SF}_6$  and  $\text{C}_2\text{ClF}_5$  plasma etch. The released structures are illustrated in Figure 2D.

## RESULTS

Several different actuator structures were designed and fabricated to serve as test vehicles for the process, including both cantilever and torsional actuators. Examples are shown in Figures 1, 3 and 4.

For the devices illustrated and tested herein, the gap heights were 10  $\mu\text{m}$  and hinge thicknesses were 150 nm.

To date, several types of cantilever designs have been successfully tested using optical and scanning electron microscopic observation [3]. Threshold voltage,  $V_{\text{th}}$ , (applied voltage for full deflection) measurements showed minimum voltages of 7V for

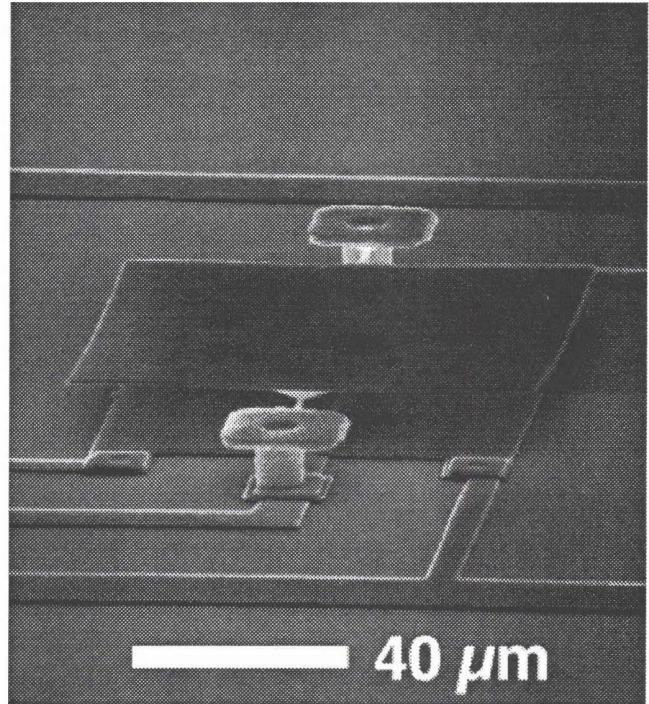


Figure 3: SEM view of a torsional Al-MEMS actuator.

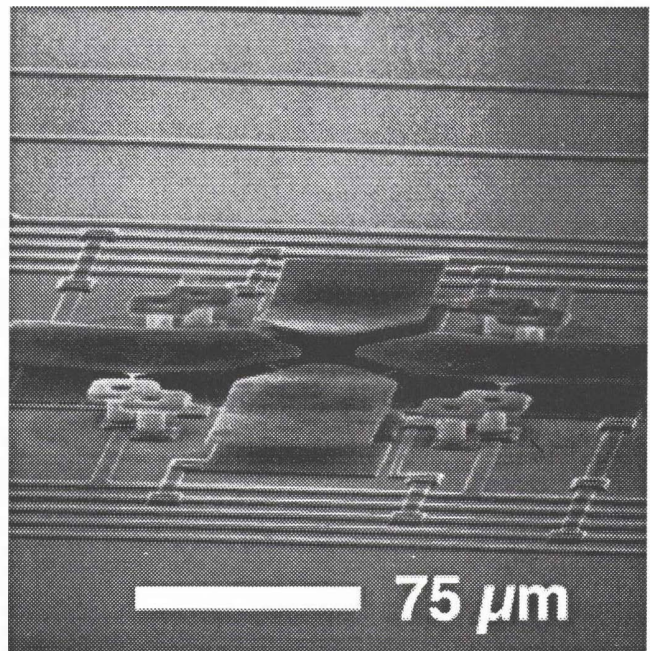


Figure 4: SEM view of a four-plate, individually-actuated torsional actuator array.

cantilever and 6V for torsional structures.

In addition, electroplated digits have been fabricated on both cantilever and torsional devices, forming actuators with out-of-plane digits, ciliary actuator arrays and accelerometer structures. A low aspect-ratio digit atop a cantilever actuator is shown in Figure 6. The additional process steps used to fabricate this device are the deposition of a thin Ti-Au-Si seed layer, application of thick photoresist, electroplating, stripping the photoresist and shorting layer, and removal of the sacrificial layer as described above.

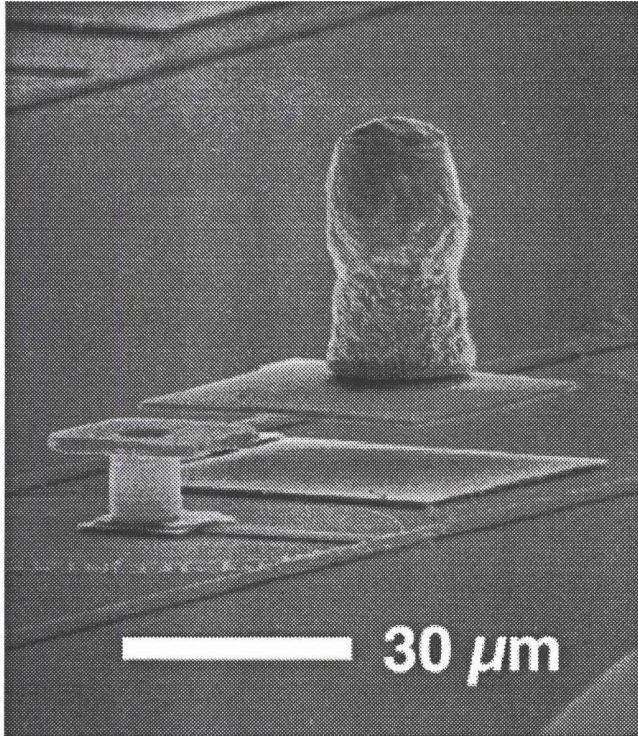


Figure 5: SEM view of a cantilever actuator with an electroplated gold out-of-plane digit.

## SUMMARY

We have presented an aluminum/organic sacrificial layer MEMS process (Al-MEMS) for the fabrication of mechanical actuators. The process is designed to be compatible with the future use of underlying, pre-fabricated CMOS circuits by relying on only process steps known to be compatible with them. Several mechanical actuator designs have been demonstrated. In addition, we have fabricated electroplated digits or proof masses on such aluminum structures.

## ACKNOWLEDGMENTS

This work was supported by the Advanced Research Projects Agency Grant Number N0014-92-J-1940-P00001, administered by the Office of Naval Research.

## REFERENCES

- [1] L.J. Hornbeck, "Deformable-mirror spatial light modulators" in Spatial Light Modulators and Applications III, *Proceedings Of The SPIE - The International Society For Optical Engineering* (1990) vol. 1150, San Diego, Aug. 1989, pp. 86-102.
- [2] W. Yun, R. T. Howe, and P. R. Gray, "Surface Micromachined, Digitally Force-Balanced Accelerometer with Integrated CMOS Detection Circuitry," *Proceedings of the IEEE Solid-State Sensor and Actuator Workshop*, Hilton Head, SC, June 22 - 25, 1992, pp. 126 - 131.
- [3] C. W. Storum, D. A. Borkholder, V. Westerlind, J. W. Suh, N. I. Maluf, and G. T. A. Kovacs, "Flexible, Dry-Released Process for Aluminum Electrostatic Actuators," to appear in the *Journal of Microelectromechanical Systems*.

# SURFACE MICROMACHINED MULTIPLE LEVEL TUNGSTEN MICROSTRUCTURES

Liang-Yuh Chen and Noel C. MacDonald  
School of Electrical Engineering and the National Nanofabrication Facility,  
Cornell University, Ithaca, New York 14853  
Tel: (607) 255-3926, Fax: (607) 255-1001

## ABSTRACT

A low temperature (440° C) selective chemical vapor deposition (CVD) tungsten process is used successfully to fabricate multiple level microstructures and microactuators. The planar, selective deposition process, combined with a mechanical micro-polishing sequence, gives excellent control of lateral feature size. The multiple level process can be used to fabricate a variety of complex, microstructures with minimum lateral dimensional constraints. The process is compatible with multiple level interconnects and plug technology used in integrated circuits. In this paper, we described the process sequence to produce three-dimensional, three level microactuators.

## INTRODUCTION

Recent advances in surface micromachining have produced many microelectromechanical systems (MEMS) and structures. Conventional microactuators consist of a biased, moving structure driven electrostatically by nearby fixed electrodes - either planar electrodes to produce a lateral motion, or a stacked electrode to produce vertical motion [1-2]. One drawback of surface micromachining is the difficulty of fabricating multilevel structures. However, these structures have many applications and provide extra design freedom in sensing and actuation [3-6]. Recent efforts using polyimide-based processes to create multilevel magnetic-meander inductors have demonstrated the importance of multilevel MEMS process technology [6-7].

The primary obstacle to the realization of multiple level microstructures by surface micromachining is the non-planar surface resulting from the fabrication of previous levels. For surface micromachining, structural layers are deposited and then patterned to define the micromachines. The resulting surface is non-planar with typical surface height variation of a few microns. This non-planar surface limits subsequent level definition and reduces processing latitude. We desire a multiple level process that produces a planar surface for the deposition and definition of each successive layer, and accommodates fine-line geometries and accurate registration. It is difficult to pattern and to plasma etch small features into a film if the resist covers non planar topography.

In this work, we discuss the use of selective chemical vapor deposition (CVD) of tungsten to fabricate multilevel, suspended microstructures. Our process allows multilevel surface micromachined structures to be fabricated with minimal geometrical constraints. The process can be scaled to submicron dimensions. Other advantages of the tungsten CVD process include low temperature deposition (440°C), and compatibility with existing silicon integrated circuit technology, and with

multiple-level metallization and plug technologies [8]. Furthermore, tungsten is less reactive with silicon and aluminum than other materials [9]. While our study concentrates on CVD tungsten, the process should be extendable to electro or electroless plating of other metals such as copper or nickel.

## FABRICATION SEQUENCE

The fabrication steps required to produce multilevel micro-mechanical structures are based on a selective tungsten CVD technology with multiple layers of CVD silicon dioxide used as support and sacrificial layers. In essence, the multiple level process is a repetition of the single level tungsten process.

### I. The Basic Process

The most favorable characteristic of the basic tungsten process is that tungsten is selectively deposited on specific regions of a wafer by chemical vapor deposition [10-11]. Selective deposition avoids additional masking and etching steps of the structural layer, enables self-aligned structures if desired, and simplifies metallization. A characteristic of our process for the fabrication of multiple level MEMS, is the achievement of a planar surface after the formation of the microstructures.

Figure 1 shows the process flow of the selective tungsten CVD process. The starting material is a three inch silicon wafer. A layer of low temperature CVD silicon dioxide (LTO), approximately 3.0  $\mu\text{m}$  thick, is used to form the trenches for selective CVD tungsten deposition. A 1000Å thick silicon nitride layer is deposited as the implantation mask (1a). The trenches for the tungsten structures are formed by reactive ion etching (RIE) the composite dielectric layers in a  $\text{CHF}_3$  ambient. The trenches are etched into the LTO to a depth of approximately 2.0  $\mu\text{m}$ , with 1.0  $\mu\text{m}$  LTO left to define the tungsten structure to substrate spacing (1b). After the resist is removed by an oxygen plasma etch step, the bottom of the trenches is made silicon rich by using ion implantation of silicon atoms at an energy of 40 KeV [11]. A silicon dosage of  $1 \times 10^{17} / \text{cm}^2$  is used to initiate the deposition of tungsten on LTO. To expose the peak silicon concentration in the implanted oxide channels, we immersed the wafer in 30:1 buffered HF. The silicon nitride mask is then removed in hot phosphoric acid at 155°C for 30 minutes (1c). A tungsten film is then selectively deposited in a Genus 8432 cold wall reactor at a temperature of 440°C (1d). Deposition pressure is 400 mTorr with gas flows of 4900 sccm  $\text{H}_2$  and 180 sccm  $\text{WF}_6$ .

The growth process for CVD tungsten is selective and only occurs on the silicon-rich bottom of the trenches. Once tungsten is deposited on the exposed silicon-rich bottom of the trenches, the process continues but deposition only occurs on the newly deposited tungsten surface, not on the surrounding insulating

surface. Another method to deposit CVD tungsten is to create a metal-rich trench floor, by evaporation of metals such as gold or palladium and resist liftoff.

Selectivity deteriorates and surface roughness increases as tungsten deposition thickness increases, resulting in the degradation of planarity for subsequent processes. These two problems are illustrated in Fig. 2 and Fig. 3(a), after a 2.5  $\mu\text{m}$  thick tungsten deposition. We have planarize such surfaces by mechanical micro-polishing. The sample is polished sequentially: 1 micron polishing compound for rough polishing, 0.3 micron for medium-fine polishing, and 0.05 micron for very fine polishing. The polishing steps are performed on three different polishing wheels. Aluminum oxide has been found to be the most suitable polishing compound. The time required for each step varies, depending on the surface roughness of the wafer. Figure 3(b) shows a planar, smooth surface after polishing. Our results show that mechanical polishing is sufficient for full planarization of selective tungsten surfaces. Other planarization techniques, such as etch-back or chemical-mechanical-polishing, are possible alternatives [12].

## II. Multilevel Process

Multiple level tungsten microstructures are fabricated by repeating the basic process. The process flow to create a three-level tungsten microstructure is shown in Fig. 4. After the first level of tungsten has been formed inside the oxide trenches and

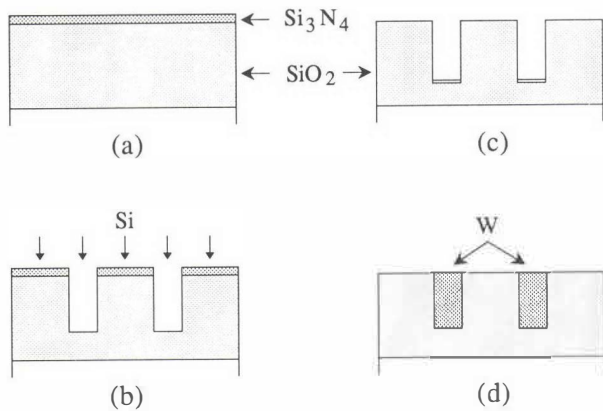


Fig. 1. Selective CVD Tungsten process cross section: (a) after CVD silicon dioxide and silicon nitride deposition; (b) after oxide trench etching and silicon implantation; (c) after silicon nitride removal, creating a silicon-rich bottom trench; and (d) after selective CVD tungsten deposition.

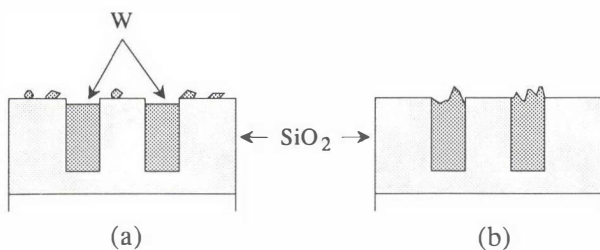
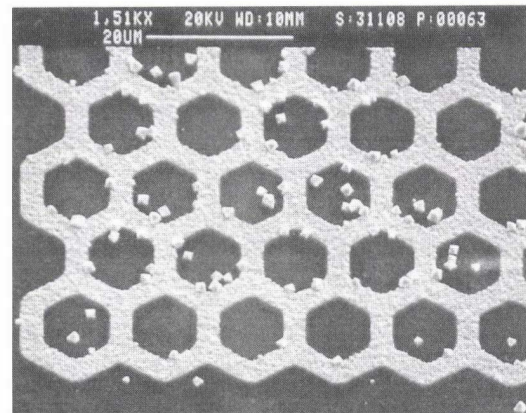


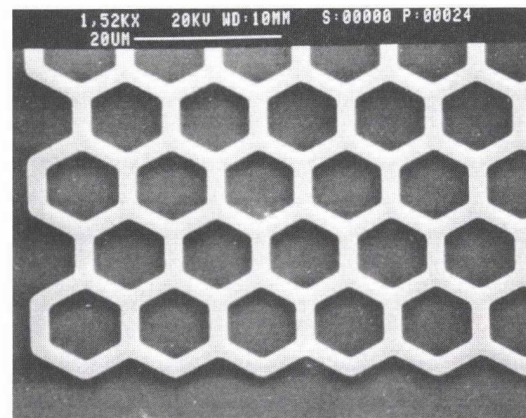
Fig. 2. Selective CVD Tungsten surface roughness issues: (a) loss of selectivity and tungsten particles; and (b) non uniform grain height.

polished to planarize the surface, a second LTO layer and 1000 $\text{\AA}$  thick silicon nitride layer are deposited (4a). The LTO thickness is equal to the thickness of the second level structure plus the air-gap spacing between the two tungsten levels. The basic process is repeated: RIE of LTO to form the second oxide trenches, silicon implantation, and removal of nitride mask (4b). The second level tungsten deposition and mechanical polishing is performed similarly as described in the previous section (4c). The gap-spacing between the two level of tungsten structures is determined by the thickness of the second LTO after RIE trench etch. The thickness of the oxide film is monitored by interferometry measurements. A third level, tungsten structure is made by again repeating the basic process again (4d). The three levels of tungsten are encapsulated in the LTO and the surface of each level is planar.

The next process sequence releases the structures and produces air gaps for the microactuators. The thick layer of sacrificial LTO is removed by a combination of dry and wet etching. First, a 0.3- $\mu\text{m}$  thick PECVD amorphous silicon carbide is deposited on the planar surface. PECVD silicon carbide has been chosen for its high selectivity to silicon dioxide in 6:1 buffered HF etchant. As the total oxide thickness for fabricating three-level tungsten



(a)



(b)

Fig. 3. SEM micrographs of tungsten wafer surface before and after the micropolish step. (a) A worst case example of surface roughness for 2.5  $\mu\text{m}$  thick tungsten deposition, and 1.5  $\mu\text{m}$  feature size; and (b) the planar wafer surface after mechanical micropolishing.

microstructures is typically greater than  $8.0\ \mu\text{m}$ , photoresist does not provide adequate masking to sustain a lengthy sacrificial oxide etch. A  $3\text{-}\mu\text{m}$  resist-mask is used to expose the tungsten contact pads and isolation released region. The steps to release the tungsten structures are performed with a combination of a dry RIE etch and a wet 6:1 BHF etch. An anisotropic etch in a  $\text{SF}_6$  plasma is used to remove the silicon carbide. This etch is followed by a  $\text{CHF}_3$  vertical RIE of LTO (4e). The photoresist is then stripped in a  $\text{O}_2$  plasma. The silicon carbide layer serves as the etch mask for the wet undercut etch-step, which removes the LTO between the tungsten structures (4f).

Figure 5 shows released, multilevel tungsten microstructures ( $1.5\ \mu\text{m}$  and  $2.5\ \mu\text{m}$  line widths) which have been fabricated using this technology. The SEM micrographs illustrate that our technology produces a variety of complex, multiple level geometric structures with minimal dimensional constraints. There are two aspects of the process that demand further attention. The time for the wet release must be properly selected. Since the dimension of the tungsten structural support is usually greater than the released part of the structure, the structure is undercut and released before significant etching of the oxide occurs under the support. The

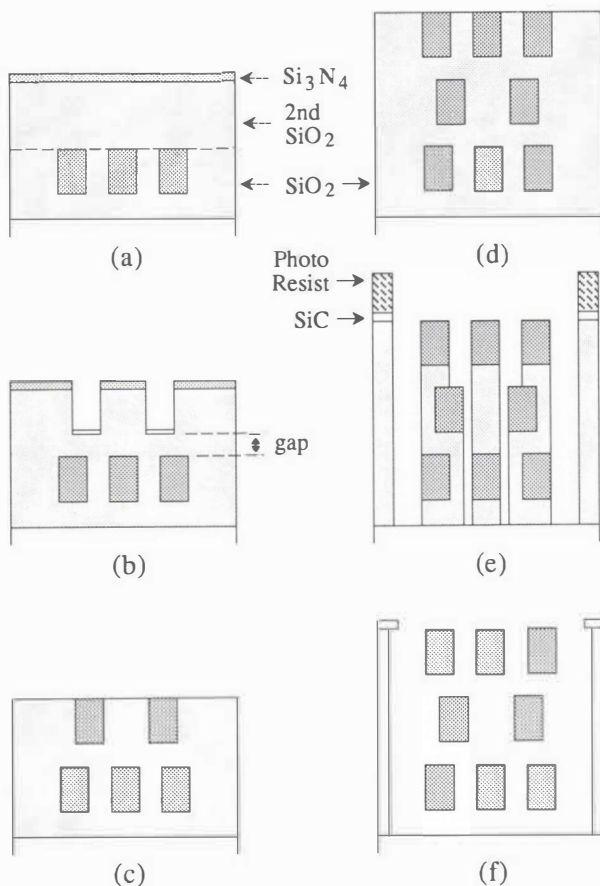


Fig. 4. Multiple level Selective CVD Tungsten process cross sections: (a) after CVD silicon dioxide and silicon nitride deposition on the first level, planar surface; (b) after composite layer trench etching and followed by silicon implantation; (c) after silicon nitride implantation mask removal and second level tungsten deposition; (d) after repeating the basic tungsten process for the third level; (e) after silicon carbide deposition and RIE dry etching of the released trench; and (f) after wet chemical etching to release the multiple-level structures.

second aspect is the projected etch-marks (middle tungsten layer) due to the RIE  $\text{CHF}_3$  etching, as shown in Fig. 5(a). Even though the etch rate is minimal, the etch chemistry of  $\text{CHF}_3$  on tungsten needs to be studied. These two problems can be simultaneously solved by using an etch-stop layer such as silicon carbide to prevent undercutting the support pads. The addition of the etch-stop layer allow longer wet chemical etching, and no RIE etch-steps would be necessary.

A three level comb-drive actuator [1, 13-15] has been fabricated as a test structure, as shown in Fig. 6. The suspended second level moving tungsten plate is placed between the first and the third level stationary electrode plates. Figure 7 shows a fabricated three level comb-drive, lateral microactuator with crab-leg flexures [15]. The multiple level structure is a large area, comb-drive ( $w = 6\ \mu\text{m}$ ) with a small gap ( $g = 1\ \mu\text{m}$ ). There are two advantages for using a multilevel electrode structures. The first advantage is a reduced driving voltage for electrostatic microactuators because of the smaller gap spacing between the electrodes, and an increased electrode surface area. By controlling the etch depth of the silicon dioxide trenches, we can obtain small gaps between the electrodes. It is not an easy process to achieve precise submicron gaps. The limitation here is not the lithography resolution but the control and monitoring of the remaining oxide thickness. The second advantage for

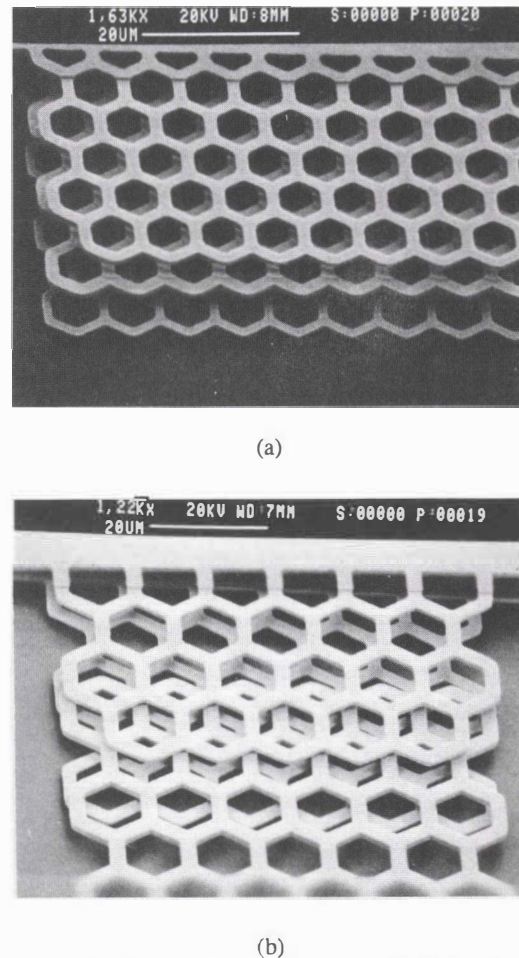


Fig. 5. SEM micrographs of released multiple-level tungsten microstructures. Three levels of tungsten with each level thicknesses  $1.5\ \mu\text{m}$ ,  $2.5\ \mu\text{m}$ , and  $2\ \mu\text{m}$ . The width of the structures are (a)  $1.5\ \mu\text{m}$ , and (b)  $2.5\ \mu\text{m}$ .

investigating multilevel electrodes is that a variety of different microactuators that require multiple level electrodes can be fabricated, such as a linear stepping motor [16].

## CONCLUSIONS

We have demonstrated the feasibility of fabricating multiple level microstructures using a low temperature, selective CVD tungsten technology. Micropolishing has been used to fully planarize the surface. The multiple level tungsten technology allows the fabrication of small-feature size, suspended beams and structures for all levels. Multiple level, comb-drive microactuators have been fabricated to demonstrate the applicability of this technique.

## ACKNOWLEDGMENTS

This work was supported by the National Science Foundation under Grant Nos. ECS-8805866 and ECS-8815775 and Advanced Research Projects Agency (ARPA). The structure fabrication was performed at the National Nanofabrication Facility (NNF) which is supported by the National Science Foundation, Cornell University, and Industrial Affiliates. The authors would like to thank Wolfgang Hofmann, Dr. Dan Haronian, Dr. Z. Lisa Zhang, and the staff of NNF for their technical assistance.

## REFERENCES

- [1] W.C. Tang, T.H. Nguyen and R.T. Howe, "Laterally Driven Polysilicon Resonant Microstructures," *Sensors and Actuators*, Vol. 20, 1989, pp. 25-32.
- [2] M. Mehregany and Y.C. Tai, "Surface micromachined mechanisms and micromotors," *J. Micromech. Microeng.* Vol. 1, 1991, pp. 73-85.
- [3] L.Y. Chen and N.C. MacDonald, "Multilevel Microdynamical Devices," presented at 36th Symposium of the American Vacuum Society, Boston, MA, Oct. 1989, pp. 109.
- [4] L. Ristic, R. Gutteridge, J. Kung, D. Koury, D. Dunn and H. Zunino, "A Capacitive Type Accelerometer With Self-Test Feature Based On A Double-Pinned Polysilicon Structure," *Dig. Tech. Papers, Transducers '93*, Yokohama, Japan, Jun. 1993, pp. 810-813.
- [5] Y. Gianchandani and K. Najafi, "Batch Fabrication and Assembly of Micromotor-Driven Mechanisms with Multilevel Linkages," *Proc. IEEE Micro Electro Mechanical Systems Workshop*, Travemünde, Germany, Feb. 1992, pp. 141-146.
- [6] C.H. Ahn and M.G. Allen, "A Fully Integrated Surface Micromachined Magnetic Microactuator with a Multilevel Meander Magnetic Core" *J-MEMS*, Vol. 2, Mar. 1993, pp. 15-22.
- [7] Y.W. Kim and M.G. Allen, "Single- and multi-layer surface-micromachined platforms using electroplated sacrificial layers," *Sensors and Actuators A*, Vol. 35, 1992, p61-68.
- [8] T. Bonifield and R. Blumenthal, "Triplelevel Metallization Using CVD Tungsten Interconnects," *Tungsten and Other Advanced Metals for VLSI/ULSI Applications*, Vol. V, pp. 145-156.
- [9] H. Itoh, T. Moriya, and M. Kashiwagi, "Tungsten CVD: Application to Submicron VLSICs," *Solid State Technology*, Nov. 1987, pp. 83-87.
- [10] L.Y. Chen, Z.L. Zhang, J.J. Yao, D.C. Thomas, and N.C. MacDonald, "Selective Chemical Vapor Deposition of Tungsten for Microdynamic Structures," *Proc. IEEE Micro*

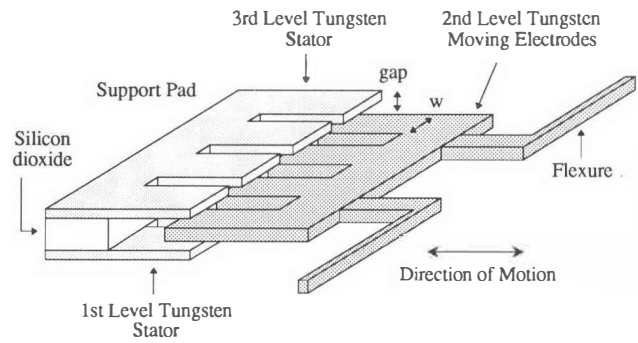


Fig. 6. Schematic view of the comb-drive with multiple-level electrodes

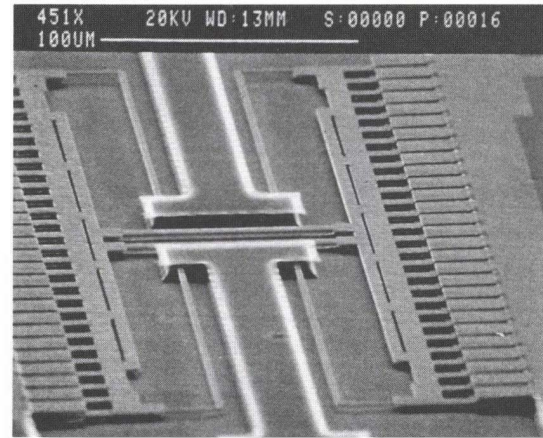


Fig. 7. SEM micrograph of released three level comb-drive microactuator with three level-thickness of 1.5  $\mu\text{m}$ , 2.5  $\mu\text{m}$ , and 2  $\mu\text{m}$ . The gap between each levels is 1  $\mu\text{m}$ .

- [11] D.C. Thomas and S.S. Wong, "A Planar Multilevel Tungsten Interconnect Technology," *IEDM. Tech. Digest*, 1986, pp. 811.
- [12] Y. Hayashi, K. Kikuta and T. Kikkawa, "A New Abrasive-Free, Chemical-Mechanical-Polishing Technique for Aluminum Metallization of ULSI Devices," *IEDM. Tech. Digest*, 1992, pp. 976-978.
- [13] T. Hirano, T. Furuhashi, K.J. Gabriel, and H. Fujita, "Design, Fabrication, and Operation of Submicron Gap Comb-Drive Microactuators," *J-MEMS*, Vol. 1, Mar. 1992, pp. 52-59.
- [14] M.W. Judy and R.T. Howe, "Highly Compliant Lateral Suspensions Using Sidewall Beams," *Dig. Tech. Papers, Transducers '93*, Yokohama, Japan, Jun. 1993, pp. 54-55.
- [15] A.P. Pisano and Y.-H. Cho, "Mechanical Design Issues in Lateral-driven Microstructures," *Sensors and Actuators*, Vol. 21, 1990, pp. 1060-1064.
- [16] T. Matsubara, M. Yamaguchi, and M. Esashi, "Stepping Electrostatic Microactuator," *Dig. Tech. Papers, Transducers '93*, Yokohama, Japan, Jun. 1993, pp. 50-53.

# Studies on the Sealing of Surface Micromachined Cavities Using Chemical Vapor Deposition Materials

Chang Liu and Yu-Chong Tai  
Electrical Engineering 116-81, Caltech, Pasadena, CA 91125

## I. INTRODUCTION

Sealing of micromachined cavities [1-12] is an important technique that has been used by many researchers to reduce air damping for electromechanical resonators [1], to establish pressure measurement references [2,3], and to make vacuum electronics [8, 11]. As a whole, many different techniques have been applied in order to seal the cavity with a predetermined pressure, including Chemical Vapor Deposition (CVD) [1-6], thermal oxidation[4], E-beam evaporation[7,8], sputtering[9], wafer anodic bonding [10,11,12], and solder glass fritting [13]. Although these many sealing procedures have been demonstrated, there is little systematic study just on the sealing methods. Here, we report our study on sealing of surface-micromachined cavities. In this work, the main focus is to find out the required thickness to seal cavities with various geometries using different CVD materials, including LPCVD silicon nitride, LPCVD polysilicon, LPCVD Phosphosilicate Glass (PSG), and PECVD silicon nitride.

## II. DESIGN AND FABRICATION

Shown in Fig. 1 are four types of test structures which are designed around a square diaphragm with different features added to it. The diaphragms are square in shape with 200  $\mu\text{m}$  by the side. Type-1 structures have different numbers (4-6) of etching channels with varying channel widths (2 to 16  $\mu\text{m}$ ) and lengths (8 to 38  $\mu\text{m}$ ). The feature of type-1 structures is that these channels may have little effect on the mechanical integrity of the diaphragms. Type 2 and 3 structures have center [6] and corner etching holes on the diaphragm, respectively. Such etching hole structures do not occupy extra space in addition to the diaphragm. A range of hole sizes (2-16  $\mu\text{m}$ ) and numbers (1,2,6) have been included in our design. Type-4 structures have one to four side openings, 120 or 180  $\mu\text{m}$  long; they are studied here because the side opening can facilitate chemicals (or gas products) to go in and come out of the cavity during sacrificial layer or silicon etching. Since our current study is based on statistical data, a large number of samples is desirable. In our design, each die ( $1 \times 1 \text{ cm}^2$ ) has 126 different cavities (72, 36, 3, 15 for type 1, 2, 3, 4 respectively). A 4" wafer has 48 dies and therefore each individual cavity has a sample space of 48.

All the test structures are fabricated in one process which is shown in Fig. 2. Starting with 4" wafers, we deposit 600 nm low-stress LPCVD silicon nitride as the insulation layer. This nitride is patterned and plasma-etched (600 nm into the silicon for the subsequent fully-recessed LOCOS process) to define the cavity wells ( $200 \times 200 \mu\text{m}^2$ ). Thermal oxide of 1.3  $\mu\text{m}$  then is grown in the wells up to silicon nitride level to maintain wafer surface flatness. PSG is deposited and patterned as the sacrificial layer; most of the wafers have a PSG of 220 nm thick but we have included other thicknesses of 280, 480, and 720 nm for studies of gap-height effects on sealing. The wafers are then deposited with 800 nm low-stress silicon nitride as the diaphragm material, which is then patterned to have etching holes ( $10 \times 10 \mu\text{m}^2$ ) for PSG etch. Using concentrated HF (49%), we etch away the PSG and thermal oxide (located only underneath the diaphragm, not the channels) in 20 minutes. Since HF etches silicon nitride inside the etching channel, the gap height is the PSG thickness plus 200

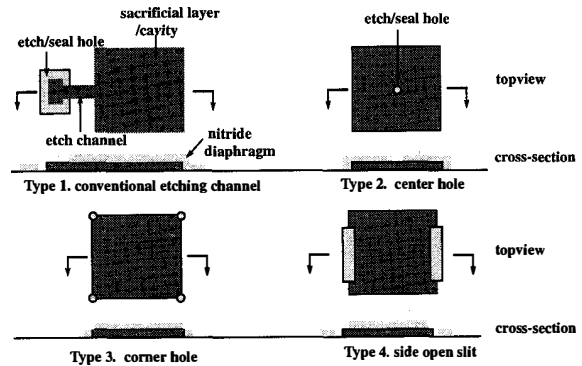


Fig.1 Schematic configurations for four different types of test structures.

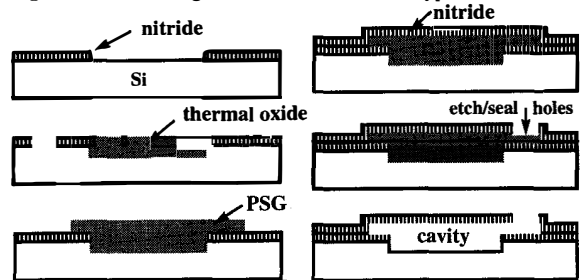


Fig.2 Major fabrication steps for micro-cavity structures.

nm (a measured value) by the end of this HF etching. Wafers are thoroughly rinsed in DI water for 20 minutes and then dried in a spin-dryer. Alley *et. al.* [14] reported a stiction problem using spin dry for their suspended polysilicon beams; however, in our case, the spin dry does not cause serious sticking problem between the diaphragm and cavity bottom (the yield is more than 95 % for all structures). Finally, wafers are baked at 400  $^{\circ}\text{C}$  in nitrogen for 10 minutes to drive out moisture in the cavities and ready for sealing experiments.

## III. EXPERIMENTS AND RESULTS

Many sequential depositions with an incremental thickness (30-60 nm) of CVD materials, including LPCVD silicon nitride, LPCVD polysilicon, LPCVD PSG, and PECVD silicon nitride, are performed to seal the cavities (deposition parameters listed in Table 1). Since the diaphragm over a sealed cavity will be deformed by the differential pressure between the atmosphere and the cavity interior, interference patterns (Newton ring) can be observed on the diaphragm. The presence of Newton Ring is thus used as an indication of complete sealing. Optical microscope pictures of sealed and unsealed structures are shown in Fig. 3. After each sealing deposition, we count the quantities of successfully sealed cavities and statistically evaluate the degree

Material	flow ratio	pressure(mTorr)	temp.( $^{\circ}\text{C}$ )/power(W)
LPCVD nitride	$\text{NH}_3/\text{DCS}-3/1$	330	820/N.A.
LPCVD Polysilicon	Silane( $\text{SiH}_4$ )	220	620/N.A.
LPCVD PSG	$\text{O}_2/\text{SiH}_4/\text{PH}_3-6:1:2$	150	450/N.A.
PECVD nitride	$\text{NH}_3/\text{SiH}_4-7:3$	400	300/50

Table1 CVD processing parameters for various sealing materials.

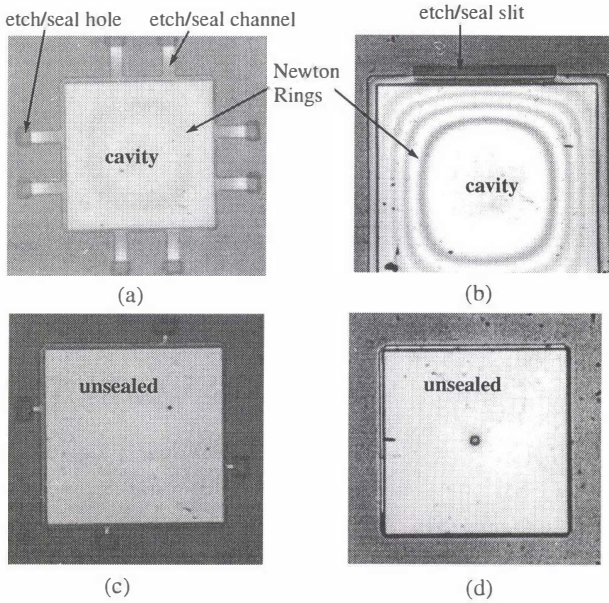


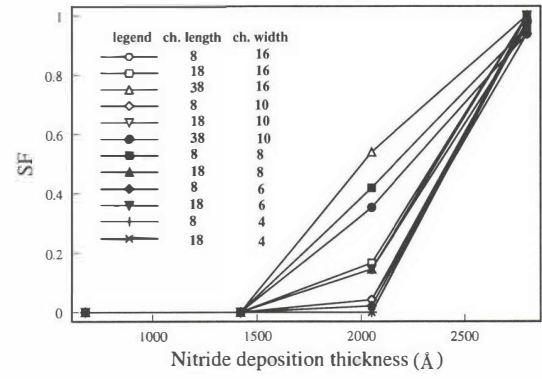
Fig. 3 Optical photographs of some test structures: (a) sealed type-1 structure, (b) sealed type-4 structure, (c) un-sealed type-1 structure, (d) un-sealed type-2 structure. Newton rings are clearly seen on sealed structures in (a) and (b), but not in (c) and (d) which not sealed.

of sealing completeness. These data points are then compared between sealing materials, deposition thickness, cavity geometry and channel heights. To quantify the sealing results of a specific structure at a cumulative deposition thickness, we define the scaling factor, SF, as the ratio between the number of sealed cavities and the total number of the cavities of its kind (48, in our case); an SF of 1 means that all 48 cavities are sealed. We also define an unitless thickness  $t_n$  as the cumulative deposition thickness normalized by the gap height. The  $t_{n,min}$  then is the minimum  $t_n$  that is required to seal a cavity with SF larger than 0.95. Because we can only deposit sealing materials with a finite thickness increment (30 60 nm), there is an inherent error associated with  $t_{n,min}$ .

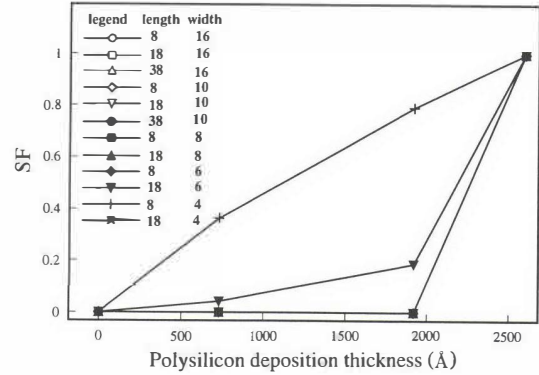
Our experiment results show that type 1 structures have been successfully sealed by all the deposition materials at certain  $t_n$ 's, whereas some structures of types 2, 3 and 4 can not be sealed by certain materials within reasonable deposition thickness range. As type-1 structures provide a larger and more complete data base compared with other types they are thus the emphasis of our sealing data analysis.

**Material Effects** — Deposited materials greatly influence the sealing results. The material effects are studied by concentrating on data analysis of type-1 structures. For example, Fig. 4abc show the SF vs. deposition thickness for three different LPCVD materials. Each figure provides information for 12 type-1 cavities, all having 8 channels with the same 420 nm gap height but different lengths and widths. One can clearly see that for each LPCVD material, there is a  $t_n$  value (0.338 for nitride, 0.173 for polysilicon, and 1.86 for PSG) that any smaller  $t_n$  will not seal the structures at all. On the other hand, there is another value (0.67 for nitride, 0.62 for polysilicon, and 4.52 for PSG) that any larger  $t_n$  will seal the structures completely. Any  $t_n$  between these two values will have partial seal of the structures.

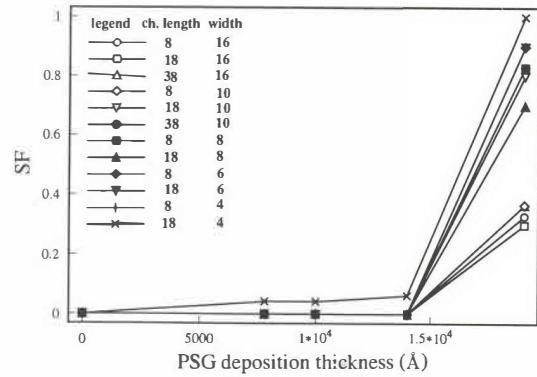
Due to size variations, SF data points scatter; therefore we compare sealing data obtained from a fixed structure to study material effects. In our case, all data points are obtained for a



(a)



(b)



(c)

Fig. 4 SF as a function of deposition thickness of three LPCVD materials for twelve type-1 structures. The channel height for the samples are all 420 nm. The lengths are 8, 18 and 38  $\mu\text{m}$  and the widths are 16, 10, 8, 6 and 4  $\mu\text{m}$ .

structure with 8 channels, each 18  $\mu\text{m}$  long and 4  $\mu\text{m}$  wide. Fig. 5 is partly extracted from Fig. 4 and, with the addition of PECVD sealing data points, shows comparison of sealing results using four different CVD materials. It is found that  $t_{n,min}$  is about 5.2 for PECVD nitride, 4.5 for LPCVD PSG, 0.67 for LPCVD nitride and 0.62 for LPCVD polysilicon. Clearly, LPCVD polysilicon and nitride require the thinnest deposition to seal the structure, thus are the most effective materials. On the other hand, although thicker deposition is required, PECVD methods have the advantage of sealing at a much lower temperature about 300  $^{\circ}\text{C}$ .

**Gap Height Effects** — For each sealing material, it is important to find out whether  $t_{n,min}$  obtained at one gap height can be applied to various other heights. Extra wafers with different gap heights (520 nm, 743 nm, and 1.01  $\mu\text{m}$ ) are prepared, and sealing tests are performed on those wafers by incremental LPCVD

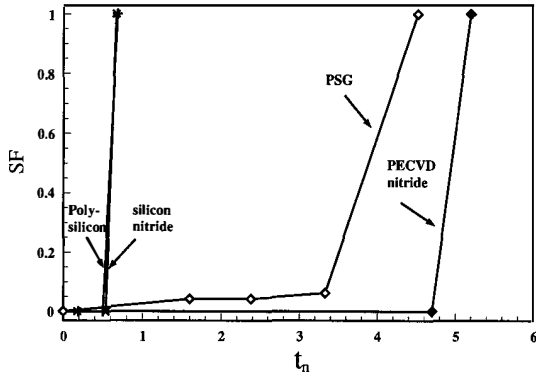


Fig.5 SF vs.  $t_n$  plots for different materials, including LPCVD nitride, LPCVD polysilicon, LPCVD PSG, and PECVD nitride. Structures under study are type-1 with eight etching channels, each  $18 \mu\text{m}$  long and  $4 \mu\text{m}$  wide. Etching channel height is  $420 \text{ nm}$ . Clearly,  $t_{n,min}$  required for successful sealing depends on the sealing materials,  $0.67$  for LPCVD nitride,  $0.62$  for LPCVD polysilicon,  $4.5$  for LPCVD PSG and  $5.2$  for PECVD nitride.

silicon-nitride deposition. Fig. 6 shows the results of  $t_{n,min}$  vs. gap heights;  $t_{n,min}$ 's are  $0.57 \pm 0.08$ ,  $0.347 \pm 0.03$ ,  $0.449 \pm 0.04$  and  $0.44 \pm 0.03$  for the four gap heights studied. Taken into account of experimental errors, the trend shows that  $t_{n,min}$  converges to a constant value of approximately  $0.44$  for larger gap. Since the incremental deposition thickness is finite, the error in  $t_{n,min}$  is thus large for small gap height and small for large gap heights.

Currently, gap height effects for other materials are not available for various reasons. For example, in the case of LPCVD PSG, thick PSG tends to fracture when the film is over  $4 \mu\text{m}$

In another case, LPCVD polysilicon becomes opaque when its thickness exceeds  $300 \text{ nm}$  and making identification of sealed structures by Newton rings impossible.

*Geometric Effects* — For type-1 structures, it is also found through our experiments that geometry could affect the sealing significantly. In fact, different materials have totally different effects. To study geometric effects, we compared sealing data of various sized type-1 structures at a fixed material deposition thickness. Fig. 7abc plots SF vs. channel length with widths ranging from  $4$ – $16 \mu\text{m}$  using three LPCVD material thicknesses. For LPCVD silicon nitride ( $t_n = 0.49$ ), Fig. 7a shows the trend that longer and wider channels can be sealed with higher seal-

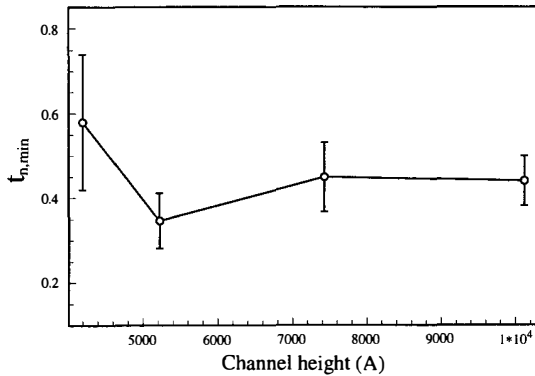
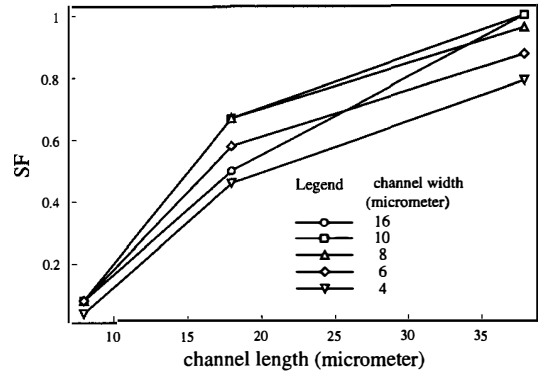
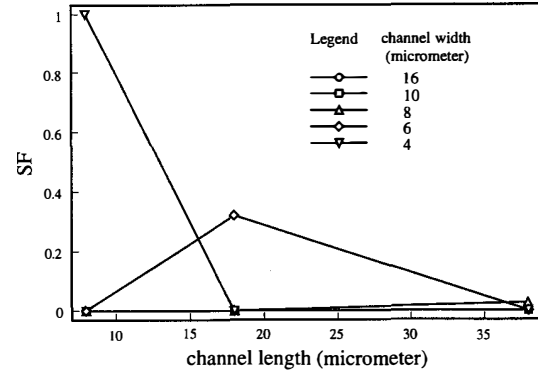


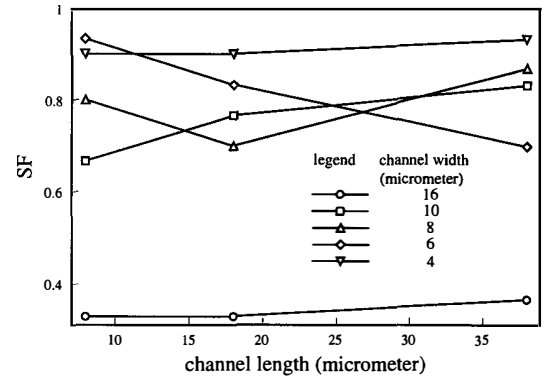
Fig. 6 Values of  $t_{n,min}$  at various channel heights ( $420 \text{ nm}$ ,  $520 \text{ nm}$ ,  $743 \text{ nm}$ , and  $1.01 \mu\text{m}$ ) using LPCVD nitride sealing. The test structure is the same one that is used in Fig. 5: a type-1 cavity with eight channels, each  $18 \mu\text{m}$  long and  $4 \mu\text{m}$  wide.



(a)



(b)



(c)

Fig. 7 SF as functions of channel lengths and widths for LPCVD silicon nitride, polysilicon and PSG sealing.

material	length	width	SF
LPCVD Nitride	↑	↑	↑
LPCVD Polysilicon	↓	↓	↑
LPCVD PSG	—	↓	↑

Table 2 For type-1 structures, trends of geometric effects on SF within the range of our current design.

ing percentage. For LPCVD polysilicon ( $t_n = 0.45$ ), however, it seems that (as shown in Fig. 7b) shorter and narrower channels have a higher SF although this trend is not as conclusive as in the silicon nitride case because of limited data points. As for LPCVD PSG ( $t_n = 4.5$ ), the narrower the channels, the better SF. Channel length has little effect. As a whole, the trends of the geometric effects of sealing type-1 structures are summarized in Table 2.

*Sealing of Types 2,3 and 4 Structures* In our work, geometric effects on sealing types 2,3 and 4 structures were also using

samples of a fixed height. Conceptually, type-2 cavities require much thicker deposition to seal than structures of other types because of the large gap height, which is 1.3  $\mu\text{m}$  thick thermal oxide plus PSG thickness. This has been confirmed using nitride and polysilicon. Type-3 structures show excellent sealing quality using all three LPCVD sealing materials. Compared with type-1 structures, type-3 structures have identical gap heights and thus comparable sealing performance; SF's for all type-3 structures exceed 0.95 at  $t_n$ 's of 0.67 (for silicon nitride), 0.62 (for polysilicon) and 4.5 (for PSG). As for type-4 structures, only cavities with one side opened survive the fabrication process for sealing analysis; cavities with more side openings tend to stick to the bottom. For a type-4 structure with one side opening 120  $\mu\text{m}$  long (60 % of the cavity side length), SF's of greater than 0.95 are achieved at a  $t_n$  of 0.67 for nitride and a  $t_n$  of 0.62 for polysilicon deposition. The general trends of sealing types 2,3 and 4 structures are summarized in Table 3.

	TYPE 2	TYPE 3	TYPE 4
LPCVD nitride	poor	good	good
LPCVD polysilicon	poor	good	good
LPCVD PSG	na	good	na

Table 3 For type 2, 3 and 4 structures, general sealing performance by the three LPCVD materials. *na* indicates that conclusive experimental results are not available.

**Sealing Profile** — Sealing qualities of cavities should be related to the step coverage of the CVD materials. Various studies on step coverage, both experimentally [16,17] and theoretically [18], have been done in the past. It has been concluded that step coverage depends on three major mechanisms: direct transport, re-emission, and surface diffusion [17].

Conceptually, knowledge on the step coverage of various materials in a etching hole or etching channel [16–18] should help to understand the material and geometric effects of sealing. In order to study the sealing mechanisms, a scanning electron microscope is used to view the cross-section at cleaved sealing holes. Initial results, for example the coverage profiles of a PSG-sealed type-1 structure at a test structure and a etching hole, is shown in Fig. 8. Cavities are sealed by PSG when the two deposition fronts meet at the entrance of the etching channel. Pictures confirm that deposition inside the cavity is very little compared with the deposition on the front of the wafer; it agrees with the conclusion of Cheng *et. al.* [17] that surface diffusion is not a strong factor in LPCVD PSG step coverage. Currently, study on sealing profiles of nitride-sealed and polysilicon-sealed samples is underway.

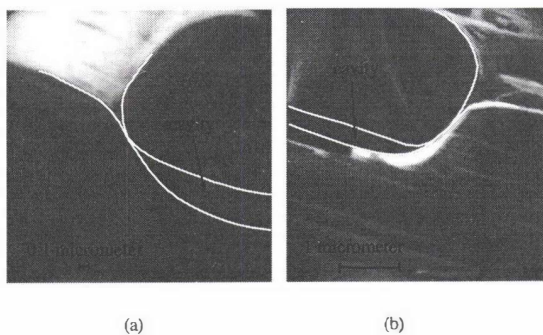


Fig. 8 SEM photographs of the sealing profile after approximately 1.9  $\mu\text{m}$  of PSG deposition. (a) A specially designed overhanging test structure; (b) a etch/seal hole of a type 1 structure. The gap height is 4200  $\text{\AA}$ . White lines indicate the contour of deposited PSG.

## IV. CONCLUSIONS

We have fabricated test structures and studied the sealing of four types of surface-micromachined cavities using LPCVD nitride, polysilicon, PSG, and PECVD nitride. Among all tested materials, LPCVD nitride and polysilicon provide the most effective sealing. LPCVD PSG and PECVD nitride requires higher  $t_{n,min}$  to seal but offers the advantage of low temperature processing. Using LPCVD nitride as the sealing material,  $t_{n,min}$  almost remains constant (0.44) for different gap heights. Qualitative geometric effects have also been studied for type-1 structures; the results point out geometric trends for designing cavity structures that are easy to seal. Sealing results for types 2,3 and 4 structures are briefly discussed; cavity structures and materials that could produce good sealing results are identified.

## V. REFERENCES

1. L. Lin, K.M. McNair, R.T. Howe, A.P. Pisano, "Vacuum Encapsulated Lateral Micro-resonators", *Digest of Tech. Papers, 7th Int. Conf. on Solid State Sensors and Actuators, Transducer '93*, p. 270, 1993.
2. J. Liu, Y.C. Tai, K.C. Pong, Y. Zohar, C.M. Ho, "Micromachined Channel/Pressure Sensor Systems for Micro Flow Studies", *Digest of Tech. Papers, 7th Int. Conf. on Solid State Sensors and Actuators, Transducer '93*, Japan, p. 995, 1993.
3. H. Guckel, "Surface Micromachined Pressure Transducers", *Sensors and Actuators*, A(28), pp. 133-146, 1991.
4. H. Guckel, C. Rypstat, M. Nesnidal, J.D. Zook, D.W Burns, D.K. Arch, "Polysilicon Resonant Microbeam Technology for High Performance Sensor Applications", *Tech. Digest., Solid-State Sensor and Actuator Workshop*, Hilton Head, SC, p. 153, 1992.
5. K.H.-L. Chau, C.D. Fung, P.R. Harris, J.G. Panagou, "High-Stress and Overrange Behavior of Sealed-Cavity Polysilicon Pressure Sensors", *Tech. Digest., Solid-State Sensor and Actuator Workshop*, Hilton Head, SC, p. 181, 1990.
6. K. Shimaoka, "Micro Pressure Sensor", *Tech. Digest of 9th Sensor Symposium*, pp. 47-50, 1990.
7. Q. Mei, T. Tamagawa, C. Ye, Y. Lin, S. Zurn, D.L. Polla, "Planar-processed Tungsten and Polysilicon Vacuum Microelectronic Devices with Integral Cavity Sealing", *J. Vac. Sci. Tec.*, B11(2), p. 493, 1993.
8. H. Busta, "Review-Vacuum Electronics -1992", *J. Micromech. Microeng.*, Vol. 2, pp. 43-74, 1992.
9. S. Zurn, Q. Mei, C. Ye, T. Tamagawa, D.L. Polla, *1991 Sealed Vacuum Electronic Devices by Surface Micromachining, Proc. IEDM 91*, pp. 205-208, Washington D.C., 1991.
10. M. Esashi, N. Ura, Y. Matsumoto, "Anodic Bonding for Integrated Capacitive Sensors", *Proc. IEEE Workshop on Micro Electro-Mechanical Systems, MEMS'92*, Travemunde, Germany, February, 1992, pp. 43-48.
11. H. Henmi, S. Shoji, Y. Shoji, K. Yosimi, M. Esashi, "Vacuum Packaging for Microsensors by Glass-Silicon Anodic Bonding", *Digest of Tech. Papers, 7th Int. Conf. on Solid State Sensors and Actuators, Transducer '93*, p. 584, Japan.
12. L. Parameswaran, V. M. McNeil, M. A. Huff, M.A. Schmidt, "Sealed-Cavity Microstructure using Wafer Bonding Technology", *Digest of Tech. Papers, 7th Int. Conf. on Solid State Sensors and Actuators, Transducer '93*, p. 274, Japan.
13. W. Ko, Q. Wang, Q.H. Wu, "Long Term Stable Capacitive Pressure Sensor for Medical Implant", *Digest of Tech. Papers, 7th Int. Conf. on Solid State Sensors and Actuators, Transducer '93*, p. 592, Japan.
14. R.L. Alley, G.J. Cuan, R.T. Howe, K.Komvopoulos, "The Effect of Release-Etch Processing on Surface Microstructure Stiction", *Tech. Digest., Solid-State Sensor and Actuator Workshop*, Hilton Head, SC, p. 202, 1992.
15. J. Liu and Y.C. Tai, J. Lee, K.C. Pong, Y. Zohar, C.M. Ho, "In Situ Monitoring and Universal Modelling of Sacrificial PSG Etching Using Hydrofluoric Acid", *Proc. IEEE Workshop on Micro Electro Mechanical Systems, MEMS'93*, Fort Lauderdale, FL, 1993, p. 71.
16. K. Watanabe and H. Komiyama, "Micro/Marcocavity Method Applied to the Study of the Step Coverage Formation Mechanism of SiO<sub>2</sub> Films by LPCVD", *J. Electrochem. Soc.*, Vol. 137, No. 4, p. 1222, 1990.
17. L.Y. Cheng, J.P. McVittie, K.C. Saraswat, "New Test Structure to Identify Step Coverage Mechanisms in Chemical Vapor Deposition of Silicon Dioxide", *Appl. Phys. Lett.*, 58(19), 1991.
18. J.J. Hsieh, "Influence of Surface-activated Reaction Kinetics on Low Pressure Chemical Vapor Deposition Conformality Over Micro Features", *J. Vac. Sci. Tech.*, A11(1), p. 78, 1993.

# Microfabricated Tweezers with a Large Gripping Force and a Large Range of Motion

Wen-Hwa Chu and Mehran Mehregany

*Electronics Design Center  
Department of Electrical Engineering and Applied Physics  
Case Western Reserve University  
Cleveland, OH 44106*

## Abstract

A new microtweezers design is presented based on bimetallic actuation and silicon bulk micromachining. The two arms of the tweezers are  $2000\mu\text{m}$  long and  $100\mu\text{m}$  wide  $p^+$  silicon cantilevers, each several microns thick. Bimetallic actuation using gold is integrated on one arm while the other arm is passive. The metal/ $p^+$  silicon thicknesses of the actuation arm are  $7800\text{\AA}/5\mu\text{m}$ . A  $30\text{mW}$  input power deflects the actuation arm by  $200\mu\text{m}$  at the tip, fully closing the tweezers. At  $30\text{mW}$  input power, the gripping force of the actuation arm is estimated near  $11\mu\text{N}$  for a  $200\mu\text{m}$ -sized object.

## 1 Introduction

Of the different thermal microactuation techniques reported, including bimetallic, thermopneumatic, and shape memory alloy, the bimetallic effect is well suited for microfabrication. Although several papers have been published on bimetallic actuation [1]–[3], basic information on the thermo-mechanical characteristics of bimetallic actuators is sparse. The primary objective of this paper is to further investigate bimetallic microactuation through a study of microfabricated bimetallic cantilever microactuators. As a vehicle for the basic studies here, we have developed and used a device (i.e., microtweezers) that utilizes bimetallic cantilever microactuators to address micromanipulation needs.

## 2 Microtweezers Design and Fabrication

A new design for microtweezers is presented in this paper and is shown schematically in Fig. 1. A brief discussion of the microtweezers design and fabrication is provided here. For details, the reader is referred to [4]. The microtweezers design utilizes two cantilevered gripping arms each  $2000\mu\text{m}$  long and  $100\mu\text{m}$  wide connected to a silicon support piece as shown in Fig. 1. The two cantilevers function as the two arms of the tweezers to clamp and release the object to be manipulated.

Heavily-boron-doped ( $p^+$ ) silicon is used as the primary structural material for the two cantilevers. The silicon support, which has a  $3\times 3\text{mm}^2$  area and is  $275\mu\text{m}$  thick, serves as the mechanical support handle of the microtweezers (Fig. 1). The two cantilevers are aligned along the  $\langle 100 \rangle$  direction, and the edges of the square silicon support are aligned along the  $\langle 110 \rangle$  direction. A  $0.45\mu\text{m}$  silicon dioxide layer is thermally grown on the top surface of the top  $p^+$  silicon cantilever arm for electrical isolation. A  $7600\text{\AA}/200\text{\AA}$  gold/chromium film is sputtered and patterned on top of the upper arm in order to provide for bimetallic actuation of that arm. The wafer is annealed in  $\text{N}_2$  at  $450^\circ\text{C}$  for 20 minutes to obtain good adhesion between the gold/chromium film and silicon dioxide, as well as to stabilize the mechanical and electrical properties of the gold [4]. The total width of the

patterned gold film is  $55\mu\text{m}$ , covering about half of the surface of the top cantilever. This sputtered gold film is also used to provide the heating resistor (Fig. 1). The tweezers structure is etched in EDP as a final step to remove the silicon between the two arms and complete the device fabrication.

The top arm of the microtweezers incorporating the bimetallic actuation is hereafter referred as the 'actuation arm'. Electric power input into the metallic strip by resistive heating will raise the temperature of the gold/ $p^+$  silicon bimetallic actuation arm. Because of the thermal expansion coefficient difference between  $p^+$  silicon and gold, the actuation arm will deform toward the lower  $p^+$  silicon cantilever. This accomplishes the gripping function of the microtweezers. When electric power is removed, the temperature of the actuation arm decreases back to room temperature and the microtweezers open.

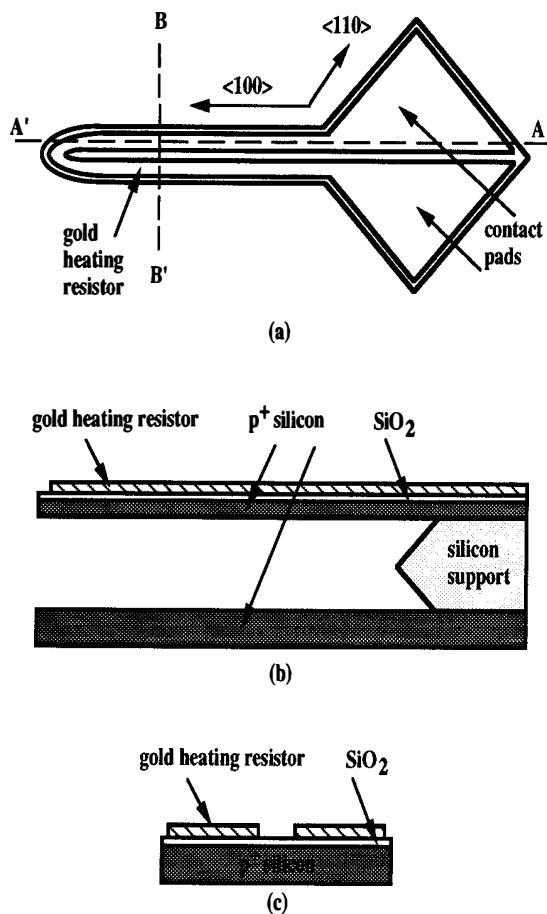


Figure 1: Schematic diagrams showing the new microtweezers design (not to scale): (a) top view; (b) cross-sectional view along line A-A'; (c) cross-sectional view along line B-B'.

In order to simplify the fabrication, only the top cantilever of the microtweezers has the metallic heating element on it. The bottom cantilever (hereafter referred to as the passive arm) is made thicker to stiffen that arm against bending during the gripping action. However, the actuation mechanism can also be applied to the bottom cantilever, in which case both arms would be actuated for the gripping action. With both arms active, a smaller temperature increase would be required to close the tweezers since each arm would only have to bend half of the initial separation distance at the tip.

The proposed microtweezers design has some advantages over previous designs [5, 6]. Bimetallic microactuation provides significantly larger gripping forces than electrostatic microactuation. The bimetallic design has a wide gripping range (e.g., over two hundred micrometers). Finally, the design presented can be integrated with strain sensors to provide direct force feedback. One major drawback of the bimetallic microtweezers is that the temperature of the microtweezers may be much higher than room temperature when gripping objects. Based on our current design, the temperature may be as high as 170°C at tweezers tip for complete closure. However, it is possible to redesign the device such that the heating resistor is well away from the grasping region.

The actuation arm of the microtweezers is made of p<sup>+</sup> silicon, silicon dioxide, and gold. Therefore, the shape (or curvature) of the actuation arm upon fabrication depends not only on the internal residual stress distribution in p<sup>+</sup> silicon but also on the stresses inside the gold film and the silicon dioxide layer. The overall bending moment generated by p<sup>+</sup> silicon, silicon dioxide, and gold determines the final shape of the actuation arm of the microtweezers. Our goal has been to develop a fabrication process to produce bimetallic microtweezers with a desired actuation arm curvature. The tweezers initial (i.e., power off) opening is determined by the actuation arm curvature and the wafer thickness (i.e., 275μm for our wafers), assuming the passive arm to be flat.

Figure 2 shows a scanning electron microscope photo of two fabricated microtweezers. The picture has been taken with the actuation arms of the two microtweezers in the lower position with respect to the passive arms. The thick (i.e., 13.5μm) p<sup>+</sup> passive arms are flat as can be seen in the figure. The bending moment generated as a result of residual stresses inside the actuation arm constituent films causes an initial curvature of this arm. The actuation arm is made thin (i.e., near 5μm thick for the p<sup>+</sup> portion) and therefore compliant to enhance its actuated motion. As a result, its curvature is sensitive to the residual stress induced bending moments.

The upper tweezers in Fig. 2 is typical of the actuation arm curvature and tweezers initial opening (which is near 200μm) which result from the baseline fabrication process. As will be seen later, tweezers with 200μm openings can be closed fully with an input power of about 30mW and display a linear opening/input power behavior. The variation in the tweezers' openings as a result of process variation on a wafer or from wafer to wafer are discussed in [4].

It is possible to vary the tweezers initial opening over a wide range by manipulating the p<sup>+</sup> diffusion and the subsequent thermal oxidation process steps. The lower tweezers in Fig. 2 demonstrates this capability. Note that the required input power, as well as the maximum temperature of the tweezers actuation arm, for closing the tweezers on an object is affected by the initial opening size of the tweezers. Correspondingly, for small objects, a small initial opening may be more desirable.

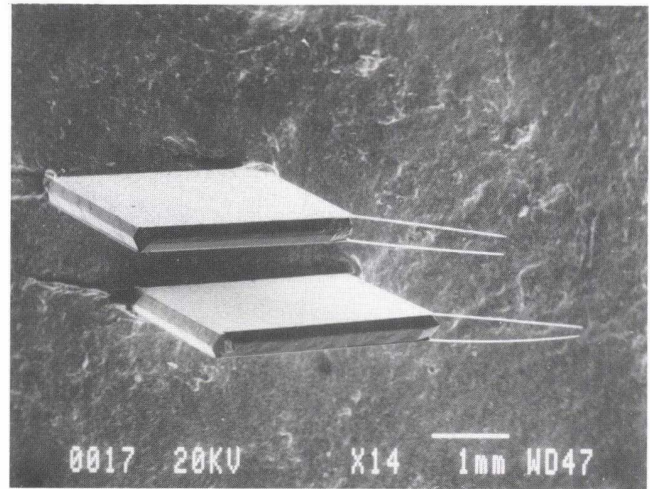


Figure 2: A SEM photo showing two microfabricated tweezers. The upper tweezers is from a typical wafer resulting from our baseline process. The lower tweezers demonstrate the capability of adjusting the microtweezers initial opening.

### 3 Thermal Characterization

The temperature profile of the actuation arm of the microtweezers is measured using a thermocouple direct contact and an infrared scanning microscope method. The data is then compared with finite element thermal analysis results from [4]. For the direct thermocouple contact method, a tiny E-type (Chromel-Constantan) thermocouple [7] with a 10μm wire diameter and a 25μm radius tip mounted on a three-axis micropositioner has been used. The micropositioner has an accuracy of 1μm about each of the three axes. The thermocouple thus can be positioned to measure the surface temperature along any axis by direct contact with the surface of device. 'TC Method' is used hereafter to indicate temperature measurements using a thermocouple.

Due to the small dimensions of the microtweezers, ordinary precision infrared pyrometers cannot be used to measure the surface temperature of the microtweezers because of the relatively large spot size (or measuring area of ordinary pyrometers). Considering the microtweezers small dimensions, CompuTherm III [8] is capable of measuring the surface temperature of the microtweezers with sufficient spatial resolution (i.e., 15μm). This instrument is an infrared scanning microscope. It uses an indium antimonide (liquid N<sub>2</sub> cooled) infrared detector to detect the emitted IR energy in the 3 to 5μm spectral range. 'IR method' is used hereafter to indicate the temperature measurements using the CompuTherm III system.

The surface temperature along the length (e.g., X-axis) of the actuation arm was measured using both TC and IR methods at different input power levels. In all temperature measurement experiments, a constant voltage source was used to supply power to the actuation arm and the current was monitored by an ammeter. The applied voltage was adjusted to obtain a desired input power with an accuracy of ±0.5 mW.

Figure 3 shows the measured temperature profiles for the bimetallic actuation arm using TC and IR methods at input powers of 18 and 20mW, respectively. Reliable data from the infrared scanning microscope measurement ends at around X=1000μm for reasons described in [4]. As can be seen from Fig. 3, both experimental methods indicate the same temperature decrease toward the mechanical support. The difference between these two

measurements for the maximum temperature is less than 10%, which is within the input power difference for the two measurements. Clearly, the silicon support acts as a heat sink, reducing the temperature toward the support end. Therefore, a constant temperature profile along the length for a bimetallic cantilever as has been assumed in previous work [1]–[3] is not accurate.

The fit to the temperature data using finite element analysis described in [4] is also shown in Fig. 3 for a 20mW input power. This temperature distribution is in good agreement with the experimental results, assuming a heat transfer coefficient ( $h_{tc}$ ) of  $480\text{W}/\text{m}^2\text{K}$ .

A point of concern in our temperature measurements using the TC method is the extent to which the thermocouple modifies the temperature distribution around the cantilever, in particular in the tip region. We have noted that the temperature data from the TC method consistently show a drop near the tip region (see Fig. 3) which is not predicted by the finite element model when a good fit is obtained toward the support end (see Fig. 3). The heat loss due to conduction through the thermocouple is thought to be responsible for this effect. A model was constructed to study (using finite element thermal analysis) the temperature change in the actuation arm due to the introduction of the thermocouple. Preliminary results from the model confirm that the presence of the thermocouple near the tip of the actuation arm results in a decrease (by as much as 20%) in the temperature of that region.

## 4 Power/Deflection Relation

As described earlier, the microtweezers typically have an initial opening near  $200\mu\text{m}$ . An input power near 30mW has typically been needed to just close the microtweezers. This input power corresponds to a maximum actuation arm temperature near  $170^\circ\text{C}$ .

The tip deflection of the actuation arm at different input powers was measured [4]. Figure 4 shows the measured tip deflection of the actuation arm under different input powers. For this measurement, the passive tweezers arm was broken off so that the actuation arm could be deflected beyond  $200\mu\text{m}$ . The fit of a thermo-mechanical model derived in [4] to the data is also shown in Fig. 4. Finite element thermal analysis is used to determine the cantilever temperature profile for each input power. A constant  $h_{tc}$  of  $480\text{W}/\text{m}^2\text{K}$  is used for the thermal analysis based on the results from the temperature measurements above. The temperature data at a given input power is then used to calculate the cantilever deflection by integrating the curvature equation derived in [9] along the cantilever length.

As seen from the experimental data, the tip deflection of the actuation arm increases linearly with input power up to around 40mW, at which point the slope of the tip deflection versus input power decreases. This general behavior is also found in the work from others [1]. The experimental tip deflection results deviate from the model also for input powers larger than 40mW. There could be two explanations for the discrepancy between the model and the experimental results at larger input powers. First, a constant heat transfer coefficient ( $h_{tc}=480\text{W}/\text{m}^2\text{K}$ ) is no longer valid in this regime. Therefore, the calculated temperature distribution is overestimated by using a lower  $h_{tc}$  value and results in a higher tip deflection.

A second explanation is the re-annealing of the actuation arm at higher operating temperatures (higher input powers). The bimetallic actuation arm fabricated in our microtweezers is annealed in  $\text{N}_2$  at  $450^\circ\text{C}$  for 20 minutes for good adhesion between the gold and  $\text{p}^+$  silicon, as well as to stabilize the electrical and mechanical properties of the gold [4]. The resistivity of the gold film would decrease with further annealing. As a result, the resistance of the heating resistor would decrease, leading to increased heat generation in parasitic series resistances and reduced heat generation in the heating resistor.

For input powers below 40mW, the tip position and the curvature of the actuation arm recover their original power-off values as the input power is removed after each cycle of operation. However, at high input powers ( $\geq 40\text{mW}$ ), the tip position and the curvature of the actuation arm do not return to their original power-off values when the input power is removed. For example, the power-off tweezers opening increases by nearly  $20\mu\text{m}$  from its original value (e.g.,  $200\mu\text{m}$ ) after it has been operated with an input power of 52mW. The maximum temperature of the actuation arm is near  $220^\circ\text{C}$  for an input power of 40mW. It seems that at temperatures above  $220^\circ\text{C}$  further annealing of the gold takes place. In addition to affecting its electrical properties, this annealing also leads to a change in the mechanical properties (e.g., residual stress) of the film, affecting the power-off tip position and curvature of the actuation arm.

Therefore, for reliable operation of the microtweezers, the maximum temperature of the actuation arm must be kept well under the annealing temperature. This condition is satisfied since an input power of 30mW is sufficient to fully close the microtweezers. In this regime of operation, the relationship between the microtweezers tip opening and input power is linear; the slope of the model tip deflection versus input power is  $6.7\mu\text{m}/\text{mW}$ . This is in good agreement with the experimental data which is  $6.9\mu\text{m}/\text{mW}$ . Thus, for the low input power regime, the thermo-mechanical models are effective tools for predicting the tip deflection of the actuation arm. The equivalent force [4] is estimated at  $15\mu\text{N}$  for an input power of 40mW, which corresponds to  $3.7\times 10^{-4}\text{N}/\text{W}$  in the linear characteristic region.

## 5 Response Time

Although the response speed is not critical for the operation of the microtweezers, it is still helpful to know the response time of the bimetallic cantilever actuator. A high speed video camera system (SP2000 [10]) is used to record and analyze the motion of the actuation arm. Figure 5 shows the step response of the tip deflection of the actuation arm during heating and cooling cycles, respectively. Although the recording speed in the measurement is 1000 frame per second, the relatively small changes in the tip deflection lead to an error of  $\pm 2\text{msec}$  in the time measurement. As can be seen from the data, the step response time for both cases is near 60msec; the heating and cooling times are nearly the same.

## 6 Manipulation of Objects

Successful demonstrations of the microtweezers operation have been made. In these demonstrations, the microtweezers were mounted on a micropositioner and used to manipulate objects under a microscope. An adjustable voltage source was used to control the opening and closure of the microtweezers to pick up or to release the objects. In one demonstration, small crystals of salt about  $100\mu\text{m}$  in size were picked up, rotated (e.g.,  $360^\circ$ ), moved around, and repositioned. In a second demonstration, grabbing and moving of an optical fiber (also around  $100\mu\text{m}$ ) into a v-groove was demonstrated. Finally, the alignment of two optical fibers by using the microtweezers to grab and align one fiber to the other was demonstrated.

## 7 Conclusion

A microtweezers design utilizing bulk micromachining and bimetallic actuation has been presented, demonstrating the potential of using bimetallic actuation to obtain large forces and deflections. It was experimentally demonstrated that the temperature distribution along the length of a bimetallic cantilever may not be constant since the support can act as a heat sink. It was noted that the re-annealing of the metal in the bimetallic cantilever may take place during operation if the input power is sufficiently high.

## Acknowledgment

This research was supported by ARPA under Contract No. DABT63-92-C-0032.

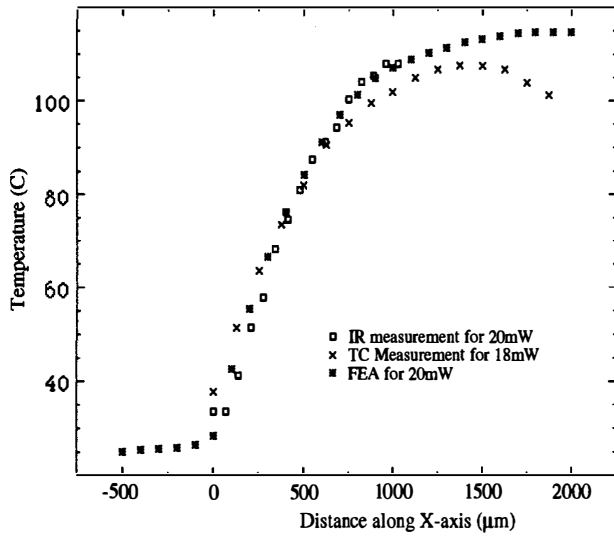


Figure 3: The temperature of the actuation arm of the microtweezers under 20mW input power. The X axis is along the length of the cantilever with X=0 at the support end and positive X toward the tip direction.

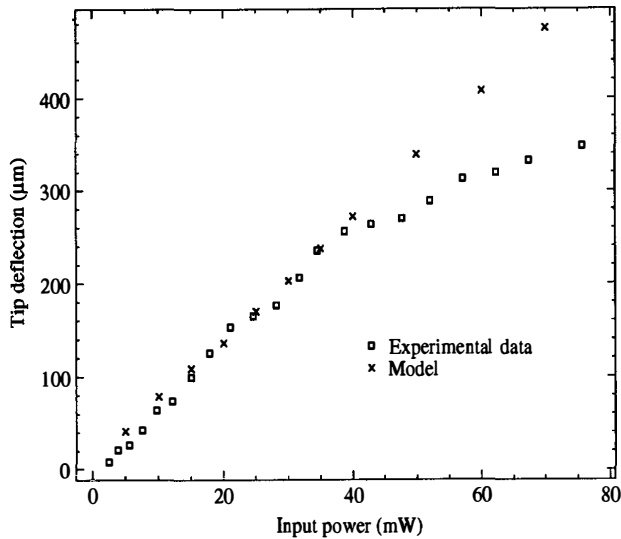


Figure 4: Experimentally measured and model tip deflections at the free end of the microtweezers actuation arm as a function of the input power.

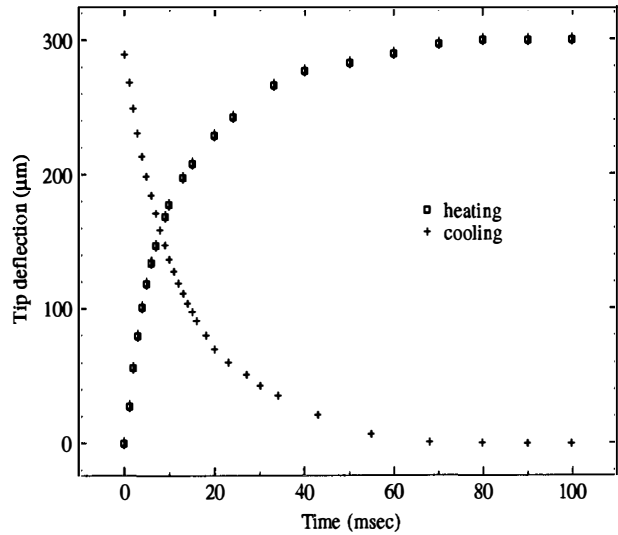


Figure 5: The step response of the tip deflection of the actuation arm during the heating and cooling cycles for an input power of 75mW.

## References

- [1] W. Riethmuller and W. Benecke, "Thermally excited silicon microactuators", *IEEE transaction on Electron Devices*, vol. 35, pp. 758-762, June 1988.
- [2] W. Benecke and W. Riethmuller, "Applications of silicon-microactuators based on bimorph structures", *Proceedings, IEEE MEMS Workshop*, Salt Lake City, Utah, pp. 116-120, Feb. 1989.
- [3] C. Doring, T. Grauer, J. Marek, M.S. Mettner, H.P. Trah, and M. Willmann, "Micromachined thermoelectrically driven cantilever structures for fluid deflection", *Proceedings, IEEE MEMS Workshop*, Travemunde, Germany, pp. 12-18, Feb. 1992.
- [4] W. Chu, "Microfabricated tweezers with a large gripping force and a large range of motion", Ph. D. Thesis, Case Western Reserve University, Cleveland, Ohio, May 1994.
- [5] L.Y. Chen, Z.L. Zhang, J.J. Yao, D.C. Thomas, and N.C. MacDonald, "Selective chemical vapor deposition of tungsten for micro electromechanical structure", *Sensors and Actuators*, vol. 20, pp. 123-133, 1989.
- [6] C.J. Kim, A.P. Pisano, and R.S. Muller, "Silicon-Processed Overhanging Microgripper", *J. of Microelectromechanical System*, vol. 1, pp. 31-36, March 1992.
- [7] Chromel-Constantant thermocouple (Type E), Omega Engineering, Inc. One Omega Drive, Stamford, CT 06907.
- [8] EDO Corporation, Barnes Engineering Division, 88 Long Hill Cross Road P.O. Box 867, Shelton, CT 06484-0867.
- [9] W. Chu, M. Mehregany, and R. L. Mullen, "Analysis of tip deflection and force of a bimetallic cantilever microactuator", *J. Micromechanical and Microengineering*, vol. 3, pp. 4-7, 1993.
- [10] SP2000 Motion Analysis System, Spin Physics, 3099 Science Park Road, San Diego, CA 92121-1101.

# A Silicon Wafer-Bonding Technology for Microfabricated Shear-Stress Sensors with Backside Contacts

H.D. Goldberg, K.S. Breuer† and M.A. Schmidt  
 Microsystems Technology Laboratories  
 Department of Electrical Engineering and Computer Science  
 † Department of Aeronautics and Astronautics  
 Massachusetts Institute of Technology  
 Cambridge, Massachusetts 02139

## ABSTRACT

Measurement of shear stress is of great importance for polymer extrusion process control, and for turbulent boundary layer modeling and control for wind tunnel research. This paper describes wall-mounted sensors for both the direct and indirect measurement of shear stress. Floating-element sensors ( $L = 140 - 500 \mu\text{m}$ ,  $W = 120 - 500 \mu\text{m}$ , and  $T = 5 \mu\text{m}$ ) and hot-wire anemometers ( $L = 65 - 650 \mu\text{m}$ ,  $W = 5 \mu\text{m}$ ,  $T = 5 \mu\text{m}$ ) were successfully microfabricated using silicon wafer bonding and etch-back technology. A new fabrication scheme has been developed to allow contact of the devices from the back side of the chip by implementing through-wafer vias. This was done to facilitate the packaging of these wall-mounted devices.

## INTRODUCTION

Flow of fluid over a rigid surface will produce a shear stress ( $\tau_w$ ) on the surface, acting in the direction of the flow. This is schematically illustrated for a simple one-dimensional case in Figure 1, where the shear stress is given by

$$\tau_w \equiv (\text{fluid viscosity}) \times (\text{shear rate}) = \mu \cdot \left( \frac{\partial V_{||}}{\partial n} \right)$$

where  $V_{||}$  is the streamwise fluid velocity and  $n$  is the direction normal to the surface. Shear stress is an important flow parameter to measure because it contains information about fluid composition (viscosity) as well as flow characteristics (shear rate).

Within many industrial extrusion processes and wind tunnel research applications, there is a growing need for wall-mounted shear-stress sensors (as in Figure 1) that allow flow properties to be measured, modeled, and controlled. A basic extrusion process involves the conversion of a suitable raw material into a product of specific cross section by forcing the material through an orifice or die under controlled conditions [1]. Shear-stress sensors can be used in extruders to determine viscosity (the near-wall fluid velocity profile is well-understood for a given extruder design), which can give an indication of the chemical composition of the polymer. For wind tunnel research, a turbulent boundary layer may extend significantly into the flow stream, but the near-wall region is considered the most important area for the production and maintenance of turbulence because this is where the maximal turbulent fluctuations and Reynolds stresses occur, and where the mean shear is the strongest [2]. Wall-

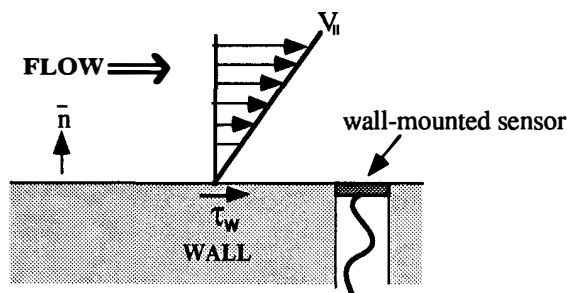


Figure 1: Schematic of a wall-mounted shear-stress sensor for determining fluid composition and flow characteristics.

mounted shear-stress sensors would provide valuable instrumentation for modeling and controlling turbulent boundary layer characteristics since they allow instantaneous shear rates to be determined (since the viscosity of air is a well-tabulated parameter). This paper describes silicon microfabricated floating-element sensors [3] (for direct shear-stress measurements) and hot-wire anemometers (for indirect shear-stress measurements) that meet the performance and packaging requirements of commercial polymer extruders (high shear-stress  $\sim 100$  kPA, high pressure  $\sim 6000$  psi, and high temperature  $\sim 300^\circ\text{C}$ ) and low-speed wind tunnels (flow velocity  $< 40$  m/s and shear-stress sensitivity  $\sim 1$  Pa).

It is imperative for these microfabricated shear-stress sensors that the transducer structure, the electrical connections to the sensor chip, and the sensor package do not form protrusions (even on the micron scale) that will perturb the flow characteristics of the system in the vicinity of the wall-mounted sensor. Micromachining permits the fabrication of very planar sensor structures that are compatible with this requirement, however, electrical connection often poses a problem. Previously, designers of wall-mounted flow sensors have addressed this concern by utilizing enlarged chip sizes or long probe stalks which attempt to locate the bonding pads sufficiently 'down stream' [3 - 6], or by implementing vertical integration schemes that require unique transducer materials [7]. Comparatively, a backside electrical contact scheme would also allow the transducer elements to be in intimate contact with the sensing environment while simultaneously maintaining electrical / physical isolation between the electrical leads and the sensing environment, but it does not specifically require an increase in the overall size of the flow sensor. Several types of integrated devices with backside electrical contacts have been fabricated and they have employed junction-isolated leads [8 - 10], dielectrically-isolated leads [11, 12], and thermomigrated aluminum interconnect [13]. To facilitate the packaging of our wall-mounted shear-stress sensors, we have successfully developed a new microfabrication process to allow contact of the device from the backside of the chip by anisotropic etching of through-wafer vias that utilize dielectrically-isolated leads to avoid high-temperature leakage effects associated with junction-isolated interconnect. It is a significant improvement in terms of process simplicity and yield over a previously described method [14].

## SENSOR DESIGN

### Floating-Element Shear-Stress Sensor

The floating-element shear-stress sensor with backside contacts was microfabricated in  $\langle 100 \rangle$  single-crystal silicon and the structure is schematically shown in Figure 2. The sensor consists of a tethered plate, or 'floating element', which can displace laterally (as a rigid body) under a shear load against the restoring force of four tethers [3]. The pressure drop across the element induces some fluid flow underneath the plate, but the shear stress generated on the bottom of the floating element can be neglected due to the small gap size (the floating element is suspended only  $1 \mu\text{m}$  above the silicon substrate). The shear force on the plate is equally distributed between the four tethers and the axial stress imparted on each tether is given by

$$\sigma_{\text{tether}} = \frac{\tau A_{\text{plate}}}{4 A_{\text{tether}}}$$

where  $A_{\text{plate}}$  is the area of the floating-element plate and  $A_{\text{tether}}$

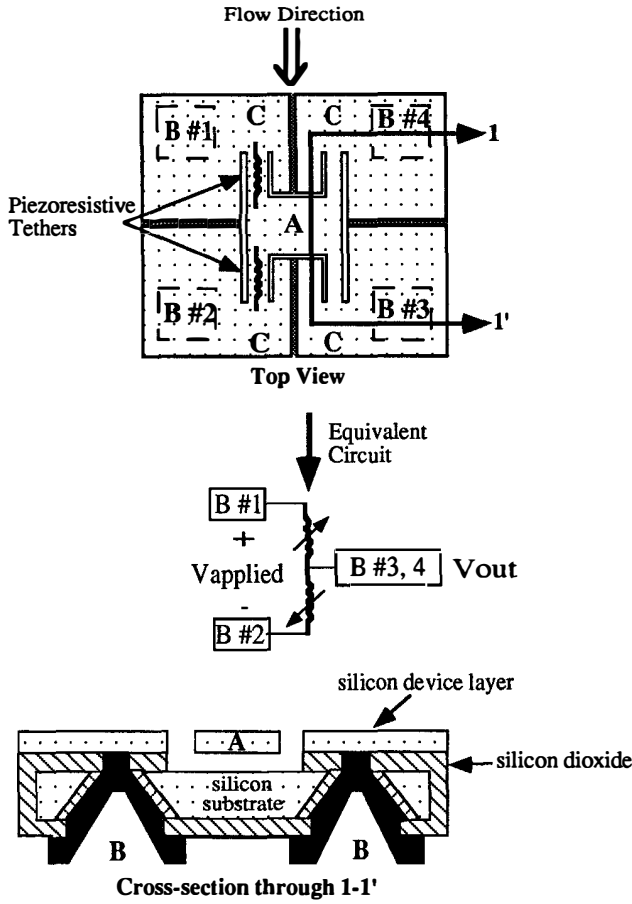


Figure 2: Top and cross-sectional schematic of the floating-element shear-stress sensor with a piezoresistive readout scheme. (Notation: A = floating-element transducer, B = backside contacts, C = microstructure anchors).

is the cross-sectional area of the tether. The resulting strain is transduced through the two piezoresistive tethers (one undergoes compressive axial strain and the other undergoes tensile axial strain). The change in the resistance of the tethers can be expressed as

$$\frac{\Delta R}{R} = G \epsilon_{\text{tether}} = G \frac{\sigma_{\text{tether}}}{E_{\text{Si}}}$$

where  $\epsilon_{\text{tether}}$  is the axial strain in a tether;  $G$  and  $E_{\text{Si}}$  are the gauge factor and Young's modulus for  $\langle 110 \rangle$  single-crystal silicon, respectively. For a half-bridge readout configuration (as shown in Figure 2), the output response ( $\Delta V_{\text{out}}$ ) is linear and is given by

$$\Delta V_{\text{out}} = \frac{V_{\text{applied}} G A_{\text{plate}}}{8 A_{\text{tether}} E_{\text{Si}}} \cdot \tau.$$

To achieve the range of device sensitivities and dynamic ranges needed for polymer extrusion, two plate sizes were fabricated ( $120 \mu\text{m} \times 140 \mu\text{m}$  and  $500 \mu\text{m} \times 500 \mu\text{m}$ ). By simply increasing the plate size, it is possible to make a sensor which approaches the sensitivity needed for wind tunnel turbulence measurements.

### Hot-Wire Anemometers

Figure 3 is a schematic of a hot-wire anemometer pair whose suspended microbridge structure is similar to surface-micromachined anemometer devices [15, 16], but in addition utilizes backside electrical contacts for flush-mounting the sensor

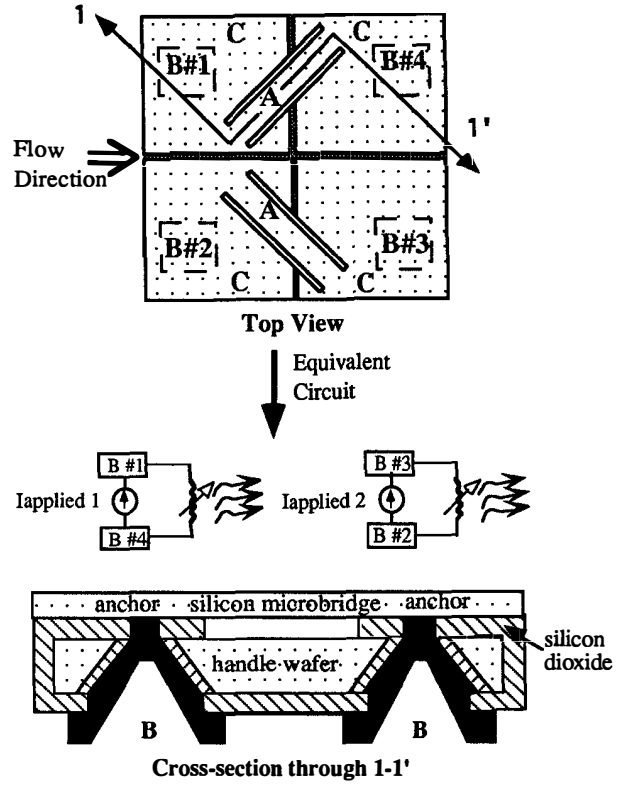


Figure 3: Schematic of the hot-wire anemometer chip. (Notation: A = hot-film element, B = backside contacts, C = microstructure anchors).

chip in a wind tunnel. The two resistive hot-wire elements are oriented at 90-degrees with respect to each other. By measuring both the common-mode and differential convective cooling of the anemometer pair, we can infer both the magnitude and direction of the local wall shear stress (assuming no reverse flow). The resistive microbridges, which form the hot-wire elements, have a nominal width of  $5 \mu\text{m}$ , a nominal thickness of  $5 \mu\text{m}$ , and lengths which vary ( $65 \mu\text{m}$ ,  $130 \mu\text{m}$ ,  $325 \mu\text{m}$ , and  $650 \mu\text{m}$ ) to set both the sensitivity and dynamic operating range of the devices. The resistive microbridges are electrically isolated from the handle wafer substrate and they are suspended  $1 \mu\text{m}$  above the handle wafer (providing thermal isolation from the substrate). Also, the backside contacts provide a relatively large surface area for conductive heat transfer to occur between the silicon microbridge anchors and the silicon substrate. This minimizes the parasitic Joule heating of the silicon microbridge anchors (please refer to Figure 3), which can influence the overall spatial and temporal resolution of the anemometer chip. The lateral gaps around the microbridge structure are nominally  $5 \mu\text{m}$  wide, which is much less than the smallest turbulent length scale of most wind tunnels (approximately  $35 \mu\text{m}$  at  $20 \text{ m/s}$ ). Thus, any flow perturbations due to the sensor can be safely ignored.

### FABRICATION

To begin the process, a  $\langle 100 \rangle$  silicon handle wafer is thermally oxidized ( $1 \mu\text{m}$ ) and an oxide gap, where the suspended microstructure will reside, is formed on the front side of the wafer. Subsequently, a handle wafer contact, for electrochemical wafer thinning (ECE), is formed on the back side of the wafer. The wafer is coated with LPCVD silicon nitride and the back side is patterned and etched to expose the regions that will form the via openings, as shown in Figure 4A. Anisotropic silicon etching ( $\text{KOH}:\text{H}_2\text{O}$ ) is used to form the through-wafer via holes. Figure 4B shows the handle wafer after the exposed oxide at the

top of the vias is removed by wet etching. The exposed  $\langle 111 \rangle$  sidewalls are then oxidized ( $\sim 7000 \text{ \AA}$ ) to provide electrical isolation, completing the handle wafer processing (the resulting structure is shown in Figure 4C). Figure 4D shows how the front side of the handle wafer is bonded [17] to the front side of a p-type device wafer which contains a n-type diffused layer ( $5 \mu\text{m}$  thick). A  $2.5\text{-}\mu\text{m}$  thick polysilicon layer is deposited and doped to form the interconnect for the backside contacts. The device wafer is selectively thinned back to the p-n junction using ECE techniques [18] (the backside contacts are exploited for making electrical connection to both the n-type device layer and handle wafer) and the resulting structure is shown in Figure 4E. A high-dose phosphorus implant was performed on the device layer to create the n+ diffusion interconnect while the piezoresistive tether regions are masked so they remain lightly-doped. The suspended sensor structure has been released using dry etching and it was thermally oxidized ( $450 \text{ \AA}$ ) to form a three-dimensional passivation coating. The finished sensor is shown in Figure 4F, where individual backside contact pads have been formed, and metal ( $1 \mu\text{m}$  of aluminum) has been deposited and patterned to facilitate external lead attachment.

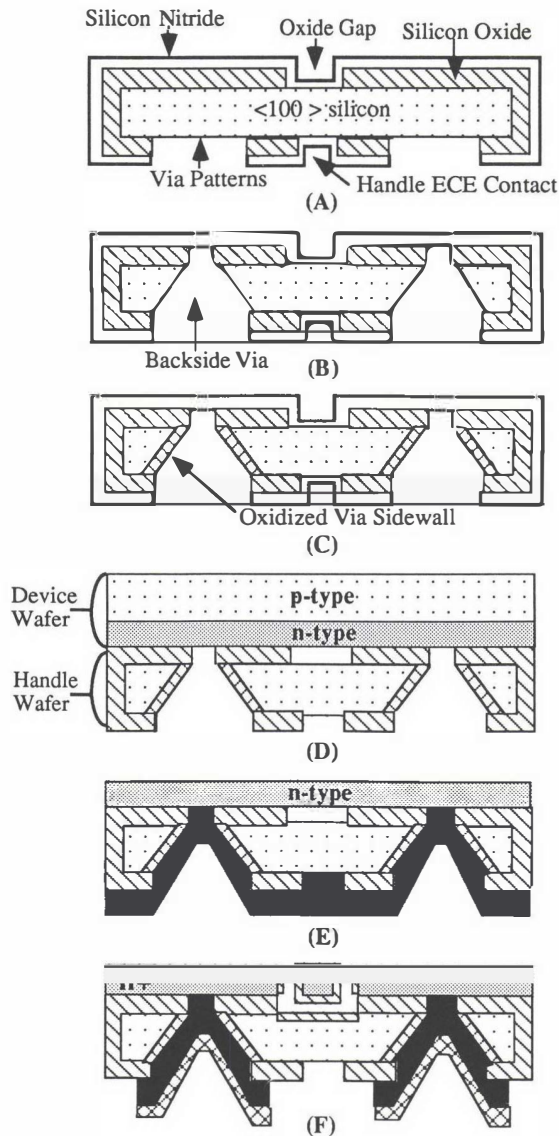


Figure 4: Sensor fabrication sequence.

The process yielded floating-element shear stress sensors and hot-film anemometers, with backside contacts that were planar microstructures. The shear stress sensor chip is  $5 \text{ mm}$  by  $5 \text{ mm}$  and a photomicrograph of a microfabricated device is shown in Figure 5 for a  $120 \mu\text{m}$  by  $140 \mu\text{m}$  floating element. The anemometer chip is the same size as the shear-stress sensor and consists of two hot-wire elements, as shown in the photomicrograph of Figure 6 for the  $325\text{-}\mu\text{m}$  long microresistors.

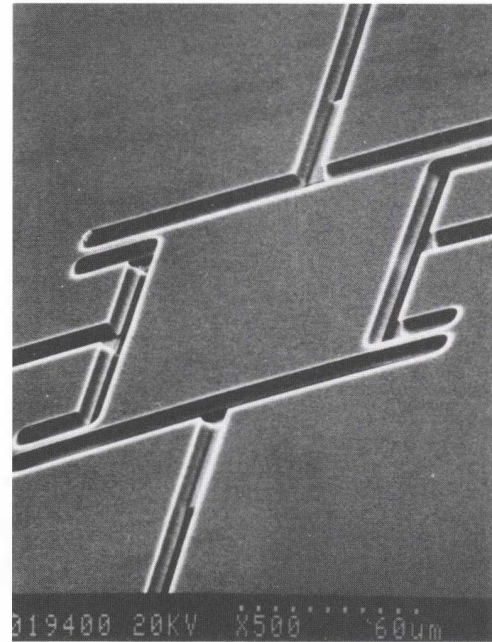


Figure 5: Photomicrograph of a microfabricated floating-element shear-stress sensor.

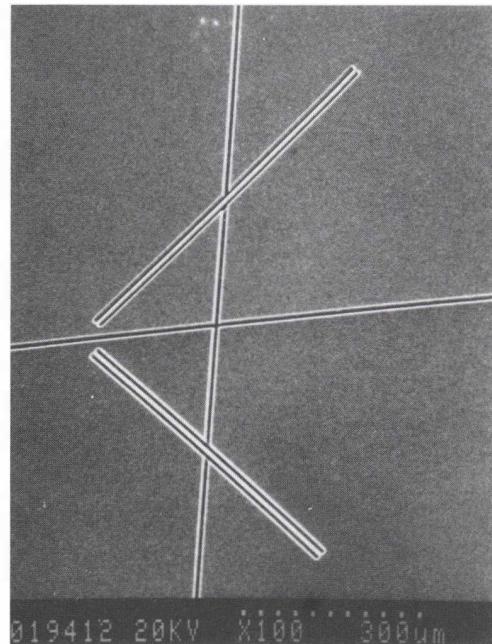


Figure 6: Photomicrograph of a microfabricated hot-wire anemometer chip.

## RESULTS AND DISCUSSION

### Electrical Functionality of the Devices

The sensors were probed to evaluate the electrical functionality of the backside contacts. The via resistance is composed of the ohmic losses within the through-wafer polysilicon interconnect and the lateral sheet resistance of the silicon anchors for the suspended microstructures. The via resistance was measured to be  $\leq 40 \Omega$  and it will not adversely affect performance of any of the sensors; the via resistance was calculated to be  $\sim 47 \Omega$  with 99.2% of this value attributed to the lateral sheet resistance of the silicon anchors. The via capacitance (i.e. via contact to handle wafer) was calculated to be 30 pF.

The measured microbridge resistances for the anemometers and the tether resistances for the shear-stress sensor are listed in Table 1. All measured values are within the range of expected values (within the accuracy imposed by the via resistances and process tolerances). Figure 7 shows typical measured current-voltage characteristics of a microfabricated anemometer during no-flow conditions. The curvature of the measured voltage curve (at the higher bias currents) demonstrates Joule heating of the microresistor. The incremental resistance, derived from the measured current-voltage characteristics, is also shown in Figure 7. Two features of this incremental resistance can be highlighted. First, the resistance increases due to the reduction in carrier mobility as the silicon heats. Second, at high enough temperature ( $\sim 900 - 1000 \text{ }^\circ\text{C}$ ), the silicon becomes intrinsic and the resistance decreases due to the extra thermally generated carriers. The linear TCR of the film was found to be  $(2.2 \pm 0.4) \times 10^{-3} / ^\circ\text{C}$  which is comparable to previously published data for the TCR of homogeneously-doped silicon samples  $((1.24 - 2.13) \times 10^{-3} / ^\circ\text{C}$ , extracted from resistivity data presented in reference [19]).

Hot-Wire Element Lengths	Average Measured Element Resistance	Average Measured Tether #1 Resistance	Average Measured Tether #2 Resistance	Average Measured Half-Bridge Resistance
65 $\mu\text{m}$	398 $\Omega$	1289 $\Omega$	1282 $\Omega$	2291 $\Omega$
130 $\mu\text{m}$	732 $\Omega$			
325 $\mu\text{m}$	1690 $\Omega$			
650 $\mu\text{m}$	3270 $\Omega$			

Table 1: Average measured hot-wire element resistances for various microbridge lengths (about 30 elements per microbridge length were measured) and average measured resistances of the piezoresistive tethers of the shear-stress sensors (about 22 sensors were measured).

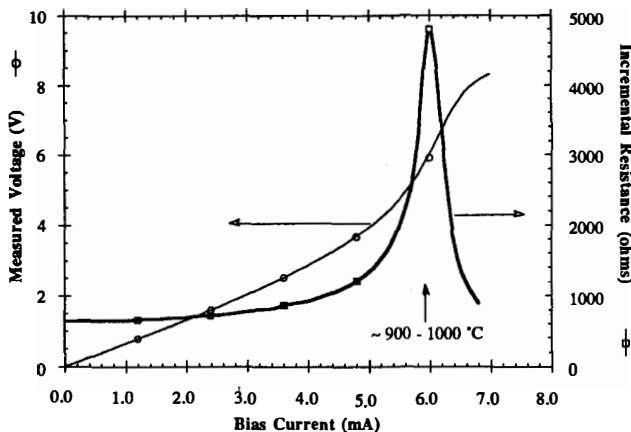


Figure 7: I-V characteristics of a 325- $\mu\text{m}$  long hot-wire anemometer during no-flow conditions at room temperature.

The first fabrication run had a functional device yield which was directly related to the sensor lead count: there was a 36% yield for the anemometer chips (composed of 2 adjacent hot-wire elements that require 2 functional backside contacts), a 50% yield for the floating-element shear-stress sensors (require 3 functional backside contacts for operation), and a 72% yield for the individual hot-wire elements (require only 2 backside contacts for operation). The dominant failure mode is electrical lead conduction to the substrate. We are investigating this phenomena, and are exploring process options to improve the yield.

### Sensor Responses

#### Floating-Element Shear-Stress Sensor

Sensors with exactly the same floating-element structures, but with frontside electrical contacts, have been previously calibrated in a cone-and-plate viscometer and have shown excellent agreement with the theoretical models [3]. Those sensors had also survived an extrusion environment (up to 20 hrs. of processing time in a polyethylene resin which was temperature-cycled to  $220 \text{ }^\circ\text{C}$  and which achieved hydrostatic pressures of 6000 psi) [3].

Currently, the new electrically-functional sensors with backside contacts are being calibrated in viscometers and are being mounted in industrial polymer extruders to evaluate their use as process control monitors. Initial shear-stress responses have been obtained by mounting the sensors in an uncalibrated nitrogen flow stream (set up on a probe station) and a typical response is shown in Figure 8. The effective shear stress was calculated, from the sensor response, to be on the order of 350 Pa and the flow noise from manual closing of the flow valve was also transduced by the sensor.

#### Hot-Wire Shear-Stress Sensors

A plastic plug package was designed to allow the sensors to be flush-mounted into our low-turbulence wind tunnel. There was a pre-drilled channel to allow access to the backside wire leads of the sensor. Wires were silver epoxied to the backside electrical contacts of the anemometer chips. The chips were flush-mounted into the chip recess of the plug and molding clay was used to fill in the gaps and to ensure that the chip surface was flush with the surface of the plug. The plugs fit into the precisely machined openings of a plastic port flush-mounted into the wall of a flat plate (the plate forms a section of the wind tunnel wall), positioned where a clean laminar boundary layer flow is established (sensors were located approximately 1 meter from the sharp leading edge of the plate). Flow speeds varied from 1 - 20 m/s.

For initial static calibration in a laminar boundary layer, the sensors were connected to standard constant-current drive

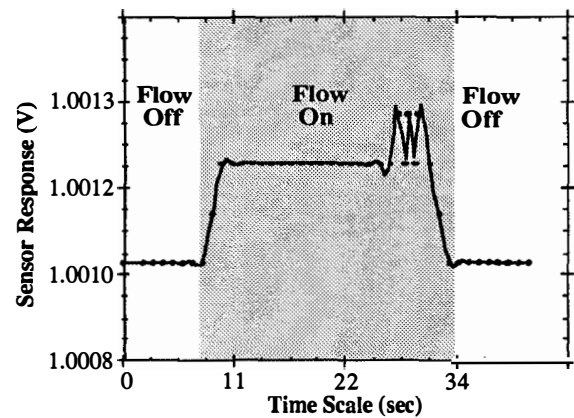


Figure 8: Response of floating-element shear-stress sensor towards uncalibrated nitrogen flow ( $500 \mu\text{m} \times 500 \mu\text{m}$  plate size, with  $V_{\text{applied}} = 2\text{V}$ ).

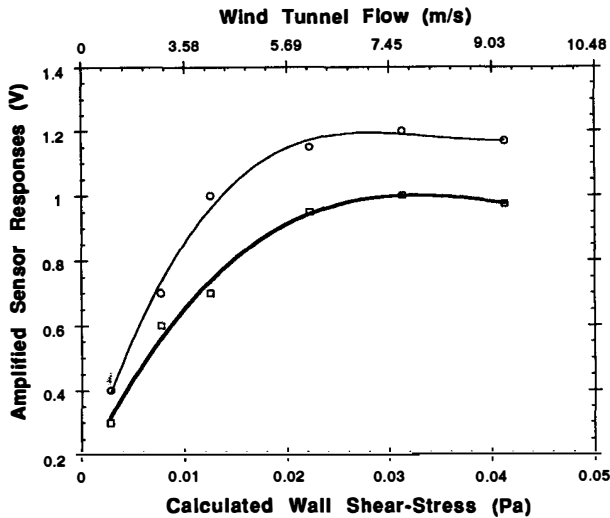


Figure 9: Characteristic laminar flow response of an anemometer chip (composed of two 325- $\mu\text{m}$  long hot-wire elements). The calculated wall shear stress is referenced against the wind tunnel flow rate (scale is non-linear).

circuitry [20] and the chips were manually oriented toward the flow as shown in Figure 3. The anemometers are functional as velocity sensors and their responses (as in Figure 9) are characteristic of constant-current mode hot-wire anemometers [20]. We believe that the variation in the individual hot-wire responses can be attributed to a slight mis-alignment of the chip toward the flow stream. Because the laminar boundary layer was previously confirmed to be a Blasius boundary layer, wall shear stress can be inferred from the near-wall velocity profile (please refer to [21]), and the shear-stress responses of the sensors can also be determined (as shown in Figure 9). Since it was demonstrated that the anemometers with backside contacts are functional sensors, constant-temperature drive circuitry is currently being designed to more effectively evaluate the dynamic response characteristics of the sensors and to allow measurements to be taken in turbulent boundary layers.

## CONCLUSION

We demonstrate the feasibility of microfabricated floating-element and hot-wire anemometer shear-stress sensors with a novel backside contact scheme. The electrical functionality and initial response characteristics of both types of flush-mounted sensors were established. Currently, the calibrated response characteristics toward shear-stress fluctuations within a polymer extruder and a wind tunnel turbulent boundary layer are being experimentally determined for the floating-element and hot-wire anemometer sensors, respectively. This new backside contact method readily lends itself to forming other microsensors (i.e. temperature and pressure), with backside contacts, that would expand the quantitative process-control arena for extrusion processes and would provide multi-sensor arrays for wind tunnel turbulence research.

## ACKNOWLEDGMENTS

We gratefully acknowledge the support of this work by the 3M Corporation, A.F.O.S.R., and the NSF Presidential Young Investigator Award Program (Prof. Schmidt). The authors would like to thank Dr. John Huizinga, Andrew Cipra, and Glen Merfeld (of 3M) for their assistance and significant involvement with the floating-element shear-stress sensor calibration and testing issues. All microfabrication was done in the Microsystems Technology Laboratories.

## REFERENCES

- [1] A. L. Griff, *Plastic Extrusion Technology*, Van Nostrand Reinhold: N.Y., 1968.
- [2] K. S. Breuer, "Active Control of Wall Pressure Fluctuations in a Turbulent Boundary Layer", presented at the *ASME Symposium on Flow Noise Modeling, Measurement, and Control*, New Orleans, USA, December 1993.
- [3] J. Shajii, K. Y. Ng, and M. A. Schmidt, "A Microfabricated Floating-Element Shear-Stress Sensor Using Wafer-Bonding Technology", *Journal of Microelectromechanical Systems*, Vol. 1 (2), pp. 89-94, 1992.
- [4] M. A. Schmidt, *Microsensors for the Measurement of Shear Forces in Turbulent Boundary Layers*, Ph.D. Thesis, M.I.T., 1988.
- [5] G. Stemme, "An Integrated Gas Flow Sensor with Pulse-Modulated Output", *Technical Digest of Transducers '87: 4th International Conference on Solid-State Sensors and Actuators*, pp. 364-367, IEEE, 1987.
- [6] L. Löfdahl, G. Stemme, and B. Johansson, "Silicon Based Sensors for Measurements of Turbulence and Wall-Pressure Fluctuations in a Two-Dimensional Flat Plate Boundary Layer", *Near Wall Turbulent Flows* (R. M. C. So, C. G. Speziale, and B. E. Launder, eds.), pp. 583-592, Elsevier Science Publishers, 1993.
- [7] H. Hsieh, A. Spietz, and J. Zemel, "Wide Range Pyroelectric Anemometers for Gas Flow Measurements", *Technical Digest of Transducers '91: 6th International Conference on Solid-State Sensors and Actuators*, pp. 38-40, IEEE, 1991.
- [8] H.-H. Van den Vlekkert, B. Kloeck, D. Prongue, J. Berthoud, B. Hu, N. F. de Rooij, E. Gilli, and P. de Croussaz "A pH-ISFET and an Integrated pH-Pressure Sensor with Backside Contacts", *Sensors and Actuators*, Vol. 14, pp. 165-176, 1988.
- [9] D. Ewald, A. Van den Berg, and A. Grisel "Technology for Backside Contacted pH-Sensitive ISFETs Embedded in a p-Well Structure", *Sensors and Actuators*, Vol. B1, pp. 335-340, 1990.
- [10] A. Merlos, J. Esteve, M. Acero, C. Cané, and J. Bausells "Low Cost Fabrication Technology for IC-Compatible Backside Contacted ISFETs", *6th Conference on Sensors and Their Applications*, Manchester, U.K., 1993.
- [11] T. Sakai, I. Amemiya, S. Uno, and M. Katsura "A Backside Contact ISFET with a Silicon-Insulator-Silicon Structure", *Sensors and Actuators*, Vol. B1, pp. 341-344, 1990.
- [12] S. Linder, H. Balthes, F. Gnaedinger, and E. Doering "Fabrication Technology for Through-Hole Interconnections and Three-Dimensional Stacks of Chips and Wafers", *Technical Digest of MEMS '94: Micro Electro Mechanical Systems*, pp. 349-354, IEEE, 1994.
- [13] T. Johansson, M. Abbasi, R. Huber, and R. Normann "A Three-Dimensional Architecture for a Parallel Processing Photosensing Array", *IEEE Transactions on Biomedical Engineering*, Vol. 39 (12), pp. 1292-1297, 1992.
- [14] J. Shajii and M. A. Schmidt, "A Backside Contact Technology for a Wafer-Bonded Liquid Shear-Stress Sensor", *2nd International Symposium on Semiconductor Wafer Bonding*, pp. 342-349, Electrochemical Society, 1993.
- [15] Y. C. Tai and R. S. Muller, "Lightly Doped Polysilicon Bridge as an Anemometer", *Technical Digest of Transducers '87: 4th International Conference on Solid-State Sensors and Actuators*, pp. 360-363, IEEE, 1987.
- [16] C. Mastrangelo, *Thermal Applications of Micro-bridges*, Ph.D. Thesis, U. C. Berkeley, 1991.
- [17] L. Parameswaran, V. M. McNeil, M. A. Huff, and M. A. Schmidt, "Sealed Cavity Microstructure Using Wafer Bonding Technology", *Technical Digest of Transducers '93: 7th International Conference on Solid-State Sensors and Actuators*, pp. 274-277, IEEE, 1993.
- [18] V. M. McNeil, S. S. Wang, and M. A. Schmidt, "Issues Regarding the Application of the Electrochemical Etch-Stop Technique to Fabricate Structures Using Wafer Bonding", *Proceedings of the Symposium on Semiconductor Wafer Bonding Science, Technology, and Applications*, Electrochemical Society, 1991.
- [19] H. Wolf, *Silicon Semiconductor Data*, p. 50, Pergamon Press: Oxford, 1969.
- [20] A. E. Perry, *Hot-Wire Anemometry*, Clarendon: Oxford, 1982.
- [21] H. Schlichting, *Boundary-Layer Theory*, McGraw-Hill Book Co.: NY, 1979.

# A COMPACT PASSIVE STRAIN SENSOR WITH A BENT BEAM DEFORMATION MULTIPLIER AND A COMPLEMENTARY MOTION VERNIER

Yogesh B. Gianchandani and Khalil Najafi

Center for Integrated Sensors and Circuits  
University of Michigan  
Ann Arbor, Michigan 48109-2122

## ABSTRACT

A new type of passive strain sensor has been developed for characterizing materials for microstructures. It basically utilizes a narrow beam slightly bent at its mid-point to amplify and transform deformations caused by intrinsic stress into a lateral displacement of the apex. Pairs of such beams, bent towards each other with vernier scales between their apices, have been used to form highly sensitive strain sensors. Analytical and finite element modeling show that strain levels below  $5 \times 10^{-5}$  (with stress  $< 8$  MPa) can be measured by a bridge only  $400 \mu\text{m}$  long. Bent beam strain sensors have been fabricated with heavily boron doped single crystal silicon and with phosphorous doped polysilicon. Strain measurements from these devices agree with those obtained by other methods.

## INTRODUCTION

A crucial aspect of characterizing the mechanical properties of materials for microstructures involves the measurement of intrinsic stress of thin films. Many different techniques to perform these measurements have been developed in past years. Measurements of wafer curvature can provide average film stress. Other methods rely on the deformation produced by external loading in specially designed structures to calculate material properties like Young's modulus and intrinsic stress. Examples of these methods are the load-deflection of composite membranes [1], electrostatic pull-in voltages of bridges [2], and frequency measurements of resonant microstructures [3, 4]. Another method utilizes strain sensors designed to operate passively, providing measurable deformation from intrinsic stresses. Passive strain sensors that have been developed in the past include bridges and rings that buckle under compressive and tensile forces respectively [5], T-shaped structures with a wide, long center stem and a thinner deformable cross that provides a measure of the deformation either directly [6] or by tilting a long cantilever [7], and bridges with an intermediate lateral displacement that rotate a long pointer when deformed [8, 9].

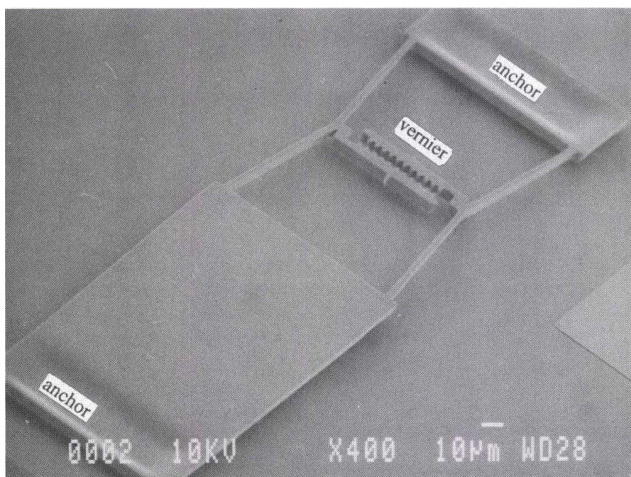


**Figure 1.** A Scanning Electron Micrograph of a Bent Beam Strain Sensor fabricated using a bulk silicon dissolved wafer process. The bridge length is  $400 \mu\text{m}$ , and its thickness about  $6 \mu\text{m}$ . The beams are at an angle of  $0.1$  radians to the x axis.

Passive strain sensors are attractive for research and development applications because they can provide quantitative readout by observing the deformation under a microscope (or some other equally simple technique). Unfortunately, all of the devices that have been developed in the past are very large ( $1\text{-}4 \text{ mm}$ ) in at least one dimension. (The buckling rings and bridges are smaller, but require great multiplicity). This means that not only do they occupy a large area, but they are also prone to clamping to the substrate in wet release processes. Furthermore, some of these devices employ long cantilevers to multiply the strain displacement [7, 8, 9]. Long cantilevers are susceptible to out-of-plane deformations, *e.g.* those caused by non-uniform stress through the cross-section of the device, making the readout more difficult and less reliable. Many of the devices developed in the past also have the additional disadvantage of only being able to measure either compressive or tensile strain, but not both. In order to overcome these problems we have developed a strain sensor using a bent-beam structure (for both tensile and compressive deformations) which offers high resolution and sensitivity as well as significant advantages in size and resistance to out-of-plane deformation. This device has been used to measure strain in polysilicon thin films and in heavily boron doped silicon. The strain has been estimated from the deformations using a simple analytical technique, and verified by finite element modeling and by comparison to measurements taken by other methods.

## DEVICE STRUCTURE AND MODELING

An SEM micrograph of a finished device is shown in Fig. 1. The device, as drawn for the lithography mask, is basically a  $400 \mu\text{m}$  long bridge clamped at both ends. Half this undercut length is relatively wide ( $100 \mu\text{m}$ ) and undifferentiated, whereas the other half is comprised of two narrow ( $4 \mu\text{m}$ ) beams bent towards each other at their midpoints, making an angle of  $0.1$  radians with the long axis of the bridge. A vernier scale is located at this point to measure deformation caused by the release of internal stresses. The vernier has a nominal resolution of  $0.2 \mu\text{m}$  and range of  $\pm 1.0 \mu\text{m}$ . A simple model for the behavior of the strain sensor is provided in Fig. 2. The elasticity of the structural material is modeled by springs  $k_1$ ,  $k_2$ , and  $k_3$  for the single wide and two narrow regions respectively. The elasticity due to bending of the two narrow beams is modeled by  $k_4$  and  $k_5$ . Fig. 2 qualitatively shows the state of each spring in the unreleased and released states. (The former corresponds to the point in fabrication just after the structural material has been deposited and patterned, and the latter corresponds to the finished structure formed when the sacrificial material is removed.) In the unreleased state the material may have some intrinsic stress, but the structure is basically not deformed. When the device is freed and responds to the internal stresses, the wide portion of the bridge relaxes, causing a deformation in the bent beam springs which is a combination of more bending and stretching. Changes in the projected axial length of the narrow beams that are caused by additional bending are amplified ( $\approx 10\times$ ) by the geometry into vertical displacements at the apex points, where the vernier is attached. (This motion is like that of parallelogram actuators [10].) The beams bend towards each other, further amplifying the apparent vernier displacement by two. The readout of the vernier provides a quantitative measure of the (tensile or compressive) intrinsic strain. Note that some of the net amplification is lost because of the elasticity of the material itself. At very small angles the elasticity of the material contributes more to the extension of the beams than does their bending.

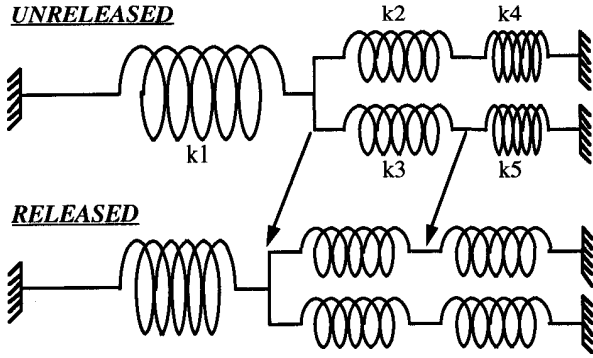


**Figure 2** A simple model for the strain sensor. The springs  $k_1$ ,  $k_2$ , and  $k_3$  represent the elasticity of the material, whereas  $k_4$  and  $k_5$  represent the bending of the narrow beams upon release. The vernier measures the extension in  $k_4$  and  $k_5$ , which is then correlated to extension in the other springs.

### Analytical Modeling

The form of a bent beam under axial loading can be approximated by the equations in Table I [11]. The  $x$  axis is along the long axis of the bridge. The change in the  $y$  coordinate of the apex can be calculated for an arbitrary axial load. The corresponding projected length of the beam along  $x$  axis can then be obtained for each axial load by using the formula [12]:

$$\Delta l = -\frac{1}{2} \int_0^l \left( \frac{\partial y}{\partial x} \right)^2 dx$$

A tensile load will increase this length, and a compressive load will reduce it. The extension due to elastic stretching of the material can also be added in, and the sum related to the strain in the bridge upon release. The vernier readout thus provides a value for the strain in the material. Prior knowledge of Young's modulus is necessary. Fig. 3a shows the relationship between strain and the vernier readout for a  $6 \mu\text{m}$  thick device with  $4 \mu\text{m}$  wide spring beams, assuming a Young's modulus of  $175 \text{ GPa}$ . The strain value corresponding to the minimum vernier reading of  $0.2 \mu\text{m}$  is about  $4.3 \times 10^{-5}$  and the stress is  $7.6 \text{ MPa}$  under these conditions. The response is linear over a large range in both tensile and compressive materials. This compares very favorably with devices that have been developed in the past, particularly if the size of the device is taken into account.

### Finite Element Modeling

Results from the analytical model for the device described above have been compared to a finite element analysis performed with ANSYS. Intrinsic stress was introduced in the model by the standard technique of applying a uniform temperature change:

$$T.E.\alpha = \sigma(1 - \nu)$$

where  $T$  = temperature change,  $E$  = Young's modulus,  $\alpha$  = the thermal expansion coefficient, and  $\nu$  = Poisson's ratio. The finite element model yields vernier displacements that are about 30% less than those obtained by the analytical technique. Comparison of linear and non-linear computations at different temperatures indicates that for stress levels of several tens of MPa, the device has an essentially linear response for both compressive and tensile materials. The results also confirm that in the released structure the wide region of the bridge sustains negligible stress, as was assumed in the analytical model.

### MEASUREMENTS

The bent beam strain sensor shown in Fig. 1 has been fabricated from boron doped silicon using a modified version of the bulk silicon dissolved wafer process that was described in ref. [4]. The finished structure rests on a glass substrate. Vernier

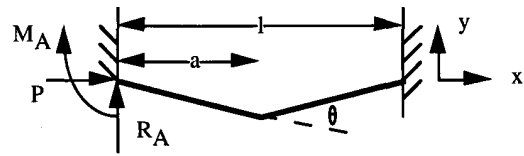
readings from different fabrication runs and corresponding values of stress and strain obtained by the analytical method are listed in Table II. The stress is in the range of  $12\text{-}25 \text{ MPa}$  (tensile), in very good agreement with previous measurements at this laboratory made using both the pull-in voltage and the resonant frequency techniques [2, 4]. For devices with beams as thick and narrow as those in Table II, we expect that one of the primary sources of error is non-uniformity in beam width along the  $x$  and  $z$  axes.

### Modified Strain Sensor

A modified version of the bent beam strain sensor has been fabricated from polysilicon using surface micromachining techniques. The structure of this device is similar to the one described above, except that the wide region of the bridge is effectively eliminated by retaining the sacrificial material underneath it. Only the narrow beams and the vernier are released. The response of a device with  $200 \mu\text{m}$  long,  $2 \mu\text{m}$  wide, and  $1.5 \mu\text{m}$  thick beams has been calculated using the analytical technique described above, and is plotted in Fig. 3b. The Young's modulus of the material was assumed to be  $160 \text{ GPa}$ . In this case the minimum vernier reading of  $0.2 \mu\text{m}$  corresponds to a strain of about  $6.2 \times 10^{-5}$ , and a stress of about  $10 \text{ MPa}$ .

The modified strain sensors were fabricated by depositing LPCVD polysilicon at  $625^\circ\text{C}$  on about  $1 \mu\text{m}$  of oxide thermally grown on a (100) silicon substrate. The samples were then subjected to different combinations of doping ( $\text{P}$ ,  $950^\circ\text{C}$ , 30 min. dep., 30 min. soak), and annealing ( $1050^\circ\text{C}$ , 60 min.), patterned, and released. Some unpatterned monitor wafers were also fabricated to permit comparative measurements by the wafer curvature technique using a Flexus 2-300 machine. The oxide and polysilicon were removed from the backside of the monitors, and the PSG was removed from their front sides. Table III shows the Flexus readings of the monitors, as well as the vernier readings of the modified bent beam devices and the corresponding stress values obtained by the analytical technique. As expected, the polysilicon was found to be in compression, with the undoped, unannealed samples showing the highest stress. An optical micrograph of the vernier for this material shows that the deflection was beyond its measurement range (Fig. 4). (It was measure<sup>d</sup> using a calibrated microscope.) Table III shows that stress values obtained analytically will require significant correction for high deflections such as this one. However, it is important to note that the Flexus and the strain sensor agree completely on the relative levels of stress in the samples.

**Table I** Equations for the form of a bent beam with fixed boundary conditions subject to axial loading [11].



$$y = \frac{M_A}{P} F_3 + \frac{R_A}{k.P} F_4 + \frac{\theta}{k} F_{a2}; \quad k = \sqrt{P/E.I};$$

$$R_A = -\theta.P \cdot \frac{C_3.C_{a1} - C_2.C_{a2}}{C_3^2 - C_2.C_4}; \quad M_A = -\frac{\theta.P}{k} \cdot \frac{C_3.C_{a2} - C_4.C_{a1}}{C_3^2 - C_2.C_4}$$

Coeff.	Tension	Compression
$C_2$	$\sinh(kl)$	$\sin(kl)$
$C_3$	$\cosh(kl) - 1$	$1 - \cos(kl)$
$C_4$	$\sinh(kl) - kl$	$kl - \sin(kl)$
$C_{a1}$	$\cosh k(l-a)$	$\cos k(l-a)$
$C_{a2}$	$\sinh k(l-a)$	$\sin k(l-a)$
$F_3$	$\cosh(kx) - 1$	$1 - \cos(kx)$
$F_4$	$\sinh(kx) - kx$	$kx - \sin(kx)$
$F_{a2}$	$\sinh k <x-a>$	$\sin k <x-a>$

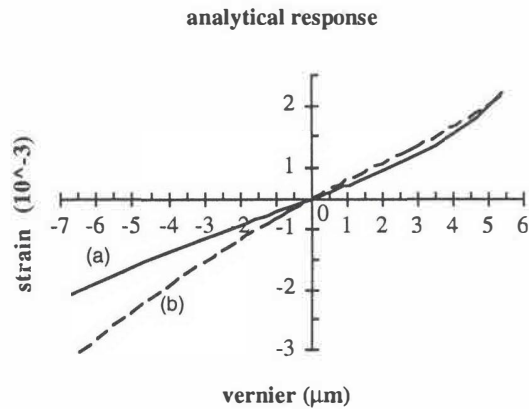


**Figure 3** Calculated strain vs. vernier readout for (a) a 400  $\mu\text{m}$  long, 6  $\mu\text{m}$  thick strain sensor with 200  $\mu\text{m}$  long and 4  $\mu\text{m}$  wide beams, assuming  $E=175\text{GPa}$ ; (b) a modified strain sensor with 200  $\mu\text{m}$  long, 2  $\mu\text{m}$  wide, and 1.5  $\mu\text{m}$  thick beams and no wide portion, assuming  $E=160\text{GPa}$ . The plots are inaccurate at high strains.

It is worth noting that although the small size (200  $\mu\text{m}$ ) of the modified bent beam sensor greatly helps to reduce its susceptibility to stiction, it does not make it immune to this problem. When the devices are thick and suspended several microns above the substrate, as in Table II, they do not clamp to the substrate. When both the structural material and the sacrificial layer underneath it are thin, as in Table III, clamping can and does occur. Although the sensors are able to respond to the intrinsic stresses before they clamp upon removal from the wet sacrificial etch, this must be recognized as a potential source of error in the readings. In order to be useful, a material characterization tool such as a local strain sensor must have higher yield than all the other micromechanical devices on the mask. We believe that the size advantage afforded by the bent beams and the complementary motion vernier (or the enhanced sensitivity at a particular size) can help accomplish this goal.

**Table II** Measurements of 400  $\mu\text{m}$  long p+ Si structures (as in Fig. 1) from different fabrication runs. Stress and strain were obtained by the analytical method. Expected stress was 15-20 MPa.

vernier ( $\mu\text{m}$ )	width ( $\mu\text{m}$ )	thickness ( $\mu\text{m}$ )	strain (analytical)	stress (MPa)
0.8	3.0	6.79	1.5 e-04	25
0.4	2.8	6.75	6.9 e-05	12
0.4	3.6	7.28	8.0 e-05	14
0.4	2.5	5.55	6.7 e-05	12
0.6	1.6	5.40	8.6 e-05	15
0.6	2.4	6.27	9.8 e-05	17
0.6	3.2	6.21	1.1 e-04	19
0.5	2.8	6.53	8.7 e-05	15
0.6	4.0	5.41	1.3 e-04	23

### CONCLUSION

Sensitive and compact strain sensors have been developed using pairs of bent beams to amplify and transform deformations caused by intrinsic stress in the structural material. The pairs are designed to cause complementary motion in a vernier scale, thereby doubling the apparent displacement. Two types of structures have been evaluated: (a) a 6  $\mu\text{m}$  thick, 400  $\mu\text{m}$  long bridge with a wide portion that is 200  $\mu\text{m}$  long and bent beams that are 200  $\mu\text{m}$  long and 4  $\mu\text{m}$  wide, and (b) a 1.5  $\mu\text{m}$  thick, 200  $\mu\text{m}$  long structure with no wide portion, and bent beams that are 200  $\mu\text{m}$  long and 2  $\mu\text{m}$  wide. The bent beams make an angle of 0.1 radians with the axis of the bridge in both cases. A simple analytical technique, based on the deflection of the beams and the elastic extension of the material, indicates that a vernier reading of 0.2  $\mu\text{m}$  corresponds to a strain of  $4 \times 10^{-5}$  in (a) and  $6 \times 10^{-5}$  in (b).

Further improvements can be expected from optimization of the bending angle and the vernier design. Finite element modeling yields results within 30% of the analytical model for values of intrinsic stress in the range of several tens of MPa. The behavior of the devices is determined to be linear for both compression and tension in this range. Bent beam strain sensors fabricated from boron doped silicon and phosphorous doped polysilicon yield results consistent with other measurement techniques.

**Table III** Vernier readings of modified strain sensors with 200  $\mu\text{m}$  long, 2  $\mu\text{m}$  wide, and 1.5  $\mu\text{m}$  thick beams and no wide region, fabricated from LPCVD polysilicon (625°C), with optional doping (P, 950°C) and annealing (1050°C). Stresses obtained analytically using  $E=160\text{GPa}$  are compared to Flexus measurements.

doped	annealed	vernier ( $\mu\text{m}$ )	strain (analyt.)	stress (MPa)	Flexus (MPa)
Y	Y	-0.4	-1.2 e-4	-20	-26.6
Y	N	-0.2	-6.3 e-5	-10	-17.4
N	Y	-0.1	-3.1 e-5	-5	-
N	N	-2.4	-8.0 e-4	-130	-231

### ACKNOWLEDGMENTS

The authors gratefully acknowledge helpful discussions with Dr. S. Crary, Mr. G.K. Ananthasuresh, and Mr. L. Saggere regarding modeling issues. This work was funded by NSF grant #ECS-8915215 and ARPA contract #92-2340.

### REFERENCES

- [1] O. Tabata, K. Kawahata, S. Sugiyama, I. Igarashi, "Mechanical property measurements of thin films using load-deflection of composite rectangular membrane," *IEEE Workshop on Microelectromechanical Systems, (MEMS '89)*, 1989, pp. 152-6
- [2] K. Najafi, K. Suzuki, "A novel technique and structure for the measurement of intrinsic stress and Young's modulus of thin films," *ibid.*, pp. 96-7
- [3] L.M. Zhang, D. Uttamchandani, B. Culshaw, "Measurement of the mechanical properties of silicon microresonators," *Sensors and Actuators A*, **29**, 1991, pp. 79-84
- [4] Y. Gianchandani, K. Najafi, "A bulk silicon dissolved wafer process for microelectromechanical devices," *JMEMS*, **1** (2), 6/92, pp. 77-85
- [5] H. Guckel, D. Burns, C. Rutigliano, E. Lovell, B. Choi, "Diagnostic microstructures for the measurement of intrinsic strain in thin films," *J. Micromech. Microeng.*, **2**, 1992, p. 86-95
- [6] M. Mehregany, R. Howe, S. Senturia, "Novel microstructures for the *in situ* measurement of the mechanical properties of thin films," *J. Appl. Phys.* **62** (9), 1 Nov. 1987, pp. 3579-3584
- [7] L. Lin, R. Howe, A. Pisano, "A passive *in situ* micro strain gauge," *IEEE Workshop on Microelectromechanical Systems*, 1993, p. 201-6
- [8] L.B. Wilner, "Strain and strain relief in highly doped silicon," *IEEE Solid-State Sensor & Actuator Workshop*, 6/92, pp. 76-7
- [9] J.F.L. Goosen, B.P. van Driehuisen, P.J. French, R.F. Wolfenbittel, "Stress measurement structures for micromachined sensors," *International Conf. on Solid-State Sensors and Actuators (Transducers '93)*, 7/93, pp. 783-6
- [10] N. Takeshima, K. Gabriel, M. Ozaki, J. Takahashi, H. Horiguchi, H. Fujita, "Electrostatic parallelogram actuators," *International Conf. on Solid-State Sensors and Actuators (Transducers '91)*, pp. 63-6
- [11] R.J. Roark, W.C. Young, *Formulas for Stress and Strain*, McGraw Hill, 1975, pp. 162-168
- [12] *ibid.*, pp. 94

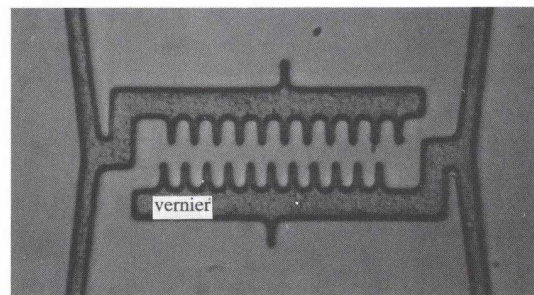


**Figure 4** A close-up top view of a large vernier deflection.

# Reliability Study of Polysilicon for Microhotplates

N. R. Swart and A. Nathan

Department of Electrical and Computer Engineering  
University of Waterloo  
Waterloo, Ontario N2L 3G1, CANADA

## Abstract

*Measurement results of resistance variations in thin film polycrystalline heating elements for thermally isolated microhotplate applications are presented for DC and AC conditions and different stress levels. The resistance variations observed were due solely to thermal effects arising from current-induced self-heating resulting in grain growth (recrystallization) of the polysilicon. Although the operating currents were low ( $I \approx 1.5\text{mA}$ ,  $J \approx 10^5\text{A/cm}^2$ ), catastrophic failure of the microhotplate was observed and this was due to microstructure damage caused by excessively high temperatures. No electromigration effects were observed.*

## 1 Introduction

Polycrystalline silicon is widely used not only in the integrated circuit (IC) technology, but also in thermal-based microsensing applications where it serves as a heating or sensing element. Although the deposition conditions and hence, the material characteristics may be identical in both categories of applications, the long term reliability issues, in the two cases, can turn out to be significantly different in view of differences in device operation. In VLSI and related applications, variations in resistance leading to failure can be attributed to electromigration arising from very large current densities ( $\approx 10^6\text{A/cm}^2$ ) (see [1, 2]). In thermal-based microsensors and related applications, the high thermal isolation with micromachining can result in high resistor temperatures even at low current densities ( $\approx 10^5\text{A/cm}^2$ ), leading to significant resistance drifts (see [3, 4]).

In general, the reliability of polysilicon is governed by the electrical current density in the material and the temperature, although the latter is a function of the electrical current itself by virtue of Joule heating [1]. At relatively lower currents, the self heating of the film results in movement of grain boundaries giving rise to grain growth (recrystallization) in regions where the local temperature exceeds some critical value [5]. This leads to a decrease in the resistance of the thin film. At higher currents and with extended operation, the temperatures become significant and an increase in resistance can be observed due to thermally-induced motion (electromigration) of impurities. This gives rise to local depletion of impurities thus significantly increasing material resistivity and eventually leading to catastrophic failure [1].

In this paper, we present measurement results of polysilicon resistance variations for different stress levels and under DC and AC conditions. The measurements were performed for microhotplate test structures comprising of two meandering resistors with one acting as control. In particular, two hot plate configurations were considered; structures with and without metallization over the active area.

## 2 Experimental Setup

A photomicrograph of the microhotplate test structure used in the experiments is shown in Fig. 1a along with its schematic in Fig. 1b. The device was fabricated using the Northern Telecom  $1.2\mu\text{m}$  CMOS process. Two symmetrical polysilicon resistors, sandwiched in oxide, with a nominal room temperature resistance of  $29.9\text{k}\Omega$ , meander in parallel over the hot plate as shown in Fig 1b. The resistors, denoted as  $R_h$  (heater) and  $R_c$  (control), have a  $1.2\mu\text{m}$  line width and a process specified sheet resistance of  $30\Omega/\square$ . The sheet resistance was found to have a scatter of

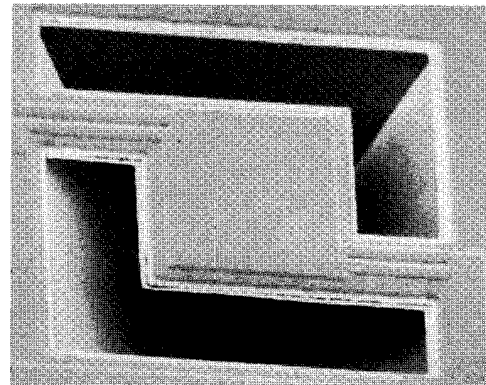


**Fig. 1a** - SEM of microhotplate structure used for reliability studies.

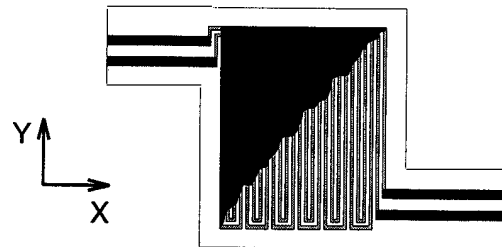


**Fig. 1b** - Schematic of microhotplate test structure with cut-away view showing  $R_h$  and  $R_c$  (see text).

less than 0.5 % over all samples tested. Power is supplied to the hot plate through metal lines along the support beams. The structure is underetched (micro-machined) using EDP to a depth of approximately  $80\ \mu\text{m}$  providing a high degree of thermal isolation from the silicon substrate. The active hot plate area (the area comprising the polysilicon resistors) is approximately  $87\ \mu\text{m} \times 71\ \mu\text{m}$ .

Two variations of the design are examined, one in which the active hot plate area is covered with two layers of metal (metal1 and metal2 in the CMOS process), and the other where the active area is non-metallized. Figures 2a and 2b are surface plots obtained from simulations of the hot plate temperature distribution under medium bias, with and without the temperature levelling metal layers. In these simula-

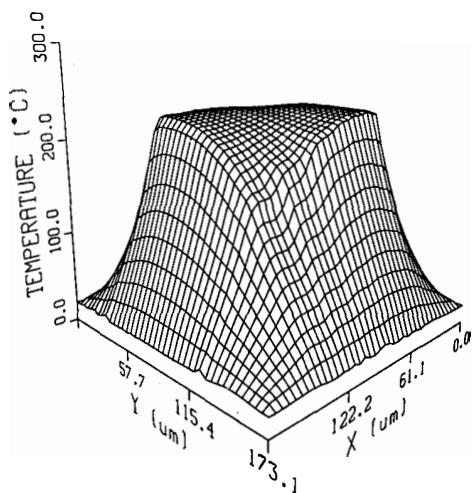


**Fig. 2a** - Surface temperature of hot plate under a medium bias with metallized active area.

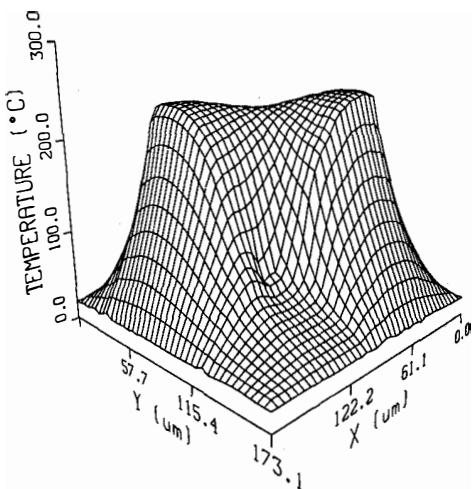


**Fig. 2b** - Surface temperature of hot plate under a medium bias without the metallized active area.

tions the ends of the support beams attached to the substrate were assumed equal to the substrate temperature ( $23^\circ\text{C}$ ). The additional metal layers lower the net thermal conductivity of the hot plate relative to the support beams resulting in a significantly more uniform temperature distribution over the active area. Without these layers, large temperature

gradients result near the two corners of the hot plate attached to the support beams as seen in Fig. 2b. As a consequence, a hot plate operated at the same average temperature with metallization layers, will have less severe hot spot temperatures than one operated without.

The normal operation of the test structure involves applying a high bias to  $R_h$  to heat the plate, and simultaneously a low bias to  $R_c$ . In this way, any electrically induced variations in  $R_h$  have minimal influence on  $R_c$  whose resistance changes are purely thermally induced. The tight thermal coupling obtained from the close spacing (approximately  $1.6\ \mu\text{m}$ ) of the two resistors, in addition to the minimal heat loss above and below the structure, ensures that  $R_h$  and  $R_c$  are at almost the same temperature along their entire length. In addition to  $R_h$  and  $R_c$ , a third resistor located (on the substrate) in close proximity to the hot plate is used to monitor the elevation of the substrate temperature during electrical stressing. For all experiments described in the next section, it was found that the substrate did not increase in temperature by more than  $3^\circ\text{C}$ . This validates the earlier assumption that the ends of the support beams at the substrate can be considered to be at room temperature; this constitutes data crucial for the boundary conditions in the numerical simulations.

All current-voltage measurements were performed at room temperature using the Keithley 236 Source Measure Units (SMU's). The SMU's can be configured to sweep a voltage or current source at precisely timed intervals, while simultaneously measuring the corresponding current or voltage. A microcomputer was used to control and retrieve data from the SMU's for the reliability studies. The resistance was constantly monitored and any changes exceeding 0.5% were recorded. In addition to the current-voltage characterisation, the temperature coefficient,  $\alpha$  of all resistors was measured before and after stressing. The temperature coefficient, defined by  $R = R_0(1 + \alpha T)$  where  $R_0$  is the resistance at  $0^\circ\text{C}$ , was found to be  $5.87 \times 10^{-4}/^\circ\text{C}$  in the range  $0^\circ\text{C}$  to  $120^\circ\text{C}$ . The measurements were performed in an oven capable of controlling the chip temperature to within  $0.5^\circ\text{C}$ . The temperature was measured using a thermocouple attached to the chip carrier. A low bias of  $35\ \mu\text{A}$  was used for the resistance measurement in order to minimise Joule heating. It was found that this bias raised the temperature of the resistor by less than  $3^\circ\text{C}$ . A total of 8 samples were measured with the scatter in  $\alpha$  being less than 1%.

### 3 Measurements and Discussion

The current voltage characteristics of the resistor  $R_h$  of both the metallized and non-metallized hot plate structures are shown in Fig. 3. The characteristics were obtained by stepping the current through the sample with a hold time of 5 ms at each bias point. At relatively low bias, one can observe that the resistance increases with increasing voltage for both structures due to the positive temperature coefficient of the polysilicon. The heater resistances in both structures are initially similar in behaviour and

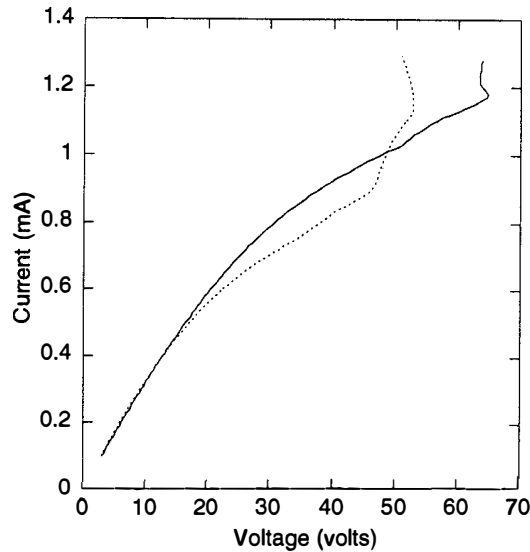


**Fig. 3** - Current-voltage characteristics of heating resistor,  $R_h$ ; solid line indicates structure with metal layers over active area, dashed line denotes structure without metal layers.

the effects of nonuniform temperature start prevailing at  $I > 0.5$  mA. The resistance of the metallized hot plate is lower in view of its lower peak temperatures; without the metallization, very high peak local temperatures (hot spots) are reached. In addition, there is more heat loss with the metallized structure occurring primarily through the supporting beams. At very high voltages, we note that the heater exhibits negative differential resistance (Fig. 3), similar to what was observed in [6, 7]. The increase in temperature at increasing currents leads to significant reduction in the grain boundary barrier potential possibly leading to formation of narrow filaments of molten silicon creating low resistivity paths for current flow.

The resistance of the heater and control resistors for both structures is shown in Fig. 4. We note a distinct

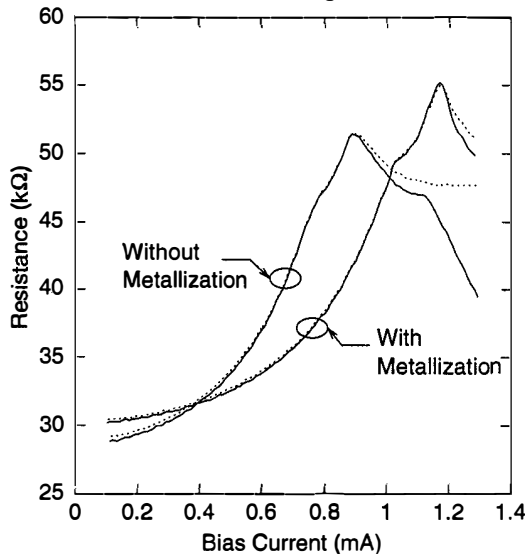


**Fig. 4** - The resistance as a function of current for the same conditions as in Fig. 3. Resistors  $R_h$  and  $R_c$  are indicated by the solid and dashed lines, respectively.

kink where after the resistance decreases sharply. Under these bias conditions, the temperature of the hot plate is much in excess of  $800^\circ\text{C}$ . At these temperatures, there is movement of grain boundaries leading to grain growth or recrystallization [5, 8]. The subsequent increase in grain size leads to lower resistivity of the thin polycrystalline film. As expected, the recrystallization points occur at higher voltages (currents) for the structure with metallization; more of the device active (resistor) area is at an isothermal state with a lower average temperature. One also observes a second kink after which we see a sharp decrease in the resistance. The reasons for this are not very clear but we suspect that this may be due to secondary recrystallization which takes place at much higher temperatures [5]. We also note that the control and heater resistances become increasingly more distinct as the bias current increases. This can possibly be attributed to thermally-induced variations after all, despite the close proximity of heater and the control, there are differences in temperature at the two locations.

So far, all electrical stressing of samples were based on variable but direct current (DC) conditions. Experiments were also performed for single bias DC and AC conditions to deduce the possible effects of electric fields. For the AC case, the polarity of the applied bias was switched at a frequency of 25 mHz. The measured resistances of heater and control in both microhotplate structures are shown in Fig. 5 as a function of stress times. The heater and control voltages were maintained at 35 V and 1.5 V, respectively. In these structures, the effect of heating is expected to be similar as before. No difference in the relative change in resistance ( $\Delta R/R_0$ ) was observed between heater and the control for both structures. Here,  $R_0$  is the respective resistance of the heater and the control, measured 1 s after the bias is applied, and  $\Delta R$  is the deviation from  $R_0$ . This indicates that the resistance variation observed is purely due to thermal effects. A direct comparison of room temperature resistance values at the start and end of a 48 hour DC

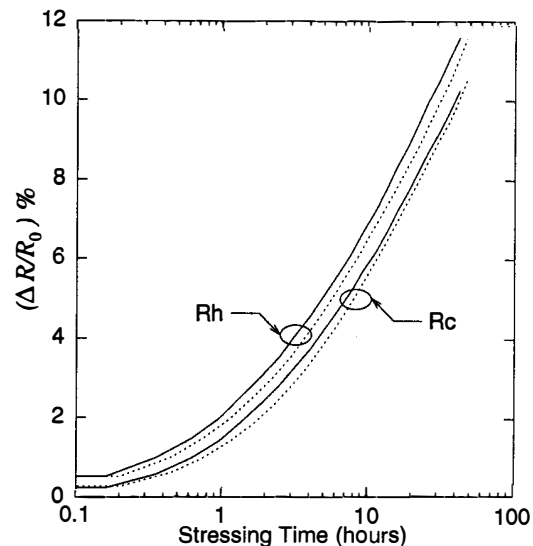


**Fig. 5** - Percentage change in heater and control resistances as a function of time for a constant voltage bias. The solid and dashed lines represent DC and AC stressing, respectively (see text).

and AC stress test is shown in Tables 1a and 1b. Also included are the values of the temperature coefficient,  $\alpha$ . No significant differences were observed between the two operating conditions. The slight discrepancy in the variation in R and  $\alpha$  may be due to intrinsic differences in the pre-test resistance and hence, in the self-heating.

	$R_h$	$R_c$	$\alpha_h$	$\alpha_s$
start	29764	29968	0.585	0.584
end	35186	34660	0.513	0.585
$\Delta$ %	18.2%	15.7%	-12.3%	-17.0%

**Table 1a** - Heater and control resistances, and corresponding temperature coefficients, measured at room temperature at the start and end of a constant DC voltage stress test.

	$R_h$	$R_c$	$\alpha_h$	$\alpha_s$
start	29868	30055	0.591	0.594
end	34871	34544	0.549	0.533
$\Delta$ %	16.8 %	14.9%	-7.1%	-10.3%

**Table 1b** - As in Table 1a, but for AC voltage stress test.

None of the structures tested exhibited electromigration for the given range of test conditions. Unlike non-thermally isolated structures, the current densities in the structures considered had to be restricted ( $J \approx 10^5 \text{ A/cm}^2$ ) due to excessive temperature build up as a result of thermal isolation. Electromigration, which is characterised by resistance increase, is caused by local depletion of impurities thus significantly increasing material resistivity and eventually leading to catastrophic failure. In our structures, catastrophic failure was observed only when the temperature of the active device area became high enough leading to damage of the microstructure due to mismatch in expansion coefficients and thermal melt down. In the structure with metallization, the damage occurred

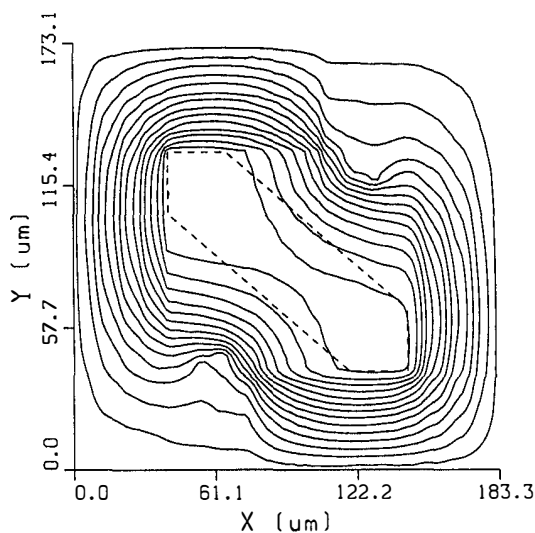


**Fig. 6** - Isotherms of hot plate without metal layers under high bias. Dashed line indicates the region of catastrophic failure of polysilicon (see text).

clearly within the region indicated by dashes in the isothermal plot (Fig. 6). For all intents and purposes, this region is an isothermal surface at a temperature in excess of 900 °C. The contour lines shown are based on simulation results and the slight asymmetry is due to asymmetries in device and resistor geometry.

## 4 Conclusions

We have presented measurement results of resistance drifts in polysilicon heating elements in thermally isolated microhotplates. Based on measurement data obtained for long stress durations, we find that safe and reliable operation, with plate temperatures around 350°C, is possible with metallization over the active hot plate area. At this temperature, the variation in heater resistance was found to be less than 1% over 100 hours of operation.

## Acknowledgements

We gratefully acknowledge the services of the Canadian Microelectronics Corporation (CMC) and Northern Telecom (NT) for the fabrication of the microheater samples. This research was supported by the Natural Science and Engineering Research Council of Canada, the National (Micronet) and Provincial (ITRC) Centres of Excellence in Microelectronics.

## References

- [1] J. R. Lloyd, M. R. Polcari, and G. A. MacKenzie, "Observation of electromigration in heavily doped polycrystalline silicon thin films," *Appl. Phys. Letts.*, vol. 36, pp. 428-430, 1980.
- [2] H. Akimori, N. Owada, T. Taneoka, and H. Uda, "Reliability study of polycrystalline silicon thin film resistors used in LSI under thermal and electrical stress," in *Proc. IEEE Int. Reliability Phys. Symp.*, pp. 276-280, 1990.
- [3] M. Parameswaran, A. M. Robinson, D. L. Blackburn, M. Gaitan, and J. Geist, "Micromachined thermal radiation emitter from a commercial CMOS process," *IEEE Electron Device Letts.*, vol. 12, pp. 57-59, 1991.
- [4] C. H. Mastrangelo, J. H. Yeh, and R. S. Muller, "Electrical and optical characteristics of vacuum-sealed polysilicon microlamps," *IEEE Trans. Electron Devices*, vol. 39, pp. 1363-1375, 1992.
- [5] C. D. Ouwens and H. Heijligers, "Recrystallization processes in polycrystalline silicon," *Appl. Phys. Letts.*, vol. 26, pp. 569-571, 1975.
- [6] D. W. Greve, "Programming mechanism of polysilicon resistor fuses," *IEEE Trans. Electron Devices*, vol. 29, pp. 719-724, 1982.
- [7] K. Ramkumar and M. Satyam, "Negative-resistance characteristics of polycrystalline silicon resistors," *J. Appl. Phys.*, vol. 62, pp. 174-176, 1987.
- [8] G. C. Jain, B. K. Das, and S. P. Bhattacharjee, "Grain growth in polycrystalline silicon," *Appl. Phys. Letts.*, vol. 33, pp. 445-446, 1978.

# A HEURISTIC APPROACH TO THE ELECTROMECHANICAL MODELING OF MEMS BEAMS

Michael R. Boyd, Selden B. Crary, and Martin D. Giles

Center for Integrated Sensors and Circuits  
EECS Department, The University of Michigan  
1301 Beal Avenue, Ann Arbor, Michigan 48109-2122  
Contacts: crary@umich.edu or madagil@umich.edu

## ABSTRACT

Approaches for calculating the capacitance of parallel plate capacitors of a variety of shapes and plate spacing are presented. Accurate solutions based on the method of subareas is compared to a new, geometry-based approximation which can be rapidly evaluated and shows excellent agreement over a wide range of capacitor configurations. The new approach reduces the computational cost of coupled electromechanical calculations of MEMS structures by essentially eliminating the cost of capacitance calculation in solving the coupled system until the final iteration.

## INTRODUCTION

Many MEMS structures utilize beams driven electrostatically. The approach advanced for the modeling of such structures, which can have substantial fringing-field effects, is coupled finite- and/or boundary-element electrostatic and mechanical calculations[1]. Such calculations incur a computational burden that should be minimized as far as possible. It is of interest and importance to find means of expressing the capacitance of MEMS beam structures in simple but accurate mathematical expressions that can be rapidly evaluated. Such expressions could be used directly for capacitance estimation. They could also be used in the initial iterations of the coupled-field solution of electromechanical systems to reduce computation time, switching to a more conventional approach for the final iteration where necessary.

Here we present approaches to the calculation of capacitance for parallel-plate capacitors of various plate shapes and plate spacings in vacuum. 3D capacitance calculations can be made directly, or approximate expressions derived by extension of 2D calculations for infinite parallel-plates. All capacitance calculations scale according to a single length parameter, so the results can be applied to structures at any length scale. Normalized results can be obtained by dividing by the capacitance of an equivalent parallel plate capacitor neglecting fringing fields.

## CALCULATING CAPACITANCE IN 2D

The mutual capacitance per unit length of a pair of infinitely-long parallel plates, or, by a familiar application of the method of images, of a single infinitely-long plate above an infinite ground plane, can be obtained exactly using the Schwartz-Christoffel transformation [2]. The capacitance in either case is given by

$$C_{\text{Palmer}} / \epsilon = K' / K$$

where  $K(k)$  is the complete elliptic integral of the first kind, and  $K'(k) = K(1 - k^2)$  is the complementary complete elliptic integral. The parameter  $k$  is an implicit function of the ratio of plate width to plate gap,  $R = w / g$ ,

$$R = \frac{2}{\pi} (K'E'(\beta, k) - E'F'(\beta, k)) \quad (1)$$

$$\sin^2 \beta = \frac{K' - E'}{(1 - k^2)K'}$$

where  $E'(\beta, k)$  is the complementary elliptical integral of the second kind and  $F'(\beta, k)$  is the complementary elliptic integral of the first kind. Since Equation 1 is not invertable, calculation for a particular value of  $R$  requires an iterative or table-lookup procedure to determine the corresponding value for  $k$ . For large values of  $R$ , an approximate capacitance formula has been derived by Love[3] effectively based on a series expansion of the elliptic integrals. This results in the expression:

$$C_{\text{Love}} / \epsilon = R + \frac{1}{\pi} (1 + \ln 2\pi R) \quad (2)$$

This gives capacitance values within 3% of the exact value for  $R > 3$ .

The zeroeth-order approximation for the capacitance per unit length is simply  $\epsilon w/g$ . Deviations from this value are called fringing-field corrections. Figure 1 shows the effect of fringing fields on the capacitance of the two beams, based on eleven evenly spaced values of the gap-to-width ratio, using the exact method. The data are labeled Exact and MSA Beams.

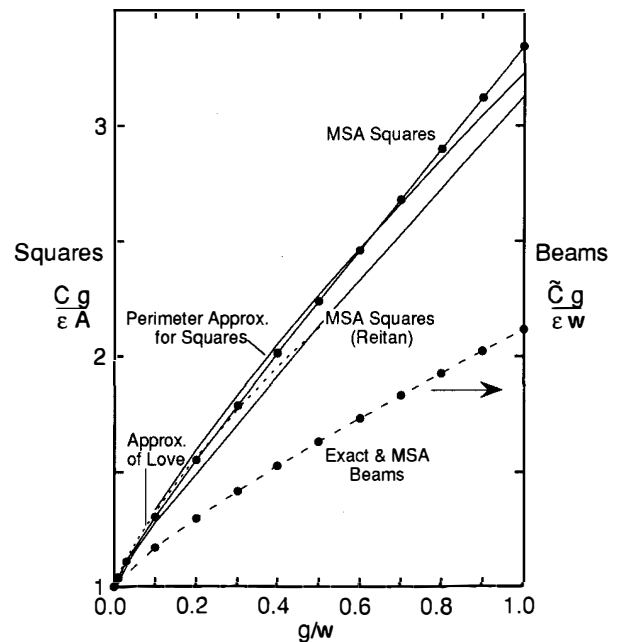


Figure 1. (Exact & MSA Beams) The mutual capacitance per unit length of a pair of infinitely long parallel plates, normalized by the mutual capacitance neglecting fringe-field effects  $\epsilon w/g$ , is shown plotted as a function of the gap-to-width ratio  $g/w$ . Straight-line segments connect points calculated using the exact method. Filled circles represent values calculated using the method of subareas. (MSA Squares) The mutual capacitance of a pair of square plates, normalized by the mutual capacitance neglecting fringe-field effects  $\epsilon A/g$  is shown in the same manner. (Perimeter approx.) The approximate formula for the capacitance of planar structures using the area and perimeter terms of the geometric expansion of Eq. 7 provides a good approximation to the actual capacitances. (Approx. of Love) Love's approximation [3] provides a series-based alternative to the perimeter approximation. (MSA Squares - Reitan) The data of Reitan using a 6x6 mesh [4] are shown for comparison.

An alternative to transformation-based methods is the method of subareas (MSA) described by Reitan[4]. This scheme subdivides the plates into a number of small subareas such that the charge density is essentially constant over each subarea. In 2D, the potential at subarea  $j$  due to charge on subarea  $i$  can be written

$$V_{ij} = \frac{-q_i}{2\pi\epsilon} \int_{-h/2}^{h/2} \ln\left(\sqrt{(x+\Delta x)^2 + (\Delta y)^2}\right) dx \quad (3)$$

where  $q_i$  is the charge per unit length on subarea  $i$ ,  $h$  is the subarea width, and  $\Delta x, \Delta y$  are the distances between the centers of the subareas along the  $x$  and  $y$  axes. This integral holds even when  $i = j$ . The total potential at subarea  $i$  is then given by

$$V_i = \sum_{j=1}^n V_{ij} \quad (4)$$

For a charged conductor at equilibrium, the potential is constant across the entire surface,  $V_i = V_0$ . In that case, Equation 4 represents a set of  $n$  simultaneous linear equations which can be solved for the individual subarea charges. By symmetry, the top and bottom plates must have equal magnitude charge distributions but opposite polarity, and charge distribution for each plate must be symmetric about the center line. Consequently, charges for only a quarter of the total subareas need be explicitly calculated. The overall capacitance is given by  $C = Q / V_0$ , where  $Q$  is the total charge on one plate.

For a gap-to-width ratio of 0.1, uniform discretizations with numbers of subdivisions  $m$  across each plate of 2, 10, 20, 30, 100, 200, 300, 1000 were used. A convergence analysis indicated that the discretization error converged to the following power law with exponent  $\beta = -1.00$ :

$$C - C_0 = \alpha h^\beta, \quad (5)$$

where  $\alpha$  is a constant determined by curve fitting. The convergence is demonstrated graphically in Figure 2.

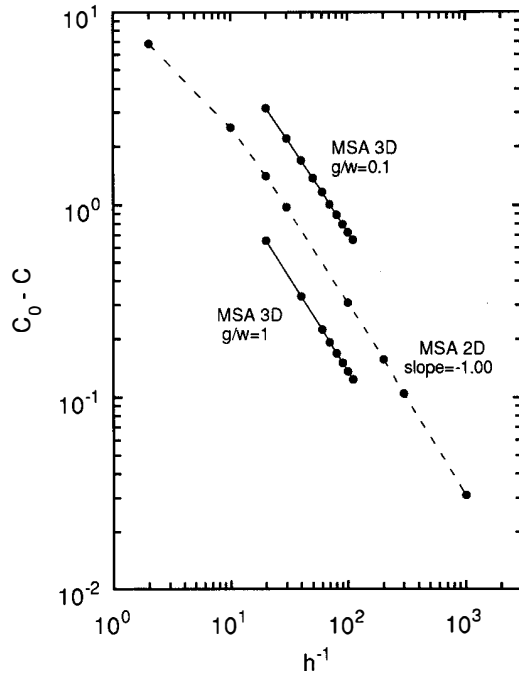


Figure 2. The results of the 2D MSA computations follow a power-law behavior with exponent -1.00, in the limit of small subdivision size  $h$ . The results of the 3D computations have not yet reached the region of asymptotic slope by  $h^{-1}=110$ , although a detailed analysis shows that the slopes themselves are converging via a power law to asymptotic values near -1.00.

Figure 1 shows as filled circles the results of eleven MSA calculations made for the same eleven values of  $g/w$  as were used for the exact calculations. The number of subdivisions across each beam was 1000. The convergence analysis indicated that these values could be used without power-law extrapolation and were accurate to 0.02%. Extrapolation via the power law could be used to reduce the error to below 0.01%.

The MSA can also be used to calculate the capacitance to infinity of a single plate in a similar manner.

### CALCULATING CAPACITANCE IN 3D

The only three-dimensional capacitance formula known is that for the capacitance to infinity of an elliptical disk. There are no formulae available for finite, parallel-plate capacitors. Approximate solutions can be obtained by applying the method of subareas in 3D. For square subareas, Equation 3 becomes

$$V_{ij} = \frac{-q_i}{4\pi\epsilon} \int_{-h/2}^{h/2} \int_{-h/2}^{h/2} \left( (x+\Delta x)^2 + (y+\Delta y)^2 + (\Delta z)^2 \right)^{-1/2} dx dy$$

where  $q_i$  is the charge on subarea  $i$ . A set of linear equations for the subarea charges is formed as before and the system solved to yield the subarea charges. Square plates have eight-fold symmetry, so only 1/16 of the total number of subareas need be explicitly calculated in that case. The rectangular and L-plate examples presented later have reduced symmetry and so require explicit calculation of a larger fraction of subareas.

Because 3D MSA computations can be expected to require many more subareas than their 2D counterparts, we made an initial set of 3D MSA runs to determine the convergence behavior for square plates with gap-to-width ratio of 0.1 at a set of increasingly fine uniform discretizations. Each square was divided into  $m \times m$  subareas, and computations were made with  $m$  ranging from 20 to 110 in steps of 10. A power-law fit to the trio of results using  $m=90, 100$ , and 110 gave a power law of  $\beta = -0.9401$ ; a fit using  $m=80, 90$ , and 100 gave  $\beta = -0.9339$ ; and a fit using the trio  $m=70, 80$ , and 90 gave  $\beta = -0.9261$ . In a similar fashion, fits to the exponent for gap-to-width ratio of 1.0 gave  $\beta = -0.9776$ ,  $\beta = -0.9759$ , and  $\beta = -0.9739$ , respectively. To test if the exponents for these two gap-to-width ratios were converging, we then performed power-law fits to the convergence of the  $\beta$ 's, under the following assumed power law:

$$\beta - \beta_0 = \gamma h^\delta, \quad (6)$$

where  $\beta_0$  is the converged value of  $\beta$  being determined. The fits gave  $\beta = -0.998$  and  $-1.007$  for gap-to-width ratios of 0.1 and 1.0, respectively.

We then tentatively assumed that the asymptotic value for  $\beta$  was unity in this 3D case, as it was in the 2D case, and we performed a variety of checks of the consistency and adequacy of this assumption. An integration of Equations 5 and 6 gave the following formula for the converged value of the capacitance  $C_0$ , based on the capacitances computed for the five finest meshes:

$$C_0 = \frac{C_3 - C_1 e^S}{1 - e^S},$$

where  $C_3$  is the capacitance computed for the middle ( $h_3$ ) of the three finest meshes of the five,  $C_1$  is the capacitance computed for the middle ( $h_1$ ) of the three coarsest meshes of the five,  $S$  is given by

$$S = \beta_0 \ln \frac{h_1}{h_3} + \frac{\gamma}{\delta} (h_1^\delta - h_3^\delta),$$

and all the other constants are determined in the course of fitting to Equation 6. This procedure gave  $C_0 = 1.3059$  for a gap-to-width ratio

of 0.1 and  $C_0=0.33429$  for a gap-to-width ratio of 1.0. Figure 2 shows the discretization error as a function of the length of a subdivision of the discretization, on the assumption that the converged values  $C_0$  are 1.3059 and 0.33429 for gap-to-width ratios of 0.1 and 1.0, respectively.

Under the assumption that  $\beta=1$ , a simpler extrapolation from the finest two discretizations, that is, from the computations at  $m=100$  and 110, gave  $C_0=115.59$ , and an extrapolation from the computations made at  $m=40$  and 60 gave  $C_0=115.61$ . Our conclusion is that extrapolations can be made from the moderately coarse discretizations of  $n=40$  and 60 using an assumed value of  $\beta=1$ , and that the error introduced in this way is less than 0.1%. The extrapolation method assuming  $\beta=1$  was then applied to computations for squares with gap-to-width ratios ranging from 0.1 to 1.0 for discretizations of  $m=40$  and  $m=60$ . The results are shown in Table 1.

Figure 1 includes a plot of the mutual capacitance of two parallel square plates, or, equivalently, of a single square plate above an infinite ground plane, as a function of the gap-to-width ratio, based on the computations and extrapolations discussed above. The normalization factor is the zeroth-order capacitance  $\epsilon A/g$ , where  $A$  is the area of one plate,  $A=w^2$ . The effect of fringing in the 3D case is roughly double that observed in 2D.

To verify the accuracy of the 3D MSA code, two calculations with known solutions were made. First, we considered the capacitance to infinity of a circular disc of radius  $r$ , which is known to be  $C = 8\epsilon r$ . Approximating the circle using a square grid with up to 110 subareas across the diameter, convergence analysis yields a capacitance of 35.337 pF for a 1 meter diameter, compared to an exact solution of 35.417 pF. Second, we considered the capacitance between two long parallel plates. As the length of the plates increases, the capacitance per unit length approaches the exact 2D result for infinite parallel plates, as shown in Figure 3.

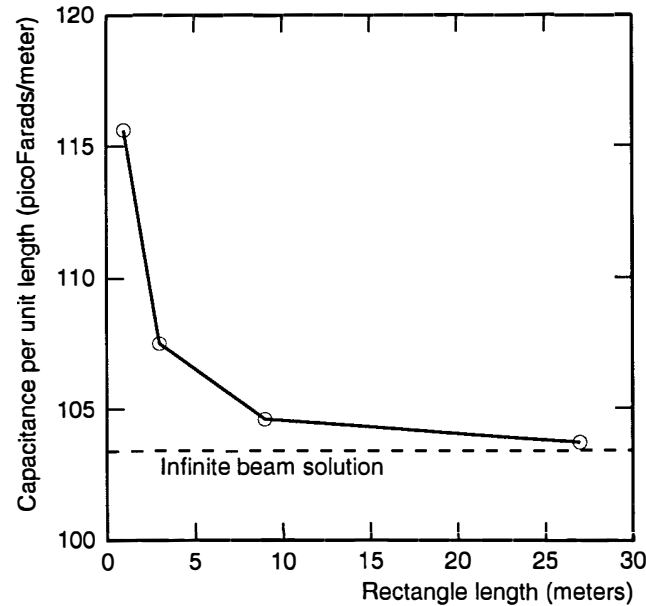


Figure 3. The capacitance per unit length of rectangular beams converges to the capacitance of an infinite beam, in the limit of the long side of the rectangle going to infinity, while holding the length of the short side constant.

Our 3D MSA code is capable of calculating capacitance for a number of different conductor shapes including rectangles, rectangles with a rectangular hole in the center, and rectangles with one quadrant removed. A plot of charge density across a 1 meter square plate of a parallel-plate capacitor with 0.1 meter gap is shown in Figure 4. The square has a 0.5 meter square hole in the center, which appears as a region of zero charge density in the plot. This clearly shows the components of the charge distribution of the capacitor: a constant

value over the area of the plate, an additional edge charge around the perimeter of the plate, a further increase in charge at exterior corners, and a decrease in charge at interior corners. These components can also be seen in the cross-sections of Figure 5.

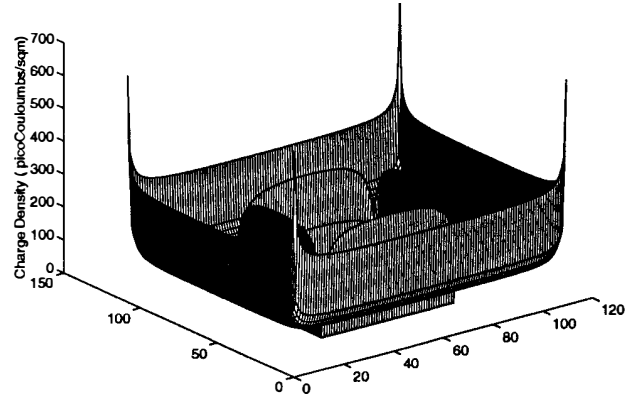


Figure 4. 3D plot of the charge density on one of two parallel square plates with holes in their centers. The plot is based on the average charge over each subarea and thus shows effects of discretization. Nonetheless, the very strong singularity in charge density at the exterior corners is observed, as are the decrease in charge density at interior corners and the singularity at the edges.

### GEOMETRIC EXPANSION

The association of capacitor charges with geometric features of the plates suggests an approach to rapidly estimating capacitance based on geometry:

$$C = A C_{area} + P C_{perim} + E C_{ext} + I C_{int} + \dots \quad (7)$$

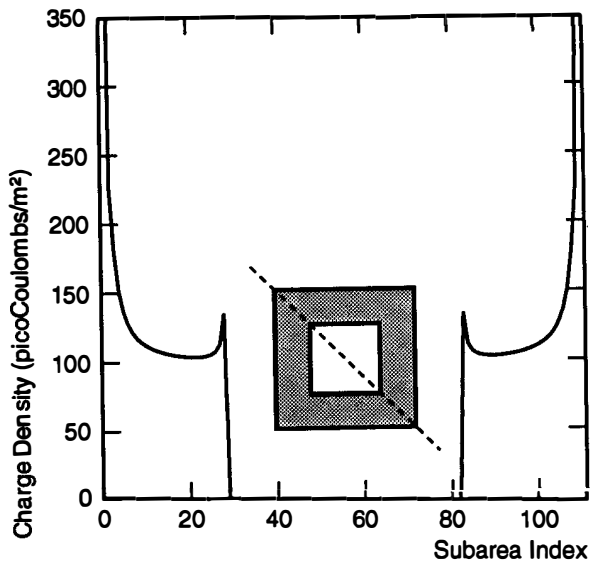
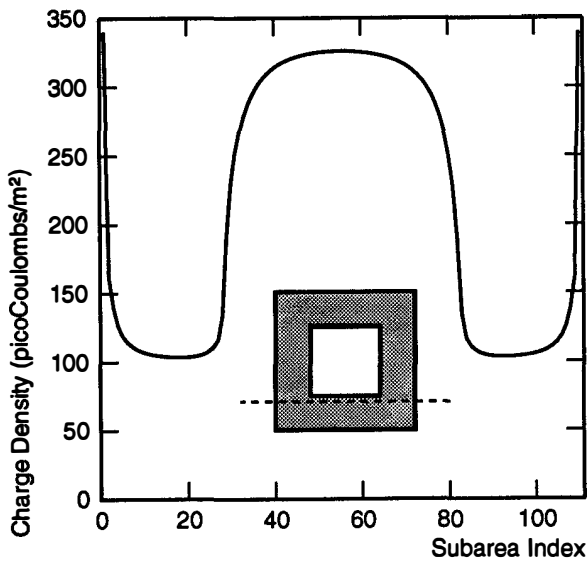
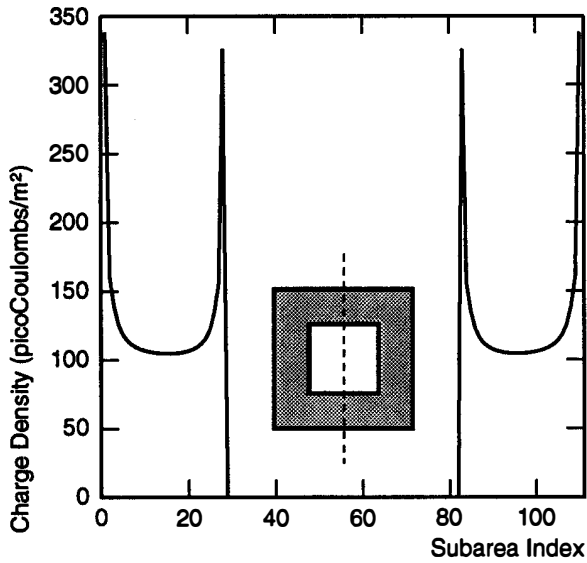
where  $A$  is the plate area,  $P$  is the perimeter length,  $E$  is the number of exterior corners, and  $I$  is the number of interior corners. The first term can be identified with the ideal capacitance expression,  $C_{area} = \epsilon / g$ . The second term can be obtained from the known capacitance of infinite parallel plates per unit length:

$$C_{Palmer} = W C_{area} + 2 C_{perim} \quad (8)$$

For hand calculations, the approximate formula of Love (Eq. 2) can also be used. Neglecting further terms in the geometric expansion, we can compare capacitances calculated using this approach with the results of MSA for parallel plate capacitors with a variety of shapes. Summaries of the results are presented in Tables 1 and 2. The simple geometric approach of Eq. 8 shows excellent agreement over a wide range of plate shapes and plate gaps.

Gap	2D Exact	3D Geometric approximation	3D MSA 7200 subareas	3D MSA extrapolated	Error
0.1	103.414	118.29	114.461	115.53	2.4%
0.2	57.470	70.67	68.089	68.71	2.9%
0.3	41.787	54.06	52.230	52.69	2.6%
0.4	33.785	45.43	44.163	44.54	2.0%
0.5	28.895	40.08	39.267	39.59	1.2%
0.6	25.581	36.40	35.979	36.27	0.4%
0.7	23.176	33.70	33.621	33.89	-0.6%
0.8	21.346	31.62	31.850	32.10	-1.5%
0.9	19.903	29.97	30.473	30.70	-2.4%
1.0	18.734	28.61	29.375	29.59	-3.3%

Table 1. Square 1x1 parallel plate capacitor calculations for a variety of plate gaps. For plate dimensions in meters, the capacitance values are in picoFarads. MSA linear extrapolation was based on 3200 and 7200 subarea calculations. The 2D Exact calculation uses Eq. 1 for infinite parallel plates of width 1 and corresponding length.



Figures 5. This figure shows the charge density across one of the two square plates with a hole in it for three different cuts, as indicated.

Shape	3D Geometric approximation	3D MSA	3D MSA extrapolated	Error
1x1 square	118.3	114.24	115.5	2.4%
3x1 rectangle	325.6	319.25	322.5	1.0%
9x1 rectangle	946.8	933.98	941.7	0.5%
2x2 L-shape	325.6	317.13	321.4	1.3%
3x3, 1x1 hole	828.3	812.38	821.3	0.9%

Table 2. Parallel plate capacitor calculations for a variety of plate shapes with plate gap 0.1. For plate dimensions in meters, the capacitance values are in picoFarads. MSA calculations used 5000 subareas and linear extrapolation between the 3200 and 5000 subarea calculations, except for the square with a hole which used 5184 and 7744 subareas.

We have also made comparisons in Figure 1 with the MSA results of Reitan [4] that used a 6x6 discretization and with the approximate equation of Love that is valid for  $g/w \ll 1$ . Finally, we made several runs using FASTCAP [5]. For beams with length 100 and width 1, the FASTCAP results were consistently low by a large margin. FASTCAP runs for a variety of squares also gave results that were also consistently low. For example, our result from a FASTCAP run for a 1x1 square with a gap of 0.1 agreed with the FASTCAP User's Guide [5], but was low by 10% compared to our 3D MSA runs.

### CONCLUSION

Geometric-based electrostatic calculations provide a simple and rapid means of calculating capacitances for MEMS, at least for the simple flat geometries discussed in this paper. Future research should be able to extend these concepts to include more realistic MEMS geometries that include thicknesses and rounded corners.

For self-consistent coupled electrostatic and mechanical modeling, the approximate expressions for capacitance presented here can be used in at least two ways. For initial exploration of system behavior, they provide a much quicker solution than a detailed capacitance calculation. For more accurate calculations they can be used in the initial iterations of the coupled system, switching to a more detailed calculation when the system is close to convergence.

### ACKNOWLEDGMENTS

This work was supported by the Advanced Research Projects Agency under Contract # J-FBI-92-149.

### REFERENCES

- [1] J. R. Gilbert, P. M. Osterberg, R. M. Harris, D. O. Ouma, X. Cai, A. Pfajfer, J. White, and S. D. Senturia, Sixth IEEE Workshop on MicroElectro Mechanical Systems, Fort Lauderdale, FL, February 1993.
- [2] H. B. Palmer, *Electrical Engineering* 56, 363 (1937).
- [3] A. E. H. Love, *Proc. London Mathematical Society*, p. 337, 1923.
- [4] D. K. Reitan, *J. Appl. Phys.* 30, 172 (1959).
- [5] K. Nabors, S. Kim, J. White, and S. Senturia, "FASTCAP User's Guide," Research Laboratory of Electronics, EECS Dept., MIT, Cambridge, MA.
- [6] S. Cray, O. Juma, and Y. Zhang, *Proc. Transducers '91*, San Francisco, CA, September 1991.

# Silicon Wafer Bonding for Micromechanical Devices

Martin A. Schmidt  
Microsystems Technology Laboratories  
Department of Electrical Engineering and Computer Science  
Massachusetts Institute of Technology  
Cambridge, MA 02139

## ABSTRACT

The process for bonding silicon wafers together at high temperature is reviewed. Specific details of the bonding process as they pertain to the formation of micromechanical devices are described. Methods of characterization of the bonded wafers are discussed.

## INTRODUCTION

Micromachining encompasses a broad range of technologies anchored in the core technology of microlithographic pattern transfer. A large fraction of the micromachining technologies are specific to the silicon material system principally due to the origins of the field, namely the silicon integrated circuit industry. In the silicon micromachining field, there have been two dominant fabrication methods, broadly classified as bulk micromachining (etching deep features into a wafer) and surface micromachining (depositing, patterning, and selective etching of films on a wafer). Fundamentally, both of these techniques rely on some form of etching or material removal. More recently, techniques have emerged for bonding or fusing of silicon wafers. As the bulk or surface micromachining technologies might be compared to material removal processes in conventional machining (end-milling, drilling), the wafer bonding processes are analogous to welding processes in conventional machining.

There is some potential for confusion in discussing wafer bonding processes since a wide range of processes exist. For example, the silicon-glass anodic bond is routinely used in many commercially available sensors. Additionally, low-temperature metal eutectic bonds are often used. While these bonds are quite useful in low temperature, back-end processes, they generally are not applicable as high temperature stable bonds. Thus the distinguishing feature between these methods and the bonding that we will discuss in this paper will be the ability of the bond to withstand high temperature processing without the need for intermediate layers, externally-applied pressure, or electrostatic fields to assist the bond. This bond can be performed between nearly any smooth surfaces [1-3], but generally, we will restrict our discussion to bonding of silicon wafers with or without silicon dioxide.

Interest in the process of wafer bonding as defined in the preceding paragraph was generated by the publications in 1985-86 of Lasky [4] and Shimbo [5]. Subsequently, a number of investigators have explored the use of this process for fabrication of electronic devices (SOI MOSFETs, Power Devices) [1-6]. Several commercially available electronic products exist today which employ silicon wafer bonding. Additionally, a number of investigators considered the application of wafer bonding to sensor and actuator structures. Two of the first sensors to be fabricated by wafer bonding were reported at the 1988 Solid-State Sensor and Actuator Workshop in Hilton Head [7,8]. These included a pressure sensor and an accelerometer. Since that time, a significant number of sensors and actuators have been reported which employ silicon wafer bonding. Several micromachined sensor products which use silicon wafer bonding are now available commercially.

## THE BONDING PROCESS

Extensive review articles have been written on the wafer bonding process, particularly as it pertains to electronic device fabrication (1-3). This section will simply summarize the major points of the process for the bonding of silicon or silicon dioxide surfaces. The silicon wafer bonding process consists of three basic steps: surface preparation, contacting, and annealing. All of the process steps are

conducted in a cleanroom environment. The surface preparation step involves cleaning the mirror-smooth, flat surfaces of two wafers to form a hydrated surface. Following this preparation, the wafers are contacted in a clean environment by gently pressing the two surfaces together at one point. The surfaces come into contact at this point and are bound by a surface attraction of the two hydrated surfaces. A contact wave is initiated at this point and sweeps across the wafer surfaces, bringing them into intimate contact over the entire surface. The exact origin of the attractive force is not universally agreed upon [3], and depends to a certain extent on whether the bond is Si-Si or Si-SiO<sub>2</sub>. The most common assumption is that a bond is formed between -OH groups on the opposing surfaces. The final step in the bonding process is a high temperature anneal of the contacted pair at temperatures between 800-1200C. While the room temperature contacted samples are well adhered, this anneal generally increases the bond strength by more than an order of magnitude. Measurements of the bond strength as a function of anneal temperature indicate three distinct regions. The first region, for anneal temperatures less than 300C, exhibits a relatively constant bond strength equal to the bond strength of the wafers prior to anneal. At temperatures greater than 300C, the bond strength increases and then levels out. It is presumed that a Si-O-Si bridging bond is formed between the surfaces and a water molecule is liberated. At temperatures greater than 800C, the bond strength begins to increase again. In this third region it has been suggested that surfaces can more easily deform (oxide flow) and trapped water may oxidize surfaces bringing them into better contact. At temperatures of 1000C or greater, the bond strength is in the range of the strength of the silicon crystal itself.

## WAFER BONDING CHARACTERIZATION

Several non-destructive and destructive techniques exist for mechanical characterization of the bonding process. These techniques are bond imaging, cross-sectional analysis, and bond strength measurement. The imaging methods are non-destructive and can be used as in-process monitors, while the cross-sectional analysis and bond strength measurements are destructive and require control wafers for characterization.

The three dominant methods for imaging a bonded pair of silicon wafers are infrared transmission, ultrasonic, and X-ray topography. Examples of the images obtained by these methods for a poorly bonded 4" silicon wafer pair are shown in Figure 1. A simplified schematic of an infrared imaging system is shown in Figure 2. It consists of an IR source (typically an incandescent light bulb), and an IR-sensitive camera. A silicon CCD camera has sufficient sensitivity in the near-IR range that it can be used when outfitted with a filter for visible light. The bonded wafer pair is located between the source and camera. Any imperfection in the bond shows up as changes in contrast in the IR image. Large un-bonded regions ('voids') appear with a characteristic 'Newton's Rings' pattern. This imaging method generally can not image voids with a separation of surfaces less than one quarter of the wavelength of the IR source. Based on a typical particle void, this translates to a spatial resolution of several millimeter. Figure 1 clearly illustrates voids not present in the IR image which do show up in the other methods. Also, this technique works for silicon wafers of moderate doping level with smooth surfaces. Highly doped layers, IR absorbing films, or rough surfaces (backside of wafer), can limit the image quality. In spite of this resolution limit, the IR method has the advantage of being simple, fast and inexpensive. It can be used directly in the cleanroom to image the wafers before and after anneal. The other two imaging methods offer higher resolution at the expense of speed, cost and incompatibility with cleanroom processing.

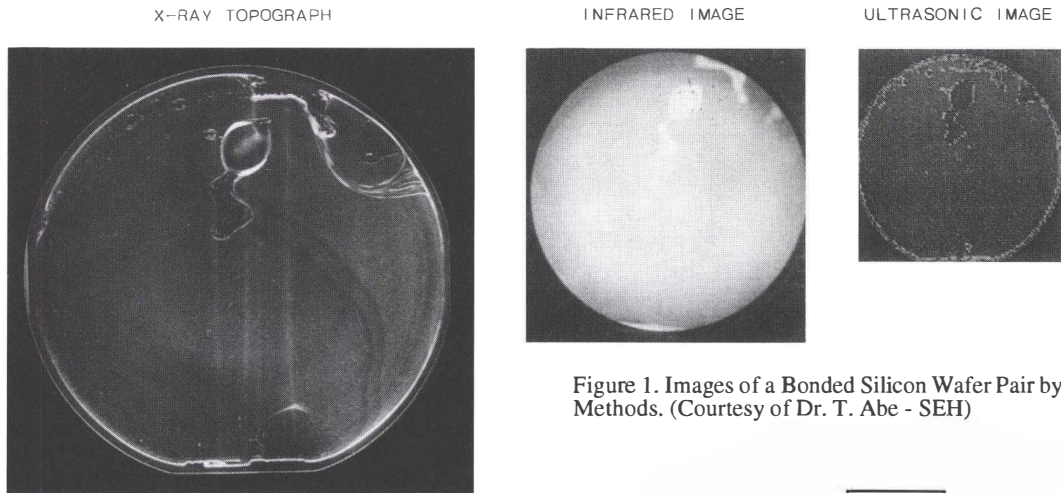


Figure 1. Images of a Bonded Silicon Wafer Pair by Several Methods. (Courtesy of Dr. T. Abe - SEH)

Cross-sectional analysis can be performed at the bonded interface by cleaving the sample. SEM and TEM techniques have been used to image the bonded interface at a submicron scale. These studies have helped to understand the composition of the bonded interface [3]. Additionally, it is possible to gain a great deal of information about the bonded interface by simply defect etching the cross-sectioned sample. Several groups have demonstrated the benefit of this approach, particularly for visualization of voids on the order of tens of microns ('microvoids') [9].

The bond strength has been characterized by a number of techniques. Figure 3 highlights the most common techniques. Pressure burst tests can often yield a number which has engineering significance in the design of sensors, but yields little information about the detailed nature of the bond due to the complicated loading of the interface. A tensile/shear test sample gives better information on the bonded interface, but is often limited by difficulties in loading and sample handling [10]. The knife-edge technique has the advantage of creating a very well defined loading on the bonded interface. A blade of defined thickness is inserted between the bonded pair in a region where a crack has been initiated. Using IR imaging methods, the length of the crack is measured, from which the surface energy can be inferred through a knowledge of the sample and blade thicknesses and the elastic properties of the wafer [11]. This method has been used with very good success. Unfortunately, the surface energy is forth power dependent on the crack length, and thus uncertainties in the crack length produce large uncertainties in the extracted surface energy. Other methods based on patterned samples have been proposed to eliminate this problem [12].

### DETAILED PROCESS ISSUES

A number of factors contribute to the success of the wafer bonding process. Some of the more important details as they pertain to application in micromechanics are summarized in this section.

#### Starting Material and Surface Preparation

The large scale and small scale roughness of the wafer surface is very important to the success of a wafer bonding process. It is difficult to establish strict requirements on the needed wafer bow and microscale surface roughness since the surface preparation and contacting methods play a large roll. Generally, people have found that VLSI grade wafers tend to be acceptable for bonding if their microscale roughness is less than 5 Å (measured optically or by STM) and the bow is of the order of 5 μm (on a 4" wafer). Abe and Masara have done careful studies of the influence of roughness [13,14]. Protrusions and particles are sources of problems. Protrusions might be present in deposited films (epi-spikes) or be formed by processes such as oxidation of etched cavities prior to bonding [15]. Wafer polishing can be employed to minimize this problem.

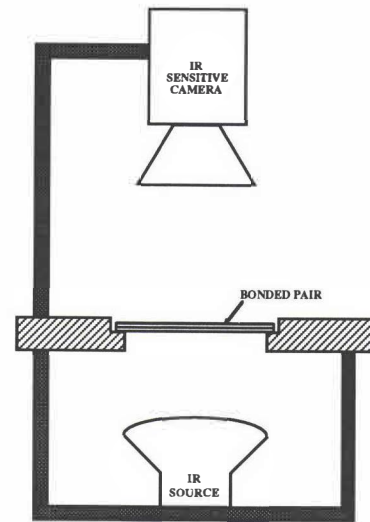


Figure 2. IR Imaging System

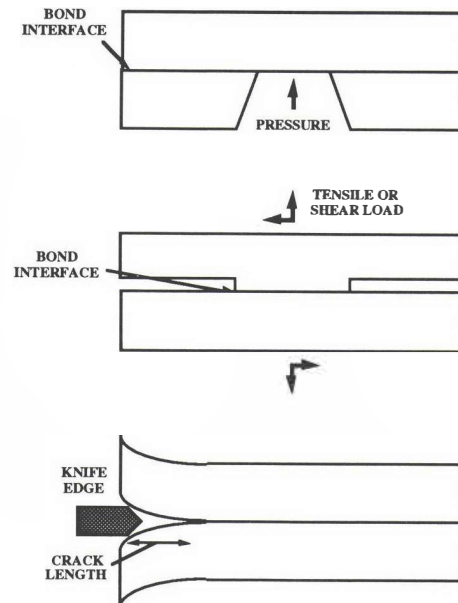


Figure 3. Examples of three bond strength measurements.

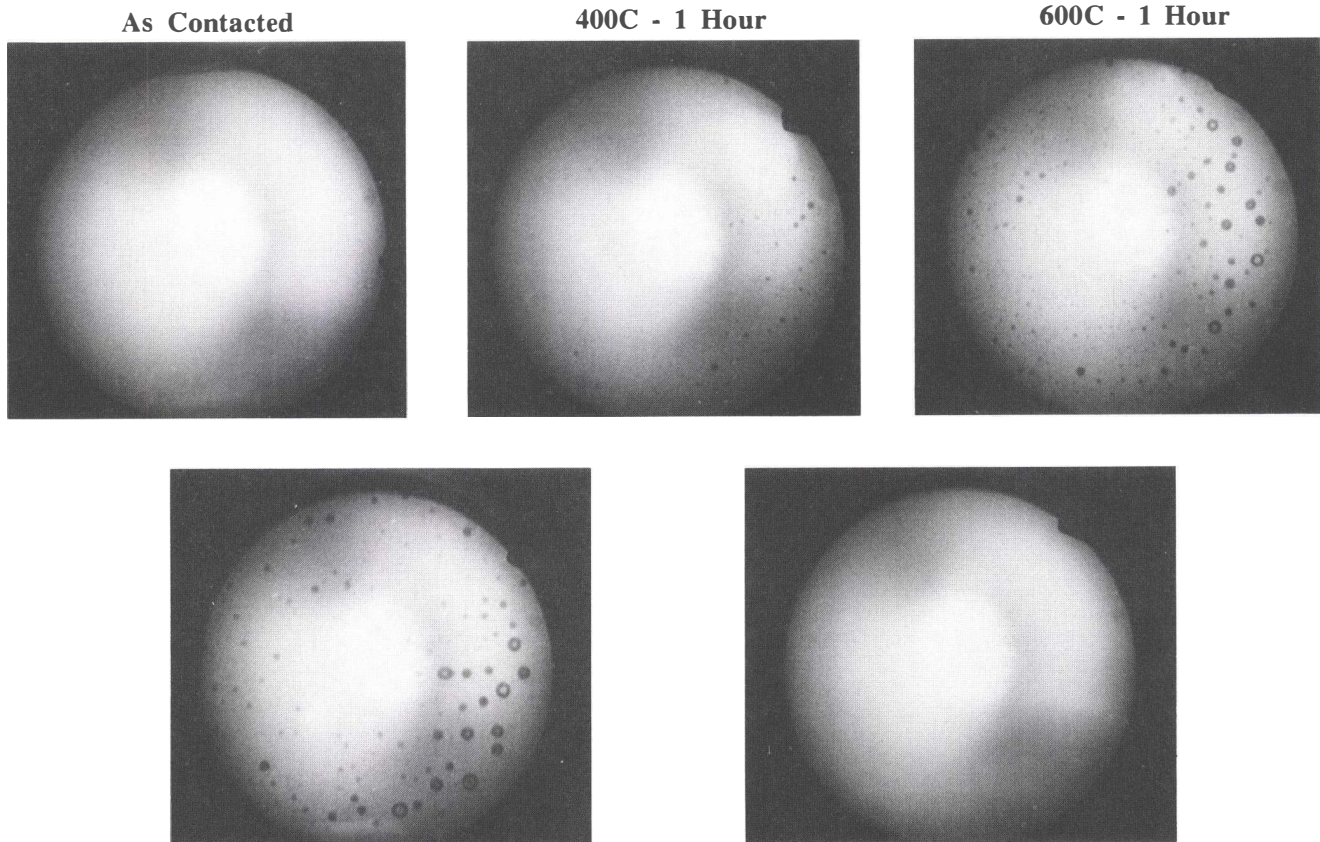


Figure 4. IR image of intrinsic voids formed in a silicon-silicon wafer bonded pair as a function of anneal temperature.

Generally, it is believed that the surface preparation should include a vigorous hydration of the surface to make it hydrophilic, followed by a de-ionized water rinse and spin dry. Processes ranging from simple water rinses to hot acid dips have been used for the hydration. However, people have also reported that HF dips, which produce a hydrophobic surface, can also be used. While the hydrophobic wafers do not contact as easily as hydrophilic wafers, there is some evidence that the final bond is better [3]. A major concern in surface preparation is hydrocarbon contamination. Exposure to plastic wafer holders has been shown to cause hydrocarbon contamination of the surfaces. These contaminants are not readily removed by standard wafer cleans, and can cause complications in the bonding as will be discussed later. Various groups have tried methods such as high temperature bakes and oxidation followed by oxide strips prior to the hydration step to minimize this problem.

#### Contacting

The contacting is performed immediately after the surface preparation to minimize contamination. This is done in a cleanroom, although some work has demonstrated the ability to do the bonding in a 'micro-cleanroom' [16] and under water [17]. The contact should be initiated at one point and allowed to propagate across the wafer surfaces. Contacting at multiple points can cause air pockets to be trapped between the wafers. As discussed later, in some instances it is desirable to contact the wafers in an ambient other than air, such as oxygen or vacuum. There is considerable interest in aligned bonding of wafers, and a variety of schemes have been proposed. These include the use of specialized alignment tools or mechanical fixtures which align to previously etched features in the wafer. Two common methods of mechanical alignment are to use optical fibers in v-grooves etched in the edge of the wafers, or to use reference flats on the wafers.

#### Annealing

In general, the highest possible anneal temperature should be used to get the best quality bond. There is very little evidence to suggest that the ambient used during the anneal has an impact on the bond quality. When processing wafers with cavities, it is important to slowly ramp the annealing temperature. Rapid temperature rises can cause the gas in the cavity to expand, building up a pressure which can separate the wafers before the bond has time to anneal. All evidence suggest that the bonding is generally complete within minutes of reaching the anneal temperature, although there is evidence that some incremental increase in bonding occurs over much longer times.

#### Structure of the Bonded Interface

When bonding silicon dioxide surfaces either to silicon or silicon dioxide, the bonded interface appears, based on TEM, to be nearly identical to a bulk silicon dioxide film or a thermally-grown silicon/silicon dioxide interface. Occasionally, there are small (micron-scale) voids or occlusions present. In contrast, the structure of the silicon-silicon bonded interface is very sensitive to surface preparation (hydrophobic/hydrophilic), the crystal alignment of the wafer, and the type of crystal (czochralski or float-zone). Bengtsson provides a detailed summary of the observations of this interface [3]. For hydrophilic surfaces, an interfacial  $\text{SiO}_x$  layer is observed (5-40 Å thick), but this layer can breakdown or form spheroids of  $\text{SiO}_x$  under conditions of perfect alignment of crystal planes. Preliminary evidence suggests that the hydrophobic surfaces do not have as much of an interfacial layer, which would be consistent with the removal of the native oxide layer during the HF dip used to create the hydrophobic surface.

## Voids

When contacting and annealing a wafer pair, voids are sometimes observed upon inspection. These voids are generally lumped in two categories; extrinsic and intrinsic. The extrinsic voids are those created by particles, protrusions on the wafers surface, or trapped air. These voids are usually observed on contact and do not change significantly during annealing. Figure 1 shows a wafer with various forms of extrinsic voids. Intrinsic voids are voids which are generated during the anneal cycle. Figure 4 is a series of IR images of a silicon-silicon bonded pair annealed at increasing temperatures. After contact, the wafer pair appears void-free. As the anneal temperature is increased, voids begin to appear above 400C, and subsequently disappear above 900C. The voids are usually only seen when bonding silicon to silicon without an intermediate oxide and they are often attributed to hydrocarbon contamination, although there is not a consensus on their origin. It has been observed that cavities in the wafers can serve to 'getter' these microvoids, thus minimizing the problem [18].

## GENERALIZED BONDING

While we have exclusively discussed bonding of silicon wafers, the same basic process steps can be applied to bonding a variety of materials. Quartz wafers can be bonded by this method [19]. Examples of bonding of dissimilar materials include the bonding of GaAs to Si [20] and Si to glass [21]. Provided the surfaces are mirror smooth and can be hydrated, the bonding proceeds in a fashion identical to Si-Si bonding. When bonding dissimilar materials, the major complication is stresses generated during the high temperature anneal due to differences in thermal coefficient of expansion of the two materials [21].

Bonding has also been demonstrated for samples with deposited films. Examples of bonding to silicon wafers with deposited polysilicon or silicon nitride have been reported [22-24]. Polishing is often needed to establish the necessary level of roughness.

## BONDING WITH SEALED CAVITIES

Nearly all micromechanical applications of silicon wafer bonding require bonding of wafers with cavities etched in one or the other wafer, thus forming sealed cavities in the wafer after the bond. The nature of gases that exist in the cavities can be very important particularly in subsequent high temperature bonding. It has been shown that when wafers are contacted in air, and subsequently annealed at high temperature, the oxygen in the cavity can react with the silicon surface and create a partial vacuum (Figure 5) [25]. When the oxygen is completely consumed (for shallow cavities), the resultant pressure inside the cavity is 0.8 atm, consistent with the consumption of the 20% oxygen in air. These results indicate that the bonding process forms rapidly enough that it can trap gasses in the cavities. Under high temperatures, the residual gases trapped in the cavities can induce plastic deformation in thin silicon membranes as the gases expand [25]. This problem can be reduced or eliminated by controlling the ambient under which the wafers are contacted. We have demonstrated that the pressure inside the cavity can be reduced by bonding the wafers in an oxygen rich ambient [26]. Alternatively, it is possible to bond the wafers in a vacuum.

## THINNING METHODS

Controlled wafer thinning is often a necessary process following the wafer bonding. This is particularly true in microelectronic applications such as SOI, but also in micromechanics. The two methods usually applied are precision grinding/polishing and chemical etching with etch-stops. Most of these techniques have been very effectively summarized in review articles on wafer bonding [1,2]. The precision grinding and polishing yield absolute

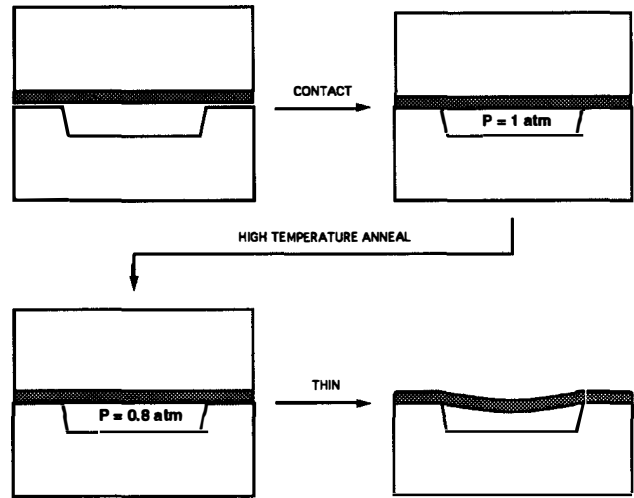


Figure 5. Sealed Cavity Formation.

thickness control between 0.25-1.0  $\mu\text{m}$ . Chemical etch-stops such as the  $p^{++}$  etch-stop have also been used with good success. However, several complications result in using this process. First, the surface roughness of a  $p^{++}$  layer is sometimes too great to achieve good bonding. Second, the residual stress in the layer can produce a large wafer bow which prevents bonding. Lastly, the  $p^{++}$  layer is formed prior to bonding, and thus the bonding temperature and time must be minimized to eliminate diffusion of the layer. Counter doping the  $p^{++}$  with Ge to reduce the stress in the material can eliminate some of these problems. Electrochemical etch-stop methods have been used successfully in a number of wafer bonding applications [27]. One disadvantage of this etch-stop is that it requires complicated fixturing.

## CONCLUSIONS

The wafer bonding process is an extremely powerful process for micromechanical devices. It complements other micromachining techniques by permitting the 'welding' of silicon wafers. This paper reviewed the methods for silicon wafer bonding. A detailed description of the process of wafer bonding has been described. Issues which impact the success of the wafer bonding process were identified. While a better understanding of the process is still possible, the bonding process is readily applicable in a broad range of devices.

## ACKNOWLEDGMENTS

The wafer bonding work at MIT has been sponsored by a number of organizations including SRC (Contract 93-SC-309), Delco Electronics, 3M, Bosch, ARPA (Contract J-FBI-92-196), Draper, and the NSF Presidential Young Investigator Award. Many of the ideas expressed in this paper are the result of extensive discussions with students and staff at MIT who worked on wafer bonding. Those persons include Errol Arkilic, Chris Bang, Mousumi Bhat, John Gilbert, Howard Goldberg, Peter Gravesen, Charles Hsu, Michael Huff, Vincent McNeil, Kay-Yip Ng, Mitch Novack, Lalitha Parameswaran, Javad Shajii, Daniel Sobek, Simon S. Wang, and Albert Young.

## REFERENCES

- [1] J. Haisma, G.A.C.M. Spierings, U.K.P. Biermann, and J.A. Pals, "Silicon-on-Insulator Wafer Bonding-Wafer Thinning Technological Evaluations," *Japanese Journal of Applied Physics*, Vol. 28, No. 8, p.1426, August 1989.
- [2] W.P. Maszara, "Silicon-on-Insulator by Wafer Bonding: A Review," *Journal of the Electrochemical Society*, Vol. 138, No. 1, p.341, January 1991.
- [3] S. Bengtsson, "Semiconductor Wafer Bonding: A Review of Interfacial Properties and Applications," *Journal of Electronic Materials*, Vol. 21, No. 8, p.841, August 1992.
- [4] J.B. Lasky, S.R. Stiffler, F.R. White, and J.R. Abernathy, "Silicon-on-Insulator (SOI) by Bonding and Etch-Back," *Technical Digest, 1985 IEEE International Electron Devices Meeting*, p.684, December 1985.
- [5] M. Shimbo, K. Furukawa, K. Fukuda, and T. Tanzawa, "Silicon-to-Silicon Direct Bonding Method," *Journal of Applied Physics*, Vol. 60, No. 8, p.2987, October 1986.
- [6] see Proceedings of the First and Second International Symposia on Semiconductor Wafer Bonding: Science, Technology, and Applications, The Electrochemical Society.
- [7] K. Petersen, P. Barth, J. Poydock, J. Mallon, and J. Bryzek, "Silicon Fusion Bonding for Pressure Sensors," *Technical Digest, IEEE Solid-State Sensor and Actuator Workshop*, Hilton Head, S.C., p. 144, 1988.
- [8] P. Barth, F. Pourahmadi, R. Mayer, J. Poydock, and K. Petersen, "A Monolithic Silicon Accelerometer with Integral Air Damping and Over-range Protection," *Technical Digest, IEEE Solid-State Sensor and Actuator Workshop*, Hilton Head, S.C., p. 35, 1988.
- [9] R.D. Horning, and R.R. Martin, "Wafer-to-Wafer Bond Characterization by Defect Decoration Etching," *Proceedings of the Second International Symposia on Semiconductor Wafer Bonding: Science, Technology, and Applications*, Vol. 93-29, p.199, The Electrochemical Society, 1993.
- [10] S.N. Farens, B.E. Roberds, J.K. Smith, and C.E. Hunt, "Analysis of Bond Characteristics in Si Direct-Bonded Materials," *Proceedings of the Second International Symposia on Semiconductor Wafer Bonding: Science, Technology, and Applications*, Vol. 93-29, p.81, The Electrochemical Society, 1993.
- [11] W.P. Maszara, G. Goetz, A. Caviglia, and J.B. McKitterick, "Bonding of Silicon Wafers for Silicon-on-Insulator," *Journal of Applied Physics*, Vol. 64, No. 10, p.4943, Nov. 1988.
- [12] R. D. Horning, D.W. Burns, and A.I. Akinwande, "A Test Structure for Bond Strength Measurement and Process Diagnostics," *Proceedings of the First International Symposia on Semiconductor Wafer Bonding: Science, Technology, and Applications*, Vol. 92-7, p.386, The Electrochemical Society, 1992.
- [13] T. Abe, M. Nakano, and T. Itoh, "Silicon Wafer Bonding Process Technology for SOI Structures," *Proceedings of the 4th International Symposium on Silicon-on-Insulator Technology and Devices*, p.61, The Electrochemical Society, 1990.
- [14] W. Maszara, B-L. Jiang, A. Yamada, G.A. Rozgonyi, H. Baumgart, and A.J.R. de Kock, "Role of Surface Morphology in Wafer Bonding," *Journal of Applied Physics*, Vol. 69, No. 1, p. 257, January 1991.
- [15] M.A. Huff, and M.A. Schmidt, "Fabrication, Packaging, and Testing of a Wafer-Bonded Microvalve," *IEEE Solid-State Sensor and Actuator Workshop, Technical Digest*, Hilton Head Island, S.C., p. 194, 1992.
- [16] R. Stengl, K.-Y. Ahn, and U. Gösele, "Bubble-Free Silicon Wafer Bonding in a Non-Cleanroom Environment," *Japanese Journal of Applied Physics*, Vol. 27, No. 12, p.L2364, 1988.
- [17] C. Parkes, E. Murray, H.S. Gamble, B.M. Armstrong, S.J.N. Mitchell, and G.A. Armstrong, "Characterization of Electronic Devices Employing Silicon Bonding Technology," *Proceedings of the First International Symposia on Semiconductor Wafer Bonding: Science, Technology, and Applications*, Vol. 92-7, p.321, The Electrochemical Society, 1992.
- [18] W. Kissinger and G. Kissinger, "Microstructures for Perfect Wafer Bonding in Different Temperature Ranges," *Proceedings of the First International Symposia on Semiconductor Wafer Bonding: Science, Technology, and Applications*, Vol. 92-7, p.73, The Electrochemical Society, 1992.
- [19] D. Sobek, S.D. Senturia, and M.L. Gray, "Microfabricated Fused Silica Flow Chambers for Flow Cytometry," *Solid-State Sensor and Actuator Workshop, Technical Digest*, Hilton Head Island, S.C., 1994.
- [20] G.G. Goetz, "Generalized Reaction Bonding," *Proceedings of the First International Symposia on Semiconductor Wafer Bonding: Science, Technology, and Applications*, Vol. 92-7, p.65, The Electrochemical Society, 1992.
- [21] T. Abe, K. Ohki, K. Sunakawa, K. Yoshizawa, S. Tanaka, and Y. Nakazato, "Bonded SOI Wafers with Various Substrates for IC Fabrication," *Proceedings of the Second International Symposia on Semiconductor Wafer Bonding: Science, Technology, and Applications*, Vol. 93-29, p.32, The Electrochemical Society, 1993.
- [22] W.G. Easter, G.T. Jones, R.H. Shanaman, and C.A. Goodwin, "Polysilicon to Silicon Bonding in Laminated Dielectrically Isolated Wafers," *Proceedings of the First International Symposia on Semiconductor Wafer Bonding: Science, Technology, and Applications*, Vol. 92-7, p.223, The Electrochemical Society, 1992.
- [23] V.M. McNeil, M.J. Novack, and M.A. Schmidt, "Design and Fabrication of Thin Film Microaccelerometers using Wafer-Bonding", *Technical Digest, 7th International Conference on Solid-State Sensors and Actuators*, Yokohama, Japan, pp. 822-825, June 1993.
- [24] C.A. Bang, J.P. Rice, M.I. Flik, D.A. Rudman, and M.A. Schmidt, "A Silicon Wafer Bonding Approach for High-Temperature Superconducting Bolometers", *IEEE Journal of Microelectromechanical Systems*, December 1993.
- [25] M.A. Huff, A.D. Nikolich, and M.A. Schmidt, "Design of Sealed Cavity Microstructures Formed by Silicon Wafer Bonding", *IEEE Journal of Microelectromechanical Systems*, Vol. 2, No. 2, 74-81, June 1993.
- [26] L. Parameswaran, V.M. McNeil, M.A. Huff, and M.A. Schmidt, "Sealed-Cavity Microstructure using Wafer Bonding Technology", *Technical Digest, Transducers '93, 7th International Conference on Solid-State Sensors and Actuators*, Yokohama, Japan, pp.274-277, June 1993.
- [27] V.M. McNeil, S. S. Wang, and M. A. Schmidt, "Issues Regarding the Application of the Electrochemical Etch-Stop Technique to Fabricate Microstructures using Wafer Bonding," *Proceedings of the First International Symposia on Semiconductor Wafer Bonding: Science, Technology, and Applications*, Vol. 92-7, p.180, The Electrochemical Society, 1992.

# Milli-Scale Polysilicon Structures

Chris Keller<sup>†</sup>, Mauro Ferrari<sup>\*</sup>

Department of Materials Science and Mineral Engineering<sup>†\*</sup>  
Department of Civil Engineering<sup>\*</sup>  
University of California at Berkeley  
Berkeley, California 94720

## ABSTRACT

Polysilicon machines composed of beams up to 110  $\mu\text{m}$  high, 18  $\mu\text{m}$  wide and 1000  $\mu\text{m}$  long have been fabricated by CVD molding. Silicon wafers are patterned by etching trenches up to 110  $\mu\text{m}$  deep to form molds of arbitrary shape. Hexagonal honeycomb geometry is used to form 3 dimensionally rigid parts. These milli-scale structures have been integrated with surface silicon devices. After etch release, the molded parts are removed from the mold, and the mold wafers are reused to fabricate more parts. This technology has been applied to produce (1) membrane particle filters with 50  $\mu\text{m}$  tall stiffening ribs, (2) 3 mm diameter, 45 to 65  $\mu\text{m}$  thick, micro tensile testing machines for transmission electron microscopy, and (3) hollow tubing, with a height to wall thickness ratio of 105, suitable for conducting fluids.

## INTRODUCTION

High aspect ratio structures that would normally be associated with LIGA can now be made of CVD polysilicon. We call this **HEXSIL** the **HEX**agonal honeycomb is an efficient geometry for making rigid structures with thin films, and **SIL**icon allows conventional surface silicon micromachines and CMOS electronics to be fabricated in subsequent overlying layers. There has long been a need to make CVD structures of arbitrary shape with dimensions perpendicular to the plane of the wafer greater than 20  $\mu\text{m}$ . The CVD process can only deposit thin films on surfaces. If those surfaces are the opposing faces of a deep narrow trench, the growing films will merge to form a solid beam. The thickness of the beam will be twice the thickness of the deposited film. A groove remains in the surface over the center of the trench where the films grew together (this can be smoothed by continuing to deposit beyond the time at which the sidewalls merge).

Figure 1 shows the basic fabrication procedure. The first step is to etch trenches in the silicon wafer. The depth of the trenches is equal to the desired height of the beams. The width of the trenches is equal to the width of the beams plus twice the thickness of the sacrificial oxide that is deposited in step 2. The trench volume that remains after oxide deposition, is filled with polysilicon (POLY 1) in step 3. The surface layer of polysilicon can be patterned if desired, but the grooves centered over the trenches make photolithography difficult. This can be remedied by lapping and polishing (step 4). A lapped and polished surface at this stage can be seen in figure 5.

The desired thickness of surface polysilicon (POLY 2) can now be deposited and patterned to make surface structures which are anchored to the HEXSIL foundation (step 5). In step 6 the sacrificial oxide is dissolved in 49% HF with about 0.1% triton X-100 surfactant. The parts are removed from the wafer, and the wafer is returned to step 2 for another mold cycle. Since the same wafer can be used to mold parts many times, a wide variety of silicon machining methods for trench forming would be economically viable, and several different levels of trench depth could be machined in the same wafer.

The central features of this work are:

### 1. Mass production of CVD parts via reusable molds

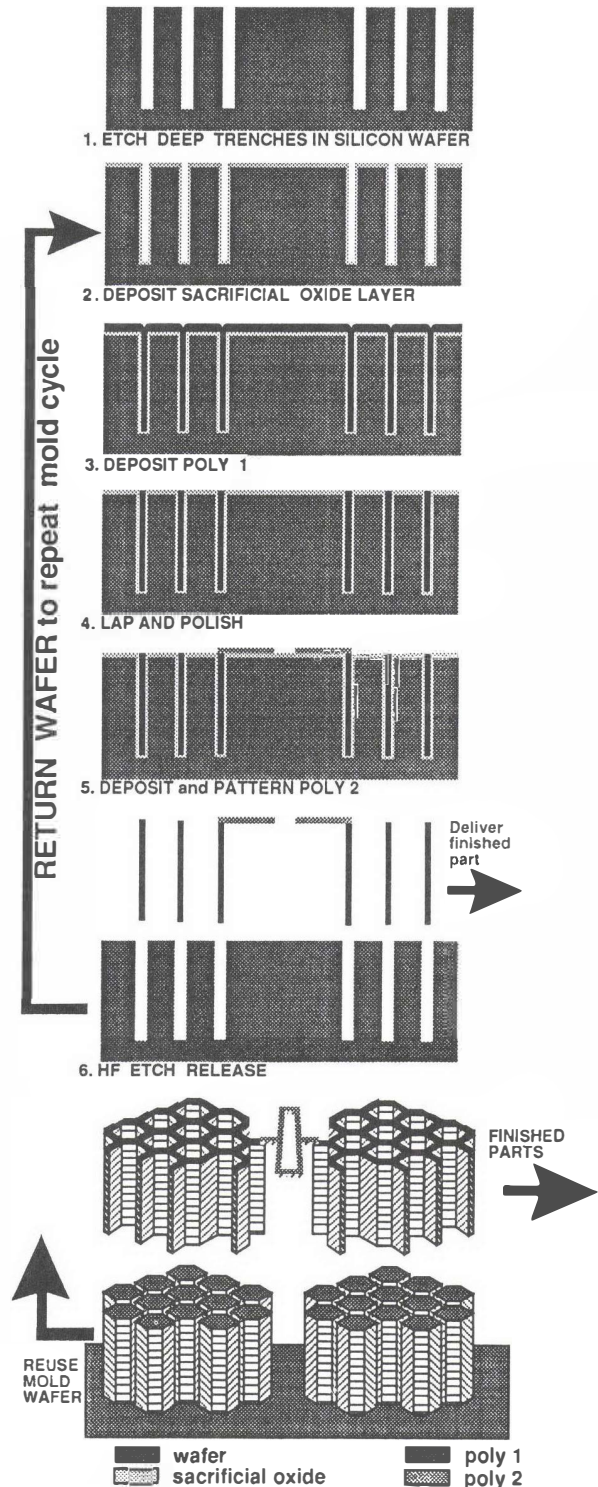


FIGURE 1. Steps in the molding cycle. Note that the mold wafer is in an "infinite loop".

2. Integration of size ranges : milli-scale structures carrying micro-scale devices which in turn support nano-scale features
3. The potential for adding electronics that conform to the molded structure in both size and mass.

Figure 2 shows a membrane particle filter (patent applied for) with nano-scale ( $<100 \text{ \AA}$ ) pore construction (not visible) interior to the  $6 \mu\text{m}$  thick surface silicon which is integrated with milli-scale support ribs  $48 \mu\text{m}$  high,  $9 \mu\text{m}$  wide, and  $500 \mu\text{m}$  long. Figure 3 shows a cross section of a stiffening rib of the filter. Lapping (processing step 4) was not done in this case. Figure 4 shows the central part of a microtensile testing machine (patent applied for) for use in the transmission electron microscope (TEM) that consists of rigid honeycomb levers connected by flexures. It is actuated by in-plane thermal expansion from resistive heating of its  $3 \text{ mm}$  diameter  $45 \mu\text{m}$  thick support frame (see also figure 14).

This work extends the range of what is achievable by means of sidewall processing strategies. Previous workers have used sidewall structures to make micro-scale devices (ref 1). Micro-scale hollow beams have also been made (ref 2). These cannot handle milli-scale forces that are of interest in many applications. Micro-scale structures have been plasma etched directly from the wafer (ref 3), but depth has been limited to less than  $20 \mu\text{m}$ . Milli-scale structures have been made by wet etching silicon, but designs are highly constrained by crystallographic planes (ref 4). LIGA (refs 5,6) provides a unique path to plated metal or molded plastic structures, but silicon parts cannot be made.

A technology is useful only to the extent that it can be economically integrated into a complete working system that performs a useful job. Integrated systems that can operate over the continuous range of forces and displacements from nano-scale to milli-scale require fabrication strategies that can yield a continuous range of machine sizes in 3 dimensions, unconstrained by crystal planes. This report offers such a strategy.

## PROCEDURE

### Trench etching:

Thermal oxide and CVD silicon dioxide have been used as masks. One  $\mu\text{m}$  of oxide is needed for each  $20 \mu\text{m}$  of depth to be etched into the wafer. A LAM Research Rainbow etcher was used in plasma etching mode (power to the top electrode). The conditions used were  $400 \text{ sccm He}$ ,  $180 \text{ sccm Cl}_2$ ,  $425 \text{ mT}$ ,  $300 \text{ W}$ , electrode gap  $0.8 \text{ cm}$ . The etch rate for silicon was  $40 \mu\text{m}$  per hour. A 7 second  $\text{SF}_6$  pre-etch ( $100 \text{ sccm}$ ,  $200 \text{ W}$ ,  $400 \text{ mT}$ ,  $1 \text{ cm}$  gap) was used to remove any native oxide. During the chlorine etch a thin layer of white material forms on the silicon side walls. When the etch depth reaches about  $45 \mu\text{m}$ , the thickness of the sidewall deposit is high enough for internal stress to make it start peeling away from the wall. This obstructs the path of ions entering the trench, and may deflect them into the sidewalls causing accelerated lateral etching. Conditions must be adjusted to maintain just enough deposit to protect the sidewalls from etching to obtain vertical sidewalls deeper than  $45 \mu\text{m}$ . The white deposit (which is insoluble in  $49\% \text{ HF}$ ,  $20\% \text{ KOH}$ , or  $120^\circ \text{ C}$  piranha) can be reduced by increasing the chlorine concentration in the plasma (e.g.,  $200 \text{ sccm Cl}_2$ ,  $350 \text{ sccm He}$ ).

Another feature of concern is the final roughness of the trench sidewalls and bottoms. After the plasma etch, the wafers are put in a tube furnace for wet oxidation at  $1100^\circ \text{ C}$  for 2.5 hours to grow 1 micron of oxide. This is then completely removed by a  $49\% \text{ HF}$  wet etch. If this smoothing treatment is not done, stress concentrations are severe enough to cause the sacrificial oxide layer to form many tiny cracks. The surface mobility of the polysilicon during deposition allows it to fill these cracks so that very thin polysilicon spikes are left protruding from the bottoms of the polysilicon beams.

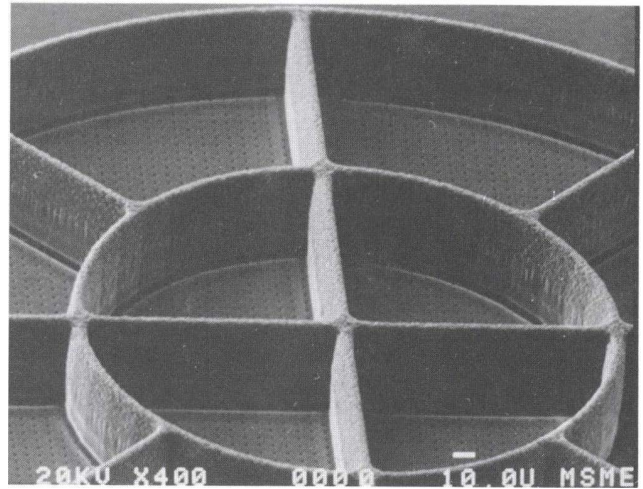


FIGURE 2. Surface silicon membrane filter integrated with  $48 \mu\text{m}$  tall molded ribs.

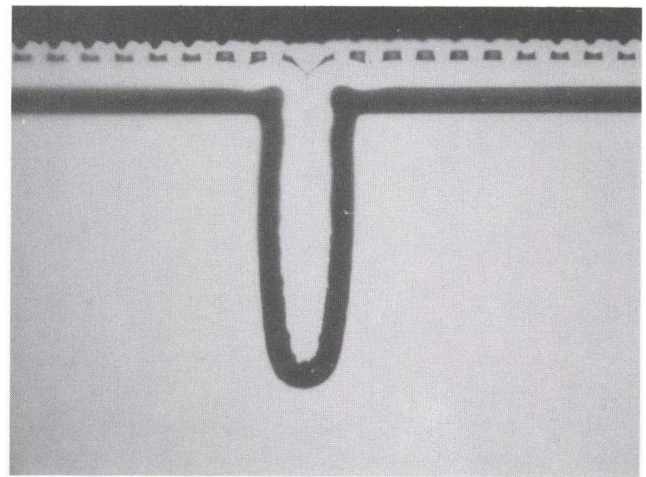


FIGURE 3. Cross section through filter membrane and  $48 \mu\text{m}$  stiffening rib prior to etch release from the wafer.

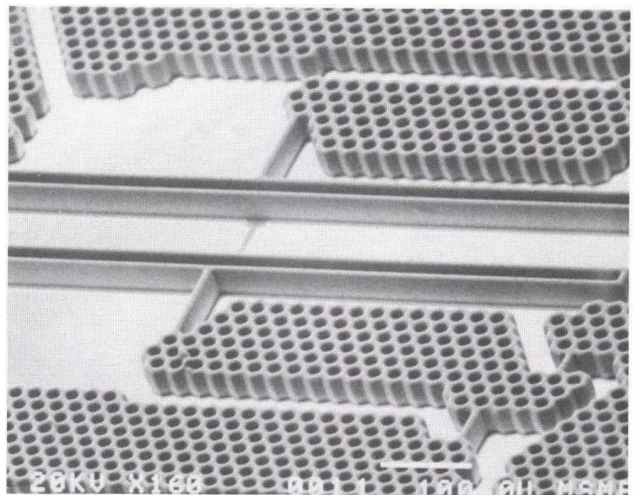


FIGURE 4. Central part of a HEXSIL microtensile testing machine  $45 \mu\text{m}$  thick and  $3 \text{ mm}$  in diameter. The thin tensile specimen is visible near the center between the long straight springs.

Smoothing has also been accomplished by timed isotropic etch with a solution of 65% nitric acid, 3% ammonium fluoride, and 32% DI water at room temperature.

An example of a mold surface that is ready for the sacrificial oxide to be deposited is shown in figure 6.

#### Sacrificial Oxide:

The methods that have been used to create the layer of sacrificial oxide are:

1. Thermal oxidation of the wafer. This consumes silicon from the mold, so it should only be done once for smoothing the etched surface.

2. CVD polysilicon ( $580^{\circ}\text{C}$ ,  $65\text{ \AA}/\text{min}$ ), followed by complete conversion of this layer to oxide by wet thermal oxidation at  $1100^{\circ}\text{C}$ . This produces a very conformal coating regardless of trench aspect ratio, and does not consume the mold. The trench can be made permanently narrower by depositing polysilicon and not oxidizing it. This allows higher aspect ratios than can be achieved directly by plasma etching.

3. CVD phosphosilicate glass (PSG) at  $450^{\circ}\text{C}$ ,  $140\text{ \AA}/\text{minute}$ , 8% phosphorous in the film. The thickness of the deposit decreases with depth in the trench. An anneal in nitrogen for 1 hour at  $1000^{\circ}\text{C}$  is done to densify the PSG. PSG provides a relatively fast etching layer (up to about  $20\text{ }\mu\text{m}$  per minute in 49% HF).

4. CVD undoped oxide (low temperature oxide, LTO) at  $450^{\circ}\text{C}$ . Conformity is comparable to that of PSG. If nonconductive polysilicon structures are needed, then a layer of LTO may be deposited over the PSG to prevent diffusion of phosphorous into the polysilicon during the stress relief anneal.

Any combination of these methods can be used depending on the requirements of the finished part. The best dimensional tolerances are achieved by oxidation of  $580^{\circ}\text{C}$  CVD polysilicon since it is extremely conformal with uniform thickness. A thin layer of PSG may be applied to decrease the time required for etch release. The thicker the PSG is, the greater are the dimensional variations that occur due to depleted deposition with trench depth, and surface tension effects during reflow. If the densification anneal is done at  $1050^{\circ}\text{C}$  the molded parts are very smooth with specularly reflecting surfaces, but then a larger scale ( $5$  to  $20\text{ }\mu\text{m}$ ) waviness develops due to surface tension of the free surface of the PSG. The oxide layer shown in figure 3 was made by first growing  $2.2\text{ }\mu\text{m}$  of thermal oxide from the mold surface. Then  $1.1\text{ }\mu\text{m}$  of PSG was deposited, and densified at  $1000^{\circ}\text{C}$  for 1 hour in nitrogen. This provides a fast etching layer. Then  $0.8\text{ }\mu\text{m}$  of CVD polysilicon was deposited at  $580^{\circ}\text{C}$ , and then completely oxidized at  $1100^{\circ}\text{C}$  in pyrogenic steam for 6 hours. It can be seen that the sharp corners at the mouth of the trench cause the PSG to increase its radius of curvature by moving material towards the center of the trench, thereby constricting it. When the polysilicon is deposited to form the molded part, it is choked off at this PSG constriction before the wider cross section down in the trench can be completely filled. This leaves a void in the middle of the beam. The thermal oxidation is not completely conformal at the trench corners either, but the major contribution to the distortion appears to be from the PSG. This should not be a problem in most structural applications.

It can be seen in figure 3 that the oxide lining is actually rougher than the walls of the etched trench. Thinner PSG and lower densification temperatures should minimize this. Oxidation of in situ phosphorous doped polysilicon may be another way to produce a fast etching layer that would be more conformal.

#### Polysilicon Deposition:

All CVD polysilicon in this work was formed undoped at  $580^{\circ}\text{C}$  with a deposition rate of  $0.39\text{ }\mu\text{m}$  per hour, 100 sccm silane, at 300 mT. The as-deposited film is expected to be essentially amorphous or very fine grained (ref 7). It has high tensile stress (judging by the cracks that open up in excessively thick deposits). Annealing

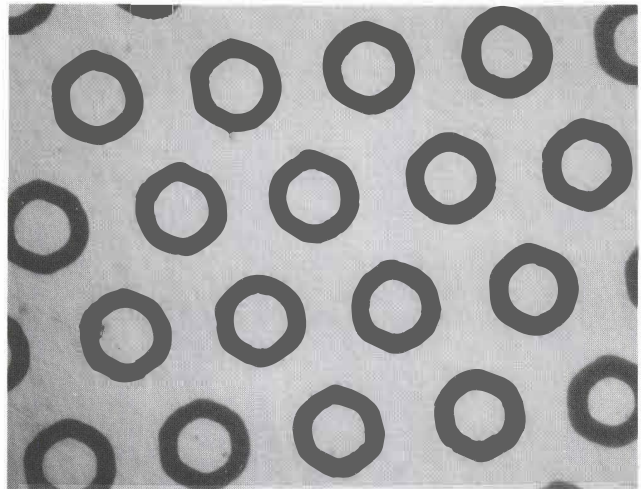


FIGURE 5. Top view after lapping back to the original wafer surface showing the tops of the single crystal silicon columns, the PSG (dark rings), and the molded polysilicon honeycomb.

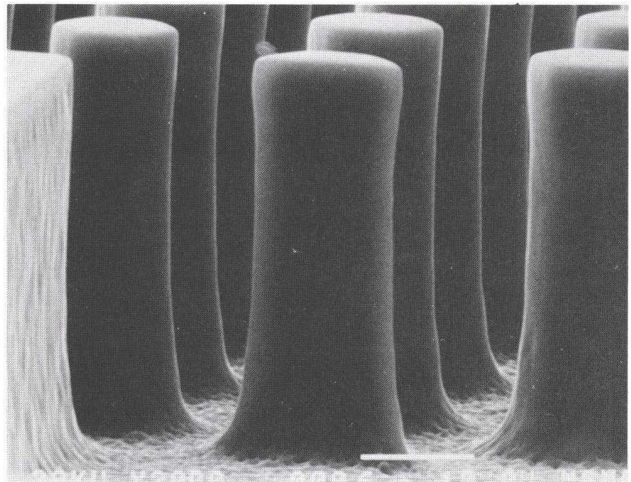


FIGURE 6. Oblique view of a region of the mold wafer that forms the honeycomb structure. Etch depth is  $45\text{ }\mu\text{m}$ , undercut  $2\text{ }\mu\text{m}$ . Hexagonal columns are located on  $25\text{ }\mu\text{m}$  centers.

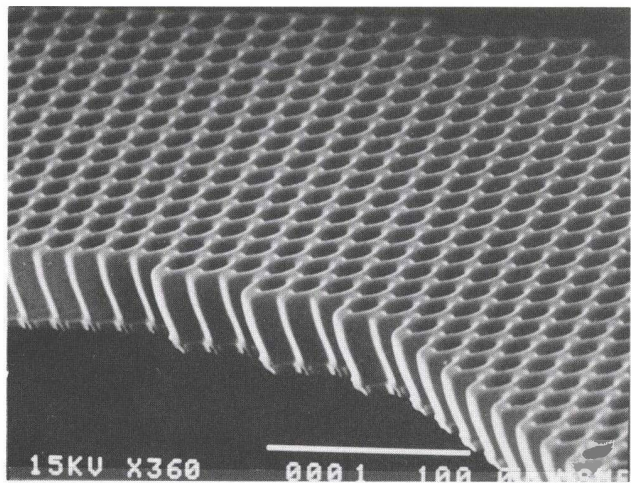


FIGURE 7. Thermal expansion frame of TEM microtensile tester. View of the bottom surface of the molded polysilicon which replicates the roughness of the sacrificial oxide.

is required to relieve the stress before removing the parts from the wafer so that they remain straight and flat. In this work, all polysilicon anneals were done at 1000° C for 1 hour in nitrogen. Polysilicon film thicknesses used have ranged from 0.9 to 8 μm. Thick films can be built up by annealing after accumulating 4 microns of growth. An attempt to grow an 8 μm thick film without an intermediate anneal resulted in cracks through the film. The opening of the cracks indicate that the stress was highly tensile. The cracks occurred during the deposition, then as polysilicon continued to form, the fragments were welded back together sufficiently for most of the machines to be usable.

Higher deposition rates could be achieved at higher temperatures, but the effects of larger grain size, deposition rate as a function of trench depth, and concentration of impurities at the grain boundaries would have to be evaluated for each particular application.

**Phosphorous Diffusion Anneal:**

Additional annealing in nitrogen may be done to increase the electrical conductivity of the polysilicon by diffusing phosphorous into it from the PSG layer. Diffusions have been done at 1000° C and at 1050° C for one hour in the case of the tensile testing machine which works by ohmic heating and therefore must be conductive.

**Lapping and Polishing:**

The most effective way to maintain flat surfaces amenable to photolithography is by lapping and polishing. In this work a slurry of 0.3 μm deagglomerated gamma alumina (Buehler Inc) in glycerin was used. The films deposited on the back of the wafer should also be lapped (alternatively they can be etched) as needed to keep the wafer flat. The wafer will warp if stressed material is removed from one side only.

**Etch Release:**

The sacrificial oxide is dissolved with 49% HF with a surfactant (triton X-100, at a concentration of about 0.1%) in complete darkness. If a surfactant is not used, the released silicon surfaces are hydrophobic and will stick together to minimize contact with the aqueous solution. Enough surfactant must be present to form a monolayer on all surfaces. The use of an opaque container is a precaution against photon induced etching of silicon.

**Mold Extraction:**

The apparatus to remove the parts from the wafer in a controlled manner has not been fabricated as yet. Several crude methods have been used for experimental purposes. The wafer can be submerged in a solution that forms gas bubbles which either float, or push the parts out. Freshly mixed piranha (5 parts sulfuric acid, 1 part 30% hydrogen peroxide) is preferred. Greater force can be obtained by soaking the wafer in saturated aqueous sodium bicarbonate, and then immersing it in 5% aqueous acetic acid. Lower temperatures or concentrations may be used to obtain gentler action.

A layer of sticky wax, or double sided tape, may be put on a glass slide and pressed lightly against the wafer. If the slide is then pulled straight up, the devices stuck to it will be pulled out of the mold.

Molded parts with a depth of 45 μm and trench wall clearance of 3 μm on each side of the beams are easy to remove by these methods.

Figure 9 shows the planned strategy of etching the trenches in an n-type silicon wafer and then using photoelectrochemical etching (refs 8,9) to form straight 5 μm diameter pores extending to the back of the wafer. Pore formation should occur only at the bottoms of the trenches since the electric field will direct the holes (generated by photons impinging on the back side of the wafer) to those locations. These pores are narrow enough to be plugged by

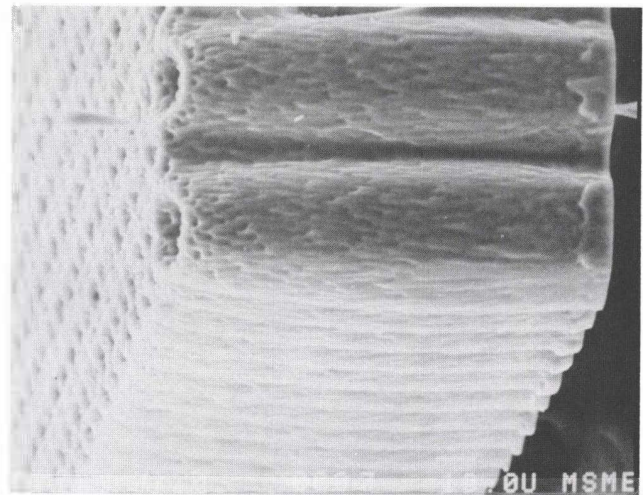


FIGURE 8. HEXSIL beam after removal from 110 μm deep mold. A smooth surface was not maintained when etching to this depth.

**Hydraulic Ejection of Molded Parts (proposed)**

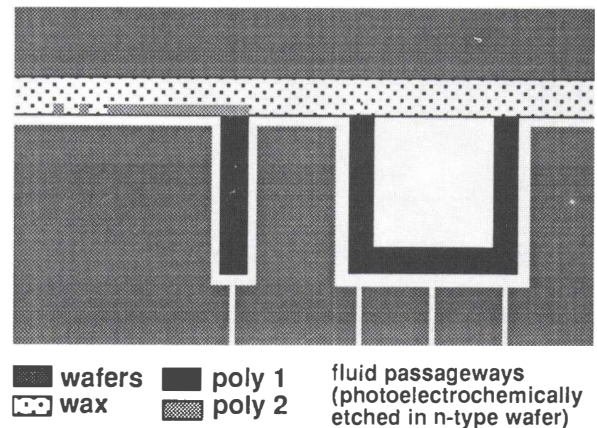


FIGURE 9. A proposed method for controlled removal of parts from the mold wafer.

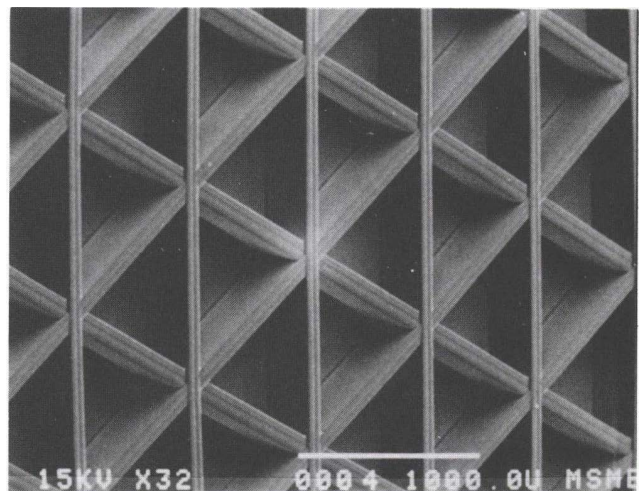
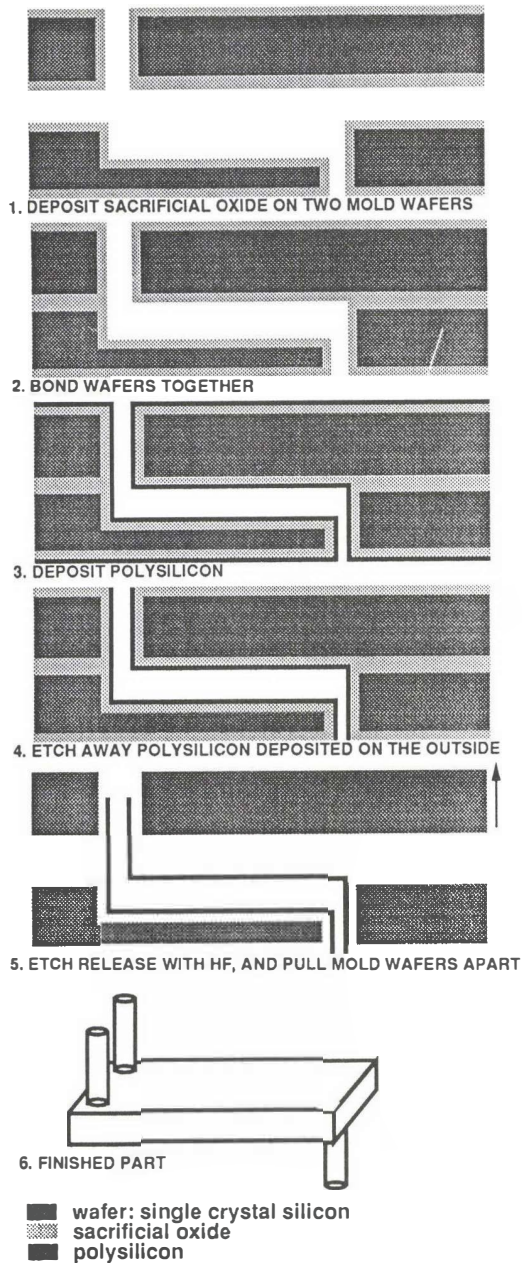


FIGURE 10. Polysilicon structural panel with 300 μm high corrugations, and 4 μm wall thickness after removal from the mold wafer.



**FIGURE 11.** Method for molding tubes and vessels

the sacrificial oxide, so polysilicon will not form in them. Then after the oxide is etched out with HF, fluid pressure applied from the back of the wafer would generate sufficient flow through the pores to carry the parts out of the mold. The overall efficiency of the molding cycle will be increased by using hydraulic ejection of parts since smaller clearances would suffice for mold extraction. Therefore a thinner layer of sacrificial oxide could be used and less time would be needed to deposit it. To preserve the organization of the parts, the front of the mold wafer may be bonded to a wax coated transfer wafer prior to etch release.

## RESULTS

The fabrication strategy described above has been used to make the following:

### Filters:

Quantitative testing remains to be done, but the stiffening rib patterns most resistant to handling breakage were found to be the hexagonal ones, and the ones with a circular outer perimeter (as

seen in figure 2). These minimize stress concentrations. The designs with square walled outer perimeters were not quite as robust.

Wafer molds for filters have been put through 2 molding cycles, and there does not seem to be any fundamental reason why they could not continue to be used for thousands of cycles.

### Tensile Testers:

10  $\mu\text{m}$  relative motion between opposing levers was achieved with 120 ma 60 Hz ac (dc current will be used in the TEM). This deflection of the 64  $\mu\text{m}$  tall, 14  $\mu\text{m}$  wide, 1000  $\mu\text{m}$  long, folded spring corresponds to a calculated force of 500  $\mu\text{N}$  applied to the test specimen. A design error caused one link in the mechanism to rotate about 10 degrees which wasted much of the pure translation that was desired. When this is corrected, performance should improve. The strategy of using in-plane thermal expansion is convenient since no additional materials have to be deposited. Rigidity in 3 dimensions is required since the thermal expansion is small and can be lost entirely if any part warps out of plane. The use of levers and flexures maximizes the output force available, in contrast to thermal bimorphs where one side has to stretch the other side creating internal stress at the expense of useful force.

### Structural Panels:

Figure 10 shows a structural panel after it was removed from the wafer on which it was formed. The polysilicon film is 4  $\mu\text{m}$  thick, and the height of the corrugations is 300  $\mu\text{m}$ . Continuous sheets up to 4 cm x 6 cm were produced. The mold wafer was patterned with a dicing saw. The saw can make deep trenches with smooth vertical side walls, but the pattern is limited to straight lines.

### Tubing Manifolds:

Figure 12 shows a free standing rectangular polysilicon tube that could be used for conducting fluids. This was made by cutting grooves in a wafer with a dicing saw, coating it with oxide, and bonding to another oxide coated wafer, with a flat surface, to form passageways open only at the periphery of the wafer assembly. Figure 11 shows the general strategy for molding vessels with tubing ports.

## FUTURE WORK

Figure 13 shows a proposed strategy for anchoring a layer of single crystal silicon (SCS) to the HEXSIL foundation. At this point the assembly looks like a conventional SOI wafer and could be processed as such to fabricate CMOS circuits. The SCS layer is then patterned to leave islands of appropriate shape to conform to the footprint of the machine. Freestanding flexible sinusoidal metallized SCS interconnects provide electrical pathways between SCS islands on different parts of the machine that will move relative to each other. After etch release from the mold wafer, this would provide a submilligram machine carrying the submilligram of electronics that interface it to the world. Thus the dead weight and volume of the silicon die is eliminated. The capability to produce such devices will be important in applications where mass or volume must be minimized. Figure 14

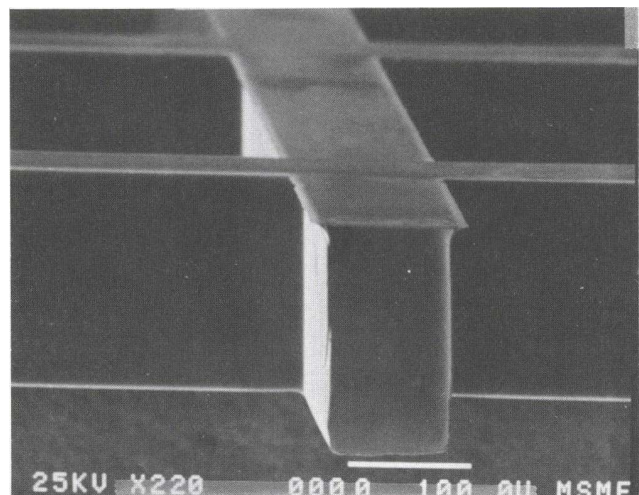


**FIGURE 12.** Rectangular grid with 1 mm spacing of rectangular polysilicon tubing 210  $\mu\text{m}$  x 110  $\mu\text{m}$  in cross section with wall thickness of 2  $\mu\text{m}$ .

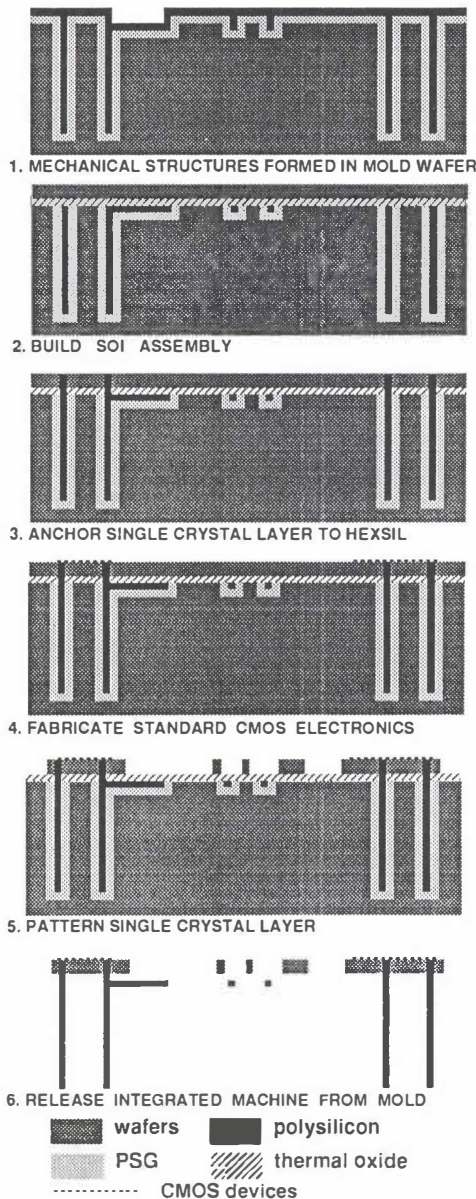


FIGURE 13. Proposed method for integrating microelectronics with micromechanics by eliminating the silicon die

schematically illustrates the application of this idea to the microtensile testing machine for use in the TEM where no space is available for a die. In this case piezoresistive strain gages, wheatstone bridges, and buffers are needed on the device.

## CONCLUSIONS

General methods for forming high aspect ratio CVD polysilicon structures with reusable molds etched in silicon wafers have been demonstrated. Parts could be made from any material that deposits conformally on trench walls, and can withstand the etch release.

Substantially vertical sidewalls were achieved with depths of 45  $\mu\text{m}$ . Dimensional tolerances could be held to 2  $\mu\text{m}$  in any direction by taking the anticipated lateral undercut and post-etch surface smoothing of the mold into account during mask design. Additional adjustment can be made to the mold by depositing 580° C polysilicon onto it to make the etched trenches narrower. In applications where curved sidewalls are acceptable, heights of 110  $\mu\text{m}$  have been achieved. This strategy provides the machine designer

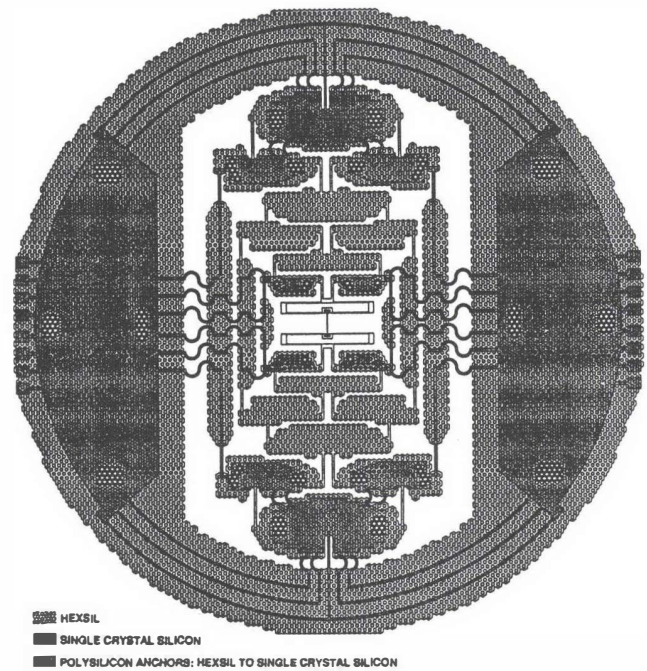


FIGURE 14. Schematic implementation of 3 mm diameter HEXSIL micro tensile testing machine with attached CMOS layer for use in the TEM.

with a pathway to milli-scale polysilicon structures which can accommodate forces and deflections in excess of 0.1 N and 10  $\mu\text{m}$  respectively.

The demonstrated devices are intended to be directly installed in the using system. There is no intervening device packaging. This improves system performance/volume, but requires careful handling prior to installation. To the extent that electronics can be built on foundations that are also mechanically functional, diverse new niches will be opened for evolving MEMS. Neural sensors (ref 10) are a well known example (although they do not have moving parts).

The economics of long-lived capital intensive molds that has been so successful in the plastics industry can now be utilized in CVD microfabrication.

## ACKNOWLEDGEMENTS

Partial support for this work was provided by the National Science Foundation, Award number ECS 9023714, and through Mauro Ferrari's National Young Investigator Award.

The students and professors of the Berkeley Sensors and Actuator Center (BSAC) and the staff of the Berkeley Microfabrication Laboratory have been extremely helpful with technical advice.

All fabrication was done at the Berkeley Microfabrication Laboratory.

## REFERENCES

1. M.W. Judy, Y.-H. Cho, R.T. Howe, A.P. Pisano, "Self-adjusting Microactuators", Proceedings, IEEE Micro Electro Mechanical Workshop, Nara, Japan, February 1991, pp. 51-56
2. M.W. Judy, R.T. Howe, "Polysilicon Hollow Beam Lateral Resonators", Proceedings, IEEE Micro Electro Mechanical Workshop, Fort Lauderdale, Florida, February 1993, pp. 265-271
3. K.A. Shaw, Z. Lisa Zhang, N.C. MacDonald, "SCREAM I: A Single Mask, Single-Crystal Silicon Process for Microelectromechanical Structures", Proceedings, IEEE Micro Electro Mechanical Workshop, Fort Lauderdale, Florida, February 1993, pp. 155-159
4. E. Bassous, "Fabrication of Novel Three-dimensional Structures by Anisotropic Etching of (100) and (110) Silicon", IEEE Transactions on Electron Devices, vol. 25, September 1978, pp. 1178-1185
5. E.W. Becker, W. Ehrfeld, P. Haggmann, A. Manner, D. Munchmeyer, "Fabrication of Microstructures with High Aspect Ratios and Great Structural Heights by Synchrotron Radiation Lithography, Galvanoforming, and Plastic Moulding (LIGA Process)", Microelectronic Engineering, 4, 1986, pp. 35-56
6. H. Guckel, T.R. Christenson, K.J. Skrobis, T.S. Jung, J. Klein, K.V. Harjojo, I. Wadajaja, "A First Functional Current Planar Rotational Magnetic Micromotor", Proceedings, IEEE Micro Electro Mechanical Workshop, Fort Lauderdale, Florida, February 1993, pp. 7-11
7. H. Guckel, J.J. Sniegowski, T.R. Christenson, "Advances in Processing Techniques for Silicon Micromechanical Devices with Smooth Surfaces", Proceedings, IEEE Workshop on Micro Electro Mechanical Systems, Salt Lake City, Utah, February 1989, pp. 126-132
8. V. Lehmann, "The Physics of Macropore Formation in Low Doped n-type Silicon", J. Electrochemical Society, Vol 140, No 10, 1993, pp.2836-2843
9. S. Cahill, W. Chu K. Ikeda, "High Aspect Ratio Isolated Structures in Single Crystal Silicon", The 7th International Conference on Solid State Sensors and Actuators, pp. 250-253 (1993)
10. A.C. Hoogerwerf, K.D. Wise, "A Three-Dimensional Neural Recording Array", Transducers '91 Digest of Technical Papers, 1991 International Conference on Solid-State Sensors and Actuators, pp. 120-123

# High Density Vertical Comb Array Microactuators Fabricated Using A Novel Bulk/Poly-Silicon Trench Refill Technology

Arjun Selvakumar and Khalil Najafi

Center for Integrated Sensors and Circuits  
Department of Electrical Engineering and Computer Science  
The University of Michigan  
Ann Arbor, MI 48109-2122

## ABSTRACT

This paper reports the development of a new fabrication technology for the implementation of electrostatically-driven vertical microactuators. It combines bulk and surface micromachining techniques to produce thick ( $>10\mu\text{m}$ ) polysilicon microstructures by depositing  $1\text{-}2\mu\text{m}$  thick polysilicon films. Deep ( $10\text{-}15\mu\text{m}$ ) and narrow ( $\sim 4\mu\text{m}$  diameter) trenches are RIE etched in a boron doped silicon chassis and are then completely refilled with polysilicon. The polysilicon microstructure and the p++ chassis are both released using EDP. This technology can be used for the fabrication of a variety of microactuators with different electrostatic drive structures that can generate large vertical motion for the polysilicon microstructure out of the plane of the wafer. In addition to allowing the simultaneous formation of polysilicon and p++ silicon microstructures, the technology allows the creation of sub-micron gaps between these two structures, which in turn allows the generation of a large amount of force. Several bridge structures have been fabricated using this technique. Polysilicon fingers and beams as thick as  $8\mu\text{m}$ , and as narrow as  $2\mu\text{m}$  have been fabricated in  $4\mu\text{m}$ -wide trenches in a p++ chassis. A vertical out-of-plane force of about  $1\mu\text{N}$  can be generated using an array of 13,  $100\mu\text{m}$ -long polysilicon beams driven with a 10V signal.

## INTRODUCTION

Microactuators have been widely used in many different devices and applications like resonant sensors, micromechanical displays, micromotors, accelerometer feedback drives, micropumps, microvalves, switches, etc. [1]. With dimensions constantly being scaled down using micromachining technology, electrostatic drives are predominantly employed for their higher energy density [1]. The most widely used and practical electrostatic drive that many microactuators utilize are the parallel plate capacitive drive [2], and the lateral interdigitated comb drive [3,4]. The former can generate a substantial amount of force when the gap spacing between the two plates of the capacitor are small ( $\leq 1\mu\text{m}$ ), however, the force that it produces is nonlinear with respect to both voltage and electrode separation, resulting in a limited range of motion (typically  $<2\mu\text{m}$ ). The latter technique, lateral comb drive [3], produces an electrostatic force that is nearly independent of displacement, and hence permits much larger motion parallel to the wafer surface. Both of these actuation techniques have been used successfully in different devices, and both have been fabricated using either surface or bulk micromachining technologies [2,5].

Surface micromachined actuators are most suitable for devices where motion lateral to the wafer surface is desirable, and where large layer thicknesses are not required. For example, the lateral polysilicon comb drives developed by Tang *et. al* [2] can be moved over a fairly large distance lateral to the wafer surface. One shortcoming of polysilicon micromachined devices is the small thickness of the mechanical structure that can be achieved, which is primarily due to the limited thickness (typically a few microns) that can be deposited using CVD techniques. Bulk micromachining technologies do not suffer from this limitation and fabrication processes have been developed that can produce laterally driven microactuators as thick as  $15\mu\text{m}$  [5]. These technologies, however, possess their own limitations, most important of which is their lack of flexibility in forming complex micromechanical systems. While laterally-driven microactuators have been fabricated using both of

these technologies, vertically driven microactuating systems have so far been limited to those that utilize parallel plate capacitive drives. By combining bulk and surface micromachining techniques, one can produce more sophisticated micromechanical devices and develop alternative vertical actuation topologies.

This paper reports on the development of a new fabrication technology that combines bulk and surface micromachining techniques by utilizing silicon micromechanics formed from both bulk silicon and deposited polysilicon. The technology allows the fabrication of thick polysilicon microstructures ( $>10\mu\text{m}$ ), without the need for large deposited layer thicknesses, by using a trench refill technique, and combining thick polysilicon and bulk micromachined microstructures to create three-dimensional micromechanical devices. Using this technology it is possible to form lateral comb drives, as well as *vertical comb arrays* that offer features similar to those produced by laterally-driven microactuators. The proposed vertical comb arrays can produce large deflections (several microns) vertical to and out of the plane of the wafer surface. The moveable comb and microstructure is made from polysilicon, while the fixed drive electrode is made out of p++ silicon. In this paper we will discuss in detail the development of this new combined bulk-silicon polysilicon technology that can be used for the development of a variety of devices, and will discuss its use in vertical comb array microactuators that can produce large motion *vertical* to the wafer surface, in much the same way that *lateral* comb drives can produce motion lateral to the wafer surface.

## DEVICE STRUCTURE

A typical microactuator structure is shown in Fig. 1, and is fabricated on a single silicon wafer. This device structure is only a representation of a range of devices that can be fabricated and is chosen because it contains all the main elements needed for different microactuators. It consists of an etch pit spanned by a two-part bridge made up of (i) a flexible mechanical polysilicon (MP) bridge which supports an array of thick polysilicon fingers (or beams), and is suspended over (ii) a rigid p++ chassis containing a number of holes (or slots) through which the fingers (or beams) pass. The MP bridge is the dynamic element of the actuator which deflects on the application of a driving signal applied between it and the p++ chassis. The MP bridge and its array of fingers (or beams) are made by refilling deep and narrow trenches etched in the p++ chassis. The gap between the MP and the p++ chassis on top and on the sidewall of the trench is defined by a LPCVD silicon dioxide and a sacrificial polysilicon (SP) layer which is removed later. Since the trenches are about  $4\mu\text{m}$  wide, it is possible to completely refill and close the trench by depositing polysilicon thin films with a thickness of about  $1\text{-}2\mu\text{m}$ . This will allow the formation of narrow (about  $2\text{-}3\mu\text{m}$ ) and thick (greater than  $10\mu\text{m}$ ) polysilicon fingers (or beams) buried within the p++ chassis. Since the thickness of the p++ boron-doped silicon chassis here (typically about  $5\mu\text{m}$ ) is smaller than the depth of the trenches (typically  $10\mu\text{m}$ ), when the bridge is undercut using a concentration-dependent etchant such as EDP, the polysilicon fingers (or beams) protrude below the lower surface of the chassis by several microns. The extent of this protrusion is defined by the depth of the trenches which can be controlled using the dry etching step that is used to form them. A protective oxide layer prevents MP from getting attacked by EDP while the chassis is undercut. The MP fingers (or beams) protruding below the p++ chassis and suspended through the holes in the chassis, are shown in the cut-away view in

Fig. 1 (the bridge is shown undercut in the figure). It is also possible to partially remove the mechanical polysilicon over the fingers (or beams) and leave these portions open but connected on the side to the main MP layer at the edges (this will be discussed in more detail later in the paper). A control polysilicon (CP) electrode (not shown in the figure) is deposited on top of the p++ chassis, and is located between the chassis and the MP layer. It is insulated by a layer of oxide, and provides a means to shield the p++ chassis from the MP layer. This is important as will also be discussed in the paper. The above structure utilizes features offered by both surface and bulk micromachining. It allows the formation of thick microstructures made from polysilicon, and provides the capability to form vertical comb arrays that can be used in a vertical drive actuation scheme similar to that used in laterally-driven comb microstructures.

### FABRICATION

The fabrication process requires seven masks, and involves both surface and bulk micromachining techniques, as illustrated in Fig. 2. On a standard, p-type <100> silicon wafer, using a thermal masking oxide, we perform deep boron diffusion at 1175°C for 2.5 hours to achieve a 5µm boron etch stop depth, which defines the thickness of the rigid p++ chassis. The boron diffusion is masked from the regions where the etch pit is to be formed to allow access to, and final etching of the undoped silicon needed for releasing the p++ chassis. This chassis functions as the skeletal frame for the refill process and as one of the two drive electrodes in the vertical comb arrays.

This is followed by the deposition of 1000Å of LPCVD silicon dioxide (#1), and 4000Å of polysilicon (which forms the control polysilicon, CP). The oxide insulates the polysilicon from the chassis. The CP layer is now doped with phosphorus, and a thin layer of oxide is grown in preparation for the second masking step. The CP layer is patterned using an RIE process to define only its outer boundaries; the RIE etch terminates on the silicon substrate below CP. Next, a thin layer of oxide is deposited on the CP layer, and the wafer is prepared for the deep RIE trench etching process. A 2500Å layer of aluminum is deposited on the wafer and patterned to expose those areas where the deep trenches are to be formed. RIE etching is now used to etch through the control polysilicon layer, the oxide layer, and the single crystal silicon underneath to form the deep trenches [5]. This RIE etch is done using 17.5sccm of SF<sub>6</sub> and 7.5sccm of O<sub>2</sub> at a pressure of 5mT, a power of 60W for about 100min; the etch rate is about 0.1µm/min. The RIE etches through the doped p++ silicon into the undoped silicon and forms a narrow

(4µm wide) and deep trench (~10µm deep). Because all etching is done through the same mask and in one step, the control polysilicon is self-aligned with the deep trench. This ensures that CP covers the top surface of the chassis everywhere.

A thin LPCVD oxide (#2, ~2500Å) is now deposited to conformally cover all the exposed silicon regions (polysilicon as well as the trench sidewall), and is followed by the deposition of a 1µm-thick sacrificial LPCVD polysilicon (SP) layer. The SP layer thickness together with the oxide #2 and oxide #3 thicknesses (oxide thicknesses are negligible) determines the finger to chassis gap distance, and can be changed easily to accommodate different gap separations between the polysilicon fingers and the p++ chassis. The fourth masking step is used to pattern the SP layer (Fig. 2b). After the SP layer is patterned and removed in the areas where anchors for the MP layer are to be created to the substrate, a 2500Å LPCVD oxide (#3) and 1.5µm LPCVD polysilicon layer (MP) are deposited. This third polysilicon layer (MP) refills the trenches and planarizes the wafer for subsequent processing. This layer when patterned forms the dynamic bridge-component of the actuator as shown in Fig. 2c. It is also possible to selectively remove part of the MP layer over the regions where the fingers or beams are located (as shown in Fig. 2c). Note that this is required for the fabrication of vertical comb arrays. In order to do this, a high pressure isotropic RIE etch is performed through a mask. This etch will remove the top part of the MP layer and part of polysilicon refill in the trenches to achieve the desired height for the polysilicon beams and fingers.

The ensuing and final furnace step is the deposition of an LPCVD oxide layer (#4) which will serve to protect the MP layer from the EDP etch. This oxide is patterned to (i) provide access through etch windows for the EDP to undercut the structure; (ii) remove the sacrificial layer, (Note that oxide layers #2 and #3 are patterned to provide a passage for EDP to etch SP and to protect MP and CP from being attacked); and (iii) provide contact openings for the metal lines and pads. After the oxide patterning step, Cr/Au is deposited and patterned to form bonding pads and make connections to the three layers (i.e. p++ silicon, MP, and CP). The final step of the process is the removal of SP and undercutting of the bridge (Fig. 2c,d). Undercutting of the bridge is possible because it is aligned 45° to the major flat of the wafer. The etch pits 'V' outward from each side of the bridge till the bridge is completely undercut which takes 3.5 hours. The SP layer is also etched in the same step, which results in releasing the MP bridge and fingers which are encapsulated by the protecting oxide shell. This oxide shell is removed by a brief BHF dip to release the final structure as shown in Fig. 2d.

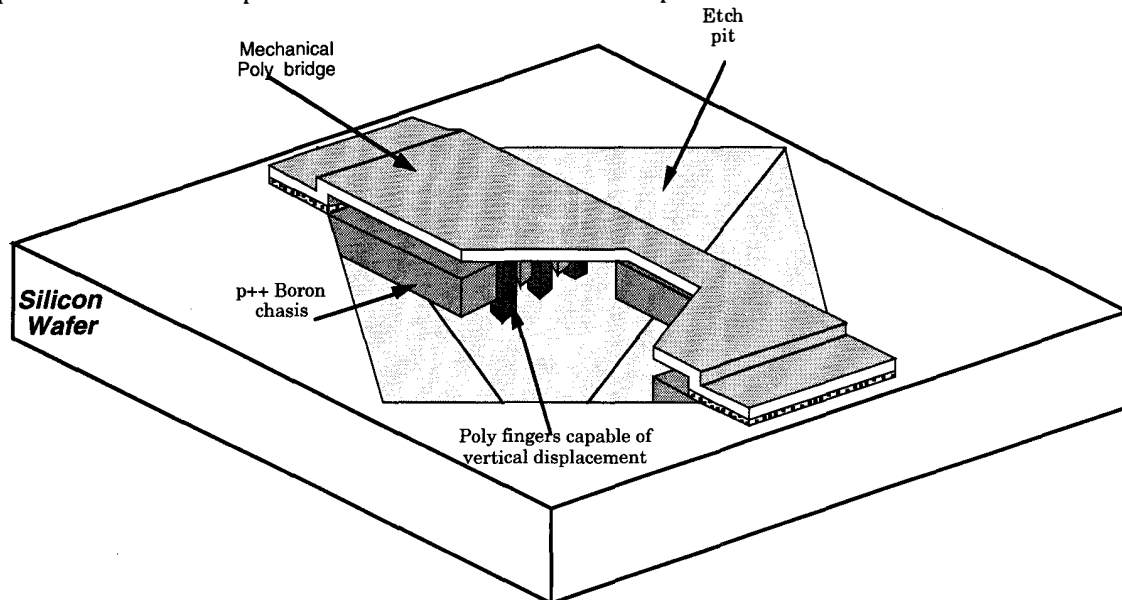


Figure 1: Three-dimensional view of a microactuator structure. It contains a p++ chassis with holes and slots through it, a mechanical polysilicon layer that is supported on the p++ chassis and fills up the holes, and a control polysilicon which shields the p++ chassis and the MP layer for proper device operation.

## FABRICATION RESULTS

The above fabrication process has been used to fabricate a number of prototype microstructures. Figure 3 shows a SEM photograph of a bridge structure fabricated using this technology. One can see the etch pit, which is about 400 $\mu\text{m}$  deep, and the combined polysilicon/p++ silicon bridge spanning the etch pit. The bridge is about 300 $\mu\text{m}$  long, 200 $\mu\text{m}$  wide. Figure 4 shows a close-up SEM view of the MP polysilicon bridge, which is about 1.5 $\mu\text{m}$  thick, and the p++ bridge which is about 5 $\mu\text{m}$  thick. One can observe the array of polysilicon fingers on the underside of the polysilicon bridge. Figure 5 shows a close-up view of one of the polysilicon fingers; note that the p++ chassis is broken to reveal the polysilicon finger. The finger is about 7 $\mu\text{m}$  high, and has a bottle-like shape. The shape is determined by the fact that the deposition of the sacrificial polysilicon is not quite conformal around the top edges of the trench and tends to build up there. Therefore, the neck is somewhat narrower than the body of the finger. This figure also shows the sidewall of the p++ chassis. Figure 6 shows a view from the underside of the p++ chassis. One can easily see the protruding fingers of polysilicon from this angle. These fingers extend below the lower side of the chassis by about 1.5 $\mu\text{m}$ . Deeper RIE etch can be used to form a deeper trench and a thicker polysilicon finger or beam.

## APPLICATIONS

The above technology allows the fabrication of a number of different actuator topologies and structures. The polysilicon finger shown in Fig. 6 can be driven electrostatically by applying a voltage between the MP layer and the p++ chassis. The control polysilicon plays an important role in any of these actuator structures. It serves as a shield between the p++ chassis and the MP layer. When the MP layer is to be attracted to the p++ chassis (Mode 1), a voltage can be applied between the CP and MP layers, thus pulling the MP bridge down (as in a parallel plate capacitive drive).

When the MP bridge is to be pushed away from the p++ (that is pushed away from the substrate), then a different actuator structure will be needed, as illustrated in Fig. 7. In this microactuator, after the MP is deposited, a portion of it is selectively removed, using an isotropic dry etching process, in areas where actuator beams are to be formed. The actuating polysilicon beams are connected to the main body of the MP bridge at their ends. The gap between the beam and the p++ chassis is defined by the thickness of the sacrificial layer. To create repulsion between MP and the p++ chassis (Mode 2), a voltage is applied between MP and the p++ chassis with CP being shorted to MP. The electric field between the chassis and the MP layer pulls the MP layer up till the top surface of the polysilicon beam is aligned with the top surface of the p++ chassis. The operation is similar to that of laterally-driven combs [3]. However, this structure can generate a much larger force per unit area than lateral actuators because: i) the polysilicon beams can be made to be several hundred microns long, and therefore provide a much longer edge between the p++ chassis and the polysilicon beam; and ii) the gap between the two layers can be easily made to be much smaller (<1 $\mu\text{m}$ ) than practical with the surface micromachined lateral combs. Analytical calculations and electrostatic simulations using FASTCAP [6] have shown that a force of about 1 $\mu\text{N}$  can be generated using only an array of 13, 100 $\mu\text{m}$  long beams with 10V drive signal.

## CONCLUSIONS

We have reported the development of a new fabrication technology for the implementation of electrostatically-driven vertical and lateral microactuators. It combines bulk and surface micromachining techniques to produce thick (>10 $\mu\text{m}$ ) polysilicon microstructures by depositing 1-2 $\mu\text{m}$  thick polysilicon films. Deep (10-15 $\mu\text{m}$ ) and narrow (~4 $\mu\text{m}$  diameter) trenches are etched in a boron doped silicon chassis and are then completely refilled with polysilicon. The polysilicon microstructure and the p++ chassis are both released using EDP or KOH. This technology can be used for the fabrication of a variety of microactuators with different electrostatic drive structures that can generate large vertical motion for the polysilicon microstructure out of the plane of the wafer. In

addition to allowing the simultaneous formation of polysilicon and p++ silicon microstructures, the technology allows the creation of sub-micron gaps between these two structures, which in turn allows the generation of a large amount of force. Analytical and electrostatic simulations using FASTCAP have shown that a force of about 1 $\mu\text{N}$  can be generated using only an array of 13, 100 $\mu\text{m}$  long beams.

## ACKNOWLEDGMENTS

The authors would like to thank Prof. M.D. Giles, Dr. S.B. Cray, and Mr. M. Boyd for their assistance in electrostatic analysis and the use of FASTCAP. They would also like to thank Ms. T. Hull and the staff of the Center for Integrated Sensors and Circuits for help in fabrication. This work was supported by the Advanced Research project Agency under contract #J-FBI-92-149.

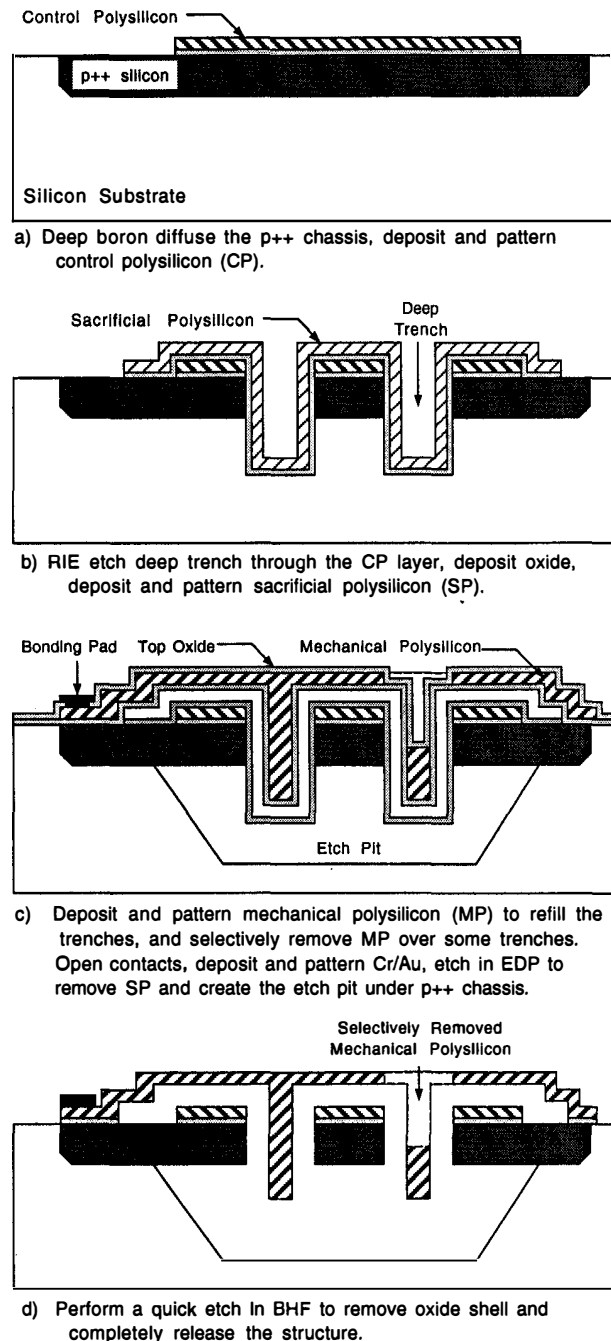


Figure 2: Fabrication process for a typical microstructure.

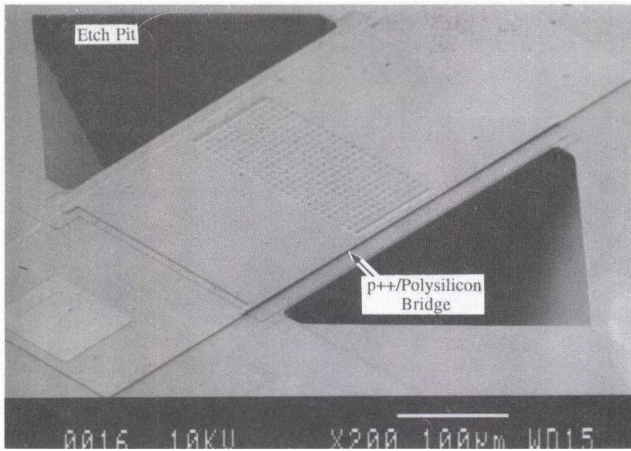


Figure 3: SEM photograph of a fabricated bridge structure, showing the 400µm deep etch pit, and the 300µm long, 200µm wide polysilicon/p++ silicon bridge spanning the etch pit.

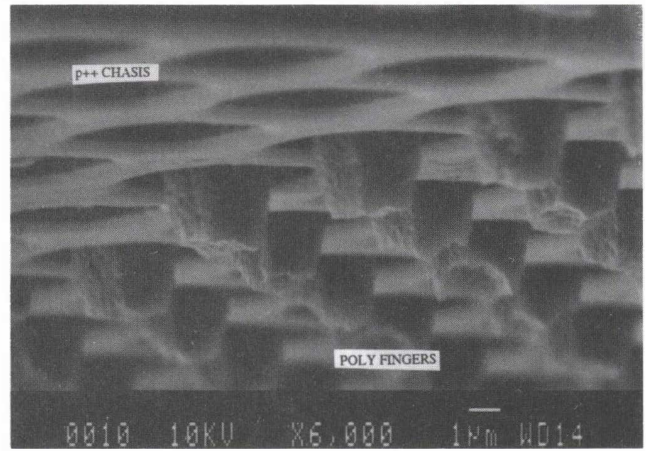


Figure 6: SEM view from the underside of the p++ chassis, showing the protruding fingers of polysilicon. These fingers extend below the lower side of the chassis by about 1.5µm.

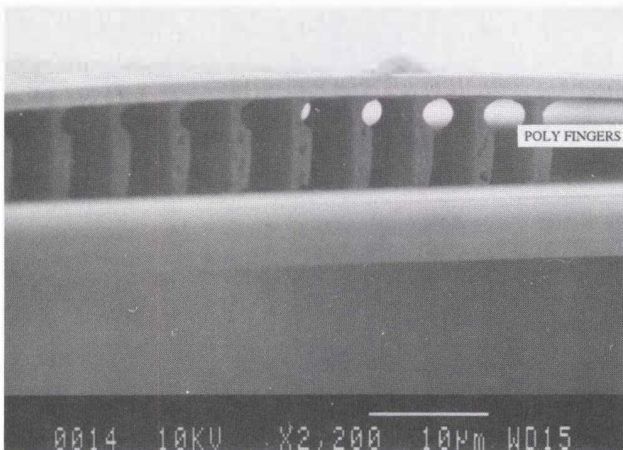


Figure 4: Close-up SEM view of the MP polysilicon bridge, which is about 1.5µm thick, and the p++ bridge which is about 5µm thick. One can observe the array of polysilicon fingers on the underside of the polysilicon bridge.

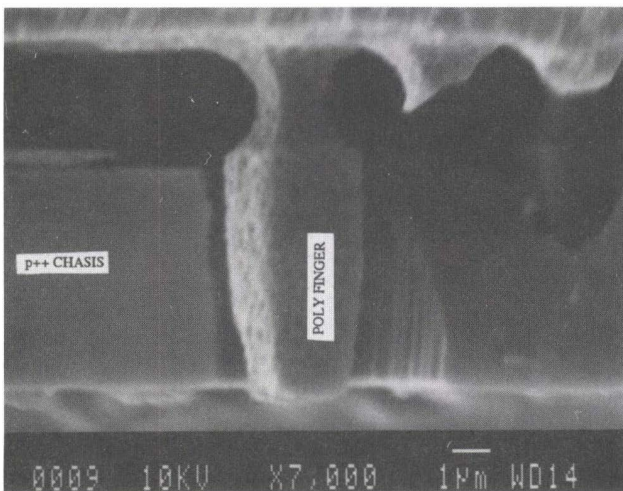


Figure 5: Close-up view of one of the polysilicon fingers; note that the p++ chassis is broken to reveal the polysilicon finger. The finger is about 7µm high, and has a bottle-like shape.

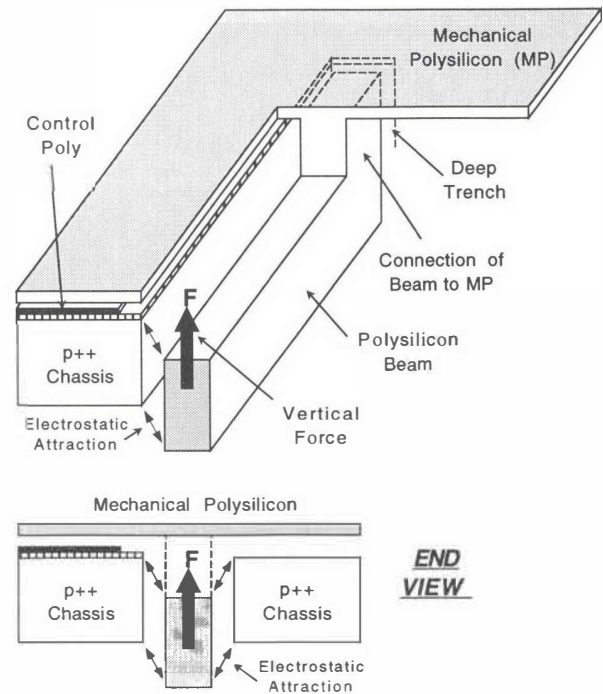


Figure 7: 3-D and end views of a vertically-driven comb array actuator. The polysilicon beam can be pulled up when a voltage is applied between it and the p++ chassis. Note that the beam has a slight overlap with the chassis, and that it is connected to the main body of the MP bridge at the ends.

## REFERENCES

- [1] H. Fujita, and K.J. Gabriel, "New Opportunities for Micro Actuators," Proceedings, Transducers '91, p. 14, San Francisco, June 91
- [2] M.W. Putty, S.C. Chang, R.T. Howe, A.L. Robinson, and K.D. Wise, "Process Integration for Active Polysilicon Resonant Microstructures," *Sensors & Actuators*, 20(1989), p.143
- [3] W.C. Tang, T-C.H. Nguyen, and R.T. Howe, "Laterally Driven Polysilicon Resonant Microstructures," *Sensors & Actuators*, 20(1989), p.25
- [4] W.C. Tang, M.G. Lim, and R.T. Howe, "Electrostatic Comb Drive Levitation and Control Method," *IEEE/ASME J. MEMS*, Vol. 1, No. 4, p. 170, Dec. 92
- [5] Y. Gianchandani, and K. Najafi, "A Bulk Silicon Dissolved Wafer Process for Microelectromechanical Systems," *IEEE/ASME J. MEMS*, Vol. 1, No. 2, p. 77, June 1992
- [6] J.R. Gilbert et. al, "Implementation of a MEMCAD System for Electrostatic and Mechanical Analysis of Complex Structures from mask Descriptions," *Digest. MEMS Workshop*. Ft. Lauderdale. Florida. p. 207, Feb. 1993

# Laser Stereo Micromachining at One-Half Million Cubic Micrometers Per Second

T. M. Bloomstein and D. J. Ehrlich  
Lincoln Laboratory, Massachusetts Institute of Technology  
Lexington, Massachusetts 02173-9108

## Abstract/Summary

We have recently demonstrated three-dimensional (3-D) micromachining of silicon using a chlorine-based microchemical reaction.<sup>1</sup> This technology achieves the necessary high degree of localization through rate nonlinearities near silicon melting. Applications are high-speed 3-D mastering and device prototyping directly from the computer-aided design environment, with no hard tooling. Figures 1–2 illustrate typical results.

Previous work has concentrated on the limiting case of slow linear scans where mass and heat transport profiles are indistinguishable from the static steady state. In this paper, we will report our findings on laser microchemical etching under conditions where transport distributions do not develop quasi-stationary profiles. Increasing the scanning velocity into this regime markedly changes the reaction dynamics. It is predicted that improvements in removal rate and surface quality will occur in this regime as the reaction zone is swept through fresh reactive gas and the melt zone extends less deeply into the bulk. Beneficial reaction zone narrowing, along with a general stabilization of dimensional control, should also occur. The chemistry used in our 3-D etching is innately among the fastest known solid/vapor interface reactions. Our study is therefore a test case for the more generally predicted benefits of using beam reactions in the transient transport regime.

This work has important implications for laser processing in the field of microelectromechanical systems and micromolding. In comparison with microelectronic applications, significantly larger volumes of material must be removed. This is expected to push laser-induced microchemical technology towards larger spot sizes to improve overall processing rates. Quasi-stationary transport profiles are, however, nonoptimal since overall removal rates can be improved only at the expense of dimensional accuracy and surface quality. Velocity-dependent transport processing is not expected to sacrifice these key aspects of the machining process and provides wider process latitude through the addition of a new process variable.

To study the laser reaction in the velocity-dependent transport domain, we have designed and constructed a new galvanometer-based laser scanning system. The output of a 15-W argon-ion laser is focused to a spot

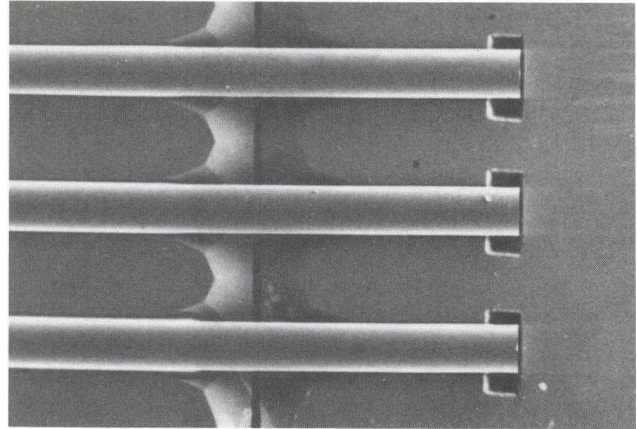


Figure 1. To improve coupling between an optical fiber and semiconductor laser, the faceted ends of the V-grooves are etched in a 100-Torr chlorine ambient using 10 W of laser power focused to a 10- $\mu\text{m}$  spot size. The V-grooves are 310  $\mu\text{m}$  wide and 110  $\mu\text{m}$  deep. The laser etched side-wall has a slope of 3°.

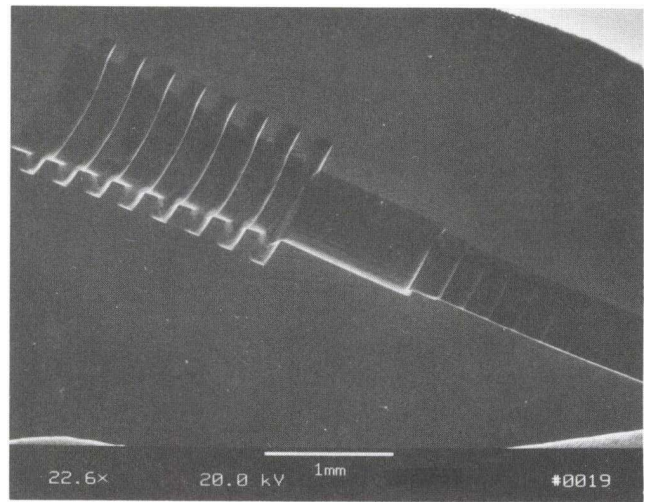


Figure 2. Prototype of the initial stage of a 490 GHz circular to rectangular waveguide mode-matching structure.<sup>2</sup> The total length of the structure shown is 4 mm and the maximum depth is 500  $\mu\text{m}$ . The total volume of the structure is approximately  $5 \times 10^8 \mu\text{m}^3/\text{s}$  and requires surface roughness values less than 0.2  $\mu\text{m}$ .

size on the order of 10  $\mu\text{m}$ . In our current arrangement, the beam can be swept across the surface at rates exceeding 10 m/s. This corresponds to a laser beam residence time of approximately 1  $\mu\text{s}$ , whereas characteristic mass and thermal transport times develop on a 10- $\mu\text{s}$  time scale. We will report the current state of the art in terms of processing speed, resolution, and

surface flatness. A volumetric removal rate of  $5 \times 10^5 \mu\text{m}^3/\text{s}$  can now be achieved by optimized scan speed and pressure conditions. Similarly, a surface roughness average of less than  $0.1 \mu\text{m}$  can be achieved on laser-etched surfaces.

## Equipment

The scanning system uses a high-performance x-y galvanometer scanner to deflect the output of a 15-W argon-ion laser running multiline (488- to 514-nm wavelength). The output of the laser is expanded to 16 mm and focused to a 10- $\mu\text{m}$  spot through a 250-mm-focal-length lens. The beam is introduced through a quartz cover glass into a stainless steel sample cell which is backfilled with chlorine gas. The sample is biased to 300 °C using a halogen lamp incident on the back side of the wafer. The sample surface is observed through the focusing optic with a charge-coupled-device camera.

The galvanometer is scanned up to angular velocities of 40 rad/s. This translates to linear velocities on the surface of 10 m/s with the current focusing optic. These optical and scan parameters were chosen to allow changes in thermal and mass transport dynamics to be evident. The mass diffusion coefficient of chlorine and the thermal diffusion coefficient of silicon near melt are both approximately 0.1  $\text{cm}^2/\text{s}$ . For a reaction zone on the order of the spot size, the characteristic transport time,  $\tau_{\text{transport}} \approx \omega_0^2/D$  where  $\omega_0$  is the spot size and D is the diffusion coefficient, is approximately 10  $\mu\text{s}$ . The resident time of the laser beam is  $\tau_{\text{residence}} \approx \omega_0/v_s$  and is a factor of ten below the transport time for scanning velocity  $v_s$ , equal to 10 m/s.

## Results

Boxes and lines were etched under several different scanning velocities ranging from 32 to 1000 cm/s to measure volumetric removal rates and lateral resolution. The transition from quasi-stationary to velocity-dependent transport conditions occurs around 100 cm/s. Figure 3 shows a graph of linewidth versus power for single passes of the laser across the surface. Results were obtained using an optical linewidth measurement system. For example, note that at the highest power, the linewidth is reduced by about a factor of three at increased scan speed. Figure 4 shows the corresponding volumetric removal rates for etched boxes taken at 1000 Torr of chlorine. Approximately the same volumetric removal rate occurs at higher powers although the resolution is better in the faster scan case. A slight improvement in rate, more pronounced at high scan velocity, is observed at 1520 Torr of chlorine. A simple model is being developed which incorporates both diffusional and convective components to the mass fluxes near the reaction zone. It predicts continued etch rate improvements as the pressure is increased in the fast scan limit. We are continuing to study the pressure dependence of the removal rate.

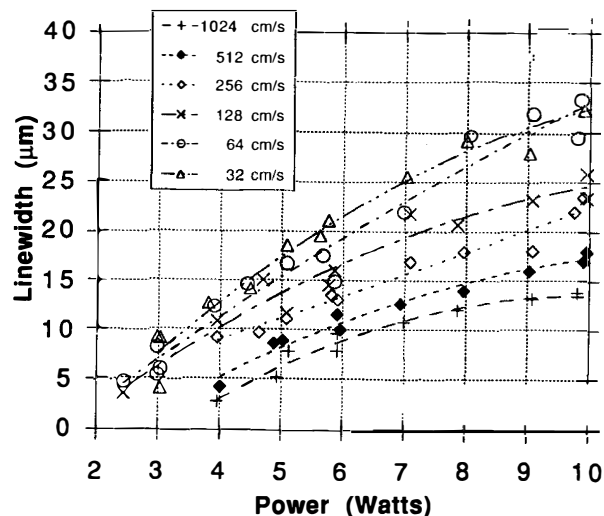


Figure 3. Linewidth of laser etched zone versus laser power. Data is presented for scan velocities of 32, 64, 128, 256, 512, and 1024 cm/s. The lower slope which occurs in the fast scan case should enable smaller features to be written with less sensitivity to laser power fluctuations.

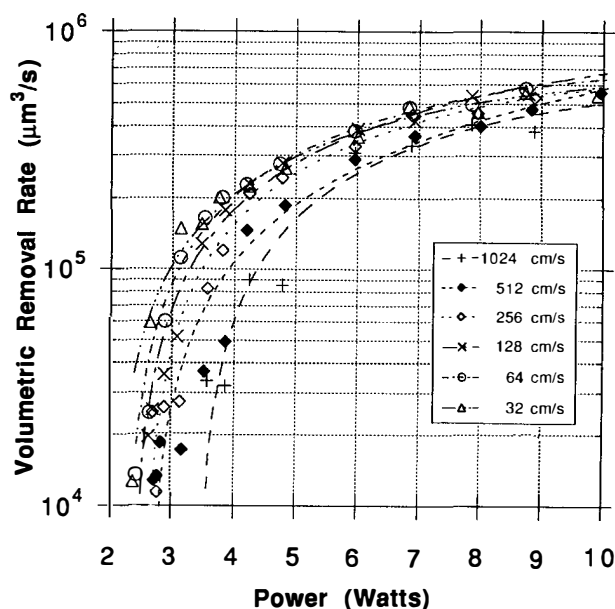


Figure 4. Volumetric removal rates versus laser power for the same variation of scan rate shown in Figure 3. At 4 Watts laser power, the slow scan case has roughly a 13- $\mu\text{m}$  linewidth, but less than half the removal rate of the fast scan case. At higher powers, roughly the same removal rates occur at all scan velocities. Typically, tens of rasters were performed in etching the boxes for the volumetric removal rate measurements. Little variation in volumetric removal rate occurred when the number of rasters was halved or doubled.

Average surface roughness values in the several tens of nanometers are typically measured under all scanning conditions with in general the smoothest surfaces occurring in the fastest scan case. At slow speeds (32–100  $\mu\text{m}/\text{s}$ ), the periodic nature of the surface texture is evident from the overlapping line scans. At intermediate speeds (100–500  $\mu\text{m}/\text{s}$ ), the surfaces have a wavy texture when viewed under Nomarski microscopy. This may be due to nonlinear optical coupling effects between

the incident power and the highly reflective molten portion of the reaction zone. In the fastest scan case, this effect appears to be reduced. One benefit from faster scanning is the significantly higher depth resolution. Thin shavings less than 0.1- $\mu\text{m}$  thick are removed per scan at the highest etch rates. Detailed studies are now in progress to characterize the laser-affected surface.

## Conclusions

We have achieved etch rates of  $5 \times 10^5 \text{ cm}^3/\text{s}$  at lateral resolutions from 13 to 33  $\mu\text{m}$ . We are continuing to study the pressure dependence of the reaction rate. Average surface roughness in the range of tens of nanometers has been achieved.

## Reference

1. T. M. Bloomstein and D. J. Ehrlich, *J. Vac. Sci. Technol. B* **10**, 2671 (1992).
2. C.K. Walker, T. M. Bloomstein, D. J. Ehrlich, to be published.

---

\*This work was sponsored by the Advanced Projects Research Agency and the Department of the Air Force, in part under a specific program supported by the Air Force Office of Scientific Research. T. M. Bloomstein is supported under a fellowship from Rockwell International Corporation. We would like to thank Marvin Tabasky at GTE for fabrication of the V-grooves and insertion of the optical fibers in the structure shown in Figure 1. We would also like to acknowledge Steven Palmacci and William DiNatale for expert technical assistance.

# INTEGRATED TEST-BED FOR MULTI-MODE DIGITAL CONTROL OF SUSPENDED MICROSTRUCTURES

G. K. Fedder and R. T. Howe

University of California at Berkeley  
Department of Electrical Engineering and Computer Sciences  
Berkeley Sensor & Actuator Center  
and the Electronics Research Laboratory  
Berkeley, California 94720

## ABSTRACT

This paper describes an integrated test-bed for research in multi-mode digital control of MEMS: a suspended polysilicon plate having four capacitive-bridge vertical position sensors, each with an integrated CMOS buffer amplifier, four differential electrostatic feedback actuators on the plate's corners, and an interdigitated comb for lateral force input. Sigma-delta ( $\Sigma$ - $\Delta$ ) force-balance control is implemented for each corner of the plate. The test bed is configured with a 0.42 N/m spring constant, 0.47  $\mu\text{g}$  mass, and a vertical resonance of 4.7 kHz. In air, vertical displacement and tilt of the plate in two axes are controlled within  $\pm 25$  nm and  $\pm 0.03^\circ$ , respectively. Measured acceleration noise is 13 milli-g rms with -73 dB dynamic range in a 50 Hz bandwidth. When operating in a low-pressure ambient, the mechanically underdamped system experiences limit-cycle oscillations, which are bounded through the use of digital lead compensation. An analytic model of the  $\Sigma$ - $\Delta$  loop, as well as simulation, successfully predicts the limit-cycle behavior.

## I. INTRODUCTION

In this paper, we present an integrated test-bed for research in multi-mode digital control of suspended microstructures. Digital closed-loop control of MEMS involves the design and simulation of mixed analog-digital, electro-mechanical systems. Prior work has focussed exclusively on the sigma-delta ( $\Sigma$ - $\Delta$ ) stabilization of single-mode microaccelerometers [1] [2] [3]. MEMS applications such as vibratory rate gyroscopes, multi-axis accelerometers and actively positioned mirrors require digital control of multiple degrees of freedom. The integrated test-bed enables the experimental verification of models and simulations of general control strategies for a suspended plate with three degrees of freedom.

The  $\Sigma$ - $\Delta$  digital control architecture is based on the high-frequency one-bit comparison between the output of a position sensor and an external reference, which generates a serial bitstream [4]. Simple digital processing of this signal then outputs a stream of high-frequency voltage pulses, which cause two quantized electrostatic force-feedback levels to act on the structure. Frequency components of the feedback above mechanical resonance are attenuated by the micromechanical mass-spring-damper. With proper attention to stability of the digital control loop, the position is stabilized, on average, at the position corresponding to the reference input. Sigma-delta control strategies linearize the electrostatic force by only applying quantized feedback levels [1]. In addition to inherent linearity,  $\Sigma$ - $\Delta$  control offers large dynamic range and eliminates the need for precision position sensing. However, digital control of a surface-micromachined structure requires integration of at least the capacitive position-sense amplifiers, in order to eliminate most of the signal degradation due to parasitic capacitance [2]. The critical circuit design issues are the position-sensor sensitivity, and speed to reduce the quantization position noise.

A fundamental limit to MEMS position control is the Brownian noise,  $x_n$  of the particular vibrational mode, in units  $\text{m}/\sqrt{\text{Hz}}$  [5]:

$$x_n = \sqrt{\frac{4k_B T \sqrt{m}}{Q k^{3/2}}} \quad (1)$$

where  $k_B$  is the Boltzmann constant and  $T$  is temperature. The Brownian noise can be reduced by increasing the spring constant,  $k$ , or quality factor,  $Q$ , or, to a lesser extent, by decreasing the mass,  $m$ . Stiffening the suspension to reduce Brownian noise necessitates a greater feedback force for a given displacement, increasing quantization noise. Surface-micromachined

structures are ideal for sub-nm position control, since the mass is small. A large micromechanical plate is usually overdamped in air. Quality factor can be increased by reducing the ambient pressure. Micromechanical quality factors up to 80000 have been reported [6], which translates into greater than a 300-fold decrease in Brownian noise.

Loop compensation is necessary to stabilize the mechanically underdamped test-bed, regardless of the sampling rate. Direct feedback from the  $\Sigma$ - $\Delta$  quantizer provides a force which is  $180^\circ$  out of phase with the displacement, resulting in uncontrolled oscillation at the resonant frequency. With compensation, the displacement stabilizes to a bounded limit-cycle oscillation. Limit cycles in conventional  $\Sigma$ - $\Delta$  modulators have been studied previously to determine the structure of quantization noise [7]. Analog lead-lag compensation was used in a bulk micromachined accelerometer designed to run in vacuum [1]. Two-bit digital compensation of a high- $Q$  micromechanical  $\Sigma$ - $\Delta$  loop was first proposed by Yun [2]. A similar digital feedback scheme is implemented in the test-bed, but, instead of a fixed two-bit gain, an adjustable gain is set to minimize the limit-cycle amplitude. Using a simple analytic model, limit-cycle amplitude and frequency as a function of system parameters are predicted, and the results agree with experimental measurements.

## II. SYSTEM DESCRIPTION AND FABRICATION

A rendering of one quarter of the test-bed is shown in Figure 1. A polysilicon plate, which measures  $360 \mu\text{m} \times 380 \mu\text{m} \times 1.6 \mu\text{m}$  in thickness, is suspended  $2.2 \mu\text{m}$  above the substrate by four serpentine springs. The springs passively constrain lateral motion of the plate. Spring compliances can be configured in seven different ways by selectively cutting fuses which anchor the springs in several locations [8]. The plate is overdamped at room-ambient pressure; damping can be reduced to nearly zero by reducing the pressure. Vertical position,  $z$ , and angular rotation about the lateral axes,  $\theta$  and  $\phi$ , are controlled by four digital feedback loops. A parallel-plate vertical-position sense capacitor is located under each quadrant of the plate, forming a bridge with a fixed reference capacitor. Use of a driven shield electrode, together with an integrated CMOS buffer amplifier, are required to detect the voltage change on the high-impedance node of the capacitive bridge. Off-chip  $\Sigma$ - $\Delta$  electronics supply digital feedback to electrostatic actuators at each corner of the plate.

Figure 2 is an optical micrograph of the die, showing the micromechanical elements integrated with CMOS circuitry. Reference capacitors are made from rigidly supported micromechanical structures which match

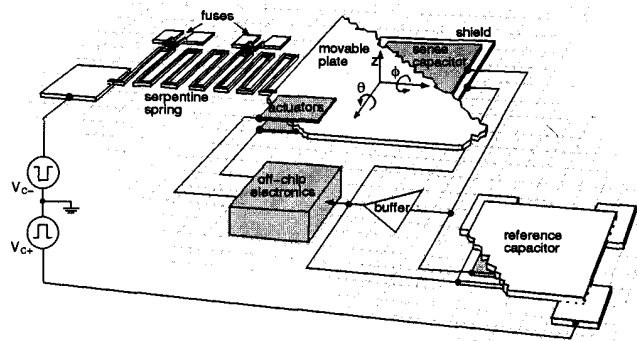


Figure 1: Schematic drawing of one quarter of the integrated test-bed.

the sense capacitor layout. Variable gain differential amplifiers, included in the layout, suffer from a design error and are not used in the system. The eight reference capacitors located at the upper and lower corners of the layout are associated with the differential amplifiers, and are also not used. Bias circuitry is shared by the four buffer amplifiers. An expanded view of

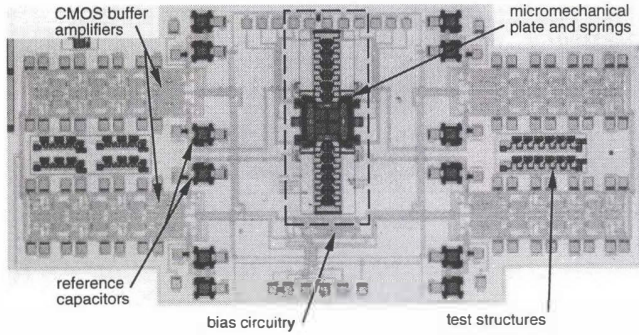


Figure 2: Die photograph of the integrated test-bed. The dashed rectangle delimits the area shown in Figure 3.

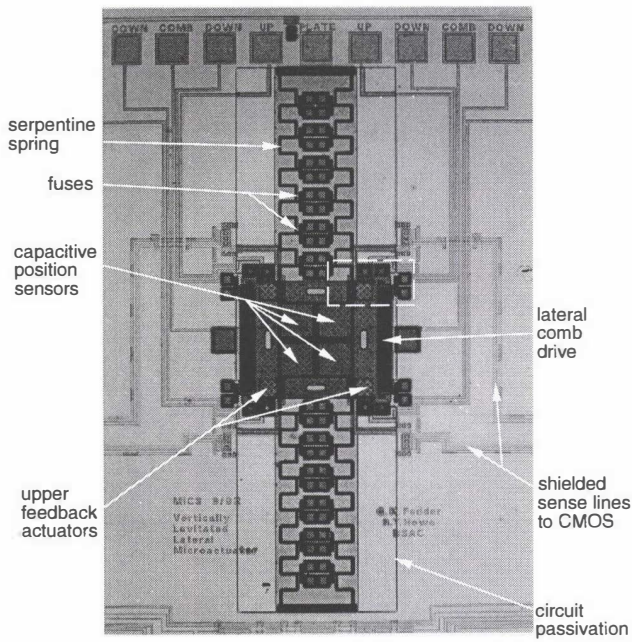


Figure 3: Expanded view of the polysilicon plate and serpentine springs. The white dashed rectangle delimits the area shown in Figure 6.

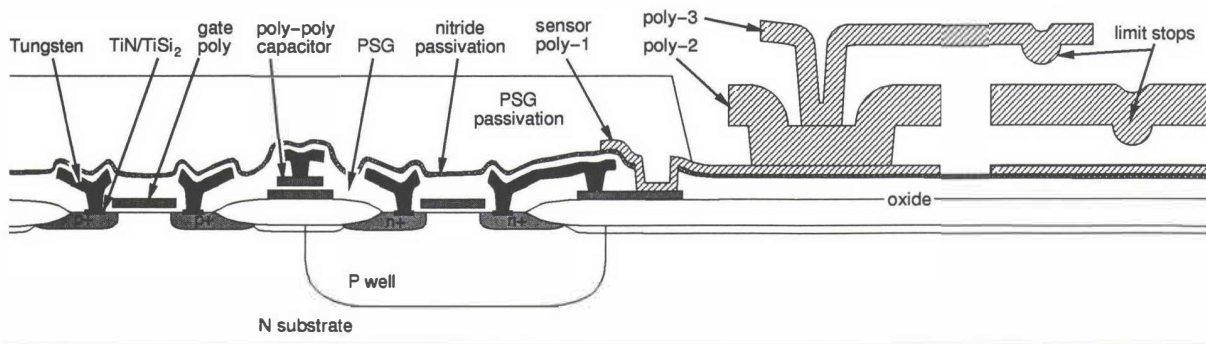


Figure 5: MICS process cross-section.

the polysilicon plate is shown in Figure 3. Two comb drives, located on two opposing sides of the plate, provide both a vertical levitation force and a lateral force for displacements up to  $10 \mu\text{m}$ . Each comb has 49,  $2 \mu\text{m}$ -wide,  $10 \mu\text{m}$ -long fingers. The four capacitive position sensors underneath the plate are identified, along with the upper and lower parallel-plate feedback actuators.

A block diagram of one of the four independent feedback channels is shown in Figure 4. Each movable sense capacitor,  $C_s$ , forms a voltage divider with a corresponding fixed reference capacitor,  $C_r$ . Balanced square-wave voltage signals,  $V_{c+}$  and  $V_{c-}$ , provide up to  $100 \text{ kHz}$ ,  $\pm 300 \text{ mV}$  modulation across the divider. A minimum area diode, connected to the buffer input, supplies a dc bias to ground. The buffer output,  $V_{\text{sense}}$ , is routed off-chip, demodulated, and amplified to generate a signal proportional to the peak-to-peak buffer output,  $V_{pp}$ . This signal is compared with an external position reference voltage,  $V_{\text{ref}}$ , quantizing the plate position into two states. The external reference enables multi-mode position control, self-test, and offset trim. The comparator output drives a level-shifting network, which generates feedback voltages containing a difference term to stabilize underdamped mechanical systems. Feedback voltage levels are adjustable, allowing experimentation with values of full-scale force and compensation. The feedback voltages are sent on-chip to the parallel-plate actuators,  $C_{up}$  and  $C_{down}$ . Digital bitstreams from the comparators are filtered and combined to form multi-mode acceleration sense signals.

Fabrication of the integrated test-bed utilizes the Berkeley MICS process: p-well  $3\text{-}\mu\text{m}$  CMOS integrated with polysilicon microstructures [2]. A MICS process cross-section is shown in Figure 5. Sputtered tungsten interconnect with  $\text{TiN/TiSi}_2$  contacts is necessary to withstand the temperature of subsequent microstructure processing steps. We have extended the original MICS process to include a second structural polysilicon layer (sensor poly-3 in Figure 5). The upper feedback actuator is made from the second structural layer, and shown in Figure 6. In order to avoid polysilicon stringer formation, the  $2.7 \mu\text{m}$ -thick sacrificial layer underlying the upper electrode is planarized by using a sandwich of spin-on glass (SOG) film and phosphosilicate glass (PSG), which is rapid-thermal annealed at  $900^\circ\text{C}$ . Upper limit stops, which prevent shorting of the actuators, are also made from the

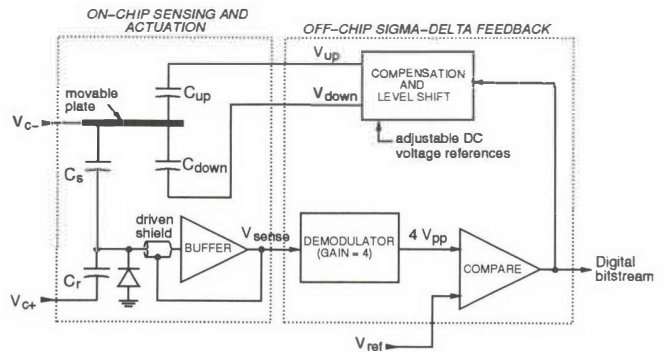


Figure 4: Block diagram of one corner of the integrated test-bed.

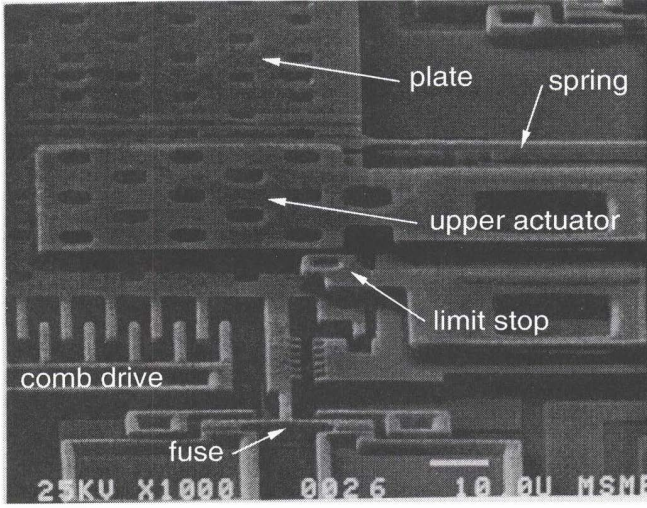


Figure 6: SEM of one corner of the movable plate, suspended below the upper actuator cantilever.

second structural layer. The spacer PSG acts as passivation for the tungsten metallization, and is only removed around the microstructure areas. Microstructure release in 5:1 BHF is done in darkness to avoid electrochemical etching of the polysilicon bonding pads.

### III. THEORY AND SIMULATION

#### A. Modeling and Simulation

There are three controllable mechanical modes of the plate: vertical displacement,  $\Delta z$ , and the two rotations,  $\theta$  and  $\phi$ , about the lateral axes. These modes are modeled with rigid-body, mass-spring-damper transfer functions.

$$H_z(s) = F(s)/\Delta z(s) = m(s^2 + 2\zeta_z\omega_z s + \omega_z^2) \quad (2)$$

$$H_\theta(s) = T_\theta(s)/\theta(s) = I_\theta(s^2 + 2\zeta_\theta\omega_\theta s + \omega_\theta^2) \quad (3)$$

$$H_\phi(s) = T_\phi(s)/\phi(s) = I_\phi(s^2 + 2\zeta_\phi\omega_\phi s + \omega_\phi^2) \quad (4)$$

$\Delta z$  is defined relative to the fabricated spacer gap of  $2.2 \mu\text{m}$ .  $F$ ,  $T_\theta$ ,  $T_\phi$  are external force and torques on the plate.  $m$ ,  $I_\theta$ , and  $I_\phi$  are plate mass and mass moments of inertia.  $\zeta_z$ ,  $\zeta_\theta$ , and  $\zeta_\phi$  are dimensionless damping factors and  $\omega_z$ ,  $\omega_\theta$ , and  $\omega_\phi$  are resonant frequencies of each mode. For an underdamped system ( $\zeta < 1/\sqrt{2}$ ), the quality factor is defined as  $Q = 1/(2\zeta\sqrt{1-\zeta^2})$ . The test-bed system is analyzed by transforming the four quad-symmetric feedback loops into the three modes. However, since there are four feedback loops and only three controllable modes, the system is over-constrained. Offsets must be precisely adjusted to avoid undesired oscillations or force limiting in one of the loops.

The test-bed can control the plate position with a large range of motion relative to the gap spacing. An accurate model of the position sensor is needed to relate each position reference input to the vertical displacement. Assuming balanced input modulation with amplitude  $V_c$ , the voltage divider peak-to-peak output is

$$V_{pp} = 2V_c \left( \frac{C_r - C_s}{C_r + C_s + C_p} \right) \quad (5)$$

where  $C_p$  is the effective parasitic capacitance of the voltage divider high-impedance node to ground. The sense capacitance has a variable, parallel-plate, component and a fixed component,  $C_{sf}$ , from interconnect.

$$C_s = C_{sf} + \frac{C_{svo}}{1 + \Delta z/z_o} \quad (6)$$

where  $z_o$  is the fabricated spacer gap, and zero angular displacement is assumed. When the plate is at the same height as the reference capacitor, the variable sense capacitance is equal to  $C_{svo}$ . By substituting Equation (6)

into Equation (5), the relation between the sensor output and displacement is derived.

$$V_{pp} = 2V_c \left( \frac{C_r - C_{svo}}{C_r + C_{svo} + C_p} \right) \left[ \frac{1 + \left( \frac{C_r - C_{sf}}{C_r - C_{svo}} \right) \frac{\Delta z}{z_o}}{1 + \left( \frac{C_r + C_{sf} + C_p}{C_r + C_{svo} + C_p} \right) \frac{\Delta z}{z_o}} \right] \quad (7)$$

where  $C_s|_{\Delta z=0} = C_{svo} = C_{sf} + C_{svo}$ .

#### B. Limit-Cycle Analysis

A simple, single-axis loop model of the test-bed is used to predict the amplitude and frequency of limit-cycle oscillations. A system block diagram of the  $\Delta z$  mode is shown in Figure 7. The position sensor, demodulator, and comparator are modeled together in the nonlinear quantizer function  $H_q(\Delta z, \omega)$ . The quantizer has an output value of +1 or -1, corresponding to the plate being above or below the position reference. Compensation and level shift of the quantizer output to provide the feedback force,  $F_{fb}$ , is modeled by  $H_{fb}(z)$ .

Limit-cycle waveforms of linearized feedback force,  $F_{fb}$ , and plate displacement,  $\Delta z$ , are given in Figure 8. After a reference crossing of the plate is sensed, a restoring force pulse of magnitude  $F_v$ , is output to the actuators. The feedback response must occur at a clock edge, and will be delayed by  $T_d$  from the time of the reference-crossing. The lead pulse lasts one sample period,  $T_s$ , after which application of a smaller force magnitude,  $F_o$ , extends until the plate crosses the displacement reference. The digital feedback compensation is expressed as a z-transform.

$$H_{fb}(z) = F_o \left[ 1 + G_v \frac{(1 - z^{-1})}{2} \right] \quad (8)$$

where  $G_v = F_v/F_o - 1$  is the adjustable lead-compensation gain.

Without compensation ( $G_v = 0$ ) and neglecting the extra delay  $T_d$ , the comparator output is exactly in phase with the displacement. The feedback force is then  $180^\circ$  out of phase with the displacement, resulting in an unstable system which oscillates at the resonant frequency. Introduction of the compensation term,  $1 - z^{-1}$ , in the feedback path, adds phase lead to the loop transfer function, and acts to stabilize the system. However, sampling of the comparator output is responsible for a phase delay in the loop, partly negating the effect of the compensation. The limit-cycle oscillation condition occurs when the phase lead from the compensation balances the phase delay due to the quantizer sampling.

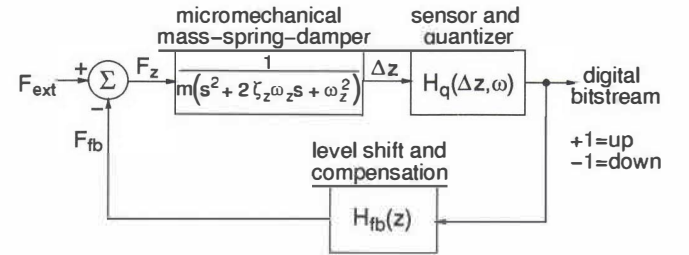


Figure 7: Loop model of the  $\Delta z$  mode for limit-cycle analysis.

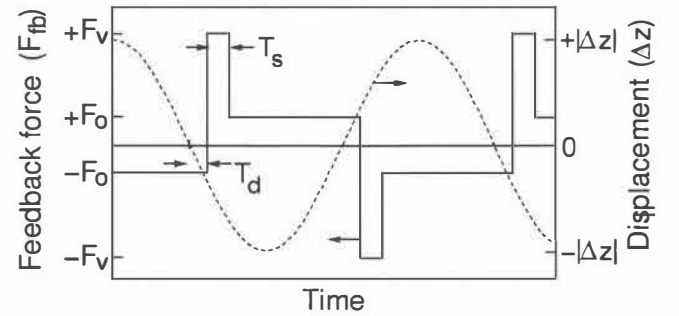


Figure 8: Limit-cycle waveforms of linearized feedback force, (solid line) and vertical plate displacement (dashed line).

Describing-function analysis [10] is used to determine the nonlinear quantizer transfer function. The describing function,  $H_q(\Delta z, \omega)$ , is obtained by relating the magnitude and phase of the fundamental frequency component of the quantizer output to a sinusoidal input signal. The quantizer gain is found by dividing the fundamental amplitude of the  $\pm 1$  quantizer output by the  $\Delta z$  amplitude.

$$H_q(\Delta z, \omega) = \frac{4}{\pi|\Delta z|} e^{-j\omega T_d} \quad (9)$$

Higher order harmonic components of the quantizer output are assumed to be attenuated through the loop by the two-pole rolloff of the mechanical system.

The system loop gain,  $L(\Delta z, \omega)$ , is the product of Equations (2), (8), and (9).

$$L(\Delta z, \omega) = \frac{4F_o e^{-j\omega T_d} [1 + G_v(1 - e^{-j\omega T_s})/2]}{\pi|\Delta z|m(-\omega^2 + j\omega_r\omega/Q + \omega_z^2)} \quad (10)$$

The magnitude,  $|\Delta z|$ , and frequency of the limit cycle are found by setting the loop gain equal to -1. For the undamped case,  $|\Delta z|$  is unbounded for  $G_v < 2T_d/T_s$ . Any sampled-data system will have a maximum delay equal to at least the sampling period, so use of  $2 - z^{-1}$  compensation ( $G_v = 2$ ) will not stabilize the system.

The quantizer phase delay,  $T_d$ , will vary because the limit-cycle frequency will never exactly equal a multiple of the sampling rate. For the test-bed system,  $T_d$  must be between  $T_s/2$  and  $3T_s/2$ , neglecting the effect of noise at the comparator input. Using these extreme values of  $T_d$ , maximum and minimum bounds for limit-cycle frequency and amplitude can be calculated. The maximum displacement amplitude is plotted versus lead-compensation gain in Figure 9(a) for the test-bed operating with a  $\pm 25$  g full-scale range. An optimal value for the lead-compensation gain is around  $G_v = 7$ , which minimizes the amplitude for  $Q = 50000$ . Lowering the  $Q$  allows the system to stabilize for lower values of compensation gain. The amplitude increases dramatically for  $G_v < 3$ , regardless of the sampling rate. Increasing the sampling rate from 100 kHz to 1 MHz reduces the limit-cycle amplitude by a factor of 100. Figure 9(b) is a plot of amplitude versus sampling rate, showing the -40dB/decade slope. The amplitude rapidly increases at sampling rates below 100 kHz, because the limit-cycle frequency approaches the resonant frequency of the test-bed (4.7 kHz). Increasing  $G_v$ , or decreasing  $Q$  or  $\omega_z$ , will lower the amplitude at sampling rates below 100 kHz. Reduction of actuator force nonlinearity to 0.1 % requires a maximum displacement amplitude of 0.5 nm, corresponding to a sampling rate of 2.1 MHz.

#### IV. EXPERIMENTAL RESULTS

We have performed characterization of the test-bed in air using  $\Sigma$ - $\Delta$  control of the three modes. Devices are packaged in 24-pin DIPs for testing. Testing is done at a probe station using a custom mounting for the device package. The plate mass is 0.47  $\mu$ g. Only the first fuse is cut from the serpentine springs, giving a vertical spring constant of 0.42 N/m and a resonant frequency of 4.7 kHz. One period of the position sensor waveform, for various reference input values, is shown in Figure 10. Tungsten contacts connecting the reference capacitor to the bridge are disconnected, due to HF attack during the microstructure release. The resulting imbalance in the capacitive divider produces a peak-to-peak sensor offset voltage of -103 mV. The interconnect leading off-chip has a capacitance value of about 10 pF, limiting the risetime to 424 ns. A source-follower circuit drives the signal off-chip, adding a dc offset of -0.81 V. Photocurrent in the diode at the input to the buffer causes the dc bias to shift more negative when the device is exposed to light. The asymmetric current-voltage diode characteristic is responsible for the output dc bias shift with increasing signal amplitude.

Vertical displacement of the plate is measured by counting fringes using laser interferometry between the top plate and underlying substrate surfaces. Each fringe occurs at multiples of a half wavelength of the He-Ne laser (316.4 nm). In previous work, interferometry with a monochromatic infrared source has been used to measure parallelism of bulk-machined surfaces [9]. The present laser interference technique is used to obtain video confirmation of closed-loop tracking of vertical position and tilt to within

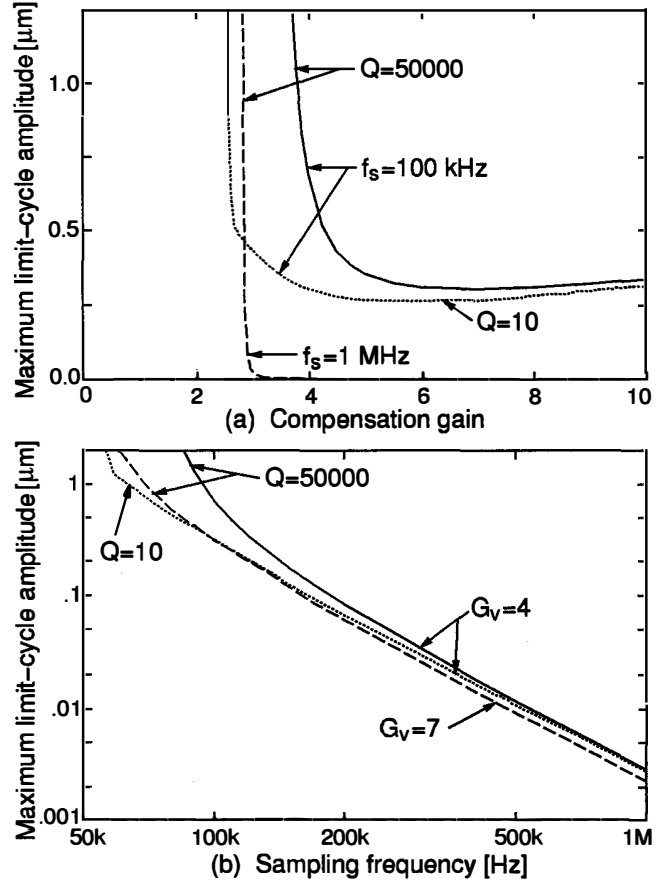


Figure 9: (a) Maximum limit-cycle amplitude,  $|\Delta z|$ , versus lead-compensation gain,  $G_v$ . (b) Maximum limit-cycle amplitude versus sampling frequency,  $f_s$ .

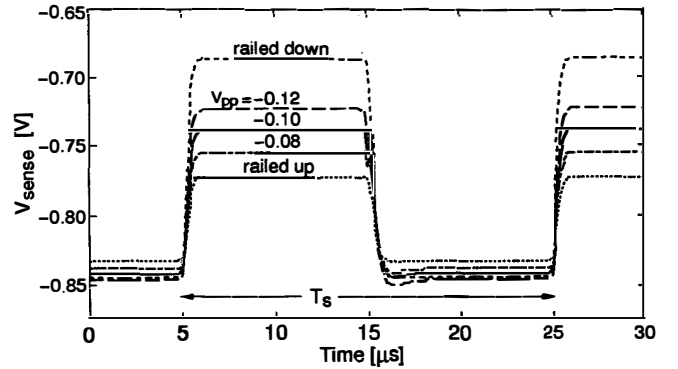


Figure 10: One period of the modulated sensor voltage, for various position reference input values.

$\pm 25$  nm and  $\pm 0.03^\circ$ , respectively.

Measured and calculated values of sensor output voltage versus displacement are compared in Figure 11. Displacement measurement error is  $\pm 25$  nm; sensor output error is  $\pm 1$  mV. Calculated sensor output values are computed from Equation (7), using  $C_{svo} = 41.4$  fF,  $C_{sf} = 4.0$  fF,  $C_r = 6.8$  fF, and  $C_p = 173$  fF. Interconnect overlap and fringe capacitance account for the reference and fixed sense capacitance. The effective parasitic capacitance value is about ten times less than the layout value, demonstrating the benefit of the driven shield. Sensitivity of the position sensor is 42 mV/ $\mu$ m at zero displacement.

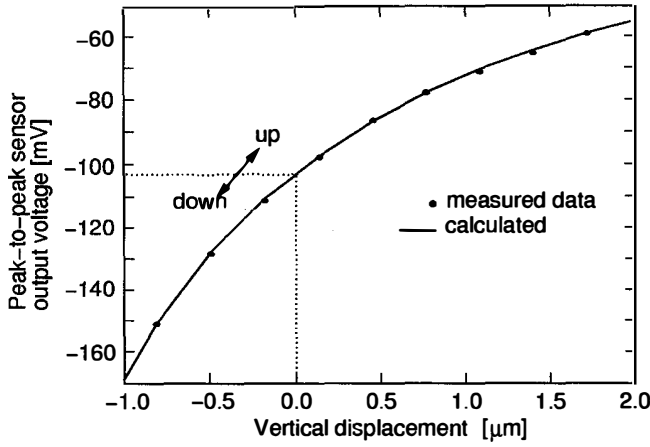


Figure 11: Measured and calculated peak-to-peak sensor voltage versus plate displacement.

Measured feedthrough between adjacent actuators and sense is a maximum of -61 dB, with two exceptions. In these two cases, the sensor high-impedance lines crossover the actuator interconnect, raising the feedthrough to -38 dB. For 10 V of actuation voltage, the sensor feedthrough is 130 mV, which is significant when compared with the signal amplitude. However, the feedthrough voltage shift lasts through multiples of a sample period, so the modulated position signal and closed-loop control should not be affected. In practice, the feedthrough must settle before the signal is sampled. Operating the test-bed above 50 kHz adds noise to the position signal during actuator switching. As an alternative control scheme, the sense and feedback cycles could be time multiplexed, at the cost of decreasing the sampling rate.

Comb-drive levitation force is used to find the open-loop step response at atmospheric pressure. When  $\Delta z = 0$ , the open-loop falltime is 2.3 ms, corresponding to a damping factor,  $\zeta_s$ , of 16. Holes in the plate are spaced only 16  $\mu\text{m}$  apart. Falltime measurements of 0.5  $\mu\text{m}$  steps reveal that mechanical damping does not have a strong dependence on gap. Open-loop measurements with larger displacements have not been measured, because of lateral comb-drive instability at higher applied voltages. Damping is approximated as a constant in simulations. The measured comb levitation force of 1.7 nN/V<sup>2</sup> is 24 % larger than the value calculated from two-dimensional finite element analysis. Fringing field capacitance is believed to be responsible for the difference in measured and calculated values.

Plots of simulated and measured closed-loop response to an 150 Hz square-wave position reference input are given in Figure 12. Operation is at atmospheric pressure without feedback compensation, and with a sampling rate of 50 kHz. Simulated results are generated by using a commercially available program for simulating dynamic systems[11]. Excellent agreement between the measured and simulated peak-to-peak sensor voltage waveforms is obtained. Limit-cycle oscillations, seen in the single-sweep waveform when the position is locked to the reference, have an amplitude of approximately 25 nm. Total Brownian noise in air is 50 times smaller than the limit-cycle amplitude value. The average quantizer output, plotted in Figure 12(d), is near zero for both of the controlled plate positions. The actuator force magnitude increases as the actuator gap is reduced, so average quantizer output does not vary linearly with position.

Acceleration performance is tested in air, with  $f_s = 50$  kHz and  $G_v = 0$ . The digital bitstreams are passed through a sinc<sup>3</sup> FIR filter, decimated by 500, and combined to provide an acceleration waveform for analysis. Measured acceleration noise is -90 dB/ $\sqrt{\text{Hz}}$ , referenced to a full-scale range of 62 g (0 dB). In a 50 Hz bandwidth, the measured noise floor is around 13 milli-g, with the measurement probably being limited by external vibration.

Underdamped system dynamics are investigated by placing the test-bed in a vacuum probe station. Our experiments are constrained to sampling frequencies up to 100 kHz and compensation gain up to 4, because of external circuit limitations. Three of the four feedback channels are activated; the fourth channel has its actuators grounded to avoid the over-constrained instability.

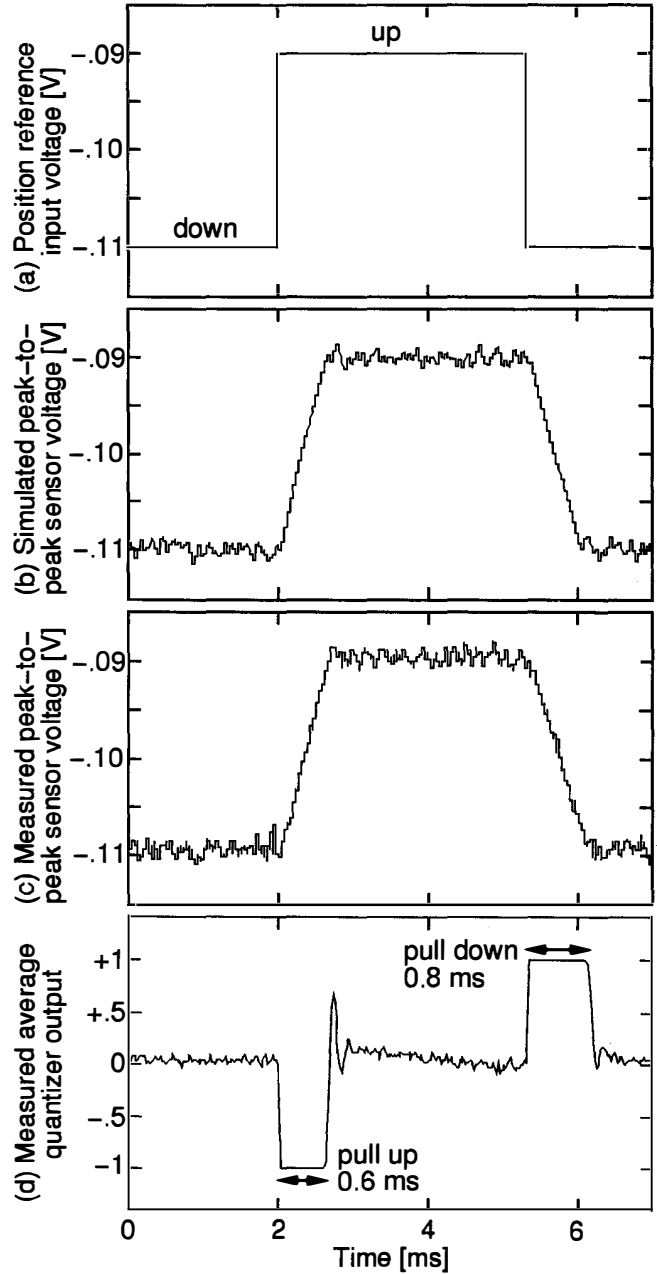


Figure 12: Closed-loop response to an 150 Hz square-wave position reference input. (a) Position reference input voltage,  $V_{\text{ref}}$ . (b) Simulated peak-to-peak sensor voltage waveform,  $V_{pp}$ . (c) Measured  $V_{pp}$  waveform. (d) Measured quantizer output, averaged over 1024 sweeps and normalized to  $\pm 1$ .

Measured peak-to-peak sensor voltage waveforms are compared with simulation and theoretical results in Figure 13, with  $f_s = 100$  kHz and  $G_v = 4$ . The waveform data is presented for three different pressure values, 10 T, 1 T, and 0.1 T, corresponding to estimated quality factors of 2.4, 24, and 240. Simulation results qualitatively match the measured waveform frequency and amplitude. The maximum limit-cycle amplitude given by the theoretical model is also in agreement with the measured data. In the P = 0.1 T case, actuator nonlinearity and added force from the sensor capacitors distort the feedback force, and is responsible for a larger measured limit-cycle amplitude than the theoretical value. With lead compensation  $G_v < 3$ , the underdamped system is unstable and rails to the limit stops, as predicted by the theory.

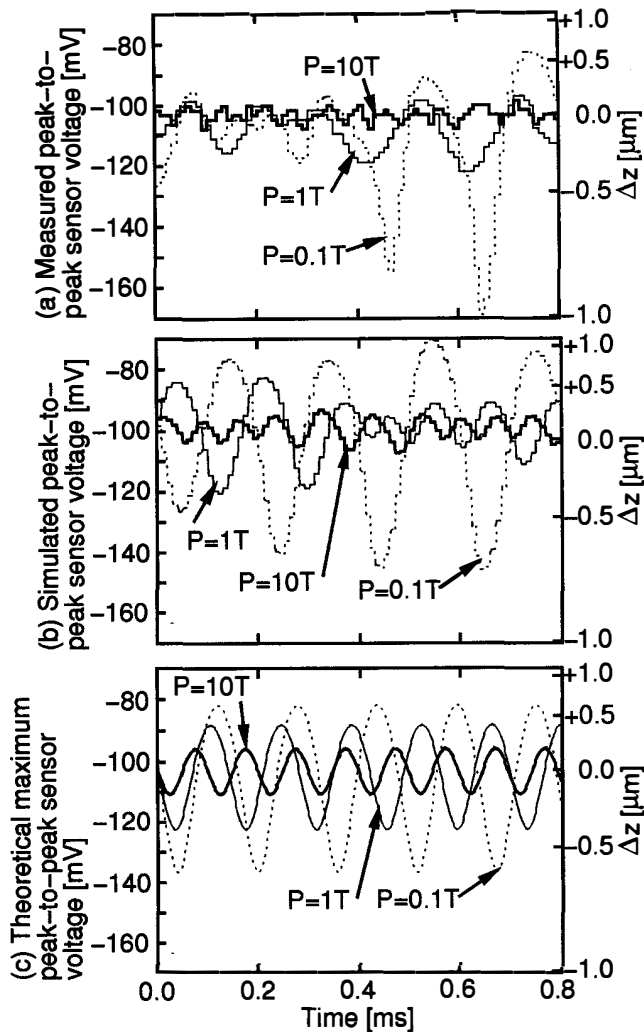


Figure 13: Measured, simulated, and theoretical peak-to-peak sensor voltage waveforms. Results are presented for three different pressure values: 10 T, 1 T, and 0.1 T.

## V. CONCLUSIONS

Digital control of a micromechanical plate is demonstrated for vertical and angular motion. Although the parallel-plate actuator force is highly nonlinear with position and voltage, the  $\Sigma$ - $\Delta$  feedback successfully controls plate position to the mechanical limit stops. For an 100 kHz sampling rate, accuracy of the position control is limited to  $\pm 25$  nm. Higher frequency circuitry is necessary to reduce the displacement amplitude below the Brownian noise level of the test-bed, which is 0.46 nm in air.

We have shown experimentally that the integrated test-bed can be operated at high- $Q$ , lowering the Brownian noise floor for digital MEMS applications. A limit-cycle model successfully predicts the behavior of the high- $Q$  system. Other types of micromechanical  $\Sigma$ - $\Delta$  loops, for example, with pulsed feedback or analog compensation, can be analyzed using the limit-cycle theory. Appropriate sampling frequency and compensation can be designed into future systems to obtain a specified maximum limit-cycle amplitude.

Further characterization of the test-bed is concentrating on the behavior of the system at reduced pressures. A redesign of the external electronics is necessary to operate above 100 kHz sampling frequency. Lowering the system spring constant will decrease the limit-cycle amplitude while operating at lower sampling rates. Exploration of the available parameter space will supply important information for future MEMS projects.

## Acknowledgements

The authors thank the U. C. Berkeley Microfabrication Facility. Special thanks to James M. Bustillo, who helped with sensor processing and developed the SOG process sequence, Shenqing Fang for completing the CMOS process steps, William A. Clark for helping construct the external electronics, and Prof. Bernhard Boser for discussions on quantization noise. This research was funded by the Berkeley Sensor & Actuator Center, an NSF/Industry/University Research Center, and ARPA.

## REFERENCES

- [1] W. Henrion, L. DiSanza, M. Ip, S. Terry, and H. Jerman, "Wide Dynamic Range Direct Digital Accelerometer," *Technical Digest, IEEE Solid-State Sensor and Actuator Workshop*, Hilton Head, SC, June 1990, pp.153-157.
- [2] W. Yun, R. T. Howe and P. R. Gray, "Surface micromachined, digitally force-balanced accelerometer with integrated CMOS detection circuitry," *Technical Digest, IEEE Solid-State Sensor and Actuator Workshop*, Hilton Head, SC, June 1992, pp.21-25.
- [3] Y. DeCoulon, T. Smith, J. Hermann, M. Chevroulet, and F. Rudolf, "Design and test of a Precision Servoaccelerometer with Digital Output," *Technical Digest, 7th Int'l Conference on Solid-State Sensors and Actuators*, Yokohama, Japan, June 1993, pp.832-835.
- [4] J. C. Candy and G. C. Temes, "Oversampling Methods for A/D and D/A Conversion," in *Oversampling Delta-Sigma Data Converters*, IEEE Press, New York, 1992, pp. 1-29.
- [5] T. B. Gabrielson, "Mechanical-Thermal Noise in Micromachined Acoustic and Vibration Sensors," *IEEE Trans. Electron Devices*, vol. ED-40, May 1993, pp. 903-909.
- [6] C. T.-C. Nguyen, "Quality Factor Control for Micromechanical Resonators," *Technical Digest, IEEE International Electron Devices Meeting*, San Francisco, CA, Dec. 13-16, 1992, pp. 505-508.
- [7] J. C. Candy and O. J. Benjamin, "The Structure of Quantization Noise from Sigma-Delta Modulation," *IEEE Trans. Commun.*, vol. COM-29, Sept. 1981, pp. 1316-1323.
- [8] G. K. Fedder, J. C. Chang, and R. T. Howe, "Thermal Assembly of Polysilicon Microstructures With Narrow Comb-Drive," *Technical Digest, IEEE Solid-State Sensor and Actuator Workshop*, Hilton Head, SC, June 1992, pp.63-68.
- [9] J. H. Jerman, "A Miniature Fabry-Perot Interferometer with a Corrugated Silicon Diaphragm Support," *Technical Digest, IEEE Solid-State Sensor and Actuator Workshop*, Hilton Head, SC, June 1990, pp.140-144.
- [10] J. K. Roberge, *Operational Amplifiers*, John Wiley & Sons, Inc., New York, 1975, pp. 217-242.
- [11] *SIMULINK User's Guide*, The MathWorks, Inc., Natick, MA, 1992.

# MICROMACHINED STRUCTURES FABRICATED USING A WAFER-BONDED SEALED CAVITY PROCESS

C.H. Hsu and M.A. Schmidt

Microsystems Technology Laboratories  
Department of Electrical Engineering and Computer Science  
Massachusetts Institute of Technology, Cambridge, MA 02139, USA

## ABSTRACT

This paper discusses silicon wafer bonding technologies for the fabrication of micromechanical devices integrated monolithically with electronics. New work aimed at processes for fabrication of "surface-micromachining-like" structures such as tuning fork gyroscopes and accelerometers is described. This work provides results on a junction-isolation scheme, dry release methods to minimize stiction problems, and mechanical properties of the resultant structures. Structures fabricated using this technology for angular rate and acceleration sensing are shown. The development of these process technologies, in combination with the front-end processes previously reported, now permits full integration of electronics on silicon wafer bonded substrates in a way which provides virtually no perturbation of the IC fabrication process.

## INTRODUCTION

Silicon wafer bonding has been used to fabricate surface-micromachining-like structures for a variety of sensors and actuators [1, 2, 3, 4, 5]. Recently, we proposed a method for fabrication of sensors with integrated electronics based on a silicon wafer bonding process [6]. Figure 1 illustrates the process. We begin by joining two silicon wafers, a device wafer containing an etch-stop layer and a handle wafer containing etched cavities, using wafer bonding. The bulk of the device wafer is then thinned to produce a wafer with sealed cavities which looks virtually identical to an unprocessed wafer. At this point the bonded and thinned structure can be returned to a standard IC facility for electronics fabrication. Following circuit processing, low-temperature back-end processes are performed to functionalize the sensors. The process has two significant features. First, the mechanical layer which results from this process has reliable, reproducible mechanical properties. Second, the electronics integration strategy is compatible with standard IC processes and equipment.

Two major front-end technology issues in using wafer bonding for the fabrication of sensors and actuators; wafer thinning processes, and the control of the residual pressure in cavities formed by bonding and etchback, have been discussed in details previously [6]. In this paper, we will discuss a modification to the thinning process to achieve electrical isolation of the mechanical layer from the substrate. The back-end processes entail etching of the mechanical layer for accelerometers/gyroscopes or etching of a pressure inlet port for the pressure sensor, followed by the low-temperature bonding of a capping wafer. This paper will discuss the etching of the mechanical layer for accelerometers/gyroscopes, and the resultant mechanical properties of this layer. Processes for etching pressure inlet ports and low-temperature capping wafer bonding are the subject of current research and will be presented in the future [7].

Thinning methods are critically important in wafer bonded micromachining processes since the thickness tolerance of the mechanical parts will be defined by this step. In our previous work [6], we described an electrochemical thinning process that produces a n-type mechanical layer on a n-type substrate. However, electrical isolation is important for a class of structures built in this technology

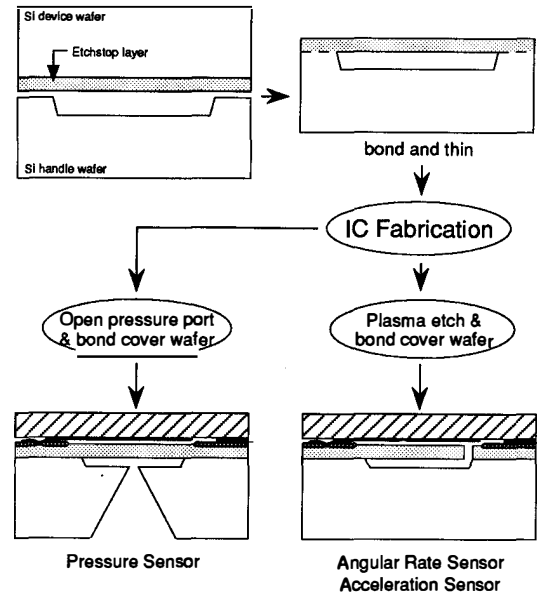


Fig. 1 MIT wafer-bonded integrated sensor process

(accelerometers and gyroscopes, for example). Two technical approaches are either to use a buried chemical etch-stop ( $p^{++}$  doping or oxide) and bonding to an oxide coated substrate wafer (*dielectric-isolation*) or to use a junction electrochemical etch-stop and a p-type substrate wafer (*junction-isolation*) as illustrated in figure 2. While the chemical etch-stop permits formation of dielectrically isolated mechanical parts, the availability, quality, and cost of either SOI starting material or buried  $p^{++}$  epi is a limiting factor. Electrochemical etch-stop methods are known to produce high quality mechanical structures, but the layers are most conveniently formed by silicon-silicon bonding, where the lower wafer provides an accessible electrical connection during the etch-stop process. This process thus precludes electrical isolation of the mechanical parts from the substrate. In an attempt to capitalize on the convenience of a silicon-silicon bonded electrochemical etch-stop, while still achieving electrical isolation of the mechanical layers, we have implemented a pnp structure for the etch-stop. This paper discusses results on the pnp electrochemical etch-stop process, and the effectiveness of the resultant junction-isolation scheme.

A second important feature of the integrated process is the ability to fabricate these parts using a completely dry release process. A resist mask is used for device patterning followed by a Si plasma etch to pattern the mechanical structure and a plasma etch to remove the resist. With this dry release method, large suspended plates have been successfully fabricated as tuning fork tines for the gyroscopes and the proof masses for the accelerometers. This paper describes this dry release process in details.

## SEALED CAVITY WAFER FABRICATION

The process in figure 1 can be segmented into three sub-processes; pre-IC fabrication, IC fabrication, and post-IC

fabrication. The IC-fabrication sub-process will not be discussed in this paper. A detailed process description for pre-IC fabrication and post-IC fabrication sub-processes is provided in the following sections.

### Pre-IC Fabrication Process

The process starts with two wafers, a handle wafer containing etched cavities, and a device wafer containing the mechanical layer. In this work, three different types of device wafers were used, as summarized in table 1. The first two (diffused and epi) are used in the junction-isolation process, and the third is used for dielectric-isolation. Each of those processes is described in further detail in the following sections.

#### A) Junction-Isolation Process

Figure 2(a) illustrates the sealed cavity process with junction-isolation. Epi wafers were formed by growing a n-type ( $5 \Omega\text{-cm}$ ) layer on a p-type ( $10\text{-}20 \Omega\text{-cm}$ ) substrate with an average thickness of  $11 \mu\text{m}$ . Diffused-junction device wafers were formed by implanting phosphorus in p-Si wafers ( $10\text{-}20 \Omega\text{-cm}$ ) followed by a 23-hour drive-in at  $1150^\circ\text{C}$  to obtain a junction depth of  $10 \mu\text{m}$ .

The handle wafers are subjected to a boron blanket implant and drive-in to heavily dope the back surface ( $> 5 \times 10^{19} \text{cm}^{-3}$ ) in order to ensure good electrical contact during the electrochemical etch and to provide ohmic contact for backside metalization later in the fabrication process. All handle wafers contain  $1\text{-}2 \mu\text{m}$ -deep trenches formed by plasma-etching.

After being hydrated with a standard RCA clean, device wafers and patterned handle wafers are contacted in a pure oxygen ambient using a single-wafer spinner with a modified Teflon chuck which can hold two wafers face-to-face, separated by Teflon shims. A detailed description on the controlled ambient bonding apparatus and procedures is provided in *reference* [6]. After the bonded wafers have been inspected for the presence of voids using an infrared camera, they are then subjected to a high temperature anneal for one hour at  $1000^\circ\text{C}$  in a nitrogen ambient to strengthen the bond.

Subsequently, the device wafer is thinned back using a two-step process. First, the wafer pair is ground and polished to remove about  $400 \mu\text{m}$  of silicon from the device wafer. The wafer surface is chemically polished until a mirror smooth finish is obtained. The wafer pair is then electrochemically etched using the procedures and apparatus identical to those described previously [6]. The process differs from previous work due to the existence of an additional diode (diode #1 in figure 3) which is incorporated to provide electrical isolation in the final structure. The electrochemical etch, however, requires positive bias on the handle wafer, which acts to forward bias this extra diode. In its forward biased state, the diode has very little impact on the operation of the electrochemical etch. Thus the etch will still terminate at the junction formed between the n-epi (or the diffused n-Si etch-stop) and the p-type substrate (diode #2 in figure 3), and will result in an n-type mechanical layer sitting on a p-type substrate. A post-KOH clean procedure, consisting of piranha clean, HF dip, and a standard RCA clean, is then performed on the etched-back wafers before they are allowed to enter the IC fabrication line.

Table 1: Three sets of device wafers and handle wafers used in this study

	Set #1	Set #2	Set #3
Device Wafer	$10 \mu\text{m}$ n-type diffused-junction	$11 \mu\text{m}$ n-type epi junction	$14.4 \mu\text{m}$ SOI
Handle Wafer	$10\text{-}20 \Omega\text{-cm}$ p-prime	$10\text{-}20 \Omega\text{-cm}$ p-prime	$10\text{-}20 \Omega\text{-cm}$ p-prime

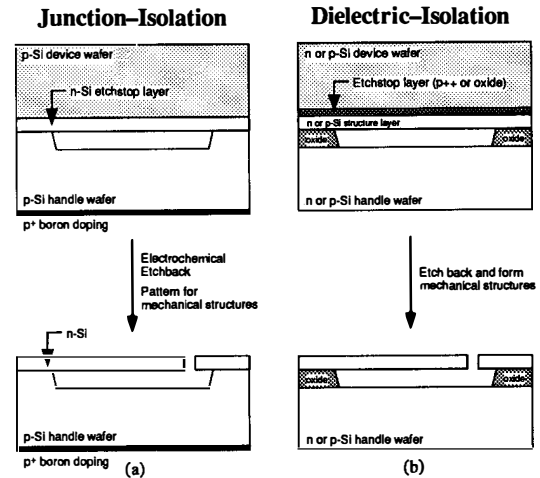


Fig. 2 Sealed cavity processes for electrical isolation of the mechanical parts from the substrate

#### B) Dielectric-Isolation Process

SOI wafers with  $0.4 \mu\text{m}$  buried oxide,  $14.35\text{-}14.42 \mu\text{m}$ -thick n-Si ( $6 \Omega\text{-cm}$ ) device layers, and n-Si ( $6 \Omega\text{-cm}$ ) substrates are used as device wafers for this process. The sealed cavity process with dielectric-isolation is illustrated in figure 2(b). The handle wafer is subjected to boron implant and drive-in as described in the previous section. Next, a layer of  $1 \mu\text{m}$ -thick thermal oxide is grown on the handle wafer. This oxide layer is then patterned and etched (BOE etch) to form cavities. The backside oxide layer is protected by a resist mask during the patterning BOE etch. This oxide layer is used as a masking material during the wafer thinning process. The device wafer and handle wafer are brought to contact in a controlled ambient as described in the previous section. After initial contact, the wafer pair is then annealed for one hour at  $1000^\circ\text{C}$  in a nitrogen ambient to strengthen the bond.

The device wafer is then ground to remove approximately  $480 \mu\text{m}$  of silicon. Next, the wafer pair is chemically etched in a  $95^\circ\text{C}$ , 20% (by weight) KOH solution until the etch terminates at the buried oxide etch-stop. The oxide etch-stop is then removed by wet-etching in BOE. Finally, the etched-back wafers are subjected to the post-KOH clean before they are returned to the IC fabrication line.

### Post-IC Fabrication Process

As shown in figure 1, two major post-IC processing steps are required to complete the integrated sensor process; a deep Si etch to form mechanical parts, and a capping wafer process to form over electrodes [7]. The silicon etch steps will be described in detail in this section.

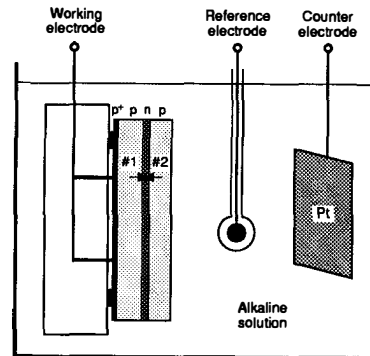


Fig. 3 Pnp electrochemical etch setup

An important feature for the wafer-bonded sealed cavity process is the ability to fabricate the mechanical parts using a completely dry release process as shown in figure 4. A resist mask is used for device patterning followed by a deep Si plasma etch (~10–15  $\mu\text{m}$ ) to pattern the mechanical structure. The sealed cavity has a partial vacuum and is etched at reduced pressure. Thus a differential pressure can exist across this mechanical layer which can cause it to fail catastrophically as the etch nears completion, particularly on very fragile structures. To eliminate this problem, a two-step approach is taken in the etching process.

A 1.1  $\mu\text{m}$ -thick resist mask is used to pattern “vent holes”, as shown in figure 4(a), on the n-type mechanical layer. These vent holes range from 3  $\mu\text{m}$  x 3  $\mu\text{m}$  to 6  $\mu\text{m}$  x 6  $\mu\text{m}$ , and they are located at remote parts away from the devices. A 5  $\mu\text{m}$ -deep Si plasma etch is used to pattern the vent holes. This is the same plasma etch chemistry which will be used to etch 10–15  $\mu\text{m}$  Si later to etch free the mechanical parts. A 2  $\mu\text{m}$ -thick resist mask is then used for device patterning followed by the 10–15  $\mu\text{m}$ -deep Si etch (figure 4(c)-(d)). This plasma etch is based on a  $\text{SF}_6/\text{C}_2\text{F}_4$  chemistry and gives an average sidewall angle of between  $83^\circ$  to  $86.5^\circ$ , an average Si etch rate of 71.4  $\text{\AA}/\text{s}$ , and a Si:resist selectivity between 7:1 to 12.5:1 due to loading effect. The vent holes are etched through first during the deep Si etch and thus balance the pressure difference and prevent the potential “blow-out” of mechanical parts.

After the deep Si etch, the resist mask can easily be removed by an oxygen plasma. Since this is a completely dry process, no adhesion problems are observed. We routinely fabricate suspended plates as large as 1 mm by 1mm as tuning fork tines and accelerometer proof masses.

## RESULTS AND DISCUSSION

### A) Pnp Electrochemical Etch-stop

It is important to be able to accurately control the thickness of the bonded and etched back layer over the cavity in order to make well-defined mechanical parts. We have previously reported that the position of the “standard” np electrochemical etch-stop relative to the metallurgical junction is a function of etchant temperature, such that an increase in the temperature results in a stop closer to the junction [6].

In order to verify this temperature dependence for the pnp electrochemical etch-stop process, full wafer samples, fabricated as described above, were etched at various etchant temperatures. A cross-sectional schematic of the sample after etchback is given in figure 5. Of interest is the value of  $x_p$ , the amount of p-type silicon remaining unetched above the metallurgical junction, since if this value is zero, the thickness of the bonded layer is determined solely by the junction depth of the etch-stop layer. Spreading resistance analysis (SRA) of the etched-back wafers was done to determine  $x_p$ . Table 2 gives a summary of the results from SRA of the samples. At our usual etching temperature ( $95 \pm 1^\circ\text{C}$ ), the etch stopping point does not reach the metallurgical junction. The measured roughness of the etch-stop surface is very dependent on etch-conditions, but roughnesses between 200 $\text{\AA}$  and 500 $\text{\AA}$  are typical.

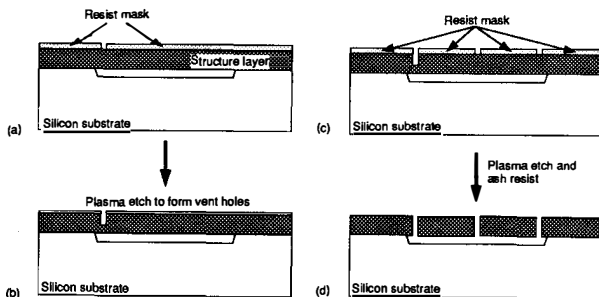


Fig. 4 Dry etch/dry release process

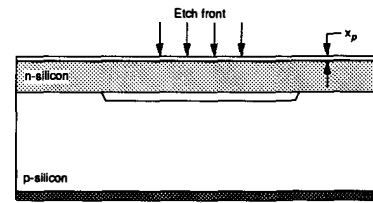


Fig. 5 Sample cross-section after electrochemical etchback

Table 2: Pnp electrochemical etch results

Etchant Temp. ( $^\circ\text{C}$ )	$x_p$ from SRA ( $\mu\text{m}$ )	
	Set #1	Set #2
$95 \pm 1$	$0.0 \pm 0.1$	$0.0 \pm 0.1$
$90 \pm 1$	$0.0 \pm 0.1$	$0.0 \pm 0.1$
$85 \pm 1$	$0.4 \pm 0.1$	$0.3 \pm 0.1$
$75 \pm 1$	$0.7 \pm 0.1$	$0.5 \pm 0.1$

- 10  $\mu\text{m}$  diffused-junction device wafer on p-Si handle wafer
- 11  $\mu\text{m}$  n-epi device wafer on p-Si handle wafer

### B) Junction-isolation Scheme

In order to evaluate the effectiveness of the junction-isolation scheme used in this study, the characteristics of diodes formed between the n-type bonded layer and the p-type substrate were measured. A total of 18 diodes per die, with variations in junction areas and perimeters, were fabricated. Figure 6 is an example of the measured I-V characteristic (n-epi sample). The diodes formed between the 10  $\mu\text{m}$  diffused layer and the p-Si substrate have an average reverse-biased breakdown voltage greater than 30V and a typical current density of 0.13  $\text{pA}/\mu\text{m}^2$  at 1V reverse-bias and 2.31  $\text{pA}/\mu\text{m}^2$  at 25V reverse-bias. For the 11  $\mu\text{m}$  n-epi samples, the average breakdown voltage is greater than 60V with a typical current density of 0.016  $\text{pA}/\mu\text{m}^2$  at 1V reverse-bias and 0.082  $\text{pA}/\mu\text{m}^2$  at 25V reverse-bias.

With an average operating voltage of  $\pm 2.5\text{V}$ , this level of reverse-bias leakage current is relatively high but acceptable. The success of this junction-isolation scheme enables us to fully utilize silicon-silicon bonding yet obtain adequate electrical isolation of the mechanical parts from the substrate.

### C) Mechanical Property

Several lateral resonant structures were fabricated and tested to demonstrate the process and measure the mechanical properties. These tuning-fork-gyroscope-like lateral resonators (illustrated in figure 7) were driven to resonance by means of comb-drive. All three types of resonators have measured resonant frequencies within 5% of the FEM calculated values, as shown in table 3, using published values for the modulus of single-crystal silicon [8].

As further evidence of this, arrays of cantilevers and fixed-fixed beams were fabricated as mechanical property test structures to extract Young's Modulus and residual stress of the bonded and etched back silicon layer. Electrostatic pull-in tests were done on these test structures. The modulus determined from these measurements was consistent with published values, and the stress was zero to within the measurement resolution of 100 kPa ( $<10^{-6}$  strain). Detailed discussion on pull-in models, theories, and test results is presented in reference [9].

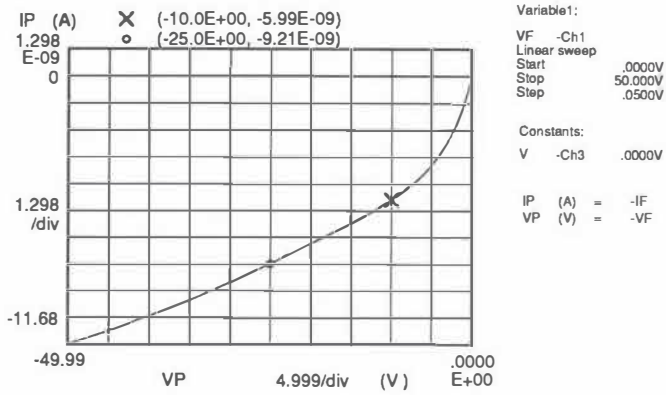


Fig. 6 A typical junction-isolation diode I-V plot

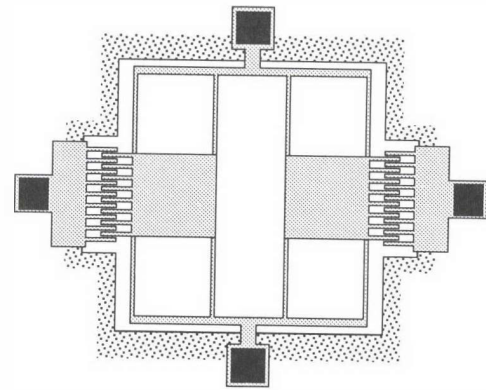


Fig. 7 Schematic and SEM photo of a tuning fork gyroscope

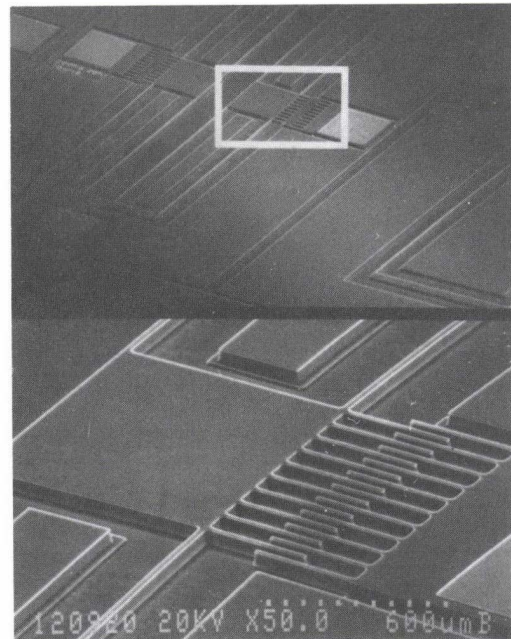
Table 3: Lateral resonator experimental results (about 6 devices per type were measured)

Device	Tine Size ( $\mu\text{m}^2$ )	Resonant Frequency (calculated)	Resonant Frequency (observed in vacuum)
Gyro Type 1	200 x 200	20 kHz	19,997.4 $\pm$ 0.1 Hz
Gyro Type 2	500 x 500	2 kHz	2047.5 $\pm$ 0.1 Hz
Gyro Type 3	1000 x 1000	2 kHz	1997.5 $\pm$ 0.1 Hz

Table 4: Device flatness measurement

	n-diffused	n-epi	SOI
Gyro Tines			
200 x 200 $\mu\text{m}^2$	63.2 $\pm$ 0.1 nm	< 24 nm	N/A
500 x 500 $\mu\text{m}^2$	478.6 $\pm$ 0.1 nm	< 33 nm	N/A
1 x 1 $\text{mm}^2$	1.158 $\pm$ 0.001 $\mu\text{m}$	< 28 nm	N/A
Proof Masses			
500 x 500 $\mu\text{m}^2$	520.2 $\pm$ 0.1 nm	< 34 nm	< 19 nm

Since we will employ a capacitive pickup detection/feedback scheme for both tuning fork gyroscopes and accelerometers, it is important to be able to fabricate ultra-flat suspended plates as tuning fork tines and accelerometer proof masses (figure 8). Plates as large as 1 mm by 1 mm have been fabricated for tines and proof masses. The flatness of the plates were measured using a Wyko Corporation's Topo-3D surface profiler [10]. Since we define "flatness" as the height difference between the center of the suspended plate and the edge of the plate, measurements of such were made on both tuning fork tines and proof masses. As discussed before, we have three different bonded layers to characterize; n-diffused, n-epi, and SOI device layers. Table 4 gives a summary of the results. Please note that there were no tuning fork tines fabricated with the SOI device layer. The values given in table 4 are average values obtained at five different dice on the wafer; center, top, bottom, left, and right respectively. We have data on a total of 6 n-diffused sample wafers (3 for tuning fork gyros and 3 for accelerometers), 2 n-epi sample wafers (1 for tuning fork gyros and 1 for accelerometers), and only one SOI sample wafer for accelerometer fabrication. All of the structures fabricated in either SOI or n-epi are flat to within the surface roughness of the sample. A warpage is clearly observable on all tuning fork tines and accelerometer proof masses fabricated on n-diffused device wafers. This "warpage" in the diffused devices is as large as 1.158  $\mu\text{m}$  for the 1 mm by 1 mm tines.



## CONCLUSION

A stable process technology for fabrication of high quality surface micromachined structures by wafer bonding has been established. It was demonstrated that the junction-isolation scheme formed by a pnp electrochemical etch-stop process can be used to achieve electrical isolation of the mechanical parts from the substrate. It was also shown that the completed mechanical parts have excellent mechanical behavior due to a negligible residual stress in the bonded layer. Furthermore, large and ultra-flat suspended plates have been successfully fabricated using dry release methods. These processes now enable the full integration of electronics monolithically with the mechanical devices.

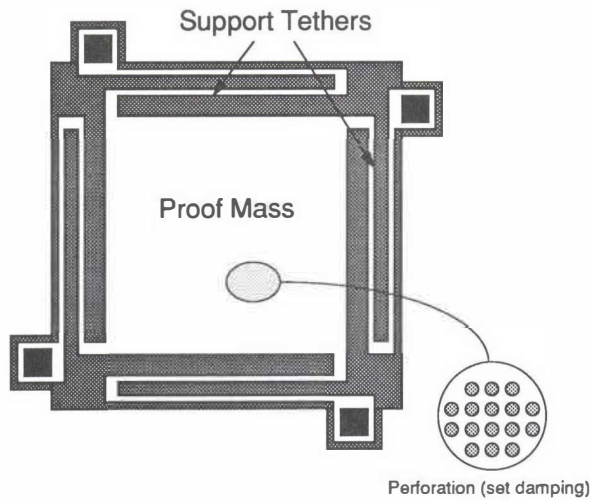
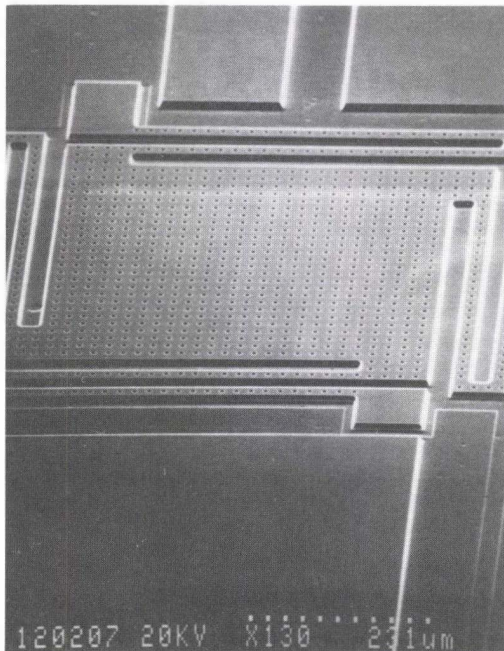


Fig. 8 Schematic and SEM photo of a microaccelerometer



#### ACKNOWLEDGMENT

Support for this work was provided by the C.S. Draper Laboratories, and the Semiconductor Research Corporation (contract 93-SC-309). Modeling work was supported by the Advanced Research Projects Agency (contract J-FBI-92-196). AT&T Reading (Bill Easter) and Motorola (Dr. Andrew Mirza) provided SOI wafers and epi wafers respectively for this research. Fabrication was carried out in the Microsystems Technology Laboratories of MIT, and we thank the staff and students of MTL for their assistance and support. We thank Dr. Robert Horning of Honeywell for the initial discussion on pnp electrochemical etch-stop process. We acknowledge the contribution of Professor S.D. Senturia, P.M. Osterberg, and R.K. Gupta to the mechanical property analysis.

#### REFERENCES

- [1] L. Christel, K. Petersen, P. Barth, F. Pourahmadi, J. Mallon, and J. Bryzek, "Single-crystal silicon pressure sensors with 500x overpressure protection," *Sensors and Actuators*, A21-23:84-88, 1990.
- [2] Y. Wang, X. Zheng, L. Liu, and Z. Li, "A novel structure of pressure sensors," *IEEE Transactions on Electron Devices*, ED-38, No. 8:1797-1801, August 1991.
- [3] K. Petersen, D. Gee, F. Pourahmadi, R. Craddock, J. Brown, and L. Christel, "Surface micromachined structures fabricated with silicon fusing bonding," *Transducers 91*, pp. 397-399, IEEE, 1991.
- [4] K. Petersen, F. Pourahmadi, and J. Brown, "Resonant beam pressure sensor fabricated with silicon fusing bonding," *Transducers 91*, pp. 664-667, IEEE, 1991.
- [5] J. Shajii, K.-Y. Ng, and M.A. Schmidt, "A microfabricated floating-element shear stress sensor using wafer-bonding technology," *Journal of Microelectromechanical Systems*, Vol. 1, No. 2, pp. 89-94, 1992.
- [6] L. Parameswaran, V.M. McNeil, M.A. Huff, and M.A. Schmidt, "Sealed-cavity microstructure using wafer bonding technology," *Transducers 93*, pp. 274-277, IEEE, 1993.
- [7] L. Parameswaran, "Silicon pressure sensor using wafer bonding technology," M.S. thesis, Dept. of EECS, MIT, September 1993.
- [8] H. J. McSkimin, "Measurement of elastic constants at low temperatures by means of ultrasonic waves - data for silicon and germanium single crystals, and for fused silica," *Journal of Applied Physics*, vol. 24, no. 8, August 1953.
- [9] P.M. Osterberg, R.K. Gupta, and S.D. Senturia, "Quantitative models for the measurement of residual stress, poisson ratio, and Young's modulus using electrostatic pull-in of beams and diaphragms," to be presented at the 1994 Solid State Sensors and Actuators Workshop, Hilton Head Island, SC.
- [10] TOPO-3D Surface Profilometer, Wyko Corporation, Tucson, AZ.

# SURFACE MICROMACHINED SHOCK SENSOR FOR IMPACT DETECTION

P. F. Man and C. H. Mastrangelo

Center for Integrated Sensors & Circuits

Department of Electrical Engineering and Computer Science

1243 EECS Bldg., University of Michigan, Ann Arbor, MI 48109-2122

## ABSTRACT

A set of copper micromachined impact sensors has been fabricated. The devices consist of a combination of suspension spring and plunger mass that impacts a stop closing an electrical circuit when subject to accelerations of 100-10,000 G's. The devices are fabricated with a three mask process using a silicon dioxide sacrificial layer and copper as the structural material. The stress in the copper films was about 20 MPa in the tensile state which makes it suitable for micromechanical devices that require a low resistance. Device length ranges from 0.2-1.5 mm. The process flow and special fabrication techniques for copper films are described. Initial experiments indicate a closing on resistance below 2  $\Omega$ .

## INTRODUCTION

Many electromechanical devices are micromachined with polysilicon or highly doped silicon because of the low stress and excellent mechanical properties of this material [1, 2]. However, silicon structures are unsuitable for devices that require the closing of an electrical contact because of the formation of a thin layer of insulating native oxide on its surface and their relatively high resistivity. Metals are ideal candidates for electromechanical switching applications where the cost of electronic controls is an important consideration. This paper presents a surface micromachined shock sensor fabricated with copper. Shock sensing devices are needed for air bag systems and in portable notebook

computers to prevent writing on their disk drives under impact. For drive failure, this threshold is between 100-200 G. Up to six shock sensors are required per disk drive; hence active devices are prohibitively expensive.

The device fabricated here is a passive mass-spring switch which closes when the impact acceleration exceeds a threshold level. Fig. 1 shows the structure of one type of shock sensor. The device consist of a plunger that is suspended by elastic folded beams [1]. The plunger is separated from an stationary electrode a short distance apart. When the device is subject to a strong acceleration, the plunger impacts the stationary contact hence closing the switch. In order to obtain a good contact with low resistance, the device is completely micromachined in copper.

Copper is an excellent candidate material for electromechanical switching because of its low resistivity ( $2 \mu\Omega - cm$ ), high current capability, and low residual stress [3-5]. The copper plunger is a symmetrically shaped, conductive proof mass, and supported  $4 \mu m$  above the substrate by folded beams  $4 \mu m$  wide anchored near the proof mass center. The folded-beam suspension design makes the device sensitive only to the translational acceleration component along the axis. The gap between the plunger and the stationary contact is 5-10  $\mu m$ . The length of the switch structures ranges from 0.2 to 2 mm. Devices with single, double folded, and simpler single beam suspensions were fabricated.

## SHOCK SENSOR CHARACTERISTICS

The device has a simple mechanical model of spring and proof mass as shown in Fig. 2. Upon the application of a positive acceleration to the structure, the plunger mass displaces in the positive direction. The threshold acceleration  $a_c$  needed for closing the switch is

$$a_c = \frac{k d}{m} \quad (1)$$

where  $d$  is the electromechanical contact gap,  $k$  the spring constant and  $m$  the plunger mass. In the device structure, the springs are folded beams with spring constant [6]

$$k = \frac{E t w^3}{N l^3} \quad (2)$$

where  $E$  is the young modulus of the beam material  $t$ , its thickness,  $w$  its width, and  $l$  its length, and  $N$  the number of folds. The plunger mass is distributed around the beams with an approximate mass

$$m \approx \rho t l^2 \quad (3)$$

Therefore the approximate device area  $A$  is

$$A \approx \left( \frac{w^3 d E}{N a_c \rho} \right)^{2/5} = c v^{4/5} \quad (4)$$

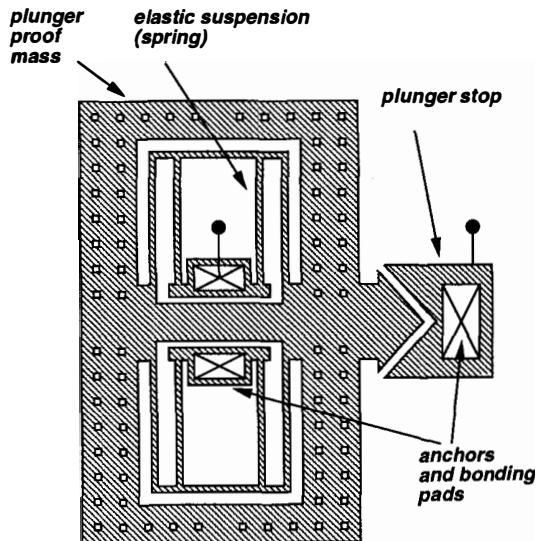


Fig. 1: top view of a shock sensor

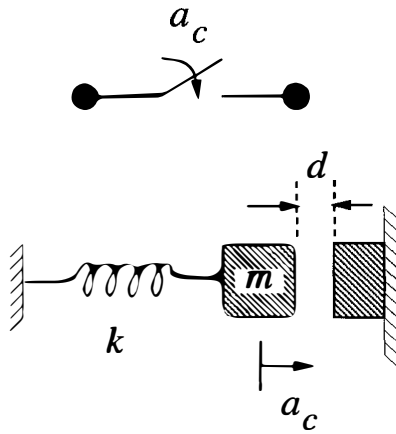


Fig. 2: shock sensor model

Where  $v = \sqrt{E/\rho}$  is the wave velocity of the material [7]. Copper has a Young modulus of approximately 110 GPa, and a density of  $8.9 \text{ g cm}^{-3}$  [8] yielding a wave velocity roughly 4.4 times smaller than that of silicon and a corresponding reduction on device area. The dynamics of the spring-mass system are determined by the second order differential equation

$$m\ddot{x} + \mu\dot{x} + kx = ma_c \quad (5)$$

Where  $\mu$  is the damping coefficient. For laterally driven structures the damping coefficient is very low [9, 10]; hence the solutions are nearly sinusoidal. Therefore the time required for switch closure is approximately

$$t_c \approx \frac{\pi}{2} \sqrt{\frac{d}{a_c}} \quad (6)$$

which for a  $10 \text{ }\mu\text{m}$  gap is approximately  $150 \text{ }\mu\text{s}$  at  $100 \text{ G's}$ . The very short closing time is a consequence of the small travel of the plunger. After the plunger impinges onto the contact, the structure will go through a series of rebounds due to the low damping coefficient; thus a latching type of circuit is needed to detect the first contact closing.

### STRESS IN COPPER FILMS

The material used for our device is sputtered copper. Copper films have been under intense investigation as an interconnect layer for VLSI circuits [11]. As a mechanical layer, copper films have in general a very low intrinsic stress [5]. Because the yield stress of copper is very low (55 MPa) [8], any stress higher than this value is essentially relaxed by plastic deformations. The ability of copper to relax its internal stress [3] is one of its most desirable features for micromechanical applications. The Young modulus of copper is 110 GPa, comparable to that of silicon, but its ultimate stress is substantially lower (230 MPa).

A set of  $1 \text{ }\mu\text{m}$ -thick copper films were sputtered on silicon substrates in an RF magnetron (Enerjet) system at a power of 800 W at various argon pressures. The stress of the copper film was then measured using an optical stress gague. Figure 3 shows the stress in the copper samples deposited at various pressures. The lowest stress samples were sputtered at 16 mT with a tensile

residual stress of 50 MPa. The stress in the samples relaxed to even lower values at room temperature after the samples were left for a period of time. The samples shown in the figure were given a short 20 min anneal at  $300 \text{ }^\circ\text{C}$  in a rapid thermal anneal system (Peak Systems ALP 3000). During this thermal cycle,

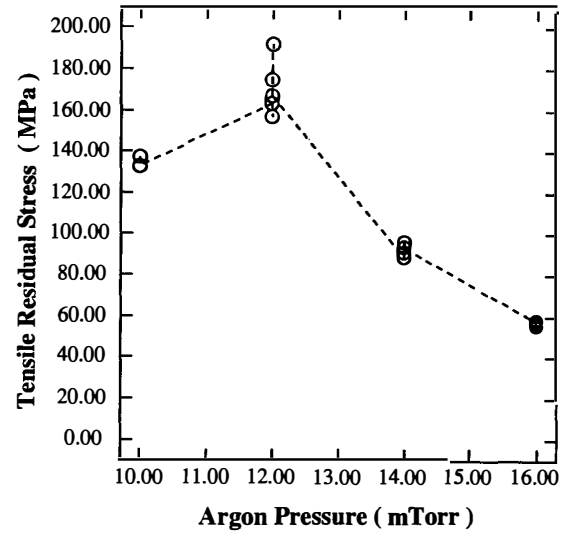


Fig. 3: copper stress

its residual stress is relaxed due to recrystallization [12,3]. The stress on the annealed samples was 10-20 MPa, low enough for most micromachining applications.

### FABRICATION

The impact sensor was constructed as shown in Fig. 4. First a uniform layer of low-stress silicon nitride [13]  $0.1 \text{ }\mu\text{m}$  thick is uniformly deposited in on n-type (100) silicon wafers with a resistivity of  $10\text{-}30 \text{ }\Omega\text{-cm}$ . The silicon nitride layer provides an insulator surface that isolates the two terminals of the impact switch. The nitride film was deposited on a LPCVD reactor at  $835 \text{ }^\circ\text{C}$  and 320 mT with  $\text{SiH}_2\text{Cl}_2$  and  $\text{NH}_3$  flows of 100 and 25 sccm. The nitride was tensile with a stress of about 150 MPa. Next, a 2.5-4  $\mu\text{m}$  thick layer of plasma-enhanced (PECVD)  $\text{SiO}_x$  was deposited as a sacrificial layer. The PECVD film was grown on a SEMI group reactor with a  $\text{SiH}_4$  flow of 24 sccm and  $\text{N}_2\text{O}$  flow of 20 sccm at 100 mT and a substrate temperature of  $200 \text{ }^\circ\text{C}$ . The power used in the deposition was 80 W, with a deposition rate of  $12 \text{ nm/min}$ .

The PECVD film was next patterned and etched  $1 \text{ }\mu\text{m}$  deep using in a plasma etch reactor. These indentations patterned in the sacrificial layer are needed to form "dimples" that reduce the adhesion of the microstructure to its substrate. The photoresist was next stripped, and the samples were cleaned. The PECVD film was next patterned and etched with diluted 5:1 BHF down to the insulating SiN to form the anchors of the structure. Using the same resist, a thin layer 50 nm-thick of evaporated Cr was deposited. The Cr layer is used as an interfacial layer that attaches to the copper [14] film. The Cr was next lifted off, and the samples thoroughly cleaned. Next a 2-3  $\mu\text{m}$ -thick layer of copper was sputtered at a power density of 800 W and at an Ar pressure of 16 mT. The samples were next annealed

at 300 °C for 20 min in a N<sub>2</sub> atmosphere to relieve the residual stress of the film.

A 2 μm layer of resist was used as a mask for patterning the copper film. After the copper film is deposited, Special precautions are required to prevent the oxidation of copper [15,16,11,17] during baking and removal of the resist. Samples that were baked at 110 °C for more than 30 min showed signs of copper oxidation. The copper was etched by several two different methods. Copper cannot be etched by plasma chemistry

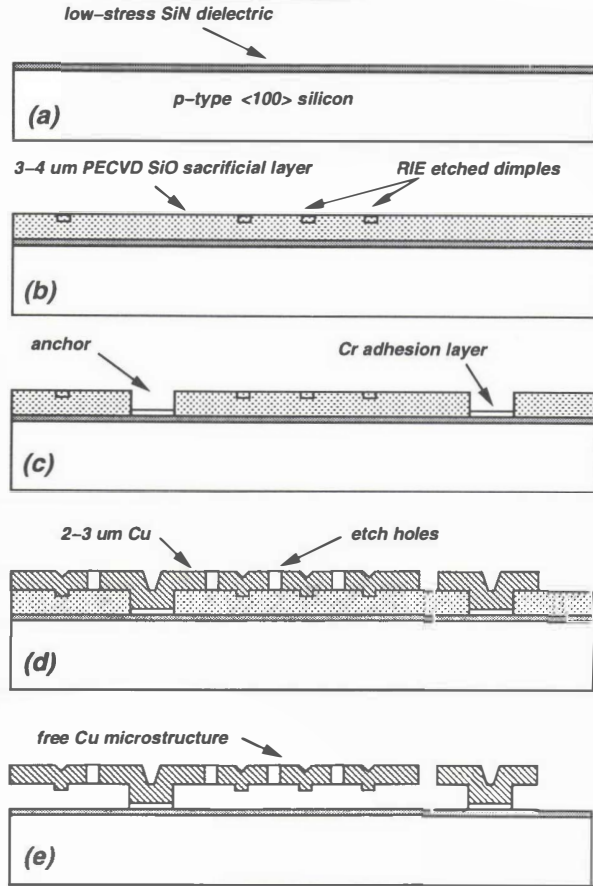


Fig. 4: process flow

easily at room temperature because it does not generate volatile reaction byproducts [18,19]. One set of samples was etched by ion-milling at 300V and 100 mA Ar beam current in a Milatron reactor. The etch rate was approximately 18 nm/min. Higher potentials caused thermal migration [11] of the copper through the PECVD oxide and excessive bombardment of the resist [1822]. A second set of samples was etched in a weak 1:2:200 HCl : H<sub>2</sub>O<sub>2</sub> : H<sub>2</sub>O<sub>2</sub> solution with an etch rate of 0.3 μm/min. The resist was removed by an acetone bath and a short 2 min O<sub>2</sub> plasma descum at 250 mT and 180 W. Resist removal with PRS1000 stripper resulted in chemical attack of the copper, and high power O<sub>2</sub> plasma stripping for long times resulted in excessive copper oxidation. The samples etched by ion milling were thoroughly rinsed and annealed a second time at 300 °C for 20 min in N<sub>2</sub> atmosphere.

The last step in the process is the sacrificial release. The PECVD oxide layer was sacrificially etched in concentrated (49%) HF which does not attack copper. The structures were released in 1.5 min. Next the samples were rinsed and let dry. San ples

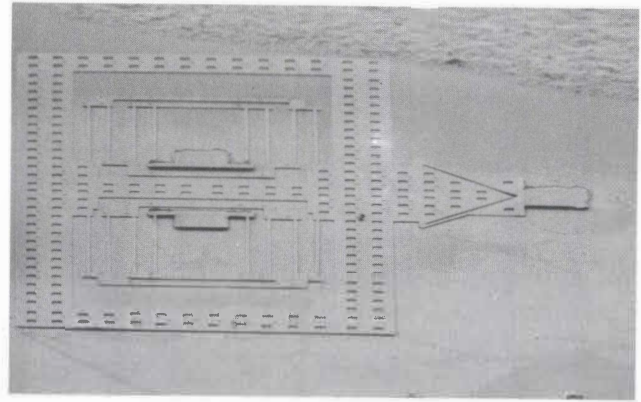


Fig. 5

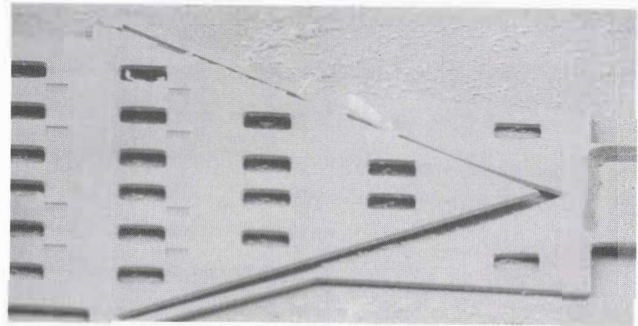


Fig. 6

etched by ion-milling were warped down indicating a change in the copper stress by the ion bombardment. Furthermore, the prolonged exposure to Ar in the ion-milling system substantially degraded the adhesion of the Cr layer yielding structures that lifted off the substrate. The flattest samples were obtained by the wet etch. Fig. 5 shows a SEM of a completed double folded device. Fig. 6 shows the tip of the plunger and copper stopper. Fig. 7 shows a 500 μm-long segment of the structure showing its flatness with some of the support beams adhering to the surface. The structures were probed, and the contact closing resistance was below 2 Ω.

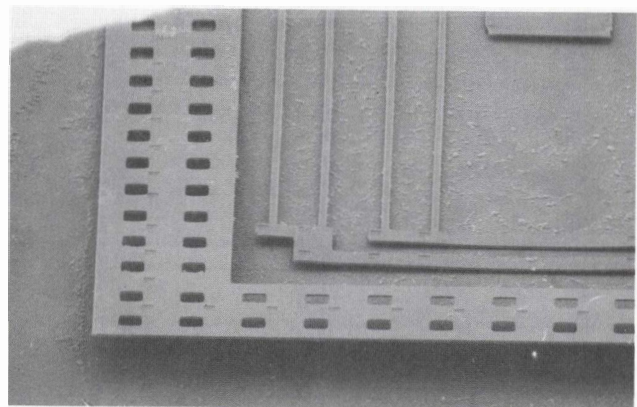


Fig. 7

## DROP TEST SETUP

The structure was next mounted on a DIP package and wire bonded. The sensor chip was mounted on a small PC board attached to a flip-flop deglitching circuit. The whole assembly was next mounted on a 0.337 kg aluminum block with a hole in the middle that rides along a vertical guide. At the base of the guide, a spring of constant  $k_s$  was inserted into the guide. The block was next dropped at different heights, and the behavior of the switch device was monitored. The impact acceleration for the switch can be determined from the properties of the spring and the height at which it was released. These are related by the equation

$$a = v_o \sqrt{\frac{k_s}{m}} = \sqrt{\frac{2Gh k_s}{m}} \quad (7)$$

Where  $v_o$  is the velocity of the block at impact and  $h$  is the release height. The copper micromachined devices are currently under testing.

## SUMMARY

A simple microelectromechanical impact sensor is described. The device consists of a copper proof mass and a spring that closes a switch when subject to a shock. The device is made of thin film copper, and it is fabricated with three lithographic steps. Processing details for the copper accelerometer switch are discussed.

## ACKNOWLEDGEMENTS

This project was partially funded by Ford Motor Company. We also acknowledge W. Baer for providing some of the packages and facilities for testing.

## References

- [1] W. C. Tang, T.-C. H. Nguyen, and R. T. Howe, "Laterally driven polysilicon resonant microstructures," in *International Workshop on Micro Electromechanical Systems (MEMS'89)*, pp. 53-59, 1989.
- [2] Y. B. Gianchandani and K. Najafi, "A bulk silicon dissolved wafer process for microelectromechanical devices," *Journal of Microelectromechanical Systems*, vol. 1, pp. 77-85, 1992.
- [3] P. A. Flinn, "Measurement and interpretation of stress in copper films as a function of thermal history," *J. Mater. Res.*, vol. 6, pp. 1498-1501, 1991.
- [4] R. Haynes, "Temperature dependence of stress for copper, copper-silver, and copper-tin films," in *Proceedings of the Materials Research Society Symposium. Thin films: Stresses and Mechanical Properties II*, vol. 188, pp. 103-107, 1990.
- [5] L. S. Fan, L. H. Lane, N. Robertson, L. Crawforth, M. A. Moser, T. C. Reiley, and W. Imano, "Batch-fabricated milli-actuators," in *International Workshop on Micro Electromechanical Systems (MEMS'93)*, pp. 179-181, 1993.
- [6] W. C. Tang, *Electrostatic Comb Drive for Resonant Sensor and Actuator Applications*. PhD thesis, University of California, Berkeley, 1990.
- [7] W. Goldsmith, *Impact*. London: Edward Arnold Ltd, 1960.
- [8] J. M. Gere and S. P. Timoshenko, *Mechanics of Materials*. New York: PWS-Kent Pub. Co., 1984.
- [9] Y.-H. Ho, B. M. Kwak, A. P. Pisano, and R. T. Howe, "Viscous energy dissipation in laterally oscillating planar microstructures: a theoretical and experimental study," in *International Workshop on Micro Electromechanical Systems (MEMS'93)*, pp. 93-98, 1993.
- [10] X. Zhang and W. C. Tang, "Viscous air damping in laterally driven microresonators," in *International Workshop on Micro Electromechanical Systems (MEMS'94)*, pp. 199-204, 1994.
- [11] Y. Schacham-Diamand, A. Dedhia, D. Hoffstetter, and W. G. Oldham, "Copper transport in thermal  $SiO_2$ ," *J. Electrochemical Soc.*, vol. 140, pp. 2427-2431, 1993.
- [12] M. Ueki, S. Horie, and T. Nakamura, "Factors affecting dynamic recrystallization of metals and alloys," *Mat. Sci. and Tech.*, vol. 3, pp. 329-337, 1987.
- [13] M. Sekimoto, H. Yoshihara, and T. Ohkubo, "Silicon nitride single-layer x-ray mask," *J. Vac. Sci. Technol.*, vol. 21(4), pp. 1017-1021, 1982.
- [14] W. R. LaFontaine, B. Yost, and C.-Y. Li, "Effect of residual stress and adhesion on the hardness of copper films deposited on silicon," *J. Mater. Res.*, vol. 5, pp. 776-783, 1990.
- [15] Y. Schacham-Diamand, J. Li, J. O. Olowofe, S. Russel, Y. Tamou, and J. W. Mayer, "Oxidation and thermal stability of thin copper layers," in *Proceedings of the 9th Biennial University/Government/Industry Microelectronics Symposium*, pp. 210-215, 1991.
- [16] J. Li, J. W. Mayer, and E. G. Colgan, "Oxidation and protection in copper and copper alloy thin films," *J. Appl. Phys.*, vol. 70, pp. 2820-2827, 1991.
- [17] K. Hauffe, *Oxidation of Metals*. New York: Plenum, 1965.
- [18] S. Wolf and R. N. Tauber, *Silicon Processing for the VLSI Era, Volume 1-Process Technology*. Sunset Beach, CA: Lattice Press, 1986.
- [19] K.-M. Chi, M. J. Hampden-Smith, and J. Farkas, "Low-temperature copper etching via reactions with  $Cl_2$  and  $PtEt_3$  under ultrahigh vacuum conditions," *J. Appl. Phys.*, vol. 73, pp. 1455-60, 1993.

# **A BULK-SILICON CAPACITIVE MICROACCELEROMETER WITH BUILT-IN OVERRANGE AND FORCE FEEDBACK ELECTRODES**

Karl J. Ma, Navid Yazdi and Khalil Najafi

*Center for Integrated Sensors and Circuits*

Department of Electrical Engineering and Computer Science

University of Michigan

Ann Arbor, MI 48109-2122

## **ABSTRACT**

This paper reports on the development of micromachined silicon accelerometers fabricated through a simple, single-sided, bulk-silicon boron etch-stop dissolved-wafer process. The fabricated structures consist of a thick ( $15\mu\text{m}$ ) inertial mass that is supported by thin beams and is suspended above a glass substrate. Metal electrodes on the glass substrate, and p++ silicon electrodes above the mass provide a means to capacitively read and electrostatically reposition the mass in response to acceleration. Bridge and cantilever structures have been fabricated which include a  $41\mu\text{gm}$  inertial mass ( $1000\times 1000\times 15\mu\text{m}^3$ ), p++ support beams ( $600\times 75\times 3.1\mu\text{m}^3$ ), and three thick ( $1000\times 300\times 15\mu\text{m}^3$ ) top p++ silicon electrodes. The mass is separated from the top and bottom electrodes by a  $1.5\mu\text{m}$  air gap. Open loop sensitivity of 0.3% obtained from CV measurements and from turnover tests using a switched-capacitor circuit correlate well with theoretical analysis.

## **INTRODUCTION**

Growing interest over the last several years in silicon micromachined accelerometers has primarily been brought about by their increased application in automobiles. Microaccelerometers are used to achieve several function in cars, among which is reliable deployment of air bags [1]. In addition, as more reliable microaccelerometers are being obtained [2], applications have grown to those in the military, medical, and aerospace industries.

Microaccelerometers have been successfully implemented using several fabrication techniques, including traditional bulk silicon devices [3], and surface micromachined polysilicon structures [4,5]. Although bulk micromachined devices have the advantage of a large inertial mass which can potentially improve sensitivity, they typically also consume too much die area because a back-side alignment is required to allow release of the final microstructure [6]. Also, corner compensation structures [7] are required to help retain orthogonal edges on the inertial mass. Lastly, specialized lead-transfer techniques are required [8] for these bulk silicon structures that utilize multiple wafers for the sensor formation. Surface micromachined accelerometers, on the other hand, avoid some of these problems, although the smaller thickness achievable using surface micromachining reduces the size of the inertial mass, which in turn limits sensitivity. In addition to standard open-loop accelerometers, there is a great deal of interest in developing force rebalanced microaccelerometers where the inertial mass is maintained in a stationary position using electrostatic attraction [5,9,10]; this will help improve the dynamic range and linearity of the device. In order to implement force rebalanced accelerometers, however, one needs to incorporate force feedback electrodes on both sides of the inertial mass to allow repositioning of the mass in either direction. As a result of this requirement, both bulk and surface micromachined accelerometers fabricated so far have resorted to multi-layer devices. For bulk silicon devices, this has forced designers to use multiple wafers using a fairly complex process, and surface micromachined technologies are being developed that utilize two levels of polysilicon, despite the fact that the size of the mass in these devices is still very small.

This paper reports on the development of a two-level, bulk silicon microaccelerometer fabricated using the dissolved wafer process developed by our group [8]. The accelerometer and its

fabrication technology offer several features, including: 1) simple, single-sided bulk silicon technology that utilizes boron etch-stop for the formation of precise microstructures; 2) a capacitive read-out scheme that allows for self-testing; 3) multiple, isolated force feedback electrodes on both sides of the mass to provide protection against overrange acceleration and for operation in a closed-loop servo mode; 4) compatibility with integrated circuitry through the use of a new electrochemical etch stop technique [11]; and 5) a highly versatile design that achieves both a heavy inertial mass ( $15\mu\text{m}$  thick mass) as well as thin suspension beams ( $2\text{-}15\mu\text{m}$ ) which are nearly as efficient as those obtained from surface micromachining. This accelerometer is also more efficient because it does not require the typical double-sided alignment needed in bulk silicon processing and ultimately yields a higher device density process. The sensor structure and its design considerations are detailed in the next section after which the fabrication process is described. Experimental results and their correlation to theoretical characteristics are then discussed, followed by a conclusion.

## **SENSOR STRUCTURE AND DESIGN**

The structure of this new type of bulk-silicon microaccelerometers is shown in Figure 1. It consists of a  $15\mu\text{m}$ -thick p++ silicon mass that is suspended above a glass support substrate using thin (typically  $2\text{-}3\mu\text{m}$ ) beams. Metal electrodes are formed on the glass substrate below the mass, while thick boron-doped silicon electrodes are formed above the mass and are attached to the glass substrate. Note that several isolated top electrodes can be formed above the mass. These electrodes not only provide a means to electrostatically reposition the mass but also provide built-in overrange protection. Note that in this structure the device area is small and only determined by the required device characteristics, unlike other conventional bulk micromachined devices. The mass is much thicker than surface micromachined devices and can hence provide better sensitivity for a given dimension. All layer thicknesses can be changed from about  $2$  to about  $15\mu\text{m}$ , thus enabling the designer to design a wide range of bulk silicon microaccelerometers. The glass substrate reduces the parasitic capacitance and improves resolution. We have designed a number of bridge and cantilever microaccelerometers using this technology.

The above device structure is based on capacitive detection and actuation, which is preferred due to both the low temperature sensitivity of capacitive devices and the ability to easily force rebalance the mass. In addition, the multielectrode, capacitive read-out and actuation available in the above structure allows the user to utilize isolated sense and force feedback electrodes thus simplifying the external circuitry. These electrodes could also be used for self-testing, calibration, and for electronically controlling the sensitivity of the device if needed. As mentioned before, the top p++ silicon electrodes also protect the device against overrange acceleration and shock. Note that the glass substrate provides protection from below and the p++ silicon electrodes provide protection from above.

A desirable feature of the fabrication technology is that it is a single-sided process that does not require critical etch control to compensate for corner undercutting. Because the bulk of the silicon wafer is etched away, this technology also provides very high density, which helps to reduce the cost, and is desirable for multi-axis accelerometer designs. The process also allows the fabrication of other sensors such as pressure, force, and flow on the same substrate without the need for any process modifications.

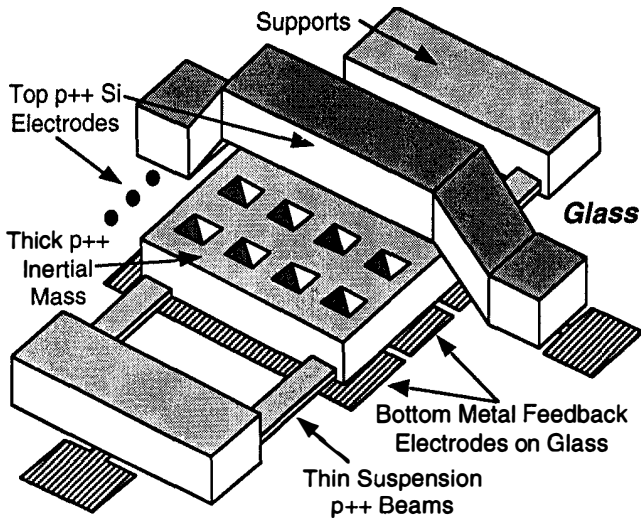


Figure 1: Structure of a bridge-type microaccelerometer implemented using the two-level bulk silicon dissolved wafer process. The device includes a perforated inertial mass suspended above a glass substrate using thin p++ beams, three metal electrodes (above), and three p++ silicon electrodes (above) the mass.

Some of the other design criteria that need to be considered when designing accelerometers include: 1) control of squeeze film damping by perforating the inertial mass; this can be done easily using this technology [12]; 2) reducing stiction problems which can be achieved by incorporating deposited oxide bushings on the mass which would help to separate it from the glass substrate; 3) reduction of cross-axis sensitivity by aligning the suspension beams with the center-of-gravity of the inertial mass; and 4) further optimization of device density through the use of folded beams to achieve the desired increase in sensitivity without the corresponding consumption of additional area. All of these features are supported by the proposed technology.

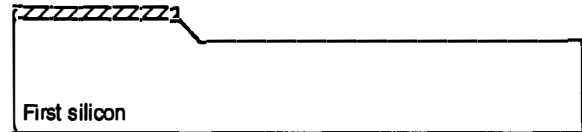
As mentioned above, we have designed and fabricated several different accelerometers each with a different set of characteristics. These designs utilize both cantilever and bridge supports and provide different sensitivities. Analytical equations for parameters such as capacitance, sensitivity, and resonant frequency are provided in a number of other papers and will not be repeated here. In the following sections we will present the fabrication technology and measured results obtained from a bridge type microaccelerometer.

### FABRICATION

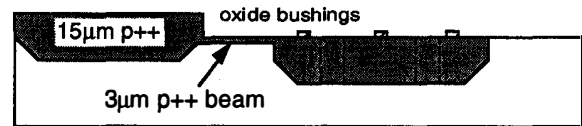
The fabrication process sequence for the accelerometer is shown in Figure 2, which requires two silicon and one glass wafer. The process starts by recessing the first silicon wafer using KOH to define the capacitive gap between the mass and the glass substrate. Next, an optional oxide masked recess could be performed to center the beams with the center-of-gravity of the inertial mass when reduced cross-axis sensitivity is needed. Following this, an oxide masked deep boron diffusion (1175°C, 16hrs. to produce a ~15µm thick silicon) is done to define the anchor regions and the inertial mass along with its perforations. Then, an oxide masked shallow boron diffusion (1175°C, 30min) is performed to define the thin suspension beams (~3µm). Next, a thick, (~1µm) LPCVD is deposited to form the oxide bushings on the mass. This completes the processing of the first silicon wafer which is now ready to be bonded to the glass wafer.

The glass wafer is prepared by evaporating Cr/Au (200Å/1200Å) into recessed trenches (~800Å) to obtain about 600Å of gold protruding over the field regions. After solvent cleaning, the silicon and glass wafers are electrostatically bonded together at

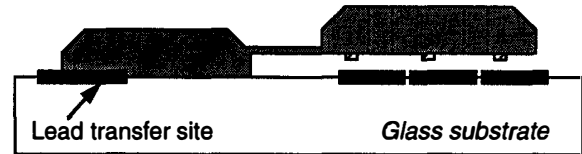
375°C and 1000V for 12min. After bonding, the sandwich is dropped in EDP [24] at 108°C to dissolve away the undoped silicon leaving the heavily boron-doped regions.



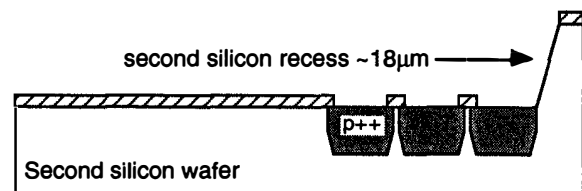
1) KOH recess to define capacitor gap.



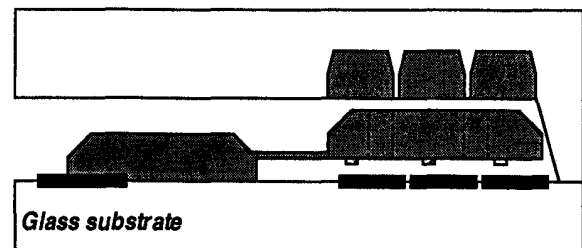
2) Deep boron diffusion for anchors and inertial mass with perforations. Shallow boron diffusion for beams and ~2000Å oxide bushings.



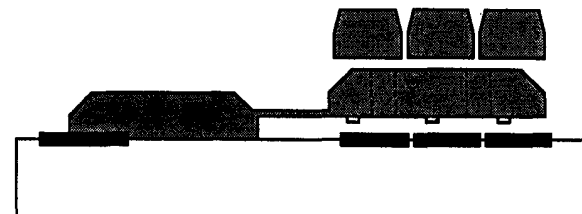
3) Glass substrate is recessed and Cr/Au is evaporated for 1000Å step height First silicon electrostatically bonded and etched back in EDP.



4) Second silicon KOH recess. Deep boron diffusion for top plate electrodes on final structure.



5) Second silicon electrostatically bonded to glass with first silicon present.



6) Second silicon etched back in EDP to reveal final structure.

Figure 2: Process sequence for the fabrication of a two-level bulk-silicon microaccelerometer with three pairs of sense electrodes and built-in overrange protection, force-feedback electrodes.

This precompleted glass wafer is then augmented with overforce electrodes by an electrostatic bonding of a second silicon wafer. An oxide masked recess is first created in the second silicon wafer to define the gap spacing of this second electrode from the inertial mass. Then, an oxide masked deep boron diffusion (16hrs. at 1175°C) is performed to define the thick electrode regions after which this silicon wafer is again electrostatically bonded to the precompleted glass substrate. It is noted that the electrostatic bonding parameters have to be increased (400°C, 1200V, 30min) in order to achieve the appropriate bonds after the first silicon wafer is dissolved away. Difficulty encountered in this second silicon bond is speculated to be due to: 1) modification of the glass surface after EDP silicon wafer dissolution and first electrostatic bond which could deplete the surface of mobile ions; and 2) distortion of the electric fields underneath the second silicon due to the presence of the first silicon microstructure.

After the second silicon wafer is bonded, the sandwich is again dropped in EDP to dissolve away the second wafer and complete the processing of the device. Note that during this second etching the first silicon is also exposed to the EDP, but because of the high etch selectivity device dimensions are not significantly changed. Following the EDP etch, the devices are rinsed, diced, and are ready for mounting and testing.

### EXPERIMENTAL RESULTS

Figure 3 shows several photographs of a fabricated bridge-type microaccelerometer at various stages in the process. Figure 3a shows a top view of the device after the first silicon bonding and EDP etch. The device contains a 41µgm inertial mass (1000x1000x15µm<sup>3</sup>) that is suspended over the metal electrodes on the substrate by four thin p++ support beams (600x75x3.1µm<sup>3</sup>). The beams are attached to the glass substrate using thick (15µm) silicon anchors. Figure 3b shows a photograph of the same device after the second silicon bond and EDP etch back. The top three electrodes are 1000x300x15µm<sup>3</sup> and are attached to the glass substrate using 100x300µm<sup>2</sup> bond anchors. The three electrodes are separated by about 20µm from one another. Figure 3c shows a SEM view of the mass, the support beam, top and bottom electrodes, and the 1.5µm air gap that separates the mass from the substrate and the top electrodes. Note that one of the top electrodes is broken away to reveal the mass and the support beams. We have fabricated several other devices (not shown here) with varying device dimensions.

In order to characterize the device performance, we have used two testing techniques: 1) we have measured device sensitivity using a CV technique by monitoring the working capacitance  $C_o$  between the inertial mass and two of glass substrate electrodes while a bias is applied (0-2V) across the mass and these electrodes. The resulting change in capacitance ( $\Delta C$ ) is then correlated to an effective g-force generated from the electrostatic voltage; and 2) we have measured actual device sensitivity using a switched-capacitor readout circuit that measures capacitance change when the device is turned over and the mass is moved under earth gravitational field.

An HP 4194A analyzer was used to monitor the capacitance between the mass and two of the three metal electrodes on the glass when a bias voltage is applied. Figure 4 shows the measured capacitance change vs. this electrostatically-generated acceleration. The sensitivity  $\Delta C/C/g$  is measured to be about 0.3%, which correlates well with theoretical results. We also tested the capability to force rebalance the mass and demonstrated that the mass could be easily moved up or down as voltage is applied to top or bottom electrodes. A voltage of 1V applied an equivalent attractive force of 4.8g to draw the mass -0.05µm away from its center position. A corresponding decrease in the sensed capacitor on the glass substrate (~0.2pF) could then be rebalanced out by applying a potential of about 1.1V to electrodes on the other side.

In addition to testing using electrostatic forces, we have designed a simple Switched-Capacitor [13] readout circuit, shown in Fig. 5, that provides an independent platform with which the turn-over test could be done. This schematic shows the circuitry used for the open-loop operation of the accelerometer and consists of a charge integrator and a gain stage. During the first clock phase ( $\phi_1$ )

the sense capacitor ( $C_x$ ) is charged up to  $V_p$  (the clock amplitude) and the first op-amp is in a unity gain configuration. During the second phase of the clock ( $\phi_2$ ), a packet of charge proportional to the difference of  $C_{ref}$  and  $C_x$  is integrated on  $C_f$ , which results in an output voltage that is then amplified using a simple inverting amplifier. The final output voltage is given by:

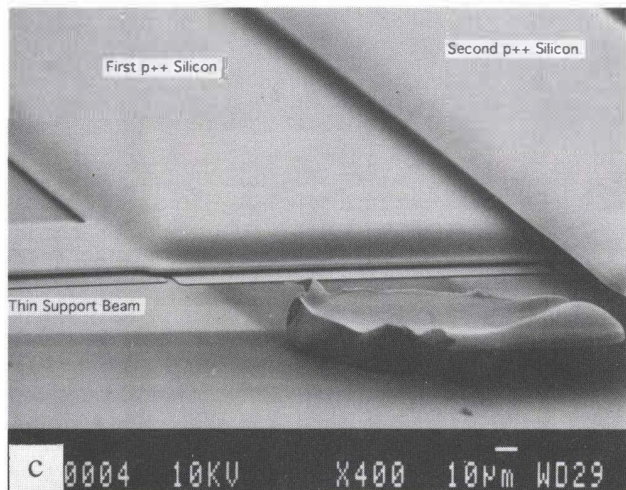
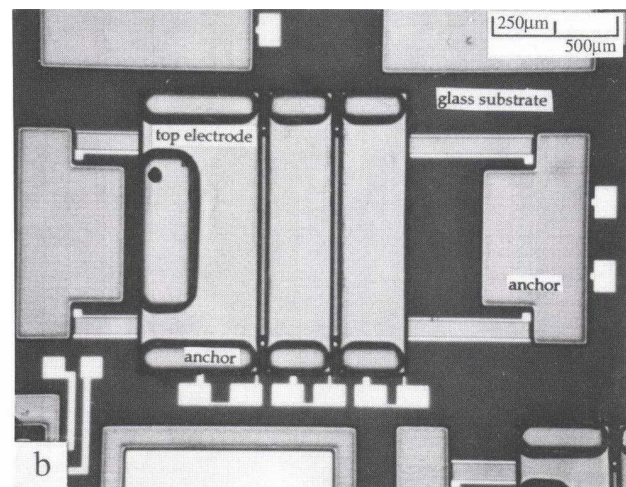
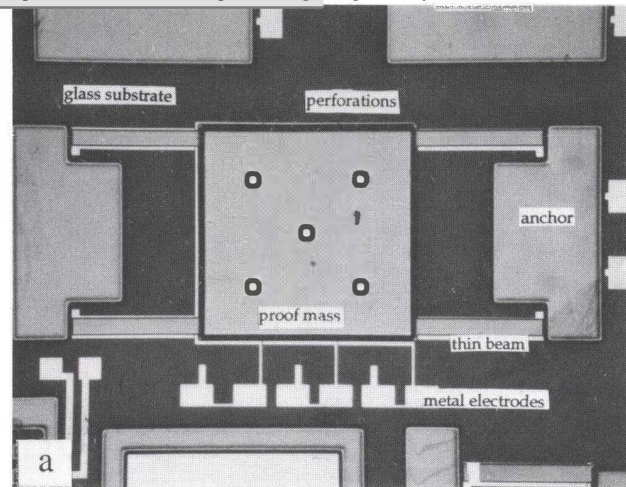


Figure 3: Optical and SEM photographs showing a bridge accelerometer: a) top view of the device after the first silicon bond and etch back; b) top view of the device after the second silicon bond and etch back; and c) SEM of the device showing the mass, the support beams, and the capacitive gaps.

$$V_{out} = -\frac{R_2}{R_1} \times V_p \times \frac{C_x - C_{ref}}{C_f}$$

The readout circuitry is implemented using commercially available discrete devices and is assembled on a printed circuit board. Using  $V_p=3V$ ,  $C_f=3pF$ , and a second stage gain of 10, it provides a measured circuit sensitivity of 1V for 100fF capacitance variation, and has a resolution of  $\sim 1fF$ .

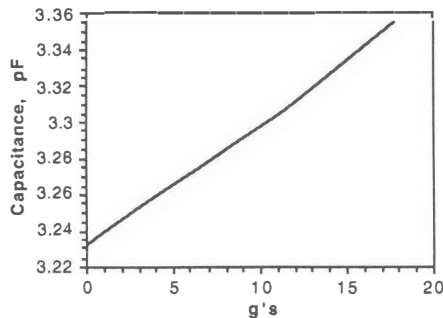


Figure 4: Measured capacitance change vs. electrostatically-generated acceleration. The sensitivity is about 0.3% per g.

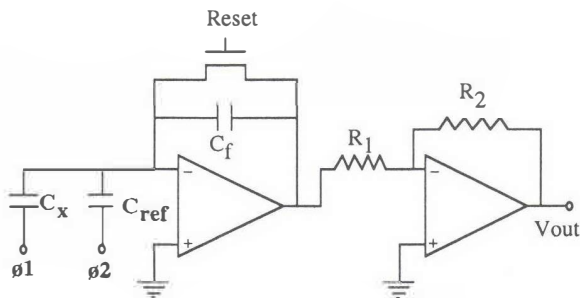


Figure 5: Schematic diagram of the switched-capacitor circuit used for testing the accelerometer.

The accelerometer is placed in a metal package and is then mounted on the circuit board. We have conducted simple turn-over tests with this device. Figure 6 shows the output of the switched-capacitor circuit (2 of 3 bottom electrodes are used) when the device is turned over, showing that the output voltage changes by  $\sim 300mV/2g$ , or  $150mV/g$ . This agrees well with both the calculated sensitivity and the resolution of the circuit. The measured and calculated results are summarized in Table 1.

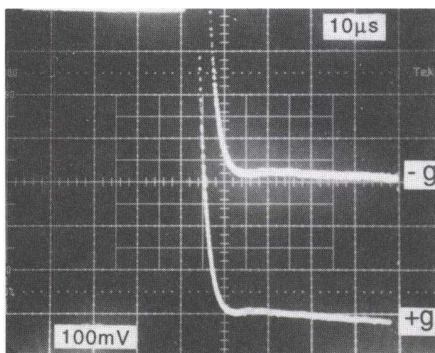


Figure 6: Output voltage of the switched-capacitor circuitry when the accelerometer is tested using the turn-over test.

In determining the durability of these devices, a dc voltage sweep (0-3V corresponding to 0-45g) was applied to the inertial mass with respect to the glass substrate electrodes and caused a periodic deflection in the structure due to the electrostatic attractive forces generated. After stressing the structure through 150,000 cycles, the sensitivity was again measured and the difference

between this value and that from before this stress test was done, yielded a figure of merit for the structure's durability.

Table 1: Measured and calculated performance characteristics of a bridge-type microaccelerometer.

Parameter	Theory	Measured
Capacitance, $C_0$	6pF	6.00pF
Sensitivity, $S=\Delta C/C/g$	0.4%	0.30%
$\pm g$ Rebalance Voltage	0.46V	0.51V
0gf Offset	0.0%	0.08%
S Temp. Var. (25-175°C)	--	0.005%/°C
0gf offset Var. (25-175°C)	--	-0.001%/°C
Stability, % change in S	--	$\leq \pm 0.02\%$

## CONCLUSIONS

A single-sided, boron-etch stop, dissolved wafer bulk-silicon process has been demonstrated and used to fabricate a number of high density microaccelerometers. These devices utilize one glass substrate and two silicon wafers to provide capacitive sensing and actuation, along with built-in overrange and force rebalance functions. The combination of thick inertial mass ( $\sim 15\mu m$ ) and thin suspension beams ( $\sim 3\mu m$ ) has helped to achieve reasonable performance characteristics. Accelerometer sensitivity was measured using both CV techniques and a switched-capacitor readout circuit and to be about 0.3% in open loop testing; and this value was stable ( $\pm 0.02\%$ ) after 3 hours of electrostatic actuation from 0-3V over 150K cycles. Furthermore, temperature variation of sensitivity (0.005%/°C) was minimal because of a capacitive readout scheme.

## ACKNOWLEDGMENTS

The authors would like to thank the staff of the Center for Integrated Sensors and Circuits for their help in device fabrication. This work was supported by the Advanced Research Projects Agency under contract 92-2340.

## REFERENCES

- [1] F. Goodenough, "Airbags Boom When IC Accelerometer Sees 50G," *Electronic Design*, August 8, 1991
- [2] World Emerging Sensor Technologies, *Frost & Sullivan Market Intelligence*, New York, 1993
- [3] M. Yoshida, T. Nomura, T. Mineta, and M. Esashi, "Capacitive Accelerometers Without Fracture Risk During Fabrication Processes," *Transducers 1993*, Yokohama, Japan, pp. 814-817
- [4] L. Ristic et al., "A Capacitive Type Accelerometer with Self-Test Feature Based on Double-Pinned Polysilicon Structure," *Transducers 1993*, Yokohama, Japan, pp. 810-813
- [5] W. Yun, R.T. Howe, and P.R. Gray, "Surface Micromachined, Digitally Force-Balanced Accelerometer with Integrated CMOS Detection Circuitry," *Digest, IEEE Solid-State Sensor and Actuator Workshop*, p. 126, Hilton-Head, SC, June 1992.
- [6] Y. Matsumoto and M. Esashi, "Low Drift Integrated Capacitive Accelerometer with PLL Servo Technique," *7th International Conf. on Solid-State Sensors and Actuators*, pp. 826-829
- [7] M. Abu-Zeid, "Corner Undercutting in Anisotropically Etched Isolation Contours," *J. Electrochem. Soc.*, Sep. 84, pp. 2138-2142
- [8] Y. Gianchandani and K. Najafi, "A Bulk Silicon Dissolved Wafer Process for Microelectromechanical Systems," *IEDM 1991*, p. 757
- [9] Y. Coulon, T. Smith, J. Hermann, M. Chevroulet and F. Rudolf, "Design and Test of a Precision ServoAccelerometer with Digital Output," *7th International Conf. on Solid-State Sensors and Actuators*, pp. 832-835
- [10] S. Suzuki et al., "Semiconductor Capacitance Type Accelerometer with PWM Electrostatic Servo Technique," *Sensors and Actuators*, A21-A23, 1990, pp. 316-319
- [11] K. Ma and K. Najafi, "A New Capacitive Electro-Chemical Etch Stop Technique," *MEMS 1993*, Oiso, Japan, pp. 158
- [12] V. McNeil, M. Novack and M. Schmidt, "Design and Fabrication of Thin-Film Microaccelerometers using Wafer Bonding," *7th International Conf. on Solid-State Sensors & Actuators*, pp. 822-825
- [13] Y. Park and K. Wise, "An MOS Switched-Capacitor Readout Circuit for Capacitive Pressure Sensors," *Proc. IEEE Custom Circuit Conf.*, May 1983, pp. 380-384

# Compatibility and Incompatibility of Chemical Sensors and Analytical Equipment with Micromachining.

Dr. Marc Madou  
Microfabrication Applications  
3680 Bryant Street, Palo Alto,  
Ca 94306 USA

## Abstract

During the past 25 years the commercialization of chemical sensors and instrumentation based on microfabrication failed to keep pace with earlier projections. In this presentation we will explore the causes that slowed down the development of micromachining to produce chemical sensors and analytical instruments and we will suggest the kinds of actions that can be taken to speed up the progress of applying micromachining tools.

Micromachining is emerging as a set of new manufacturing tools to solve specific industrial problems rather than as a monolithic new industry with generic solutions for every manufacturing problem. Based on some concrete examples we will show that, whereas mechanical sensor manufacture is moving towards more integration, embodied in increased reliance on surface micromachining, chemical and biosensors are moving away from integration toward hybrid technology. In the case of instrumentation there is a trend toward using laser machining and some early exploration of LIGA use.

Micromachining in the chemical and micro-instrumentation area has the stigma of a technology used in backrooms only. To change this it will be important to describe most new results as fine-tuning of micromachining skills rather than as the latest breakthrough in analytical instrumentation. A more thorough understanding of the application is needed to make it easier to decide upon the correct manufacturing technique.

### Introduction

We are focusing this presentation on the microfabrication of chemical sensors and analytical instruments that promise to become successful market opportunities i.e. biomedical and some selected industrial applications. The commercialization of chemical sensors and instrumentation based on microfabrication over the last 25 years has not kept pace with earlier projections while progress in biosensors and analytical instrumentation, based almost exclusively on classical manufacturing techniques, has been significant. In the industrial arena, characterized by less aggressive R&D efforts, the progress in developing new sensors and equipment based on

micromachining was even more restricted than in the biomedical arena.

Concurrent with the above developments the number of tools made available to fabricate small devices has grown dramatically. Some important techniques for chemical sensor and instrumentation construction are compared in Table 1. This presentation shows that in contrast to mechanical sensors where the excellent mechanical properties of single crystalline Si tend to favor Si technology, the choice of the optimum material and manufacturing technology for chemical sensors and micro-instrumentation is far less evident. We can point out the following trends. Whereas mechanical sensors (pressure, acceleration, temperature etc.) are moving toward more integration embodied in surface micromachining, chemical and biosensors are moving away from integration and toward hybrid technology. Where instrumentation is concerned there is a move toward using laser machining and some early exploration of LIGA use. In this presentation we want to explore what was lacking in the application of micromachining to chemical sensors and analytical instruments, what can be done to speed up the progress and how to correctly apply the manufacturing tools in Table 1.

### Chemical Sensors in Table Top and Hand-Held Analytical Equipment

The progress enabling the development of small table top medical diagnostic instruments was mainly based on the development of solid-state stabilized reagents (over 30 dry reagent chemistries are available for detection of biological compounds) and to a minor extent on advances in thin-film technology [1]. It was anticipated that micromachining would play a more prominent role in the development of sensors for the smaller, next-generation, hand-held, portable diagnostic instruments. In reality, the micromachining and Si sensor content in the more advanced, hand-held, biomedical products has been surprisingly limited. We will describe a few representative examples of micromachined chemical sensors for such instruments.

### Ion Selective Electrodes (ISE's).

In vitro - Some of the biggest hurdles in silicon based ISE development are the construction of a true on-board external reference electrode in the same plane as a FET device (Field Effect Transistor), a stable internal reference, a simple calibration scheme, incompatibility of sensor materials with Si processes, electrolyte shunting the electronics, high fabrication cost at low volumes and packaging [2]. Another reason for the slow commercialization of silicon-based ISE's is that the currently available chemical sensing technologies are proven and cost effective. After

25 years of R&D, the ISFET (Ion Sensitive Field Effect Transistor) only has found some limited niche applications. Its research in the US seems at a standstill for now.

Most sensor experts have come to appreciate that for chemical sensors one should only implement on-board electronics if it is absolutely essential for the integrity of the signal. The extended gate field effect transistor (EGFET) device was conceived to avoid some of the problems associated with the leakage problems of an ISFET [3]. By depositing the ISE membranes a short distance away on conducting lines extending from the FET gates, encapsulation was made easier. This seemed like an elegant solution at the time. But i-STAT abandoned the EGFET approach and eliminated all on-board electronics. The Portable Clinical Analyzer from i-STAT uses Si only as a substrate for the chemical sensors and as a contacting base, clearly a more economical approach. The sensor electrodes, gels and membranes are all deposited with semiconductor type processes [4].

Another problem in the manufacture of Si chemical sensor arrays manifests itself in the decrease in manufacturing yield with increasing number of array elements. When depositing the sensor materials associated with the different array elements, each new layer added to the wafer reduces the yield of the finished product, especially since the materials involved are mostly non-standard. To increase the manufacturing yield dramatically, one would need to fabricate a different wafer with only one type of sensor, combining the individual sensors into an array, e.g. with pick and place techniques. This automatically would make the sensor array larger though and the Si approach would lose some of its attractiveness.

The success of i-STAT's product introduction [5] renewed the interest in making planar ISE's. Efforts by this author in collaboration with SENSORS 2000! at NASA and efforts at the Center for Emerging Cardiovascular Technologies (CECT)[6] focus on depositing ISE components on inexpensive non-Si substrates (ABS and Kapton respectively). At NASA we are comparing silkscreening and drop-delivery systems to deposit ISE membranes and hydrogels.

*In vivo*. Cost of disposable sensors for in-vivo use does not represent as big a concern as for in-vitro disposable sensors. It is estimated that a catheter based pH, CO<sub>2</sub> and O<sub>2</sub> sensor may cost up to \$250.00 and would serve a market of well over \$300 M a year in the U.S. alone [7] [8]. Unfortunately the warm, wet, saline in-vivo environment exemplifies perhaps the most severe environment in which silicon sensors might be used. Si based in-vivo chemical sensors are not

commercially available today. Biocompatibility is the single most complex issue facing in-vivo sensor development. As biocompatibility is the main concern it should be addressed up front. In the following example we, at first, neglected to do just that. For 4 years (\$6 M research fund) we attempted to develop an in-vivo pH, CO<sub>2</sub> and O<sub>2</sub> probe, the so-called RT-MECSS (i.e. the Micro Electronic Chemical Smart Sensor) shown in Fig. 1 [9]. The RT-MECSS attempted to put chemistry and electronics on separate planes while keeping the signal line as short as possible. This linear electrochemical array fitted inside a 20-gauge catheter (705 μm in diameter) without taking up so much space as to distort the pressure signal monitored with a pressure sensor outside the catheter. A classical (macro) reference electrode, making contact with the blood through the saline drip, was used for the pH signal while the CO<sub>2</sub> and O<sub>2</sub> had their internal reference electrodes. Results obtained in saline solutions were encouraging but funding for continued research stopped before serious biocompatibility efforts could be started. In order to avoid this type of situation we have launched an ambitious program where we are addressing the biocompatibility issue of a catheter based electrochemical sensor up front [10]. If biocompatibility results warrant such an endeavor, the RT-MECSS design will be put back into the catheter.

The catheter shown in Fig. 2 is used for those biocompatibility studies with animals. The internal dual lumen structure shown has a working and a reference chamber. The reference chamber has a hole contacting the external medium, and the working electrode chamber has a hole contacting the ion selective membrane (see also Fogt et al. [11]). The membrane for the pH ISE is based on PVC doped with tridodecylamine as the ionophore. The purpose of the external 'sleeve' shown in Fig. 2 is the incorporation of a reservoir for slow release of an anticoagulant such as Heparin or Heparin. The catheter is further interfaced with a 450 kHz amplitude-modulated (AM) implantable telemetry transmitter which incorporates a high impedance (> 10<sup>12</sup> ohm) preamplifier and allows for nearly continuous measurement of pH and temperature at a distance of two feet from the animal. In-vivo and in-vitro telemetric pH data will be presented.

**Immunosensors.** Whereas for ISE devices and enzyme based sensors electrochemical techniques are preferred [2], optical techniques are more prevalent for immunosensing today. A comparison of optical and electrochemical immunosensors is presented in reference [12]. Two major issues facing any immunosensor are its inherent irreversibility and non-selective

protein binding. Almost all immunochemical reactions are irreversible given the large association constants ( $K_a$ ) that are involved in an antigen-antibody binding reaction (typical  $K_a$  values range between  $10^5$  and  $10^9$   $M^{-1}$ ). The Ag-Ab association constants are composed of large forward ( $k_1$ ) and small reverse ( $k_{-1}$ ) rates. These kinetic parameters make antibodies very selective for the analyte of interest but also make them quite irreversible.

The best way to avoid non-specific binding effects in immunosensors is to make a reference as similar to the sensing surface as possible i.e. a reference that is subject to all the same non-specific protein binding phenomena as the sensor surface itself except for the antigen-antibody of interest. This enables the best possible correction for non-specific binding. An interesting way of implementing this idea is to create an optical grating pattern with the antigen-antibody binding modulation providing the grating structure. The reference in this grating is based upon the loss of antigenicity by UV radiation as observed by Panitz and Giaver [13]. They found that the antigenic sites on proteins are very sensitive to ultraviolet radiation in air. By using a photomask, alternating bands of antibodies can be inactivated by creating a biological diffraction grating. A CD-type He-Ne laser beam diffracts from the grating with an intensity related to the antigen concentration. This technology is being pursued by Idetek (1993) [14].

Barnard et al. [15] introduced an ingenious way to make an assay continuous. They used fluorescein-labeled antibody (F-Ab) and Texas Red-labeled immunoglobulin G antigen (TR-Ag) in a competitive immunoassay based on fluorescence energy transfer. To circumvent the inherent irreversibility of this assay Barnard et al. used a controlled-release delivery system capable of sustaining a constant release of fresh immunochemicals (similar to our approach to biocompatibility illustrated in Fig. 2). In cases where continuous monitoring is of major importance but response time is not very critical this technique seems very promising.

Examples of optical and electrochemical immunosensors developed by this author are shown respectively in Fig. 3 and 4. Our one-step electrochemical immunosensor combines the fundamentals of enzyme immunoassay, electrochemistry, and gel filtration [16]. To make the components as cheap as possible, thick film technology on a plastic substrate has been used. The detection limit of the FAD/apoglucose oxidase system used in the sensor in Fig. 3 is well below  $10^{-10}$  M which is adequate for the analysis of a majority of analytes. A further challenge is to find reproducible ways

of layering the different organic materials shown in Fig. 3. This challenge has little to do with Si micro-machining but everything with learning how to stack and manipulate hydrogel materials.

Our optical immunosensor is based on Langmuir-Blodgett technology [12]. The difference in thickness of two adjacent steps as shown in Fig. 4 corresponds to a double layer of stearate (approximately 48 Å) and forms an interference based color gauge which sensitively tracks thickness increases. Steps can be built using etching techniques in inorganic materials with optimum refractive indices for maximum interference effect [17]. We experimented with both Si and glass substrates. This system can follow antigen-antibody binding in a simple and inexpensive way. Langmuir-Blodgett deposition is a difficult manufacturing proposition. More recently we found a better way: a substrate was pulled at a uniform rate from an etchant solution making a continuous optical wedge rather than a staircase type structure.

In general optical thin film immunosensors are quite amenable to IC type micro-machining techniques (e.g. for protein patterning) but for electrochemical immunosensors hybrid approaches seem more appropriate.

**Gas Sensors-Dry.** Solid state gas sensors for industrial applications i.e. zirconia based oxygen sensors for the automotive, toxic and combustible gas sensors for the chemical and petrochemical industry and humidity sensors for the energy conservation market (e.g. all drying operations) constitute a sizable industrial market served by, with few exceptions, mediocre products [18]. With the automotive world as the driving force, significant efforts in using microfabricated gas sensors are under development. So far results have been disappointing.

We developed a planar zirconia oxygen sensor for automotive applications fabricated by using plasma-spray deposition [19],[20]. Although not exactly micromachining, the use of plasma spraying might enable the batch fabrication of such sensors at a cost below \$2.00 rather than the current \$12.00 and up. Controlling the plasma spray process to form the porosity gradient in the sensor is still a major challenge.

The use of a ceramic tube in a classical Taguchi sensor maximizes the utilization of the heater power, so that all power is used to heat the tin oxide. The tin-oxide paste is applied on the outside of the ceramic body over thick film resistance measuring pads and is sintered at high temperature. The sintering stabilizes the intergranular contact where the sensitivity of the gas sensor resides. The design is not suited for mass production as it involves excessive hand

labor. The problems with the thick film structure are mainly in the area of reproducibility: compressing and sintering a powder, the deposition of the catalyst, the use of binders and other ceramics (e.g. for filtering) are all very difficult to control. Application of IC techniques could improve the state of the art dramatically if one could make a thin semiconductor-oxide film (e.g. tin-oxide) with the same sensitivity as the thick film. Micromachining the heater elements would further improve reproducibility and the absolute power budget needed to heat the thin film. Such thermal efficiency and low power budget is obtained by thermally isolating the heater. It has proven to be very difficult to make a thin film as sensitive as the ceramic type thick films.

The use of the intergranular contact potential as the resistance-determining parameter is required for maximum sensitivity [2]. When making thin films, the films have to be thin enough so that extraction of electrons has a significant effect on the overall film resistance. Obviously thickness control becomes a key factor here. Another problem is that the resistance is not controlled by the bulk electron density, but by grain boundaries in the films. Again intergranular contact resistance is involved in determining the resistance of the film, and because oxygen cannot directly reach the intergranular contact (as it does in the powder case) it must diffuse in and out at the grain boundary. This makes for long time constants unless the grain boundaries are completely blocked.

Finally the currently available devices, already quite small and inexpensive, only will be replaced quickly by newer technology in terms of: reproducibility, cost, sensitivity, response time, concentration range, specificity, reversibility, stability and power consumption.

At this time the best course for future progress in the Taguchi sensor R&D area is to optimize sensitivity of thin film oxide semiconductors, use planar silicon devices (reproducibility and cost) and concentrate on implementing less power-consuming microheater elements. These devices will cost more than the planar ceramic devices but they will outperform them in terms of power needs and reproducibility. For the short term thick film planar devices on ceramic substrates are the best way to go.

Wet. We have attempted to make faster responding electrochemical gas sensors by innovative methods of exposing the triple points to gas media [21]. The intent was to make the liquid path through which the gas must diffuse to reach the triple point as short as

possible or even do away with it completely. We believed it was possible to create gas sensors that combine some of the positive characteristics of both electrochemical and solid state gas sensors. The sensor we invented is the Back-cell™ [22] (Fig. 5). Two versions of the back cell sensors were investigated: sensors using a porous ceramic substrate and those based on a silicon substrate with micromachined pores. A thin layer of Nafion or a hydrogel was deposited over the metal electrodes on the front of the porous slab and the gas to be detected only was allowed to reach the sensing electrode from the back of the porous substrate. The details of the microfabrication procedure were explained elsewhere [21], [23].

The response of this sensor to a step change in oxygen concentration from 0 to 100 % exhibits a 90 % response time of 300 msec; this is extremely fast compared to other amperometric sensors (typical response time 30 to 90 seconds). Gas does not need to diffuse through a thick layer of electrolyte to reach the triple points where they react. In other words the triple point is almost dry (as water is involved in the reaction, gas probably still diffuses through a few monolayers of water to react at the metal). The recovery of the sensor back to baseline upon a step change in oxygen concentration from 100 % to 0 % is slightly slower than the initial response—400 msec.

For ease of manufacturing the ceramic approach is preferable. The major problem with the current device is water management. The fast response of the sensor gets lost when water fills the pores on the back of the metal electrodes.

## Instrumentation

From the time a gas chromatograph, the size of a matchbox, was printed on the cover of the April issue of Scientific American in 1983 [24] (Terry and Angell built a first prototype between 1974 and 1975), there has been a continued effort to micromachine analytical instruments. Today there are only two commercially available 'micro-instruments' with some key components based on micromachining. The first is the gas chromatograph by MTI, looking significantly different than the device shown on the Scientific American cover (e.g. the column itself is not micromachined). Second are a class of instruments based on Molecular Devices' patented LAPS (Light-Addressable Potentiometric Sensor) technology [25]; a silicon based microphysiometer i.e. the Cytosensor: capable of measurement of the metabolism in living cells and the immuno assay; Threshold: for rapid quantitation of a variety of analytes at sub-femtomole levels. In the LAPS devices the Si

content is a minute contributor to the \$80,000 dollar price tag but it is the most essential part (very much like the Si tips in AFM and STM). For most of the other micro-instrumentation listed the verdict on the wisdom of using Si micromachining is still out.

#### Gas Chromatography (Mini-GC).

The first integrated GC, consisting of a long separating column, a sample injection valve, and a thermal conductivity detector, all fabricated on a single silicon wafer, was developed at Stanford in 1974. MTI's commercial Mini-GC based on that original work uses a classical capillary column but has retained all the other micromachined components.

Column diameter profile is an important issue not adequately addressed with micromachining. The smoothness of the film coating on the inside of a capillary column is a function of the profile symmetry and is extremely important. Rectangular columns and columns made by joining two cylinder halves tend to accumulate coating on the corners or joints leading to a less perfect separation [26]. Analytes might spend a longer time in areas where the coating is thick compared to places where it is thin, leading to a broadening of peaks. As we will discuss in our lecture, miniature Joule-Thomson cryogenic refrigerators [27] and micro electrophoresis units [28] are not as sensitive to the column diameter profile but other problems are associated with these two instruments. Since traditional columns are perfectly adequate for the mini-GC, the focus has shifted to other problem arenas where micromachining could help. For example a GC only works properly if the volume of the injected gas is small compared to the volume of the column so that a miniature sample-injection valve needs to be built. Also the volumes between column and detector and valve and detector need to be minimized. Large dead volume in analytical equipment leads to a high power budget and too slow response time. To accept a range of gas volatilities the injector column assembly needs to be heated uniformly. Fast heating and cooling rates are very important creating the following challenge for micromachinists i.e to add and remove heat locally, fast and uniformly (a requirement also for building the next generation of PCR units). In the Personal Chromatograph or PC [29] injector temperatures up to 220°C are possible and the chromatographic column assembly consists of a 3 meter 100 μm i.d. tubular column with an ultra low thermal mass column oven heater and RTD sensor in intimate contact with the column. Through efficient thermal management heating rates to 5°C per second over temperatures up to 230°C can be

obtained. The controller maintains the carrier gas pressure at the head of the column by electronic pressure control using a fluistor (Redwood Microsystems) and manages flow of sample and carrier gas through the entire system by appropriate sequencing of flow control valves.

We are considering LIGA to integrate the column, heater and sensor of the PC in one simple monolithic structure.

#### Mini-Ion Mobility Spectrometer (Mini-IMS)

In an ion mobility instrument, ions, produced at atmospheric pressure in an ionization cell by a  $^{63}\text{Ni}$  beta source, are accelerated in a drift chamber (uniform field of 150-250 V/cm), where they are separated according to their mobilities and detected as a current on a Faraday plate and plotted on a time axis in accordance to their time of arrival (see Fig. 6). About six years ago we set out to micromachine some critical components of an IMS instrument. Field uniformity, temperature and pressure, we recognized, could be controlled with miniature Si sensors. Our principal aim though was to substitute the  $^{63}\text{Ni}$  ionization source with a less fragmenting ionization source (a "soft" field ionization technique (FI)), mainly creating parent ions ( $M^+$ ) and thus simpler spectra for complex environmental gas mixtures. Considering the extreme electric fields required for FI, one might expect that under atmospheric pressure conditions, catastrophic electrical breakdown would occur. The idea for the new ionizer was based on the peculiar behavior of micro electrodes when operating at the left side of the Paschen curve. In Fig. 7, the Paschen curves, the sparking potential as a function of  $pd$  (where  $p$  is the pressure of the gas phase between the two electrodes and  $d$  the inter electrode distance) for a variety of gases are shown. Interestingly, with  $d$  small, the sparking potential goes up dramatically. This can be understood by recognizing that when the distance is too short to allow an electron avalanche to gather enough electrons, no spark between the two electrodes results. The minimum of the curve shown at atmospheric pressure in air is 6.4 μm.

An array of 10\*10 microvolcanoes was fabricated with a typical throat opening of 1 μm. Given the small dimensions of the microvolcanoes, the intense electric fields required for field ionization can be produced with significantly lower voltages than macro FI sources. Referring back to the Paschen curve in Fig. 7, it is clear that the microvolcano sources should operate at atmospheric pressure with voltages up to several hundred volts and perhaps as high as a kilovolt. We have shown that these sources can indeed resist electrical breakdown at atmospheric pressure and produce

positive ions and usable current levels in a set-up as shown in Fig. 6 (we experimented with butane, toluene and pyridine). On the basis of these observations we believe that a strong possibility exists to make a working ion mobility spectrometer using an atmospheric field ionization source.

In a separate effort [30] we also have shown that negative ions can be formed at atmospheric pressure as well.

#### Discussion

There is no doubt that the chemical sensor and analytical instrument market constitutes a potentially larger market than mechanical sensors, not in the least because sensors here are often disposable and cost is usually less of an issue with analytical equipment. Despite the slow progress, the search to make sensors and instrumentation smaller, less expensive, faster, more sensitive etc. will continue.

From the above it is clear that in chemical sensors hybrid technology is becoming more important. Also for instrumentation and for many chemical sensors one micromachining tool does not represent a deus-ex-machina. All tools shown in Table 1 need to be considered. In many cases a better fundamental understanding of the application is needed before a manufacturing technique is decided upon. Often the influence of miniaturization on device performance can be studied independently from the manufacturing technique, e.g. by laser machining (fast turn around prototyping).

The following is a good definition for micromachining in the application field of mechanical devices. Microfabrication, micromachining or micro-manufacturing comprises the use of a set of manufacturing tools mostly based on electronic integrated circuit (IC) manufacturing technologies, often enhanced or modified, to build devices such as sensors, actuators and other micro-components and microsystems. In the case of chemical sensors and microinstrumentation this definition must be expanded to include, in a wide variety of materials using parallel batch lithography as well as serial direct write and thick film (hybrid) techniques.

The direct write techniques may indeed become economically viable solutions for microsystem applications. Micromachining has matured around Si and Si processes, further development of sensors and actuators will require the adaptation of many different materials to the micromachining process and hybrid technology will actually become more important for the construction of chemical sensors. The need to incorporate new materials is especially urgent for progress in chemical sensors and biosensors.

#### References

- [1] J.F. Roe, *Pharmaceutical research*, vol.9, No.7, pp.835-844, 1992
- [2] M.J. Madou and S.R. Morrison, 1989, *Chemical Sensing with Solid State Devices*, Academic Press
- [3] Lauks, I., Van der Spiegel, Sansen, W., and Steyaert, M., in *Transducers'85, Proc. of the Int. Conf. on Solid-State Sensors and Actuators*
- [4] Lauks, I. in *Microsensors: Transferring Advanced Technology to Industry*, SRI, Nov.7, 1986
- [5] *In Vito, The Business and Medicine Report*, pp.1-4, May 1992
- [6] CECT, Duke University, UNC, Case Western, New Mexico State University Fifth Annual Report, October 8, 1992
- [7] *The Genesis Report/Dx, Microsensors : Applications and Commercialization*, June 1991
- [8] *Sensor Business Digest*, Vol.3, No.1, October, 1993, ISSN 1060-1902
- [9] M.J. Madou and T. Otagawa, *AICHE Symposium Series*, 267 Volume 85, 1989, pp.7-14
- [10] H.L.Kim, M.Madou, and J.Hines, *Proc. of 207 th ACS, San Diego, Ca*, March 13-18, 1994
- [11] E.Fogt, J.Kelley, J.Lund, M.S.Norenberg, M.Schwinghammer, *Sensors and Actuators*, 1990, pp.267-271
- [12] M.J. Madou and J. Joseph, *Immunomethods* 3, 134-152, 1993
- [13] Panitz and Giaver in *Structure and Motion : Membranes, Nucleic Acids&Proteins*, Eds. Clementi, E., Corongiu, G., Sarma, M.H., and Sarma, R.H., 1984, *Adenine Press*, pp.87-99
- [14] *Idetek, R&D Magazine*, March 1993, p.51
- [15] Barnard, S.M., and Walt, D.R. (1991) *Science* 251, 927
- [16] Joseph, J., Jina, A., and Madou, M. (1991) *Separation-Free Electrochemical Immunosensor*, Paper presented at the Annual meeting of the AIChE, Anaheim, CA
- [17] Joseph, J., and Itoh, K. (1992) *US Patent* 5, 169, 599
- [18] M.J. Madou, *World Markets for Solid State Gas Sensors* September 8-9, 1993, NIST Special Publication 1993, Stephen Semancik Editor
- [19] S. Oh and M. Madou, *Sensors and Actuators B*, Vol.13-14, 1992, pp.581-582
- [20] S. Oh, *Sensors and Actuators B*, Vol.20, 1994, pp.33-41
- [21] Maseeh, F., Tierney, M.J., Chu, W.S., Joseph, J., Kim, H.-O.L., Otagawa, T., *Transducers '91, San Francisco*, p.359, IEEE Catalog Number 91CH2817-5
- [22] M.J. Madou and T. Otagawa, *US Patent* 4, 812, 221

- [23] Otagawa, T., Madou, M., Wing, S., Rich Alexander, J., Kusanagi, S., Fujioka, T., Yasuda, A., Sensors and Actuators, B1, (1990)319
- [24] Angell, J.B., Terry, S.C and Barth, P.W., Scientific American, pp. 44-54, April 1983
- [25] L.J. Bousse, D.L. Miller, J.C. Owicki, and J.W. Parce, Transducers '91, San Francisco, IEEE Catalog Number 91CH2817-5 see also D.G. Hafeman, J.W. Parce and H.M. McConnell, 27 May 1988, Volume 240, pp.1182-1185
- [26] E.B. Overton, April 1994, Private communication
- [27] Hollman, R.; Little, W.A. NBS Conf. Refrigeration for Cryogenic Sensors and Electronics Systems, 1980; Special Publications 607, p.160.
- [28] Futuretech, No.166, October 1993, Technical Insights, Inc., Fort Lee, New Jersey also Seiler, K., Harrison, D.J., Manz, A. 1993, Analytical Chemistry, 65, pp.1481-1488 and D.J. Harrison, K. Fluri, K. Seiler, Z. Fan, C.S. Effenhauser, A. Manz, Science, Reports, Vol.261, 13 August 1993
- [29] K.R. Carney, E.B. Overton, R.L. Wong, M.A. Jackisch, C.F. Steele, ACS Symposium Series, E. Winegar and L. Keith ed. p.21-38, Lewis Publishers, 1993
- [30] M.J. Madou and S.R. Morrison, p.145-149, Transducers '91, San Francisco, p.359, IEEE Catalog Number 91CH2817-5

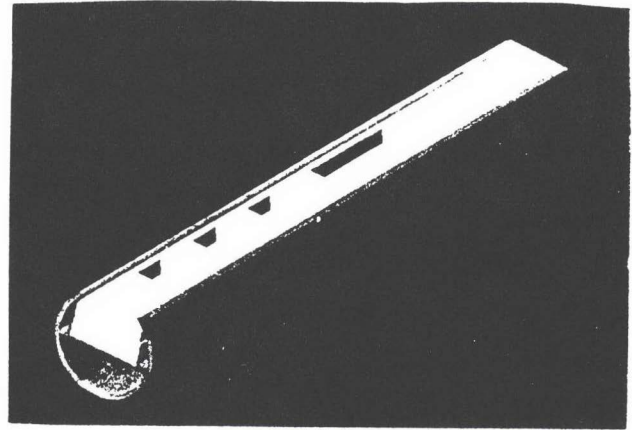


Figure 1. Array of electrochemical cells etched in Si to accommodate sensors for e.g. pH, O<sub>2</sub>, CO<sub>2</sub>.

Table 1. Machining Tools.

	Surface $\mu$		Wet Bulk $\mu$	Dry Bulk $\mu$ (e.g. SCREAM*)	LIGA**	Laser	Hybrid
	Poly-Si	SOI					
Z-Height	< 10 $\mu$ m	up to 100 $\mu$ m	Single wafer : 600 $\mu$ m	up to 100 $\mu$ m	Up to 1 mm was reported	Very wide range	Less than 20 $\mu$ m is difficult
X, y-Shapes	Free	Free	Limited	Free	Free	Free	Free
IC Comp.	Good	Good	Poor	Good	Not demonstrated	Good	Not applicable
Materials	Poly-Si	SCS***	SCS	Free	Some choice	Free	Lot of choices
Maturity	Fair	New	Mature	New	New	Very new	Mature
Cost	Low	Fair	High	Fair	?(low with replication)	High	Low
Access	Good	Not yet	Good	Good	Poor	Fair	Good
Parallel (P)/ Serial (S)	P	P	P	P	P	S	P

\* Single Crystal Released Etched and Metallized  
 \*\* From the German acronym for lithography, electro deposition and molding.  
 \*\*\* Single Crystal Silicon

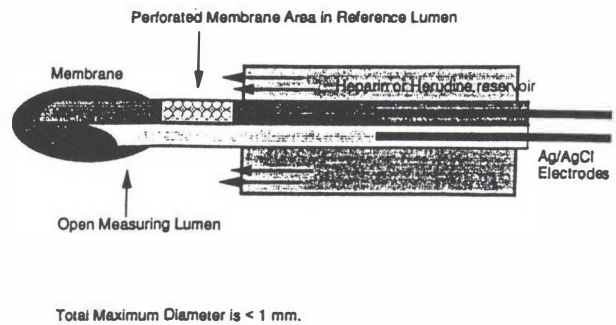


Figure 2. PH sensitive catheter used for biocompatibility experiments (telemetric transmitter and receiver are not shown).

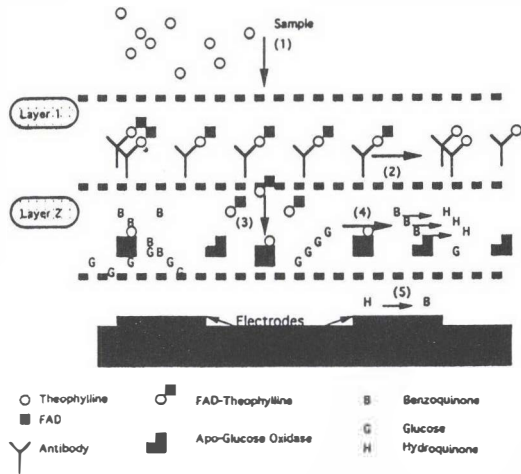


Figure 3. Layer configuration of the immunosensor using theophylline as example  
 Reaction scheme: (1) Theophylline sample diffuses into 1st layer, (2) free theophylline displaces pre-bound FAD-theophylline conjugate, (3) FAD-theophylline diffuses into the second layer and activates Apo-Glucose Oxidase, (4) Benzoquinone consumed and Hydroquinone produced, (5) Hydroquinone is oxidized at the metal electrode leading to an increase in current.

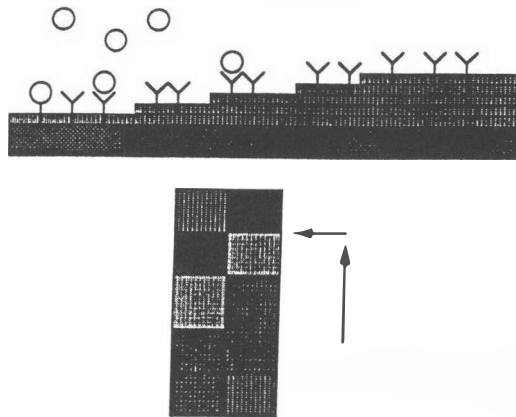


Figure 4. Interference based immuno sensors (staircase).

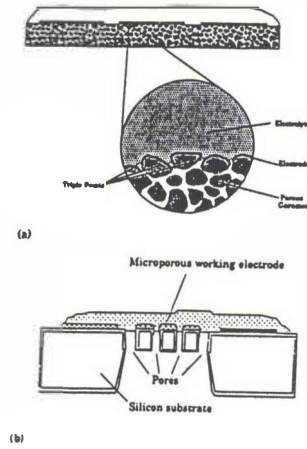


Figure 5. Backcell configurations :  
 (a) Back cell sensor in porous ceramic substrate;  
 (b) Back cell sensor with a silicon micromachined substrate.

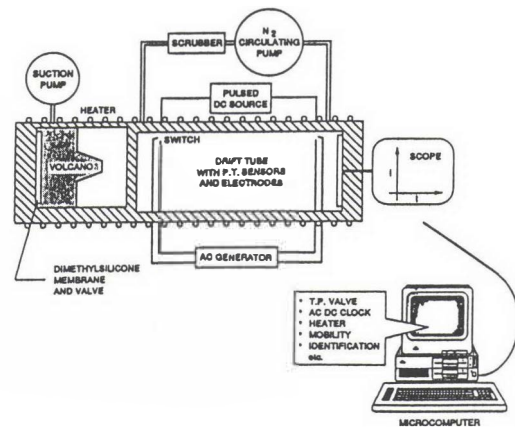


Figure 6. IMS set-up for testing of micro volcanoes.

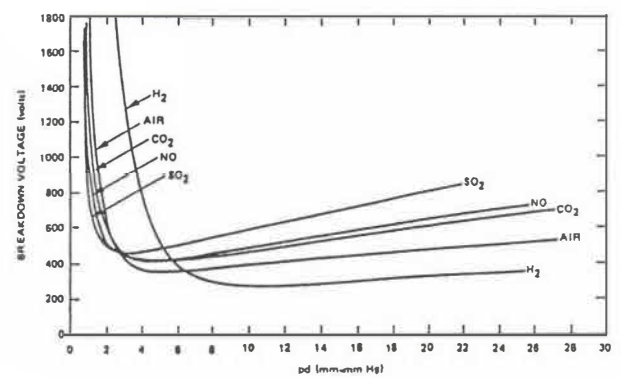


Figure 7. Paschen curves for various gases.

# Diamond Film Based Structure for Gas Sensing Applications

W. P. Kang, Y. Gurbuz, J. L. Davidson and D. V. Kerns

Department of Applied and Engineering Sciences, Vanderbilt University,  
Nashville, TN 37235

Fax: (615)322-7996, Tel: (615)322-0952 E-mail:wkang@vuse.vanderbilt.edu

## Abstract

A new microelectronic gas sensor utilizing plasma enhanced chemical vapor deposited (PECVD) diamond in conjunction with a catalytic metal has been built and tested for gas detection. The device is fabricated in a layered Pd/ i-diamond/ p-diamond Schottky diode configuration on a variety of supporting substrates. The performance of the device for H<sub>2</sub> detection has been examined in terms of sensitivity, linearity, response rate, and response time as a function of temperature and hydrogen partial pressure. Analysis of the steady state reaction kinetics confirm that the hydrogen adsorption process is responsible for the barrier height change in the diamond Schottky diode. The use of diamond film technology opens the door to the development of a microelectronic gas sensor which can operate at a wider and higher temperature range than the present silicon technology.

## I. Introduction

Catalytic-gate microelectronic gas sensors such as the Schottky diode, MOS capacitor, and MOSFET using silicon based technology have been investigated extensively<sup>1-7</sup> in the past decade. Many interesting applications have been demonstrated and practical devices have been commercialized. Extensive research has been performed to improve gas sensitivity and selectivity through the use of a perforated gate structure<sup>8</sup>. And most recently, by the incorporation of catalyst and adsorptive oxide layers into the MOS system<sup>9-10</sup>. However, the relatively limited temperature operating range (<150°C) of the silicon based device has prevented the widespread utilization of these sensors, particularly for the detection of toxic gas for the combustion process and *in situ* emission control at high temperature. Recent advances in the plasma enhanced chemical vapor deposition (PECVD) process have resulted in the realization of high quality polycrystalline diamond films for device applications. Microelectronic devices such as Schottky diodes, and field-effect-transistors FETs<sup>11</sup> have been fabricated for high temperature applications. It would thus be possible to utilize the diamond technology for gas sensors operating at considerably higher temperatures than those based on silicon technology.

In this paper, we present the first prototype polycrystalline diamond based gas sensing structure for hydrogen gas detection. Major advantages of using the polycrystalline diamond thin film based structure for gas sensing applications are wider (or higher) temperature operating range, simplicity in the fabrication process, flexibility in the choice of substrates, and compatibility with silicon microfabrication technology. Moreover, PECVD diamond films possess many desirable material properties such as good thermal conductivity, chemical inertness, electrical stability, and compatibility with hostile environments.

## II. Sensor Fabrication and Characterization Method

The diamond-based gas sensor was fabricated in a layered Pd/ i-diamond/ p-diamond Schottky diode configuration as shown in Fig. 1. The PECVD diamond film can be deposited on a variety of substrates such as W, Mo, Si, SiN, etc. Boron doped p-type polycrystalline diamond films 5-10µm thick were deposited on the prepared surface of the substrates via *in situ* boron compound solid source doping method using PECVD. A thin intrinsic (undoped) diamond interfacial layer was then deposited on the p-diamond layer. Typical process parameters for the growth of these films were: pressure, 40 torr; substrate temperature, 850°C; gas flow rate, 500 sccm hydrogen and 5 sccm methane; microwave power, 1500 watts. The growth rate was nominally 0.5 microns per hour. Films were then annealed for one minute at 850°C in argon. Raman spectroscopy of these diamond films is shown in Fig. 2. The film shows the typical characteristic Raman peak of a diamond at 1332cm<sup>-1</sup>. Finally, a palladium electrode 1000 Å thick and 1mm in diameter was thermally evaporated on the diamond surface.

The device-under-test was placed on a probe station equipped with a heated stage in an atmosphere controlled test chamber. A predetermined amount of hydrogen was introduced into the chamber. The steady state and transient responses of the devices to H<sub>2</sub> were measured as a function of H<sub>2</sub> partial pressure and temperature by I-V and ΔI-t methods using a Hewlett Packard 4145 meter. The operating temperature of the device was controlled to ±1°C of the desired temperature during the measurement.

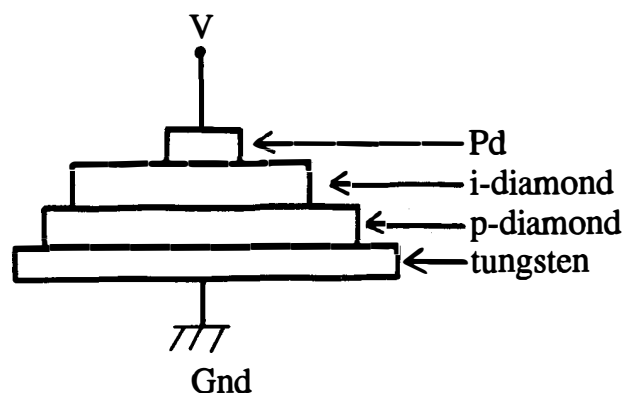


Fig. 1. Diamond based gas sensor fabricated in a layered Pd/ i-diamond/ p-diamond Schottky diode

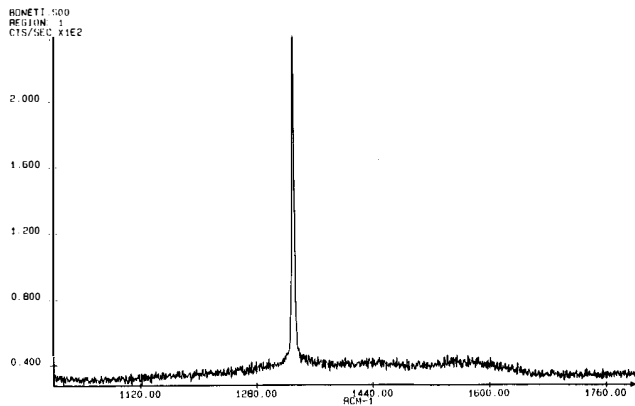


Fig. 2. Raman Spectra of PECVD Diamond

### III. Results and Discussion

#### A. H<sub>2</sub> Sensing Characteristic

Typical I-V characteristics of the polycrystalline diamond based gas sensor before and after exposure to H<sub>2</sub> are shown in Figs. 3, and 4 for two type of devices operating at 55 and 200°C, respectively. The figures show a large change in the I-V characteristics of the sensor, shifted from near ohmic to rectifying behavior upon the devices exposure to the H<sub>2</sub> gas. The effect is reproducible and repeatable upon adsorption/ desorption of hydrogen gas. Figure 5 shows the detection sensitivity,  $\Delta I$ , versus hydrogen partial pressure for the device operated at 55°C, under a fixed (-0.4 V) forward bias voltage. The figure shows a rapid increase in  $\Delta I$  upon H<sub>2</sub> adsorption at low hydrogen partial pressures, followed by a trend to saturation at higher H<sub>2</sub> partial pressures.

Adsorption transient behavior of the diode upon exposure to hydrogen gas was measured by monitoring the current of the device as a function of time, at fixed forward bias voltage. Typical transient responses of the diode as a function of H<sub>2</sub> partial pressures at a constant room temperature and at fixed H<sub>2</sub> partial pressure for several operating temperatures are shown in Figs. 6 and 7, respectively. In general, the initial adsorption rate,  $[\Delta(\Delta I)/\Delta t]_{\text{initial}}$ , increases with hydrogen partial pressure or temperature, while the adsorption time constant, (time required for the measured  $\Delta I$  to reach  $e^{-1}$  of its saturation value) decreases with increasing hydrogen partial pressure or temperature. At room temperature, as the concentration of hydrogen increases from 0.1 torr to 2 torr, the initial adsorption rate increases from 0.002 mA/sec to 0.022 mA/sec with the corresponding response time decreasing from 168 sec to 22 sec. As the temperature increases, the initial adsorption rate increases from 0.019 mA/sec to 0.069 mA/sec and the response time constant decreases from 20 sec to 9 sec.

A typical repeatability test of the sensor for the detection H<sub>2</sub> (concentration: 100%, flow rate: 10 ml/min) in an open air (1 atm.) background is shown in Fig. 8. The device shows a response and recovery time in seconds upon turning of the H<sub>2</sub> gas on/off, exhibiting that the response to hydrogen is fast, sensitive, reproducible, and repeatable.

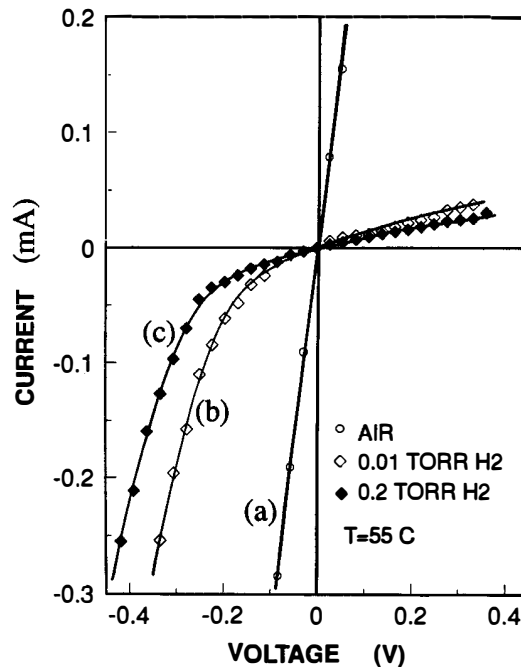


Fig. 3. I-V Characteristics of Pd/ i-Diamond/ p-Diamond Schottky Diode Hydrogen Sensor at T=55°C: (a) in air, (b) in 0.01 Torr H<sub>2</sub>, and (c) in 0.2 Torr H<sub>2</sub>.

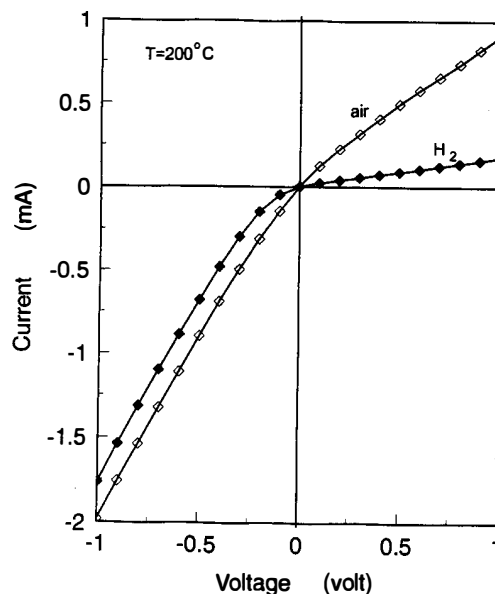


Fig. 4. I-V Characteristics of Pd/ i-Diamond/ p-Diamond Schottky Diode Hydrogen Sensor at T=200°C: (a) in air, (b) in H<sub>2</sub>.

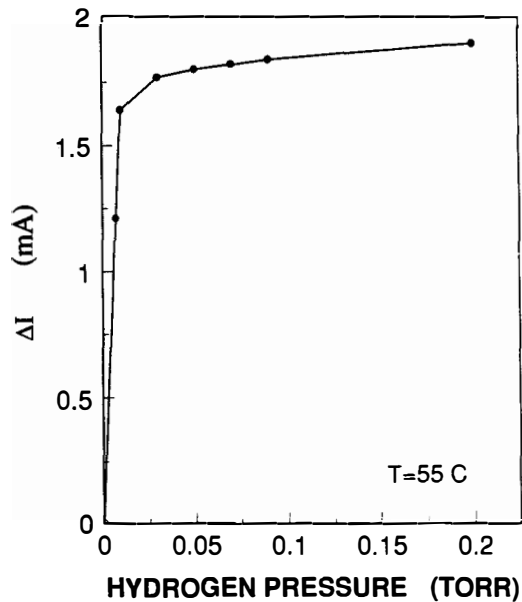


Fig. 5. Detection Sensitivity,  $\Delta I$ , versus hydrogen partial pressure at 55°C.

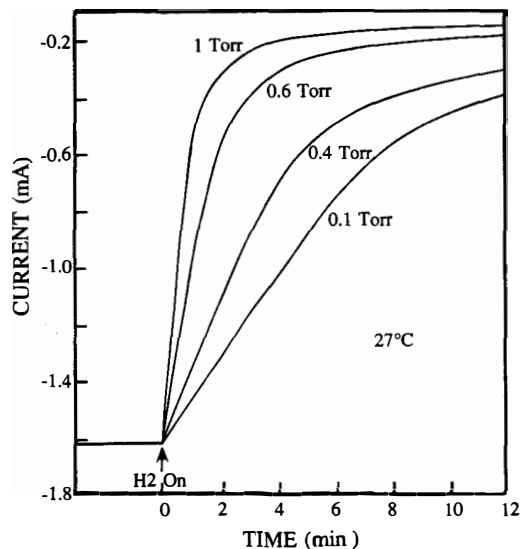


Fig. 7. Adsorption Transient Behaviors of Pd/ i-Diamond/ p-Diamond Hydrogen Sensor upon Exposure to various Hydrogen concentration at a constant temperature

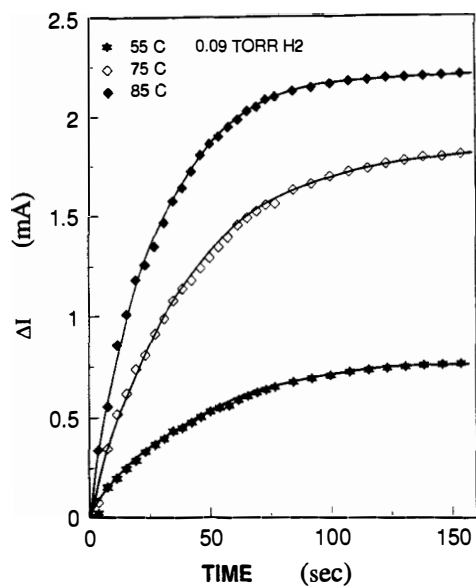


Fig. 6. Adsorption Transient Behaviors of Pd/ i-Diamond/ p-Diamond Hydrogen Sensor upon Exposure to 0.09 Torr Hydrogen at Various Temperatures.

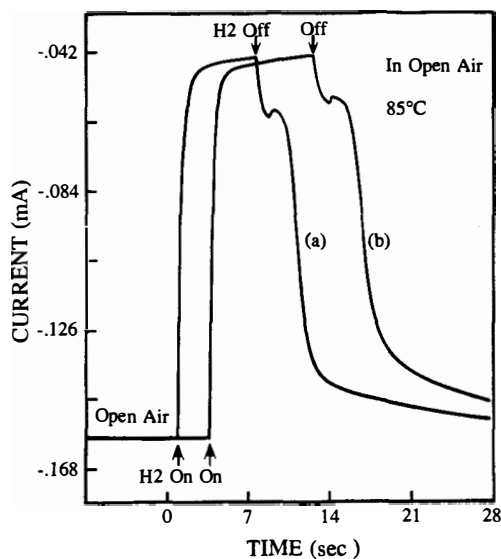
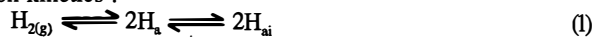


Fig. 8. Repeatability Test of Pd/ i-Diamond/ p-Diamond Hydrogen Sensor for Hydrogen Detection in Open Air Environment.

### B. Detection Kinetic Analysis

The hydrogen reaction kinetic on the Pd-diamond based structure can be explained by considering the following hydrogen reaction kinetics<sup>1</sup>.



where  $g$  and  $a$  stand for gaseous and adsorbed species, respectively. In this case, Eq. (1) describes the  $H_2$  dissociative chemisorption on the Pd surface, solid state diffusion of atomic hydrogen through the metal film, and finally adsorption of atomic

hydrogen at the Pd-diamond interface. Since the measured adsorption time constant is much larger than the hydrogen diffusion time through the 1000Å Pd film (solid state diffusion coefficient of atomic hydrogen in the metal<sup>12</sup> is  $10^{-6} \text{ cm}^2 \text{ s}^{-1}$ ), we can assume that the equilibrium between hydrogen adsorbed on the surface,  $H_a$ , and hydrogen adsorbed on the Pd-diamond interface,  $H_{ai}$ , is established rapidly. Then, under the steady state condition in Eq. (1), the hydrogen coverage,  $\theta$ , at the interface can be put in the form

$$\theta/(1-\theta) = (c_1/d_1)^{1/2}(P_{H_2})^{1/2}. \quad (2)$$

But the barrier height of a Schottky barrier diode is related to the I-V characteristics<sup>13</sup> by

$$I = AA^{**}T^2 \exp(-\phi_b/\phi_T)[\exp(V/n\phi_T) - 1][1 - \exp(-V/\phi_T)] \quad (3)$$

where  $k$  is the Boltzmann constant,  $T$  is in °K,  $A^{**}$  is the effective Richardson constant,  $A$  is the junction area,  $n$  is the ideality factor, and  $\phi_T = kT/q$ . Therefore, if we assume that the change in barrier height,  $\Delta\phi_b$ , induced by hydrogen adsorption is proportional to the hydrogen coverage,  $\theta$ , i.e.  $\Delta\phi_b = \Delta\phi_{max} \theta$ . Where  $\Delta\phi_{max}$  is the maximum barrier change, and  $\theta$  is defined as  $0 < \theta < 1$ . Then Eq. (2) can be reduced to

$$(1/\Delta\phi) - (1/\Delta\phi_{max}) = (1/\Delta\phi_{max})(d_1/c_1 P_{H_2})^{1/2}. \quad (4)$$

Thus, according to the I-V relation of the Schottky diode (Eq. 3), under a fixed temperature and low bias voltage, the change in barrier height  $\Delta\phi_b$  due to hydrogen adsorption is

$$\Delta\phi_b = \phi_T \ln(I_o/I_{og}) \quad (5)$$

and it follows that,

$$\Delta\phi_{max} = \phi_T \ln(I_o/I_{og(max)}) \quad (6)$$

where  $I_o$  and  $I_{og}$  are the current measured in the environment without and with hydrogen gas respectively.  $\Delta\phi_{max}$  is the maximum barrier height change and  $I_{og(max)}$  is the corresponding current measured at a fixed temperature.

Substituting Eqs. (5) and (6) into Eq. (4), we get

$$1/(\ln(I_o/I_{og})) = 1/(\ln(I_o/I_{og(max)})) + [1/(I_o \ln(I_{og(max)}/I_o))](d_1/c_1)P_{H_2}^{1/2}. \quad (7)$$

Thus Eq. (7) describes a linear plot of  $1/\ln(I_o/I_{og})$  versus  $(1/P_{H_2})^{1/2}$ . Figure 9 shows that the plots of  $1/\ln(I_o/I_{og})$  versus  $(1/P_{H_2})^{1/2}$  for the Schottky diode is indeed linear. Thus, the experimental data obtained in this work from I-V measurements confirms the hydrogen reaction kinetics in the Pd-diamond based Schottky diodes is consistent with that in the silicon based Pd-MOS system<sup>1</sup>.

The activation energy  $E_a$  for  $H_2$  detection can be obtained by investigating the device initial transient response rate,  $\Delta I/\Delta t$ , upon exposing the device to a fixed  $H_2$  pressure with temperature ranging from 27°C to 85°C. According to the Lennard-Jones model, the initial rate of the adsorption process is given by  $\Delta\theta/\Delta t = k_{ads} \exp(-E_a/kT) = (1/\ln(I_{og(max)}/I_o))(1/I_{og})(\Delta I_{og}/\Delta t)$ . (8) Thus, the adsorption activation energy of hydrogen can be determined from the slope of  $\ln[(1/I_{og})(\Delta I_{og}/\Delta t)]$  versus  $1/T$  plot. The adsorption activation energy is 2.95 kcal/mole in 0.09 torr  $H_2$ . The low hydrogen adsorption activation energy of the device explains the observed high sensitivity and fast response to the hydrogen gas at low temperatures utilizing the Pd-diamond based structure.

#### IV. Conclusions

The utilization of PECVD diamond technology for gas sensing application is achieved. Hydrogen detection performance of the device at low, medium, and high temperature ranges (27°C, 85°C, 200°C) have been demonstrated and analyzed. The hydrogen sensitivity is high, repeatable, and reproducible. This study has shown that the barrier height of the Pd-diamond Schottky diode increases upon hydrogen adsorption. This effect leads to the change of the I-V characteristics from near ohmic to rectifying behavior. Hydrogen reaction kinetics have been analyzed. This polycrystalline diamond based hydrogen sensing technology should have many applications due to its reproducibility, sensitivity, and performance over a wide temperature range. The findings open the door for the development of diamond based high temperature gas sensor which could be used for detection of combustible gas and *in situ* emission control.

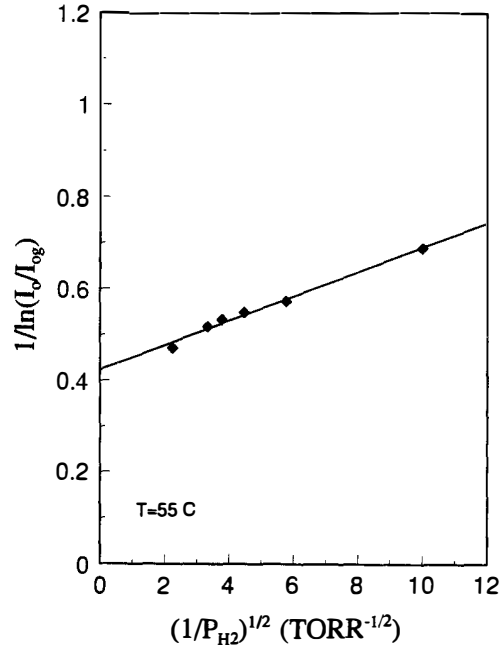


Fig. 9. Hydrogen Reaction Kinetic Analysis under Steady State Condition for Pd/ i-Diamond/ p-Diamond Hydrogen Sensor: Plot of  $1/\ln(I_o/I_{og})$  versus  $(1/P_{H_2})^{1/2}$ .

#### Reference

- [1] I. Lundstrom, S. Shivaraman and C. Svensson, *J. Appl. Phys.*, vol. 46 (1975) 3876-3881.
- [2] T. Poteat and B. Lalevic, *IEEE Trans. Electron Devices*, vol. 29 (1982) 123-129.
- [3] A. D'Amico, G. Fortunato, G. Petrocco and C. Caluzza, *Sensors and Actuators*, 4 (1983) 349-356.
- [4] P. F. Ruths, S. Ashog, S. J. Fonash and J. M. Ruths, *IEEE Trans. Electron Devices*, vol. 28 (1981) 1003-1009.
- [5] B. Karamati and N.J. Zemel, *J. Appl. Phys.*, 53 (1982) 1091.
- [6] R. C. Hughes, W. K. Schubert, T. E. Zipperian, J. L. Rodriguer and T. A. Plut, *J. Appl. Phys.*, 62, (1987) 1074.
- [7] I. Lundstrom, A. Spetz, F. Winqvist, U. Ackelid and H. Sundgren, *Sensors and Actuators B*, 1 (1990) 15-20.
- [8] K. Dobos and G. Zimmer, *IEEE trans. Electron Devices*, vol. 32 (1985) 1165-1169.
- [9] W. P. Kang, J. F. Xu, B. Lalevic and T. L. Poteat, *IEEE Electron Device Lett.*, vol. 8 (1987) 211-213.
- [10] W. P. Kang and C. K. Kim, *J. Electrochem. Soc.*, 140 (1993) L125-L127.
- [11] J. L. Davidson, Invited paper, *International Symposium on Diamond Science and Technology (Electrochemical Society Meeting)*, Hawaii, May (1993).
- [12] H. Katsuta and R. B. Mcllellan, *J. Phys. Chem. Solids*, 40, (1979) 697
- [13] S. M. Sze, *Physics of Semiconductor Devices* (Weley-Interscience, New York, 1981).

# Fabrication and Properties of a Si-based High Sensitivity Microcalorimetric Gas Sensor.

M. Zanini, J.H. Visser, L. Rimai, R.E. Soltis  
A. Kovalchuk, D.W. Hoffman, E.M. Logothetis  
U. Bonne<sup>†</sup>, L. Brewer<sup>\*</sup>, O.W. Bynum<sup>\*</sup>, M.A. Richard<sup>\*</sup>  
Ford Research Laboratory MD3028, P.O. Box 2053, Dearborn, MI 48121-2053  
<sup>†</sup>Honeywell Technology Center, Bloomington, MN 55420  
<sup>\*</sup>Advanced Sensor Devices, Mountain View, CA 94043

## Abstract

This paper discusses the design, fabrication, and testing in a laboratory flow-bench of a Si-based differential microcalorimeter to detect combustible gases at low concentrations. Design parameters most affecting the device sensitivity are reviewed.

## Introduction

Calorimetric sensors for combustible gases, such as methane (CH<sub>4</sub>) and carbon monoxide (CO), are commercially available in various forms [1,2]. A Pellistor, for example, consists of a small ceramic body impregnated with a noble-metal catalyst and a platinum resistor thermometer imbedded in it. This type of catalytic sensor measures the heat generated during combustion of the reactant with oxygen in the atmosphere by measuring the temperature rise induced on the ceramic element. Under appropriate conditions [1], the magnitude of the temperature rise is related to the combustible concentration. To compensate for environmental temperature fluctuations, differential structures are most commonly employed so that the reactant concentration is proportional to the temperature difference between a catalytically active element and another inactive element of (nearly) identical thermal characteristics.

Although successfully employed for years, catalytic-bead calorimeters have typical response times of several seconds because of their thermal mass and type of encapsulation, require hundreds of mW to operate, and the two elements have to be matched by sorting [1]. These devices are mainly used to detect thousands of ppm of combustible gases, such as CH<sub>4</sub>, although sensors with higher sensitivity but longer response time have also been reported [2].

Silicon micromachining offers the opportunity of fabricating well-matched devices with lower power consumption at potentially lower manufacturing costs. A micromachined device can also have a faster response time because the sensing element has a smaller thermal mass. On the other hand, the capability of micromachined devices to measure very low concentrations of combustible gases has not yet been established [3,4]. Devices capable of measuring 100 ppm of HC or lower are desirable for pollution monitoring applications.

This paper describes the design, fabrication, and evaluation in a laboratory flow bench of a Si-based microcalorimeter for the detection of combustible gases in the concentration range 0 to 4000 ppm. The device evaluation was

carried out under steady state conditions by externally heating the gas stream to better characterize the device behavior under well controlled conditions.

## Design and Fabrication

The average temperature rise in a microcalorimeter is dictated by the balance of heat produced by the chemical reaction and the heat lost to the environment. In order to maximize the detection limit of the sensor, effects such as the reactant mass transfer, the reaction kinetics at the catalyst, the heat loss by conduction/convection to the ambient gas and by conduction to the substrate, thermal fluctuations in the environment, and the electrical characteristics of the thermometer must all be taken into account.

The key elements of a Si-based microcalorimeter are the catalyst, the temperature sensing element, the heater, and the supporting structure for all of the previous elements. The structure consists of a silicon frame with either a membrane or a more complex plate/teeter element which is obtained by

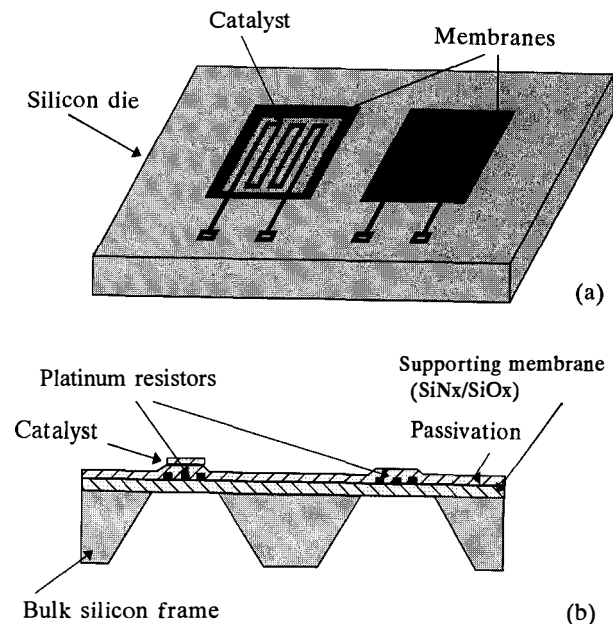


**Fig. 1.** (a) Perspective view and (b) schematic cross section of the microcalorimeter design used in the experiments reported in this paper.

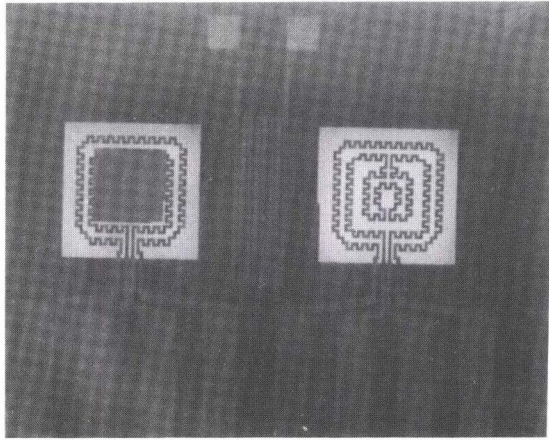


**Fig. 2** The photograph shows another type of microcalorimeter with separate Pt resistors for the heater and the thermometer. A Pd film catalyst covers part of the membrane on the left.

etching the underlying bulk silicon. The membrane should have a small thermal mass for fast response time, but must be mechanically robust to support the thermometer and the catalyst and survive temperature cycling, pressure shocks, water mist and small particles impingement. It should also be configured in such a way as to minimize the heat loss to the silicon frame and to the ambient gas for increased sensitivity. The catalyst should have a large specific surface area for the device to operate in mass-transport limited regime. In this case, some catalyst aging can be tolerated without causing the sensor output to change. Good thermal contact between the catalyst and the underlying temperature sensing element is also important for increased sensitivity. The catalytic layer should not substantially change the thermal characteristics of the membrane otherwise the sensor temperature compensation may be compromised. For greater sensitivity, the thermometer should mainly sense the central region of the substrate where the temperature rise due to the reaction is the greatest, without substantially contributing to conductive heat loss. A thin-film resistor with stable resistance and temperature coefficient of resistance (TCR) is desirable as the temperature sensing element. The film resistor is patterned as a winding element to increase its resistance (i.e., the output signal) and distribute the stress induced by the thermal mismatch with the substrate.

The microcalorimetric devices studied in this work utilize thin dielectric membranes. Similar structures have been recently reported by other authors [3,4]. However, the membranes of devices that we have investigated are much larger, ranging from 1 to 4 mm<sup>2</sup> to facilitate various deposition techniques for a variety of catalysts. The larger size is achieved by using low residual-stress dielectric films. Our simplest design, shown in Figs. 1a and 1b, uses a 1.2x1.2 mm<sup>2</sup> membrane. The die includes two identical membranes separated by 1 mm on the silicon frame to minimize thermal cross-talk. The membranes are kept relatively thick (up to 1 μm total thickness) for robustness, in order to support thick catalytic layers (up to a few μm) and to withstand stress induced by mismatch in thermal expansion coefficients. The temperature sensor is a Pt-film in a serpentine pattern that covers approximately 50% of the

membrane area. Another design shown in Fig. 2 uses double element (heater/thermometer combination) with a wave-like pattern in order to distribute thermal stresses. A thermopile-based device, using Pt and Pt/Chromel, was also fabricated to evaluate the advantages of this alternate temperature sensing method. This paper, however, reports only results obtained on devices as depicted in Fig. 1a.

As schematically shown in the device cross-section of Fig. 1b, the supporting membrane is deposited first on a silicon wafer, 100 mm in diameter, 400 μm thick. We have used either a 0.6 μm thick layer of low-stress LPCVD silicon nitride, or a composite of PECVD silicon oxide/nitride layers (about 0.5 μm and 0.1 μm, respectively) deposited over 0.1 μm of LPCVD nitride. After annealing at 600 °C, the latter composite layer, has a small residual stress (tensile) of about  $6 \times 10^8$  dynes/cm<sup>2</sup>, the compressive state of the oxide being compensated by the tensile nitride. A Pt film, 100 nm thick, is then sputter deposited in argon after an ion-milling step, which removes approximately 20 nm of the top silicon nitride film, to improve the adhesion of Pt to the substrate. Alternatively, a film of Ti/Pt, consisting of a 10 nm Ti layer and a 100 nm Pt layer, is prepared by e-beam deposition. The film resistors, acting as temperature sensors and/or heaters, are delineated by lithography and wet etching. After annealing the Pt resistors at 500 °C in nitrogen to stabilize their resistance and temperature coefficient of resistance (TCR), the wafers are coated with 0.2-0.3 μm of PECVD silicon nitride for passivation and annealed at 500 °C. The passivation is then removed on the contact pads with plasma etching. While defining the opening for the contact pads, an etch-mask pattern is also defined on the back side of the wafer using a double-sided aligner. A 30% aqueous solution of KOH at 80 °C is used to completely etch the silicon underneath the membranes. The membranes have sufficient mechanical strength to allow the wafer to be diced with a diamond saw. For ease of handling, a die size of 7x7 mm<sup>2</sup> is used, although only a 3.5x3.5 mm<sup>2</sup> area is needed for the device with the smallest membranes. For maximum flexibility, the catalyst is deposited after dicing on single devices, either by sputtering through a shadow mask (mainly Pt and Pd) or using solutions/slurries impregnated with the appropriate catalytic material.

### Microcalorimeter Thermal Sensitivity

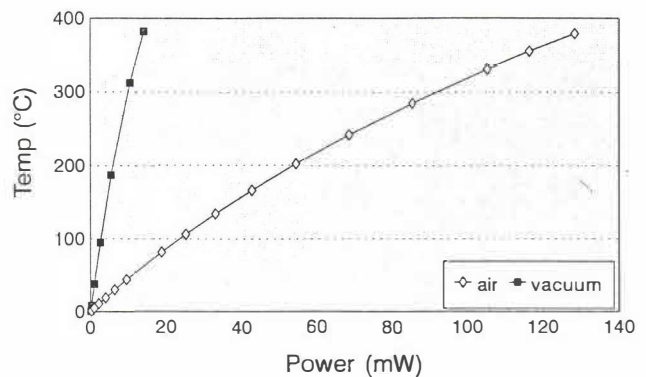


**Fig. 3.** Thermal sensitivity of the device measured in stagnant air and in vacuum.

## Catalytic Differential Microcalorimeter Sensitivity

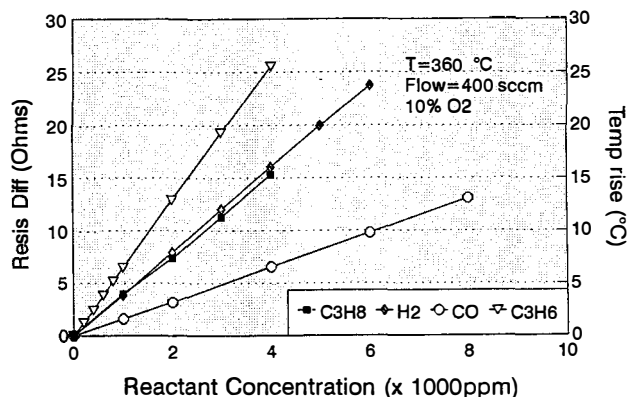


**Fig. 4.** The resistance difference between the active and the reference temperature sensing elements of the microcalorimeter (left vertical axis) is plotted as a function of propylene, propane, hydrogen, and carbon monoxide concentration by volume. The right axis shows the corresponding average temperature rise produced by the reaction on the membrane.

### Characterization

The devices were characterized both for their thermal and chemical response. The thermal sensitivity of the device was determined from the temperature rise detected by the Pt thermometer when 1mW electrical power was dissipated through it. The chemical sensitivity for a given combustible gas is defined as the average temperature difference between the two membranes when the device is exposed to 1000 ppm of reactant at a given temperature. In both cases, the temperature change was determined from the change in resistance of the Pt thermometer and its previously measured TCR. Since the temperature rise generated on the catalyst at the gas concentrations of interest was less than 30°C, a linear relation between resistance  $R$  (ohms) and temperature  $T$  (degrees Celsius) was assumed as given by

$$R(T)=R(0)[1+\alpha T]$$

Typical values for  $\alpha$  (TCR), as measured in a furnace under steady-state conditions between room temperature and 400°C, are 2500 ppm/°C for the Ti/Pt resistors and 3000 ppm/°C for the Pt resistors. Fig. 3 shows the temperature rise observed on the device as a function of power input, both in air, under stagnant conditions, and in vacuum. The thermal sensitivity in air is 5°C/mW and 38°C/mW in vacuum, demonstrating that the major heat loss mechanism for these micromachined "hot plates" is conduction to the ambient gas.

The device response to different gases was measured in a steady-state flow reactor in which the gas stream was kept at constant temperature by an external heater. The tubular flow chamber was made of quartz and the sample was positioned in the center by an alumina rod axially inserted in the tube opposite to the end where the gas stream entered the flow chamber. The silicon die was cemented to an alumina plate and

wire-bonded to screen-printed interconnects on the substrate. The devices were usually mounted several millimeters away from the leading edge of the substrate. The gas stream was prepared by mixing nitrogen and oxygen with one or more reactants using mass-flow-controllers. The flow rates were varied between 100 and 1000 sccm. The cross section of the reactor was approximately 10 cm<sup>2</sup>, and the average flow velocity in the quartz chamber could be changed from about 0.2 to 2.0 cm/s. The volume of the chamber was approximately 2000 cm<sup>3</sup>.

Hydrogen (H<sub>2</sub>), carbon monoxide (CO), propane (C<sub>3</sub>H<sub>8</sub>), and propylene (C<sub>3</sub>H<sub>6</sub>) were used for the characterization. Typical reactant concentrations were in the range 0 to 4000 ppm. The tests were run with excess oxygen, either 2% or 10% by volume. The flow stand was controlled by computer which was also used for recording the device output as a function of time. In a typical run, the gas concentration was changed stepwise every 5 minutes, while the flow and temperature of the gas stream were kept constant. In other runs, the reactant concentration was kept constant and the flow rate was changed.

The sensor output was measured in two different modes. In one case, a constant current of 1mA was passed through the two resistors connected in series and the voltage drop across each one was recorded and converted to a resistance difference by the computer. In the other case, the active and the reference elements were connected in a Wheatstone bridge configuration to two external resistors, approximately equal in value to the reference resistor at the temperature of the measurement. The voltage difference across the reference and active resistor and the bridge offset voltage were recorded and converted by the computer to resistance values. The sensor output was sampled with a 180 ms integration time every 20 s, or faster, with the average of the last 10 points used to generate the response vs. concentration curves, as shown in Fig. 4. The standard deviation of the same 10 data points was taken as a measure of the signal variability. The gas concentration in the large-volume flow chamber could not be changed fast enough at the flow rates allowed by the equipment to measure the true chemical response time of the device. Characterization at higher flow rates is under way.

### Results and Discussion

Fig. 4 shows typical results on the sensitivity of a device which uses a small-mass agglomerate of fine powders as a catalyst, the same material used in a macroscopic commercial device [2]. The catalyst covered about 80% of the area defined by the thermometer. Fig. 4 plots the device output, measured as a resistance difference, as a function of the concentration for four different gases. The average temperature rise is shown on the right axis. The data were collected at a gas temperature of 360 °C. The device sensitivity to C<sub>3</sub>H<sub>6</sub> is 6.2 °C/1000 ppm, while the relative sensitivities to C<sub>3</sub>H<sub>8</sub>, C<sub>3</sub>H<sub>8</sub>, H<sub>2</sub>, and CO shown in Fig. 4 are 3.9 : 2.3 : 2.4 and 1. For diffusion-limited operation, it is expected that the device sensitivities to different gases scale as the product of the enthalpy of combustion and the diffusion coefficient of the reactants. The respective enthalpies of combustion for these gases are 458, 486, 57, and 67 Kcal/mole, while the binary diffusion coefficient at 350 °C are 0.56, 0.54, 0.75, and 2.7 cm<sup>2</sup>/s, respectively. The products of

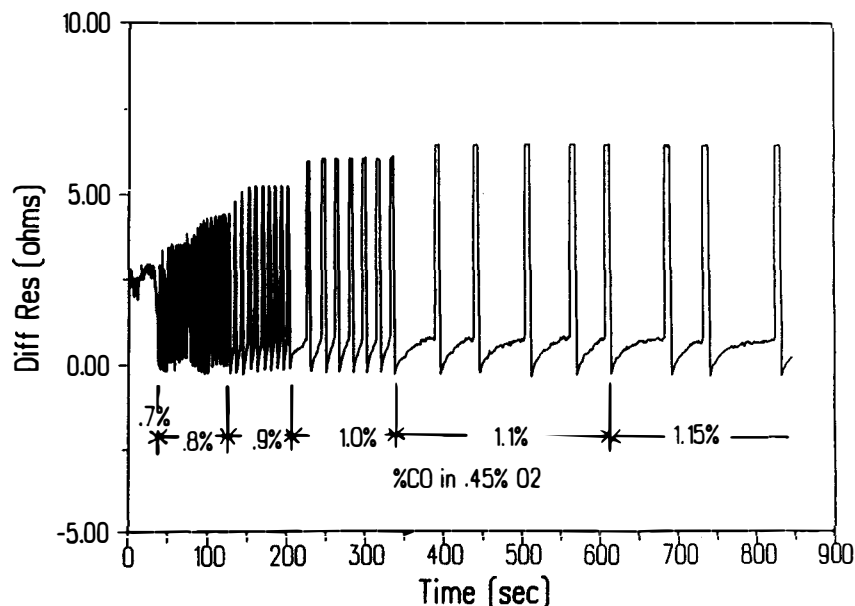


**Fig. 5.** Oscillatory reactions observed for the oxidation of carbon monoxide on the surface of a microcalorimeter using a Pd film catalyst.

the diffusion coefficient and enthalpy for the different gases scale as 5.1 : 5.2 : 3.1 : 1. These values are close to the measured relative sensitivities but not in the right order. The discrepancies may signify that the device response depends on the reaction rate at the catalyst surface, at least for some of the gases. However, the device output is nearly temperature independent above certain values (for  $H_2$  and  $C_3H_6$ , about 150 and 300 °C, respectively), which supports the model that the device is mass-transport limited above certain temperatures. Further studies are being carried out to clarify these discrepancies.

The detection limit for this device is defined here as the standard deviation of ten successive measurements carried out with short integration time (180 ms). For propylene, a maximum standard deviation value of 53 mΩ was measured, corresponding to a detection limit of 8 ppm. The standard deviation of the sensor output measured in a bridge configuration was found to be about a factor of five smaller.

Similar results were obtained for devices having a 400 nm Pd film as the catalyst, covering an area slightly larger than that occupied by the thermometer. The output signal, normalized to a temperature rise, was approximately 30% less than that found for an equivalent device with the commercial catalyst. In addition, the response to propane was very small and saturated quickly by increasing the reactant concentration.

A thermal response time of 20 ms was measured for the devices used in the measurements described in this paper. In another flow stand capable of higher flow rates, the chemical response time was found to be of the order of 1 s.

Oscillatory reactions for CO and  $C_3H_6$  were observed for the device using a Pd film catalyst at 300 °C. Fig 5 shows the device output changing from low to high in less than 1s. Notice that the period of the oscillations is affected by the reactant concentration, as expected for chemical oscillatory phenomena [5].

Some devices were also evaluated in the self-heated mode by passing current through the thermometer. The results of these measurements were similar to the data reported above. Almost no convective cooling was detected for flow velocities comparable to those used in the previous experiments.

## CONCLUSIONS

The present results show that the detection limit of a Si-based differential microcalorimeter can be, under laboratory conditions, of the order of 2 ppm of propylene and that response times of the order of 1 s can be achieved. The device sensitivity to different gases depends on the catalyst used. The device output is relatively insensitive to temperature and flow, consistent with mass-transport limited behavior. This is the desirable operating mode for a calorimetric device to minimize changes induced by catalyst aging. However, we have found some discrepancies between the measured values for the relative sensitivities to various gases and the values calculated for a simple diffusion model.

## REFERENCES

- [1] E. Jones, "The Pellistor Catalytic Gas Sensor", in Solid State Gas Sensors, P.T. Moseley and B.C. Tofield eds., A. Higler (Bristol and Philadelphia) 1987.
- [2] R. Dalla Betta and W. O. Bynum, "A New Combustion Control Sensor", Sensors, April 1989.
- [3] M. Gall, "The Si-Planar-Pellistor: a Low-power Pellistor Sensor in Si Thin-film Technology", Sensors and Actuators **B4**, 553-538 (1991).
- [4] P. Krebs and A. Grisel, "A Low Power Integrated Catalytic Gas Sensor", Sensors and Actuators **B12**, 155-158 (1993).
- [5] F. Schuth, B.E. Henry, and L.D. Schmidt, "Oscillatory Reactions in Heterogeneous Catalysis", Advances in Catalysis **39**, 51 (1993)

# NEW MATERIALS AND MULTIDIMENSIONAL CLUSTER ANALYSIS FOR SAW CHEMICAL SENSOR ARRAYS

Antonio J. Ricco, Gordon C. Osbourn, and John W. Bartholomew  
Microsensor R&D and Vision Science Depts., Sandia National Laboratories  
Albuquerque, New Mexico, USA 87185-0351

Richard M. Crooks and Chuanjing Xu  
Department of Chemistry, Texas A&M University  
College Station, Texas, USA 77843-3255

Ronald E. Allred  
Adherent Technologies, Inc.  
Albuquerque, New Mexico, USA 87123

## ABSTRACT

We use six-element arrays of 97-MHz ST-quartz surface acoustic wave (SAW) devices to detect changes in thin-film mass and mechanical properties resulting from sorption of analytes by films representing two new classes of chemical sensor interface: self-assembled monolayers (SAMs) and plasma-grafted films (PGFs). While these materials do *not* display exceptional chemical selectivity, various combinations of the 7 different SAMs and 8 PGFs examined do produce distinct response patterns for each of 13 analytes. The analytes include aliphatic, aromatic, and chlorinated hydrocarbons; alcohols; ketones; organophosphonates; and water. Evaluation of the SAW array data using multidimensional cluster analysis techniques (1) shows that each chemical species can be correctly identified 100% of the time over the 9%-to 49%-of-saturation range using data from many combinations of four or more films.

## INTRODUCTION

Chemical sensor arrays can obviate the difficult and costly process of developing a new thin film with high chemical specificity for each prospective analyte. Effective array technology hinges on two active research areas: new thin-film materials, and advanced mathematical techniques to identify the response patterns. In this paper, we describe the fabrication and application of two classes of thin-film materials, SAMs and PGFs, that we are evaluating for chemical sensing applications. Response data are reported for SAW devices coated with these materials during exposure over a range of concentrations to organic analytes representing several chemical classes.

For chemical sensor array data to be utilized efficiently, and also to guide the development and improvement of chemically sensitive films used with such arrays, requires effective pattern-recognition (PR) techniques. One promising technique for the analysis of chemical sensor array data has recently been adapted from multivariate cluster analysis software that mimics the way in which human beings group sets of objects together as a consequence of their spatial relationships to one another. This

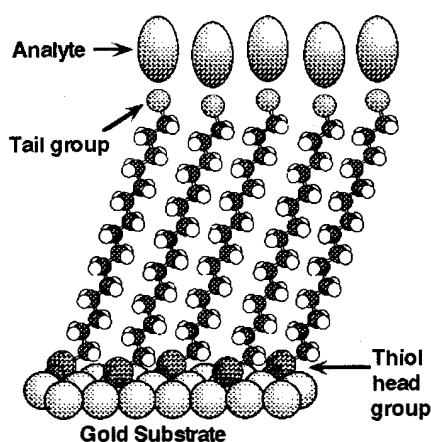


Figure 1. Schematic of interaction between self-assembled monolayer and analyte.

PR technique, developed by Sandia National Laboratories' Vision Science Dept., is described in detail in another paper in this Digest (1); only general results and trends obtained using the technique are reported here.

Self-assembled monolayers are ordered, molecular thin films (Figure 1) that can be prepared with a range of terminal groups to confer chemical preference for particular classes of analytes. The SAMs we have studied all include a thiol (-SH) head group separated by a seven- to 16-carbon chain from the terminal group. They are prepared on a gold film located between the launching and receiving sets of interdigital transducers (IDTs) on a SAW delay line surface. The two interactions responsible for the spontaneous assembly of these ordered films are (i) chemisorption of the thiol head group on the Au surface, and (ii) van der Waals forces between the long alkyl chains, maximized when the chains line up in the same relative orientation. As reported previously (2), combination of these materials with SAW devices allows monitoring of the kinetics of the monolayer assembly process, characterization of single-monolayer chemical reactions, and the construction of sensitive chemical detectors. Our current study includes SAMs with several terminal groups: methyl (CH<sub>3</sub>); carboxylic acid (COOH); carboxylate-coordinated metal ions ((COO)<sup>-</sup><sub>2</sub>M<sup>2+</sup>, M = Fe, Ni, and Cu); cyano (CN); and amine (NH<sub>2</sub>).

Plasma-grafted films are a little-studied class of polymeric materials with the potential to incorporate a wide range of functional groups in an open, permeable matrix (3). These films are formed (Figure 2) by plasma polymerization of a thin (one to several monolayers), highly

crosslinked base layer that is sufficiently hydrogen-rich for a stable population of free radicals to persist after the plasma is extinguished. Following base layer formation, grafting occurs in the absence of plasma upon introduction of a suitably unsaturated

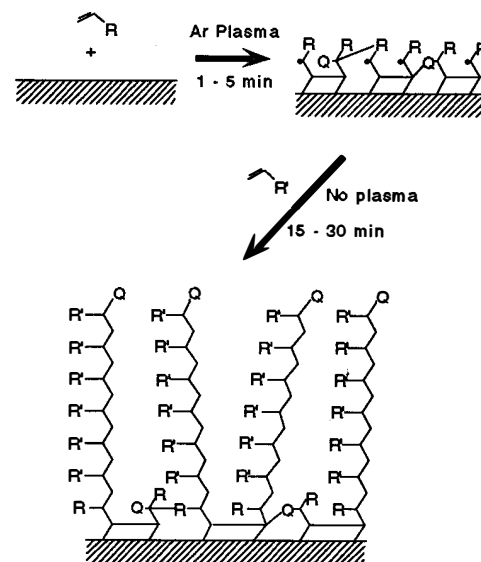


Figure 2. Formation of plasma-grafted film. Q is a free-radical quencher.

monomer—e.g. one containing a vinyl functionality—in the gas phase. Residual free radicals on the base layer initiate a chain polymerization process; with appropriate monomers, polymerization is mainly straight-chain in nature, yielding the kelp-forest-like morphology shown in Figure 2. Grafting ceases when the gaseous monomer is removed and/or the radicals are quenched by O<sub>2</sub> or by recombination with one another. We have examined films derived from acrylic acid grafted onto a plasma-polymerized base layer of poly(isobutylene) or of acrylic acid itself. We have also investigated plasma-polymerized films of eugenol and vinylphosphonic acid.

The organic analytes studied include representatives of environmental pollutants, common industrial solvents, and chemical weapons simulants and precursors. Grouped according to general chemical class, they are cyclohexane and *i*-octane (aliphatic hydrocarbon); benzene and toluene (aromatic hydrocarbon); carbon tetrachloride and trichloroethylene (chlorinated hydrocarbon); methanol, *n*-propanol, and pinacolyl alcohol (alcohol); acetone (ketone); DIMP and DMMP (the organophosphonates diisopropylmethylphosphonate and dimethylmethylphosphonate, respectively); and water.

## EXPERIMENTAL METHODS

SAW devices were designed and fabricated at Sandia National Laboratories (SNL) on ST-cut quartz substrates with propagation in the *X* direction. Devices have two interdigital transducers, each composed of fifty finger-pairs with  $\Lambda = 32 \mu\text{m}$  periodicity;  $v_0$  is 3.16 km/s, yielding a center frequency of 98 MHz. Transducers are defined photolithographically from 200 nm-thick Au on Cr; finger length is 50  $\Lambda$  and center-to-center separation between transducers is 230  $\Lambda$ . For SAM-coated devices, a 200 nm-thick layer of Au (with a Cr or Ti adhesion layer) was thermally or electron-beam deposited in the wave path using a shadow mask. Each SAW device was configured as the feedback element in an oscillator loop as described in detail elsewhere (4). This arrangement yields short-term frequency stability that allows the detection of mass changes of approximately 100 pg/cm<sup>2</sup> (4). The relationship between the frequency shift of a SAW delay-line oscillator circuit and the mass loading of the SAW is given by

$$\frac{\Delta f}{f_0} = \kappa \frac{\Delta v}{v_0} = -c_m f_0 \Delta(m/A), \quad [1]$$

in which  $f_0$  is the unperturbed oscillation frequency,  $v_0$  is the unperturbed SAW velocity,  $\kappa$  is the fraction of the center-to-center distance between transducers perturbed,  $c_m$  is the coefficient of mass sensitivity (1.3 cm<sup>2</sup>/g-MHz for ST-cut quartz), and  $\Delta(m/A)$  is the change in mass/area. In addition to monitoring the SAW velocity using a frequency counter, we monitor the amplitudes of the input and output signals to/from the SAW device using a vector voltmeter, enabling the insertion loss (and hence SAW attenuation) to be measured (4). Each of the six oscillator loops used with the SAW array was connected in sequence to the frequency counter and vector voltmeter using a RF multiplexer (HP 3488A/44478A) that otherwise terminates the connections from each oscillator loop with 50 ohm loads.

Sets of six coated SAW devices were secured in a custom-fabricated test fixture utilizing spring-loaded pin contacts to the IDT bonding pads. Impedance matching consists of a single series inductor for one comb of each IDT; the other comb is grounded. With this configuration, total insertion loss of about 12 dB is attainable with the Cr/Au IDT SAW delay lines.

A manifold within the test fixture delivers the test gas stream to all six devices in parallel; a gas-tight O-ring seal encircles each SAW device. Vapor streams were provided by a computer-con-

trolled gas-flow system, with the organic compound entrained by passing high-purity N<sub>2</sub> through a gas-washing bottle with a 50-mm diameter fritted disk; the vapor-saturated gas stream was diluted as required with additional N<sub>2</sub>. Total flow rates were 1 l/min; the gas, organic liquid, and the SAW device were all maintained at 23° C.

Prior to deposition of the Au film and monolayer self assembly, SAW devices were silanized using ClSi(CH<sub>3</sub>)<sub>3</sub> (Petrarch) to prevent interactions between polar compounds and the quartz substrate from complicating interpretation of the response. SAMs of mercaptoundecanoic acid (MUA, HS(CH<sub>2</sub>)<sub>10</sub>COOH; Aldrich) were produced by soaking Au-coated SAW devices in a dilute solution of the thiol in ethanol overnight. Amine and cyano-terminated monolayers were similarly prepared. Transition metals were coordinated to the MUA films by dipping for several minutes in a dilute ethanol solution of the perchlorate salt, then rinsing.

To form a plasma-polymerized acrylic acid base layer, a flask containing the monomer (Polysciences) was heated to 120 °C. A flow of 5 L/min of Ar entrained the compound, carrying it into a quartz plasma-deposition chamber, which was continuously pumped to maintain a pressure near 1 Torr (TC gauge). The 13.56-MHz plasma was maintained at a forward power of approximately 50 W. After plasma polymerization of the base layer (1 - 5 min), the RF generator was switched off and grafting of acrylic acid onto the base layer allowed to continue for 15 - 30 min at an indicated pressure of 1 Torr. Poly(isobutylene) base layers were produced using similar methods to the acrylic acid, except the monomer was obtained from a gas cylinder of isobutylene (Aldrich) at room temperature. Vinylphosphonic acid (Hoechst-Celane) and eugenol (Polysciences) plasma-polymerized films were prepared analogously to the acrylic acid base layer, with the monomers held at approximately 80 °C in both cases.

## RESULTS AND DISCUSSION

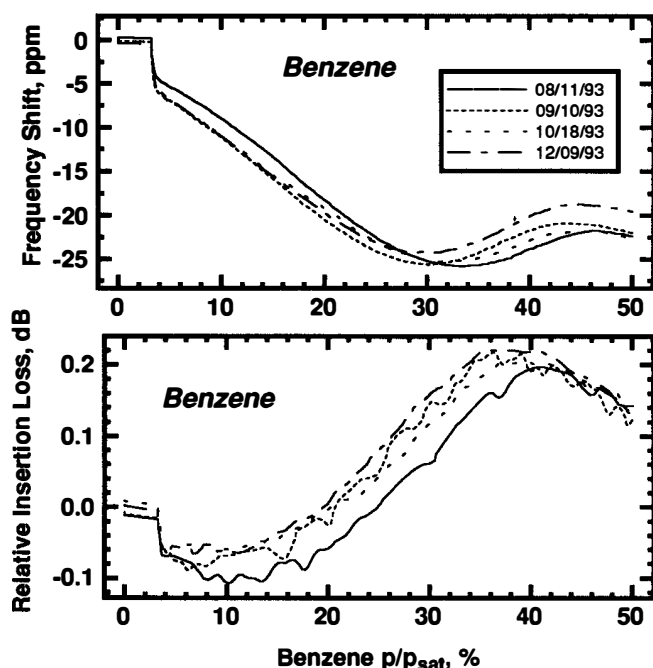
To obtain the maximum information from the coated SAW devices, both the velocity and the attenuation of the acoustic wave are continuously monitored (5). For each analyte, a four-hour adsorption/desorption isotherm was obtained, over the course of which the concentration of analyte slowly varied from 3% to 50% and back to 3% of its saturation vapor pressure,  $p_{\text{sat}}$ . For the isotherms shown below, note that data between 0% and 3% are not "real", because the flow system steps abruptly from 0 to 3%.

Figure 3 shows a set of four benzene adsorption isotherms obtained at approximately 30-day intervals using a single MUA-coated SAW device; frequency shift vs. partial saturation pressure is at the top, relative insertion loss vs.  $p/p_{\text{sat}}$  at the bottom. During the time periods between the isotherms of Figure 3, this coated device was exposed to the various other analytes in the test group, so the extent of reproducibility includes the effects of exposure to a range of chemicals. Variation of the isotherms from one measurement to the next is representative of the better films we have examined; many others behave nearly as well.

In Figure 3, the nonmonotonic nature of the frequency-shift isotherms and the peak in the relative-insertion-loss isotherms are both indicative of a non-mass-loading response, a result of either resonant energy transfer to the film or a relaxation process in the film. Such effects occur at particular concentrations of adsorbed analyte because mechanical film properties (sound velocity, relaxation times) are influenced by the quantity of adsorbate. Significantly, nonmonotonic isotherms such as those in Figure 3 do not pose any difficulty for our PR algorithms (1).

Figure 4 presents a series of isotherms representing four of the chemical classes we have studied: aromatic and chlorinated hydrocarbons, alcohols, and organophosphonates. For each compound,

a set of six isotherms is presented for frequency shift vs.  $p/p_{\text{sat}}$ , and another set of six for relative insertion loss. For clarity, only the adsorption branches are shown in each case. Each of the six curves represents a different chemically sensitive film; the legends and the caption describe the films. Note that all twelve of the curves for a given analyte are obtained simultaneously using our array system; tens of concentration points are recorded for each film/analyte combination.



**Figure 3.** Benzene adsorption isotherms for a MUA self-assembled monolayer. Frequency data are in the top panel, corresponding insertion loss data at the bottom. The four isotherms were obtained on the dates in the legend; exposure to many other analytes occurred during the intervening time periods.

Examination of the six sets of six curves in Figure 4 reveals very significant qualitative differences in the pattern of responses for the four analytes. Each concentration of each analyte yields its own set of 12 responses; it is left as an exercise for the reader to show that each such set of 12 data points is unique.

The set of six films represented in Figure 4 gives flawless identification of each of the 13 analytes over the  $p/p_{\text{sat}} = 9\% - 49\%$  concentration using the "leave-one-out" approach with our PR technique (1). In this method, the data for each concentration of an analyte are represented by a  $k$ -dimensional vector, where  $k$  is the number of different responses collected. In the example shown by Figure 4,  $k = 6$  because, at present, only the frequency-shift data for the six films are used. A cluster of all the (appropriately normalized (1)) data vectors but one is created for the analyte under consideration, and the full clusters are created for all other analytes. In the present example, 21 concentrations were used for each analyte (20 for the leave-one-out species). The concentration left out is then tested to see which cluster it groups with; for the example discussed here, the answer is invariably correct. Note that this sort of evaluation is rapid and straightforward with our PR technique, in contrast to some approaches—e.g., neural nets—in which complete "retraining" is required to evaluate each and every data point.

The relative insertion loss response provides useful information, both regarding the nature of the coating/analyte interaction, and for the purpose of correctly identifying the analyte. Note in

particular the prominent peaks in the attenuation curves in three of the sets of isotherms, and the corresponding sigmoidal deflections in the frequency-shift data. As discussed above, this indicates a non-mass-loading response; it also serves as a signature for a particular analyte/film pair. Unfortunately, the higher noise level apparent in the relative insertion loss data makes use of this information more challenging. Nevertheless, we are working to include these data, which should allow use of a smaller number of films (array elements) to provide an equivalent level of certainty, thus reducing system cost, size, and complexity.

The six films represented in Figure 4 are equally divided among the two materials categories, SAMs and PGFs, a consequence of an evaluation using our PR system to find the best set(s) of films. This result supports our claim that chemical orthogonality of films is maximized when disparate film categories are included, and we therefore plan to broaden the film categories under examination to include metals, ceramics, coordination complexes, and others.

## CONCLUSIONS

Combination of a SAW array with the appropriate chemically sensitive films and pattern-recognition algorithms provides a powerful method to monitor many different species without the need to custom design and synthesize a large number of custom thin films. The ability to handle often non-linear-with-concentration data produced by coated SAW devices is a strength of our multidimensional PR technique. We are currently exploring application of this combination of technologies for: detecting lower analyte concentrations; quantifying analytes; and analyzing simple chemical mixtures.

Helpful technical discussions with, and collaboration on the design of the six-device array fixture by, Stephen J. Martin of SNL are gratefully acknowledged, as is the excellent technical assistance of Alan W. Staton, Mary-Anne Mitchell, and Mark Hill, all of SNL, and Brent Gordon of Adherent Technologies. This work was supported by the U.S. DOE under contract DE-AC04-94AL85000.

## REFERENCES

1. G. C. Osbourn, J. W. Bartholomew, G. C. Frye, and A. J. Ricco, "Clustering-Based Pattern Recognition Applied to Chemical Recognition Using SAW Array Signals", *Technical Digest of the 1994 Solid-State Sensor and Actuator Workshop*, Hilton Head Isl., SC, 6/13-16/94, Transducer Research Foundation, Cleveland (1994).
2. A. J. Ricco, L. J. Kepley, R. C. Thomas, L. Sun, and R. M. Crooks, "Self-Assembling Monolayers on SAW Devices for Selective Chemical Detection", *Technical Digest of the 1992 Solid-State Sensor and Actuator Workshop*, Hilton Head Island, SC, 6/21-25/92, IEEE, New York, pp. 114-117 (1992).
3. Y. L. Hsieh and M. Wu, "Residual Reactivity for Surface Grafting of Acrylic Acid on Argon Glow-Discharged Poly(Ethylene Terephthalate) (PET) Films", *J. Appl. Polymer Sci.*, **43**, 2067 (1991).
4. A. J. Ricco and S. J. Martin, "Thin Metal Film Characterization & Chemical Sensors: Monitoring Electronic Conductivity, Mass Loading, and Mechanical Properties with SAW Devices", *Thin Solid Films*, **206**, 94 (1992).
5. S. J. Martin and A. J. Ricco, "Effective Utilization of Acoustic Wave Sensor Responses: Simultaneous Measurement of Velocity and Attenuation", *Proc. 1989 IEEE Ultrasonics Symp.*, 621 (1989).

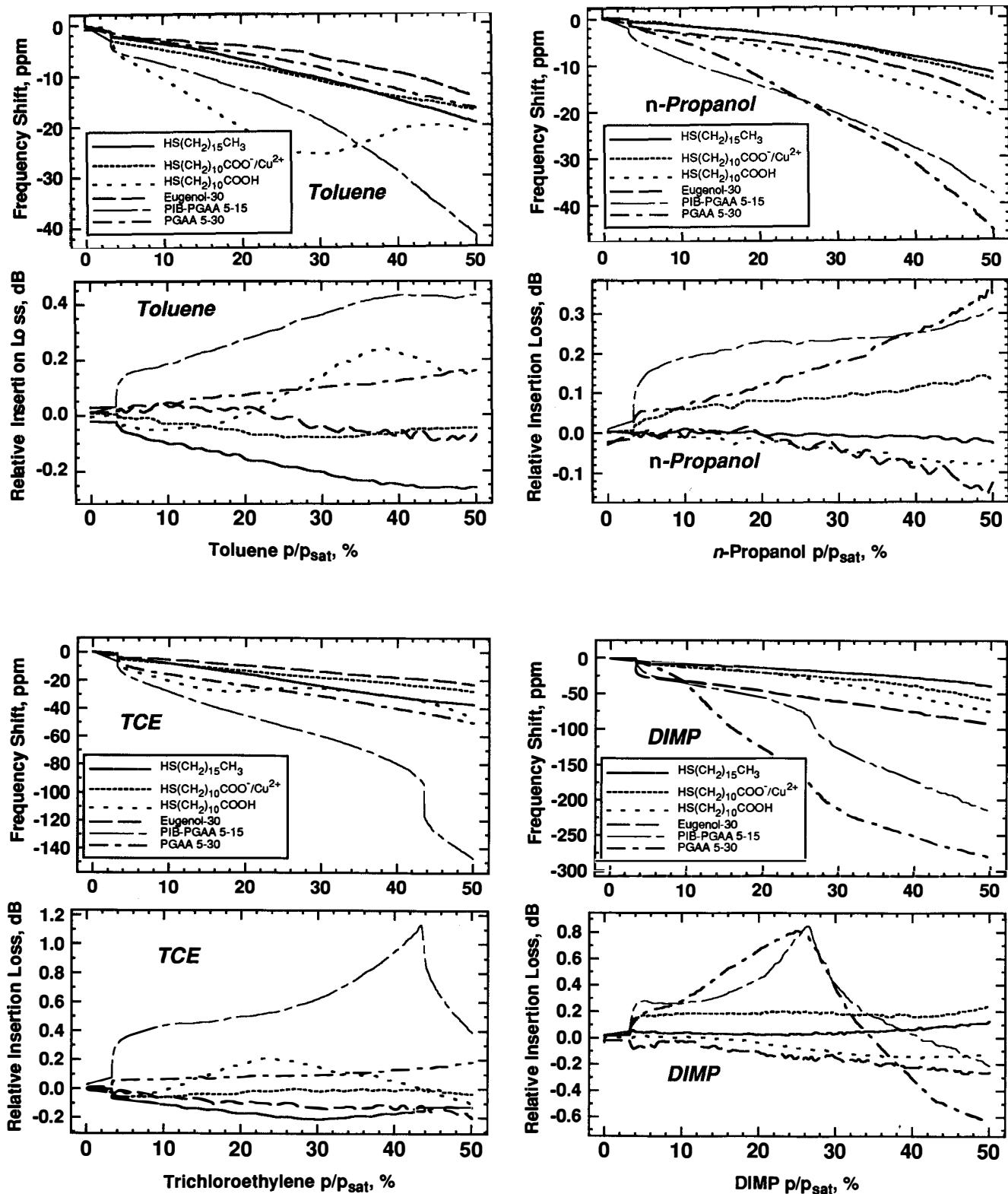


**Figure 4.** Six-SAW array adsorption isotherm sets for toluene (upper left), trichloroethylene (lower left), n-propanol (upper right), and DIMP (lower right). Frequency shift data are above relative insertion loss data for each analyte. This set of six films (identified in the legends) gives 100%-accurate identification of these and 10 other analytes in conjunction with our pattern-recognition technique. The first three films in the legends are SAMs; eugenol-30 is a 30-min plasma-polymerized film of 2-methoxy-4-(2-propenyl)phenol; PIB-PGAA is a 5-min plasma-polymerized base layer of poly(isobutylene) + a 15-min graft of acrylic acid; and PGAA 5-30 is a 5-min base layer of plasma-polymerized acrylic acid + a 30-min graft of acrylic acid.

# Quantitative Models for the Measurement of Residual Stress, Poisson Ratio and Young's Modulus Using Electrostatic Pull-in of Beams and Diaphragms

Peter M. Osterberg, Raj K. Gupta, John R. Gilbert and Stephen D. Senturia  
Microsystems Technology Laboratories  
Massachusetts Institute of Technology, Cambridge MA 02139, USA

## ABSTRACT

This paper presents an analysis of the use of electrostatic pull-in of suspended microstructures for the measurement of material properties, and demonstrates the approach with experiments.

## INTRODUCTION

Access to accurate and reliable material property data for Young's modulus, Poisson ratio and residual stress is crucial to the design of MEMS [1]. The problem is that many properties, especially residual stress, can depend not only on the specific process step used for forming a material, but also on subsequent thermal processing [2]. Even single-crystal silicon can exhibit a doping-dependent stress and stress gradient which can lead to modifications of structural stiffness and to warpage of suspended structures [3,4].

The goal of the work presented here is the design of standard "drop-in" mechanical test structures, analogous to transistor test structures used for extraction of device parameters, where the intent is to be able to measure material properties *in-situ*. There are three uses for such test structures: (1) determination of experimental engineering quantities of importance to design, such as beam stiffness, which depend on a combination of material properties and structural dimensions; (2) extraction of the primary material properties from those quantities for use in design and simulation; and (3) routine monitoring of repeatability of a complex processing sequence for MEMS devices.

If the mechanical drop-in pattern is to achieve general utility, it should be possible to perform the testing at the wafer level using ordinary wafer probe equipment and microscopes. One possible way to meet this criterion is to use electrostatic deflection and pull-in of microstructures, detected either electrically or optically. Najafi and Suzuki [5] have already proposed this approach and have presented results on various microelectronic materials. Their work, however, was based on simple analytical models of beam behavior and electrostatic applied loads. We are now revisiting this subject using more intensive 2-D and 3-D numerical modeling tools developed for the MIT MEMCAD system [6-8].

At MEMS 94, we reported a hierarchy of models for electrostatic pull-in [8]. In this work, we significantly extend those models, both by the development of closed-form expressions for pull-in voltage of cantilevers, fixed-fixed beams, and clamped circular diaphragms, and by the inclusion of a first-order correction for electrostatic fringing fields (following a suggestion of Cray [9]). The closed-form expressions permit a succinct discussion of the benefits and limitations of electrostatic pull-in as a method for material property extraction. The method is then illustrated using measurements on suspended fixed-fixed beams processed in wafer-bonded single-crystal-silicon [10], and on suspended fixed-fixed beams of aluminum-coated silicon nitride [11].

## MODELS OF ELECTROSTATIC PULL-IN

**Previously Reported Models.** As presented in [8], we use a hierarchy of models to explore the pull-in behavior of cantilevers, fixed-fixed beams, and clamped circular diaphragms insulated from and suspended above a ground plane by a gap  $g_0$ . These structures are illustrated in Figure 1. The simplest model of electrostatic actuation of these structures is a 1-D parallel-plate capacitor with one fixed plate and one plate suspended from an ideal linear spring as shown in Figure 2. If we neglect fringing fields, we can write the force balance for this system as

$$K(g_0 - g) = \frac{\epsilon_0 V^2 A}{2g^2} \quad (1)$$

where  $g$  is the gap between the structure and the ground plane,  $g_0$  is the initial gap,  $K$  is a lumped mechanical spring constant for the structure,  $V$  is the applied voltage,  $\epsilon_0$  is the permittivity, and  $A$  is the area of the capacitor plate. This system has a well-known pull-in instability, as illustrated in Figure 3, which plots the gap normalized to its initial value versus the applied voltage normalized to the pull-in voltage,  $V_{PI}$ . For voltages less than  $V_{PI}$ , the structure is stable. As  $V$  approaches  $V_{PI}$  and  $g$  approaches  $2g_0/3$ , the plate position becomes unstable, and collapses to the ground plane. The expression for pull-in voltage is

$$V_{PI} = \sqrt{\frac{8Kg_0^3}{27\epsilon_0 A}} \quad (2)$$

The importance of this 1-D model is that it provides a closed-form expression for the pull-in voltage in terms of parameters such as a "spring constant", "capacitor gap", and "capacitor area". Note that the spring constant  $K$ , which typically includes both structural dimensions and material properties, appears in a product with  $g_0^3$ . This means that a measurement of  $V_{PI}$  alone cannot separate the material properties from the geometric quantities, even if the area  $A$  is systematically changed. We will discuss this point in greater detail later.

As demonstrated in [8], when we attempt to determine  $K$  from the small-deflection beam or diaphragm differential equations by applying a uniform pressure load and finding the maximum deflection, we find that the pull-in voltage predicted by Eq. 2 is significantly in error. The primary reason is that the rigid-parallel plate capacitor is a bad model for a bending beam or diaphragm. Instead, we used the beam and diaphragm differential equations (in effect, a 2-D structural model) with a position dependent electrostatic load. The load was derived from the expression for the force on an incremental parallel-plate capacitor whose value varies inversely with the position-dependent gap,  $g$ . A similar force model has been previously used by Artz and Cathey [12] in conjunction with finite-element simulations. As an illustration, the

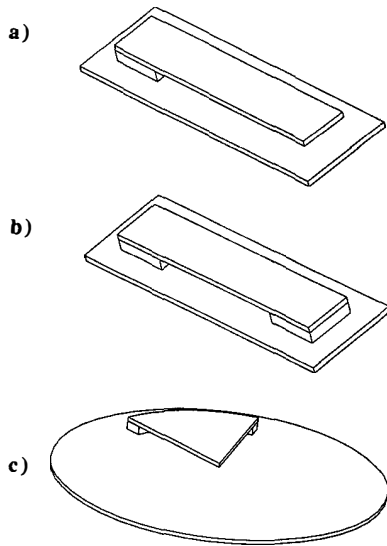


Figure 1. Test structures: (a) cantilever beam, (b) fixed-fixed beam, (c) clamped circular diaphragm (cut-away view).

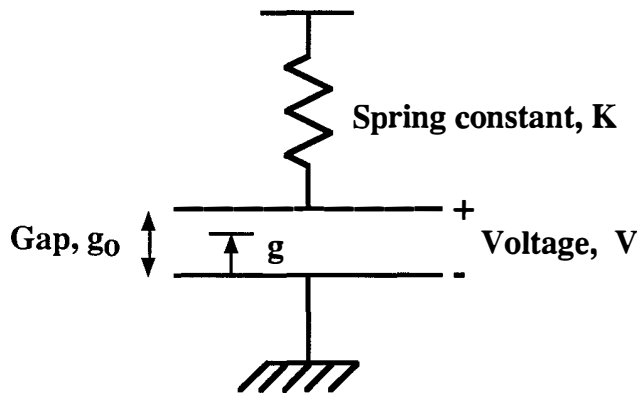


Figure 2. 1-D lumped parallel-plate capacitor model.

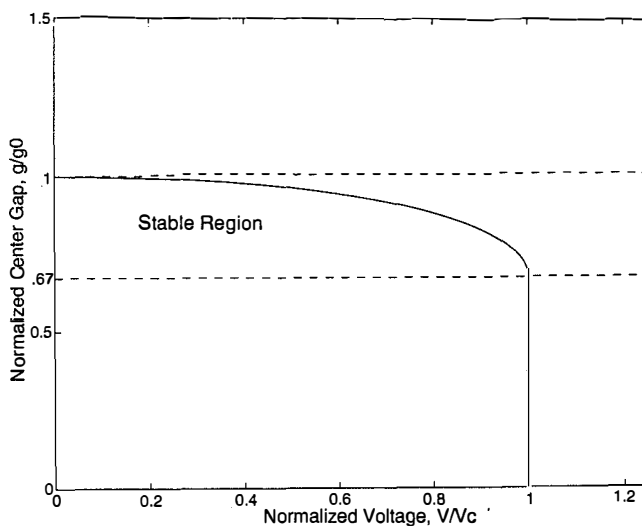


Figure 3. Normalized plot of the gap vs voltage for the 1-D lumped model. Stability requires a normalized gap,  $g/g_0$ , greater than  $2/3$ .

differential equation for a fixed-fixed beam under this assumption becomes

$$EI \frac{d^4 g}{dx^4} - T \frac{d^2 g}{dx^2} = -\frac{\epsilon_0 V^2}{2g^2} \left( 1 + 0.65 \frac{g}{w} \right) \quad (3)$$

where  $E$  is Young's modulus,  $I=(1/12)wt^3$ ,  $T=\sigma_0(1-\nu)wt$ ,  $w$  is beam width,  $t$  is beam thickness,  $\sigma_0$  is the biaxial residual stress presumed present before the beam shape was etched,  $\nu$  is the Poisson ratio, and the factor in parentheses on the right-hand side is a new fringing-field correction, explained below.

While it was acceptable in [8] to neglect fringing fields when studying clamped circular diaphragms, it is more important to examine fringing when analyzing the behavior of beams, since the fringing fields occur in a region which is changing shape due to deflection. The origin of the correction term in Eq. 3 is an analytic expression for the capacitance of a zero-thickness stripline over a ground plane, as obtained by Morgenthaler [13]. Morgenthaler's capacitance formula was then differentiated with respect to gap to give the fringing-field enhancement of the electrostatic force for a parallel plate capacitor. The result is the right-hand side of Eq. 3. This correction does not take into account the finite thickness of the beam, but preliminary studies on two-dimensional electrostatic geometries of beam structures show that a correction to account for thickness will not increase capacitance values more than a few percent for  $g/w < 0.1$ . Nevertheless, the effect of finite thickness may slightly modify the calculated pull-in voltages reported here for beams and cantilevers; study of these details is continuing.

Numerical finite-difference solution of Eq. 3 (and of the corresponding equations for cantilevers and clamped circular diaphragms) was performed using Newton's method implemented in MATLAB [14]. In [8] it was shown that the gap vs. voltage and the value of the pull-in voltage from the 2-D numerical model for a clamped circular diaphragm agreed well both with a full 3-D self-consistent electromechanical simulation and with experimental data on a suspended diaphragm consisting of a tensioned polymer membrane with a thin aluminum coating. We also expect the 2-D models with fringing correction to be reasonably accurate for cantilevers and beams over ground planes when the aspect ratio (gap relative to beam width) is small, and when the gap is small enough so that the pull-in instability is reached before the beam bending enters the large-deflection regime.

#### Closed-form models for mechanical property extraction.

In order to use the 2-D simulations for mechanical property extraction, we have captured the results of numerical analysis into closed-form expressions which make explicit the dependence of key model parameters on material properties and structural dimensions. In previous work, we have used this approach to establish a quantitative basis for the load-deflection method for extracting residual stress and biaxial modulus,  $E/(1-\nu)$ , of tensile suspended membranes [15,16]. The approach in the present work is to find the analytical form of the "effective spring constant" from a solution of the beam or diaphragm equation with a uniform distributed load, and replace the numerical constants in the solution by fitting parameters which, if successful, can capture the corrections needed to allow for the fact that when the structure deflects, the load is no longer uniform. The results of the 2-D numerical simulations are then fitted to the analytical expression, leading to a semi-numerical closed-form expression for pull-in voltage as a function of both material properties and structural dimensions.

**TABLE I.** Closed-form expressions for pull-in voltage of suspended structures defined in terms of the numerical constants in TABLE II and parameters in TABLE III. The index  $n$  equals 1 for cantilevers, 2 for fixed-fixed beams, and 3 for clamped circular diaphragms.  $L$  is either length (for cantilevers and beams) or radius (for diaphragms). In the stress-dominated limit,  $k_n L \gg 1$ , and in the bending dominated limit,  $k_n L \ll 1$ .

	General	Stress Dominated	Bending Dominated
$V_{PI}$	$\sqrt{\frac{\gamma_{1n} S_n}{\epsilon_0 L^2 D_n(\gamma_{2n}, k_n, L) \left[ 1 + \gamma_{3n} \frac{g_0}{w} \right]}}$	$\sqrt{\frac{\gamma_{1n} S_n}{\epsilon_0 L^2 \left[ 1 + \gamma_{3n} \frac{g_0}{w} \right]}}$	$\sqrt{\frac{4\gamma_{1n} B_n}{\epsilon_0 L^4 \gamma_{2n}^2 \left( 1 + \gamma_{3n} \frac{g_0}{w} \right)}}$

$$\text{where } D_n = 1 + \frac{2\{1 - \cosh(\gamma_{2n} k_n L/2)\}}{(\gamma_{2n} k_n L/2) \sinh(\gamma_{2n} k_n L/2)} \quad \text{and} \quad k_n = \sqrt{\frac{12S_n}{B_n}}$$

**TABLE II:** Numerical constants for the closed form expressions of TABLE I.

Numerical Constants	$n = 1$	$n = 2$	$n = 3$
$\gamma_{1n}$	0.28	2.79	1.55
$\gamma_{2n}$	N/A	0.97	1.65
$\gamma_{3n}$	0.42	0.42	0

Tables I-III contain the closed-form models. Table I shows the general form of the pull-in voltage, where the index  $n=1$  refers to cantilevers,  $n=2$  to fixed-fixed beams, and  $n=3$  to circular diaphragms. The analytical form depends on two parameters,  $S_n$  and  $B_n$ , which combine geometric factors with either stress or modulus, respectively (see Table III). The ratio,  $S_n/B_n$ , appears in the factor  $k_n$ , which is a measure of the relative importance of stress versus bending. The stress-dominated limit is  $k_n L \gg 1$  and the bending dominated limit is  $k_n L \ll 1$ . Asymptotic forms for these two limits are also shown in Table I.

For each structure type, several thousand self-consistent calculations of pull-in voltage versus were carried out using the 2-D model on MATLAB, systematically varying  $S_n$  and  $B_n$ . The results of these simulations for each structural type ("the virtual data") were then fit to the form in Table I using three parameters  $\gamma_{1n}$ ,  $\gamma_{2n}$ , and  $\gamma_{3n}$  (except that the fringing term is not used for circular diaphragms). The resulting values are shown in Table II. Figure 4 illustrates a typical comparison between the 2-D numerical simulations and the fit from the closed-form model. The typical agreement of  $V_{PI}$  is within 10 mV or better.

#### EXTRACTION OF MATERIAL PROPERTIES

**Strategy.** In a typical MEMS process, structural thicknesses and gap heights are fixed. Structural widths and lengths can be readily varied by mask design. A useful strategy, therefore, is to measure  $V_{PI}$  versus beam length (or diaphragm radius). In order to extract material properties, it is first necessary to fit the experimental data to the form of the expressions in Table I by determining numerical values for  $S_n$  and  $B_n$ . Then, using known values of thickness and initial gap, one can extract material properties.

**TABLE III:** Stress and Bending Parameters for the closed-form expressions of TABLE I.

	$n = 1$	$n = 2$	$n = 3$
$S_n$	0	$\sigma_o(1-\nu)tg_o^3$	$\sigma_o tg_o^3$
$B_n$	$Et^3 g_o^3$	$Et^3 g_o^3$	$\frac{Et^3 g_o^3}{(1-\nu^2)}$

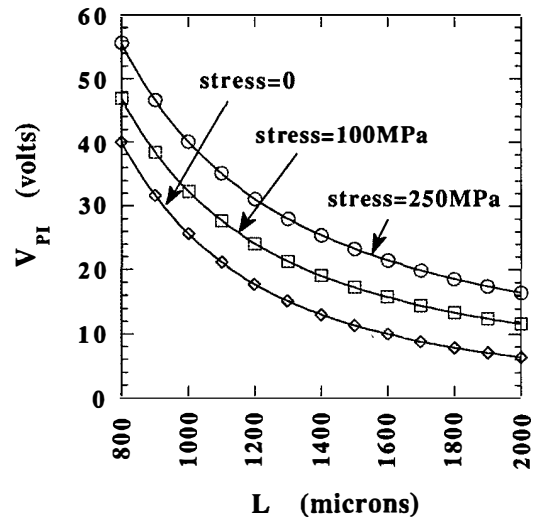


Figure 4. Comparison of closed-form model (solid line) to 2-D MATLAB simulated pull-in (points) for three fixed-fixed beams with varied stress ( $E=169$  GPa,  $\nu=0.3$ , width=50 $\mu\text{m}$ , thickness=14.4 $\mu\text{m}$  and  $g_0=1\mu\text{m}$  in each case). Agreement is typically within 10 mV.

If only cantilevers are used, then only  $B_1$  can be determined ( $S_1$  is always zero). The other two structures in general will yield values for both  $S_n$  and  $B_n$ , although for extreme values of  $k$ , one of these may be very noisy (see below). If  $S_2$  and  $S_3$  can be found, then their ratio yields  $(1-\nu)$  without any additional dependence on geometric factors. Similarly,  $B_2/B_3$  equals  $(1-\nu^2)$ . However, extraction of either  $E$  or  $\sigma_0$  requires independent determination of  $t$  and  $g_0$ . Further, since  $S_n$  and  $B_n$  depend on  $g_0^3$ , errors in  $g_0$  appear amplified by a factor of 3 in the extraction of  $\sigma_0$  from  $S_n$  or  $E$  from  $B_n$ . Errors in  $t$  appear similarly amplified in the extraction of  $E$  from  $B_n$ . We now examine how this works in practice.

**Experimental Methods.** We obtained from Hsu [10] a wafer containing silicon fixed-fixed beams fabricated in a dielectrically isolated wafer-bonding process. The beams are  $14.4 \pm 0.2 \mu\text{m}$  thick,  $50 \mu\text{m}$  wide and are suspended above the ground plane by an initial gap of  $1.015 \pm 0.01 \mu\text{m}$ . Beam lengths varied between  $900 \mu\text{m}$  and  $1500 \mu\text{m}$ , using drawn mask dimensions for length.

To measure pull-in, a slowly ramped voltage was applied between the beam and the substrate, and the current was recorded. Pull-in was indicated by the appearance of contact current. Figure 5 shows an example output from a typical pull-in experiment using this technique. Pull-in voltage could be determined in this fashion to within better than  $0.1 \text{ V}$ . A total of nine die, each containing five beams of different lengths, were tested.

**Experimental Results.** Figure 6 shows a plot of pull-in voltage versus beam length for a series of five beams from one die located near the center of the wafer. The solid curve is the fit to the closed-form model using the non-linear least-squares algorithm in Kaleidagraph [17]. The result indicated a very small value for  $S_2$  with a large relative error ( $S_2 = 2 \pm 1 \times 10^{-20} \text{ Pa}\cdot\text{m}^4$ ) and a relatively accurate value for  $B_2$  ( $5.4 \pm 0.1 \times 10^{-22} \text{ Pa}\cdot\text{m}^6$ ). The fact that  $S_2$  is not statistically well defined suggests that the behavior is bending dominated. Therefore, as a test, we assumed  $S_2=0$  and did an independent fit to the asymptotic form of the bending dominated expression in Table I. In that case only the factor  $B_2$  enters, and we obtained  $5.3 \pm 0.1 \times 10^{-22} \text{ Pa}\cdot\text{m}^6$ . The good agreement between the two fitting procedures indicates that numerical artifacts are not dominating the results, and that the stress in the silicon is small.

Extraction of Young's modulus and residual stress from this one die depends directly on the accuracy with which the geometric parameters are known. Using the stated experimental uncertainties on  $t$  and  $g_0$ , we calculate a range for Young's modulus:  $E=173 \pm 13 \text{ GPa}$  and an upper bound for residual stress:  $\sigma_0(1-\nu) < 100 \text{ KPa}$  (estimated from the tolerance of the fitting routine). On other die, we found larger tolerances corresponding to a bound of  $\sigma_0(1-\nu) < 10 \text{ MPa}$ , but we never obtained a well-defined non-zero value for  $S_2$ . The value of modulus agrees well with the known Young's modulus of  $169 \text{ GPa}$  for a  $[110]$  directed beam in a  $\langle 100 \rangle$  single crystal plane [18], but has a much larger uncertainty than the  $B_2$  value because of the amplified uncertainties in  $t$  and  $g_0$ .

In examining die-to-die variation, we find a range of  $B_2$  between  $4.1$  and  $5.4 \times 10^{-22} \text{ Pa}\cdot\text{m}^6$  for die near the center of the wafer, and much larger variation near the edge of the wafer. The variations are substantially larger than the precision with which  $B_2$  can be determined for each die, and therefore suggest that there are variations in structural geometry from die to die. This is being examined further.

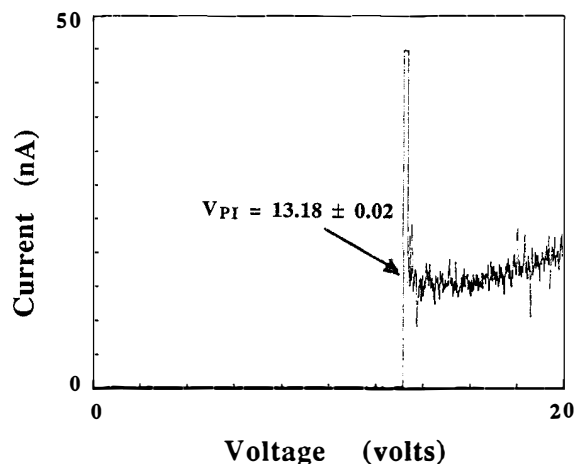


Figure 5. Current-voltage characteristic of a dielectrically isolated fixed-fixed silicon beam (length= $1500 \mu\text{m}$ , width= $50 \mu\text{m}$ , thickness= $14.4 \mu\text{m}$ ,  $g_0=1 \mu\text{m}$ ). Pull-in is indicated by the abrupt jump in current.

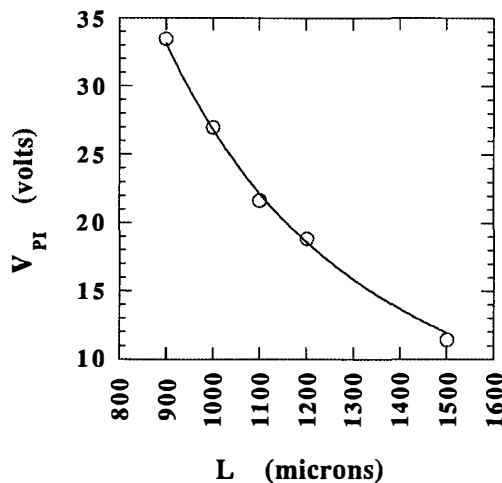


Figure 6. Experimental pull-in data vs beam length for a series of five beams from one die. Solid line is the fit to the closed-form model which yields:  $B_2 = 5.4 \pm 0.1 \times 10^{-22} \text{ Pa}\cdot\text{m}^6$  and  $S_2 < 1 \times 10^{-19} \text{ Pa}\cdot\text{m}^4$ .

A second set of samples was obtained from Bloom at Stanford [11]. The structures were fixed-fixed beams of LPCVD silicon nitride (nominally  $1325 \text{ \AA}$  thick and  $1.25 \mu\text{m}$  wide) coated with aluminum ( $200 \text{ \AA}$  thick), suspended  $1325 \text{ \AA}$  above a ground plane. Beam lengths ranging from  $28 \mu\text{m}$  to  $40 \mu\text{m}$  were tested. Pull-in of these structures was observed visually by microscope. In contrast with the silicon beams, which were bending dominated, a fit to the  $V_{PI}$  vs  $L$  data yielded good precision on  $S_2$  ( $6.0 \pm 0.1 \times 10^{-20} \text{ Pa}\cdot\text{m}^4$ ), and a small value for  $B_2$  ( $5.0 \pm 1.0 \times 10^{-29} \text{ Pa}\cdot\text{m}^6$ ). Their ratio indicates that this case is tension dominated. Because of substantial uncertainties in geometry for these devices, including some underetching of the supports at the ends and ambiguity on how to define the value of  $g_0$  in this dual-dielectric structure, we did not attempt a quantitative study of residual stress.

## DISCUSSION AND CONCLUSIONS

We have presented closed-form models for the electrostatic pull-in behavior of suspended cantilevers, fixed-fixed beams, and clamped circular diaphragms. These models are based on 2-D numerical simulation of beam deflection, including a first-order fringing-field correction. The expressions are directly usable by designers for prediction of pull-in. We have further shown that experimental data on such structures can be used to extract parameters ( $S_n$  and  $B_n$ ) which depend on combinations of mechanical properties and structural geometry. These parameters are very useful indicators of structural stiffness, and show directly whether the behavior is stress-dominated or bending dominated. They can also serve to monitor the repeatability of a fabrication process. However, because these quantities depend on thickness and initial gap to a higher power than Young's modulus or residual stress, errors in geometric parameters generate relatively larger errors in the extracted mechanical properties. Thus, it is clear that this method puts a stringent demand on the metrology of structural dimensions. An important next step is the examination of *in-situ* methods for monitoring critical dimensions, so that the precision of the extracted mechanical properties can be improved.

## ACKNOWLEDGMENTS

This work was supported in part by the Semiconductor Research Corporation (Contract 93-SC-309) and by ARPA (Contract J-FBI-92-196). The authors wish to thank Charles Hsu and Prof. Martin Schmidt of MIT and Dr. David Bloom and Dr. Raj Apte of Stanford for providing devices used in this work, and for helpful technical discussions. Measurements were made using Prof. Schmidt's test station. The authors also wish to thank Dr. Selden Crary of the University of Michigan for his suggestion of an approach to the problem of fringing-field corrections.

## REFERENCES

- [1] S. D. Senturia, "Microfabricated structures for the measurement of mechanical properties and adhesion," *Proc. Transducers '87*, Tokyo, Japan, June 1987, pp. 11-16.
- [2] S. D. Senturia, "Mechanical properties of microsensor materials: How to deal with the process dependencies?" *Mat. Res. Soc. Symp. Series*, **239**, 3-11 (1992).
- [3] W.-H. Chu and M. Mehregany, "A study of residual stress distribution through the thickness of p+ silicon films," *IEEE Trans. Elec. Dev.*, **40**, 1245-1250 (1993).
- [4] F. Maseeh and S. D. Senturia, "Plastic deformation of highly doped silicon," *Sensors and Actuators*, **A21-A23**, 861-865 (1990).
- [5] K. Najafi and K. Suzuki, "A Novel Technique and Structure for the Measurement of Intrinsic Stress and Young's Modulus of Thin Films," *Proc. MEMS 89*, Salt Lake City, Feb. 1989, pp. 96-97.
- [6] J. R. Gilbert, P. Osterberg, R. Harris, D. Ouma, A. Pfajfer, J. White, and S.D. Senturia, "Implementation of a MEMCAD System for Electrostatic and Mechanical Analysis of Complex Structures from Mask Descriptions", *Proc. MEMS 93*, Fort Lauderdale, Florida, Feb. 1993, pp. 207-212.
- [7] X. Cai, H. Yie, P. Osterberg, J. Gilbert, S. D. Senturia, and J. White, "A Relaxation/Multipole-Accelerated Scheme for Self-Consistent Electromechanical Analysis of Complex 3-D Microelectromechanical Structures," *Intl. Conf. Computer Aided Design*, Santa Clara, CA, Nov. 1993, pp. 270-274.
- [8] P. Osterberg, H. Yie, X. Cai, J. White and S. Senturia, "Self-Consistent Simulation and Modeling of Electrostatically Deformed Diaphragms", *Proc. MEMS 94*, Oiso, Japan, Jan. 1994, pp. 28-32.
- [9] Dr. Selden Crary, private communication.
- [10] C. H. Hsu and M. A. Schmidt, "Micromachined Structures Fabricated Using Wafer-Bonded Sealed Cavity Process", *1994 Solid-State Sensor and Actuator Workshop*, Hilton Head, SC, June 1994 (this volume).
- [11] O. Solgaard, F. S. A. Sandejas, and D. M. Bloom, "Deformable grating optical modulator," *Optics Letters*, **17**, 688-690 (1992).
- [12] B. E. Artz and L. W. Cathey, "A Finite Element Method for Determining Structural Displacements Resulting from Electrostatic Forces", *IEEE Solid-State Sensor and Actuator Workshop*, Hilton Head, SC, June 1992, pp. 190-193.
- [13] F. R. Morgenthaler, "Theoretical Studies of Microstrip Antennas, Vol. 1: General Design Techniques and Analyses of Single and Coupled Elements", U. S. Dept. of Transportation, Federal Aviation Administration Report No. FAA-EM-79-11, I, September 1979.
- [14] Matlab is a commercial product from The Mathworks Inc, Natick, MA, USA. Matlab scripts for the solution of the 2-D case for cantilevers, fixed-fixed beams and circular diaphragms, including the fringing-field correction, are available from the authors.
- [15] P. Lin, *et. al.*, "The in-situ measurement of biaxial modulus and residual stress of multi-layer polymeric thin films", *Mat. Res. Soc. Symp. Series*, **188**, 41-46 (1990).
- [16] Jeffrey Y. Pan, PhD Thesis, Department of Electrical Engineering and Computer Science, Massachusetts Institute of Technology, September 1991; also J. Y. Pan and S. D. Senturia, "Suspended-membrane methods for determining the effects of humidity on the mechanical properties of thin polymer films," *Soc. Plast. Eng. 49th Annual Tech. Conf., (ANTEC '91)*, Montreal, Canada, April 1991.
- [17] Kaleidagraph Version 2.1.3, Adelbeck Software.
- [18] W. A. Brantley, "Calculated elastic constants for stress problems associated with semiconductor devices," *J. Appl. Phys.*, **44**, 534-535 (1973).

# A METHODOLOGICAL APPROACH TO THE DESIGN OF COMPLIANT MICROMECHANISMS

G. K. Ananthasuresh\*, Sridhar Kota\*, and Yogesh Gianchandani†

\*Design Laboratory, Department of Mechanical Engrg. & Applied Mechanics

†Center for Integrated Sensors and Circuits, Department of Electrical Engrg. & Computer Science  
The University of Michigan, Ann Arbor, MI 48109

E-Mail: sureshgk@caen.engin.umich.edu, sridhar.kota@um.cc.umich.edu,  
yogesh@caen.engin.umich.edu

## ABSTRACT

At micro level, *compliant mechanisms*—flexible structures that generate desired motions through elastic deformation—provide a superior alternative to simple cantilever and diaphragm based flexible micromechanisms and rigid body mechanisms. The attractive features of compliant micromechanisms include joint-less, single-piece construction that is amenable for easy fabrication, and minimal detrimental effects due to friction, wear and backlash. The deformation capability of compliant micromechanisms is attributed to the *topology, shape* and *size* of their structure. In this research, we formulate a systematic method to the design of such mechanisms using the *structural optimization* approach. An emerging topology optimization technique, called *homogenization method*, is used to solve the synthesis problem with least dependence on designer's intervention. The proposed method is thus a valuable *synthesis* tool for automating the design of optimal micromechanical devices. The concept of compliant mechanisms and the proposed design methodology are both illustrated with a microcompliant crimping mechanism that has been fabricated and tested.

## 1. INTRODUCTION

Many deformable microstructures that have been developed over the years for sensor related applications are mainly comprised of simple cantilever and diaphragm like configurations [1]. The ability to perform general mechanical tasks, i.e. mechanical motions beyond simple rotations and translations, was thus very limited. Nevertheless, the flexure in a structure can be further exploited by suitably choosing the *form*, i.e. *topology, shape* and *size*, to generate wider variety of motions under the action of the applied forces (Figure 1). In such generalized deformable structures, the compliance (or flexibility) of the structure is *distributed* as opposed to *lumped* compliance as in structures with *flexural pivots*. These are emerging as a new class of mechanical systems under the name of '*compliant mechanisms*' [2]. These are, however, not yet in widespread use—perhaps due to the lack of design methods to synthesize them. In this paper, we propose a systematic design methodology for compliant mechanisms to generate *form* from the intended *function*.

Compliant mechanisms are particularly suited for micro applications as their unitized construction without rigid joints

(hinges, sliders, etc.) makes their manufacture extremely simple using *any* of the existing microfabrication processes, and also the frictional effects that dominate at micro level are reduced to a minimum, if not completely eliminated. Furthermore, wear, backlash, lubrication and assembly problems are alleviated. As flexure is permitted in these mechanisms, they can be readily integrated with non-mechanical actuation such as thermal, fluid pressure, piezo-electric and even shape-memory alloys. It is also possible to integrate the sensors within the mechanism; for instance, using piezo-electricity concept. Owing to these advantages, many potential uses of *compliant micromechanisms* in the controlled mechanical manipulation of micro objects and micro sensor related tasks can be realized.

## 2. SYNTHESIS OF COMPLIANT MECHANISMS

To use compliant mechanisms as superior substitutes for multi-membered rigid link mechanisms or locally flexible microstructures, it is necessary to generate a suitable structural form to perform the same function as the latter. It is usually done intuitively and iteratively as this synthesis process is still not systematized. We meet this shortcoming through a systematic procedure as explained below.

First, we abstract the *function* in terms of applied forces and output deformations that constitute the input-output behavior of a compliant mechanism. Thus, here *function* (or intended behavior) means that certain portion of the structure should deform in a prescribed direction under the application of external loads. The input to the problem would then be input forces, required output deformations and the available design domain. Second, we adapt a formal structural optimization technique called *Homogenization Method* [3] to synthesize a *form* that generates the desired behavior.

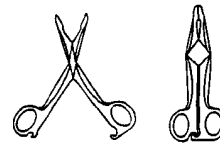


Figure-1 a  
Compliant forceps [6]

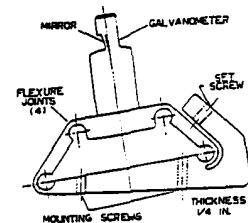


Figure-1 b  
Compliant four-bar  
adjustment mechanism [7]

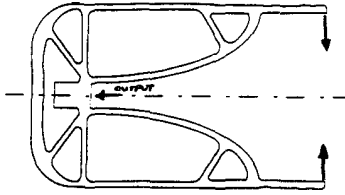


Figure-1c  
Compliant crimping  
mechanism

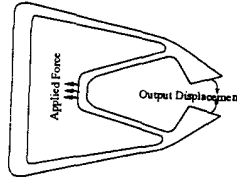


Figure-1d  
Compliant gripper

The task of generating a form to the structure that has the desired deformation behavior entails *designing structures for given deflection*. This deflection requirement distinguishes the compliant mechanism synthesis problem from the traditional structural optimization problems wherein structures are designed to be stiff, i.e. with least overall deformation [4]. The basis for our approach to compliant mechanism synthesis problem is in the search for the stationary value of the *Mutual Potential Energy (MPE)* [5] in the setup of an optimization problem (**P**) in which we can also incorporate criteria such as maximum mechanical advantage.

Mutual potential energy, as its name implies, is the mutual energy of a structural system under two different loadings. When the specified applied forces constitute one loading, and a unit dummy load applied at the point where a prescribed deflection is required in the required direction of deflection is the second loading, MPE is same as the actual deflection of the point where unit dummy load is applied. It is often referred to as the *unit dummy load method*. We use MPE in formulating the deflection as a constraint or an objective in the optimization problem in explicit form. Next, the objective of the optimization problem could be one of the following as necessitated by a given specific problem: minimize weight, minimize compliance (work done by external forces), minimizing deflection at the point of interest, etc. Choosing one of these as an objective function, e.g. minimum deflection at a point, the statement of the optimization problem would assume the following form:

$$\begin{aligned}
 &\text{Minimize Deflection at the point of interest} \\
 &\text{Subject to} \\
 &\quad \text{Volume constraint} \\
 &\quad \text{Equilibrium equations}
 \end{aligned}
 \tag{p}$$

Here, the intent is to design a structure that has prescribed upper limit on volume of material and to have least deformation at one prescribed point of interest. This fits in with the “design for deflection” formulation. Furthermore, as can be seen in (p), the structure should also satisfy equilibrium equations and traction forces on the boundary. Body forces, if any, can also be included.

The tensor  $\epsilon_{ij}$  denotes the strain field (two normal strains and a shear strain in a planar problem) due to the applied external loads and  $\bar{\sigma}_{ij}$  is the stress field due to the unit dummy load. The strain tensor,  $\epsilon_{ij}$ , can also be written in terms of the displacement field  $u_i$  as:

$$\epsilon_{ij} = \int_{\Omega} \frac{1}{2} \left( \frac{\partial u_i}{\partial x_j} + \frac{\partial u_j}{\partial x_i} \right)$$

MPE, or equivalently the deflection at a point, is written as in integral sum of product of  $\epsilon_{ij}$  and  $\bar{\sigma}_{ij}$  taken over the entire volume,  $\Omega$ . The elasticity tensor,  $E_{ijkl}$ , contains both material properties and design variables of the problem. It appears in the equilibrium equations as shown below. There are two sets of equilibrium equations: one to satisfy the applied external loads (the  $\epsilon_{ij}$  equation) and the other to satisfy the unit dummy load (the  $\bar{\sigma}_{ij}$  equation). The optimization problem statement can now be rendered in mathematical form as follows:

$$\begin{aligned}
 &\text{Minimize Design variables MPE} = \int_{\Omega} \epsilon_{ij} \bar{\sigma}_{ij} d\Omega = \int_{\Omega} \frac{1}{2} \left( \frac{\partial u_i}{\partial x_j} + \frac{\partial u_j}{\partial x_i} \right) \bar{\sigma}_{ij} d\Omega \\
 &\text{Subject to}
 \end{aligned}$$

$$\begin{aligned}
 &\text{Continuum mechanics Equilibrium equations} \quad \frac{\partial}{\partial x_j} \left( E_{ijkl} \frac{\partial u_i}{\partial x_k} \right) = 0; \quad \frac{\partial \bar{\sigma}_{ij}}{\partial x_j} = 0
 \end{aligned}$$

(External loads appear as surface traction forces in the form of boundary conditions.)

$$\begin{aligned}
 &\text{Volume constraint} \quad \int_{\Omega} \rho d\Omega \leq W_0
 \end{aligned}
 \tag{P}$$

Independent variable:  $x$  in  $\Omega$  (spatial coordinates)  
 State variables:  $u, \bar{\sigma}$  (displacement and stress)  
 External loads: surface tractions, unit dummy load  
 Design variables:  $E_{ijkl}$  parameterized as  $a, b, \theta$

Design variables in  $E_{ijkl}$ , can be size related features such as length, width, thickness, area of cross section, etc., or intrinsic features such as density. We use a microstructural model that has recently been shown to have the capability to vary topology of the structure in addition to shape and size.

### 3. SOLUTION TECHNIQUE

To implement this optimization problem, we use a computational technique called homogenization method. In this method, the design domain is parameterized using *cellular microstructure* (Figure 2) and the optimization method arrives at optimal values for the parameters of each cell ( $a, b$  and  $\theta$ ). Thus, there will be  $3n$  variables in the optimization problem if there are  $n$  elements (cells) in the domain. If the optimized hole dimensions  $a$  and  $b$  reach their limit values, i.e. the length and width of the cell, a hole will be generated; if  $a$  and  $b$  are zero, then a solid cell is created and intermediate values give rise to porous regions. This gives the method the ability to generate *any topology, shape and size* that are optimal for given problem specifications which include applied forces, desired output displacements and the amount of material to be distributed in a prescribed design domain.

The stationarity conditions for the above optimization problem (**P**) are obtained by using variational calculus approach (Euler-Lagrange equations) and Karush-Kuhn-Tucker necessary conditions for constrained optimality. Considering the large number of variables in the problem, an optimality criteria method is used rather than a mathematical programming type search technique. To facilitate iterative numerical solution, update formulas for  $a_i, b_i$  and  $\theta_i$  ( $i = 1, 2, 3$ . number of cells) are derived to satisfy the stationarity conditions of (**P**). For details, see [3].

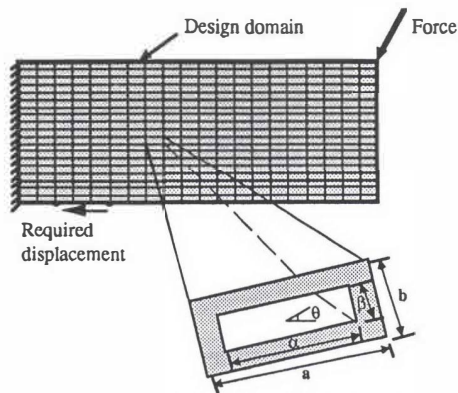


Figure-2 Parameterization of the design domain with microstructural cells having rectangular holes

#### 4. AN ILLUSTRATIVE EXAMPLE

The systematic design method is illustrated by synthesizing a microcompliant crimping mechanism whose functional specifications (Figure 3a) lead to the *homogenized* image (Figure 3b) where optimal parameter values of each square cell are converted to a density measure and are shown in gray scale. Figure 3c is an interpretation of the homogenized image. As can be observed in Figure-3c, the interpretation of the homogenized image requires some designer's intuition. The devices in Figures 1c and 1d are obtained in this manner by relying on intuition to some extent. At this stage of development, the proposed systematic technique immensely helps in synthesizing compliant mechanisms for given functional behavior with little human intervention. However, it is believed that the interpretation step can also be made completely systematic by improving the formulation, computational procedure and even the functional abstraction of the original intended task.

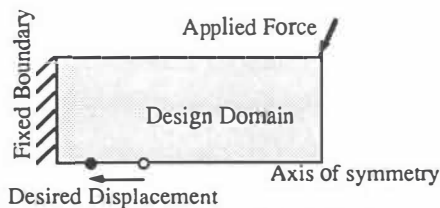


Figure-3a Functional Specifications

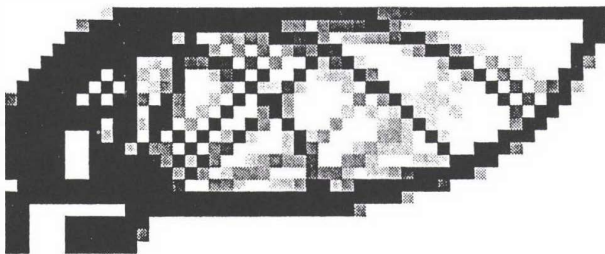


Figure-3b The generated homogenized image (The density of each cell is in gray scale)

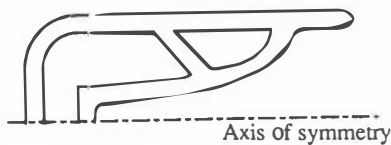


Figure-3c Interpretation of the homogenized image

The mechanism shown in Figure-3c has been fabricated using the *boron-doped bulk-silicon dissolved wafer process* [6]. The purpose of this device is to hold and/or crimp the micro object placed in the gap on the left when the handles on the right are pressed together (Figure 4 and Figure 1c). The device has been qualitatively tested with probe tips and quantitatively analyzed for performance characterization. Figure 5 shows the deformed configuration of the half-model of the device.

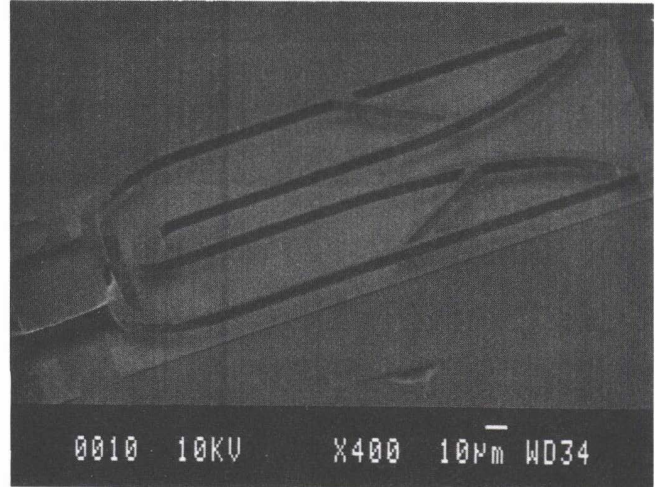


Figure-4 Scanning Electron Micrograph of the microcompliant crimping mechanism

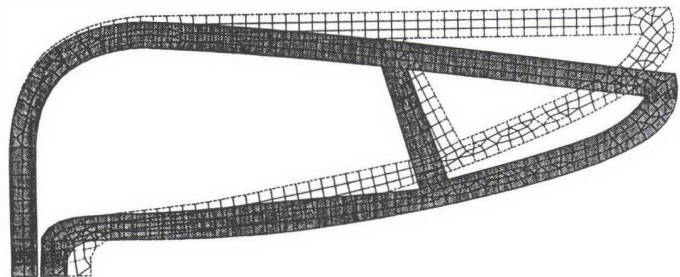


Figure-5 Finite element deformation analysis of the half-model of the device (The configuration prior to deformation is superimposed with empty grid)

#### 5. MECHANICAL ADVANTAGE ISSUES

Unlike in rigid link mechanisms, mechanical advantage (ratio of  $F_{out}$  to  $F_{in}$ ) is not an intrinsic character of the mechanism alone; it also depends on the properties of the workpiece operated by the mechanism. For the type of compliant mechanisms treated in this paper, the mechanical advantage (MA) is a nonlinear function of the stiffness of the workpiece (Figure 6). The device shown in Figure 4 has a peak mechanical advantage of 2.41 for a workpiece whose modulus of elasticity is 1/20th of that of the material of the device. Displacement at the output port decreases with increased stiffness of the workpiece, but MA rises up to a limit (Table-1) indicating a tradeoff between crimping and grasping applications. This device can potentially be used in biochemistry applications to crush macromolecules or to manipulate micro organisms in biomedical applications.

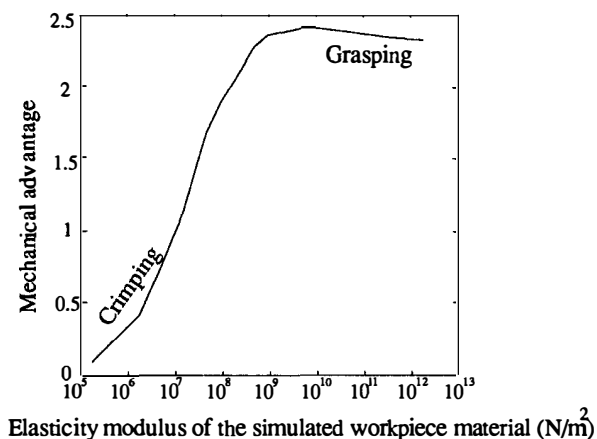


Figure 6 Variation of the mechanical advantage with stiffness of the workpiece

$E_{Si}$ = Elasticity Modulus of Si = $175e9 \text{ N/m}^2$ $E_w$ = Elasticity Modulus of workpiece material		
$E_w \text{ (N/m}^2\text{)}$	Output Disp. ( $\mu$ )	MA = $F_{out}/F_{in}$
175e3	8.92	0.07
175e4	7.67	0.41
525e4	6.40	0.75
875e4	5.67	0.95
126e5	5.16	1.08
438e5	3.14	1.68
875e5	2.14	1.89
438e6	0.65	2.27
875e6	0.36	2.36
525e7	0.08	2.41
875e7	0.06	2.41
175e8	0.04	2.40
438e8	0.02	2.38
875e8	0.01	2.37
175e9	0.007	2.35
350e9	0.004	2.34
175e10	0.0018	2.33

Table 1 Simulated performance of the device using Finite Element software ANSYS

## 6. CLOSURE

*Compliant mechanisms* are flexible structures that generate a wide variety of mechanical motions through elastic deformation. In this research, the concept of compliant mechanisms is applied to the micro regime. Frictionless, backlash-free and easily manufacturable compliant micromechanisms are clearly more advantageous than rigid link and rigid joint micromechanisms, and are also more versatile than simple cantilevers and diaphragms that also depend on the flexural capability. For a given task, the suitability of a compliant mechanism is determined by the configuration or *form* of its structure. Specifically, the topology, shape and size together provide the ability to deform in the desired manner. The design of compliant mechanisms would then involve generating suitable topology, shape and size for a given application. A systematic design method has been proposed here for a general synthesis task abstracted in terms of applied loads and desired deflections.

The synthesis problem is formulated as an optimization problem using the *mutual potential energy* principle [5]. The *homogenization* method is used as the computational tool to generate topology, shape and size in a single step and in a systematic manner. The feasibility of the method is demonstrated by designing and fabricating a micro-crimping mechanism. This device can potentially be used for grasping, crimping and other manipulative tasks. Using the concept of compliant micromechanisms, a variety of micro devices with built-in actuators and sensors can be created for easy manufacture and superior performance.

## ACKNOWLEDGMENTS

The authors would like to express their sincere thanks to Dr. Selden B. Cray, Professor Noboru Kikuchi and Professor John E. Taylor for their invaluable help and encouragement during the course of this work. We also thank Professor Kensall D. Wise and Professor Khalil Najafi for providing the microfabrication facilities. This research was supported by NSF under #DDM-931333 to the second author, and Horace H. Rackham Predoctoral Fellowship at The University of Michigan, to the first author.

## REFERENCES

- [1] Petersen, K. E., "Silicon as a Mechanical Material," *Proc. IEEE*, Vol. 70, No. 5, May 1982, pp. 420-457.
- [2] Midha, A., "Chapter 9: Elastic Mechanisms," *Modern Kinematics*, A. Erdman (ed.), John Wiley Inc., New York, 1993.
- [3] Bendsøe M. P. and Kikuchi, N., "Generating Optimal Topologies in Structural Design Using a Homogenization Method," *Computer Methods in Applied Mechanics and Engineering*, 71 (1988), North Holland, pp. 197-224.
- [4] Ananthasuresh, G. K., Kota, S. and Gianchandani, Y., "Systematic Synthesis of Microcompliant Mechanisms—Preliminary Results," *Proc. The Third National Applied Mechanisms and Robotics Conference* held at Cincinnati, OH, Nov. 8-10, 1993, Vol. 2, Paper 82.
- [5] Shield R. and Prager W., "Optimal Structural Design for Given Deflection," *ZAMP: Journal of Applied Mathematics and Physics*, 21, 1970, pp. 513-523.
- [6] Gianchandani, Y. and Najafi, K., "A Bulk Silicon Dissolved Wafer Process for Microelectromechanical Devices," *Journal of Microelectromechanical Systems*, Vol. 1, No. 2, June 1992, pp. 77-85.
- [7] Salamon, B. A., "Mechanical Advantage Aspects in Compliant Mechanisms Design," M. S. Thesis, Thesis Advisor: Midha, A., Purdue University, 1989.
- [8] Towfigh, K., "The Four-bar Linkage as an Adjustment Mechanism," *Proc. Applied Mechanisms Conference*, Paper No. 27, Stillwater, Oklahoma, July 1969.

# CLUSTERING-BASED PATTERN RECOGNITION APPLIED TO CHEMICAL RECOGNITION USING SAW ARRAY SIGNALS

G. C. Osbourn, J. W. Bartholomew, G. C. Frye and A. J. Ricco

Sandia National Laboratories  
Albuquerque, N.M. 87185

## ABSTRACT

We present a new pattern recognition (PR) technique for chemical identification using arrays of microsensors. The technique relies on a new empirical approach to k-dimensional cluster analysis which incorporates measured human visual perceptions of difficult 2-dimensional clusters. The method can handle nonlinear SAW array data, detects both unexpected (outlier) and unreliable array responses, and has no user-adjustable parameters. We use this technique to guide the development of arrays of thin-film-coated SAW devices that produce optimal PR performance for distinguishing a variety of volatile organic compounds, organophosphonates and water.

## INTRODUCTION

There is much current interest in the use of pattern recognition (PR) techniques to identify and quantify chemical analytes based on the multivariate responses of chemical microsensor arrays [1,2]. PR techniques used previously measured array responses of the class categories of interest, called training set data, to infer the class category associated with new array measurements (test data). The class categories can be the chemical identities of the analytes and can also represent the analyte concentrations. Each sensor in the array provides one dimension of the multidimensional data vectors. The application of PR techniques to microsensor-based chemical sensing is motivated by two advantages: (i) chemical identification is possible using only partially chemically selective microsensors rather than highly selective (and more difficult to develop) microsensors; (ii) PR can in principle identify a large number of chemical species using a small, fixed set of sensors.

The desired arrays of sensors are those that yield distinctive response patterns for different chemicals, i.e. so that the clusters of pattern vectors associated with different chemical classes are spatially separated and distinguishable in the pattern vector space. However, not all arrays yield useful separations of the chemical classes, so much of the work required to develop a useful chemical pattern recognition scheme is in finding a useful combination of chemical sensors.

Surface acoustic wave (SAW) devices that have been coated with different partially selective films are of current interest for array applications [2-4]. The variety of coatings that can be fabricated suggests the possibility of detecting a wide range of analytes with SAW devices. However, coated SAW devices often respond nonlinearly and occasionally nonmonotonically as a function of analyte concentration [5]. These devices also do not necessarily yield additive responses to chemical mixtures. Such responses present severe difficulties for conventional chemometric techniques, which work well for linear response signals.

We describe a new PR technique which can treat nonlinear and nonmonotonic sensor responses. The technique is computationally efficient, provides warning for new data points that are atypical or that cannot be reliably identified, and requires no user-adjustable parameters. We demonstrate the technique with the optimization of arrays of coated SAW devices for identifying volatile organic compounds (VOCs), organophosphonates and water. VOC detection and monitoring is of interest for a number of industrial and DOE applications [4] and the organophosphonates are simulants for chemical warfare agents [3]. We describe the selection of SAW coating combinations and compute estimates of the expected performance of the arrays on new data. The arrays are developed and

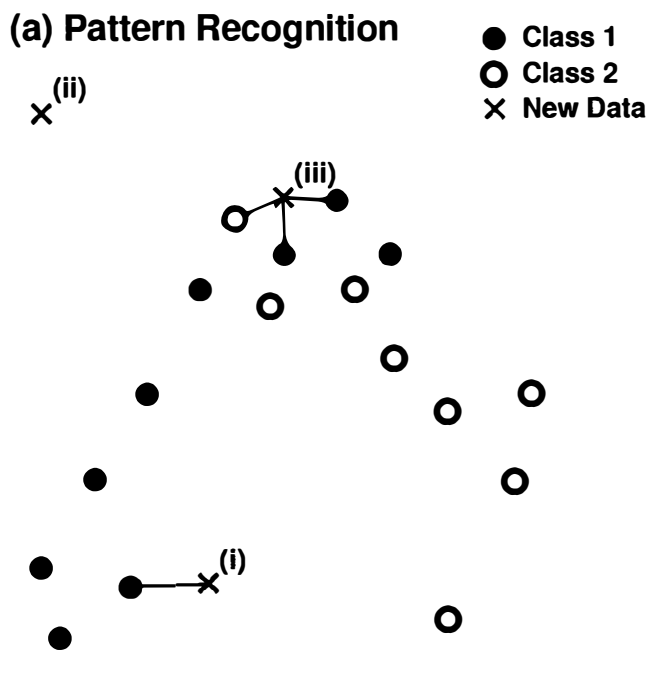
demonstrated using chemicals presented individually. The performance of this approach for array responses to complex mixtures remains the subject of future study.

## PATTERN RECOGNITION TECHNIQUE

Our technique relies on a new empirical approach to k-dimensional cluster analysis that incorporates measured human visual perceptions of difficult 2-dimensional clusters [6]. We use this new clustering method because it: (i) mimics human cluster perception; (ii) requires no prior knowledge about the final cluster result (e.g. the number of clusters); (iii) outperforms commercially available cluster methods on benchmarking tests [6]. Here we describe the use of the clustering results to carry out PR or to evaluate the expected PR performance using sets of coated SAW sensor responses. Details of the clustering method are described in Ref. 6.

PR using the cluster results is illustrated in Fig. 1a. The open and closed circles represent hypothetical training data for two classes and the x symbols represent hypothetical test data points of unknown chemical class identity. The two dimensions of the data correspond to simultaneous responses of two different sensors. Computed clusterings of the test points are indicated by the lines connecting the points. Three possible cases occur for the class assignment of each new test point: (i) The new point is clustered only with training data of a single class and is assigned that same class -- this is the desired result; (ii) The new point is clustered with none of the training data and is not assigned a class -- these outlier points can result from detection of a new chemical class that is not present in the training data set, although sensor measurement errors can also produce outliers; (iii) The new point is clustered with training points from multiple classes -- these points occur where the training set classes overlap and cannot be reliably distinguished, so that the class assignment is ambiguous. We note that cases (ii) and (iii) provide useful information that is often unavailable or unreliable from existing PR techniques.

It is usually necessary to estimate the expected performance of the sensor array using only the measured training data set. We use the "leave-one-out" approach [7], where each data point is individually removed from the complete training set and examined as a new test point by the PR technique. This approach maximizes the use of the available training data and avoids the favorable bias of the results that occurs by including the point that is being classified. This approach is not always convenient in some PR methods that require additional computations for each version of the training set with a point removed (e.g. retraining a neural net). Fig. 1b illustrates how the cluster results are used for the leave-one-out computations. The known class identity of each training data point is compared with the result inferred from the clustering approach shown in Fig. 1a. There are again three possible cases which can arise: (i) The point is clustered only with other training data of the correct class -- such points are correctly identified; (ii) The point is clustered with none of the other training data -- these outlier points are too far away from other points in the same class for clustering to occur. Outlier points in the leave-one-out analysis are usually due to inadequate sampling of the class in the parts of pattern vector space near the outliers, and suggest the need for more training points. However, these can also result from sensor measurement errors; (iii) The point is clustered with other training points from one or more classes that do not match the correct class. These points identify overlaps between classes in pattern vector space where the sensor array is unable to reliably



**(b) Leave-One-Out Analysis**

● Class 1  
○ Class 2

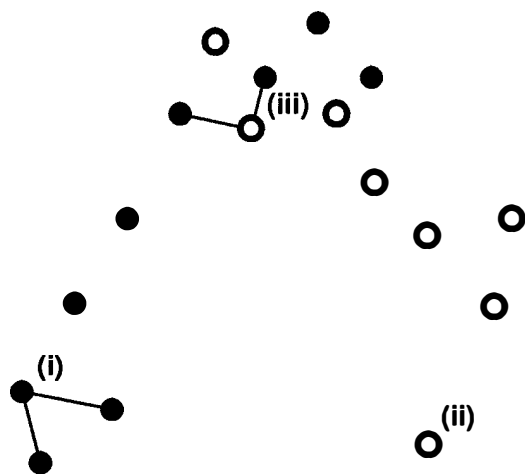


Fig 1. (a) Illustration of the use of cluster results for PR. Open and closed circles are training data, × symbols are test data. Computed clusterings of test points with training data are indicated by connecting lines. The three cases illustrated are: (i) recognized; (ii) outlier; and (iii) ambiguous or incorrect. (b) Use of cluster results for leave-one-out analysis on the same training data. The three illustrated cases are: (i) correctly recognized; (ii) outlier; and (iii) incorrect.

distinguish chemical identities. Statistics on these three cases for the entire training set provide three separate figures of merit for the sensor array under consideration, i.e. the percentage correctly identified, the percentage that indicates inadequate training set sampling, and the percentage that indicates class overlap. These figures of merit are used here to optimize the selection of the array sensors.

## EXPERIMENTAL PROCEDURES

We analyze experimental results from two sets of coated-SAW arrays and analytes. In both studies we make use of only the frequency shifts which result from the uptake of the analyte by the SAW device coatings. Other measurable responses, e.g. attenuation [4], are also available for PR, and we will examine these in future work.

The first set of chemicals includes water, an alcohol (isopropanol), a ketone (acetone), non-chlorinated hydrocarbons (d-limonene, n-hexane, and toluene) and chlorinated hydrocarbons (CCl<sub>4</sub>, TCE, and chloroform). These analytes are sensed using SAW devices coated with ethyl cellulose, polyisobutylene and nafion polymer films. The data are acquired by alternating between a chemical-free purge stream and a stream at a constant chemical concentration. Chemical concentration is controlled by the relative flow rates of a chemical-free mix-down stream and a saturated stream (obtained by passage through a bubbler containing the chemical). Four concentrations per chemical were obtained. This produced 12 data points for both the chlorinated and non-chlorinated classes.

The second set of chemicals includes water, organophosphonates (DIMP, DMMP), a ketone (acetone), aromatic hydrocarbons (benzene, toluene), chlorinated hydrocarbons (CCl<sub>4</sub>, TCE), aliphatic hydrocarbons (cyclohexane, isooctane), and alcohols (methanol, pinacolyl alcohol, n-propanol). These analytes are sensed using SAW devices coated with nine self-assembled monolayer (SAM) films and plasma-grafted polymer films (PGFs). These films and the data acquisition method are described in a companion paper [8]. We retained 21 points per chemical, with concentrations ranging from 9% to 49% of the saturation vapor pressure.

## DATA PREPROCESSING FOR CLUSTERING-BASED PATTERN RECOGNITION

It is common for coated SAW devices to yield ranges of responses that are quite different in magnitude. In order for each device to have a comparable effect on the class separations in pattern vector space, the magnitudes of the device responses must be comparable. We equalize the responses of each sensor by a multiplicative scale factor, so that the largest absolute training data response of each sensor is unity.

The coated SAW sensor responses and the lengths of the multivariate pattern vectors generally increase as the chemical concentrations are increased. This tends to spread the class vectors away from the origin and each other as the chemical concentrations are increased. We improve the clusterings of the sensor data by normalizing the pattern vectors to unit length after the device responses have been equalized. A comparison of PR performance for the raw and normalized data are described below.

## DETERMINATION OF OPTIMAL ARRAYS

A key element in the successful development of a pattern recognition system is the selection of a useful set of measurements that can separate the classes in pattern vector space. This corresponds to selecting a set of SAW coatings and a set of chemical concentrations to include in the training set. One might expect that arrays with larger numbers of distinct sensor signals,  $k$ , would always be preferable for PR applications. This is not true for two reasons. From a practical viewpoint, arrays with the fewest devices are likely to require simpler fabrication and data acquisition procedures. This motivates the use of the smallest arrays that provide the desired performance. From a PR performance viewpoint, discriminating ability peaks and then declines as  $k$  is increased beyond approximately  $N/2$ , where  $N$  is the number of training data points per class. The reasons for this well-known behavior of PR systems are discussed in Ref. 7. Here we emphasize that the number of SAW films that can be usefully included in an array is limited by the number of chemical concentrations per class that is included in the training data set. This well-known condition for reliable PR analysis of arbitrary  $k$ -dimensional data is often not satisfied in published sensor PR work. We also note that estimates of PR performance that

do not remove examined points from the training data when computing their class identities, i.e. that do not use the leave-one-out approach, will exhibit increasingly perfect performance as  $k$  increases. Such biased estimates are not representative of the PR performance on future data.

For large sets of distinct devices, we must search for the smallest subsets that produce good separation of the chemical classes of interest in a leave-one-out analysis. We do this directly for the nine SAMs and PGFs by examining all combinatorial sets of arrays. The computations are done on a SPARC 10 workstation. The primary figure of merit we seek to minimize is the percentage of incorrect leave-one-out points in the data set. We also seek to minimize the number of outliers among the array combinations with the smallest incorrect percentages. The number of data points per chemical class is sufficient to usefully include all of the SAM-coated and PGF-coated SAW devices in the array, but we are interested in identifying the smallest subset of devices with the best PR performance.

## RESULTS

The leave-one-out results for the ethyl cellulose, polyisobutylene and nafion coatings yield no incorrect points for the class combinations chosen. The locations of the training points are shown in the plot of Fig. 2. Note that this is one perspective of a

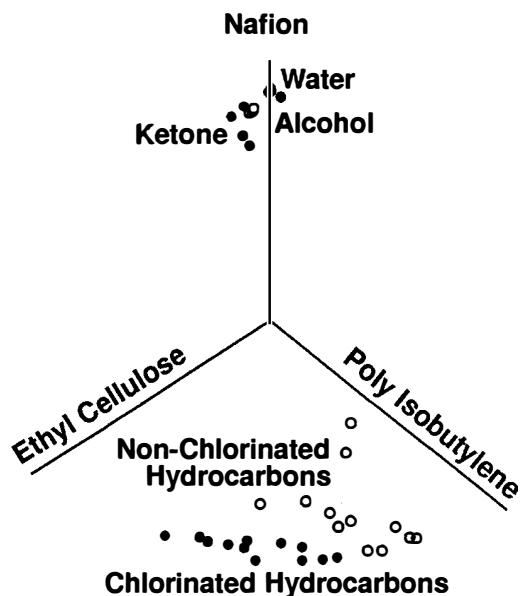


Fig 2. One view of a three-dimensional pattern vector space plot of 3-film SAW array data. All of these chemical classes are distinguished. The alcohol and ketone classes are seen to separate when viewed along the nafion axis. The 3 types of chemicals within the chlorinated and non-chlorinated classes are too similar to be distinguished with this array.

three-dimensional plot. These results show that a variety of chemical classes can be distinguished using these three SAW coatings. The ketone and alcohol classes appear to overlap from this viewing orientation, but can be seen as distinct when viewed along the nafion axis direction. The three individual chemicals within the chlorinated and non-chlorinated VOC classes are not reliably separated, so that additional measurements are needed to distinguish these chemicals. However, more concentration values are required for the individual chemical classes to achieve this improvement.

Figs. 3a-d show the statistics obtained from the nine SAMs and PGFs. The number of array combinations that yields a particular percentage of incorrect identifications is plotted for arrays with 3 to 6 films in Figs. 3a-d, respectively. Again it is seen that all three-film

## Array Optimization

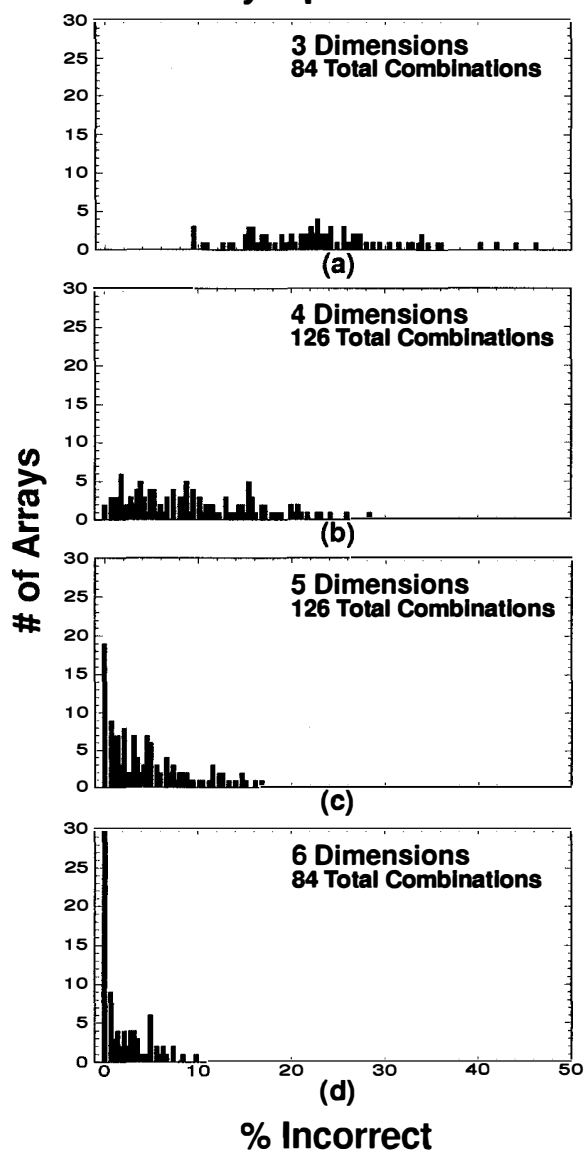


Fig 3. Histograms of number of arrays vs percentage incorrect from the leave-one-out analyses for the SAM-coated and PGF-coated SAWs. Panels (a)-(d) show results for arrays with three to six films per array, respectively.

arrays generate some incorrect chemical identifications. The overall PR performance improves as films are added, and the number of array combinations exhibiting no incorrect responses is nonzero for four or more films in the arrays. The best three-to-six film combinations are [HS(CH<sub>2</sub>)<sub>10</sub>COO<sup>-</sup>/Cu<sup>2+</sup>, Eugenol-30, PIB-PGAA 5+15], [HS(CH<sub>2</sub>)<sub>15</sub>CH<sub>3</sub>, PGAA-PGAA 5+15, Eugenol-30, PIB-PGAA 1+15], [HS(CH<sub>2</sub>)<sub>15</sub>CH<sub>3</sub>, HS(CH<sub>2</sub>)<sub>15</sub>CH<sub>3</sub>, PGAA-PGAA 5+15, PGAA-PGAA 5+30, PIB-PGAA 1+15], [HS(CH<sub>2</sub>)<sub>10</sub>COOH, HS(CH<sub>2</sub>)<sub>10</sub>COO<sup>-</sup>/Cu<sup>2+</sup>, HS(CH<sub>2</sub>)<sub>15</sub>CH<sub>3</sub>, Eugenol-30, PIB-PGAA 1+15, PIB-PGAA 5+15], respectively (see ref. 8 for an explanation of the film abbreviations). Since the higher-dimensional results can not be graphically displayed, we show the best three-film case in Fig. 4. This three-film set is not able to separate all of the chemicals. For clarity, we show only some of the chemical classes which are non-overlapping in Fig. 4.

Finally, we have examined the effect of normalizing the pattern vector lengths on these results. This is done by computing results with

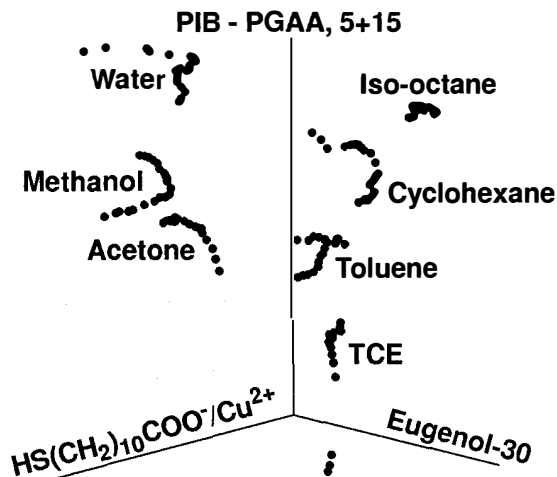


Fig 4. One view of a three-dimensional pattern vector space plot of the best 3-film SAW array from Fig. 3a. Not all of the individual chemicals are correctly identified, and for clarity we show only some of the non-overlapping chemical data.

a range of scaling values ranging from 1, corresponding to raw data, to  $1/(\text{vector length})$ , corresponding to a completely normalized vector length. Fig. 5 plots the number of incorrect responses as a function of the degree of normalization for the three-film array shown in Fig. 4. The PR performance is best for nearly normalized vector lengths and is worst for the raw data.

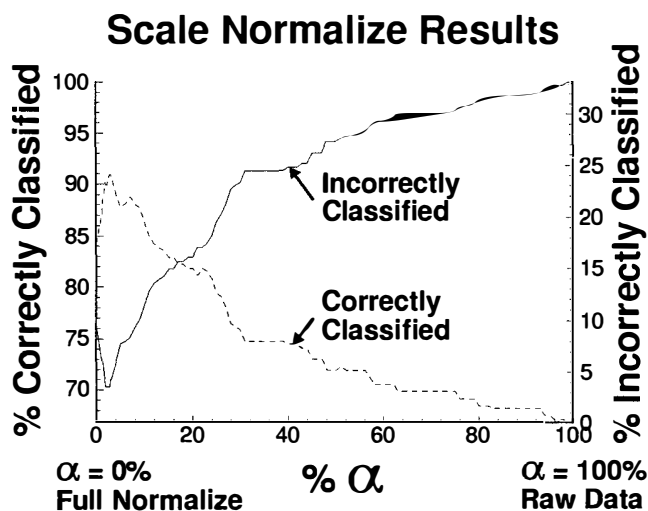


Fig 5. Effect of the amount of pattern vector normalization on the results of the three-film array of Fig. 4. Each pattern vector is multiplied by  $1/(L+\alpha(1-L))$ , where  $L$  is the length of the pattern vector and  $\alpha$  determines the degree of normalization.

## CONCLUSIONS

We present a new PR technique for chemical identification using arrays of microsensors. The technique relies on a new empirical approach to  $k$ -dimensional cluster analysis which incorporates measured human visual perceptions of difficult 2-dimensional clusters. The method can handle nonlinear SAW array data, detects both unexpected (outlier) and unreliable array responses, and has no

user-adjustable parameters. We use this technique to develop small arrays of thin-film-coated SAW devices which produce optimal PR performance for distinguishing a variety of volatile organic compounds, organophosphonates and water. We find that three-film arrays are sufficient to distinguish a number of distinct chemical classes, but are unable to distinguish closely similar chemicals in the non-chlorinated and chlorinated hydrocarbon classes. For vapor concentrations greater than 9% of saturation, arrays with as few as 4 selected films give 100% correct classification for these chemical classes and the individual chemicals. In addition, many different five-film combinations give 90-100% correct identifications for the individual chemicals.

## ACKNOWLEDGEMENT

Work supported by the US DOE under contract DE-AC04-94AL85000.

## REFERENCES

- (1) X. Wang, J. Fang, P. Carey, S. Yee, "Mixture analysis of organic solvents using nonselective and nonlinear Taguchi gas sensors with artificial neural networks", *Sensors and Actuators B*, 13, 455 (1993).
- (2) S. L. Rose-Pehrsson et. al., "Detection of hazardous vapors including mixtures using pattern recognition analysis of responses from surface acoustic wave devices", *Anal. Chem* 60, 2801 (1988).
- (3) A. J. Ricco, C. Xu, R. M. Crooks, and R. E. Allred, "Chemically sensitive interfaces on SAW devices" in *Chemically Sensitive Interfaces*, ACS Symposium Series No. 561, Amer. Chem. Society, Washington, D. C. (1994), in press.
- (4) G. C. Frye, S. J. Martin R. W. Chernosek and K. B. Pfeifer, "Portable acoustic wave sensor systems for on-line monitoring of volatile organics", *Int. J. of Environ. Conscious Manufacturing*, 1, 37 (1992).
- (5) G. C. Frye and S. J. Martin, "Velocity and attenuation effects in acoustic wave chemical sensors", *Proc. 1193 Ultrasonics Symposium (IEEE, 1993)* p.379.
- (6) G. C. Osbourn and R. F. Martinez, "Empirically defined regions of influence for clustering analyses", Sandia Report SAND 94-0210.
- (7) D. J. Hand, *Discrimination and Classification*, John Wiley and Sons, New York 1981.
- (8) A. J. Ricco et. al., this proceedings.

# Nongimbaled Solid-State Compass

Gregory J. Olson, Robert B. Smith, Gordon F. Rouse,  
Howard B. French and James E. Lenz  
Honeywell Technology Center  
3660 Technology Drive  
Minneapolis, MN 55418

## Abstract

We have developed and evaluated a new solid-state nongimbaled electronic compass. Typical high-accuracy (1-deg resolution) compasses use a mechanical gimbaling method to hold two orthogonal magnetic sensors in a horizontal plane. The limited range of motion of the gimbal restricts the angular operation of the compass but, on the other hand, simplifies the compensation of the compass for its own tilt-related distortions of earth's magnetic field. The challenge of building a rugged and nongimbaled compass involves measuring the three components of earth's field and the gravity vector simultaneously and then developing three-dimensional tilt compensation and magnetic calibration algorithms to correct the measurement for tilt and for the self distortion of earth's field introduced by ferrous materials within the package. We demonstrated better than  $\pm 1$ -deg accuracies under a variety of field exercises.

## Introduction

Historically many different magnetic sensor concepts have been used in compass applications. These range from low-cost, low-sensitivity Hall-effect sensors to more sensitive, complex, and expensive fluxgate sensors. These compasses typically contain a gimbal mechanism that keeps the sensor horizontal during the measurement. In the case of the fluxgate compass, a point pivot and fluid-filled compartment are often used to provide the gimbal effect. When a compass cannot be gimbaled, then some means of measuring its tilt or orientation must be provided. Our recent development of a nongimbaled solid-state compass builds directly on our experience in magnetic sensing and our development of magnetoresistive (MR) permalloy material. The MR sensing bridges are produced by IC techniques and can be made on microminiature scales. Although the MR sensors are unique and provide an excellent sensitivity to magnetic fields, they also must maintain a level orientation during the compass measurement, or at least have a measured and accounted for tilt. We have added accelerometer-based tilt sensors and the appropriate compensation algorithms to allow elimination of the gimbal.

Our electronic compass was developed to replace a previously used gimbaled fluxgate compass for a personal navigator concept. This personal navigation system is shown in Figure 1. In this system, the compass must operate quickly, reliably, and accurately while being handheld. Unfortunately, earlier versions of this system used a gimbaled compass and had to contend with the damping and response time issues of the gimbal. We found that the combination of handheld compass operation with gimbal-related delays created a difficult situation. We often found ourselves forced to hold the system steady for several seconds while the gimbal settled out. When the compass gimbal finally stabilized, the heading could be registered and used in the system calculations. We would have preferred to get an instantaneous reading of heading while briefly sighting the compass. In addition, as the personal navigator breadboard evolved toward smaller and smaller package volumes, our MR sensors appeared to be perfectly suited to the application. The new nongimbaled solid-state compass easily met our requirements for the personal navigator.

The personal navigator compass is constructed from a three-axis set of MR transducers to sense magnetic field strength and orientation and a three-axis set of piezoresistive accelerometers to sense the

gravity vector. The system incorporates a calibration algorithm to take out local and fixed magnetic field disturbances while actively sensing and compensating for tilt. The magnetic sensing transducers have been packaged with reset coils used to initialize the films for maximum sensitivity, and with feedback coils for closed-loop operation. The piezoresistive accelerometers were chosen for their dc response characteristics. The magnetometer suite, accelerometer package, and analog compass circuitry are shown in Figure 2. The actual size of the magnetometer suite is 0.75 in.  $\times$  0.75 in.  $\times$  2.5 in. The majority of this volume is occupied by the reset and feedback coils. We have since designed on-chip straps for switching the magnetization vector, and open-loop operation may eliminate the need for the feedback coils. Ultimately, we envision a two-IC package that would contain four magnetoresistive bridges and provide for proper packaging of the three orthogonal sensing axes required for compassing applications.



Figure 1. Personal Navigator System Containing Solid-State Compass

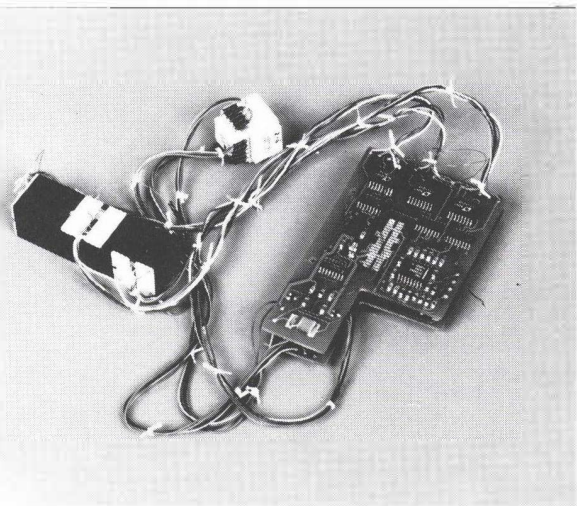


Figure 2. Solid-State Compass Components

### Magnetometer Detail

Honeywell's permalloy magnetometer uses the anisotropic magnetoresistive (AMR) effect in thin-film permalloy (a nickel-iron alloy). In this effect, the resistance of a ferromagnetic material depends on the angle between the current flow direction vector and the magnetization vector in the material ( $\theta$ ). This resistance variation has an amplitude of about 2% and has the form  $\cos^2\theta$ , maximum when the current and magnetization are parallel (or antiparallel) and minimum when they are perpendicular. The highest sensitivity (maximum slope) occurs for  $\theta = 45$  deg. The amplitude of this sensitivity depends on both the total (percentage) change in resistance and on the magnetic "stiffness" of the film (the field needed to rotate the magnetization by 90 deg). Because both the current and zero field magnetization will normally tend to align with the long dimension of the film, this high sensitivity can only be obtained if a "biasing" technique is used to rotate one or the other by 45 deg.

The magnetization can be rotated by a bias field generated by a coil, or by a permanent magnet deposited directly onto the film. The biasing method used for this compass (called barberpole biasing because of its appearance) uses high-conductivity "shorting bars" at a 45-deg angle on the film. The current will generally flow along the shortest paths between the shorting bars, or at about 45 deg to the long dimension. The full transducer is a Wheatstone bridge in which all four resistors have the same sensing axis, but have the shorting bars slanting in opposite directions in the two sets of legs such that one set increases in resistance while the other decreases. A

barberpole-biased transducer is shown schematically in Figure 3, along with its response to a magnetic field along the sensing axis.

### Compass Detail

The MR compass magnetometers provide voltages  $v_x$ ,  $v_y$ , and  $v_z$  with magnitudes representative of their vector components of earth's magnetic field. In addition, the tilt sensor provides  $a_x$ ,  $a_y$ , and  $a_z$  signals whose magnitudes represent their respective components of earth's gravitational field and are used to define  $G$ . These vector relationships are shown in Figure 4. Basically, north is shown as the Magnetic North plane defined by  $H_{East}$  and  $G$ . The level plane represents the ideal orientation of the compass package where no tilt compensation is required. However, the tilted rectangle represents the more general tilt and magnetic orientation of the compass package. Assuming that the magnetometers and accelerometers have a fixed orientation within the package, the system microprocessor then samples these signals at an appropriate rate and does a series of vector manipulations to determine the magnetic heading and tilt correction for the package. These manipulations will now be described in greater detail.

The task of nongimbaled compassing must take into account the following issues:

- Heading calculation and tilt compensation,
- Magnetic calibration,
- Temperature compensation.

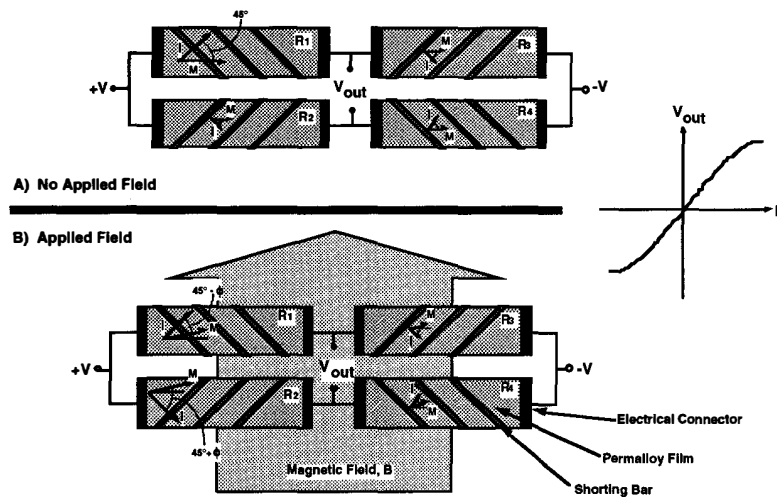


Figure 3. "Barberpole" Biasing with A) No Applied Field and B) Applied Field

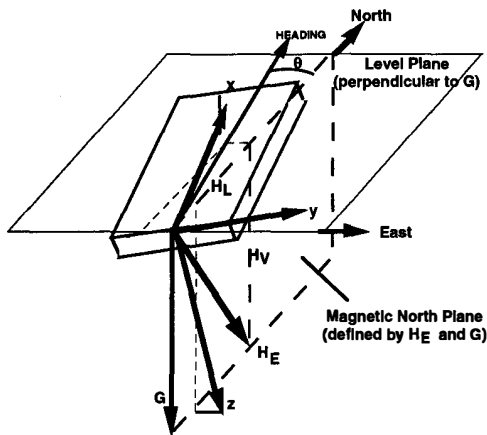


Figure 4. Compass Vector Diagram

### Compass Heading Computation and Tilt Compensation

The output of the three magnetic sensors provides a vector of three numbers for the total magnetic field of the earth,  $H_e$ , as measured in the  $x, y, z$  coordinate system of the package. ( $H_e$  is the total earth field, including a large vertical component, not just the horizontal components.) Three accelerometers, or a two-axis tilt sensor, provide a vector  $G$ , for the direction of gravity, also expressed in the package coordinate system. From these two vectors the horizontal components of  $H_e$  may be calculated to determine the heading of the compass module. The  $x$  axis of the module is taken along the long axis and defines the heading. Normal orientation will define the  $y$  axis to the right, and  $z$ , down. The compass heading for the module package is defined by the direction of a vertical plane through the longitudinal  $x$  axis of the package and  $G$ , regardless of some roll tilt of the package.

Compass heading in the presence of tilt is calculated as follows. All vectors are three-element numerical vectors expressed in the

package coordinate system. For brevity, all vectors are assumed to be normalized unit vectors. First, we calculate the four intermediate vectors below. The products are vector cross-products, with the resulting vector being perpendicular to the two arguments. For these calculations,  $H_e$  must first be compensated for case-induced magnetic errors as described above.

- Calculate a horizontal vector pointing east regardless of package orientation, defined as perpendicular to both  $G$  and  $H_e$ :  $E = (G \times H_e)$ .
- Calculate a horizontal unit vector pointing to the right in the package, defined as perpendicular to both  $G$  and  $X$  (the package axis):  $Y_H = (G \times X)$ .
- Calculate a horizontal vector pointing to magnetic north regardless of package orientation, defined as perpendicular to both  $G$  and  $E$ :  $N_H = (E \times G)$ .
- Calculate a horizontal vector pointing along the heading of the package, defined as perpendicular to both  $Y_H$  and  $G$ :  $X_H = (Y_H \times G)$ .

From these four vectors, calculate the cosine and sine of the heading angle as vector dot products (giving the cosine of the angle between them):

$$\begin{aligned} \text{Cos}\theta &= +(Y_H \cdot E) = +(X_H \cdot N), \\ \text{Sin}\theta &= -(Y_H \cdot N) = +(X_H \cdot E) \end{aligned}$$

Finally, the heading angle or compass bearing for the package is calculated as:

$$\theta = \arctan(\text{Sin}\theta/\text{Cos}\theta)$$

(four-quadrant arc tangent function)

### Magnetic Calibration

Specifically, magnetic errors can and often do arise from misalignment of the magnetic sensing axes within the magnetometer package, from metals collocated within the package that introduce an induced magnetization dependent upon their orientation to earth's field, from other magnetized objects (i.e., batteries) also within the package, and finally, from fixed external structures such as those encountered with any vehicle-mounted compass. Fortunately, we have found that our formulation compensates for both sensor errors and magnetic perturbations simultaneously and thereby eliminates the need for separate treatment.

The calibration approach proceeds with the following manipulation of vector quantities.

The magnetometer output, the measured fields  $H_{\text{measured}}$ , are given by:

$$\begin{aligned} H_{\text{measured}} &= H_{\text{earth}} + H_{\text{perm}} + H_{\text{induced}} \text{ (heading error)} \\ &= H_{\text{earth}} + H_{\text{perm}} + M \cdot H_{\text{earth}} \\ &= H_{\text{perm}} + K \cdot H_{\text{earth}} \text{ with } K = (I + M) \end{aligned}$$

Under ideal conditions,  $H_{\text{measured}} = H_{\text{earth}}$ , and the heading can be calculated from the measured horizontal components. However,  $H_{\text{perm}}$  is a constant term that arises from some residual permanent magnetization of box components, and it rotates with the case.  $H_{\text{induced}}$  is a term induced by earth's field magnetizing some package components, and its magnitude and direction changes with the orientation of the package. The values for  $H_{\text{perm}}$  and  $K$  and some form of calibration procedure to obtain them are needed for compensation. These values can be obtained by doing an eight-point compass swing and recording the measured values internally. For the sake of brevity, we do not describe the mathematics for obtaining the coefficients  $H_{\text{perm}}$  and  $K$  from the calibration measurements.

In practice, the compass calibration typically requires that the compass be carefully leveled while measurements are made at the

eight cardinal points (0, 45, 90, 135, 180, 225, 270, and 315 deg). This can be done by placing the compass on a test fixture that accurately selects the eight orientations. High accuracy is not required. A sampling loop generated in software rejects the magnetometer data until the device is indeed level. This forces the calibration coefficients to be computed from values not distorted by tilt.

The magnetic compensation formulation is: Given values for the compensation coefficients  $H_{\text{perm}}$  and  $K$ , then the compensated values for earth's field are given by inversion of the above expression:

$$H_{\text{earth}} = K^{-1} \cdot (H_{\text{measured}} - H_{\text{perm}}) = L \cdot (H_{\text{measured}} - H_{\text{perm}})$$

where  $L = K^{-1}$  is the inverse of  $K$ . Values for  $H_{\text{perm}}$  and  $L$  are stored and used repeatedly until they are replaced by a new set of values from a recalibration.

### Temperature Compensation

Sensor offset bias and linearity often show a temperature dependence. Unfortunately, these effects can also result in erroneous heading information if no precautions are taken. Honeywell has devised a proprietary switched-magnetization technique that separates the temperature-induced errors from magnetic sensing errors, thereby allowing the sensor drifts due to temperature to be canceled out. This process has been successfully demonstrated in past compass applications.

### Compass Performance

As stated above, compass errors arise from package-induced magnetic effects and from scale factor and alignment errors within the sensors themselves. Figure 5 shows compass measurements taken before and after the magnetic calibration process. Shown in trace A is a precalibration scan where a nearby source of magnetic distortion results in compass errors ranging from -6 to +8 deg. Following a calibration run with the distortion still in place, trace B now shows accuracies within  $\pm 1$  deg for the total 360-deg scan. Clearly, this type of calibration is necessary for reliable compass operation when attached to or positioned near ferrous materials (i.e., vehicle platforms).

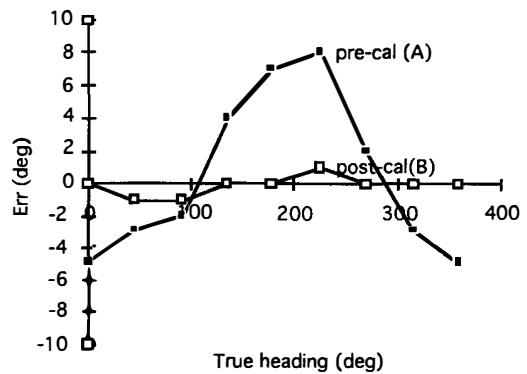


Figure 5. Compass Calibration Plots

Magnetic heading can be defined as the direction of earth's field measured in a horizontal reference plane. However, the elimination or lack of a gimbal means that the magnetic sensors can no longer be assumed to be horizontal. When the three magnetometers that detect their respective components of earth's field are incorrectly assumed to be level, the erroneous field magnitudes they measure will be applied to the calculation of magnetic heading. These incorrect field measurements cannot help but lead to an incorrect compass heading.

We determined that a *calibration* done with an intentional tilt of as little as 1 deg subsequently introduced compass errors of up to 6 deg during later measurements; that is, an incorrect set of calibration and compensation measurements was generated. At this point, our tilt compensation has been demonstrated successfully for normal handheld operation with a single horizontal calibration. In fact, with these calibration and compensation routines, our solid-state compass continued to perform with better than 1-deg accuracy over a variety of tests and field experiments where nominal handheld tilt angles ranged to  $\pm 5$  deg. Unfortunately, the laboratory measurements shown in Figure 6 confirm that tilts ranging to  $\pm 30$  deg will require a more complete development of our tilt compensation routines.

### Conclusions

A solid-state nongimbaled compass has been developed from Honeywell's MR sensors with the inclusion of a three axis accelerometer to measure the tilt orientation. We have found under conditions of handheld operation that the device provides heading accuracies of  $\pm 1$  deg. Furthermore, the response time of this device is currently limited only by the switching period of the electronics that switch the materials magnetization vector. We can easily

sample magnetic heading in excess of 50 Hz. This rapid response time lets us avoid the typical time delays encountered in other compassing devices while waiting for the gimbals to settle out. The development of our nongimbaled solid-state compass significantly enhanced the performance of the personal navigator and resulted in very consistent and reliable heading accuracies.

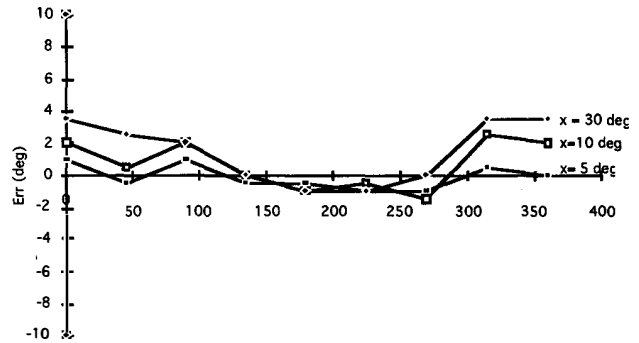


Figure 6. Compass Measurements in the Presence of Tilt

# BULK-SILICON TUNNELING-BASED PRESSURE SENSORS

Chingwen Yeh and Khalil Najafi

Center for Integrated Sensors and Circuits  
Solid-State Electronics Laboratory  
Department of Electrical Engineering and Computer Science  
University of Michigan  
Ann Arbor, Michigan 48109-2122

## ABSTRACT

This paper discusses the development, design, fabrication, and testing of bulk-silicon tunneling-based pressure sensors. A boron etch-stop bulk-silicon dissolved wafer technology is used for the fabrication of two levels of silicon and one level of glass. The first silicon wafer is used to form a boron-doped, thin, and free standing cantilever beam to support a tunneling tip made from platinum, while a second silicon wafer is used to form a boron-doped pressure-sensitive diaphragm and to act as a counter-electrode for sustaining a tunneling current to the tip located on the beam. A glass wafer is used to support a metal electrode for electrostatic deflection of the beam, and the two boron-doped silicon microstructures. The deflection in the diaphragm brought about by pressure change modulates the tunneling current that provides an indication of pressure change. The fabrication technology allows the implementation of a variety of sensor designs with different dimensions and thicknesses for the diaphragm and the support beam, thus allowing the development of practical low-voltage tunneling-based pressure sensors. Several sensors have been fabricated using this technology. One design utilizes a  $700 \times 700 \times 3.5 \mu\text{m}^3$  diaphragm and a straight beam  $3.5 \mu\text{m}$  thick to measure pressures from 1mTorr to 10Torr and provides a current sensitivity to pressure of  $0.2 \text{nA/mTorr}$ .

## INTRODUCTION

Development of high sensitivity and large dynamic range sensors has become an important goal for different application areas, including transportation, biomedicine, space, and avionics. Among parameters that need to be measured with high resolution and sensitivity using a small sensor are pressure and acceleration. During the past decade a number of very sensitive capacitive pressure sensors have been developed [1,2]. These capacitive sensors are simple in structure and fabrication and utilize very thin ( $< 1 \mu\text{m}$ ) and large area diaphragms (a few mm on a side) to improve sensitivity to pressure changes. Improvements in fabrication technology and capacitance measurement techniques have allowed these sensors to continually provide improved performance and reliability. Recently a new category of sensors has been developed by researchers at JPL that utilize the tunneling current between a tunneling tip and a moveable diaphragm or beam to sense their deflection [3,4]. These tunneling-based sensors are potentially more sensitive, smaller, and have a larger dynamic range than conventional capacitive and piezoresistive sensors since the tunneling current is a very sensitive function of the separation distance between the tunneling tip and counter electrode (which is typically a movable microstructure). Although tunneling-

based sensors can produce sensitivity that approaches or exceeds that of the capacitive designs, one of more interesting features is that they can do so without the need for either super thin or large area diaphragms or beams. This feature obviously simplifies the fabrication of the necessary microstructures and potentially improves uniformity and yield. Prototypes of accelerometers and infrared detectors based on the tunneling current have been fabricated using conventional bulk-silicon micromachining technology [3,4]. However, the fabrication technologies used do not allow the full potentials of these tunneling sensors to be realized because the final devices have been typically large, require double-sided processing of several silicon wafers, and do not provide the needed reproducibility and uniformity. This paper presents the development and fabrication of tunneling-based pressure sensors using a bulk-silicon boron-doped dissolved wafer process [5]. The fabrication technology and device structure allow the implementation of pressure sensors with mTorr sensitivity in a small area, and provide flexibility in setting device characteristics by changing process and layout parameters. In the following we will discuss the proposed sensor structure and operation, analytical design and modeling of sensor performance and characteristics, the dissolved-wafer fabrication technology, and will finally present preliminary measurement results.

## SENSOR STRUCTURE AND OPERATION

The bulk-silicon tunneling-based pressure sensors incorporate two levels of silicon and one level of glass as shown in Fig. 1a. The first silicon is formed as a cantilever beam supporting a tunneling tip, and the second silicon is formed as a thin diaphragm, which can be deflected by external pressure. The glass substrate supports a metal electrode and is used to deflect the beam down using electrostatic attraction. Initially, the beam is deflected up, by applying a tunneling voltage,  $V_{\text{tun}}$ , between it and the diaphragm and producing an equivalent electrostatic force,  $P_b$ , to bring the tip close enough to the diaphragm and to cause electron tunneling from the tip to the counter-electrode on the diaphragm, as shown in Fig. 1b. When an external pressure  $P$  is applied, the diaphragm deflects, and the tunneling current will change at a constant  $V_{\text{tun}}$ . The sensor can be operated in a closed-loop mode when needed. In this mode the tunneling current is kept constant when the diaphragm moves by applying an appropriate deflection voltage,  $V_{\text{def}}$ , between the beam and deflection electrode. The deflection voltage generates an electrostatic pressure,  $P_d$ , which counters the external pressure, and can be tuned to compensate for the pressure change and maintain a constant tunneling current, thereby a constant separation between the tip and diaphragm (the tunneling voltage remains unchanged). Pressure changes can be measured by reading out the deflection voltage.

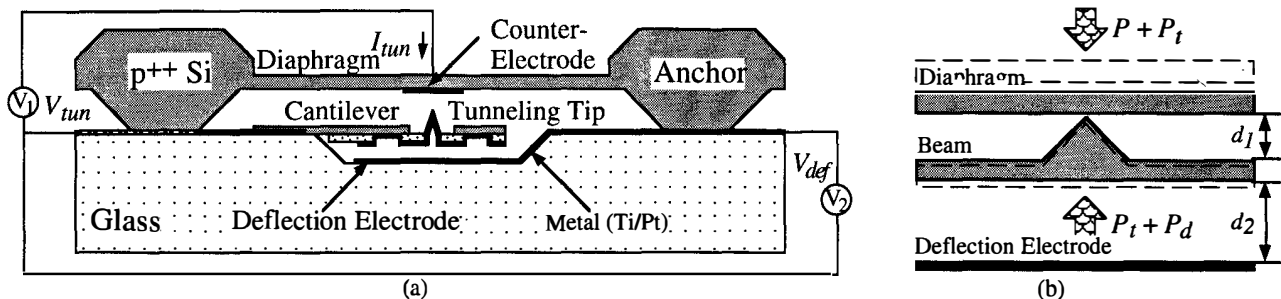


Figure 1: Structure and operation of a two-level bulk-silicon tunneling-based pressure sensor implemented using the dissolved wafer process.

## ANALYTICAL DESIGN AND MODELING

In order to analyze the performance of the sensor and its pressure sensitivity, analytical and finite element modeling has been performed. The following provides simple analytical equations to study the performance of the sensor. For these calculations, we consider one of the sensor designs that have been fabricated. The sensor incorporates a straight cantilever beam 400 $\mu\text{m}$  long, 14 $\mu\text{m}$  wide, and 3.5 $\mu\text{m}$  thick, and a thin boron-doped diaphragm that is 700x700x3.5 $\mu\text{m}^3$ . The target pressure range for the sensor is from 1mTorr to 10Torr. The operating voltages are less than 20V and the target tunneling current is around 1 $\mu\text{A}$ .

For a rigidly clamped square diaphragm, which is free from built-in stress, the approximate load-deflection characteristic is given by [1]:

$$p \cong \frac{E}{1-\nu^2} \frac{h_d^4}{a^4} \left( \frac{4.20d_c}{h_d} \right) \quad (1)$$

where  $p$  is the uniform applied pressure,  $E = 1.88 \times 10^{11}$  N/m<sup>2</sup> is the Young's modulus,  $\nu = 0.3$  is the Poisson's ratio,  $a$  is half of the width and length of the diaphragm,  $h_d$  is the diaphragm thickness, and  $d_c$  is the central bending of the diaphragm, which is calculated to be about 1 $\mu\text{m}$  at a pressure of 10Torr. The separation of the beam from the diaphragm is 2 $\mu\text{m}$  and the tip extends 1 $\mu\text{m}$  above the beam. The amount of deflection of the free end of the beam,  $s$ , under electrostatic attraction can be calculated from [6]:

$$s = \frac{3wL^4}{2Ebh_b^3} \quad (2)$$

where  $w$  (force per unit length) is the uniform load on the straight beam.  $L$ ,  $b$ , and  $h_b$  are the length, width, and thickness of the straight beam. In addition, the applied force per unit length,  $w$ , is [7]:

$$w = \frac{\epsilon_0}{2} \left( \frac{V_{tun}}{d_1} \right)^2 b \quad (3)$$

where  $\epsilon_0$  is the permittivity of free space,  $V_{tun}$  is the applied voltage between the straight beam and diaphragm, and  $d_1$  is the separation of the straight beam from the diaphragm. An applied force per unit length of  $3 \times 10^{-3}$  N/m (corresponding to a voltage of 15V) can deflect the free end of the straight beam up 1 $\mu\text{m}$ . Consequently, the applied voltage between the beam and diaphragm, which can produce an electrostatic force large enough to bring the tip close to the diaphragm to establish the tunneling current, is less than 20V. Similarly, the separation of the beam from the deflection electrode is 2 $\mu\text{m}$  such that the deflection voltage between the beam and deflection electrode required to bring the beam down and respond to external pressure is also less than 20V.

As mentioned above, when pressure is applied on the diaphragm, the sensor is operated at a constant  $V_{tun}$  and  $I_{tun}$  by tuning  $V_{def}$  to keep the tunneling gap unchanged in the closed-loop mode. Assuming that the deflection of the beam by  $V_{def}$  is much less than the separation of the beam from the deflection electrode, the  $P$ - $V_{def}$  characteristic of the sensor can be calculated:

$$p \cong \frac{4.20}{1-\nu^2} \frac{h_d^3}{a^4} \left( \frac{3\epsilon_0 w L^4}{4h_b^3} \right) \left( \frac{V_{def}}{d_2} \right)^2 \quad (4)$$

where  $d_2$  is the separation of the straight beam from the deflection electrode. The  $P$ - $V_{def}$  curve is plotted in Fig. 2 and a sensitivity of about a few mV/mTorr can be obtained theoretically.

## FABRICATION

The fabrication process is shown in Fig. 3. Two p-type (100) silicon wafers of moderate doping ( $>1\Omega\text{-cm}$ ) and one #7740 Corning

glass wafer are used in a ten-mask process (four masks for each of the silicon wafers and two masks for the glass wafer). First, the first silicon wafer is subjected to a masked shallow boron diffusion (3 $\mu\text{m}$ ) at 1175 $^\circ\text{C}$  for about one hour to define the beam thickness; the tip area is left undoped. An anisotropic etching using ethylenediamine-pyrocatechol-water (EDP) follows to form a pyramidal cavity about 4.5 $\mu\text{m}$  deep. EDP instead of KOH is used because the former has better etching selectivity between doped and undoped silicon. Silicon dioxide is deposited on the beam and patterned to prevent short circuiting of the beam to the metal electrode on the glass substrate. Next the tip metal (30nm Ti/50nm Pt/ 200nm Au) is evaporated into the pyramidal cavity, and lifted off from the field regions to form the tunneling tip. This produces a sharp tip that is suitable for these tunneling applications, since a super sharp tip is not required [3,4]. Finally, reactive ion etching (RIE) utilizing a mixture of SF<sub>6</sub> and O<sub>2</sub> at a pressure of 5mTorr and a power density of 60mW/cm<sup>2</sup> is used to define the shape of the beam with smooth and nearly vertical sidewalls. The etching rate is about 80-85nm/min and etching must traverse entirely through the boron diffused areas into the undoped silicon. A 150nm thick aluminum is used as a mask for etching. Processing of the second silicon wafer starts by creating a recess in it using KOH. This recess has a depth of about 5 $\mu\text{m}$  and defines the cavity height. Two boron diffusions follow; the first is a 12-15 $\mu\text{m}$  deep diffusion, which defines the bond anchor, and the second is a shallow diffusion (3.5 $\mu\text{m}$ ), which determines the thickness of the diaphragm [8]. The multi-metal system used for the first silicon wafer is evaporated and lifted off from the field regions to form the counter-electrode.

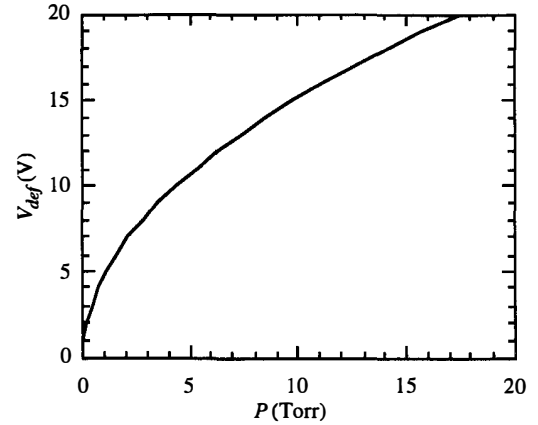


Figure 2: Theoretical relationship between the readout voltage  $V_{def}$  and pressure for the sensor.

For the glass wafer, a 2 $\mu\text{m}$  recess is etched using HF:H<sub>2</sub>O to form a cavity under the tunneling beam. Positive photoresist cannot be used directly as a mask for an etching depth of over 1 $\mu\text{m}$  due to attack and peeling by the hydrofluoric acid. A 25nm chromium layer is deposited between the glass and photoresist to improve adhesion. Then 30nm of Ti and 70nm of Pt are evaporated and lifted off from the field regions to define the deflection electrode. In order to facilitate the electrostatic bonding, an 80nm shallow recess is etched using buffer HF before metal evaporation to limit the protrusion of metal above the glass to about 20nm to establish a good Pt/Ti ohmic contact (a few hundred ohms for a 50 x 50 $\mu\text{m}^2$  area) with the boron-doped silicon after electrostatic bonding.

Before electrostatic bonding, all silicon and glass wafers are solvent cleaned. In addition, the silicon wafers are thinned down to about 150 $\mu\text{m}$  using HF-nitric-acetic acid to reduce etching time in EDP. The first electrostatic bond between the first silicon and the glass is performed at 400 $^\circ\text{C}$ , with 1000V applied across the silicon-glass sandwich. The bonded sandwich is then immersed in EDP to dissolve the undoped silicon away and leave the heavily boron-doped beams resting on the glass. The glass with the first level of silicon is subjected to another organic clean and placed in BHF for a few seconds to remove Ti (Pt exposed) on the tip for bonding to the second silicon. The second silicon is aligned and bonded at a temperature of 420 $^\circ\text{C}$  such that the diaphragm and anchor region can

cover the beam that has been bonded on the glass. Another EDP etching releases the diaphragm and the fabrication is completed.

Figure 4a shows the SEM view of a straight beam supporting a tunneling tip. Figure 4b and 4c show closer SEM views of the sharp tunneling tip. Figure 4d shows the SEM view of a two-level bulk-silicon tunneling-based pressure sensor, where the diaphragm is cut in half to allow observation of the straight beam. The diaphragm is about 700 $\mu\text{m}$  on a side and the cantilever beam is 400 $\mu\text{m}$  long.

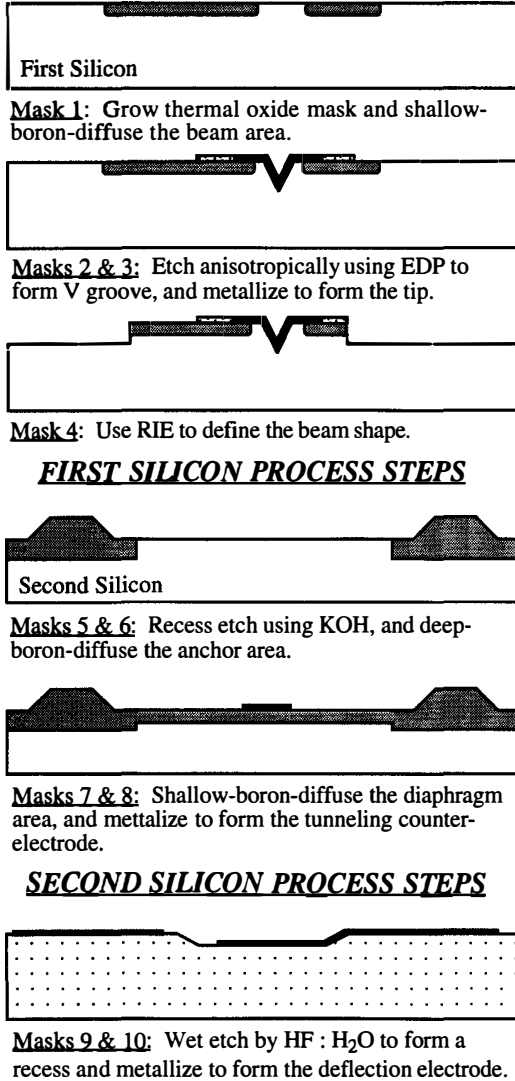


Figure 3: Fabrication sequence for the bulk-silicon tunneling-based pressure sensor.

### EXPERIMENTAL MEASUREMENTS AND TESTS

Experimental measurements were carried out at several points in the process. Before the second silicon bond, capacitance change between the beam and deflection electrode as a function of the deflection voltage was measured using an HP 4194A gain-phase/impedance analyzer to be 0.35fF/V, and the pull-in voltage was measured to be 13.5V. After the second silicon bond, capacitance change between the beam and diaphragm as a function of the tunneling voltage was also measured to be 0.34fF/V.

After device fabrication, the full electrical characteristics of the device were measured using the HP-4145B semiconductor parameter analyzer. Figure 5 shows the tunneling current as a function of the tunneling voltage between 0 and 50V as the deflection voltage is

modulated from 0 to 40V. In these measurements the tunneling current is limited to less than 1 $\mu\text{A}$  to avoid accidental damage to the tip, although these tips can tolerate a higher current level. Note that as the deflection voltage is increased, thus pulling the beam away from the diaphragm, the current exponentially reduces. An increase of 10V in either the deflection voltage or the tunneling voltage can produce two orders of magnitude change in the tunneling current.

These measurements are also used to determine the pressure sensitivity of the device, since an appropriate pressure measurement setup that can generate sub-Torr pressure changes cannot be reliably implemented. On the basis of the above  $I$ - $V$  measurement and the equations presented previously, at a tunneling voltage of 22V, the following relationship can be derived from Fig. 5:

$$\frac{\Delta I_{tun}}{\Delta V_{def}} \cong \frac{1\mu\text{A} - 0.03\mu\text{A}}{10\text{V}} = 97\text{nA/V} \quad (5)$$

where  $I_{tun}$  is the tunneling current and  $V_{def}$  is the deflection voltage. One can also show that:

$$\frac{\Delta I_{tun}}{\Delta s} = \frac{\Delta I_{tun}}{\Delta V_{def}} \frac{\Delta V_{def}}{\Delta s} \cong 0.21\text{nA/\AA} \quad (6)$$

where  $d$  and  $V_{def}$  are taken to be 3 $\mu\text{m}$  and 10V respectively. Since a deflection of 1 $\text{\AA}$  in the diaphragm corresponds to an increase of 1mTorr in external pressure, one can obtain:

$$\frac{\Delta I_{tun}}{\Delta P} = \frac{\Delta I_{tun}}{\Delta s} \frac{\Delta s}{\Delta P} \cong 0.21\text{nA/mTorr} \quad (7)$$

The pressure sensitivity of the tunneling current has been plotted in Fig. 6. These data have been obtained from the measured results in Fig. 5 and from the equations discussed previously which are used to convert the deflection voltage to an equivalent pressure. As can be seen from Fig. 6, the tunneling current changes drastically with pressure. Therefore, it is indicated that one needs to operate the sensor at a larger tunneling current to get a higher sensitivity. As a larger pressure change (corresponding to a larger value of the deflection voltage) separates the diaphragm too far from the tunneling tip to result in a considerable tunneling current, the sensitivity of the tunneling current to pressure will become extremely low at a larger pressure range. This apparent reduction in sensitivity of course will not happen in the closed-loop mode because the tunneling current is maintained at a constant value.

Finally, based on the above equations and our measurements, one can also show that the average sensitivity of the deflection voltage to pressure is about 1mV/mTorr, which agrees with the calculations presented before. The results clearly demonstrate that high sensitivity can be obtained using these devices without either super thin or large diaphragms. We are currently conducting tests to determine the long-term stability and temperature sensitivity of these devices.

### CONCLUSION

Tunneling-based pressure sensors have been fabricated using a bulk-silicon dissolved wafer process. The fabrication technology utilizes boron diffusion and boron etch-stop to form a cantilever beam supporting a tunneling tip and a thin pressure-sensitive diaphragm, both of which are attached to a glass substrate. The process is simple, single-sided, and allows the implementation of a variety of pressure sensor designs. These sensors can be operated in both the constant-voltage open-loop mode (where the change in the tunneling current is used to provide an indication of pressure change) and the constant-current closed-loop mode (where the feedback voltage between the beam and deflection electrode can provide an indication of pressure change). The sensitivity and dynamic range of these sensors can be varied over a large range by changing diaphragm and beam dimensions. A sensor with a 10Torr dynamic range was fabricated and tested and provides a current sensitivity of several hundred pA per mTorr, and voltage sensitivity of about 1mV per mTorr (without amplification).

## ACKNOWLEDGMENTS

The authors would like to thank Y. Gianchandani, K. Ma, and A. Selvakumar for useful discussions, and Ms. Terry Hull and W. H. Juan for their assistance in the fabrication and SEM photography. This work was supported by the Advanced Research Projects Agency under Contract # J-FBI-92-149.

## REFERENCES

- [1] H.L. Chau and K.D. Wise, "Scaling Limits in Batch-Fabricated Silicon Pressure Sensors," *IEEE Trans. Electron Devices*, vol. 34, p. 850, April 1987.
- [2] S.T. Cho, K. Najafi, and K.D. Wise, "Internal Stress Compensation and Scaling in Ultrasensitive Silicon Pressure Sensors," *IEEE Trans. Electron Devices*, Vol. ED-39, p. 836, April 1992.
- [3] H.K. Rockstad, T.W. Kenny, J.K. Reynolds, W. J. Kaiser, and T.B. Gabrielson, "A Miniature High-Sensitivity Broad-Band Accelerometer Based on Electron Tunneling Transducers," *Proc. Transducers '93*, Yokohama, Japan, p. 836, June 1993.
- [4] T.W. Kenny, W.J. Kaiser, S. B. Waltman, and J. K. Reynold, "Novel Infrared Detector Based on a Tunneling Displacement Transducer," *Appl. Phys. Letters*, vol. 59, p. 1820, 1991.
- [5] Y. Gianchandani and K. Najafi, "Batch-Assembled Multi-Level Micromachined Mechanisms from Bulk Silicon," *J. Micromech. Microeng.*, vol. 2, UK, p. 80, 1992.
- [6] W.C. Young, *Roark's Formulas for Stress and Strain*, 6th ed., New York: McGraw-Hill, 1992.
- [7] G. Blasquez, P. Pons, and A. Boukabache, "Capabilities and Limits of Silicon Pressure Sensors," *Sensors & Actuators*, vol. 17, p. 387, 1989.
- [8] S.T. Cho, K. Najafi, C.E. Lowman, and K.D. Wise, "An Ultrasensitive Silicon Pressure-Based Flowmeter," *IEEE Trans. Electron Devices*, vol. ED-39, p. 825, April 1992

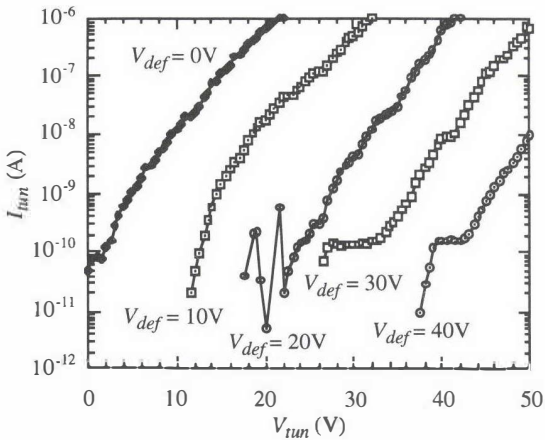


Figure 5: Measured tunneling current as a function of the tunneling and deflection voltages.

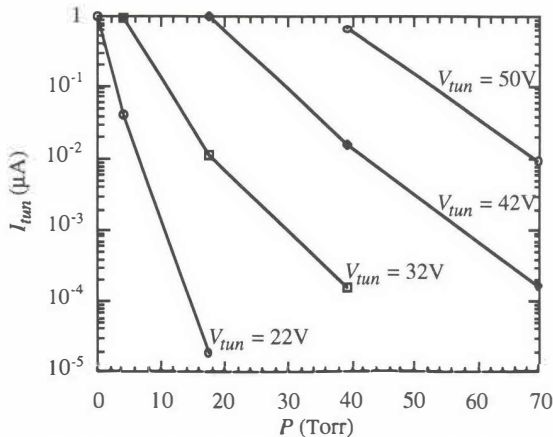


Figure 6: Relation of  $I_{tun}$  with  $P$  at a constant  $V_{tun}$  for the open-loop operation.

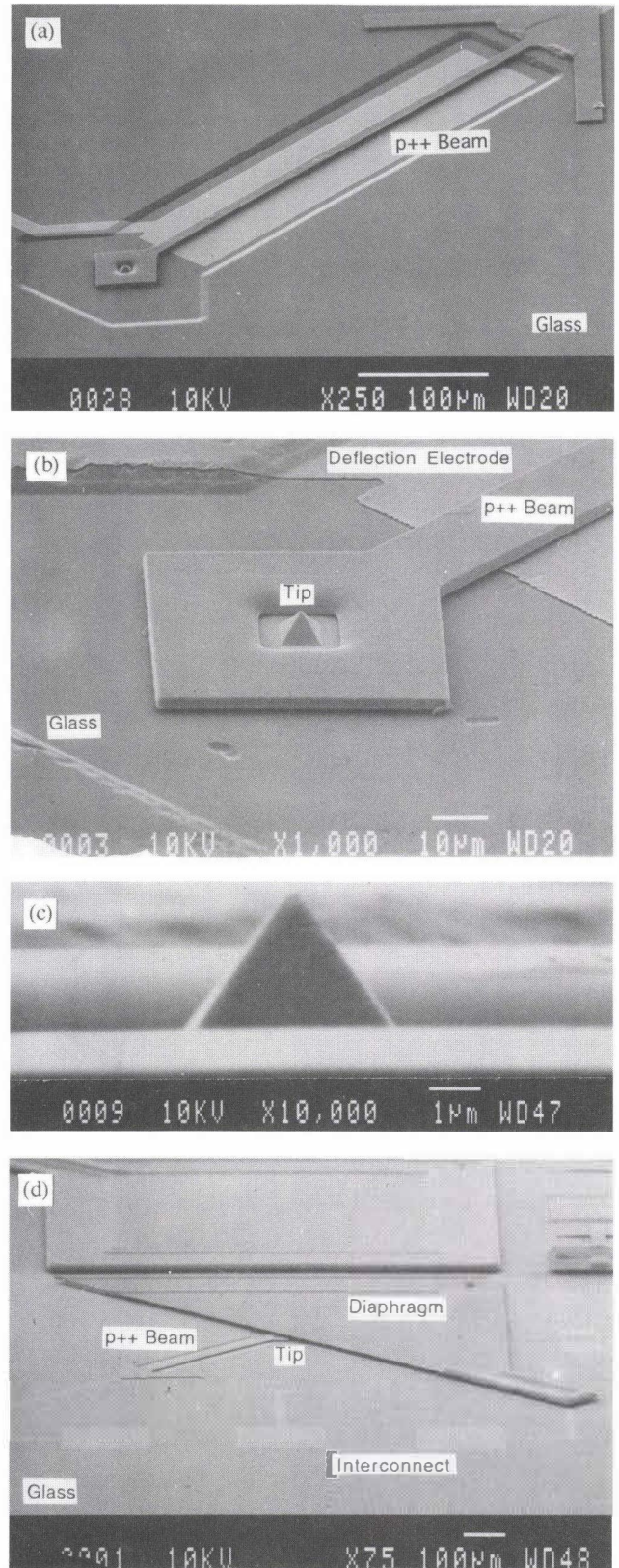


Figure 4: a) SEM view of the  $400 \times 14 \times 3.5 \mu\text{m}^3$  straight beam that supports a tunneling tip; b) and c) magnified SEM views of the sharp tunneling tip made from platinum. The tip protrudes from the upper side of the beam by  $1 \mu\text{m}$ ; d) complete two-level bulk-silicon tunneling-based pressure sensor. The  $700 \times 700 \times 3.5 \mu\text{m}^3$  diaphragm is cut in half to allow observation of the beam.

# AN ULTRA-SENSITIVE CAPACITIVE PRESSURE SENSOR WITH A BOSSED DIELECTRIC DIAPHRAGM

Yafan Zhang and Kensall D. Wise

Center for Integrated Sensors and Circuits  
The University of Michigan  
Ann Arbor, MI 48109-2122

## ABSTRACT

This paper reports the development of an ultra-sensitive pressure sensor for a very small (<5cc) portable microinstrumentation cluster for environmental monitoring and process control. The device utilizes a thin stress-compensated dielectric diaphragm with a silicon boss. For a device with a 2.0mm-diameter 0.3μm-thick diaphragm and a 1.2mm-diameter 3.0μm-thick boss, the measured pressure sensitivity is more than 10,000ppm/Pa (5fF/mTorr), at least five times greater than other recent devices. The minimum resolvable pressure is 0.1mTorr, while the temperature coefficients of the zero-pressure offset and the pressure sensitivity are 910ppm/°C and -2900ppm/°C, respectively. These temperature coefficients can be reduced to 15ppm/°C and -63ppm/°C using digital compensation implemented through a six-term polynomial.

## INTRODUCTION

As micromachining and wafer processing technology have improved, it has become possible to fabricate silicon pressure sensors with steadily-improving sensitivities. Such devices are needed for a broad variety of applications, including microphones for use in hearing aids [1-3], manometers for tracking barometric pressure variations, and instruments for use in automated process control [4]. Some of these applications require the sensors to be physically very small, to respond to very low differential pressures, and yet to operate over a considerable dynamic range. To satisfy these sometimes conflicting requirements, the research reported here has explored the use of a capacitive pressure sensor having an ultra-thin diaphragm and a center boss which serves as the conducting plate. The resulting devices have achieved pressure sensitivities as high as 5fF/mTorr, at least five times higher than other recent devices [1,4]. This paper describes the design approach used and discusses in detail the effects of such factors as diaphragm internal stress, device geometry, ambient temperature, and long-term operating drift. Digital compensation techniques are used for reducing temperature effects, and the present pressure resolution is compared to fundamental noise limits.

## DESIGN AND FABRICATION

To achieve high sensitivity and wide operating range in a micromachined capacitive pressure sensor, one possible design approach is to use an ultra-thin diaphragm with a center boss. This approach has several advantages: 1) An ultra-thin diaphragm offers very high sensitivity; 2) A center boss enlarges the operating range and yields improved linearity; and 3) A nearly parallel-plate capacitor is obtained using the center boss. It is difficult, however, to analyze and optimize this structure. Earlier work [5] has expressed the center deflection of a circular diaphragm having a center boss as:

$$y = A_p \left( \frac{Pa^4}{Eh^3} \right) \quad (1)$$

$$A_p = \frac{3(1-\nu^2)}{16} \left( 1 - \frac{b^4}{a^4} - 4 \frac{b^2}{a^2} \log \frac{a}{b} \right) \quad (2)$$

where  $y$  is the center deflection,  $P$  is the applied pressure,  $E$  is Young's modulus for the diaphragm material, and  $a$  and  $h$  are the radius and the thickness of the diaphragm, respectively.  $A_p$  is a stiffness coefficient which is a function of the so called "solidity ratio of boss and diaphragm radii" ( $b/a$ ). In (2),  $\nu$  is Poisson's ratio and  $b$  is the boss radius. These two equations, however, assume that the diaphragm deflects linearly with applied pressure. In addition, they do not account for effects due to a finite diaphragm boss thickness and internal stress.

To accurately predict the device performance so an optimum design could be achieved with respect to both high sensitivity and dynamic range, an approach based on the finite-element method (FEM) was adopted in this work. An FEM software tool, CAEMEMS-D [6], was used to search for the best combination of the center boss dimension and the diaphragm thickness. The analysis has led to the following findings: 1) The linearity of the load-deflection characteristic improves as the boss thickness increases. This improvement is minor when the boss thickness is less than five times the diaphragm thickness but becomes significant when the boss thickness is about ten times the diaphragm thickness because with that thickness ratio, the center boss can, like a plate, deflect uniformly under load. 2) There is a trade-off in selecting the best solidity ratio ( $b/a$ ) because it affects both the operating range and the pressure sensitivity. The center boss is designed to serve as a conducting plate for the capacitive pressure sensor; hence, when it is too small, a smaller than desired output signal ( $\Delta C$ ) results. On the other hand, too high a solidity ratio can make the diaphragm too stiff, degrading the sensitivity. After many design-simulation iterations, a near-optimum design was obtained which achieves high sensitivity, appropriate diaphragm rigidity, and a large output signal. In this design, the device has a gap of 2.76μm. The diaphragm is circular, 2mm in diameter, and 0.3μm in thickness. The center boss is also circular with a 1.2mm-diameter and a thickness of 3μm.

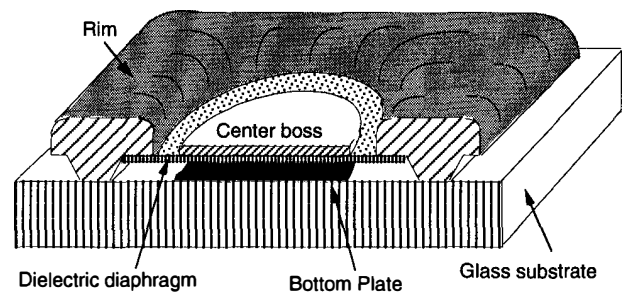


Fig. 1: A three-dimensional view of the ultra-sensitive capacitive pressure sensor

Figure 1 provides a three dimensional view of the capacitive pressure sensor. The device is composed of a glass base with patterned metal electrodes and an ultra-thin diaphragm with a center boss. The device is fabricated using a six-mask silicon bulk-micromachined dissolved-wafer process. The rim of the device is first defined using a deep boron diffusion, after which the recess defining the capacitor gap is formed by dry etching. The center boss is formed using a shallow boron diffusion, and the dielectrics which

form the diaphragm are deposited by LPCVD ( $\text{Si}_3\text{N}_4\text{-SiO}_2\text{-Si}_3\text{N}_4$ , 600Å/1800Å/600Å) and patterned using dry etching. The wafer is then metallized to connect the center boss to the chip rim, inverted, and anodically bonded to the metallized glass plate. The device is then completed using an unmasked etch in EDP to remove the portions of the silicon wafer that are not etch-stopped. The top view of an actual device is shown in Fig. 2.

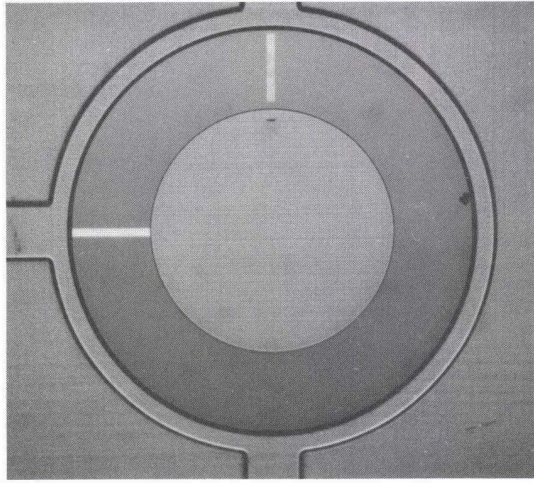


Fig. 2: Top view of a device having a 2mm diaphragm diameter

## DEVICE PERFORMANCE

### Device Linearity and Pressure Sensitivity

This ultra-sensitive capacitive pressure sensor design has been extensively tested. Figure 3 shows the measured capacitance change versus applied pressure. As can be seen, the capacitance change is highly linear because of the design of the center boss. Since the boss is ten times as thick as the diaphragm, most of the diaphragm deformation comes from stretching and bending of the dielectric layer. The minimum measured pressure sensitivity of the device is 5fF/mTorr, and the equivalent boss deflection is 25Å/mTorr. The minimum resolvable pressure is 0.1mTorr. The operating range of the device has been studied from 0 to 1000mTorr (0 - 130 Pa), which covers the range of sound pressure levels [7] and complements existing barometric devices.

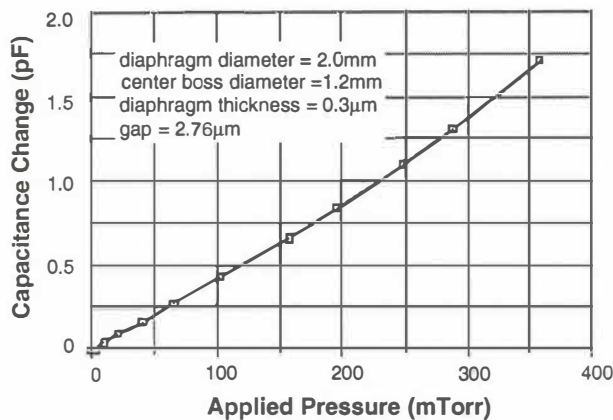


Fig. 3: Capacitance change versus applied pressure for a pressure sensor with a 2mm-diameter circular diaphragm

### Diaphragm Internal Stress and Pressure Sensitivity

To investigate the effect of diaphragm internal stress on pressure sensitivity for an ultra-thin diaphragm with a center boss, the device has been compared with another fabricated device in which the diaphragm was formed using a two-dielectric sandwich of  $\text{Si}_3\text{N}_4\text{-SiO}_2$  (2100Å/900Å). As an approximation, the average internal stress for the composite diaphragm structure is given by [8]:

$$\sigma_{\text{avg}} = \frac{\sigma_1 h_1 + \sigma_2 h_2}{h_1 + h_2} \quad (3)$$

where  $\sigma_1$  is the internal stress for  $\text{Si}_3\text{N}_4$ ,  $\sigma_2$  is the internal stress for  $\text{SiO}_2$ , and  $h_1$  and  $h_2$  are the corresponding layer thicknesses.

The calculated internal stress of the diaphragm for the ultra-sensitive device is only 60MPa, a stress level compatible with that for boron-doped silicon (40MPa), whereas the internal stress of the second diaphragm is 575MPa, about ten times higher. Figure 4 shows the measured capacitance change as a function of applied pressure for these two devices. As can be seen, the pressure sensitivity is 5fF/mTorr for the ultra-sensitive device and only 0.33fF/mTorr for the second device. The gap difference accounts for about a factor of two in this sensitivity reduction, while the increased diaphragm internal stress is responsible for a factor of more than seven.

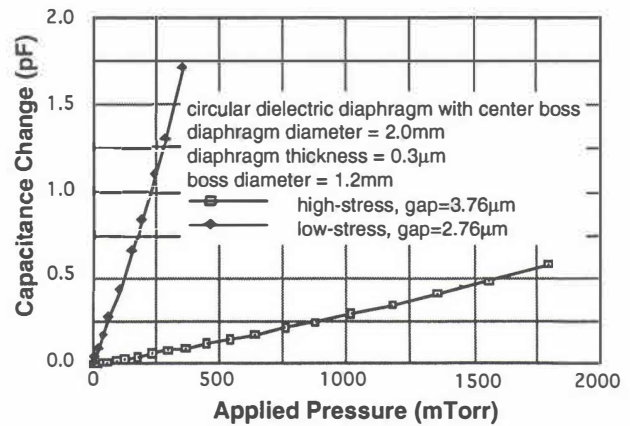


Fig. 4: Capacitance change vs. applied pressure for two capacitive pressure sensors with different diaphragm internal stress

Another important observation is that the device with a  $\text{Si}_3\text{N}_4\text{-SiO}_2$  diaphragm structure also exhibited a large zero-pressure offset. A possible explanation is that when  $\text{SiO}_2$  is deposited on top of the  $\text{Si}_3\text{N}_4$  layer, the internal stress gradient in the thickness direction in the composite diaphragm will change from tensile on the top to compressive on the bottom (near the glass). When the diaphragm is released from its silicon substrate, a deformed diaphragm results due to this stress distribution in the diaphragm thickness direction, leading to a large zero-pressure offset. On the other hand, the zero-pressure offset observed for the ultra-sensitive device using the balanced  $\text{Si}_3\text{N}_4\text{-SiO}_2\text{-Si}_3\text{N}_4$  diaphragm has been negligible.

### Device Geometry and Pressure Sensitivity

For a device with a given diaphragm thickness and internal stress level, the size of the diaphragm and the capacitive gap distance become the main factors affecting the pressure sensitivity. To investigate these effects, the ultra-sensitive device was compared with a similar device which differs only in its diaphragm and boss diameters (1.5mm and 0.9mm). The measured pressure sensitivity is 5fF/mTorr for the ultra-sensitive device and 1.83fF/mTorr for the smaller diaphragm, reflecting a 63.4% loss for a 0.5mm reduction in

the diaphragm diameter. This sensitivity loss is less than 83.5% calculated using Eqs. (1) and (2) in which the diaphragm internal stress and the boss thickness are ignored.

To study the effect of device gap changes on the pressure sensitivity, the ultra-sensitive device and a similar device with a larger gap (4.76 $\mu$ m) were compared. The minimum pressure sensitivity measured is only 1.25fF/mTorr for the second device. The pressure sensitivity therefore drops by 75% when the gap is increased by 2 $\mu$ m. According to the pressure sensitivity definition:

$$S_{cap} = \frac{1}{C_0} \frac{\Delta C}{\Delta P} \quad (4)$$

where  $\Delta C$  and  $\Delta P$  are the changes in capacitance and pressure, and  $C_0$  is the zero-pressure capacitance. The calculated pressure sensitivity drop here is 69.9% as the gap changes from 2.76 $\mu$ m to 4.76 $\mu$ m. The experiment results are thus in good agreement with the theory. To achieve very high sensitivity, the gap should be designed to be as small as possible, consistent with dynamic range requirements.

### Temperature and Pressure Sensitivity

The pressure sensitivity and accuracy of a capacitive pressure sensor can easily be degraded due to operating temperature changes which are often not controllable. To study these temperature effects, a representative device was tested from 25°C to 100°C. Figure 5 illustrates the capacitance change as a function of applied pressure for different temperatures. An increase in temperature causes the response to decrease, probably due to the increasing diaphragm internal tensile stress as well as the thermal expansion of the glass base. According to [9], the thermal expansion coefficients for SiO<sub>2</sub>, Si<sub>3</sub>N<sub>4</sub>, and glass are 0.5x10<sup>-6</sup>/°C, 2.8x10<sup>-6</sup>/°C, and 3.2x10<sup>-6</sup>/°C, respectively. Since Si<sub>3</sub>N<sub>4</sub> possesses a tensile stress on silicon and SiO<sub>2</sub> is compressive, the larger thermal expansion coefficient in Si<sub>3</sub>N<sub>4</sub> results in a larger tensile stress in the diaphragm as temperature increases. Similarly, because the silicon rim is anchored to the glass base, the larger thermal expansion coefficient in the glass base induces additional tensile stress onto the diaphragm. Although these temperature effects are undesirable, the responses are repeatable; hence, they can be minimized using digital compensation techniques [10].

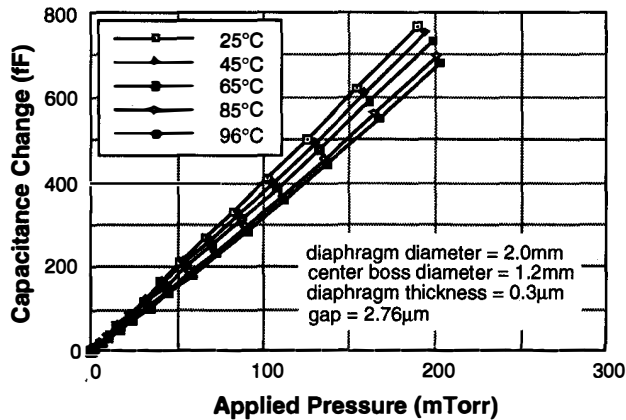


Fig. 5: Capacitance change versus applied pressure for a 2mm diameter diaphragm at temperatures from 25°C to 100°C.

### Long-Term Stability

The nature of its application as a precision measurement device requires that an ultra-sensitive pressure sensor be stable during its operating lifetime, meaning that its response surface does not move beyond a given tolerance range. In order to evaluate the stability of the fabricated sensor, a long-term test has been conducted

on a representative device. In the test, a periodic square pulse (voltage) was applied to the diaphragm to induce deflection electrostatically. The pulses were equivalent to an applied pressure of 200mTorr. Alternating positive and negative square pulses were used so that any charge built up in the device during charging and discharging could be eliminated. The device was tested continuously for 1.93 million pulse cycles at a frequency of 1.49Hz. The capacitance versus applied pressure response was examined before and after the test; no noticeable change was found in the device response surface (zero-pressure offset or sensitivity). Any changes were less than the 0.05mTorr resolution imposed by the measurements, indicating that the dielectric diaphragms are mechanically stable, at least when operated over a limited pressure range (0-1000mTorr).

### DIGITAL COMPENSATION

As discussed earlier, the capacitance response of the sensor is affected by temperature. Such an effect constitutes a shift in the response surface. Since the device is very sensitive and is designed for use over a low range of pressures, even a small amount of offset or drift in the response surface can be very detrimental to its performance. To correct the device response for temperature variations, digital compensation techniques have been used with this sensor. As a first step, the device was fully tested over a pressure range of 0-500mTorr and over a temperature range from 25°C to 100°C using a total of 80 test points. The measurement data were then analyzed using a statistical software package, RS/1, and were fitted with a quadratic model using multiple variable regression. Through analysis, the device compensation model was generated as a function of both the applied pressure and temperature:

$$C_{reg}(P,T) = 3.537068 + 0.004158P + 0.003795T - 0.000010P \cdot T + 9.542191 \times 10^{-7}P^2 - 0.000004T^2 \quad (5)$$

where  $C_{reg}$  (in pF) is the predicted capacitance from this model,  $P$  (in mTorr) is the applied pressure, and  $T$  (in °C) is the external temperature. Figure 6 is a plot of the uncompensated response surface for the device with respect to both applied pressure and temperature. The device was digitally compensated, reducing the temperature coefficient of sensitivity from -2900ppm/°C to -63ppm/°C (0.05mTorr) over all the measurement points. The temperature coefficient of zero-pressure offset was reduced from 910ppm/°C to 15ppm/°C.

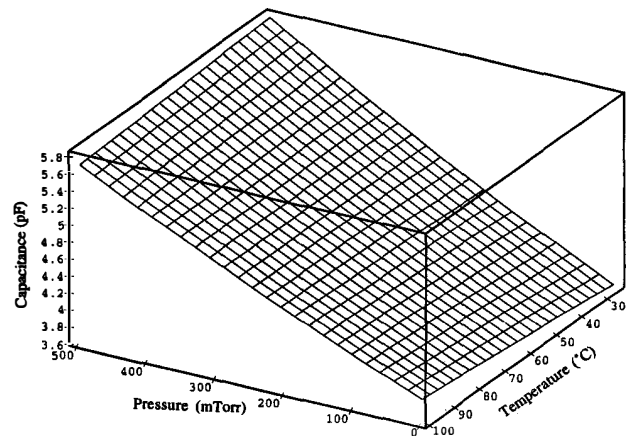


Fig. 6: Response surface of the ultra-sensitive pressure sensor

### NOISE ESTIMATION

When developing an ultra-sensitive pressure sensor, the effects of noise should be estimated as a measure of how much

further it is feasible to consider pushing the response of such a device. In our study, three important types of noise have been considered: Brownian noise,  $kT/C$  noise, and noise induced by voltage source (readout) variations. Brownian noise is mechanical-thermal noise resulting from the thermal agitation of molecules bombarding the diaphragm. The diaphragms of ultra-sensitive capacitive pressure sensors are especially susceptible to this type of noise. Since this molecular agitation of the medium surrounding the diaphragm creates local variations in pressure, it determines the minimum pressure resolution possible for a given measurement. The two-side power spectral density of the pressure fluctuation in the medium due to the thermal noise is defined as [11-13]:

$$\frac{S_p(f)}{\delta f} = \frac{2\pi k T \rho f^2}{c} \quad (6)$$

where  $f$  is the frequency,  $k$  is the Boltzmann's constant,  $T$  is the absolute temperature, and  $\rho$  and  $c$  are the density and the speed of sound in the medium. As can be seen, the power spectral density of the pressure fluctuation is strongly frequency-dependent. It has been calculated that the root-mean-square thermal-noise pressure in air at room temperature and ambient pressure over the audio-frequency band (20-20KHz) is only  $4.2 \times 10^{-3} \mu\text{Torr}$ . Therefore, this noise can be neglected for low frequency applications.

The second type of thermal noise arises from the thermal agitation of the free electrons in an electrical conductor. For a capacitive pressure sensor, the spectral density of the thermal-noise voltage appearing across the sensor is given by [14]:

$$\frac{v_t^2}{\delta f} = \frac{4kTR}{1 + (\omega CR)^2} \quad (7)$$

where  $k$  and  $T$  have the same definition as above,  $R$  is the resistance,  $\omega$  is the angular frequency, and  $C$  is the capacitance from the sensor. The total mean-square noise voltage across the device throughout the complete frequency spectrum is  $kT/C$ . It can be calculated that the root-mean-square thermal-noise voltage at room temperature is  $0.034\text{mV}$ , which reflects a pressure fluctuation of  $0.001\text{mTorr}$ . This noise therefore does not limit the performance of the device studied here since it is two orders of magnitude lower than the minimum device resolution.

The third noise source arises from the bias voltage applied to the pressure sensor during readout. The resulting electrostatic pressure acting on the diaphragm during readout is a function of this bias voltage. It is estimated that the fluctuations in this bias voltage can be controlled to well below  $1\text{mV}$ . If the bias voltage fluctuates  $\pm 1\text{mV}$ , the induced worst case equivalent fluctuation in pressure for the device would be  $0.025\text{mTorr}$ . This type of noise therefore dominates all other noise sources for the present device.

## CONCLUSIONS

The performance and the characteristics of an ultra-sensitive pressure sensor have been presented and discussed. The device exhibits a highly linear pressure-capacitance response. The measured pressure sensitivity is  $5\text{fF/mTorr}$ . The sensor can resolve minimum input pressures as low as  $0.1\text{mTorr}$  and can be used in very low pressure applications (0 to  $1000\text{mTorr}$ ). The temperature coefficient of sensitivity of this ultra-sensitive device can be digitally compensated to  $-63\text{ppm}/^\circ\text{C}$ . Long-term tests show no noticeable change in the device characteristics after 1.9 million  $200\text{mTorr}$  cycles at room temperature.

## ACKNOWLEDGMENTS

The authors would like to express their thanks to Mr. Wayne Baer for his help in device testing and to Dr. Selden Crary for many helpful discussions of digital compensation. This work is supported by the Advanced Research Projects Agency under contract 92-2340.

## REFERENCES

- [1] J. Bergqvist, F. Rudolf, J. Maisano, F. Parodi, and M. Rossi, "A silicon condenser microphone with a highly perforated backplate," *Digest of Technical Papers*, Transducers'91, San Francisco, pp. 266-260.
- [2] E. S. Kim, J. R. Kim, and R. S. Muller, "Improved IC-compatible piezoelectric microphone and CMOS process," *Digest of Technical Papers*, Transducers'91, San Francisco, pp. 270-273.
- [3] A.G.H. van der Donk, A.J. Sprenkels, W. Olthuis and P. Bergveld, "Preliminary results of a silicon condenser microphone with internal feedback," *Digest of Technical Papers*, Transducers'91, San Francisco, pp. 262-265.
- [4] S. T. Cho and K. D. Wise, "A high-performance microflowmeter with built-in self-test," *Sensors and Actuators*, A, 36, pp. 47-56, 1993.
- [5] M. Di Giovanni, *Flat and Corrugated Diaphragm Design Handbook*, Marcel Dekker Inc., New York, 1982.
- [6] Y. Zhang, S. B. Crary, and K. D. Wise, "Pressure sensor design and simulation using the CAEMEMS-D module," *Digest IEEE Solid-State Sensors and Actuator Workshop*, Hilton Head, S.C., pp. 32-35, June 1990.
- [7] W. Kühnel and Gisela Hess, "A silicon condenser microphone with structured back plate and silicon nitride membrane," *Sensors and Actuators*, A, 30, pp. 251-258, 1992.
- [8] O. Tabata, K. Kawahata, S. Sugiyama, and I. Igarashi, "Mechanical property measurements of thin films using load-deflection of composite rectangular membrane," *Proc. IEEE Workshop on Microelectromechanical Systems*, pp. 152-156, Feb. 1989.
- [9] S. T. Cho, "An Ultrasensitive Silicon Pressure Based Microflow Sensor," Ph.D. Dissertation, The University of Michigan, April 1991.
- [10] S. B. Crary, W. G. Baer, J. C. Cowles and K. D. Wise, "Digital compensation of high-performance silicon pressure transducers," *Sensors and Actuators*, A21-A23, pp.70-72, 1990.
- [11] F. V. Hunt, "Thermal noise in acoustic medium," in *American Institute of Physics Handbook*, 2nd ed., New York: McGraw-Hill, 1963.
- [12] H. L. Chau and K. D. Wise, "Noise due to Brownian motion in ultrasensitive solid-state pressure sensors," *IEEE Transactions on Electron Devices*, vol. ED-34, No. 4, April 1987.
- [13] T. B. Gabrielson, "Mechanical-Thermal Noise in Micro-machined Acoustic and Vibration Sensors," *IEEE Trans. on Electron Devices*, Vol. 40, No. 5, May 1993.
- [14] A. B. Gillespie, *Signal, Noise and Resolution in Nuclear Counter Amplifiers*, New York: McGraw-Hill Book Co., Inc. 1953.

# FABRICATION OF ULTRASENSITIVE FORCE DETECTORS

S. Hoen, O. Züger, C.S. Yannoni, H.J. Mamin, K. Wago, D. Rugar

IBM Research Division, Almaden Research Center  
650 Harry Road, San Jose, CA 95120

## ABSTRACT

We have developed micromechanical cantilevers capable of detecting sub-femtonewton forces. These cantilevers have been used to detect nuclear magnetic resonance (NMR) signals from microscopic samples, inaugurating a technique which is several orders of magnitude more sensitive than conventional NMR schemes. The cantilevers are fabricated from low stress silicon nitride grown on <110> oriented silicon using low-pressure chemical vapor deposition. After an anisotropic wet etch, the fixed end of the cantilever is determined by a vertical slow-etching (111) plane, eliminating the need for backside alignment or anodic bonding. The release process is completed by a critical point drying step which is necessary to protect these delicate structures from meniscus forces. Using this process, we have fashioned 200Å thick silicon nitride cantilevers with thickness to length ratios of 1:2500 and spring constants of ~10<sup>-5</sup> N/m. Their thermally limited force sensitivity is 2.4 × 10<sup>-17</sup> N/√Hz at room temperature. Damping measurements have been made as a function of temperature for 600Å thick nitride cantilevers.

## INTRODUCTION

With the advent of modern micromachining techniques and the atomic force microscope, the interest in the detection of extremely small forces has multiplied. Sensitive force sensors are required for micromachined accelerometers, atomic force microscopes (AFM's), and other scanning probe devices. Typical forces measured by micromachined accelerometers vary from 10<sup>-8</sup> N/√Hz for large (~1mg) Si proof masses to 10<sup>-14</sup> N/√Hz for accelerometers using tunneling detection.[1] Since Albrecht's construction of the first micromachined AFM cantilever,[2] AFM's have been routinely used to detect forces from 10<sup>-6</sup> N to 10<sup>-12</sup> N.[3]

One of the most demanding applications of force detection is magnetic resonance force microscopy (MRFM). Sidles has proposed using a sensitive force sensor to detect nuclear magnetic resonance (NMR) with an ultimate goal of detecting NMR signals from individual nuclei.[4, 5] This technique requires a force sensor which is many orders of magnitude more sensitive than a conventional AFM. In this paper, we describe the fabrication of silicon nitride cantilevers ranging in thickness from 900Å to 200Å. These cantilevers are capable of detecting sub-femtonewton forces at room temperature and attonewton scale forces at low temperatures. Recently, the 900Å thick cantilevers have been used to detect NMR via magnetic force.[6]

In the optimal case, the absolute sensitivity of a cantilever is limited only by the thermal noise in the mechanical system. This thermal noise is readily detected as a

"Brownian" type motion of the cantilever deflection. Its magnitude can be determined by a Nyquist type argument since the cantilever is in thermal equilibrium with its surroundings.[7] The only three parameters needed to characterize the response of the oscillator near resonance are the resonant frequency  $f_o$ , the quality factor  $Q$ , and the spring constant  $k$ . [8] Setting the minimum detectable force,  $F_{min}$ , equal to the effective noise force, one finds [4, 9]

$$F_{min} = \left( \frac{2k_B k_B T}{\pi Q f_o} \right)^{1/2}, \quad (1)$$

where  $B$  is the measurement bandwidth,  $k_B$  is Boltzmann's constant and  $T$  is temperature. Equation (1) holds for both resonant and off-resonant force detection as long as the damping is relatively frequency independent. For sensitive force detection, it is desirable to have a small spring constant while maintaining a large  $Q$  and  $f_o$ . An attractive option is a micromachined cantilever since it can have a very low spring constant while maintaining a high resonant frequency. A rectangular cantilever of Young's modulus  $E$  and density  $\rho$ , has a spring constant  $k = Ewt^3 / 4L^3$  and a fundamental resonant frequency  $f_o = 0.161 (wt/L^2) \times (E/\rho)^{1/2}$ , where  $w$ ,  $t$ , and  $L$ , are the cantilever width, thickness, and length, respectively.[10] Equation (1) can then be rewritten in terms of cantilever geometry as

$$F_{min} = \left( \frac{wt^2 B k_B T}{QL} \right)^{1/2} (\rho E)^{1/4}. \quad (2)$$

The cantilever force detector should thus have minimal width and thickness and large  $Q$  and  $L$ . In this paper, we focus especially on the reduction of cantilever thickness.

## PROCESSING

We have incorporated several innovations in producing silicon nitride cantilevers with thicknesses ranging from 900Å to 200Å. Low stress silicon nitride is grown on <110> oriented silicon in a silicon rich atmosphere (4:1 dichlorosilane to ammonia) using low-pressure chemical vapor deposition. The nitride is subsequently patterned with an SF<sub>6</sub> reactive ion etch. An anisotropic wet etch in 60°C KOH releases the cantilevers from the underlying Si. The low temperature (60°C) maximizes the relative <110>/<111> etch rate.[11].

Figure 1 shows the completed chip with the attached cantilevers on the upper and lower faces. The fixed end of the cantilever is determined by a slow-etching (111) plane which is perpendicular to the wafer surface. Thus, access

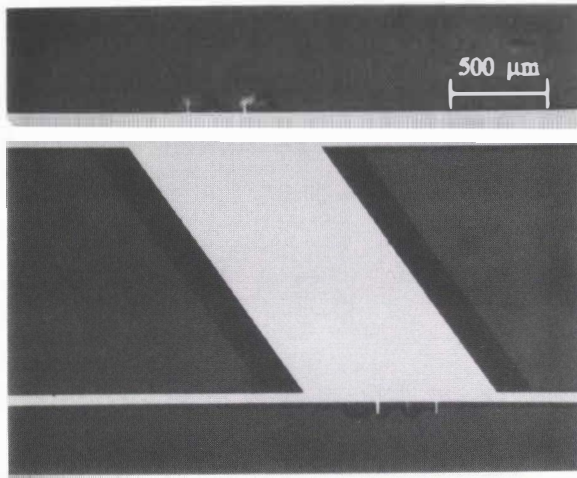


Figure 1. Optical micrograph of bulk micromachined chip with attached cantilevers formed by a KOH etch of patterned nitride on <110> oriented silicon.

is provided to both sides of the released cantilever without any need for backside alignment or wafer bonding. The overall shape of the chip is not rectilinear because the remaining (111) planes do not run parallel to the vertical direction. An additional benefit of this design is that the chip is held to the remainder of the frame by thin (~30μm) legs, allowing easy removal of the chip from the frame. Two 900Å thick paddles, on which samples can be mounted, are shown in more detail in Figure 2. The silicon nitride exhibits excellent integrity, and some underetch is visible as a white band bordering the chip. The thicker paddle has a spring constant of  $2 \times 10^{-3}$  N/m and a resonant frequency of 9.3 kHz.

One drawback of using <110> oriented Si is that the (111) surface exposed during the anisotropic etch is unstable with respect to the formation of asperities. One such asperity is shown in Figure 3. A cantilever causes enough perturbation of the upper etch surface to prompt their formation. They are bounded on one side by a slow etching (111) plane oblique to the surface and, as the upper surface of the silicon is etched away, they grow until the wafer is etched entirely through. Clearing these asperities requires a 30% overetch.

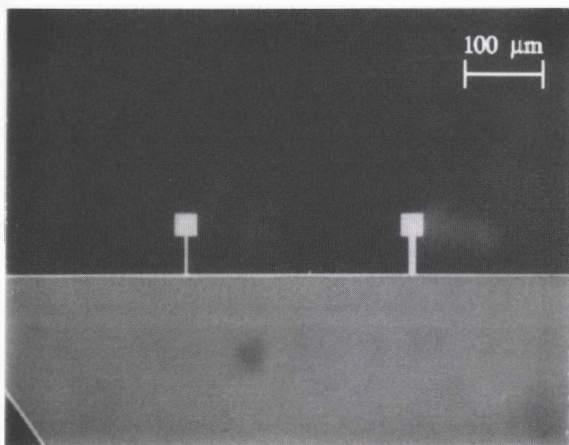


Figure 2. Optical micrograph of two 900Å thick silicon nitride paddles. Access to both sides of the paddle is provided by the vertical (111) etch face at the cantilever base.

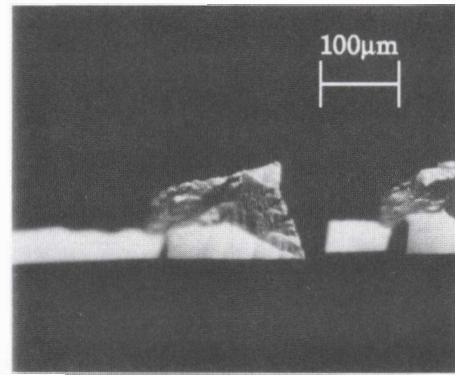


Figure 3. Optical micrograph of asperity formed along (111) face during the etch. The left hand side of the "nose" is formed by a slow etching (111) plane.

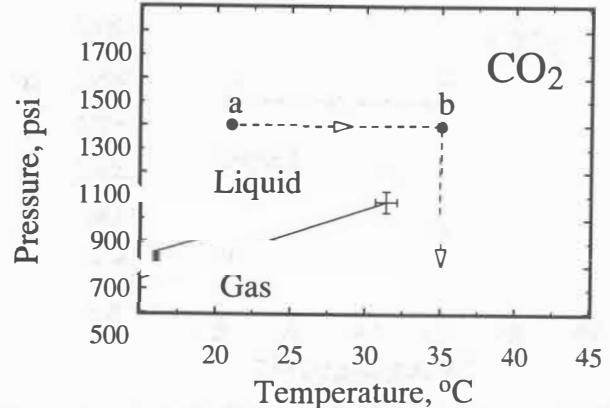


Figure 4. Schematic diagram of critical drying process using CO<sub>2</sub>. Initial dilution of methanol surrounding the sample occurs at point a. The CO<sub>2</sub> is next heated to point b and then the pressure is reduced to atmospheric.

With the original 900Å thick cantilevers, we found yields of ~5% with the wet etching process. The low yields were caused by surface tension effects in removing the cantilevers from the release bath. To circumvent the need to cross a liquid/vapor interface, we designed and built a critical point drier using CO<sub>2</sub> as the fluid system.[12] This drying process is shown schematically in Figure 4. To stop the etch, the KOH is first exchanged with distilled water which is then incrementally diluted with methanol. The wafer is placed in a pressure vessel and the methanol is replaced with liquid CO<sub>2</sub> at high pressure (point a in Figure 4). By increasing the temperature, the CO<sub>2</sub> is raised above the critical point (1070psi, 31.3°C) and there is no longer any distinction between the gas and liquid phases (point b in Figure 4). The high pressure fluid is then vented and the cantilevers are freed without ever experiencing a liquid/vapor interface. This process has increased the yields of the 900Å thick cantilevers from 5% to 95%, and it has proved essential for the release of thinner cantilevers.

The 900Å thick paddles have a slight curvature and are bent down at their ends by ~3 μm, visible as a defocussing in Figure 2. Figure 5 shows the measured silicon nitride curvature as a function of thickness for cantilevers grown on bare <100> and <110> oriented Si. Thinner cantilevers exhibited substantially more curvature and cantilevers grown on <100> Si showed ~40% more bending than on <110> oriented Si. The curvature of the 200Å cantilevers

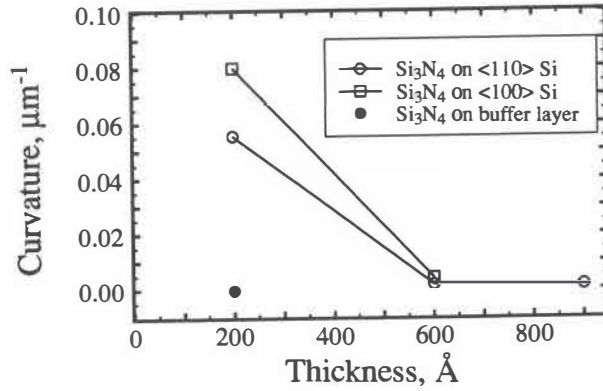


Figure 5. Curvature of the released cantilevers plotted as a function of silicon nitride thickness. To reduce curvature, a buffer layer of 1000Å of oxide was first grown on the silicon.

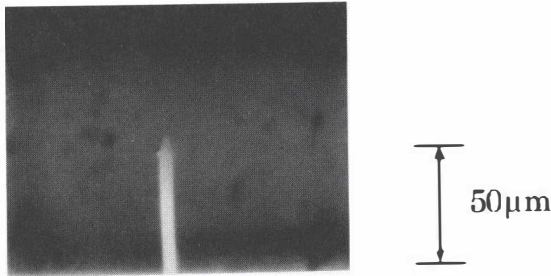


Figure 6. Optical micrograph of 200Å thick silicon nitride cantilever grown on 1250Å SiO / <110> Si. The end of the cantilever is pointed to allow mounting of a magnetic film.

grown on bare Si renders them unusable. The curvature is due to a residual stress gradient in the cantilever material which probably arises from the lattice mismatch between the Si substrate and the deposited nitride. We overcame this problem by growing a ~1000Å thermal oxide layer on the bare Si before the nitride deposition. Thermal oxide is an excellent buffer layer since it provides a more amorphous surface on which to grow the nitride and it etches slowly in KOH. Figure 6 shows an optical micrograph of a 200Å thick cantilever grown on a 1250Å thick oxide layer over <110> oriented Si. The curvature has been reduced to that of the original 900Å thick cantilevers. This cantilever has an aspect ratio of 1:2500 and a spring constant of ~10<sup>-5</sup> N/m.

### FORCE SENSITIVITY RESULTS

The ultrathin cantilevers produced by the preceding process show considerable promise as force detectors. To

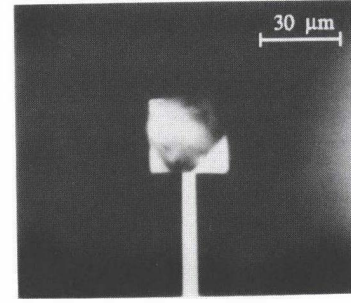


Figure 7. Optical micrograph of 900Å thick silicon nitride cantilever with a 12ng ammonium nitrate sample attached.

properly quantify their sensitivity, measurements of resonant frequency and  $Q$  were made in vacuum (< 1 mtorr). In this pressure range, the value of  $Q$  depends only on the internal friction of the nitride and the losses at the boundary. Because we see very little change in  $Q$  under varied boundary conditions, it appears that the  $Q$  is determined only by the internal friction.

Table I presents measured values of  $Q$  and  $f_o$  for the silicon nitride cantilevers along with calculated values of  $k$  and  $F_{min}$ .  $F_{min}$  was calculated using equation (1) and the experimentally determined values of  $f_o$  and  $Q$  for all thicknesses except 200Å. For the 200Å thick cantilevers,  $F_{min}$  was calculated using equation (2) and assuming a  $Q$  of 3000. The measured values of  $f_o$  are within ~5% of those calculated from simple beam theory assuming  $E = 140$  GPa and  $\rho = 3$  gm/cm<sup>3</sup>. The extraordinary sensitivity (< 1 fN/√Hz) of these cantilevers arises from their small spring constants.

The cantilever  $Q$  was also studied as a function of temperature because magnetic resonance force microscopy will ultimately require cooling below 4K. Between room temperature and 4.2K,  $Q$  showed a moderate increase for the 600Å thick cantilevers. This is expected since, for most materials, energy dissipation mechanisms freeze out as temperature is lowered, increasing  $Q$ . The overall force sensitivity increased by a factor of 13 in this same temperature range because of the Boltzmann term which enters equation (1).

### MAGNETIC RESONANCE FORCE MICROSCOPY

Cantilevers of the type shown in Figure 2 have already been used to detect the NMR signal arising from a microscopic sample.[6] Figure 7 shows one such 900Å thick cantilever with an attached 12ng ammonium nitrate sample. The physical characteristics of this cantilever are

TABLE I. Physical Parameters of Micromachined Cantilevers

Thickness (Å)	Width (μm)	Length (μm)	Geometry	Temperature (K)	$k$ (μN/m)	$Q$	$f_o$ (kHz)	calculated $F_{min}$ (fN/√Hz)
900	10	50	paddle	295	2000	3000	9.23	0.43
900	5	50	sample	295	1000	3000	1.8	0.77
600	10	50	paddle	295	600	1270	2.23	0.753
				77	600	2200	2.23	0.29
				4.2	600	2900	2.14	0.059
200	5	55	cantilever	295	8			0.024

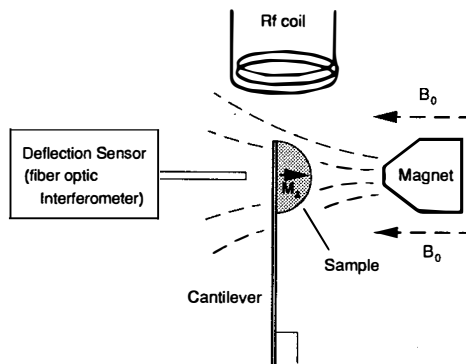


Figure 8. Schematic diagram of magnetic resonance force detection technique. See text for description of elements.

included in Table I. Equation (1) predicts an  $F_{min}$  of 0.39 fN in a 0.25 Hz bandwidth. The experimental configuration for MRFM is shown schematically in Figure 8. An external field  $B_0$  of 2.4 T polarizes the nuclear spins and an additional field gradient of 6 G/ $\mu\text{m}$  is produced by a nearby magnetic tip. As in NMR, an rf field applied at the correct frequency will flip the nuclear magnetic moments. Using cyclic adiabatic inversion, by fm modulating the rf field, the nuclear magnetic moments are caused to oscillate at the cantilever resonant frequency. The resulting change in the sample magnetic moment applies an oscillating force on the cantilever. The resulting cantilever displacement is detected by a fiber optic interferometer.[13] In principle, the interferometer noise contributes to the overall noise; however, its effect is small because the thermal vibration of the cantilever is on the scale of angstroms, several orders of magnitude larger than our interferometer sensitivity.

Figure 9 shows the cantilever vibration amplitude as a function of time where the nuclei of the sample were excited during the indicated interval. The cantilever achieved an amplitude of 110Å, corresponding to a magnetic force of  $1.1 \times 10^{-14}$  N. The 5Å vibration noise corresponds to a minimum detectable force of  $5 \times 10^{-16}$  N,

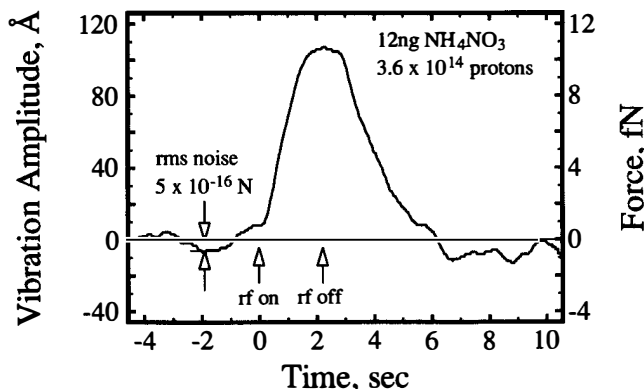


Figure 9. Cantilever vibration amplitude plotted as a function of time. At 0 seconds, the rf field was turned on and z-component of the sample magnetic moment was induced to oscillate at the cantilever resonant frequency. At 2 seconds, the rf field was turned off. The ring down time was determined by both the cantilever  $Q$  and an applied electronic damping.

similar to our estimate. The noise floor implies a minimum resolution of  $10^{13}$  nuclear spins in a 0.25 Hz bandwidth, which is two orders of magnitude more sensitive than conventional NMR techniques. This experiment clearly demonstrates the phenomenal sensitivity mechanical detection can achieve.

## CONCLUSIONS

To our knowledge, these cantilevers provide the most sensitive force detection to date and should move magnetic resonance force microscopy significantly closer to the goal of atomic scale resolution. Measuring the NMR signal from a single nuclear spin will require a force sensitivity of  $1.5 \times 10^{-18}$  N in a field gradient of 100G/Å.[4] This is already close to the sensitivity of a 200Å cantilever if it were cooled to 1K. This temperature range will also be required to have the proper NMR relaxation times. The cantilevers should already sensitive enough to detect single electron spin resonance at 4.2K.

We acknowledge the Berkeley Microfabrication Laboratory for growth and patterning of the low-stress silicon nitride. We thank H.-M. Vieth, and R.D. Kendrick for their contributions to the NMR experiment. We also thank Tom Albrecht, Long-Sheng Fan, Debra Hebert, and Greg Mulhern for many helpful conversations.

## REFERENCES

- [1] T.W. Kenny, *et al.*, *IEEE Solid-State Sensor and Actuator Workshop* (Hilton Head, SC, USA, 1992) p. 174.
- [2] T.R. Albrecht, *et al.*, *J. Vac. Sci. Technol.* **A8**, 3386 (1990).
- [3] H.K. Wickramasinghe, *J. Vac. Sci. Technol.* **A8**, 363 (1990).
- [4] J.A. Sidles, *Appl. Phys. Lett.* **58**, 2854 (1991).
- [5] J.A. Sidles, *Phys. Rev. Lett.* **68**, 1124 (1992); and J.A. Sidles, J.L. Garbini, and G.P. Drobny, *Rev. Sci. Instrum.* **63**, 3881 (1992).
- [6] D. Rugar, *et al.*, (submitted to *Science*).
- [7] F. Reif, *Fundamentals of Statistical and Thermal Physics* (McGraw-Hill Book Company, New York, 1965).
- [8] J.A. Sidles and D. Rugar, *Phys. Rev. Lett.* **70**, 3506 (1993).
- [9] U. Dürig, O. Züger, and A. Stalder, *J. Appl. Phys.* **72**, 1778 (1992).
- [10] W. Weaver, S.P. Timoshenko, and D.H. Young, *Vibration Problems in Engineering* (John Wiley and Sons, New York, 1990).
- [11] H. Seidel, *et al.*, *J. Electrochem. Soc.* **137**, 3612 (1990).
- [12] G.T. Mulhern, D.S. Soane, and R.T. Howe, *1993 International Conference on Solid-State Sensors and Actuators: Transducers '93* (Yokohama, Japan, 1993).
- [13] D. Rugar, H.J. Mamin, and P. Guethner, *Appl. Phys. Lett.* **55**, 2588 (1989).

# A Micromachined Vibrating Ring Gyroscope

Michael W. Putty and Khalil Najafi\*

General Motors Research and Development Center  
30500 Mound Rd., Warren, MI, 48090-9055, USA

\*Center for Integrated Sensors and Circuits, University of Michigan,  
1301 Beal Ave., Ann Arbor 48109-2122, USA

## Abstract

A new micromachined gyroscope based on a vibrating ring is described. The device measures rotation rate or whole angle inertial rotation by monitoring the position of node lines in a vibrating ring. To sense rotation, the ring is electrostatically forced into an elliptically shaped vibration mode and the position of the node lines are capacitively monitored. When the device is subjected to rotation, the node lines, lag behind the rotation due to the Coriolis force. The control and readout circuitry monitors this lag and develops a corrective voltage, that is proportional to the rotation rate, to hold the position of the node lines fixed. The device is fabricated using a low-cost process based on metal electroforming techniques that allows large amounts of circuitry to be included with the sensor. A resolution of approximately  $0.5^\circ/\text{sec}$  in a 10 Hz bandwidth, limited by the on-chip electronics, has been obtained with this new sensor. Further improvements in the on-chip electronics and sensor materials are expected to push the resolution to below  $0.5^\circ/\text{sec}$  in a 50 Hz bandwidth.

## Introduction

Gyroscope devices for measuring angular rotation or rotation rate have been the subject of extensive research and development over the past several decades. With the development and proliferation of low-cost miniature silicon micromachined accelerometers, attention is naturally turning to the development of a low-cost companion micromachined gyroscope since many applications exist for these devices. Some of the applications being considered for these miniature devices include: automotive applications such as traction control systems and ride stabilization systems; consumer electronic applications such as video camera stabilization and model aircraft stabilization; computer applications such as an inertial mouse; as well as robotic applications; and military applications [1]. Generally the requirements for these sensors are a resolution between  $0.1^\circ/\text{sec}$  to  $1^\circ/\text{sec}$ , a full scale range of  $50^\circ/\text{sec}$  and a response bandwidth of 50 Hz at a cost of 10\$ to 20\$ per sensor. Given the large number of potential applications for medium performance gyroscopes many groups are currently developing micromachined designs to meet this need [2,3].

Over the years many different gyroscope concepts have been conceived and successfully developed. The traditional gimballed spinning wheel and the ring laser gyroscope are two well-known designs that have been widely applied and proven in inertial navigation applications [4]. Although highly accurate, these devices are currently too expensive for many of the low-cost applications. Some low-cost fiber optic gyroscopes are currently under development but it is uncertain whether these devices can meet the cost goals of many applications even in large scale production volumes [5]. Another class of successful gyroscope designs, known as vibratory gyroscopes, use vibrating mechanical elements to sense rotation [6]. Although less well known, these devices find many applications in the medium performance range and one vibratory gyroscope, the Hemispherical Resonator Gyroscope (HRG) [7], has achieved inertial navigation performance levels rivaling and even exceeding that of the best ring laser gyroscopes. Almost universally when low-cost is the goal, gyroscope devices are based on vibrating mechanical elements due to their simple structure. Since vibratory gyroscopes have no rotating parts that require bearings they can be readily miniaturized and batch fabricated using micromachining techniques to produce a low-cost device. Furthermore, with the precision of micromachining techniques it is still possible to produce a

medium to high performance device. For these reasons most groups are basing their micromachined designs on vibrating mechanical elements.

In this paper we present a new low-cost micromachined vibratory gyroscope based on a vibrating ring that is designed for medium performance applications [8]. To understand the operation of this device we first review the principles of vibratory gyroscopes using the familiar Foucault pendulum to present these concepts. We then discuss the various types of vibratory gyroscope designs to get a clearer understanding of the advantages and disadvantages of the ring design. After this the more detailed design and fabrication of the ring gyroscope is presented emphasizing the reasons for choosing the ring design for a micromachined device. We next discuss the operation of the sensor with its closed loop electronics. Experimental results are then reported for the rotation response of the sensor and electronics followed by some concluding remarks.

## Vibratory Gyroscope Principles

Vibratory gyroscopes use the Coriolis acceleration or force that arises in rotating reference frames to sense rotation. Similar to the centrifugal acceleration, familiar to all amusement park lovers, the Coriolis acceleration is one of the accelerations that are used to describe motion in a rotating reference frame and accounts for radial motion. Its effects must be considered in many phenomena where rotation is involved and can even account for the differences in the motion of air over the earth's surface in the northern and southern hemispheres. To understand how vibratory gyroscopes use Coriolis acceleration it is instructive to first examine a simple vibratory device, the well known Foucault pendulum [9]. This discussion provides the base for understanding the principles of vibratory gyroscopes in general and the ring gyroscope in particular. During the discussion the normal mode method for modeling vibratory gyroscopes is introduced and discussed [10]. Later this model is used to describe the operation of the ring gyroscope. Three ways of operating vibratory gyroscopes are then presented and discussed in terms of the normal mode model followed by a discussion of desired characteristics of vibratory gyroscopes to achieve the best performance.

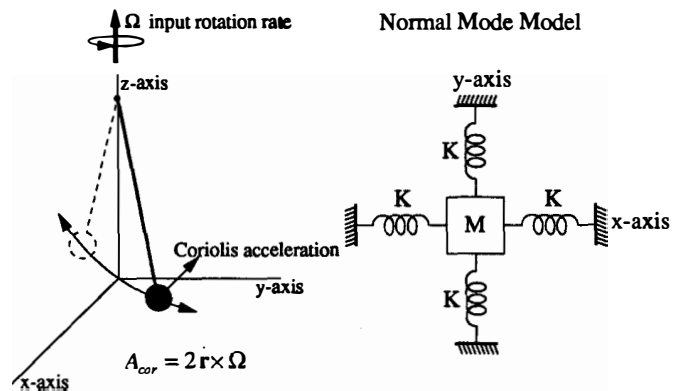


Figure 1 Foucault pendulum and normal mode model

### Foucault Pendulum and the Normal Mode Model

In 1851 the French scientist Leon Foucault used a large pendulum to study earth's rotation. As the earth rotated under the pendulum, the plane of the pendulum's swing appeared to rotate or precess at a rate equal to earth's vertical rotation rate. Foucault correctly reasoned that the Coriolis acceleration due to earth's rotation caused the precession of the pendulum. Mathematically this precession phenomenon can be modeled by two independent harmonic oscillators that are coupled by the Coriolis acceleration as shown in Figure 1. This method of describing the Foucault pendulum is known as the normal mode method in vibration theory and the independent oscillators are called the normal modes of the system [10]. In this model the pendulum's swing is resolved into two orthogonal amplitude components  $x$  and  $y$ , one for each oscillator or normal mode. The path of the pendulum's swing is then obtained as a linear superposition of these two independent motions.

How Coriolis acceleration causes precession in this model can be understood as follows. Consider the case when the pendulum's swing is initially aligned with the  $x$ -axis. At this time all the energy or amplitude of vibration is stored in the first normal mode. In the absence of rotation the pendulum swing would stay aligned with the  $x$ -axis and all the stored vibration energy would remain in the first normal mode. However, under rotation the normal mode equations reveal that the Coriolis acceleration will transfer energy between the two normal modes causing the pendulum to precess. Solving the normal mode equations for the case of constant rotation shows that the pendulum would precess at a constant rate equal to the rotation rate. This principle of the transfer of energy between two vibration modes of a structure caused by the Coriolis acceleration is the basic operating principle underlying all vibratory gyroscopes [6].

### Modes of Operation

So far we have considered the case when the pendulum swing is allowed to freely move under rotation. In this mode of operation, called the whole angle mode, the pendulum operates as a rate-integrating gyroscope and measures the angle of rotation. Vibratory gyroscopes including the Foucault pendulum can also be operated as rate gyroscopes to measure rotation rate in an open-loop or force-to-rebalance mode.

To measure rotation rate, the pendulum would be continuously driven to a fixed amplitude in the first vibration mode along the  $x$ -axis. In the absence of rotation there would be no vibration amplitude in the second mode along the  $y$ -axis. Under rotation, however, the Coriolis acceleration will cause energy to be transferred from the first mode to the second mode. In the open-loop mode of operation the second-mode amplitude is allowed to build up to a steady state value and provides a measure of the rotation rate. In the force-to-rebalance mode of operation the secondary vibration amplitude is monitored and continuously driven to zero by applying the necessary force along the  $y$ -axis to rebalance the Coriolis acceleration. Which operating mode is used in a particular vibratory gyroscope depends on the application and the particulars of the device design.

### Design Goals

All vibratory gyroscopes are based on the rotation-induced transfer of energy between two vibration modes of the structure. Independent of the mode of operation, highest performance for vibratory gyroscopes is obtained when these two vibration modes have the same natural frequency and a long damping time or high quality factor [6]. When this is the case, the response to the very small Coriolis acceleration is amplified or multiplied by the quality factor of the resonance which can exceed 50,000, thereby improving the overall sensor performance. Not all vibratory gyroscopes use this principle of matched vibration mode frequencies in their design. Tuning fork designs, for example, often do not match the resonant frequencies of their two vibration modes and still achieve good performance. They do this by careful design that involves detecting small motions. However, the highest performance vibratory gyroscope, the HRG, has used this principle of matched frequencies to achieve inertial-navigation performance levels demonstrating the potential of this design principle [7].

The design goal of matching the vibration mode frequencies is most easily obtained in symmetric structures that naturally have two identical modes of vibration such as the Foucault pendulum or the vibrating shell designs discussed shortly. To obtain a long damping

time for these devices, isolated structures that do not radiate acoustic energy and which are fabricated from low-loss materials are desirable [11]. Also, the damping time is increased as the resonant frequency of the structure is lowered. Consequently, lower natural frequency structures are desirable as well, however, the natural frequency of the structure is generally chosen to be above the environmental noise to improve vibration sensitivity. In this paper we describe a new micromachined vibratory gyroscope design that uses these principles.

## Types of Vibratory Gyroscopes

Vibrating elastic bodies can sense rotation just as the Foucault pendulum and many different designs for these structures have been developed. These vibratory gyroscope designs generally fall into one of five classes; vibrating prismatic beams, tuning forks, single or dual accelerometers, vibrating shells, and rotated piezoelectric crystals [6,12]. Each of these classes are represented by commercial or research devices with the highest performance belonging to the vibrating shell class. Since the rotating piezoelectric crystal devices use bearings that are currently unavailable in micromachining technology, this class of devices will not be discussed further. To put the ring gyroscope into perspective, examples of each of these other classes will be discussed highlighting the advantages and disadvantages of each class.

### Vibrating Prismatic Beams

Probably the simplest vibratory gyroscope is the vibrating rectangular beam that operates like the Foucault pendulum and uses the two identical primary bending modes of the beam to sense rotation (Fig. 2). Experience with these devices has revealed that they are difficult to mount, have large temperature sensitivities due their construction, and are sensitive to spurious vibrations [12].

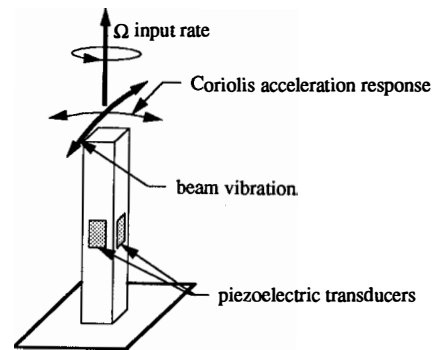


Figure 2 Vibrating prismatic beam gyroscope

### Tuning Forks

To overcome the difficulties encountered with vibrating beam gyroscopes, designers have worked with gyroscopes based on tuning forks which being balanced devices are easy to mount and not sensitive to linear vibrations. In operation, the tines of the tuning fork are differentially driven to a fixed amplitude and, when rotated, the Coriolis acceleration causes a differential sinusoidal force to develop on the individual tines orthogonal to the main vibration (Fig. 3). Depending on the design of the device, this force is detected either as differential bending of the tuning fork tines or as a torsional vibration of the tuning fork stem. Due to fabrication difficulties and temperature drift problems, the input and output mode natural frequencies of tuning fork gyroscopes are generally not matched, limiting the device sensitivity [6]. Another problem encountered with tuning fork gyros is large bias errors caused by a misalignment of the mass centers of the individual tines [6]. If the centers of mass are not precisely in the plane of the tine vibration, their inertia produces a vibration response that is indistinguishable from the Coriolis acceleration. To minimize this error, tuning fork devices are often individually mechanically trimmed. In spite of these difficulties a high-quality micromachined quartz device is available from Systron Donner and a silicon-micromachined device has been developed by Draper Labs with impressive sensitivity [3].

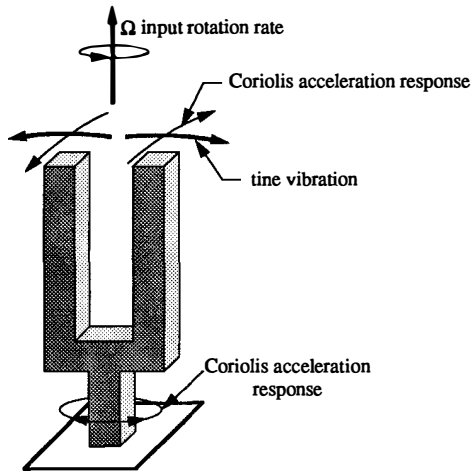


Figure 3 Tuning fork vibratory gyroscope

### Single and Dual Accelerometers

Dual-accelerometer gyroscopes are essentially tuning fork gyroscopes whose tines are constructed from identical accelerometers (Fig.4). These devices are operated by vibrating the accelerometer proof masses antiphase in one plane and measuring the resulting differential Coriolis acceleration in an orthogonal plane. Since this class of devices is so similar to the tuning fork class, they share many of the same advantages and disadvantages, although, they can also measure acceleration, which is an important advantage in many applications. For less demanding applications a single accelerometer can be used to measure the Coriolis acceleration but like the prismatic beam this device is more sensitive to spurious vibrations.

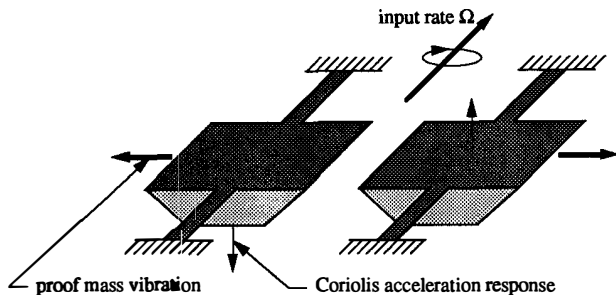


Figure 4 Dual accelerometer vibratory gyroscope

### Vibrating Shells

Tuning fork gyros are based on the rotation-induced transfer of energy between two different vibration modes of the structure. This can cause the device to have low sensitivity or a large temperature drift. In contrast, vibrating-shell gyroscopes transfer energy between two identical modes of the structure just as the Foucault pendulum does, thus avoiding these problems [6,7,12]. Because of their shape, vibrating shells have two identical modes of vibration with nominally equal resonant frequencies. They may be shaped like a wine glass (HRG), like a cylinder, or like a ring [6]. Although the vibrating disk is not, strictly speaking, a vibrating shell it can be included in this category as well [12].

The rotation sensing principles of the vibrating-shell gyroscope were first analyzed by G. H. Bryan in 1890 and are best illustrated by the ringing wine glass vibrating in its fundamental flexural mode shown in Figure 5 [13]. In this mode of vibration, the lip of the wine glass vibrates in an elliptical-shape mode that has two nodal diameters. When the wine glass is rotated, the node lines lag behind the rotation or precess much like the swing of the Foucault pendulum precesses. During a 90° rotation, the node lines are observed to precess by about 27°. The precession rate is a geometric constant

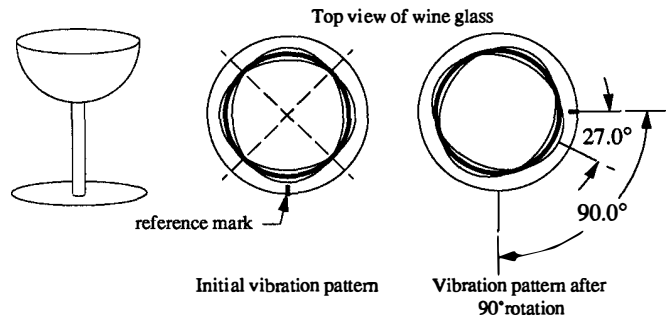


Figure 5 Vibrating shell gyroscope

for each type of vibrating shell gyroscope-called the angular gain-and is approximately 0.3 for a wine glass.

Due to their shape, vibrating-shell gyroscopes are inherently rugged but are still highly sensitive to rotation. They are less sensitive to spurious vibration than other vibratory gyroscopes for, ideally, spurious vibrations do not couple to the shells identical vibration modes. Only when the shells have mass or stiffness asymmetries, can environmental vibrations induce a spurious response. Vibrating shell gyroscopes can be operated in either the whole angle, the open-loop, or the force-to-rebalance mode depending on the demands of the application [1,6,7,12].

### Device Description

Given the many advantages of vibrating-shell gyroscopes, we chose to develop a micromachined, vibrating-shell gyroscope to explore the potential of such a device. After some consideration we based our device on a vibrating ring; rather than a hemisphere, cylinder, or disk, as micromachining versions of the other shapes can be problematic. Although hemispherical wine-glass shapes can be micromachined, it would be difficult to fabricate attached versions of these structures with the associated capacitive drivers and pickoffs in a batch process. Furthermore, to obtain low natural frequencies with long damping times, cylinder structures would require very tall, thin walls that demand special, expensive fabrication techniques such as LIGA. The main difficulty found in fabricating these two structures is their three-dimensional nature which demands special micromachining techniques. Although disk structures are more two dimensional, they would still have to have very large diameters to obtain reasonable natural frequencies as their vibration mode is primarily extensional. In contrast, the ring structure that we have developed is a small quasi-two dimensional device that can be easily batch fabricated, thus avoiding the difficulties associated with these other structures. As we shall see, the ring gyroscope can be fabricated with a simple inexpensive process using conventional process equipment based on electroforming.

The ring gyroscope, shown in Figure 6, consists of three main elements; the ring itself, the support springs, and the drive pickoff and control electrodes [8]. Like the vibrating wine glass device, this device uses the two primary flexural vibration modes of the ring to sense rotation. In these modes the ring vibrates in the plane of the substrate in an elliptically-shaped pattern with two node lines. The device can be operated in the whole angle mode, the open-loop mode or the force-to-rebalance mode, although in this paper we will concentrate on the force-to-rebalance mode of operation.

To suspend the ring above the silicon substrate, we have developed a novel support arrangement using eight semicircular springs that attach the ring to the substrate at the ring center. This spring arrangement supports the ring without drastically restricting its in-plane motion, thus allowing the ring to still vibrate in a low-frequency, elliptically-shaped mode. Symmetry considerations require at least eight springs to support the ring to give a balanced device with two identical modes that have the same natural frequency. The attachment point in this structure forms a balanced isolated support for the ring that is similar in spirit to the base in tuning fork designs. As a result of this isolation, the support structure is compatible with high Q, long time constant devices for high performance applications. Another feature of the support structure is its released design which eliminates the effects of package-induced stress on the device.

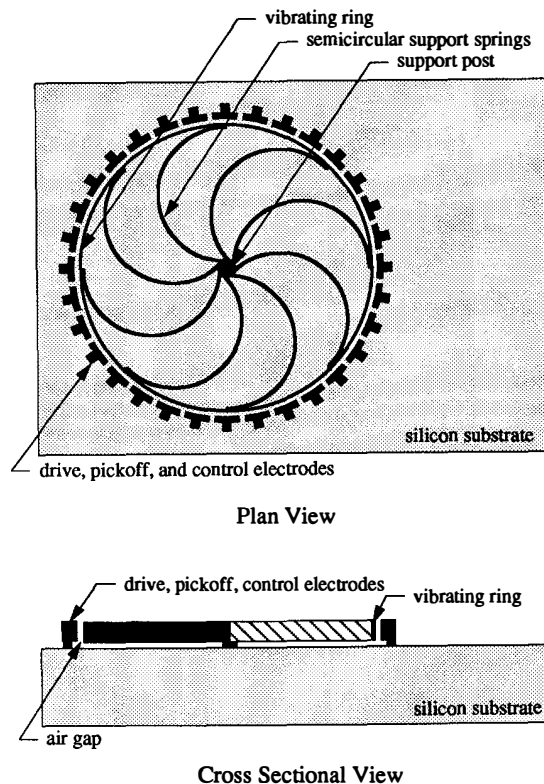


Figure 6 Plan and cross sectional views of ring gyroscope

Since the vibrating ring is a shell structure, it naturally has two identical modes that have nominally equal resonant frequencies. To obtain two identical frequencies in either tuning fork or beam structures, it is necessary to match both the thickness and width of the structure which is difficult, if not impossible, to do with the required precision in a batch-fabricated process. In contrast, to obtain two identical frequencies in the ring device, it is not necessary to precisely control any dimension of the device, rather, it is only necessary that the device be uniform in its dimensions and material properties at the die level. This makes fabrication of the ring gyroscope much simpler as these requirements are easy to achieve in a batch fabrication process.

Thirty-two capacitive electrodes are located around the outer circumference of the ring to drive, sense, and control its vibration. The electrostatic drive and detection scheme used in this device is ideal for a micromachined device and results in a clean, simple, one-element mechanical structure [14]. In developing the ring gyroscope, we have used these electrodes in two different sets; a simple unbalanced set and a balanced set. The balanced electrode set uses all thirty-two electrodes in a symmetrical arrangement that electronically cancels the electrostatic effects of rigid body motions of the ring on the sensor's operation. It is envisioned that this complete electrode set would be used when vibration performance of the sensor is crucial. Otherwise, the simpler unbalanced electrode set would be used. As discussing both electrode sets would be redundant, we will discuss the simpler set in this paper. All the basic operating principles of the device are covered in this discussion without loss of generality using this electrode set. For a further discussion of the balanced set the interested reader is referred to [8].

In the simple electrode set, two pickoff electrodes, located at  $0^\circ$  and  $45^\circ$ , are used to capacitively sense the ring vibration. Two electrodes located across from the sense electrodes at  $180^\circ$  and  $225^\circ$  are used to electrostatically drive the ring vibration. Four electrodes located at  $67.5^\circ$ ,  $90^\circ$ ,  $112.5^\circ$ , and  $135^\circ$  are used to electrostatically balance the ring so that the two flexural vibration modes of the ring have the same natural frequency. Ideally, these two modes are identical and would have the same natural frequency. However,

actual rings usually have some imperfections that cause these two frequencies to be slightly different. By applying the proper voltages to the balancing electrodes, as discussed shortly, this frequency split can be removed [7]. The remaining electrodes are not used and are held at ground potential.

The ring gyroscope design is more compliant than wine glass designs or cylinder designs due to its support structure. This makes the ring gyroscope somewhat more sensitive to spurious vibrations than other shell designs since three vibration modes of the structure have resonant frequencies below the flexural mode frequencies used to sense rotation. The first vibration mode of the ring gyroscope is a torsional mode in which the ring remains rigid and rotates about the support center. Often when people are first exposed to this sensor they mistakenly assume that this is the vibration mode used to sense rotation. However, for the range of rotational accelerations normally encountered when using this sensor the torsional mode is not excited and the ring structure faithfully follows the applied rotation. The second and third vibration modes of the ring gyroscope are x- and y- translational modes in which the ring remains rigid. In perfectly balanced devices these modes do not contribute to the rotation response of the device. However, when mass or stiffness asymmetries exist in the sensor structure these modes can cause the device to be sensitive to environmental vibration [15]. In demanding applications, rigid-body motions of the ring can be electronically rejected using the balanced electrode set to further improve sensor performance in high vibration environments.

Out-of-plane vibration modes of the ring can be moved to high frequencies by using high aspect ratios in the sensing element. When these modes have high frequencies, they do not significantly contribute to the sensitivity of the sensor to spurious vibrations. It is, therefore, desirable to use a high-aspect ratio process to fabricate the sensor element such as the electroforming process described later. At this time, it should be remembered that even the high performance HRG shell design has torsional and translational modes that lead to unwanted vibration sensitivity [15]. The ring gyroscope support structure only lowers these frequencies. This design trade-off is one compromise in the sensor design. Although, hemisphere or cylinder shells do not require this compromise the ring gyroscope is much easier to fabricate as mentioned earlier.

## Device Operation and Control and Readout Electronics

Just like the Foucault pendulum, the operation of the ring gyroscope can be understood from the normal mode model. For the ring, the two identical modes of the structure have an elliptical shape with their antinodes lying  $45^\circ$  apart. For the purposes of this discussion we will initially consider a balanced device in which case one mode, which we will call the primary mode, can be considered to be aligned with  $0^\circ$  pickoff; and the other mode, which will be called the secondary mode, will then be aligned with the  $45^\circ$  pickoff.

The ring gyroscope uses electrostatic drive and detection biased by a polarization voltage applied to the ring. Each pickoff electrode incorporates a low-input capacitance, unity-gain, buffer amplifier to sense the small capacitance changes due the ring vibration [16]. The pickoff electrode capacitor and the input capacitance of the buffer amplifier form a capacitive voltage divider which is biased by the ring polarization voltage. This circuit arrangement converts the ring vibration into a buffered output voltage for the control and readout electronics. For simplicity and ease of fabrication, the initial device design has used a source follower for the unity gain amplifier shown in Figure 7. Resolution of the sensor is currently limited by noise in the buffer amplifier and could be improved with an improved buffer design [16]. In the current design, with large  $7\ \mu\text{m}$  electrode gaps, the polarization voltage is 60V. This voltage can be reduced to more conventional IC voltages by scaling the device to reduce its gap sizes.

The block diagram of the control and readout electronics for operating the ring gyroscope in the force-to-rebalance mode is shown in Figure 8 [1,6,12]. To sense rotation rate, the primary mode is driven to a fixed amplitude at the ring resonant frequency with a phase-locked loop, oscillator circuit and an amplitude control loop. The primary or main drive loop incorporates an amplitude control

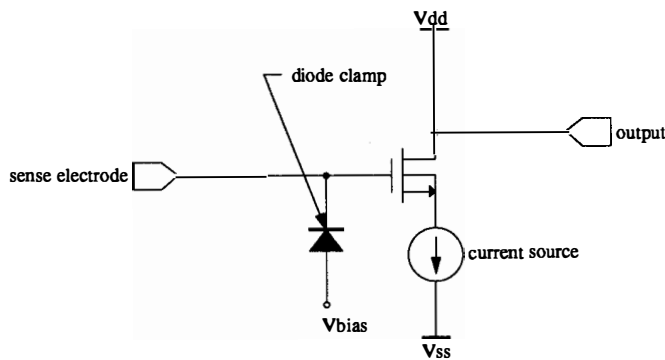


Figure 7 On-chip source follower buffer amplifier

loop to set the primary mode amplitude to a predetermined level. Since the scale factor of the sensor is proportional to the amplitude of the primary mode it is important to control this amplitude to eliminate the effects of device parameters, such as  $Q$ , on the sensor response [1].

When the device is not rotating, the secondary mode will not be excited and therefore has zero amplitude. Rotating the ring causes the secondary mode to be excited by the Coriolis acceleration and to build up amplitude. The sensor could be operated in this open-loop mode with the amplitude in the secondary mode giving the rotation rate. However, in this mode of operation the response to a step change in rotation rate would not be instantaneous, since time is required for the amplitude to build up. The amplitude build up is approximately exponential with a time constant given by

$$\tau = \frac{2Q}{\omega}$$

where  $Q$  is the quality factor of the resonance and  $\omega$  is the angular natural frequency [1,6].

This response time may be too slow for some applications so the sensor electronics includes a second control loop to continuously force the secondary mode amplitude to zero thus operating the sensor in a force-to-rebalance mode [1,6]. With this feedback control arrangement, the sensor response time and damping are entirely controlled electronically, as the control system can apply large drive forces to rapidly and continuously rebalance the Coriolis acceleration. The rebalance voltage is used to measure the rotation rate and is given by

$$\frac{v_b}{v_d} = 4A_s Q \frac{\Omega}{\omega}$$

where  $v_b$  is the secondary mode drive voltage required to rebalance the device,  $v_d$  is the primary mode drive voltage,  $A_g$  is the angular gain, and  $\Omega$  is the rotation rate to be measured.

Up to this point in the discussion we have been considering ideal balanced rings with two equal normal mode frequencies. Actual rings usually have some mass or stiffness asymmetries that split these two frequencies somewhat. Without compensation, this small frequency split produces a scale factor error and, if the split is large, the sensitivity of the sensor is greatly reduced since then there would be no  $Q$  amplification. To balance the device, voltages are applied to the balancing electrodes to force the normal mode frequencies to be equal [7]. Placing voltages on the balancing electrodes can be thought of as adding 'electrical' springs to the ring at the electrodes to compensate for device asymmetries. When the vibrating ring deforms at a biased electrode there is net force tending to make it deform still further due to the nonlinear electrostatic force. For small vibrations of the ring this additional displacement is modeled as a negative 'electrical' spring.

How balancing of the ring is performed can be understood by considering the simple nonsymmetrical mass distribution, shown in Figure 9, with extra mass at  $0^\circ$ . For this simple mass distribution the primary mode located at  $0^\circ$  has a lower natural frequency than the secondary mode located at  $45^\circ$ . To balance this extra mass, a negative electrical spring is applied to the secondary mode thereby reducing its frequency to match that of the primary mode. All asymmetries, whether due to mass or stiffness variations in the ring,

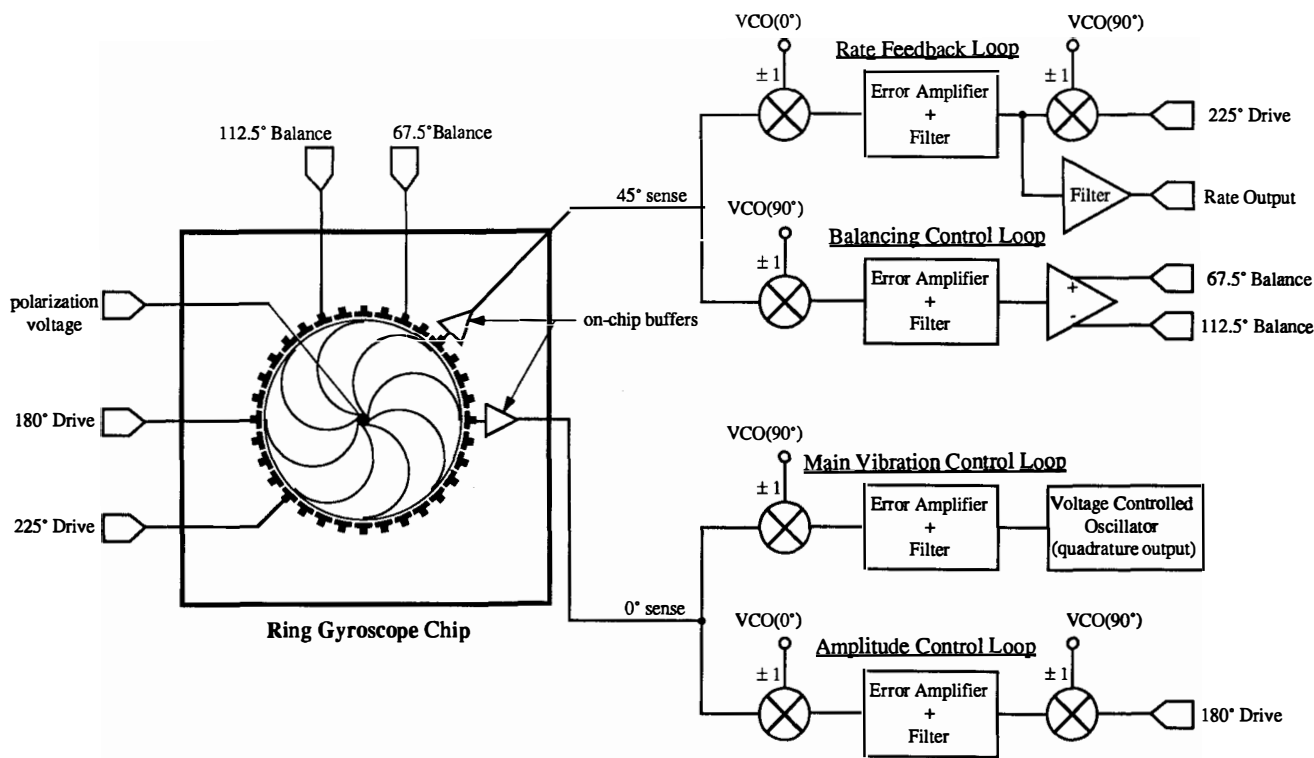


Figure 8 Block diagram of control and readout electronics

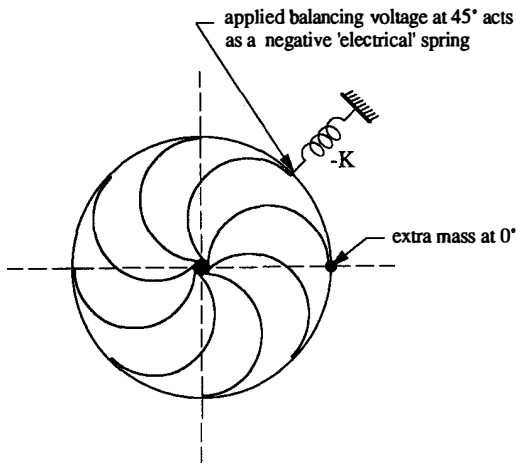


Figure 9 Balancing of simple nonsymmetrical mass distribution

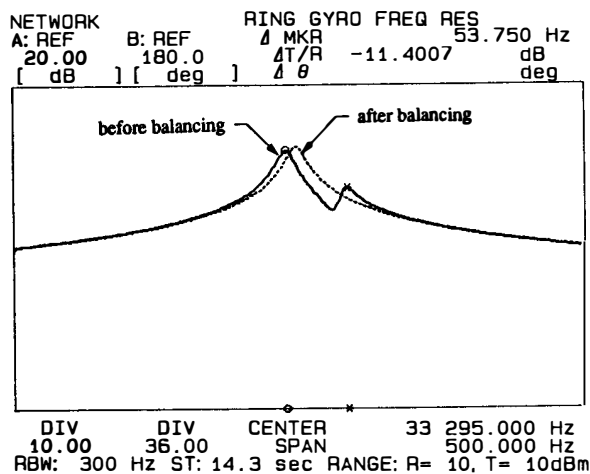


Figure 10 Frequency magnitude response before and after balancing

can be balanced in this manner as long as the frequency split is not excessively large. Initially, sensors are open-loop trimmed for course balance (Fig. 10) and, in operation, the control electronics uses the quadrature imbalance to continuously balance the device. [7].

Ultimately, the resolution of the sensor is limited by Brownian motion of the ring itself. However, this resolution has not been obtained in the current design due to noise in the buffer amplifier. The sensitivity of the device can be improved with a higher Q and by improving the buffer amplifier design.

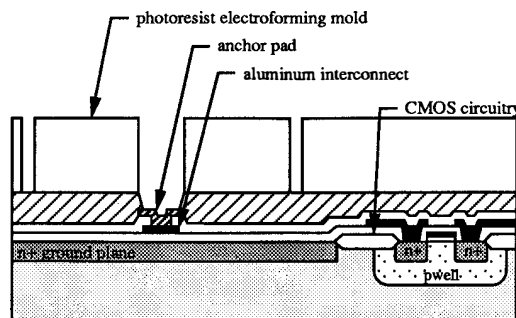
### Fabrication

To fabricate the ring gyroscope, we have developed a LIGA-like post circuit process for incorporating high aspect-ratio, electroformed metal microstructures with CMOS circuitry [17]. In the electroforming process a nonconducting mold is fabricated into which metal is electroplated to form the sensor element. Although other micromachining techniques exist for fabricating high aspect-ratio structures [18,19], we have selected electroforming because of the ease of integration and potential low-cost of this process. Our general approach is to fabricate the on-chip circuitry using a state-of-the-art standard CMOS technology, and to add the gyroscope in a series of low-temperature, post-circuit fabrication steps without any disturbance to the underlying circuitry. This partitioned approach enables one to include a large amount of on-chip circuitry with the sensor for signal readout, compensation, calibration, and external

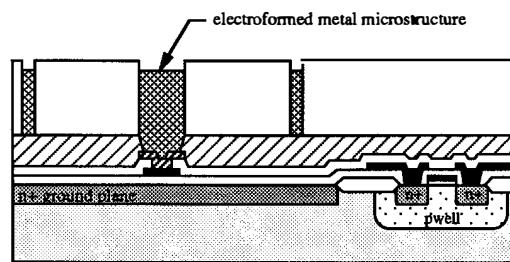
interfacing without sacrificing overall yield or increasing cost. The process is simple and uses only conventional techniques and standard equipment and can, therefore, be implemented on most IC fabrication lines with minimal additional equipment.

Fabrication of microstructures by electroforming, although not new, is currently experiencing a revival of interest for fabricating novel, high aspect-ratio microstructures. Several electroforming processes have been developed ranging from the very high aspect-ratio LIGA process to lower aspect-ratio low cost processes [17,20,21]. Similar techniques were developed over a decade ago and are now being used to fabricate thin film magnetic recording heads for computer disk drives [22]. These processes are based on fabricating a nonconducting mold into which the metal structure is electroplated. Movable microstructures are fabricated in these processes by including sacrificial spacer layers for surface micromachining.

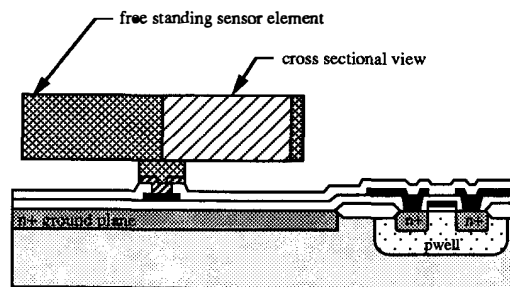
The basic process, shown in Figure 11, for fabricating the ring gyroscope begins with a standard CMOS process to fabricate the on-chip buffer circuitry. After completion of the CMOS, the aluminum metallization is passivated and anchor regions where the sensor elements are attached to the silicon substrate are defined. Next, a conductive sacrificial spacer is deposited and patterned. This layer defines the movable portions of the sensor element and also serves as a plating base layer for electroforming the microstructure. At this point, the electroforming mold is defined, and the sensor element is formed by selective electroplating in the open mold areas. The mold and sacrificial layer are then removed, completing the sensor process.



1. Electroforming mold defined by UV exposure



2. Electroforming of sensor element



3. Mold and sacrificial spacer removed

Figure 11 Electroforming fabrication sequence

The most important step in the ring gyroscope process is the formation of the electroplating mold. Initially, in the development of the ring gyroscope, we used a polyimide layer that was patterned by reactive ion etching for the electroforming mold [8]. Currently, we are using a contrast-enhanced, optical lithography process to fabricate the electroforming mold. The process uses a thick positive photoresist of high viscosity and high transparency that is defined with conventional UV lithography equipment. This is a low-cost mature technology that was originally developed for the thin film magnetic recording head industry and is, therefore, well suited to fabricating sensors [22]. Molds fabricated with this technology have nearly vertical walls with aspect ratios of about 7, almost matching the quality of molds produced by reactive ion etching (Fig.12).

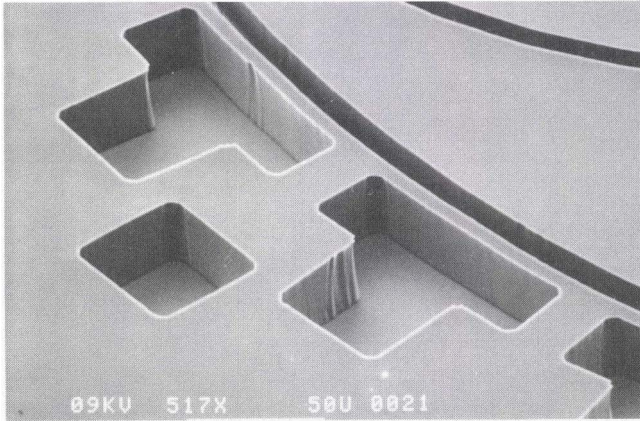


Figure 12 SEM photograph of photoresist electroplating mold

A concern with this process is that a metal structure is used for the vibrating sensor element that may exhibit creep, fatigue, or long-term drift problems. One could legitimately ask why even consider a metal sensor element, after all silicon is an excellent mechanical material and many techniques are available for micromachining this material. Certainly a high aspect-ratio polysilicon fabrication could be used to fabricate the ring gyroscope and produce a high quality device. However, one should not prematurely rule out using a metal element for the sensor, given the integration and cost advantages of the electroforming process. Furthermore, using metal structures for vibrating elements is not without precedence as many resonator devices have metal elements including a macroscopic vibratory gyroscope [1]. For these applications metal alloys are available that have been specifically designed with elastic moduli independent of temperature so that the natural frequency of these devices does not vary with temperature.

In the ring gyroscope process, we have initially used nickel as the material for the sensor element. Nickel was selected because of the ease with which it can be electroformed and because of its moderate hardness. We have found that nickel is not an ideal material for the sensing element. Ring gyroscopes have a maximum Q of around 4000 which limits the performance of the device. To improve the sensor's performance we are investigating other electroplated materials for the sensing element that potentially have a higher Q. Even with a lower Q, the gyroscope devices have shown a sensitivity of 0.5°/sec in a 10 Hz bandwidth.

Fabrication of the ring gyroscope is not limited to this electroforming process. Other micromachining techniques, including LIGA, surface micromachining of polysilicon, or reactive ion etching of bulk silicon could be used and may be advantageous for some applications [17,18,19]. The LIGA process could produce very tall devices with larger pickoff capacitors and, consequently, better sensitivity. Polysilicon devices would have higher Q and, therefore, better sensitivity. If the Young's modulus variation with crystal orientation of heavily doped silicon is not excessive the dissolved wafer process could be used to fabricate very high Q ring gyroscopes. With better materials and processes the ring gyroscope could potentially be used in low grade, short term, inertial navigation applications such as belt-buckle size, personal navigation systems.

## Experimental Results

The ring gyroscope with integrated CMOS buffer amplifiers has been fabricated using the electroforming process and the sensor has been tested. Figure 13 shows a die photo of the fabricated device including the on-chip buffer amplifiers. The ring has a diameter of 1mm, a thickness of 19 μm, a width of 5 μm, with electrode gaps of 7 μm. Circuit performance was evaluated by wafer probing before and after the electroforming process and no change in the circuit performance was observed confirming the integration potential for this fabrication process.

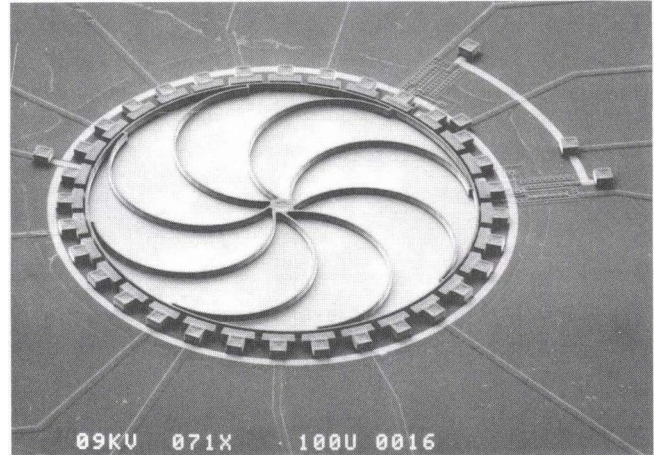


Figure 13 SEM photograph of ring gyroscope sensor

The device has been operated in the force-to-rebalance mode using the closed loop circuitry described earlier. Initial electrostatic balancing of the device was performed manually and then further automatically trimmed with the balancing control loop. Figure 14 shows the results of rotation testing of the complete sensor system and plots the analog output voltage as a function of the applied rotation rate. For these tests the device was packaged in a 24-pin ceramic DIP and continuously pumped using a metal lid with an o-ring seal. This arrangement gave a marginal vacuum level that reduced the Q of the device to 2000 down from its intrinsic Q of 4000. The sensor system shows excellent linearity and moderate sensitivity. Resolution of the system is approximately 0.5°/sec in a 10 Hz bandwidth limited by noise from the on-chip buffer amplifiers and by the low Q of the device. Using the measured secondary mode rebalance voltage and the measured primary mode drive voltage the angular gain of the ring gyroscope is found to be approximately 0.3 which is in good agreement with theoretically calculated value of 0.33 [8]. The step response of the sensor is shown in Figure 15 which shows the analog output voltage of the sensor as the rotation rate is stepped from 0°/sec to 10°/sec to 0°/sec to -10°/sec and back to 0°/sec demonstrating the transient performance of the system.

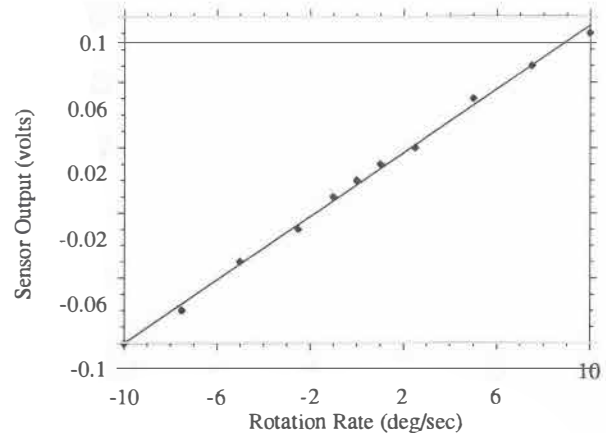


Figure 14 Measured rotation response of sensor

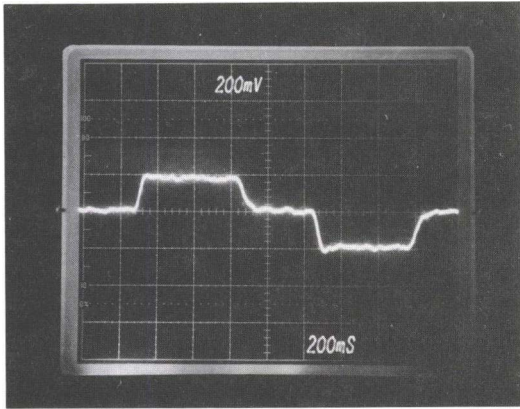


Figure 15 Step response of sensor for 10°/sec changes

## Conclusions

Micromachined gyroscopes are currently receiving a great deal of attention as many applications exist for these devices. In this paper, we have described a new, low-cost, micromachined gyroscope based on a vibrating ring. The vibrating ring design is small and naturally suited to fabrication by micromachining. It is fabricated by a simple mature process that allows for the inclusion of large amounts of on-chip circuitry, thus lowering the unit cost. Precise control of the device dimensions and material properties is not required as it is only necessary that the device be uniform—something that is easily achieved in a batch fabricated process. The device design is inherently insensitive to secondary parameters such as linear acceleration, and package-induced stress, simplifying the overall system design. Control and readout electronics for the device are relatively simple and could potentially be integrated with the device producing a reliable, low-cost, total sensor system with autocalibration and self-test features.

In comparing the ring design with other micromachined designs such as the tuning fork design [3] each device is seen to have advantages and disadvantages. The ring device is a shell design with two identical modes, so the response of this device is amplified by the quality factor  $Q$ . For a given amount of driven motion there is more motion to detect in the ring device than in the tuning fork device. However, this motion is measured in a smaller capacitance in the ring device. At this point in time, due to the low  $Q$  of the device and the buffer amplifier design, the ring gyroscope is less sensitive than the tuning fork design. As  $Q$  increases, however, the ring and tuning fork designs become more competitive in terms of raw sensitivity and then additional features of the ring gyroscope, such as its simple low-cost fabrication process and high integration potential, become very attractive.

Currently, the resolution of the ring gyroscope is about 0.5°/sec which is suitable for some, but not all, of the perceived applications. This performance level represents our initial experience with this new device and we feel many options are available to greatly improve the device. Simply increasing the device diameter lowers the resonant frequency and increases the pickoff capacitance, improving the sensitivity of the device. Reducing the electrode gaps reduces the voltage requirements for the device to more reasonable IC voltage levels without decreasing sensitivity. As mentioned earlier, the resolution of the sensor is presently limited by noise from the on-chip buffer amplifier. Better buffer designs with lower input capacitances will further improve the sensor performance. Further improvements in the sensor's performance can be obtained by increasing the quality factor of the device. Already we have measured a  $Q$  of 10,000 on some of our nickel structures and we have reason to believe that the  $Q$  for the ring will ultimately be above this level when we incorporate new materials in our electroforming process. Combining all these potential improvements we feel that a resolution below 0.05°/sec can be obtained with this device structure and fabrication process, opening up many new applications for this new sensor.

## Acknowledgements

The authors would like to express their appreciation to General Motors Corporation for their support of this research. Mr. Putty would like to acknowledge his colleagues at General Motors: Shih-Chia Chang, David S. Eddy, David B. Hicks, Andrew M. Mance, Larry M. Oberdier, and Qian Shi whose contributions and timely discussions made this reported work possible. He would especially like to thank David S. Eddy and Linos J. Jacovides for their support of his continuing education and would also like to thank the people at Delco Electronics for allowing this work to be published.

## References

- [1] "The Vibrating Structure Gyroscope," British Aerospace Systems and Equipment report #TR5102, March 1993
- [2] J. Bernstein and M. Weinberg, "A Micromachined Comb-Drive Tuning Fork Gyroscope," *21st Joint Serv. Data Exchng for G. N. and C.*, Palm Springs, California, Oct. 1992
- [3] J. Bernstein et al, "A Micromachined Comb-Drive Tuning Fork Gyroscope," *Digest IEEE/ASME Micro ElectroMechanical Systems (MEMS) Workshop*, Ft. Lauderdale, Fl., pp. 143-148, February 1993
- [4] A. Lawrence, *Modern Inertial Technology Navigation Guidance and Control*, Springer-Verlag, New York, 1993
- [5] T. Kumagai, "Development of Optical Fiber Gyroscopes for Industrial Use," *Hitachi Cable Review*, No. 9, pp. 43-48, August 1990
- [6] A. Lawrence, *Modern Inertial Technology Navigation Guidance and Control*, Springer-Verlag, New York, 1993, pp. 148-161
- [7] E. J. Loper and D. D. Lynch, "Projected System Performance Based on Recent HRG Test Results," *Proceedings 5th Digital Avionics System Conference*, Seattle, Washington, Nov. 1983
- [8] M. W. Putty, "A Micromachined Vibrating Ring Gyroscope," *Ph.D. Thesis*, University of Michigan, Ann Arbor, MI, to be published
- [9] R. R. Ragan and D. D. Lynch, "Inertial Technology for the Future, Part X: Hemispherical Resonator Gyro," *IEEE Transactions on Aerospace and Electronic Systems*, Vol. AES-20, No. 4, pp. 432-434, July 1984
- [10] S. Timoshenko, D. H. Young and W. Weaver, *Vibration Problems in Engineering*, 4th ed., John Wiley and Sons, New York, 1974
- [11] E. P. EerNisse and J. M. Parcos, "Practical Considerations for Miniature Quartz Resonator Force Transducers," *Proceedings, 28th International Instrumentation Symposium*, pp. 33-34, 1982
- [12] J. S. Burdess and T. Wren, "The Theory of a Piezoelectric Disc Gyroscope," *IEEE Transactions on Aerospace and Electronic Systems*, VOL. AES-22, No.4, pp. 410-418, July 1986
- [13] G. H. Bryan, "On a Revolving Cylinder or Bell," *Proceedings of the Royal Society (London)*, 47, 1890
- [14] R. T. Howe, "Resonant Microsensors," *Proc. 4th Int. Conf. Solid-State Sensors and Actuators (Transducers '87)*, Tokyo, Japan, pp. 843-848, June 25, 1987
- [15] D. D. Lynch, "Vibration Induced Drift in the Hemispherical Resonator Gyro," *Annual Meeting of the Institute of Navigation*, Dayton, Ohio, June 1987
- [16] W. Yun, R. T. Howe and P. R. Gray, "Surface Micromachined, Digitally Force Balanced Accelerometer with Integrated CMOS Detection Circuitry," *Tech Digest, Solid State Sensors and Actuators Workshop*, Hilton Head, S. C., pp. 126-131, June 1992
- [17] H. Guckel, et al, "Deep X-Ray and UV Lithographies for Micromechanics," *Tech Digest, Solid State Sensors and Actuators Workshop*, Hilton Head, S. C., pp. 116-122, June 1990
- [18] D. Kobayashi et al, "An Integrated Lateral Tunneling Unit," *Proceedings, IEEE Workshop on Micro Electro Mechanical Systems (MEMS' 92)*, Travemunde, Germany, pp. 214-219, Feb. 1992
- [19] Y. Gianchandani and K. Najafi, "A Bulk Silicon Dissolved Wafer Process for Microelectromechanical Systems," *Digest, International Electron devices Meeting*, Washington, D. C., Dec. 1991
- [20] G. Engelmann, et al, "Fabrication of High Depth-to-Width Aspect Ratio Microstructures," *Proceedings, IEEE Workshop on Micro Electro Mechanical Systems (MEMS' 92)*, Travemunde, Germany, pp. 93-97, Feb. 1992
- [21] A. B. Frazier and M. G. Allen, "High Aspect Ratio Electroplated Microstructures Using a Photosensitive Polyimide Process," *Proceedings, IEEE Workshop on Micro Electro Mechanical Systems (MEMS' 92)*, Travemunde, Germany, pp. 87-92, Feb. 1992
- [22] J. Bond, "The Incredible Shrinking Disk Drive," *Solid State Technology*, Vol. 36, No. 9, pp. 39-45, Sept. 1993

# A Digital Pressure Sensor Based on Resonant Microbeams

D. W. Burns, J. D. Zook, R. D. Horning and W. R. Herb  
Honeywell Technology Center  
10701 Lyndale Ave S., Bloomington, Minnesota 55420

H. Guckel  
University of Wisconsin Center for Applied Microelectronics  
Madison, Wisconsin 53706

## Abstract

A quasi-digital pressure sensor based on polysilicon resonant microbeams has been demonstrated. Pressure sensitivities of nearly 4,000 counts per second per psi have been attained on a 10-psi device with a base frequency of 233,000 Hz. The microbeams are fabricated with their own integral vacuum cavities, allowing high-Q operation in the differential pressure mode or in contact with liquids such as silicone oil. Design considerations include the effects of internal strain and lead to a push-pull layout configuration independent of microbeam strain or diaphragm thickness. Fabrication technology incorporates fine-grained polysilicon, surface micromachining, and reactive sealing. Packaging into precision avionics headers is being used for preliminary testing. Testing results indicate suitability for precision avionics, industrial, and commercial applications. Optical methods have been used to test resonant microbeam pressure sensors and verify the push-pull design methodology.

## Introduction

Pressure sensors are second only to temperature sensors as the most important and widely used type of sensors being sold today. They are used to measure not only pressure but flow, fluid level, and acoustic intensities. More than ten different uses for pressure sensors have been identified in automotive applications. Honeywell introduced piezoresistive silicon sensors in the mid-1960s that, with continuous improvements, have been used extensively for precision pressure measurement in industrial controls and aircraft guidance controls. The trend in both of these areas is to increase the number of measurement points and the accuracy of the measurements under the premise that better information leads to better control.

Improvements in precision silicon micromachining technology during the past decade have led to a wide range of improved sensing structures, including the use of resonant microbeams as strain transducers.<sup>1-7</sup> With resonant sensors, the output is in the form of a robust sinusoidal signal whose frequency changes with pressure. The output is quasi-digital in the sense that it can easily be converted to digital form using a high frequency clock. Strain-sensitive mechanical-grade polysilicon resonators have been fabricated monolithically on silicon pressure diaphragms with integral vacuum-sealed cavities (see Figure 1) for differential or absolute pressure sensors that are usable in a wide range of applications.

Precision pressure applications now require "smart" transmitters that provide calibrated, temperature-compensated output in a specified format. Compensation for temperature and pressure nonlinearities requires calibration constants that must be stored in look-up tables and processing capability to execute the data correction algorithms. This capability is included in the package of a smart transmitter but not on the sensor chip. Use of a separate microcontroller chip that is interconnected to the sensor chip inside the package offers much greater flexibility and much faster time to market than combining them on the same chip. In this way, separate manufacturing processes can be used for each chip and there is no need to compromise the sensor or IC design or processing to achieve a merged process. In the case of the resonant sensors, it is possible to integrate the oscillator on the sensor chip using simple analog electronics. At the present time, however, we are using discrete surface-mount elements for the oscillator electronics.

## Pressure Sensor Design

Static and dynamic structural modeling of the resonant microbeam and the sensor microstructure have been used extensively to guide

the design of the resonant pressure sensor devices. Simplified analysis of a resonant microbeam pressure sensor requires a model of the deflection profile of the pressure diaphragm under load, the resulting applied strain to the microbeam(s) as a function of the position on the diaphragm, and the shift in resonant frequency of the microbeam with applied strain. With these basic elements, the microbeam frequency response as a function of applied pressure can be predicted as a function of geometry and material properties.

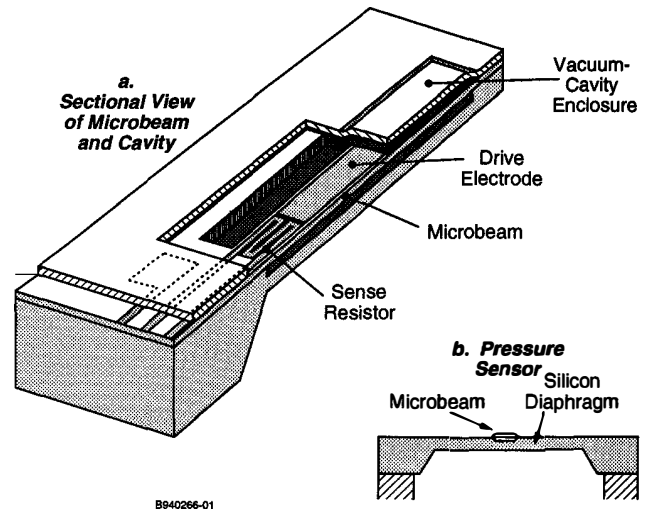


**Figure 1. Cutaway view of a resonant microbeam.** The sectional view in (a) shows the microbeam inside its vacuum-cavity enclosure with a central drive electrode and a position sensing microbeam at one end. A small ac voltage applied to the drive electrode electrostatically excites the microbeam, which is maintained by external drive/sense electronics. The resonant frequency of the microbeam shifts with applied axial strain. Selective positioning on a silicon diaphragm provides a large shift in frequency with differential pressure applied across the diaphragm.

The response of a undamped resonant microbeam element is governed by the following differential equation,<sup>1,6</sup> which includes the effects of intrinsic and applied strain:

$$EI\partial^4w/\partial x^4 - (\epsilon_0 + \epsilon_{app})EA\partial^2w/\partial x^2 = -\rho A\partial^2w/\partial t^2 \quad (1)$$

where  $w(x,t)$  is the lateral, time-dependent displacement of the beam along its length,  $E$  is Young's modulus of the beam material,  $I$  is the moment of inertia,  $\epsilon_0$  is the internal or residual strain,  $\epsilon_{app}$  is the applied strain to the beam ends,  $A$  is the beam cross-sectional area, and  $\rho$  is the mass density. This equation does not yield exact solutions, but approximate solutions can be found using energy or Rayleigh methods, which give the resonant frequencies of the beam. The resonant frequencies of a rectangular beam element of length  $l_b$  and thickness  $h_b$  are then given by Eq. 2 for doubly supported beams (clamped-clamped) and Eq. 3 for cantilever beams:

$$f_r = (b_n/2p)(E/\rho)^{1/2}(h_b/l_b^2)(1 + \gamma_n(l_b/h_b)^2(\epsilon_0 + \epsilon_{app}))^{1/2} \quad (2)$$

$$f_r = (c_n/2p)(E/\rho)^{1/2}(h_b/l_b^2) \quad (3)$$

The coefficients for the fundamental frequency and the first two overtones are summarized in Table 1.

**Table 1. Coefficients of resonant microbeams.**

	$b_n$ Doubly Supported	$\gamma_n$ Doubly Supported	$c_n$ Cantilever
Fundamental	6.4586	0.2949	1.0150
First Overtone	17.8034	0.1453	6.3608
Second Overtone	34.9018	0.08119	17.8104

To determine the applied strain to the microbeam, a model of the pressure sensor microstructure is required. With the pressure diaphragm in the form of a thin circular plate, the displacement profile under uniform applied pressure may be found in standard references<sup>8</sup> as:

$$w(r) = 3p_{app}(1 - \nu^2)(a^2 - r^2)^2/16Eh_d^3 \quad (4)$$

where  $w$  is the diaphragm deflection,  $p_{app}$  is the applied pressure,  $E$  and  $\nu$  are Young's modulus and Poisson's ratio for the silicon diaphragm,  $a$  and  $h_d$  are the diaphragm radius and thickness, and  $r$  is the radial coordinate from the center. The corresponding strain distribution at the diaphragm surface is:

$$\epsilon_r(r) = -(h_d/2)\partial^2 w/\partial r^2 = -3p_{app}a^2(1 - \nu^2)(1 - (r/a)^2)/8Eh_d^3 \quad (5)$$

For a microbeam mounted to the surface of the diaphragm, the strain applied to the beam may be calculated as the average diaphragm strain over the beam length. Eq. 6 and 7 give this result for two specific cases. Eq. 6 gives the applied strain to a microbeam of length  $l_b$  with one end mounted at the diaphragm edge and extending inward, while Eq. 7 gives the result for a beam centered on the diaphragm:

$$\epsilon_a = 3p_{app}a^2(1 - \nu^2)[2 - 3(l_b/a) + (l_b/a)^2]/8Eh_d^2 \quad (6)$$

$$\epsilon_a = -3p_{app}a^2(1 - \nu^2)[1 - (l_b/2a)^2]/8Eh_d^2 \quad (7)$$

By combining Eq. 6 and 7 with Eq. 2, the change in microbeam resonant frequency with applied pressure may be determined for a variety of sensor layouts. For a dual-beam sensor layout, the sign difference between Eq. 6 and 7 implies a push-pull configuration, where the center- and edge-mounted microbeams undergo opposite applied strain and frequency shift with applied pressure.

To optimize the push-pull pressure sensor configuration, a sensitivity factor was defined to quantify the beam frequency response as

$$s_f = \Delta f/f_0/\Delta p_{app} \quad (8)$$

where  $\Delta f$  is the total frequency shift with pressure,  $f_0$  is the base frequency, and  $\Delta p_{app}$  is the change in pressure. Eq. 6, 7, and 8 may be used to calculate the sensor pressure sensitivity as a function of the beam length to diaphragm radius ratio. Figure 2 plots  $s_f$  versus  $l_b/a$  for the edge and center microbeams, and the combined push-pull configuration with equal length edge and center beams, with an assumed intrinsic strain value of 300 microstrain. This factor is maximized in the push-pull configuration for an  $l_b/a$  ratio of 0.4, a result that is independent of the beam and diaphragm thickness. This design choice also results in equal length beams, which provides first-order cancellations of microbeam nonlinearity and temperature effects.

An alternative sensor configuration with a single active beam on the diaphragm and a reference beam mounted off the diaphragm was also studied. Referring again to Figure 2, a sensor with a single center-mounted beam would have an optimum  $l_b/a$  ratio of about 0.6, a somewhat longer beam length than the optimal push-pull configuration. Unlike the push-pull configuration, the optimal singly active center-mounted design length varies significantly with the microbeam intrinsic strain level.

The design analysis was used to select the microbeam length-to-diaphragm diameter ratios to optimize the nominal frequency sensitivity of the resonant pressure sensor. The specific pressure sensor ranges can then be attained by varying diaphragm thickness

without changing the layouts. The overall device performance has many other influences, including the microbeam drive/sense configuration. The details of the microbeam design and layout are further influenced by processing considerations, drive/sense electronics and packaging. Interconnects to the microbeam drive and sense lines are configured to minimize parasitic resistances and capacitances. The piezoresistor length is optimized to maximize the change in resistance with beam deflection. The electrostatic drive electrode may be optimized to selectively excite the fundamental mode and discourage higher order modes. Processing constraints affect the design rules for the microbeam, affecting in turn the minimum beam length and width. Packaging effects such as mechanical and thermal hysteresis are reduced by isolation techniques and the push-pull configuration.

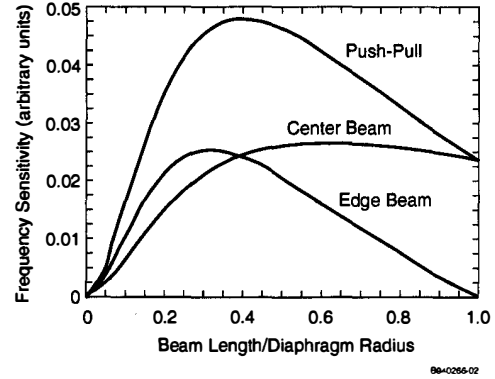


**Figure 2. Pressure sensitivity of a resonant microbeam pressure sensor. The normalized shift in output frequency is plotted versus the microbeam length normalized to the diaphragm radius. The sensitivity of a center-mounted and an edge-mounted microbeam increases with length due to the increase in gage factor of the microbeam with increased aspect ratio (length/thickness) to a maximum value, then decreases due to a rapid reduction in the average applied strain. At the ratio  $l_b/a = 0.4$ , the frequency sensitivities of the two microbeams are equal in magnitude but opposite in sign, allowing subtraction and cancellation of first-order effects.**

## Sensor Fabrication

Resonant microbeam pressure sensors are fabricated on an n-type silicon epitaxial layer that is grown on a p-type substrate. The resonant microbeams are formed first, followed by diaphragm etching. Initial microbeam process steps include the growth and patterning of a thin oxide and deposited silicon nitride. Two local oxidations are done in the lower cavity region.<sup>9</sup> The first oxidation forms a depression in the silicon and is stripped off. The second oxidation deepens the depression to about 7500 Å and fills it in. The oxide forms a sacrificial layer upon which the beams are formed. The thin oxide film surrounding the depressions is patterned into narrow lines, forming channels for introduction of the sacrificial etchant later in the process. A 2- $\mu$ m-thick film of mechanical-grade polysilicon, deposited over the oxide films and implanted, will form the resonant beam. The polysilicon piezoresistors are deposited and patterned over the beam poly. Following the piezoresistor formation, the beam poly is etched to define the exact beam dimensions, typically 46  $\mu$ m wide  $\times$  200  $\mu$ m long. A low-temperature oxide is then deposited and patterned to form a sacrificial layer above the beam. Another 2- $\mu$ m-thick polysilicon film is deposited and patterned to form a shell over the beam and sacrificial layers. An HF solution penetrates through patterns etched in the shell and through the oxide channels. All oxide in the cavity is etched away, freeing the microbeams for vibration. After careful rinsing in water and cyclohexane baths, the wafers are placed in a vacuum chamber for sublimation of the solidified liquid in the shell. Following sublimation, the wafers are immediately placed in an LPCVD furnace to be evacuated and reactively sealed. Finally, contact openings are made to the substrate, piezoresistor, and shell, and PtSi contacts are formed in the openings. Aluminum is used for pads and for connection to the contacts. This completes the resonant microbeam formation, as shown in Figure 3.

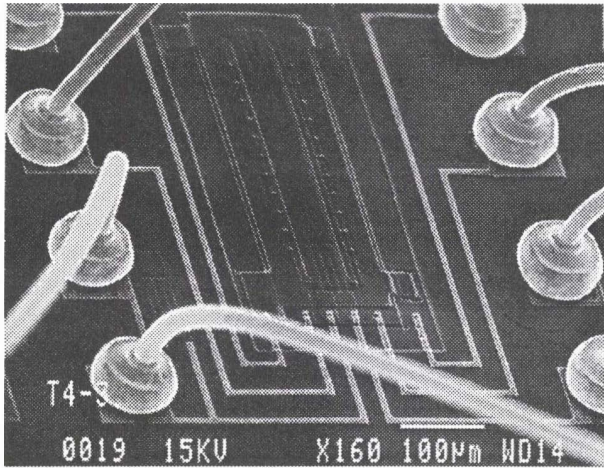


Figure 3. SEM of a wire-bonded resonant microbeam. Electrical interconnects are made to the drive line and sense lines of the 400- $\mu\text{m}$ -long and 46- $\mu\text{m}$ -wide microbeam.

An HF-based anodic etch is used to form the diaphragms. The backsides of the wafers are ground and polished to a thickness of about 280  $\mu\text{m}$ . A Pt film is deposited and patterned with openings for the diaphragm etch. Additional pinhole protection is provided by a sputtered nitride film. The Pt acts as both the mask for the etching and as the contact to the p-type substrate. Etching is carried out in an HF-based electrolyte containing  $\text{H}_2\text{SO}_4$  to allow higher current density.<sup>10</sup> The wafer is biased anodically at about 2–2.5 V with respect to a Pt counter electrode in the solution. The p-type substrate etches readily; etch stop occurs when the etch front reaches the n-type epilayer. This procedure forms a circular diaphragm with thickness determined by the initial epilayer thickness. Following removal of the backside nitride and Pt and the frontside protection layers, the wafer is diced and mounted in packages for testing.

### Packaging and Test Results

Completed resonant microbeam pressure sensor wafers are probed optically to verify microbeam operation, frequency, and Q.<sup>11</sup> This noninvasive measuring technique requires the modulation of incident laser light around the microbeam resonant frequency. Reflected light is detected by a simple photodetector to locate microbeam resonances and determine Q.

Select die are electrically probed to verify drive line and piezo-resistor impedances. The die are thermoelectrically bonded to a Pyrex tube, mounted in a Honeywell avionics product header, and wire bonded. A die with select microbeams wire bonded is shown in Figure 4. A metal lid can be welded on under vacuum to provide a vacuum reference for absolute pressure sensor measurements, or omitted for differential or gage pressure operation. The sensor die and header are mated with associated drive/sense electronics, as shown in Figure 5. The drive/sense electronics excite the microbeam into resonance and maintain it there as pressure is changed. The output is buffered for external data acquisition and analysis. The output frequency of a single microbeam as pressure is varied using a commercially available transfer standard is shown in Figure 6.

Linearity, span shift, null shift, and thermal hysteresis measurements are now under way on first units. Long-term testing on resonant microbeam devices have now exceeded 24,000 continuous operating hours without failure. Periodic checking of base frequency and Q shifts show little alterations. Continuous data taken on resonators suspended in a constant temperature bath show short-term stability as low as 0.01 ppm based on the fundamental resonant frequency. Frequency noise data for a typical microbeam is shown in Figure 7. The data represent nearly 100,000 measurement points. This device is being operated long term and has over 7,000 continuous operating hours.

Optical interrogation of the resonant microbeam pressure sensor has been demonstrated using the packaging and fixturing described

above. Modulated incident laser light excites the microbeam into resonance. Resonances are detected by reflected light, as shown in Figure 8. Pressure applied to the backside of the diaphragm shifts the resonant frequencies of the microbeams to provide a measure of applied pressure, as shown in Figure 9. Optical testing shows high Q, high sensitivity, and excellent stability.

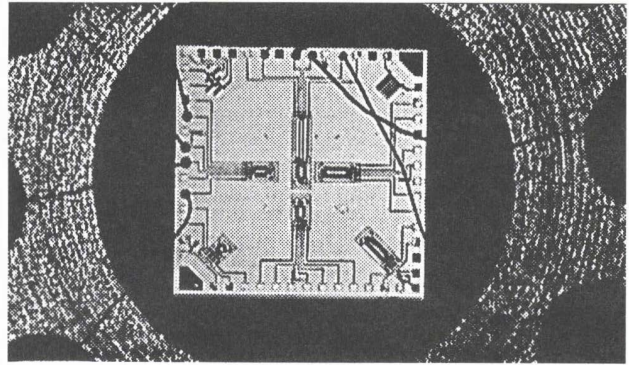


Figure 4. Resonant microbeam pressure sensor die. A multiplicity of resonant microbeams are located at the center and periphery of an isotropically etched silicon diaphragm and are selectively wire bonded for testing purposes. The die measures 3.3 mm  $\times$  3.3 mm.

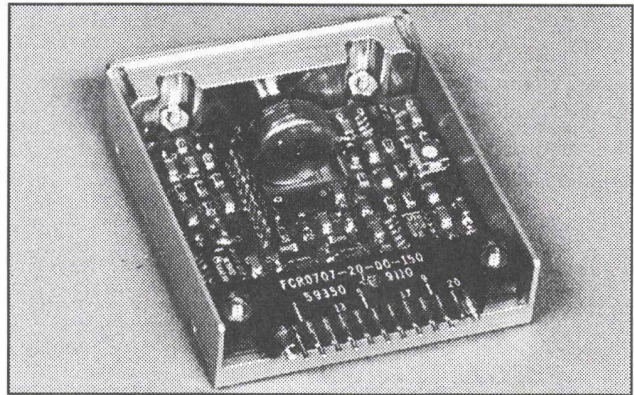


Figure 5. Packaged pressure sensor with digital output. The resonant microbeam pressure sensor die is located inside the circular metal can surrounded by the drive/sense electronics. The sensor is driven with standard  $\pm 12\text{-V}$  supplies and a buffered frequency output is available at one of the pins. The pressure port is located on the opposite side of the stainless steel manifold.

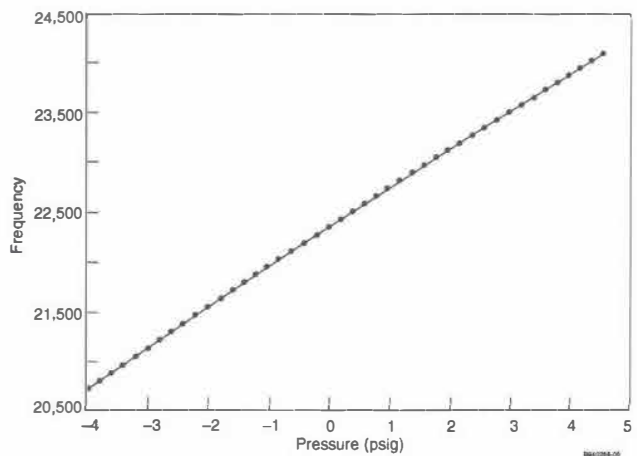
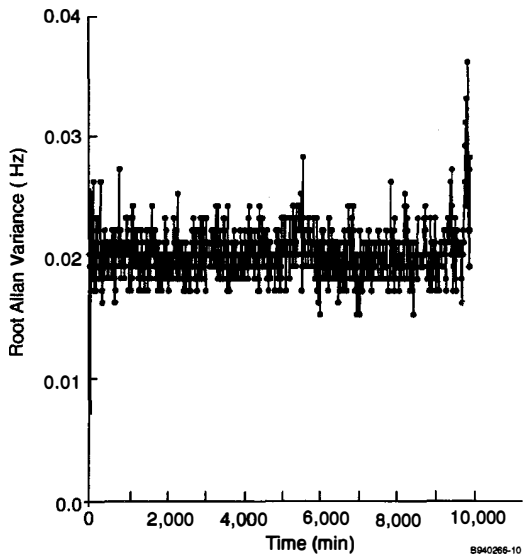
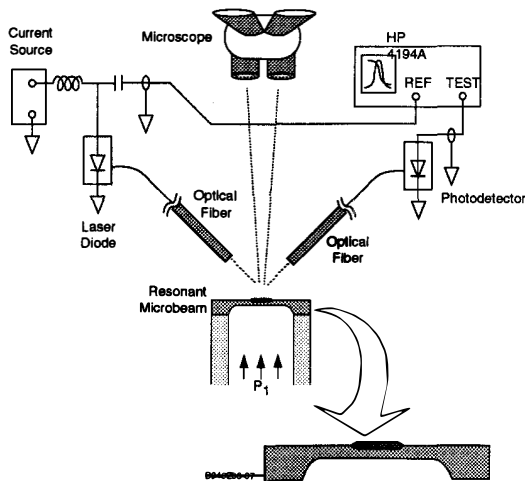


Figure 6. Frequency output in differential mode. Operating at a base frequency of 223,000 Hz, the pressure sensitivity is 3,880 Hz/psi.



**Figure 7.** Root Allan variance of a resonant microbeam. This plot is a compilation of 100 consecutive paired variance data taken every 10 min over the time frame of a week, showing short-term stability of 0.02 Hz for a base frequency of 625,000 Hz.



**Figure 8.** Optical test arrangement for resonant microbeam pressure sensor. An isotropically etched silicon die with polysilicon resonators is mounted on a Pyrex tube. Pressure applied up the tube creates bending stresses in the diaphragm that cause shifts in the resonant microbeam frequency. Excitation of the microbeam is achieved with modulated incident laser light and sensed with a simple photodetector.

## Results and Conclusions

Resonant microbeam technology combines precision polysilicon microbeam strain sensors with conventional silicon microstructures to produce high-quality silicon sensors that integrate the digitizing function directly at the sensor. Interconnection with digital control systems is possible via electrical or optical means, allowing remote operation in harsh environments where immunity to EMI or intrinsic safety is required. The large gage factors of a resonant microbeam and its integral vacuum cavity to maintain high-Q operation allow large signals to be obtained with minimal strain for avionics and industrial applications such as differential pressure sensors.

## Acknowledgments

The authors wish to acknowledge the Wright Laboratory Electronic Technology Directorate for partial funding of this activity. We would also like to acknowledge Jerry Huber and Bob Martin for sensor processing, Cindy Bassett for testing, and the Honeywell

Solid State Electronics Center for providing precision packaging and wire bonding of the sensors.

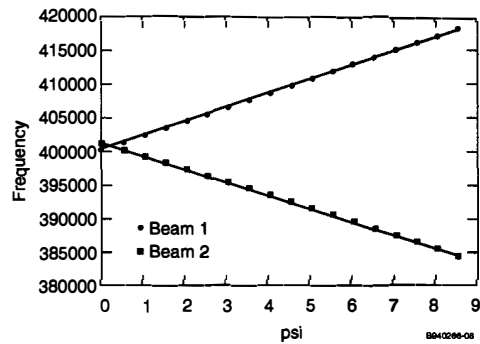


**Figure 9.** Output frequencies for the optical resonant microbeam pressure sensor. Two microbeams in the push-pull configuration are independently tested while pressure to the backside of the diaphragm is altered. The base frequencies of each microbeam is just over 400,000 Hz with a pressure sensitivity of nearly  $\pm 2,000$  Hz/psi.

## References

1. Sniegowski, J.J., "Design and Fabrication of the Polysilicon Resonating Beam Force Transducer," PhD Dissertation, University of Wisconsin-Madison, 1991.
2. Ikeda, K.; Kumayama, H.; Koboyashi, T.; Wanabe, T.; Nishikawa, T.; Yoshida, T.; and Harada, K., "Silicon Pressure Sensor Integrates Resonant Strain Gauge on Diaphragm," *Sensors and Actuators*, A21-23 (1990), pp. 146-150.
3. Petersen, K.; Pourahmadi, F.; Brown, J.; Parsons, P.; Skinner, M.; and Tudor, J., "Resonant Beam Pressure Sensor Fabricated with Silicon Fusion Bonding," *Transducers '91, Proceedings of the 1991 IEEE Conference on Solid-State Sensors and Actuators*, San Francisco, June 24-28 1991, pp. 664-667.
4. Guckel, H.; Rypstat, C.; Nesnidal, M.; Zook, J.D.; Burns, D.W.; and Arch, D.K., "Polysilicon Resonant Microbeam Technology for High-Performance Sensor Applications," *IEEE Solid-State Sensor and Actuator Proceedings*, Hilton Head Is., SC, June 22-25, 1992, pp. 153-156.
5. Zook, J.D.; Burns, D.W.; Guckel, H.; Sniegowski, J.J.; Engelstad, R. L.; and Feng, Z., "Characteristics of Polysilicon Resonant Microbeams," *Sensors and Actuators*, A35 (1992), pp. 51-59.
6. Tilmans, H.A.C., "Micromechanical Sensors Using Encapsulated Built-in Resonant Strain Gauges," PhD Dissertation, University of Twente, Enschede, The Netherlands (1993).
7. Nikolich, A.D., and Senturia, S. D., "A Wafer-Bonded Silicon Load Cell Operating in the Tensioned-Wire Regime," *IEEE Solid-State Sensor and Actuator Proceedings*, Hilton Head Is., SC, June 22-25, 1992, pp. 157-160.
8. Timoshenko, S., *Theory of Plates and Shells*, 2nd edition, McGraw-Hill, 1959.
9. Sniegowski, J.J.; Guckel, H.; and Christensen, T.R., "Performance Characteristics of Second-Generation Polysilicon Resonating Beam Force Transducers," *IEEE Solid State Sensor and Actuator Workshop*, Hilton Head Is., SC, June 1990, pp. 9-12.
10. Wen, C.P., and Weller, K.P., *J. Electrochem. Soc.*, 119, 547, 1972.
11. Guckel, H.; Nesnidal, M.; Zook, J.D.; and Burns, D.W.; "Optical Drive/Sense for High-Q Resonant Microbeams," *Transducers '93, Proceedings of the 7th International Conference on Solid State Sensors and Actuators*, Yokohama, Japan, June 7-10 1993, pp. 686-689.

# Piezoelectrically Activated Resonant Bridge Microaccelerometer

David B. Hicks, Shih-Chia Chang, Michael W. Putty and David S. Eddy

Electrical and Electronics Department  
General Motors Research and Development Center  
Warren, MI 48090-9055

## ABSTRACT

As the complexity of automotive systems increases, there has been a concurrent increase in demand for motion sensors. Vibratory sensors, capable of measuring linear and angular motion, have the potential of satisfying these demands. A resonant bridge microaccelerometer has been developed to test two design innovations. The first involves the incorporation of thin film zinc oxide to piezoelectrically excite and detect bridge resonance. The primary advantage of moving away from electrostatic excitation and detection to the piezoelectric approach is the elimination of squeeze-film damping. Higher Q values have been obtained as a result and offers the potential for device operation at reduced vacuum levels. The second innovation turns the device inside out by placing the proof mass around the perimeter of the device rather than at the center. This new cantilever-like configuration decouples the resonant bridges from the effects of package-induced stress and also provides a proof mass that is six times heavier than its central proof mass counterpart.

## INTRODUCTION

Sensors based on beam resonance have attracted more and more attention over the past few years due to the quasi-digital nature of the output signal and the better sensitivity/bandwidth product of the sensors [1-4]. So far, beam resonance has been most often activated by electrostatic force. Simple device structure and IC process compatibility are the advantages of this approach. However, the close proximity of the beam to the drive-sense electrodes ( $\sim 2 \mu\text{m}$ ) necessitates vacuum packaging ( $\leq 10$  mTorr) to minimize squeeze film damping effects so as to achieve a high quality factor (Q). In addition, the electrically measured resonant frequency is a strong function of the electrode gap distance, and hence, it is more sensitive to processing variations associated with the construction of resonant structures [5].

As an alternative to electrostatics, we have experimented with sputter-deposited zinc oxide (ZnO) thin films to piezoelectrically drive and sense bridge resonance. With drive voltages of a few millivolts, a clear bridge resonance was observed even at one atmosphere. The measured Q value was 300. Q increased to 1800 when the measurement was done under a vacuum of  $\sim 100$  mTorr, which is two to three times greater than the Q values achieved with the electrostatically driven devices. In this work, the established ZnO thin film technology is applied to the fabrication of a resonant bridge microaccelerometer. Simple on-chip circuitry, consisting of a diode and a n-channel depletion mode MOSFET is incorporated for signal conditioning and amplification.

## SENSOR CONCEPT

The device is a two-axis accelerometer which employs two pairs of silicon bridges orthogonally attached to a common proof mass to measure in-plane acceleration. This acceleration causes differential axial loads on opposing bridge pairs, thereby shifting their resonant frequencies. The acceleration component aligned

with a pair is measured by the difference in resonant frequencies. By monitoring both bridge pairs simultaneously, direction can also be determined. In-depth discussions on the device concept and theory of operation have been reported previously [4].

In this version of the accelerometer, bridge resonance is driven and detected piezoelectrically. When an electric field is applied vertically across the ZnO drive element, a stress is induced in the film laterally (through piezoelectric coupling,  $d_{31}$ ). This stress bends the bridge which, in turn, produces a strain in the sensing element. The resulting change in the charged state of the ZnO sensing element is detected and amplified by the on-chip circuitry.

## DEVICE DESCRIPTION

Plan and cross-sectional views of the overall structure of the accelerometer are shown in Fig. 1 (a-c). The dimensions of the various components are given below, along with brief descriptions:

### 1. Proof mass

12 mg (peripheral)    2 mg (central)

Two different proof mass arrangements were devised: a central proof mass (Fig. 1b), and a peripheral proof mass (Fig. 1c). For a given chip size, the peripheral proof mass is approximately six times heavier than the central proof mass which translates into greater sensitivity. The accelerometer with the peripheral proof mass is essentially a released structure and inherently is less affected by package-induced stress.

### 2. Drive-Sense Elements

thickness =  $1 \mu\text{m}$     area =  $9600 \mu\text{m}^2$  (per pad)

The transducing elements are positioned in two different configurations as shown in Figs. 2a and 2b. In both cases, the ZnO pads are positioned such that they do not cross the points of inflection of the fundamental flexure mode of the bridge. The configuration shown in Fig. 2b provides a larger ZnO area, and, hence, a larger sensor signal is expected. The drive and sense elements are sandwiched between silicon dioxide and silicon nitride layers to prevent charge leakage, thus ensuring device performance in the low frequency spectrum.

### 3. Bridges

	<u>Length</u>	<u>Width</u>	<u>Thickness</u>
Resonant bridge:	500 $\mu\text{m}$	100 $\mu\text{m}$	5 $\mu\text{m}$
Constraining bridge:	1200 $\mu\text{m}$	100 $\mu\text{m}$ ,	10 $\mu\text{m}$

The resonant bridges as well as the constraining bridges are made of heavily boron-doped single crystal silicon.

## FABRICATION

Figure 3 shows the principal processing steps in sequence. The thicknesses of the resonant and constraining bridges are defined by two separate deep boron diffusion operations (Fig. 3a). The on-chip circuitry (a diode and a n-channel depletion mode MOSFET) is closely positioned to the resonant bridge with the diode-gate lead connected to the sensing element (Fig. 3b). The ZnO pads are deposited by rf magnetron sputtering and patterned with either phosphoric acid or ammonium chloride etchants [6]. The ZnO is sandwiched between a silicon dioxide layer and a plasma nitride layer before aluminum metallization (Fig. 3c). The proof mass, resonant and constraining bridges are formed simultaneously by etching in an ethylene diamine-pyrocatechol (EDP) etchant (Fig. 3d). Figures 4a and 4b are photomicrographs of the fabricated accelerometers showing both proof mass configurations.

## RESULTS AND DISCUSSION

Figures 5a and 5b show the frequency response of the resonant bridge associated with the central proof mass when operated at one atmosphere and at 100 mTorr, respectively. Bridge resonance is clearly detected at one atmosphere, however, the quality factor (Q) is low. Q increases to 1,800 when the device is operated at 100 mTorr. Similar results are obtained for the device with a peripheral proof mass. The measured resonant frequency,  $f_m$ , is  $\geq 200$  kHz, which is somewhat higher than the expected natural frequency,  $f_o$ , of an unstressed bridge as estimated by the equation,

$$f_o = 1.03 \sqrt{\frac{E}{(1-\nu^2)\rho}} \left(\frac{t}{l^2}\right) \quad (1)$$

where E is Young's modulus,  $\nu$  is Poisson's ratio,  $\rho$  is the density, t is the bridge thickness, and l is the length of the bridge. Neglecting the effects of the various layers comprising the bridge and using  $E = 1.5 \times 10^{12}$  dyne/cm<sup>2</sup>,  $\nu = 0.25$ ,  $\rho = 2.328$  g/cm<sup>3</sup>,  $t = 5\mu\text{m}$ , and  $l = 500\mu\text{m}$ , the calculated resonant frequency is  $\sim 165$  kHz. The built-in tensile stress can be estimated from the following relationship,

$$f_m = f_o \sqrt{1 + 0.293 \left(\frac{\sigma}{E}\right) \left(\frac{l}{t}\right)^2} \quad (2)$$

and comes out to be  $\sim 2 \times 10^6$  dyne/cm<sup>2</sup>, which is comparable to the values reported by Ding, et al, for heavily boron-doped silicon [7].

Figures 6a and 6b show single-bridge responses to static in-plane accelerations of  $\pm 1g$  for the different proof mass configurations. The measured frequency shifts are  $\sim 36$  Hz and 12 Hz for devices with the peripheral proof mass and central proof mass, respectively, as compared with the calculated values of 130 Hz and 20 Hz. The causes of these large discrepancies between the measured and calculated responses are not clear at this point. It may be attributed to the fact that the resonant bridge is formed by five layers of different materials: B<sup>+</sup> doped silicon / silicon dioxide / ZnO / plasma nitride / aluminum.

## CONCLUDING REMARKS

The results obtained in this work clearly demonstrate that piezoelectric thin film ZnO is a viable transduction material for a resonant bridge accelerometer and that sensor designs exploiting the piezoelectric effect offer some advantages over prior developments using electrostatics. In the piezoelectric design, the electrodes are an integral part of the resonant bridge, thus eliminating the bridge-to-electrode air gap required for electrostatic devices. Consequently, device performance is not limited by squeeze film damping nor by nonlinear effects associated with changing air gap dimensions. When measuring the quality factor (Q) for both devices at 100 mTorr, the new device yields 5 times the Q value of its electrostatic predecessor. The direct benefit of the new design is that vacuum packaging requirements may be relaxed -- or eliminated -- for some applications.

Finally, there are two advantages to the peripheral proof mass configuration: a) it eliminates the coupling of package-induced stress to the resonant bridges which simplifies the packaging process, and b) it yields a heavier proof mass for a given die size when compared to its central proof mass counterpart, thus making more efficient use of silicon real estate.

## REFERENCES

1. W. Yun and R. T. Howe, "Recent Development in Silicon Microaccelerometers," *Sensors*, 2, 10 (1992) p. 31.
2. S. Bouwstra, R. Legtenberg, H. A. C. Tilmans and M. Elwenspeck, "Resonating Microbridge Mass Flow Sensor," *Sensors and Actuators*, A21-A23 (1991) p. 332.
3. R. A. Buser and N. F. Derooij, "Very High Q-factor Resonators in Monocrystalline Silicon," *Sensors and Actuators*, A21-A23 (1991) p. 323.
4. S. C. Chang, M. W. Putty, D. B. Hicks, C. H. Li and R. T. Howe, "Resonant-Bridge Two-axis Microaccelerometer," *Sensors and Actuators*, A21-A23 (1991) p. 342.
5. M. W. Putty, D. B. Hicks, S. C. Chang, "An Integrated Microaccelerometer for Automotive Sensing Applications," *GM Internal Research Report* (1990).
6. S. C. Chang, D. B. Hicks and R. C. O. Laugal, "Patterning of Zinc Oxide Thin Films," *Technical Digest, IEEE Solid-State Sensor and Actuator Workshop, Hilton Head, SC, 1992*, p. 41.
7. X. Ding, W. H. Ko, Y. Niu and W. He. "A Study on Silicon-Diaphragm Buckling," *Technical Digest, IEEE Solid-State Sensor and Actuator Workshop, Hilton Head, SC, 1990*, p. 128.

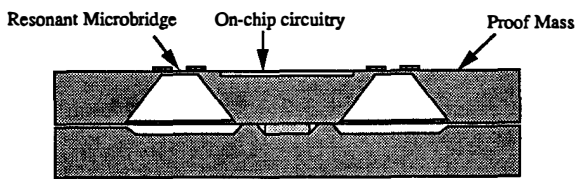
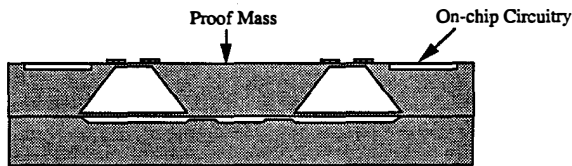
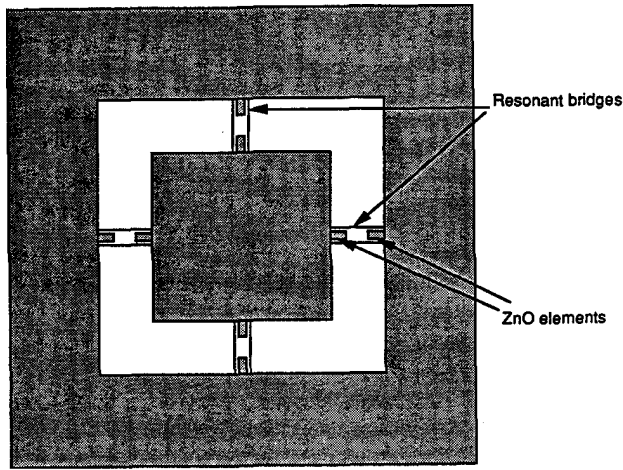


Fig. 1 Schematic diagram of a piezoelectrically driven and sensed resonant bridge microaccelerometer with alternative proof mass configurations: a) top view, b) cross sectional view of central proof mass configuration, c) cross sectional view of peripheral proof mass configuration.

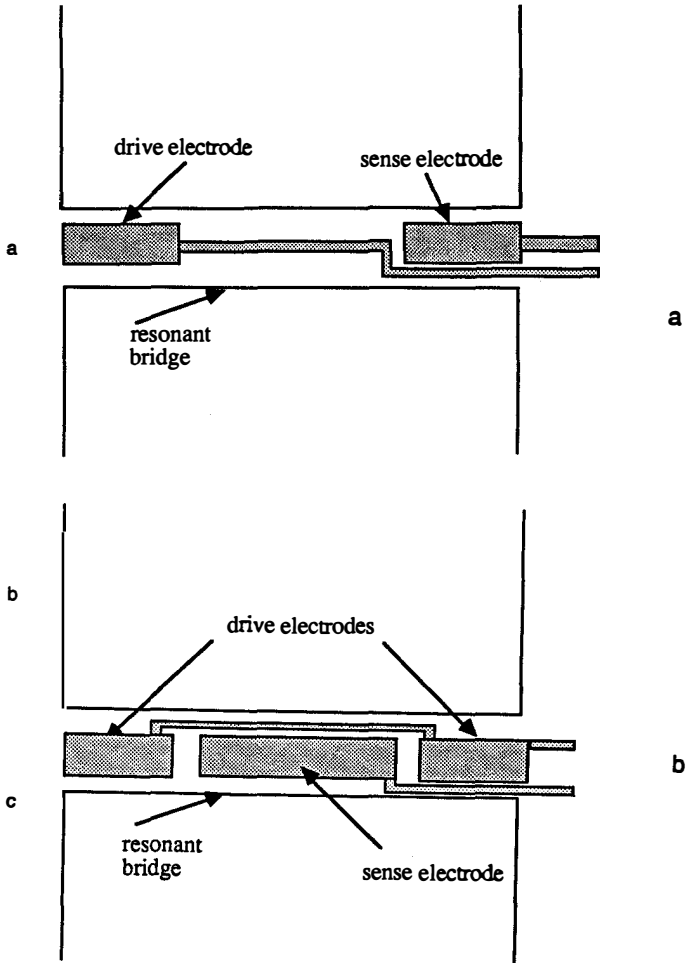
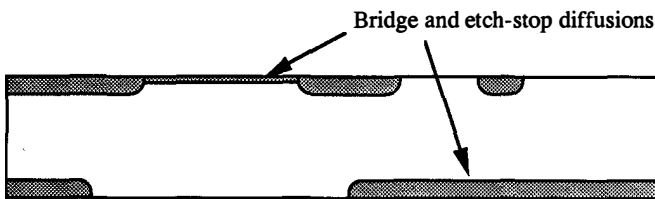
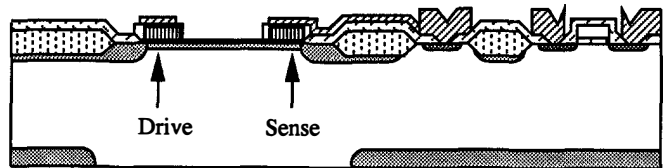


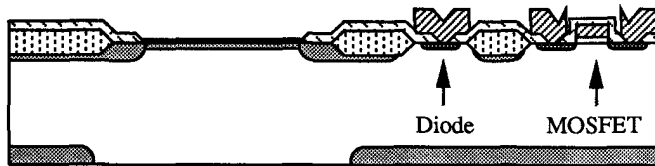
Fig. 2 Two different arrangements of thin film zinc oxide transducing elements.



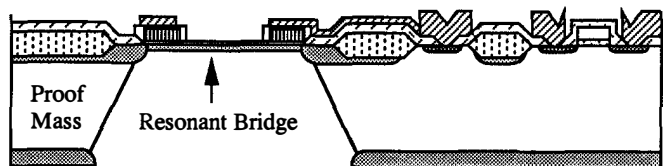
(a.)



(c.)



(b.)



(d.)

Fig. 3 Major processing steps for device fabrication: a) the dimensions of the resonant and constraining bridges are defined by two consecutive boron diffusions, b) the on-chip circuitry consists of a diode and a depletion mode n-channel MOSFET, c) the ZnO thin films are sandwiched between SiO<sub>2</sub> and Si<sub>3</sub>N<sub>4</sub> to prevent charge leakage, d) proof mass, constraining bridges and resonant bridges are formed simultaneously by etching in EDP.

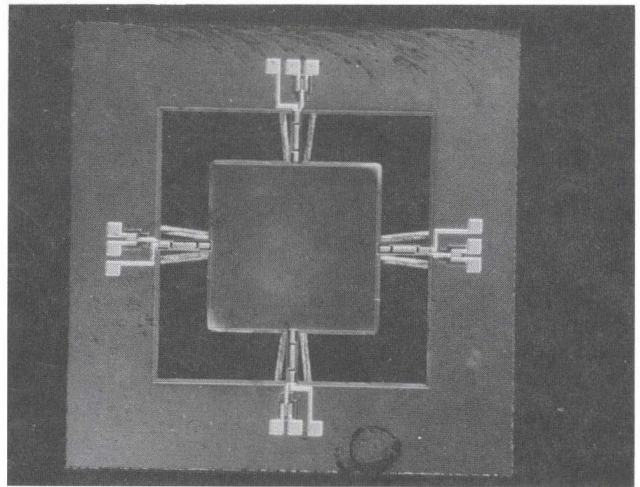
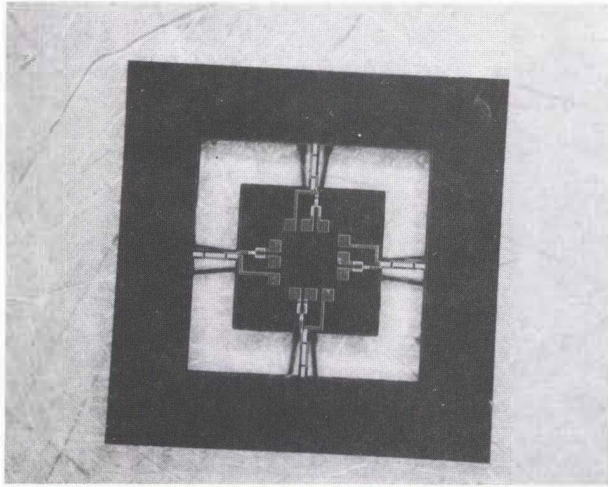


Fig. 4 Photographs of fabricated microaccelerometers: a) peripheral proof mass configuration, b) central proof mass configuration.

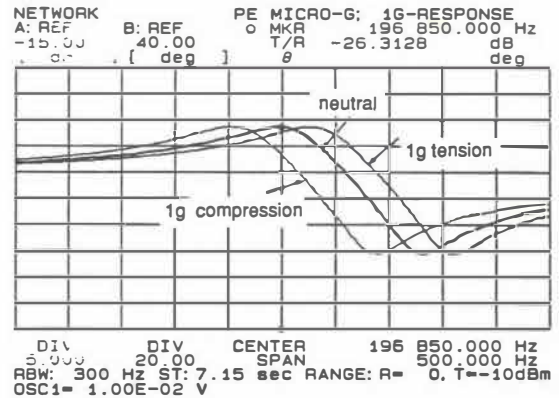
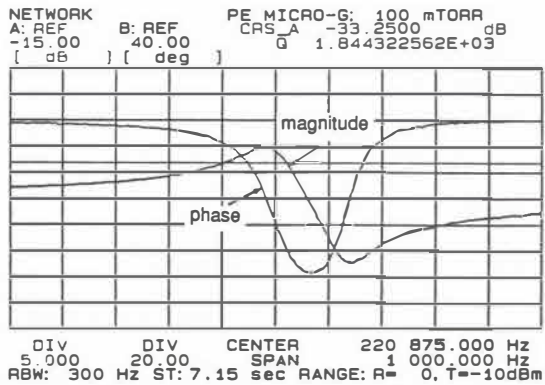
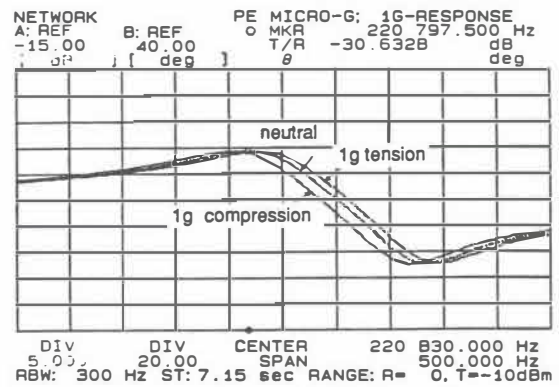
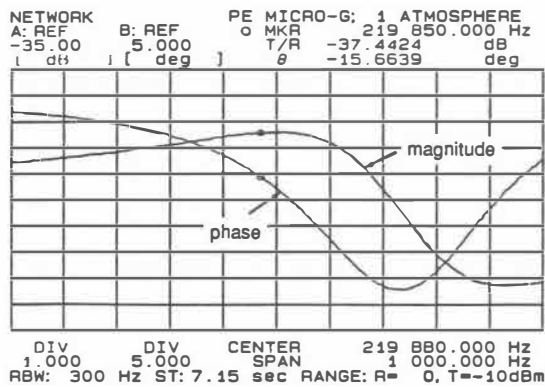


Fig. 5 Frequency responses of the resonant bridge associated with central proof mass when operated at: a) one atmosphere pressure, and b) 100 mTorr.

Fig. 6 Frequency shifts of the resonant bridges when the proof mass is subjected to static acceleration of  $\pm 1g$  in the direction parallel to the length of the bridge: a) central proof mass configuration,  $\Delta f = 12$  Hz, b) peripheral proof mass configuration,  $\Delta f = 36$  Hz.

# MICROTEXTURED RESONATORS FOR MEASURING LIQUID PROPERTIES

Stephen J. Martin<sup>1</sup>, Gregory C. Frye<sup>1</sup>, Richard W. Cernosek<sup>1</sup>, and Stephen D. Senturia<sup>2</sup>

(1) Microsensor Research and Development Department  
Sandia National Laboratories, Albuquerque, New Mexico 87185-0351

(2) Department of Electrical Engineering and Computer Science  
Massachusetts Institute of Technology, Cambridge, MA 02139

## ABSTRACT

The response of smooth- and textured-surface thickness-shear mode (TSM) quartz resonators in liquid has been examined. Smooth devices, which viscously entrain a layer of contacting liquid, exhibit a response that depends on the product of liquid density and viscosity. Textured-surface devices, with either randomly rough or regularly patterned features, also trap liquid in surface features, exhibiting an additional response that depends on liquid density alone. Combining smooth- and textured-surface resonators in a monolithic sensor enables simultaneous extraction of liquid density and viscosity.

## INTRODUCTION

A TSM resonator typically consists of a thin disk of AT-cut quartz with circular electrodes patterned on both sides (Fig. 1). Due to the piezoelectric properties and crystalline orientation of the quartz, the application of a voltage between these electrodes results in a shear deformation of the crystal. The crystal can be electrically excited into several resonant modes, each corresponding to a unique standing shear wave pattern (eigenmode) across the thickness of the crystal. The fundamental thickness-shear mode is shown in Fig. 1. For each of these modes, displacement maxima occur at the crystal faces, making these devices sensitive to surface mass accumulation and contacting fluid properties.

A major obstacle to adapting piezoelectric resonators to liquid sensing applications arises from mechanical damping by the liquid medium. Resonators with a surface-normal displacement component generate compressional waves in the contacting liquid.

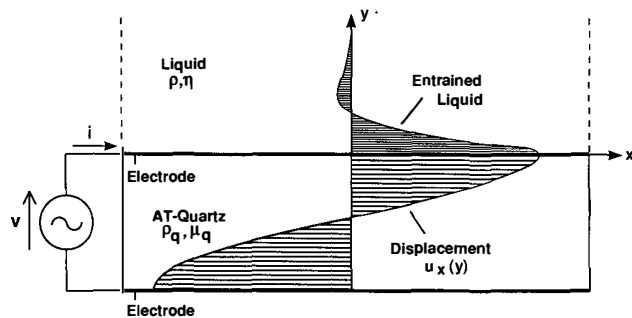


Fig. 1. Cross-sectional view of a smooth TSM resonator with the upper surface contacted by a liquid. Shear motion of the smooth surface causes a thin layer of the contacting liquid to be viscously entrained.

This causes acoustic energy to be radiated away, leading to severe resonance damping. Thickness-shear modes, with only in-plane surface displacement, suffer much less acoustic coupling to a contacting liquid and a tolerable amount of resonance damping.

Oscillator circuits have been designed for the TSM resonator that overcome the damping contributed by low viscosity liquids (1). Since the mass sensitivity of the resonator is nearly the same in liquids as in air or vacuum, the device can be used as a sensitive solution-phase microbalance (2). In addition, the sensitivity of the TSM resonator to contacting fluid properties enables it to function as a monitor for these properties. Kanazawa and Gordon (3) have shown that the TSM resonant frequency decreases with liquid immersion as  $(\rho\eta)^{1/2}$ , where  $\rho$  and  $\eta$  are liquid density and viscosity, respectively. Muramatsu *et al.* (4) demonstrated that resonance damping also increases as  $(\rho\eta)^{1/2}$ . Martin *et al.* (5) derived an equivalent-circuit model to describe the electrical behavior of the TSM resonator in terms of the contacting fluid properties.

This paper will describe the mechanical interactions between smooth- and textured-surface TSM resonators and a contacting liquid. These interactions influence device response in a way that depends on liquid properties, providing a means for measuring these properties.

## RESPONSE WITH A SMOOTH SURFACE

When a smooth TSM resonator is operated in contact with a liquid, the shear motion of the surface couples to the contacting liquid, radiating a critically-damped shear wave into the liquid, as shown in Fig. 2a. The decay length  $\delta$  of this shear wave is (3):

$$\delta = \left( \frac{2\eta}{\omega\rho} \right)^{1/2} \quad (1)$$

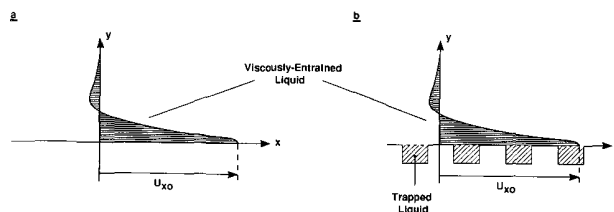


Fig. 2. Cross-sectional view of a resonator surface in contact with a liquid: (a) smooth, showing viscous entrainment, and (b) textured, showing both viscous entrainment and trapping.

where  $\omega$  is angular frequency ( $2\pi f$ ). For reference,  $\delta = 0.25 \mu\text{m}$  in water at  $20^\circ\text{C}$  when  $f = 5 \text{ MHz}$ . The liquid entrained by the oscillating smooth surface undergoes a progressive phase lag with distance from the surface and is described as "viscously coupled."

Liquid entrainment leads to energy storage and power dissipation in the contacting liquid and affects resonator response. An equivalent circuit model can be used to describe the electrical response of the dry or liquid-contacted resonator (Fig. 3). This modified Butterworth-Van Dyke circuit (6) consists of a "static" capacitance  $C_o^*$  (includes any parasitic capacitance) in parallel with a motional branch ( $L_1$ ,  $C_1$ ,  $R_1$ ,  $L_2$ ,  $R_2$ , and  $L_3$ ). The static capacitance arises between electrodes across the insulating quartz. The motional impedance is due to electrical excitation of a shear-mode mechanical resonance in the piezoelectric quartz. Liquid coupling to the surface modifies this motional impedance. For a smooth surface, viscous coupling introducing a motional inductance ( $L_2$ ) and a resistance ( $R_2$ ). These are related to the density  $\rho$  and viscosity  $\eta$  of the contacting fluid (5,7):

$$L_2 = \frac{N\pi}{4K^2\omega_s C_o} \left( \frac{\rho\eta}{2\omega_s \mu_q \rho_q} \right)^{\frac{1}{2}} \quad (2a)$$

$$R_2 = \frac{N\pi}{4K^2 C_o} \left( \frac{\rho\eta}{2\omega_s \mu_q \rho_q} \right)^{\frac{1}{2}} \quad (2b)$$

where  $N$  is the resonator harmonic number (1, 3, 5, ...),  $\omega_s$  is the angular series resonant frequency, while  $\rho_q$ ,  $\mu_q$  and  $K^2$  are the quartz density, shear stiffness, and electromechanical coupling factor, respectively. Eqs. 2 are for one-sided liquid contact; for two-sided contact,  $L_2$  and  $R_2$  are doubled. Electrical energy storage

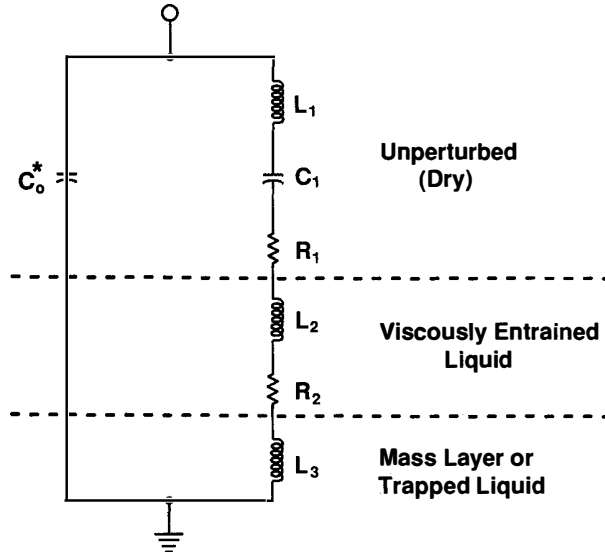


Fig. 3. Equivalent-circuit model to describe the electrical characteristics (for  $\omega$  near  $\omega_s$ ) of a TSM resonator with liquid loading. Contributions arise from both viscously-coupled liquid ( $L_2$  and  $R_2$ ) and liquid trapped by surface features ( $L_3$ ).

in  $L_2$  arises from the kinetic energy of the viscously-entrained liquid layer (with effective thickness  $\delta/2$ ); power dissipation in  $R_2$  arises from shear wave radiation into the liquid.

The equivalent circuit model in Fig. 3 can be used to derive the changes in series resonant frequency  $\Delta f^{(S)}$  and motional resistance  $\Delta R^{(S)}$  contributed by viscous coupling to liquid by the smooth (superscript S) resonator surface (5,7):

$$\Delta f^{(S)} = -\frac{L_2 f_s}{2L_1} = -\frac{2f_s^2}{N\sqrt{\mu_q \rho_q}} \left( \frac{\rho\eta}{4\pi f_s} \right)^{\frac{1}{2}} \quad (3a)$$

$$\Delta R^{(S)} = R_2 = \frac{\omega_s L_1}{N\pi} \left( \frac{2\omega_s \rho \eta}{\mu_q \rho_q} \right)^{\frac{1}{2}} \quad (3b)$$

Eq. 3a is in agreement with Kanazawa and Gordon (3).

Eqs. 2 and 3 indicate that the response of a smooth TSM resonator depends only on the product ( $\rho\eta$ ) of liquid density and viscosity. Thus, density and viscosity *cannot* be individually resolved from smooth resonator measurements alone.

#### RESPONSE WITH A TEXTURED SURFACE

Devices with textured surfaces, either randomly rough or regularly patterned, trap a quantity of fluid in excess of that viscously entrained by a smooth surface (7-9). Vertical features constrain this trapped liquid to move synchronously with the oscillating crystal surface, rather than undergoing a progressive phase lag as occurs with viscously coupled liquid. Thus, this trapped liquid behaves much like an ideal mass layer contributing an areal mass density  $\rho_s = \rho h$ , where  $\rho$  is the liquid density and  $h$ , the effective thickness of the trapped liquid layer, is dependent upon the vertical relief of the surface texture.

We can approximate the response of a textured-surface resonator in liquid by separating the solid/liquid interface into two regions, as shown in idealized fashion in Fig. 2b. If we imagine a boundary connecting peaks of the textured surface, then liquid below this boundary is "trapped" and moves synchronously with the surface; liquid above this boundary is viscously coupled (as if by the boundary) and undergoes a progressive phase lag with distance from the boundary.

Liquid trapping by surface texture gives rise to an additional motional impedance element ( $L_3$ ) in the equivalent-circuit model of Fig. 3 (5,7):

$$L_3 = \frac{N\pi \rho h}{4K^2 \omega_s C_o (\mu_q \rho_q)^{1/2}} \quad (4)$$

Electrical energy storage in  $L_3$  arises from the kinetic energy of the trapped liquid moving synchronously with the oscillating device surface.

The changes in series resonant frequency and motional resistance arising from liquid contacting a textured (superscript T) surface are (5,7):

$$\Delta f^{(T)} = -\frac{(L_2 + L_3)f_s}{2L_1} = -\frac{2f_s^2}{N\sqrt{\mu_q\rho_q}} \left[ \left( \frac{\rho\eta}{4\pi f_s} \right)^{\frac{1}{2}} + \rho h \right] \quad (5a)$$

$$\Delta R^{(T)} = R_2 = \frac{\omega_s L_1}{N\pi} \left( \frac{2\omega_s \rho \eta}{\mu_q \rho_q} \right)^{\frac{1}{2}} \quad (5b)$$

**Response Measurements** From Eqs. 5, surface texture is expected to increase the frequency shift caused by liquid contact, in proportion to  $\rho h$ , without changing the motional resistance. Fig. 4 shows the changes in series resonant frequency  $\Delta f$  and motional resistance  $\Delta R$  measured vs. the liquid parameter  $(\rho\eta)^{1/2}$ . Measurements were made using a network analyzer on a smooth and a rough device as water/glycerol solutions contacted one side. The different degrees of surface roughness were obtained by polishing the quartz crystals with various abrasive particle sizes before depositing the conformal Cr/Au electrodes. Surface roughness was quantified using a Wyko RST (Tucson, AZ) profiler (7). The smooth device has an average roughness  $< 10$  nm—much smaller than the liquid decay length  $\delta$  (250 - 1200 nm for the glycerol solutions tested). For this device, the measured changes in frequency and motional resistance are nearly equal to the predictions for an ideally smooth surface (dashed lines, Eqs. 3). The rough device has an average roughness of 243 nm, comparable to the liquid decay length. Extrapolating the data to  $(\rho\eta)^{1/2} = 0$  shows that this device exhibits a large additional frequency shift of approximately 0.87 kHz due to liquid trapping in the randomly-rough surface. From Eq. 5a, this gives  $h = 150$  nm, or roughly 63% of the optically-measured surface roughness. The motional

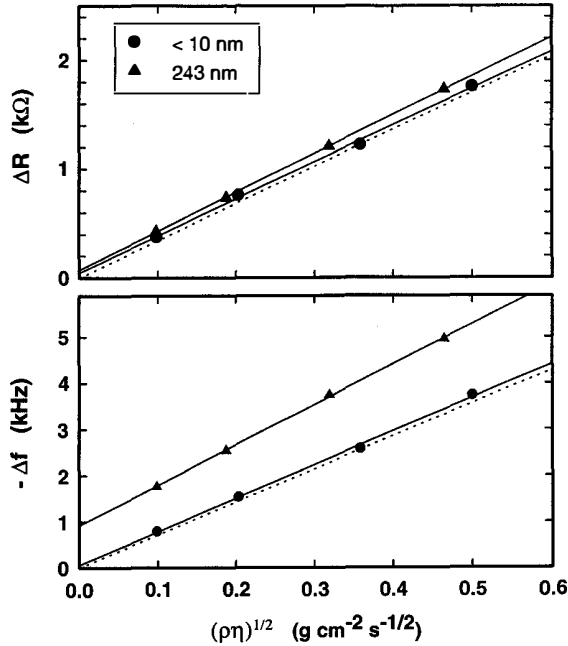


Fig. 4. Change in series resonant frequency ( $\Delta f$ ) and motional resistance ( $\Delta R$ ) vs. the liquid parameter  $(\rho\eta)^{1/2}$  for TSM resonators with two different surface roughnesses.

resistance is also slightly larger with the rough device. This indicates increased power dissipation by the rough surface, thought to arise from compressional wave generation by surface asperities (7). For very rough devices, these additional  $\Delta R$  responses can be significantly larger than those shown in Fig. 4 (7).

#### DENSITY AND VISCOSITY EXTRACTION

Comparison of Eqs. 3a and 5a indicates that density and viscosity *can* be individually resolved by using a pair of TSM resonators, one smooth and one textured. Since the response due to viscous entrainment of liquid is common to both devices, the difference in response measured upon immersion eliminates this contribution and, in effect, *weighs* the trapped liquid. Subtracting Eq. 3a from Eq. 5a yields the liquid density:

$$\rho = -\frac{N\sqrt{\mu_q\rho_q}}{2f_s^2 h} [\Delta f^{(T)} - \Delta f^{(S)}] \quad (6)$$

where  $\Delta f^{(T)}$  and  $\Delta f^{(S)}$  are the frequency shifts measured upon immersion of the textured and smooth resonators. Using Eq. 6 for liquid density, the frequency change of the smooth device (Eq. 3a) is used to determine liquid viscosity:

$$\eta = \frac{2\pi h N \sqrt{\mu_q \rho_q} (\Delta f_s)^2}{f_s |\Delta f^{(T)} - \Delta f^{(S)}|} \quad (7)$$

Alternatively, if the change in motional resistance  $\Delta R^{(S)}$  is measured, liquid viscosity can be determined from this parameter:

$$\eta = \frac{\rho_q \mu_q}{2\omega_s \rho} \left( \frac{N\pi \Delta R^{(S)}}{\omega_s L_1} \right)^2 \quad (8)$$

#### MONOLITHIC SMOOTH AND TEXTURED RESONATOR PAIR

Fig. 5 shows a monolithic quartz sensor that includes a smooth and a textured TSM resonator to measure liquid density and viscosity. Since these liquid properties (especially viscosity) are temperature dependent, a meander-line resistance temperature device (RTD) is included to measure the liquid temperature. Texture in the form of a surface corrugation is formed on one device by electrodepositing periodic gold ridges on top of the gold electrodes. In order to trap liquid and insure that it moves synchronously with the surface, these ridges are oriented perpendicular to the direction of surface shear displacement (+X crystalline direction).

In fabricating the dual-resonator device, a Cr/Au (30 nm/200 nm) metallization layer is first deposited on both sides of an optically polished AT-cut quartz wafer. This metallization layer is photolithographically patterned to form the resonator electrodes (both sides) and the meander-line RTD (one side). To form a surface corrugation on one resonator, a periodic resist pattern is formed on opposing electrodes. Gold is then electrodeposited, to a thickness of 1.5  $\mu\text{m}$ , onto the electrode between resist strips. When the photoresist is removed, a corrugation pattern remains

with channels approximately 5  $\mu\text{m}$  wide for trapping liquid. Fig. 6 is an SEM micrograph of the sectioned surface, showing the surface corrugation.

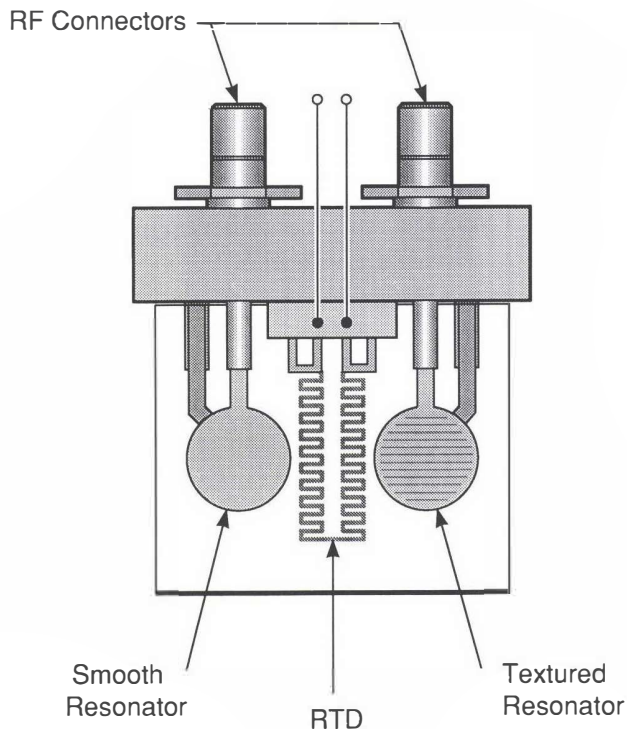


Fig. 5. Monolithic sensor that includes a smooth and textured TSM resonator to measure liquid density and viscosity along with an RTD to measure temperature.

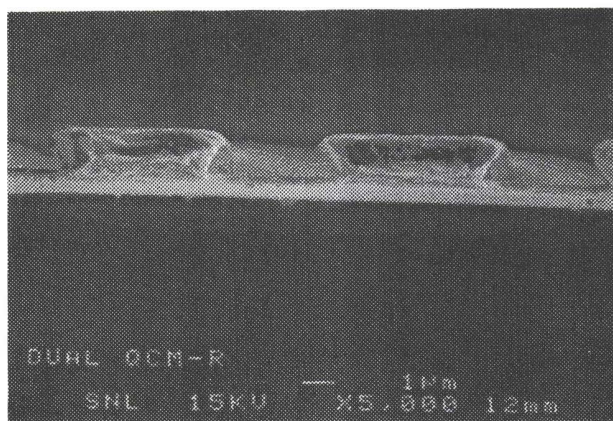


Fig. 6. SEM micrograph of surface corrugation, formed from electrodeposited gold, for trapping liquid at the surface.

An oscillator circuit has been designed to operate the TSM resonator in liquid media and provide outputs indicating the resonant frequency and motional resistance. The oscillator, described by Wessendorf (1), provides an rf output indicating the the series resonant frequency of the crystal, and a dc voltage proportional to the motional resistance  $R = R_1 + R_2$ . The oscillator circuit will sustain oscillation for motional resistances up

to approximately 2 k $\Omega$ . Using Eq. 3b, and assuming  $\rho = 1 \text{ g/cm}^3$ , this enables resonator operation in liquids with viscosity values up to 34 cP for one-sided contact or 8.6 cP for two-sided contact.

In instrumenting the dual-resonator sensor, each resonator is driven by an independent oscillator circuit. The RF outputs from the oscillators are read by frequency counters while the DC voltages and RTD resistance are read by multimeters. These signals are input to a personal computer. The baseline responses are determined by measuring frequency and motional resistance for each device before immersion. Changes in responses are then measured for the smooth ( $\Delta f^{(S)}$ ,  $\Delta R^{(S)}$ ) and textured ( $\Delta f^{(T)}$ ,  $\Delta R^{(T)}$ ) devices upon immersion. Eqs. 6 and 7 or 8 are then used to determine density and viscosity.

Fig. 7 illustrates the *densitometer function* of the dual-resonator sensor of Fig. 5. The difference in responses  $|\Delta f^{(T)} - \Delta f^{(S)}|$  measured between the textured and smooth resonators upon immersion (two-sided liquid contact) is shown vs. liquid density. The response difference is linear with density, despite variations in viscosity between the test liquids. This indicates that liquid trapping is independent of liquid viscosity, as assumed in the simple trapping model outlined above.

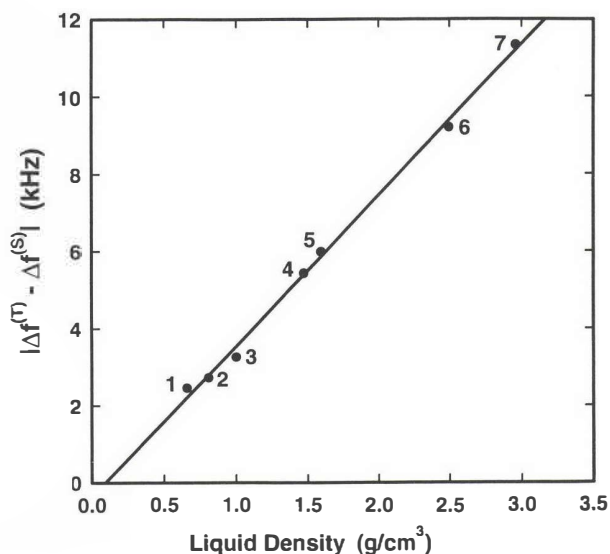


Fig. 7. The difference in frequency changes  $|\Delta f^{(T)} - \Delta f^{(S)}|$  measured between the textured and smooth resonators (Fig. 5) upon immersion vs. liquid density. Liquids tested: (1) hexane, (2) butanol, (3) water, (4) chloroform, (5) carbon tetrachloride, (6) dibromomethane, and (7) tetrabromoethane.

Fig. 8 shows a "scatter diagram" that compares liquid densities and viscosities extracted from dual-resonator measurements (circles) with literature values (squares). For  $\rho\eta > 0.08 \text{ g}^2 \text{ cm}^{-4} \text{ s}^{-1}$  (8 cP-g/cm<sup>3</sup>), the crystal is damped too severely to sustain oscillation. This data illustrates that liquid density and viscosity can be extracted from measurements made by a pair of quartz resonators—one smooth and one with surface texture. When compared to the literature values, the average measured density

error in this data set was 5.3% and the average viscosity error was 19.5%.

Interestingly, the points in Fig. 8 divide into density bands according to chemical class: the lowest set (A - J) are hydrocarbons, the middle set (K - M) are chlorinated solvents, while the upper point (N) is a brominated solvent. This data suggest the possibility of identifying pure liquids on the basis of density and viscosity measurements.

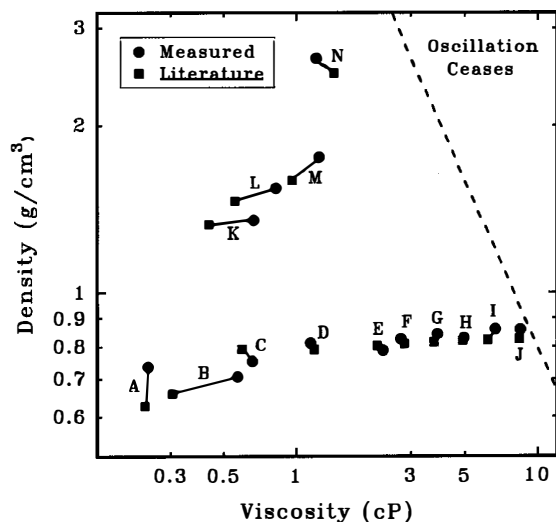


Fig. 8. Scatter diagram comparing the extracted (circles) and literature (squares) values of liquid density and viscosity for organic liquids: (A) n-pentane, (B) n-hexane, (C) methanol, (D) ethanol, (E) n-propanol, (F) n-butanol, (G) n-pentanol, (H) n-hexanol, (I) n-heptanol, (J) n-octanol, (K) dichloromethane, (L) trichloroethylene, (M) carbon tetrachloride, (N) dibromomethane.

#### CONCLUSION

Quartz resonators with smooth surfaces can be operated in liquids to measure the density-viscosity product of a contacting fluid. Surface texture causes fluid trapping and an additional response proportional to liquid density. Comparing the responses of a pair of resonators—one smooth and one textured—enables liquid density to be extracted. Once density is known, the response of a smooth device yields liquid viscosity.

#### ACKNOWLEDGEMENTS

The authors wish to thank L. Casaus and K. Rice of Sandia National Laboratories for technical assistance. This work was performed at Sandia National Laboratories, supported by the U.S. Department of Energy under contract No. DE-AC04-94AL8 5000.

#### REFERENCES

- (1) Wessendorf, K. O. *Proc. 1993 Frequency Control Symp.* (IEEE, New York, 1993) pp. 711-717.
- (2) Numura, T.; Minemura, A. *Nippon Kagaku Kaishi* **1980**, 1621.
- (3) Kanazawa, K. K.; Gordon II, J. G. *Anal. Chem.* **1985**, *57*, 1770-1771.
- (4) Muramatsu, H.; Tamiya, E.; Karube, I. *Anal. Chem.* **1988**, *60*, 2142-2146.
- (5) Martin, S. J.; Granstaff, V. E.; Frye, G. C. *Anal. Chem.* **1991**, *63*, 2272-2281.
- (6) Rosenbaum, J. F. *Bulk Acoustic Wave Theory and Devices*; Artech: Boston, 1988; Sect. 10.5.
- (7) Martin, S. J.; Frye, G. C.; Ricco, A. J.; Senturia, S. D. *Anal. Chem.* **1993**, *65*, 2910-2922.
- (8) Beck, R.; Pitterman, U.; Weil, K. G. *J. Electrochem. Soc.* **1992**, *139*, 453-461.
- (9) Schumacher, R.; Borges, G.; Kanazawa, K. K. *Surface Science* **1985**, *163*, L621-L626.

# The Development of Polysilicon Micromotors for Optical Scanning Applications

K. Deng, H. Miyajima<sup>1</sup>, V.R Dhuler<sup>2</sup>, M. Mehregany,  
S.W. Smith, F.L. Merat, and S. Furukawa<sup>3</sup>

*Electronics Design Center  
Department of Electrical Engineering and Applied Physics  
Case Western Reserve University  
Cleveland, OH 44106*

## Abstract

This paper reports preliminary results on the development of polysilicon micromotors for optical scanning applications. The scanner structures studied are similar to conventional mechanical polygon scanners but utilize micromotors with diameters up to one millimeter. The optical elements are hollow polygonal nickel reflectors plated up to 20  $\mu\text{m}$  tall on the rotor of the micromotor. The optical axis of reflection corresponds to the axis of rotation of the micromotor. Optical measurements have been done at visible wavelengths (633 nm) using multi-mode optical fibers roughly in the plane of the substrate for the source illumination. The scanned, reflected radiation was detected via scattering from the substrate or by a television camera in the plane of the substrate.

## Introduction

Significant improvements in polysilicon micromotor operational characteristics allows them to be considered for a variety of applications [1,2]. The development of polysilicon micromotors for optical scanning applications is a good match to the small size and low cost of batch fabricated micromotors with the low-load requirements imposed by optical elements such as polygon mirrors. Typical optical scanners (e.g., supermarket scanners) are large, complex systems requiring careful alignment. A micromechanical scanner implementation could reduce the weight and size of existing scanners by two orders of magnitude with significant decrease in cost due to batch fabrication. This paper focuses on demonstrating the feasibility of using polysilicon micromotor for optical scanning applications.

## Microscanner Designs

We are investigating two types of microscanners based on polysilicon micromotors: a micromotor polygon scanner and a micromotor grating scanner. Figure 1 presents schematic drawing of a polygon scanner with optically reflective rotor segments. Figures 2 and 3 show a SEM photograph of a typical microscanner fabricated on a salient-pole micromotor and a cross-sectional schematic of the microscanner. The polygon scanner can scan in a straight line in a plane, but requires high-aspect-ratio fabrication of metallic microstructures for the reflective surfaces and careful optical design to efficiently transmit optical radiation through small dimensions of the microstructure. A polygon scanner such as described here can also be used for inexpensive optical switches.

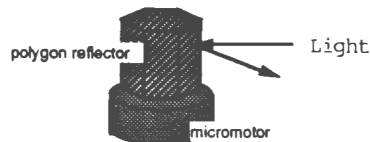


Figure 1: Schematic drawings of a rotating polygon scanner with optically reflective rotor segments.

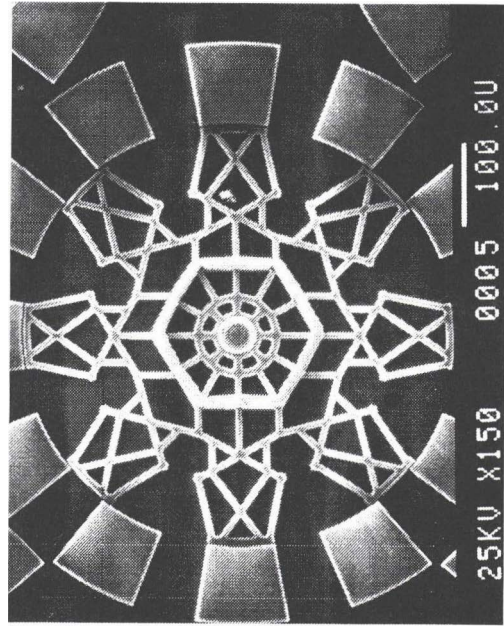


Figure 2: SEM photo of a typical optical microscanner which was fabricated by electroless-plating of nickel reflecting surfaces on the rotor of a 0.5 mm-diameter salient-pole micromotor. The thickness of the nickel is 20  $\mu\text{m}$  and the width of the nickel line is 10  $\mu\text{m}$ .

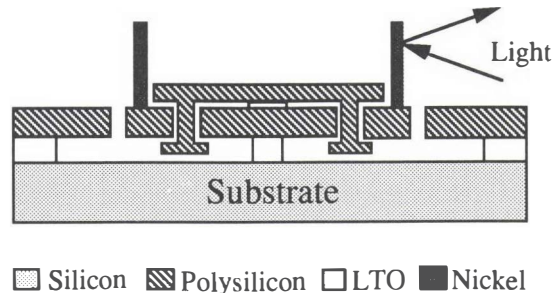


Figure 3: Cross-sectional schematic of a typical microscanner (e.g., Fig. 2) after release showing illumination of the nickel surface with a laser beam.

A micromotor grating scanner replaces the plated optical element with a diffractive element. Figure 4 presents schematic drawing of a micromotor grating scanner. The source illumination will come from out of the plane of the substrate depending upon the application. Depending upon the optical wavelength and the substrate material, a rotating grating scanner will be capable of being operated in either the transmission mode or reflection mode. Because the optical source can be perpendicular to the substrate plane and the grating structure will be of millimeter dimensions, the optical design will not be as complex as that for the micromotor polygon scanner. In addition, arrays of gratings rotated by synchronized micromotors would be capable of scanning large diameter optical beams (larger than one millimeter).

<sup>1</sup> On leave from Olympus Optical Co., LTD., Tokyo, Japan  
<sup>2</sup> Current address: Center for Microelectronics Systems Technologies, Research Triangle Park, NC  
<sup>3</sup> On leave from Electronics Materials & Devices Laboratory, Asahi Chemical Industry Co., LTD., Kawasaki, Japan

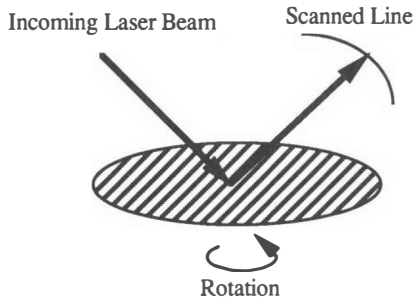


Figure 4: Schematic drawing showing the concept of a micromotor grating scanner in the reflection mode.

In general, the micromotor polygon scanner scans in a straight line in a plane, and the micromotor grating scanner scans in a curved line out of the plane of the grating. The former requires high-aspect-ratio optical elements to limit diffraction losses, and the source must lie in the same plane. This also poses strict requirements on the optical source in terms of efficiently coupling the optical energy to the reflecting elements of the polygon. The most promising sources are optical fibers as we describe here or integrated optical waveguides. The grating scanner requires well defined grating lines and precise control of the grating depth during fabrication. However, coupling the optical energy to the grating is relatively simple. Processing of a grating scanner for transmission mode requires that the substrate to be transparent to the optical radiation. This paper describes preliminary development results for the polygon scanners. The grating micromotor scanners are still under development and will be reported on in the near future.

### Fabrication of the Microscanners

The microscanner structures described in this paper are based upon the development of millimeter-sized polysilicon micromotors and the integration of a high-aspect-ratio electroless nickel plating process with polysilicon surface micromachining to fabricate the optical elements.

#### Millimeter-Sized Polysilicon Micromotor

In order to support optical elements large enough to have acceptable diffraction losses, we have developed large diameter (up to one millimeter) micromotors. Figure 5 shows SEM photograph of a typical microscanner fabricated on the rotor of a 1.0 mm-diameter wobble micromotor, which is the largest side-drive, polysilicon surface micromachined electrostatic motor reported to date. In our work, typical motor dimensions are rotor diameters 0.5 to 1.0 mm, rotor/stator gaps 1.5 to 2.5  $\mu\text{m}$ , and rotor/stator thicknesses of 5  $\mu\text{m}$ .

Figure 6 presents a cross-sectional schematic of a millimeter-sized micromotor before release. Millimeter-sized motors were fabricated using the rapid prototyping process described in [2] which results in flange bearing wobble and salient-pole motors. The rotor/stator and bearing were fabricated from a 5  $\mu\text{m}$ -thick phosphorus-doped polysilicon film. A 2.4  $\mu\text{m}$ -thick Low temperature oxidation (LTO) film was used for substrate/stator isolation, as well as the sacrificial layer under rotor. The bearing clearance was created by a 0.5  $\mu\text{m}$  thermal oxidation step.

#### Fabrication of the Reflector

A high-aspect-ratio lithography process was developed in conjunction with an electroless nickel plating process to fabricate the polygon reflectors on the rotor of the polysilicon micromotors prior to release. Of key importance is the compatibility of the reflector fabrication process with that of the micromotor process, in particular during the release step. Additionally, a large area smooth reflective surface is desired.

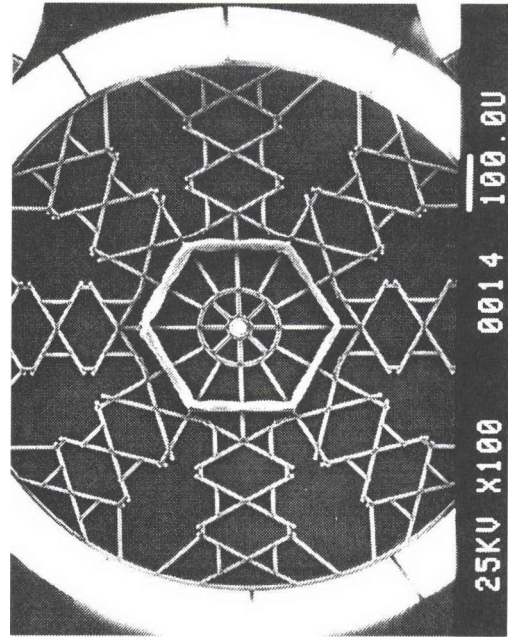


Figure 5: SEM photo of a typical optical microscanner which was made by electroless-plating of nickel reflecting surfaces on the rotor of a 1.0 mm-diameter wobble micromotor. The thickness of the nickel is 20  $\mu\text{m}$  and the width of the nickel is 10  $\mu\text{m}$ .

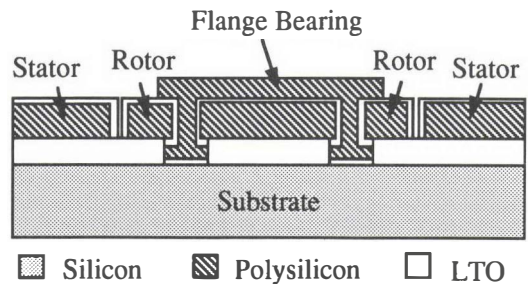


Figure 6: A schematic drawing of the cross-sectional view of the millimeter-sized micromotor before release.

Figure 7 presents a schematic of the reflector fabrication process. After the motor is fabricated (Fig. 6), the oxide layer on rotor/stator is removed in BHF. A thick (up to 23  $\mu\text{m}$ ) photoresist layer is then spun cast and patterned to make the mold for plating (Fig. 7(a)). Electroless plating of nickel is then performed (Fig. 7(b)), and the photoresist mold is removed. The microscanners are then released in hydrofluoric acid (HF) for 10 minutes (Fig. 7(c)). The release process does not alter the reflective properties of the nickel structures in our work.

In the photolithography process for the plating mold (Fig. 7(a)), large heights, smooth vertical sidewalls, and material compatibility with the electroless plating chemicals were required. Our photolithography process used a positive photoresist of high transparency and high viscosity with multiple coats to obtain thick photoresist films and planarized surfaces. The softbake, exposure, and development conditions were controlled to obtain near vertical sidewalls. A standard high pressure mercury ultraviolet source was used for exposure. Figure 8 shows a close-up of the photoresist mold pattern on the rotor. The thickness of the photoresist is 23  $\mu\text{m}$ ; the mold opening is 7  $\mu\text{m}$ .

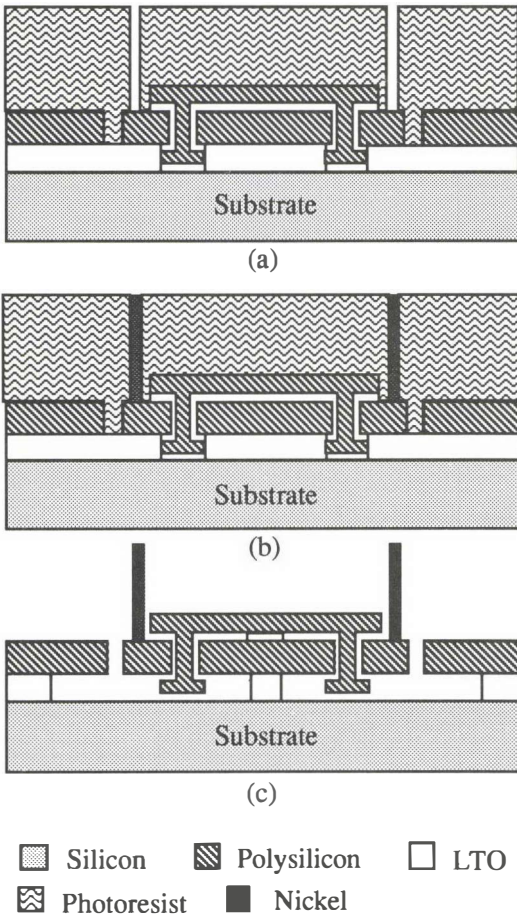


Figure 7: Cross-sectional schematics describing the reflector fabrication process: (a) after thick photoresist process to create the reflector mold; (b) after electroless plating of nickel; and (c) after release.

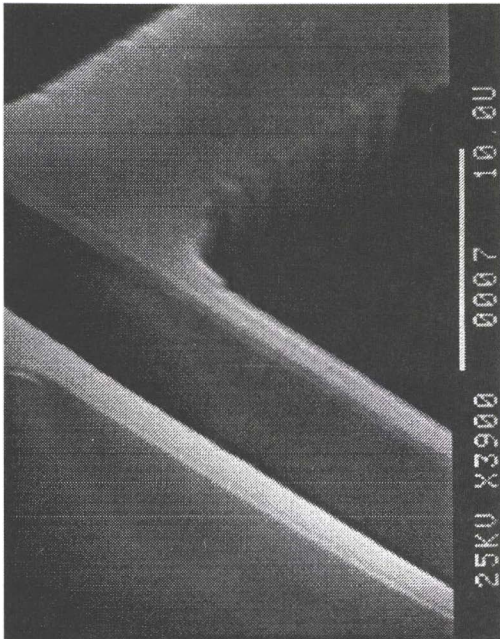


Figure 8: A magnified view of the thick photoresist pattern where the reflector is to be plated. The thickness of the photoresist is 20 μm; the mold opening is 7 μm.

Before plating, the polysilicon surface was pretreated. In our work, this pretreatment includes: (a) a 45 second etch in a solution of  $\text{HNO}_3$ , HF, and  $\text{H}_2\text{O}$ ; (b) a 9 minute deposition of Pd as a starting catalyst from a solution of  $\text{PdCl}_2$ ,  $\text{SnCl}_2$ , and  $\text{HCl}$ ; (c) 15 seconds in  $\text{HCl}$  to removal the Sn oxide complex; and (d) a 2 minute rinse in deionized water. In (a), etching of the polysilicon surface takes place, which has been determined to be critical for the uniformity of the plating process and for adhesion. The adhesion force between nickel and polysilicon seems to be primarily mechanical (not chemical) in nature. The etch rate and surface morphology vary depending on the polysilicon grain size which is, in turn, affected by the LPCVD deposition conditions, as well as subsequent thermal treatment. For short etch times, plating will not be initiated uniformly. For long times, the polysilicon film thickness is reduced significantly, affecting the mechanical integrity of the rotor.

After the surface treatment step, electroless plating was carried out in a mixture of  $\text{NiSO}_4$ ,  $\text{NaH}_2\text{PO}_2$  (as reducing agent), and  $\text{CH}_3\text{COONa}$  (as a buffer and mild complexing agent for Ni) [3]. A fresh plating solution was used for each experiment to keep the nickel concentration constant and to avoid contamination from the solution itself, photoresist, and/or substrate. Electroless plating on polysilicon was conducted at  $90^\circ\text{C}$  in the pH of 5 electroless plating solution with a pH of 5. Figure 9 is an example of a nickel-plated beam on a polysilicon rotor. The thickness of the nickel is 20 μm. The polygon beam width is 7 μm.

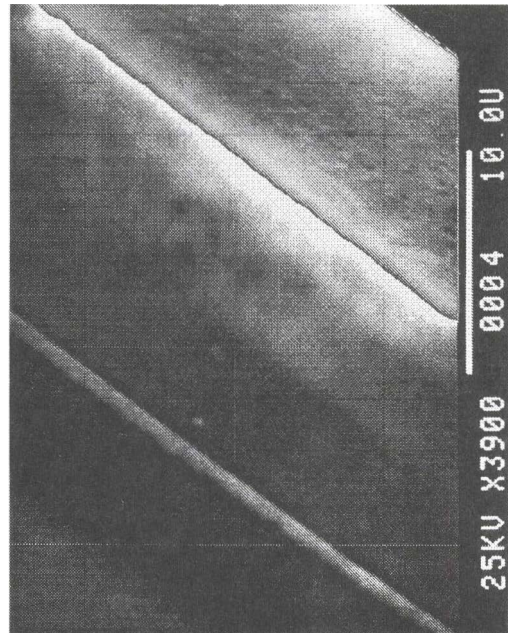


Figure 9: SEM photo showing a magnified view of the sidewall and top surface of a 20 μm-thick nickel reflector on a polysilicon rotor.

## Polysilicon Microscanners

### Preliminary Mechanical Measurements

The microcanners fabricated from millimeter-sized motors operate smoothly and reproducibly in room air for extended periods (e.g., several months) after release. Minimum voltages can be as low as 12V, while maximum rotor speeds have been 100 rpm for microscanners fabricated on millimeter-sized wobble motors and 2500 rpm for those fabricated on millimeter-sized salient-pole motors. These large motors have motive torques over an order of magnitude larger than previously reported polysilicon micromotors [4].

Figure 10 presents typical experimental gear ratios as a function of excitation voltage for loaded (e.g., nickel plated) and unloaded (e.g., unplated) wobble motors. As expected, the gear ratio increases with increased load, since the load increases friction

at the flange contact by increasing the normal contact force. The increased flange friction leads to increased rotor slip [5.6]. The load was estimated near  $72 \mu\text{N}$  using pure nickel density of  $8.9 \text{ g/cm}^3$ . The increase in the gear ratio at the smaller excitation voltages (and hence smaller motive torques) is due to increased rotor slip as well.

Figure 11 presents typical step transient data for salient-pole motors with load and without load. Stroboscopic dynamometry was used to measure the step response of the motors [7]. The step response is overdamped for these motors due to the increased viscous drag caused by the larger rotor as compared to our previous micromotors [7]. The rise time of the step response is one order of magnitude larger than that for our previous micromotors which are one tenth the size of these motors [7]. As expected, the step response of the motor with load is slower due to the increased inertia and friction.

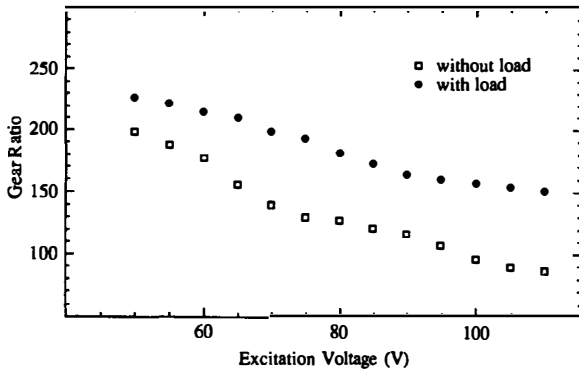


Figure 10: Gear ratio versus excitation voltage for  $0.5 \mu\text{m}$ -diameter wobble micromotors with load (e.g., nickel plated) and without load (e.g., unplated). The rotor/stator gaps are  $2.5 \mu\text{m}$ . An excitation speed of 909 rpm was used. The rotor gear ratio was measured by dividing the excitation speed by the average steady-state rotor speed.

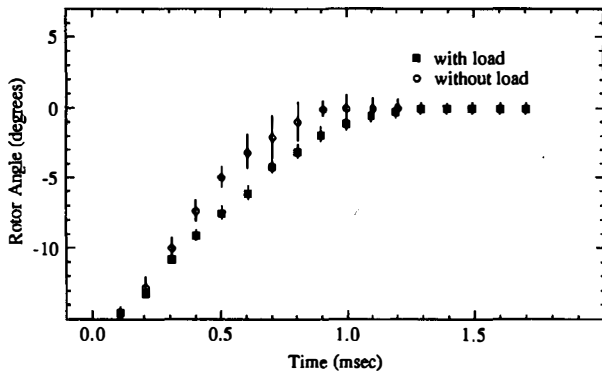


Figure 11: Step transient data for  $0.5 \mu\text{m}$ -diameter salient-pole micromotors with load (e.g., nickel plated) and without load (e.g., unplated). The rotor/stator gaps are  $1.5 \mu\text{m}$ . An excitation voltage of 95V was used.

### Preliminary Optical Measurements

We have performed preliminary optical testing of the microscanners using a 633 nm He-Ne laser coupled into a multi-mode optical fiber. The core of the optical fiber was  $20 \mu\text{m}$  in diameter and the cladding was  $125 \mu\text{m}$ . The laser beam was mechanically chopped to facilitate subsequent optical detection. The optical fiber was positioned approximately in the plane of the substrate 1.5 millimeters from the axis of rotation of the motor. The scanned optical radiation was detected using a photo detector (Milles Griot #13 DSI 007). Absolute power measurements have not yet been performed to determine the optical efficiency of the microscanners. Figure 12 presents a schematic diagram of the instrumentation for optical measurements on the microscanners.

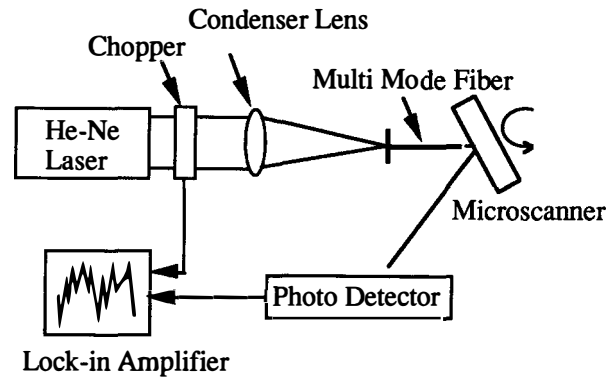


Figure 12: Instrumentation for optical measurement on the microscanners.

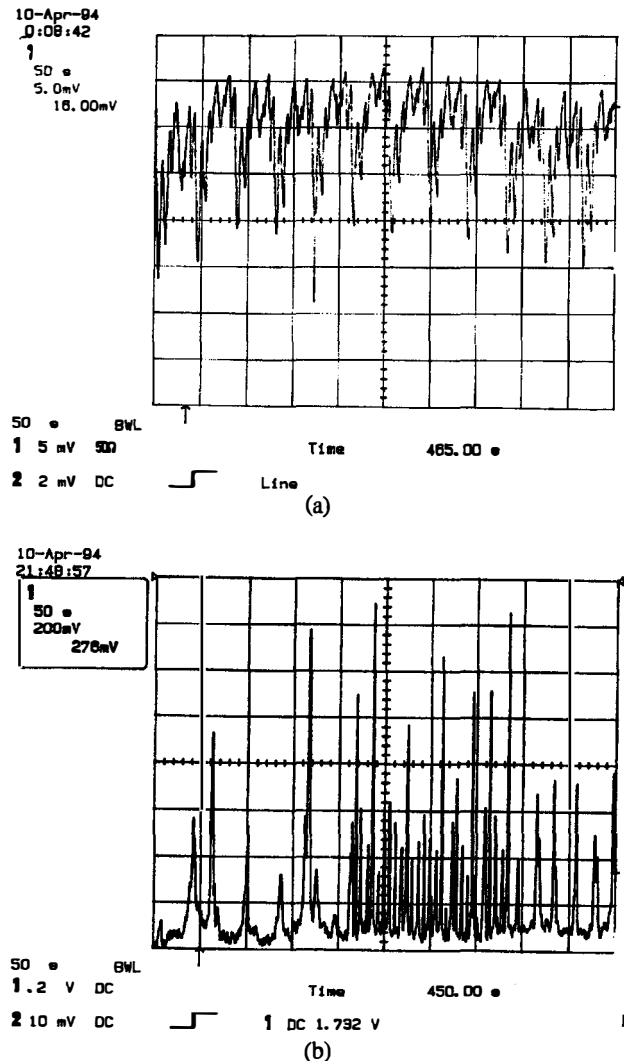


Figure 13: Detected optical radiation from a rotating polygon scanner: (a) a 0.5 mm-diameter rotor with constant rotational speed; and (b) a 1.0 mm-diameter rotor with different operating rotor speeds during measurement. The vertical axis for these measurements is arbitrary.

Figures 13(a) and (b) show the detected radiation reflected by microscanners fabricated on wobble micromotors. The diffraction pattern of the scanned radiation is repeatable. The intensity variation in the scanned radiation may be due to wobbling of the micromotor on its rotational axis. The potential of the micromotor scanner is most clearly seen in Fig. 14 which is a digitized photo of a laser beam reflected from the microscanner. The image was captured using a common camcorder with a macro lens approximately in the plane of the scanner and about six inches from the micromotor. The diffraction pattern is observed in Fig. 14.

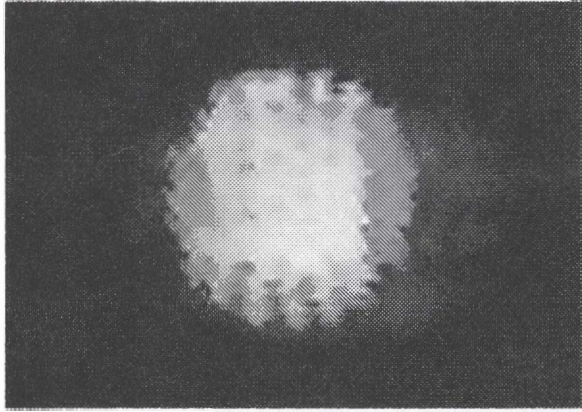


Figure 14: Visible optical radiation pattern from a rotating polygon scanner. The scanner is a 1 mm-diameter wobble micromotor, with a 20  $\mu\text{m}$  tall nickel plated polygon reflector approximately 300  $\mu\text{m}$  in diameter. The image was detected with a television camera in the plane of the substrate. The diffraction pattern can be observed.

## Discussion

Our results clearly demonstrate the ability of the micromotors to rotate optical elements capable of directing laser beams. However, polygon reflectors which are much taller, i.e. on the order of 100-300  $\mu\text{m}$ , are more desirable. Such large structures could be made by the LIGA process but the weight of such structures and the corresponding frictional effects as they relate to the performance of the micromotors must be studied. Furthermore, the optical scanners described in this paper have the polygon reflector located a considerable distance from the outer dimensions of the rotor. This design is not efficient for coupling the source radiation to the reflector for either scanning or switching applications. We recommend placing the reflecting surfaces near the outer rotor of the micromotor. For optical switching applications, the source and detected radiation could be transmitted through optical waveguides fabricated on the substrate, dramatically improving the optical efficiency of the device.

## Acknowledgment

This work was supported in part by ARPA under Contract No. F49620-94-C-0007 and by NSF under Grant No. ECS-9109343.

## References

- [1] M. Mehregany and Y.C. Tai, "Surface micromachined mechanisms and micromotors," *J. of Micromechanics and Microengineering*, vol. 1, pp. 73-85, 1991.
- [2] K. Deng, M. Mehregany, and A.S. Dewa, "A simple fabrication process for side-drive micromotors," in *Technical Digest, 7th Int. Conf. Solid-State Sensors and Actuators*, (Yokohama, Japan, June 1993), pp. 756-759.

- [3] S. Furukawa, H. Miyajima, M. Mehregany, and C.C. Liu, "Electroless plating of metals for micromechanical structures," in *Technical Digest, 7th Int. Conf. Solid-State Sensors and Actuators*, (Yokohama, Japan, June 1993), pp. 66-69.
- [4] M. Mehregany, S.D. Senturia, J.H. Lang, and P. Nagarkar, "Micromotor fabrication," *IEEE Trans. Elect. Dev.*, vol. 39, pp. 2060-2069, Sept. 1992.
- [5] V.R. Dhuler, M. Mehregany and S.M. Phillips, "A comparative study of bearing designs and operational environments for harmonic side-drive micromotors," *IEEE Trans. Elect. Dev.*, vol. 40, pp. 1985-1989, Nov. 1993.
- [6] V.R. Dhuler, M. Mehregany and S.M. Phillips, "An experimental technique and a model for studying the operation of harmonic side-drive micromotors," *IEEE Trans. Elect. Dev.*, vol. 40, pp. 1977-1984, Nov. 1993.
- [7] S. F. Bart, M. Mehregany, L. E. Tavrow, J. H. Lang, and S. D. Senturia, "Electric Micromotor Dynamics," *IEEE Transactions on Electron Devices*, vol. 39, pp. 566-575, March 1992.

# Microchopper-Modulated IR Microlamp

Peter Y. Chen and Richard S. Muller

*Berkeley Sensor & Actuator Center  
Department of Electrical Engineering and Computer Sciences,  
University of California, Berkeley*

## ABSTRACT

We describe the design, fabrication, and operation of a chopped microincandescent IR source which can be used in applications demanding a modulated IR output at a fairly high frequency (typically above 1kHz). Such a source is typically required to reduce background noise and to improve signal amplification. The chopper and source are formed primarily using surface micromachining in a continuous batch process to produce a microencapsulated polysilicon filament IR source similar to that described by Mastrangelo and Muller [1] and an overlying shutter based upon the resonator structures first introduced by Tang and Howe [2]. Although Tabata et al [3] have used bulk micromachining to produce a resonating comb-drive shutter to chop IR entering a detector, this research is the first to combine fabrication of an IR source and chopper and to make extensive use of surface micromachining. Experimental choppers were operated between 9 and 15 kHz.

A nine-mask process produced the shuttered microlamp. Six of the masks were used to fabricate the incandescent source and the remaining three produced the shutter positioned above it. The six-mask microlamp process is slightly modified from that of Mastrangelo [1]. Aside from layout changes, the new process replaces a potassium hydroxide etch with a nitric acid/hydrofluoric-acid mixture to form a trench below the filament in the substrate and it uses *n*-type dopants for the filament. Post-fabrication tests and measurements show that device yield is approximately 98% for the microlamp. Yields for the shutter processing were above 80% when 3-micrometer features were employed, but dropped to about 50% when 1-micrometer features were used. Although radiative output peaks in the IR, visible output radiation, becoming quite intense at higher filament voltages, was clearly observable during microlamp testing even under normal indoor illumination as will be shown in a video. To avoid polysilicon recrystallization that would permanently change the filament resistance, the drive voltage must be kept below a "reversible" region that can be found by characterizing the *I-V* characteristic of the microlamp. When the applied voltage is held below the

recrystallization voltage, the microlamp operates for over four hours with less than 10% change in its current.

The measured shutter resonant frequencies matched closely those obtained through simulations. We designed a total of 81 different shutters having resonant frequencies from 1 to 10kHz. Deviations between the measured and calculated resonant values were smaller than 2%. In contrast, the measured bandwidths (~200Hz), were an order-of-magnitude smaller than the calculated bandwidths (~2kHz). In addition, measured displacements ranging from 1 to 10 $\mu$ m were larger, also by an order-of-magnitude, than simulated expectations. The matches in resonant frequencies, combined with the mismatches in bandwidths and displacements, suggest that the damping effect modeled in simulation has been overestimated. The polysilicon shutters were found to absorb most of the visible output radiation although an infrared-absorbing metal layer would be needed in order to extinguish completely all IR output.

## INTRODUCTION

Since their introduction in the work of Tang and Howe [2], resonant polycrystalline-silicon microflexures, driven by electrostatic comb structures, have proven themselves as reliable frequency standards [4]. With design modifications, these microstructures can also function as micro-chopping elements that can be produced compatibly with electronic components to function as key elements in a number of special-purpose MEMS. An early example is the miniaturized electrostatic voltmeter or "field mill" described by Hsu and Muller [5] which was later improved by Loconto and Muller [6]. The microchopper in the "field mill" interrupts an electric field which gives rise to currents in a detector electrode that are proportional to the difference in voltage between a test surface and the detection electrode. Choppers are also key components for photoemissive and photosensing systems where they can be used as shutters to chop the optical signals and enable phase-locked system designs. By making such systems suitable for MEMS, microchoppers open important new engineering applications.

Mastrangelo [1] has introduced a

microincandescent source that is suitable as a very tiny infrared emitter. Its construction can be combined, using surface micromachining, with the resonant-shutter technology to produce a microshuttered IR source. The source may have applications in sensors, remote controls and communications, and as nonlinear components in circuits that operate under hostile environments.

## DESIGN and FABRICATION

The microlamp has a similar design to that of Mastrangelo [1] and consists of two main elements: a

suspended *microbridge* filament that is anchored at both ends, and a *microshell* that hermetically seals the filament under low pressure. The filament is made of polycrystalline silicon coated with a layer of silicon nitride. Another layer of silicon nitride acts as the window material. Mastrangelo measured a radiant power of ~ 300 microwatts peaked strongly in the infrared with a filament power of 5 mW [7]. The sources produced in this work are noticeably brighter although measurements of brightness have not been carried out as yet.

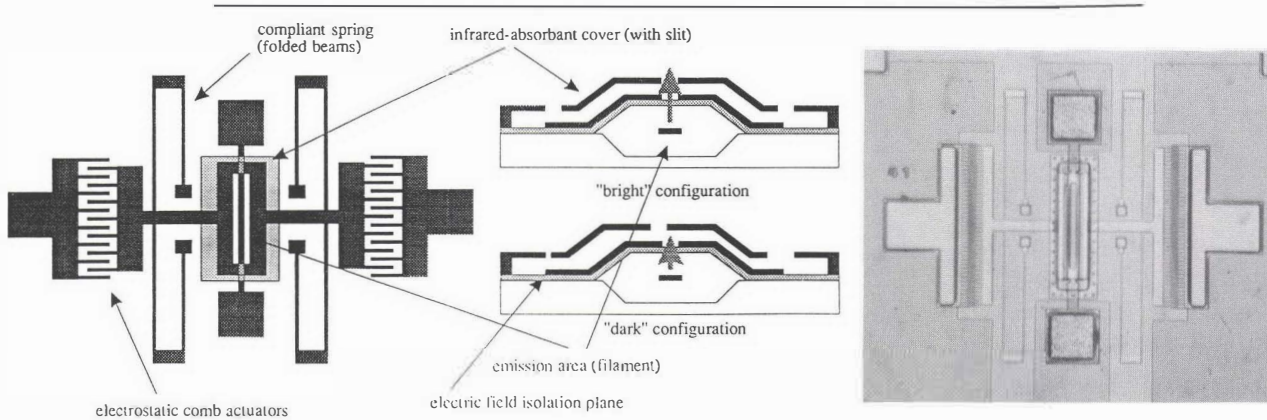


**Figure 1.** Layout, cross section, and die photograph of a microchopped IR source. The microlamps are  $100\mu\text{m}$  by  $300\mu\text{m}$  and the overall width of the assembly is 1.05 mm.

Figure 1 shows a layout, cross section and photograph of the microchopper IR source. The fabrication process for it uses eleven layers and nine masks. The microlamp is formed in seven layers and six masks, while the shutter is built in the remaining four

layers and three masks. Figure 2 provides a processing summary. The process uses a *p*-type,  $\langle 100 \rangle$  silicon wafer as substrate and begins with the deposition of 500 nm of low-stress silicon nitride on it. This layer of nitride forms the bottom half of the coat that protects the polysilicon filament. The undoped filament is 1  $\mu\text{m}$  thick. A

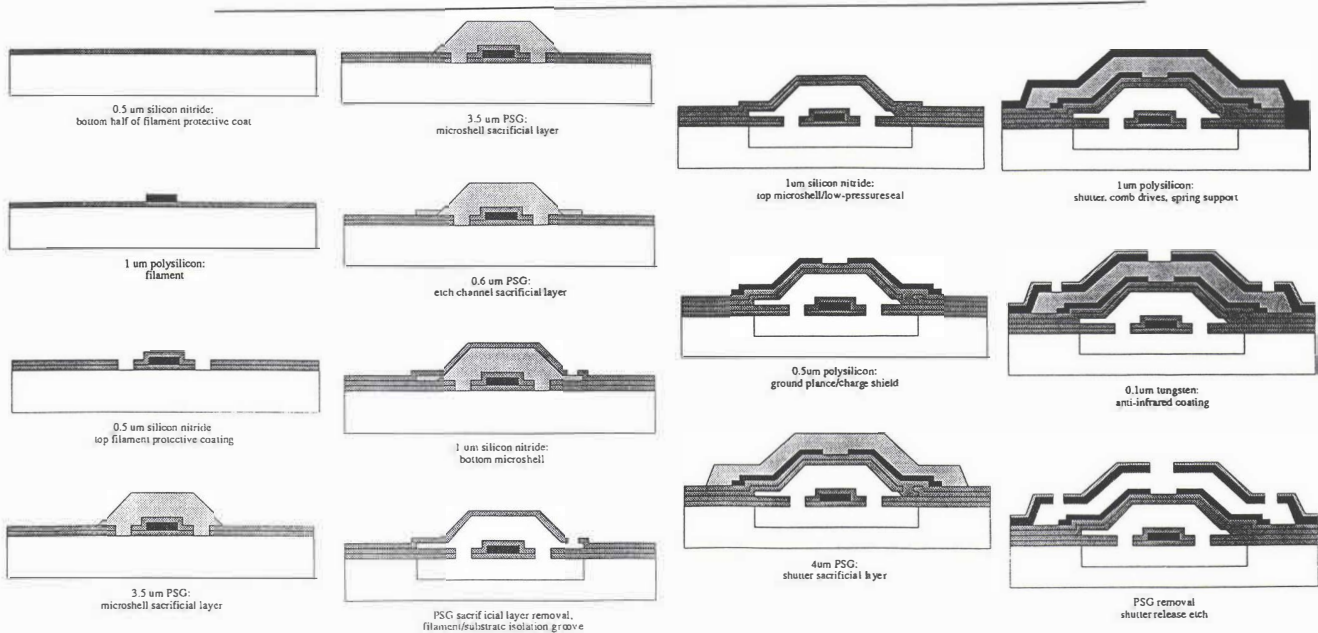


**Figure 2.** Processing steps for the microchopped IR source.

phosphorus-rich silicon dioxide layer (PSG) is then deposited above the filament, and from it phosphorus is driven into the filament in a two-hour, 1050C anneal. The PSG layer is then removed and a 500nm silicon nitride deposition above the filament completes the filament protective coating. The two silicon nitride layers are patterned and etched, near the filament, to provide an opening to the substrate. Silicon etchant used in subsequent steps opens an isolation groove under the filament.

A thick PSG sacrificial layer, for the microshell, is followed immediately by a thin PSG layer for the etch channels. The silicon nitride microshell is next deposited, in two 1 $\mu$ m depositions. Etch channels are defined above the thin PSG after the first 1 $\mu$ m deposition. The wafer then undergoes a long 5:1 BHF immersion, during which the BHF attacks and removes the PSG sacrificial layers enclosed in the shell. Another immersion step, in a VLSI silicon etchant (consisting of, 50:20:1 HNO<sub>3</sub>:H<sub>2</sub>O:HF by weight) follows the BHF dip to form the underlying isolation groove. Since this silicon etchant is isotropic, prolonged immersion undercuts the substrate below the filament so that a cavity is formed in which the filament is suspended. The second 1 $\mu$ m silicon nitride deposition forms the top half of the microshell and hermetically seals the microshell at  $\sim$ 300mtorr, the LPCVD deposition pressure for low-stress silicon nitride. A silicon nitride etch, not shown in the figure, opens the filament contact and completes the improved microlamp process.

A 500nm undoped polysilicon layer is then deposited and patterned. It will act as the charge-shielding ground plane. The sacrificial PSG layer for the top shutter, 4 $\mu$ m-thick, follows the ground-plane deposition and shutter-support anchors to the substrate are defined in this step. The final polysilicon layer, 1 $\mu$ m thick, constitutes the shutter and the actuator. The two polysilicon layers are doped during a high-temperature anneal that drives the dopant from the PSG sacrificial layer into the polysilicon. To ensure doping symmetry, another PSG layer is deposited above the polysilicon to act as the upper dopant source for the shutter. A thin tungsten coat (100nm) is sputtered above the polysilicon shutter and the two layers are patterned in one step. Wet-etching the wafer in 5:1 BHF removes the PSG and frees the shutter.

Eighty-one shuttered microlamps, of varying component sizes, were designed using the KIC layout generator. Variations include three filament sizes (widths of 4, 10, and 20 $\mu$ m), different electrostatic comb sizes (1, 2, and 3 $\mu$ m), comb gaps (1, 2, and 3 $\mu$ m), and compliant supports of varying widths (1, 2, 3 $\mu$ m).

## MEASUREMENTS and CHARACTERIZATION

Only those microlamps with 10 $\mu$ m-wide filaments were tested for yield. Of 324 microlamps tested in the 12 central dice of the wafer, all but four survived the 6-mask process and are functional (two of the four "dead" microlamps had broken microshells, while the other two had broken filaments). Consequently, the 6-mask microlamp process yielded 98.8%. The lamps were surprisingly robust; all 320 were operational after the shutters were fabricated. Fabricating the shutter (3-mask process) was more difficult than fabricating the microlamp, primarily due to difficulty in the final release etch. Because of their large surface areas and relatively fragile beam supports, many shutters were torn from their anchors during rinsing. Even though precautions were taken to insure minimal rinse-deionized-water flow, approximately 50% of the shutters were lost. We believe that significant yield improvement would follow the use of the supercritical drying technique described by Mulhern et al [8].

Figure 3 is a plot of microlamp lifetime measurements as performed on the HP4145B. The lifetime values were obtained by applying a constant voltage across the filament until the current across the filament changed by more than 10% of its normalized value. Each data point is the average of three

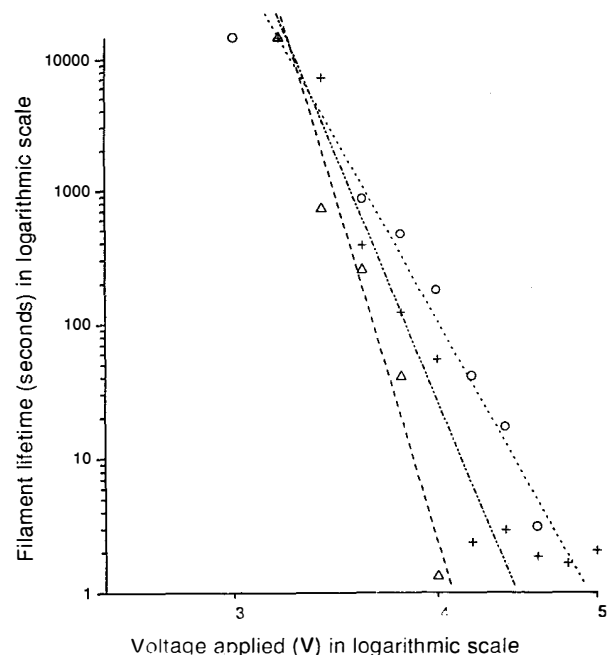


Figure 3. Measured lifetimes of micro-IR sources as a function of voltage drive. Lifetime terminated if current changes by greater than 10% of nominal value. Plotted values are averages of 3. Filament widths: 4  $\mu$ m o, 10  $\mu$ m  $\Delta$ , 20 $\mu$ m +.

measurements. Due to time constraints on equipment usage, lifetime measurements at the lowest voltage were stopped after 4 hours for all filament widths, which is why the extrapolated lines for these measurements seem to converge at approximately 4 hours. However, at low voltages (~ 3 volts), the filament resistance changes very little for all microlamps, and we expect them to last much longer than 4 hours. The log voltage vs. lifetime plot for the polysilicon filament consists of only one line with a single slope, suggesting that a single mechanism dominates the filament-degradation process, most likely polysilicon evaporation.

Eleven of the 27 shutter designs survived the release etch and were operational. Of the 27 shutters designed for the 10 $\mu$ m-wide filament, most of the 9 designs that use 1 $\mu$ m-wide folded beams did not survive the release etching and rinsing. Those that were fabricated could not be powered without a failure caused by the overly flexible driver combs becoming stuck to the substrate. In fact, we found that thin beams and small gap spacings led to failures in all 1  $\mu$ m-gap beams whereas nearly 100% of the 2  $\mu$ m-gap shutters were functional. For the 11 shutter designs that operated, the resonant frequencies match very closely to predicted values [9]; deviations from theory are less than 5%. Such close matches in resonant frequencies suggest that modeling of the folded-beam spring constants and the shutter mass used in the simulation is very accurate. However, the observed bandwidths for all these shutters (approximately 200Hz) are much lower than those obtained by simulation, implying that the simulation may overestimate shutter damping. The narrow bandwidth makes it necessary to tune very carefully in order to drive these microchoppers at their resonant peak. The largest displacement measured was 30 $\mu$ m (peak-to-peak) at 10.25 kHz.

## CONCLUSIONS

The design, fabrication, and operation of a microchopped luminous source has been demonstrated for the first time. Both a vacuum-encapsulated source and an overlying resonant polysilicon microflexure chopper have been produced in a nine-mask continuous batch-fabrication process. Yields of nearly 100% were achieved in the first steps of the process which produced the encapsulated IR sources. The silicon nitride-windowed microcavities proved adequately robust for further steps needed to fabricate the resonant microchoppers. The critical release-etch step was successful for shutters having feature sizes above 2 $\mu$ m, but generally failed for 1 $\mu$ m features. Additional failures of greater than 50% of the shutters were experienced in the final-rinse step.

The measured resonant frequencies for the completed microchoppers agree well with the predictions of simulations, indicating accurate modelling of the folded beams and shutter masses. The simulation, however, substantially underestimates the measured mechanical quality factor and the maximum shutter displacement. Both inaccuracies are thought to result from improperly modeling damping in the system. Several design changes leading to more simplified processing and improved performance have become evident in carrying out this research. These changes, which will reduce the mask count and modify the shutter design, should move the microchopped IR source closer to system applications.

## ACKNOWLEDGMENTS

Advice and experimental help from Gary Fedder of BSAC and from Drs. Damien Gray and Paul Lum of Hewlett-Packard is warmly appreciated. Assistance by the staff of the Berkeley Microlab was essential to the success of this project. This work was partially supported by the State of California CALTRANS PATH project.

## REFERENCES

- [1] C.H. Mastrangelo and R.S. Muller, "Vacuum-Sealed Microfabricated Silicon Incandescent Source." *Tech. Digest: 1989 IEEE Electr. Devices Mtg.*, 503-506, Washington D.C., 4-6 Dec. 1989.
- [2] W.C. Tang, T.-C. Nguyen, and R.T. Howe, "Laterally Driven Polysilicon Resonant Microstructures," *Sensors and Actuators*, 20, 25-32, 1989.
- [3] O. Tabata et al, "Electrostatically Driven Optical Chopper Using SOI Wafer," *Tech. Digest: TRANSDUCERS '93*, 124-127, Yokohama, Japan, 7-10 June, 1993.
- [4] T.-C. Nguyen, and R.T. Howe, "Microresonator Frequency Control and Stabilization Using an Integrated Micro-Oven," *Tech. Digest: TRANSDUCERS '93*, 1040-1043, Yokohama, Japan, 7-10 June, 1993.
- [5] C.H. Hsu and R.S. Muller, "Micromechanical Electrostatic Voltmeter," *Tech. Digest: TRANSDUCERS '91*, 659-662, San Francisco, CA, 24-27 June, 1991.
- [6] D.P. Loconto and R.S. Muller, "High-Sensitivity Micromechanical Electrostatic Voltmeter," *Tech. Digest: TRANSDUCERS '93*, 878-881, Yokohama, Japan, 7-10 June, 1993.
- [7] C.H. Mastrangelo, J.H.-J. Yen, and R.S. Muller, "Electrical and Optical Characteristics of Vacuum-Sealed Polysilicon Microlamps," *IEEE Trans. Electr. Devices*, 39, 1363-1375, June 1992.
- [8] G.T. Mulhern, D.S. Soane, and R.T. Howe, "Supercritical Carbon Dioxide Drying of Microstructures," *Tech. Digest: TRANSDUCERS '93*, 296-299, Yokohama, Japan, 7-10 June, 1993.
- [9] W. Tang, *Thermal Applications of Microbridges*, PhD Thesis, Dept't of EECS, Univ. of California, Berkeley, December 1990.

# Micromachined Jets for Manipulation of Macro Flows

David J. Coe and Mark G. Allen  
*School of Electrical and Computer Engineering*

Mark A. Trautman and Ari Glezer  
*George W. Woodruff School of Mechanical Engineering*

Georgia Institute of Technology  
Atlanta, GA 30332

## Abstract

This paper describes the successful fabrication and initial characterization of micromachined jets (microjets) fabricated for use in macro flow control and other applications. The microjets were fabricated using standard silicon micromachining techniques and consist of an orifice situated atop an actuator cavity which is bounded by a flexible membrane. Typical microjet orifice sizes range from 150-300 microns. Vibration of the membrane using either electrostatic or piezoelectric drive results in a nominally round turbulent air jet formed normal to the microjet orifice. An important feature of the jet is that it is formed without net mass injection by an oscillatory flow that is acoustically induced near the edge of the orifice. Initial characterization was performed using a miniature total pressure tube and a conventional miniature hot wire sensor. Microjets with velocities of 17 m/s and coherent to lengths exceeding 500 diameters were achieved. The microjet Reynolds number at a distance of 15 diameters is estimated at approximately 1400.

## Introduction

While there is no question that one of the most important application areas for microactuators is the control of macro-events, these actuators usually generate insufficient force to directly realize control authority. Thus, some type of mechanical amplification is required. An attractive means for the amplification of the actuator output is its coupling to inherently unstable pressure or flow systems. If system operating points are carefully chosen, the relatively small forces generated by a microactuator can be used to create large disturbances in either static, pressure-balanced systems or in free- and wall-bounded shear flows. These concepts have been exploited for years in a number of static and dynamic macro systems such as pressure regulators and fluidic actuators, respectively. More recently Huff et al. [1] have demonstrated the adaptation of a pressure-balanced system to an electrostatically-actuated microvalve.

An example of flow control that illustrates a scaling hierarchy which can be adopted for microactuators is in the area of

jet thrust vectoring. Recent experiments by Green and Glezer [2] have demonstrated the utility of millimeter-scale surface actuation for thrust vectoring of larger jets having characteristic length scales that are at least two orders of magnitude larger. Vectoring is accomplished by exploiting hydrodynamic instabilities of the macro-jets near the flow boundary such that the energy necessary for their manipulation is extracted from the mean flow and thus the power input to the actuators is of the order of several milliwatts [3-4]. The efficacy of this technique has been demonstrated in an air jet emanating from a rectangular orifice (7.62 x 1.27 cm) as shown in contour plots of the measured streamwise velocity component in the cross-stream plane (Figure 1a-1c). The unforced jet is shown in Figure 1a for reference. In Figure 1b, the jet is forced by and vectored away from the bottom actuators. Time-periodic vectoring is achieved when the input waveforms to the top and bottom actuators are modulated out of phase (Figure 1c). Recent jet vectoring experiments at Georgia Tech (Smith and Glezer, unpublished) in which the mechanical actuators were replaced with millimeter-scale zero mass flux surface jets have suggested the concept of cascaded control. Namely, that micromachined jet actuators (microjets) be used to manipulate millimeter-scale jets which, in turn, will control larger jets. Arrays of micromachined jets are particularly attractive for such applications because they can be individually addressed and phased. In this paper, we describe some design and fabrication concepts of micromachined jet actuators and include some preliminary measurements of their performance.

## Jet Operation

In the present investigation a nominally round turbulent air jet is formed normal to an orifice in a flat plate. An important feature of the jet is that it is formed without net mass injection by an oscillatory flow that is acoustically induced near the edge of the orifice. As in larger-scale geometries (e.g., Ingard and Labate [5]) the jet is synthesized by a train of vortex rings. Each vortex is formed during the half cycle of the acoustic wavetrain when the orifice velocity is in the streamwise direction and is advected away from the plate under its self-induced velocity. The vortices are

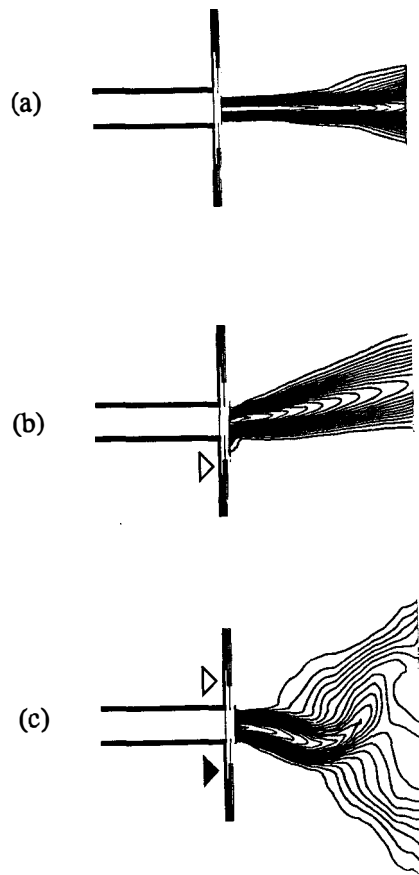


**Figure 1** Measured contours of streamwise velocity for a rectangular air jet with dimensions 7.62 cm x 1.27 cm. ( $U_{exit} = 6.5$  m/s).

formed at the excitation frequency and the jet is synthesized by their interaction downstream from the orifice. In the present work, the acoustic excitation is provided by a diaphragm that is mounted at the bottom of a sealed shallow cylindrical cavity under the orifice plate as described below.

### Fabrication

A cross-section of the prototype microjet is shown in Figure 2. In this design, the orifice and actuator are incorporated into the same wafer. Both electrostatic and piezoelectric drive can be used in this configuration. Although only a single jet is shown in this configuration, extension of this concept to addressable arrays of microjets is straightforward and has been realized by us.

The microjet orifice and actuator hole were anisotropically etched in the wafer as pictured in Figure 3. Starting with a high resistivity two inch <100> silicon wafer that was polished on both sides, a layer of silicon dioxide 1 micron in thickness was formed using wet thermal oxidation. On the front side a 3000 Å layer of aluminum was deposited using DC sputtering. Photolithography was then used to pattern a square orifice hole in the aluminum. This hole was designed to be 265 microns on a side. Using the

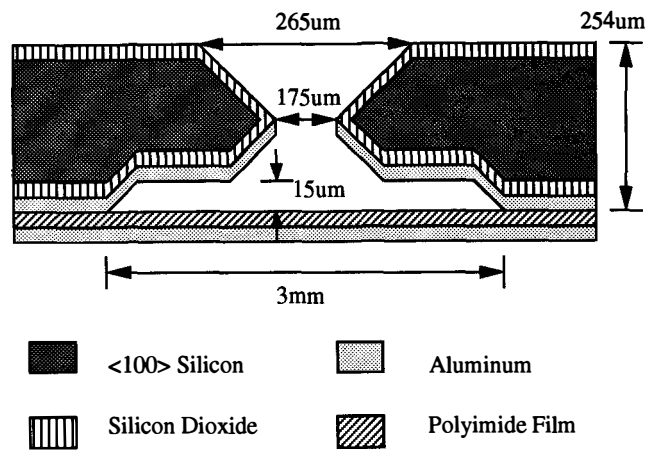


**Figure 2** Cross-section of fabricated microjet.

patterned aluminum as a mask for infrared alignment, a matching orifice hole was created on the back side of the wafer using photolithography. Using the patterned silicon dioxide as an etch mask, the jet orifice was anisotropically etched using a 20% potassium hydroxide solution in water at 60 °C (Figure 3b).

Photolithography was then used to pattern a square actuator hole in the back-side oxide 3 mm on a side (Figure 3c). This hole was anisotropically etched to a depth of 15 microns using a timed etch consisting of 20% potassium hydroxide in water at 50 °C (Figure 3d). The wafer was then re-oxidized using thermal oxidation such that a layer of 2500 Å of silicon dioxide was formed in the etched region. A layer of aluminum 3000 Å in thickness was then sputtered on the back side of the wafer to act as an electrode for electrostatic actuation. A layer of polyimide film was bonded to the back side of the wafer to form the flexible actuation diaphragm. This polyimide film was then coated with a layer of 3000 Å of aluminum using DC sputtering to provide the second electrode for electrostatic actuation (Figure 3e).

For electrostatic actuation, application of voltage between the diaphragm electrode and the electrode on the back side of the wafer was used to realize diaphragm actuation. Alternatively, a ground plane below the wafer could also be used for actuation; in this case, voltage is applied between the diaphragm electrode and the ground plane. For piezoelectric actuation, the back side of the wafer was fitted with non-vented standoffs and bonded to a commercial piezoelectric transducer. Vibration of the piezoelectric transducer caused pressure fluctuations in the transducer-actuator wafer cavity, thus realizing diaphragm actuation. Both electrostatic and piezoelectric actuation were successful in the creation of microjets. In the case of piezoelectric actuation, the jet output could be modified by the electrostatically actuatable diaphragm. In the jet measurements described below, piezoelectric actuation is used.

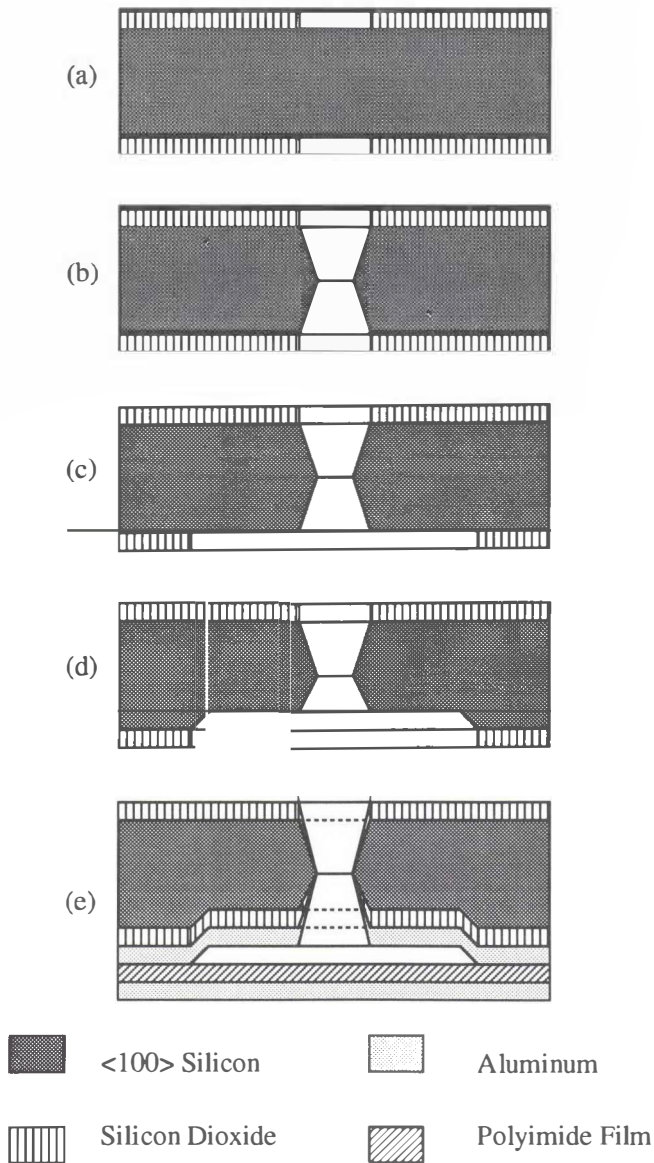


**Figure 3** Microjet fabrication sequence.  
 a) Prior to etching orifice  
 b) After etching orifice  
 c) Prior to etching actuator cavity  
 d) After etching cavity  
 e) After membrane attachment and metallization

#### Initial Measurement of the Jet Flow

In all experiments reported here, the piezoelectric driver is operated at its nominal 1.3 kHz resonance frequency in its first axisymmetric mode of vibration using a laboratory function generator and a high voltage (max. 120 Vrms) broad band DC amplifier (the present measurements were taken at an excitation level of 42 Vrms). Figure 4 is a smoke visualization photograph of the jet where the smoke is injected radially near the orifice edge. The field of view measures 89 mm in the streamwise ( $x$ ) direction and thus corresponds to nearly 500 jet diameters. The jet appears to become turbulent at or near the orifice, and spreads almost

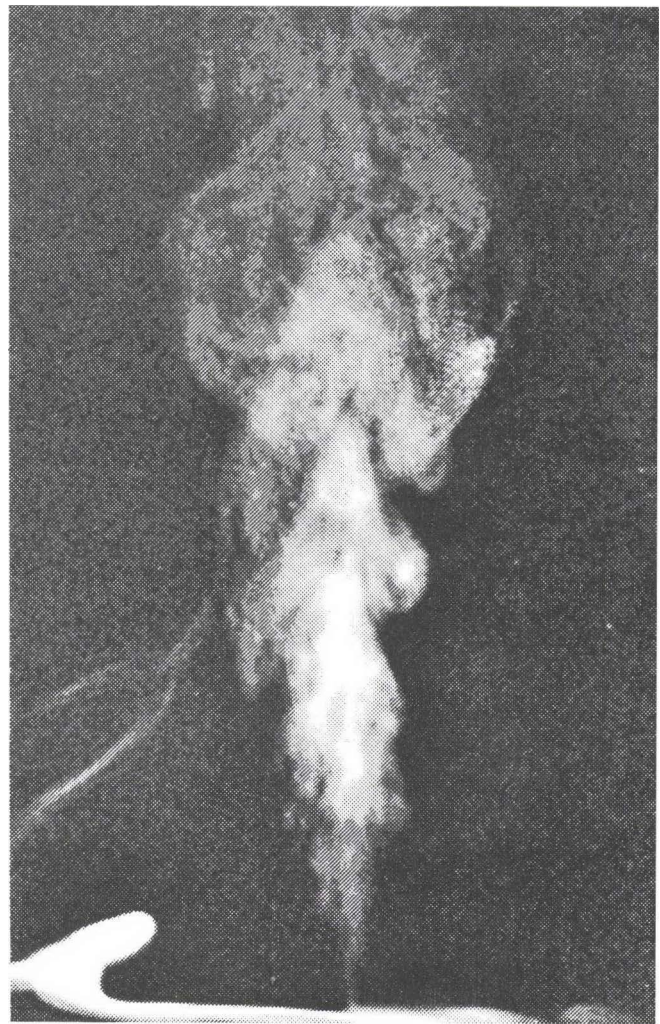


**Figure 4** Smoke visualization of operational microjet.

linearly with streamwise distance. Large coherent vortical structures are apparent in the far field of the jet. The Reynolds number of the jet based on the centerline velocity and its width at  $x/D = 15$  (see velocity profiles in Figure 5) is approximately 1400.

The streamwise velocity component was measured using a miniature total pressure tube having inner and outer diameters of 212  $\mu\text{m}$  and 340  $\mu\text{m}$ , respectively. Radial profiles of the time-averaged streamwise velocity were measured at  $x/D = 15, 25,$  and 35 using a three-axis traversing mechanism and are shown in Figure 5. Despite the obvious limitations in spatial resolution and sensor interference, these profiles suggest that the jet is reasonably symmetric about its centerline, and furthermore, when these profiles are plotted in the usual similarity coordinates (Figure 5b), they appear to collapse reasonably well on top of each other, suggesting that the jet is self-similar. The self-similarity of the flow is further supported by the linear decay of the centerline velocity with streamwise distance for  $x/D > 15$  as shown in Figure 6 (a line with a slope of -1 is shown for reference). Measurements at  $x/D < 15$  are included for reference as an indication of the the spatial limitations of the sensor.

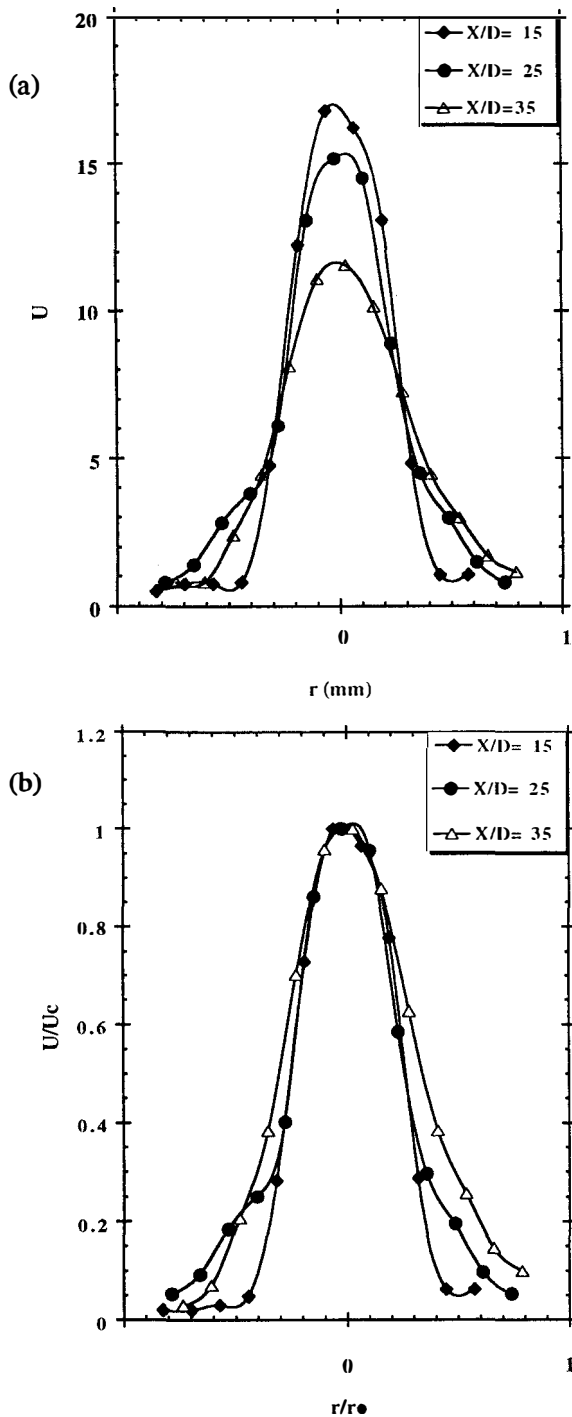


**Figure 5** Measured time-averaged streamwise velocity of the microjet.  
 a) Plotted using radial coordinates ( $U$  in m/s).  
 b) Plotted using similarity variables.

Finally, a spectrum of the centerline (streamwise) velocity was measured at  $x/D = 40$  using a conventional miniature hot wire sensor and is shown in Figure 7. The spectral component at the excitation frequency and its higher harmonics shows that an oscillatory component of the fluid velocity is prominent even in the far field of the jet. It is noteworthy that the spectrum is virtually

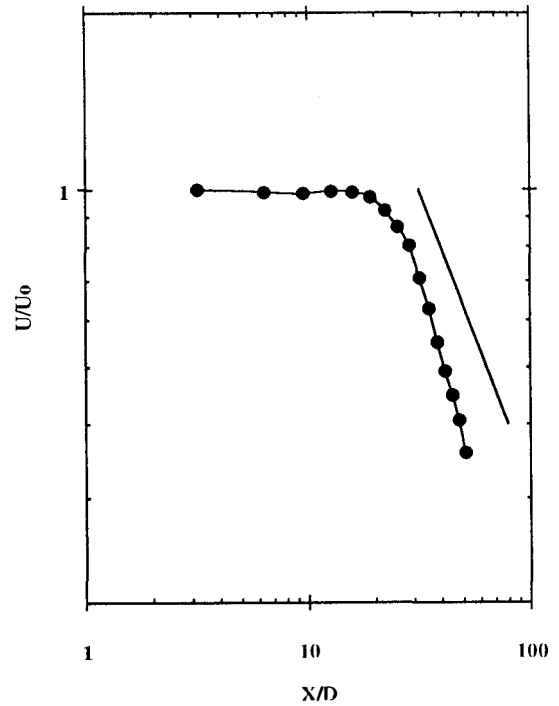


**Figure 6** Measured centerline streamwise velocity decay of microjet.

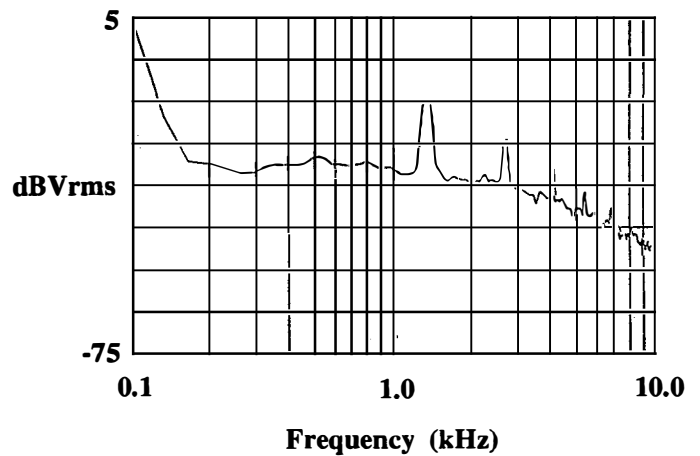


**Figure 7** Frequency spectrum of microjet measured at  $x/D = 40$ .

featureless below 1000 Hz and that no subharmonics of the excitation frequency are present.

### Conclusions

Micromachined jets and jet arrays have been realized using silicon micromachining techniques. These jets can be driven piezoelectrically or electrostatically and can produce velocities on the order of 17 m/s within 15 orifice diameters, and remain established up to 500 diameters or more. Each jet is produced with no mass injection at the edge of an orifice by a vibrating diaphragm and is synthesized by the interaction of a train of vortex

rings. Although these jets are formed by the strong oscillatory motions, they appear to become self similar within fifteen orifice diameter from the actuator surface. These microjets show great promise as vehicles by which macro-scale effects can be influenced by microactuators.

### **Acknowledgments**

This work was supported in part by the Air Force Office of Scientific Research under Grants F49620-92-J-0518 and F49620-93-1-0495, monitored by Dr. J. M. McMichael. The authors would like to thank E.I. Dupont, Inc. for donation of polyimide materials used in this work. Microfabrication was carried out at the Georgia Institute of Technology Microelectronics Research Center (MiRC), and the authors would like to acknowledge the support of the MiRC staff.

### **References**

- [1] Huff, M.A., Mettner, M.S., Lober, T.A. and Schmidt, M.A., "A pressure-balanced electrostatically-actuated microvalve," Proceedings of Solid State Sensors and Actuators Conference, Hilton Head, SC, June, 1990.
- [2] Green, S. M., and A. Glezer, "Manipulation of a High Aspect Ratio Rectangular Jet," presented at the APS/DFD Meeting, Florida State University, Tallahassee, Florida, November 1992.
- [3] Wiltse, J. M. and Glezer, A "Manipulation of free shear flows using piezoelectric actuators," *J. Fluid Mech.*, **249**, 261, 1993.
- [4] Jacobs, J.W., James, R. D. Ratliff, C. T. and Glezer A. "Turbulent jets induced by surface actuators," AIAA Paper 93-3243.
- [5] Ingard, U. and Labate S. "Acoustic circulation effects and the Nonlinear Impedance of orifices" *J. Acoust. Soc. Am.* **22**, 211-219, 1950.

# A Robust Normally-Closed Silicon Microvalve

Phillip W. Barth\*, Christopher C. Beatty†, Leslie A. Field\*, James W. Baker†, and Gary B. Gordon\*

\*Hewlett-Packard Laboratories, 3500 Deer Creek Road, Palo Alto, California 94304

†Hewlett-Packard Little Falls Site, Wilmington, Delaware 19808-1610

## ABSTRACT

A nickel-silicon bimetallic microvalve intended for use in analytical instrumentation has been designed, fabricated, packaged, and tested. This valve's range of operation constitutes an order-of-magnitude increase in both pressure and flow as compared to the performance of previous bimetallically actuated valves. System requirements of 0-200 psi and 0-600 sccm have been met or exceeded with air, He, N<sub>2</sub>, and H<sub>2</sub>.

## INTRODUCTION

The design of a robust gas-control valve is subject to a complex group of constraints. Proportional control of gas flow at moderately high pressures (5-200 psi) and moderately high flow rates (0.1-1000 sccm) requires significant mechanical motion and adequate stiffness in the mechanical structure used for flow control. For a poppet valve in which a flat valve face moves in opposition to an orifice surrounded by a seat, typical dimensions required are an orifice diameter on the order of 200-400  $\mu\text{m}$  and total face motion (stroke) on the order of 50-100  $\mu\text{m}$ . Control of low flows at the high end of the pressure range, where the valve face is nearly in contact with the valve seat, requires that the structure be stiff enough to resist closing as the face approaches the seat, and stiff enough in the opposite direction for insensitivity to environmental vibrations which would otherwise open the valve by the action of a mechano-pneumatic positive feedback loop. In many applications safety considerations dictate that a valve should go to a no-flow mode when power fails. For reliability the dirt-sensitive mating area between face and seat should be as small as possible, and reliability should be sufficient to permit millions of operating cycles. Finally, as in all engineering endeavors, the fabrication cost should be minimized within other constraints.

Historically such valves have been solenoid actuated and have been fabricated by traditional macro-scale manufacturing techniques. More recently several microvalves fabricated using MEMS techniques have been developed [1-7]. The valve presented in this work is a candidate for use in future gas chromatography systems and has generated considerable interest within Hewlett-Packard [8,9]. Its simplicity of fabrication and its rugged structure make it a strong contender for many gas-phase applications.

## MICROVALVE DESCRIPTION

Figures 1 and 2 illustrate cross-sectional and top views of the valve. Figure 3 is a photograph of the bottom side of the actuator chip which comprises the top half of the valve, and Figure 4 shows a detail of the orifice and seat combination in the bottom orifice chip.

The actuator chip [10] comprises a central silicon boss surrounded by a radial array of bimetal legs of plated nickel 25-50  $\mu\text{m}$  thick on single-crystal silicon also 25-50  $\mu\text{m}$  thick. The "spider legs" of the actuator act to relieve hoop stress during actuation, so that a greater valve stroke is achieved than would otherwise be possible. Each leg connects at its peripheral end to a torsion-bar suspension of plated nickel, which in turn is attached to a silicon frame. The suspension

allows rotation of the end of the leg while resisting vertical motion, in a manner which approximates a simply-supported boundary condition. The long, thin suspension arms also provide high thermal resistance between the legs and the frame for reduced power consumption.

In operation the actuator is heated by a thin-film nickel heater situated near the central ends of the spider legs. The heater sits on the silicon surface between areas of plated nickel, and comprises two resistors in a parallel electrical configuration. Contact to the ends of the resistors is made at points 180° apart by two electrically isolated plated nickel regions connected to bonding pads, and the resistor current splits from the contact points to flow both clockwise and counterclockwise along the meandering path. Although the resistor region is thinner than the plated nickel regions, the meander shape adds stiffness and prevents excessive bending in this region.

Because the actuator chip contains no diffusions or contact holes, its fabrication process uses only four photomasks in three photomasking steps. Actuators can be electrically tested and optically inspected in wafer form, minimizing testing costs.

A separate chip containing a square orifice framed by a square valve seat sits beneath the actuator chip. This chip requires two photomasks in its fabrication process. Like the actuator chips, orifice chips can be inspected and marked in wafer form.

The orifice chip consists of a square raised seat area which frames a central orifice. In contrast to previous orifice chips, the seat and orifice (patent pending) are formed in a self-aligned manner so that the inner perimeter of the seat exactly defines the minimum cross-sectional area of the orifice, maximizing the orifice area in relation to the seat area and providing several benefits. The small seat area relative to the orifice area maximizes the head pressure which the valve can open against for a given actuator force. Conversely, the large orifice area relative to the seat inner perimeter maximizes flow through the valve at a given head pressure and valve stroke. In addition, the small seat area relative to the orifice area minimizes heat flow from the actuator chip to the orifice chip when the valve face is in contact with the valve seat, minimizing the thermal power required to open the valve. This last consideration is especially important in a thermally actuated valve.

The two chips are separately fabricated and diced out of their wafers, and are placed together during packaging. While a hermetic seal is required between the bottom of the orifice chip and the package base, no hermetic seal is required between the actuator chip and the orifice chip. This characteristic provided much freedom in design and testing, since several variants of actuator and orifice chips could be mated to evaluate flow and pressure characteristics.

In production the chips can be packaged in a metal can suitable for manifold mounting, with an internal volume of 1.2 cm<sup>3</sup>. To create a

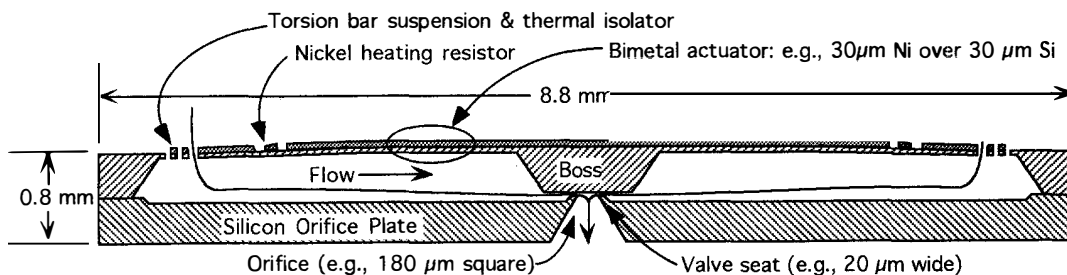


Figure 1. Cross section of silicon microvalve.

packaged valve the actuator and orifice chips are stacked on top of one another on the package base and leads are attached, then a cap is welded on. Gas inlet and outlet are through the base of the package, as are electrical leads. The flow path occurs around the entire perimeter of the actuator chip's suspension area, which maximizes sweeping of the upstream volume of the package.

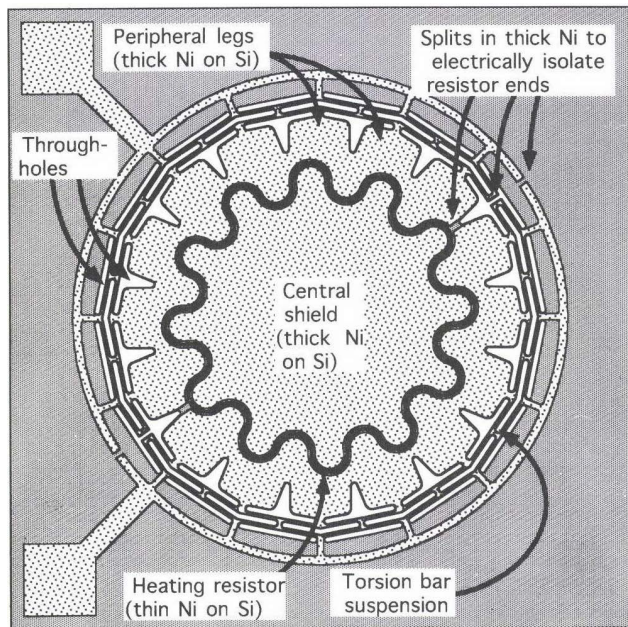


Figure 2. Simplified plan view of an actuator chip.

#### MODELLING, DESIGN, AND FABRICATION

The valve chip and orifice were designed by a combination of hand calculations, finite element simulations of both mechanical and thermal characteristics using ANSYS software from Swanson Associates on HP Unix systems, and equation-based computer models using TKSolver Plus. Layout was performed using DW2000 software from Design Workshop, and a combination of optically generated and electron-beam generated photomasks was used in contact and proximity lithography on a Karl Suss MA-25 double-sided mask aligner.

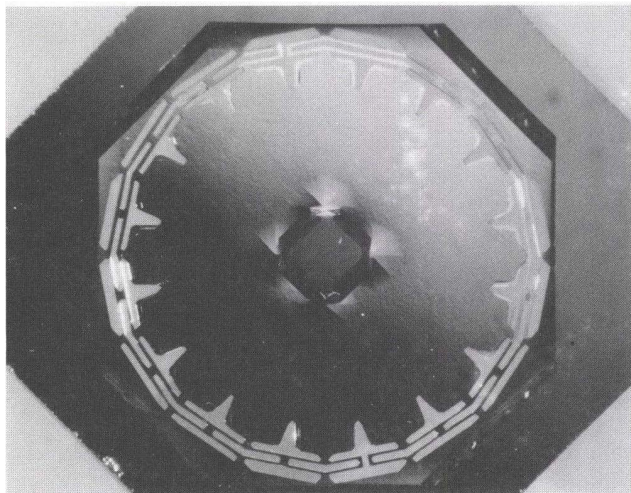


Figure 3. Photograph of the back surface of an actuator chip.

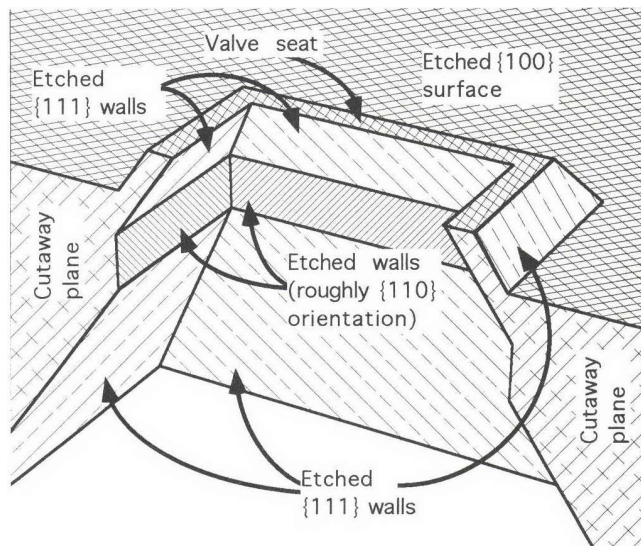


Figure 4. Cutaway detail of an orifice  $200\ \mu\text{m}$  square surrounded by a valve seat  $20\ \mu\text{m}$  wide.

#### OPERATION & PERFORMANCE

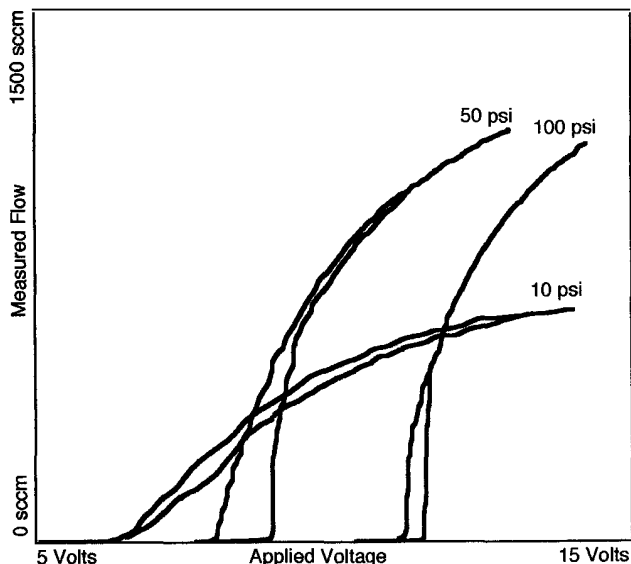
The valve operates in a normally-closed fashion. With no power applied, the central boss of the actuator covers the orifice and contacts the valve seat, preventing gas flow. When power is applied to the heating resistor the central boss rises as much as  $100\ \mu\text{m}$  out of contact with the valve seat, permitting gas flow.

Figure 5 is a set of experimental curves showing flow versus applied voltage at several different head pressures, with helium used as the flowing gas. Each curve shows roughness because voltage was controlled by manually turning a potentiometer. In addition, each curve shows hysteresis because it takes more power to open a cold valve than it does to hold a warm valve open. At higher pressures (e.g., 50 and 100 psi) a thermal feedback loop is evident on the right-hand side of the curves: as the valve face lifts off of the valve seat in a regime where pressure has held it closed until appreciable power is supplied, thermal conductance between the face and seat decreases rapidly. The decreased conductance causes the actuator to warm rapidly at an essentially constant input power, and the valve opens more quickly than it would in the absence of this rapid warming. This feedback effect operates slowly enough (transients on the order of 100 ms) to indicate that it is not a mechano-pneumatic feedback effect due to insufficient structural stiffness.

As with any thermal actuator, there is a tradeoff between actuation speed and power consumption, and speed is in any event slow compared to that of a solenoid actuator. By applying a large power pulse it is possible to move a thermal actuator rapidly in one direction, but the rate of movement in the opposite direction is limited by cooling through conduction and convection. Rapid cooling requires high thermal conductance, and high thermal conductance requires higher applied power to open the actuator. In the present valve the thermal conductance has been designed to limit the power requirement to 1 Watt for the desired pressure and flow ranges, and actuation time (full open to full closed) is thus several hundred milliseconds. This speed is not rate limiting in setting flows for gas-phase analysis systems, since compressible gases flowing through small-bore tubing result in pneumatic time constants on the order of hundreds of milliseconds to seconds.

Laser doppler velocimetry was used to characterize the mechanical resonances of the valve actuator as evidence of high structural stiffness. Figure 6 shows a plot of amplitude versus frequency for an actuator chip placed on a shaker table; the laser was focused on the top of the actuator at a point 1.9 mm from the center of the chip. The fundamental piston mode at 7.39 KHz is in fair agreement with ANSYS modelling which predicted a first resonance at 8 KHz; the lower experimental resonance frequency is thought to be due to thinner nickel and silicon in the fabricated device than in the ANSYS model. Modes 2 and 3 are rocking modes; their separation in

frequency is thought to be caused by the slight asymmetry introduced by the suspension split used to isolate the two ends of the heating resistor. Additional characterization up to 50 KHz (not shown) revealed ten higher-order modes.



**Figure 5.** Flow versus applied voltage in helium at 10, 50, and 100 psi head pressures.

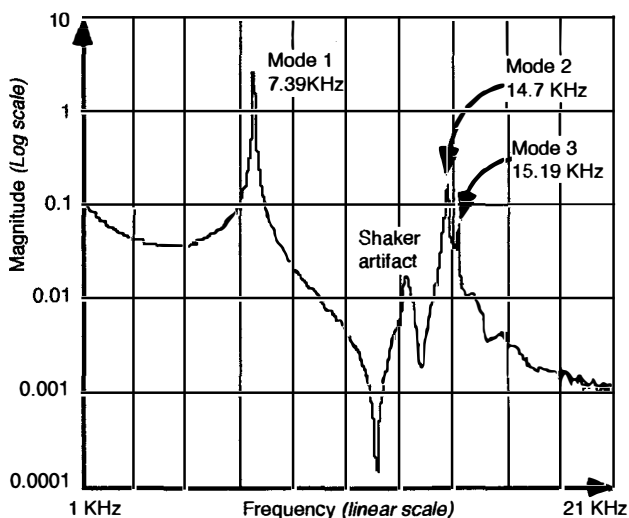


**Figure 6.** Experimental frequency response curve obtained using a laser doppler velocimeter focused on a valve actuator chip.

## CONCLUSIONS

A robust silicon microvalve meeting the many criteria for use in gas phase analysis systems has been developed. This valve's range of operation constitutes an order-of-magnitude increase in both pressure and flow as compared to the performance of previous bimetallically actuated valves [3,4] and is in the same range as that of thermally actuated valves employing fluid expansion [1,5,7] or shape-memory alloy [2,6]. The improvement compared to previous bimetallic valves is made possible by an actuator using a torsion-bar suspension and a nickel-and-silicon bimetal combination, which allow larger valve dimensions and higher stress levels for consequent longer stroke and higher force. In addition, a novel orifice and seat configuration minimizes the requirements for force and power.

The authors believe that the simple fabrication process for this valve combined with its high reliability will provide a significant contribution to gas phase analysis systems.

## REFERENCES

- [1] M.J. Zdeblick and J.B. Angell, "A Microminiature Electric-to-Fluidic Valve," Proc. 4th Int. Conf. on Solid-State Sensors and Actuators, June 1987, pp 827-829.
- [2] John D. Busch and A. David Johnson, "Prototype Microvalve Actuator," Proc. 1990 IEEE Micro Electro Mechanical Systems Workshop, Lib.Cong. No. 89-82431, pp 40,41.
- [3] Hal Jerman, "Electrically-Activated, Micromachined Diaphragm Valves," Technical Digest, 1990 IEEE Solid State Sensor and Actuator Workshop, pp 65-69.
- [4] Hal Jerman, "Electrically-Activated Normally Closed Diaphragm Valves," Technical Digest, 1991 Int. Conf. on Solid-State Sensors and Actuators, Lib.Cong. No. 89-81740, pp 1045-1048.
- [5] Mark J. Zdeblick, "A Revolutionary Actuator for Microstructures," SENSORS Magazine, Helmers Publishing, 174 Concord St., Peterborough, NH, February 1993.
- [6] "Thin-Film Ni-Ti Alloy Powers Silicon Microvalve," Design News Magazine, July 7, 1993, pp 67-68.
- [7] Mark Zdeblick, *et al*, "Thermopneumatically Actuated Microvalves and Integrated Electrofluidic Circuits", *this workshop*.
- [8] Hewlett-Packard Corporation 1993 Annual Report, cover photograph.
- [9] Hewlett-Packard Corporation First Quarter Report, 1994, cover photograph.
- [10] Gary B. Gordon and Phillip W. Barth, "Thermally-Actuated Microminiature Valve," U.S. Patent 5,058,856, May 1991.

## ACKNOWLEDGEMENTS

Many people have made this work possible. We give special thanks to Jerome Beckman, Roger Brown, Diane Burriesci, Sam Burriesci, Bill Collins, Filiz Crocker, Ray Dandeneau, Yogesh Desai, Michael Greenstein, Bob Henderson, Dick Henze, Rolf Jaeger, Gladys Koke, Hermann Luechinger, Farid Matta, Carl Myerholtz, Slav Rohlev, Lori Tully, T.K. Wang, Barry Willis, and Dave Yates.

## Thermopneumatically actuated microvalves and integrated electro-fluidic circuits

Mark J. Zdeblick, Rolfe Anderson, Joe Jankowski, Bob Kline-Schoder, Lee Christel, Robin Miles, Walter Weber  
Redwood MicroSystems, Inc.  
1030 Hamilton Court  
Menlo Park, California

### Abstract

An electro-fluidic multi-chip module (E/F MCM) technology incorporating microfabricated sensors and actuators has been developed for diverse research and commercial applications. The first E/F MCM incorporates a thermopneumatically actuated valve, a piezoresistive pressure sensor, and feedback electronics to create a complete electronically programmable pressure regulator. Both the operation of the valve and the pressure regulator are described. By routing chemicals between various reaction vessels and detectors, future E/F MCM's may be used to process chemical information in a manner analogous to the way computers manipulate electronic information.

### Introduction

The idea of using silicon as an electro-fluidic substrate for chemical analysis evolved in the laboratory of Professor James B. Angell at Stanford University in the late 1970's and early 1980's<sup>1</sup>. In that same laboratory, other microfluidic devices were built<sup>2,3,4</sup> and the first complete integrated microvalve was produced<sup>5,6</sup>. Later, the concept of using silicon as a substrate for multiple valves, electronics, and detectors to perform chemical operations as complex as DNA analysis evolved<sup>7,8,9</sup>. Others have built micropumps<sup>10,11,12</sup>, microvalves with a variety of actuation mechanisms<sup>13,14,15</sup>, flow sensors<sup>16</sup>, and electrophoresis separators<sup>17</sup>. A nice review paper documenting the surge of interest in microfluidics has recently been published<sup>18</sup>. This paper focusses on thermopneumatically-actuated microvalves and their role in integrated circuits that have fluidic as well as electronic elements, enabling chemical instrumentation of increasing complexity but decreasing size.

### Principles of Operation

An Electro-Fluidic Multi-Chip Module (E/F MCM) may be comprised of five functional groups: 1) a fluid management system including flow channels, valves, mixers, and reaction chambers; 2) one or more sensors for measuring any of a number of parameters, including pressure, flow, pH, optical properties, and electrical properties; 3) separation systems for refining chemical products from reagents; 4) interface and control electronics; and 5) a multi-chip module manufacturing technique that integrates these electronic and fluidic functions. In the example of an E/F MCM described herein, the fluid management system is comprised of a thermopneumatic-microfabricated valve, an orifice, input and output ports, and a flow channel connecting them; the sensor is a pressure sensor; the separation system is omitted; the electronics are an analog feedback control circuit that provide pressure regulation; the MCM manufacturing technique is a direct extension of standard PC board manufacturing methods used in the IC industry.

### Operation of the microfabricated valves

The key component of a microfabricated thermopneumatically actuated valve is a silicon diaphragm made by etching a precisely controlled recess in a silicon substrate. A Pyrex wafer with a resistor fabricated onto its surface covers the liquid-filled recess, creating a hermetically sealed control cavity. Dissipating energy in the resistor heats the liquid, increasing the pressure inside of the sealed vessel, increasing the volume of the vessel. This pressure is used to modulate the flow of either gas or liquid in the adjacent channel. In a Normally Open (NO) configuration (Figure 1), the edges of the diaphragm are fixed in space. Increasing control cavity volume pushes the silicon membrane towards the valve seat. In a Normally Closed (NC) configuration (Figure 2), a point on the diaphragm is fixed in space. Increasing control cavity volume causes the edges of the diaphragm to move away from the valve seat. The devices shown in Figures 1 & 2 are both designed for gaseous operation. Similar devices optimized for liquid operation prevent the liquid from contacting the electrical connections.

Since the NO and NC valves are made using a similar process, only the Normally Closed process is illustrated in Figure 3.

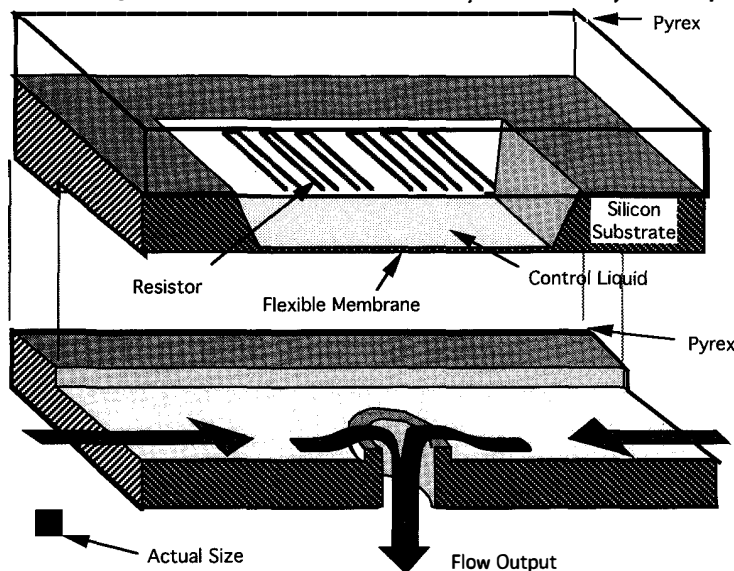


**Figure 1 :** The Normally Open thermopneumatically actuated Fluistor™ Microvalve features a liquid filled cavity which when heated, forces a silicon diaphragm outward over valve seat.

These drawings represent an illustrative cross-section through a single device; typically nearly one hundred devices are made simultaneously on a single wafer. Figure 3a) shows the top pyrex wafer after one side has been coated with 1000Å Pt and patterned into a resistor. It also shows an electric / fluidic via through the pyrex. Figure 3b) shows the first step in the processing of the silicon wafer. Here a thick (1.2 μm) layer of SiO<sub>2</sub> is grown in a humid environment at 1100°C and photolithographically patterned as shown. Figure 3c) shows the silicon wafer after it has been etched in a hot (80°C) solution (33% w/w) of KOH, defining the control cavity and membrane. A second lithography and etch is performed, leaving a 40 μm thick silicon membrane and sealing ring, as shown in Figure 3d). The bottom wafer, shown in Figure 3e) is made of pyrex, which is ultrasonically drilled and polished. Figure 3e) shows the three wafers after they are bonded together. After being filled with the control liquid, Figure 2) illustrates how the cap seals the liquid in the control cavity. The complete valve, pictured in Figure 4, measures 6.3 x 6.6 x 2.0 mm.

One of the advantages of thermopneumatic actuation over other micro-actuated mechanisms — such as thermal bimorph, electrostatic or piezoelectric — is the independence of the actuation and the object being actuated. In this case, the object being moved is a diaphragm, whose flexibility, chemical inertness, and other properties can be completely optimized independently of the actuator. The actuator, i.e., the cavity full of gas and or liquid, can also be optimized independently from the membrane for a particular application by adjusting cavity shape, boiling point of the control liquid, quantity of both gas and liquid molecules, and other properties. The dynamic range of the device can thus be quite broad: vacuum pressures to hundreds of atmospheres; gas, liquid, and corrosive fluids; ultra-low (μl/min of gas) to industrial (10's slpm) flow rates. Valves of this type have been built that control liquids at 204 bar (3000 psig). Flow rates of similar valves have been built that exceed 15 slpm of N<sub>2</sub> at 7 bar (103 psid).

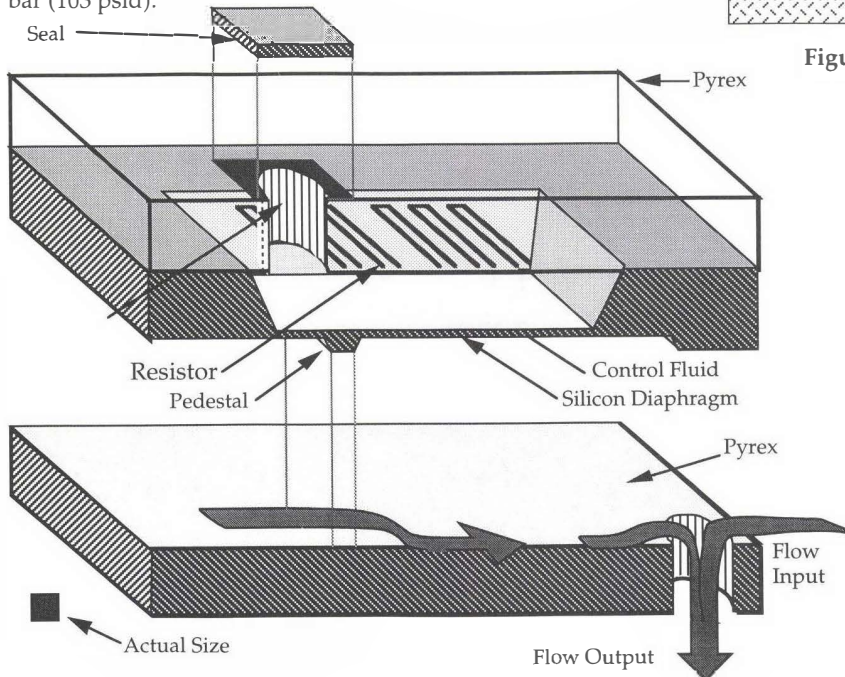


**Figure 2:** Normally Closed thermopneumatically actuated Fluistor™ Microvalve features a liquid filled cavity which when heated, flexes a silicon diaphragm forcing the valve cover to lift off the valve seat.

Compared to other microvalve technologies, thermopneumatic actuation exerts tremendous force through a long stroke. The maximum displacement of a NO valve is about 50 μm. Since the upper portion of a NC valve rotates, its maximum vertical displacement is about 150 μm. A thermopneumatic actuator is capable of providing significant force throughout this displacement — over 20 N (200 bar x 6900 N/m<sup>2</sup>/bar x 1.6 x 10<sup>-5</sup> m<sup>2</sup>) through a 50 μm stroke has been demonstrated in the case of the NO valve.

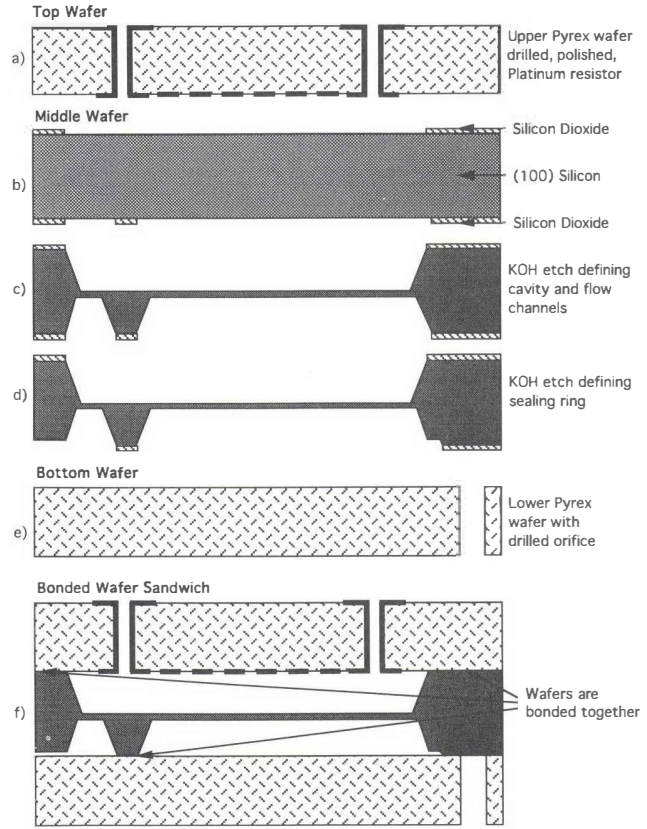


**Figure 3:** Process flow of a normally closed valve

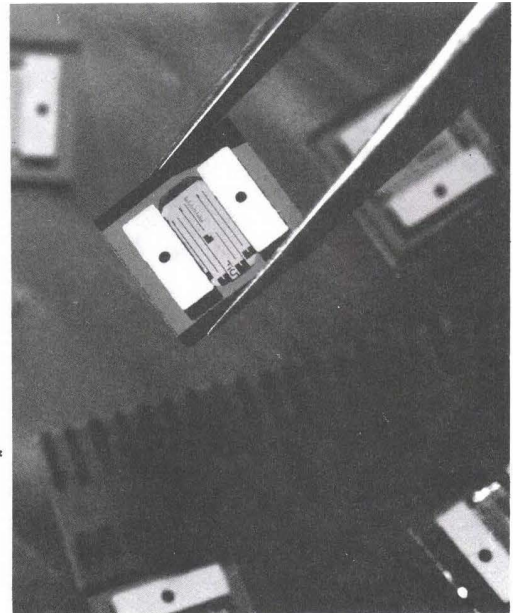


**Figure 4:** Photograph of a Fluistor™ microvalve.

This long stroke allows a thermopneumatically-actuated microvalve to control high flow rates and pressures relative to other microvalve technologies. The high operating pressure capability not only extends its application to high pressure applications, it allows the use of significant force for preventing leaks across the valve seat. Long stroke and smooth actuation allows stable control of flow rate over a wide dynamic range: single valves are capable of controlling stable flow rates continuously from 0.001 sccm to 10 slpm. Flow v. pressure at a variety of ambient temperatures and flow v. applied power at a variety of supply pressures are shown in Figure 5a & 5b (Normally Open) and Figure 6a & 6b (Normally Closed).

### Pressure Sensor

The sensor used in this E/F MCM is a piezoresistive, silicon membrane device (SenSym, Milpitas CA). The silicon sensor is encapsulated in a plastic "button" package that facilitates PC-board mounting. The sensor has a linearity and accuracy of about 1%. Linearity and precision may be extended to about 0.1% through the use of well-established digital compensation techniques that correct for nonlinearities in the sensor caused by temperature and pressure variations.

### Feedback electronics

The analog control circuit provides the necessary power signal for the pressure sensor and conditions the sensor output appropriately for the implementation of the pressure control system. The analog pressure control system calculates a valve control signal as the sum of three terms; one term proportional to the pressure error, one term proportional to the integral of the pressure error, and one term proportional to the filtered derivative of the pressure error. Therefore, the controller is a classical PID (proportional-integral-derivative) controller. Since the system is non-linear, however, the gains have been set to maximize the time of response without unduly sacrificing transient overshoot or steady-state performance. The selected gains result in a controller which closely resembles a modified-bang-bang controller: bang-bang control until the operating point is within range of linear behavior at which point the PID control behavior dominates. The output of the control electronics is a 0 - 15 Volt signal which serves as the command to the valve chip drive electronics. As the valve membrane deflects due to changes in the voltage applied to the heater, the flow through the valve will vary, changing the sensed pressure, which is used by the controller to continually adjust the valve heater voltage until the sensed pressure matches the desired pressure.

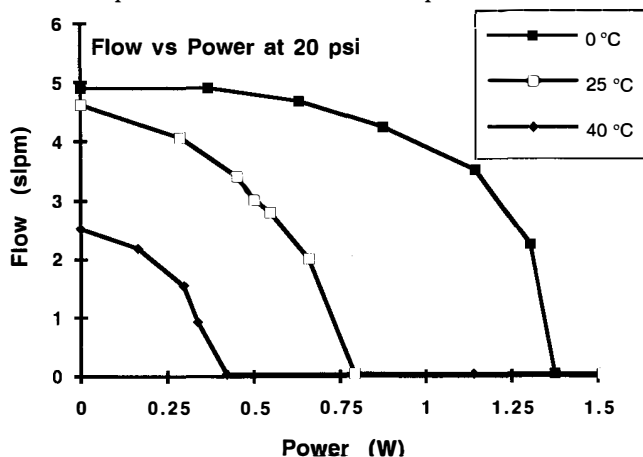


Figure 5a: Flow vs. Power for a Normally Open valve at 20 psig supply pressure and a variety of ambient temperatures.

### E/F MCM Manufacturing technique

Multi-Chip Module is a widely known manufacturing technique in the electronics industry for integrating electronic chips together at the die-level to reduce the volume of the package and improve the performance of the system. Non-packaged silicon die are bonded to a substrate, which provides electrical connections. In this way, a system designer has the flexibility of purchasing functionally specialized components or systems from different vendors and integrating them in an optimal way. Lower system cost, smaller size, greater reliability, higher frequency response, and electro-optic transduction are all attributes that make MCMs higher value-added products.

Here, we demonstrate an MCM for electro-fluidic circuits, i.e., consists of fluidic and electronic elements. The construction and choice of materials of the fluidic element has an influence on the performance of the valve in the module. Since currently available micromachined valves are thermal devices, the thermal mass and heat conduction of the manifold materials plays an important role in the response time and stability of the system. Ideally, the package should be a perfect heat sink, i.e. the chip interface stays near ambient temperature while dissipating heat from the chip.

Since fluidic interfaces (input/output ports) for E/F MCMs must conform to industry standard fluidic fittings and tubing, these interfaces prevent shrinking the modules even further. For high density packaging requirements, a manifold with flange seal type O-rings is often the best choice. This format can eliminate fittings and tubing since the module can be pressed directly against larger manifolds or instrument bulkheads. In some applications, in-line connections with tube fittings are required — a solution that allows easy interface but sacrifices size efficiency.

The MCM substrate contains milli-flow channels that are used to interconnect various fluidic and electro-fluidic components. This E/F MCM uses three such components: the microvalve, the pressure sensor, and an optional microfabricated capillary or orifice for relieving pressure applications. These three devices are interconnected with a channel buried in the substrate. Electronic traces are patterned on the surface of the substrate using standard PC-Board manufacturing techniques. The first example of an E/F MCM to use both microactuators and microsensors is shown in Figure 7 — the Mini Pressure Regulator.

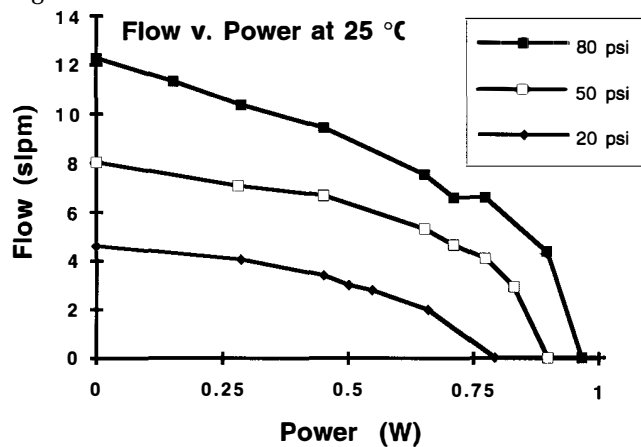


Figure 5b: Flow vs. Power for a Normally Open valve at a variety of supply pressures and 20°C ambient temperature.

Pressure regulators built using E/F MCM technology have excellent performance characteristics including electronic pressure programmability, broad dynamic range of flow (100,000:1), excellent supply pressure rejection (>100dB) and flow rate rejection (<0.1% full scale pressure/full scale flow), temperature insensitivity (<0.1% full scale pressure/°C), minimal ripple (0.01% full scale pressure), and long term stability (variations <0.1% full scale pressure/year). When compared with manual mechanical regulators, these performance characteristics are striking. Mechanical devices typically have small dynamic range (100:1), less supply pressure rejection (<40 dB), lower flow rate rejection (0.5% full scale pressure/full scale flow rate), reduced temperature insensitivity (1.0% full scale pressure/°C), and poor long term stability (variations greater than 1.0% full scale pressure/year). Although small in size — measuring 6.3 x 8.6 x 1.2 cm — it is capable of regulating continuously over a range of 0 to 100 psig with 0.5% accuracy. The full performance specifications are summarized in Table 1.

Virtually all of the closed-loop performance limitations of the E/F MCM pressure regulator arise due to the sensor calibration limitations. Higher performance E/F MCM pressure regulators will be based on digital control electronics and will incorporate accurately calibrated pressure sensors. Off-the-shelf pressure sensors with minimal compensation yield pressure signals which are accurate to no better than 1.0% full scale pressure. Advanced digital calibration techniques will result in a pressure sensor with accuracies of at least ± 0.1% full scale pressure over a wide range of temperatures. Incorporation of a microprocessor for control opens up the possibilities of using intelligent control algorithms which can more easily implement nonlinear functions making fuzzy logic and neural network-based controllers attractive. Further, the use of high accuracy pressure sensors combined with a microprocessor makes the development of a flow regulator a simple extension of the pressure regulator.

One of the key advantages of the E/F MCM technology is the efficient use of space. Since these modules can be made compactly, individual units can be combined to form more complex systems without sacrificing cost or size over specifically dedicated designs. For example, a manifold of pressure regulators can be efficiently constructed by mounting numerous E/F MCM pressure regulators to a common input gas line. This type of configuration is required by numerous industries including analytical instrumentation,

gas chromatography, and other mixing applications. More complex modules for regulating pressure and flow of gases and liquids will be developed offering greatly reduced size, lower cost and higher performance than systems utilizing mechanical valves.

#### Application of E/F MCM's in Medical Instrumentation

The trend in the Medical marketplace is constantly towards reducing size and costs. Medical applications more commonly involve carrying liquids not gases and require on-off switching rather than proportional control. For these applications, E/F MCM materials require a higher degree of corrosion resistance and the feedback circuitry must close the control loop very quickly.

There are numerous medical applications where current E/F MCMs can perform proportional control of gas pressure. Anesthesia machines can be upgraded to perform automatic gas mixing and flow control — functions which today are still performed with manual valves and regulators. Insufflators, instruments which inflate the abdominal cavity during surgery, can be equipped with Micro Pressure Regulators to provide dynamic closed-loop control of pressure during surgery, replacing larger, more expensive and lower performance electro-mechanical valve-based systems. For Non-Invasive Blood Pressure monitoring (NIBP), E/F MCMs can be used to rapidly inflate and deflate pressure cuffs in a stable and predictable manner to facilitate rapid and accurate blood pressure measurement — the size and affordability of the E/F MCMs will enable the NIBP industry to utilize closed-loop control of pressure to replace unstable, open-loop solenoid valve systems.

Future E/F MCM's designed for liquid operation could provide a new platform on which a variety of clinical chemistry operations could be performed. A concept sketch of such a "Universal chemical processor" is shown in Figure 8. Such a processor would have a number of different elements: an array of input ports to connect to a supply of reagents and samples; an array of valves to route selected chemicals to and from various nodes; a number of temperature controlled reaction chambers where the chemical reactions would take place; an array of separation devices for separating certain chemicals from each other; an array of detectors that sense the presence of chemical products; an array of output ports for disposing of waste materials as well as any chemicals that have been synthesized. A number of these microfabricated elements have been developed by various researchers around

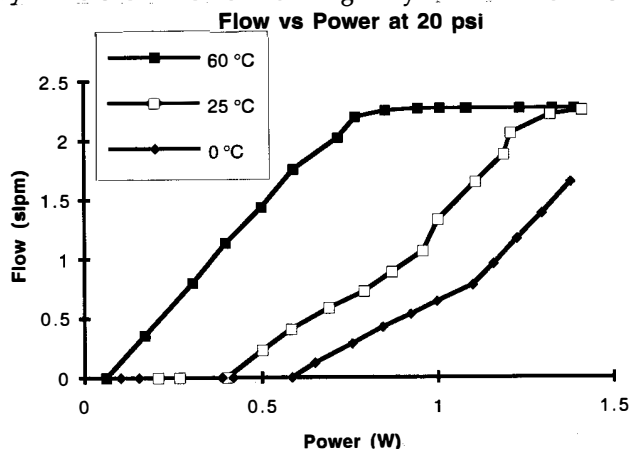


Figure 6a: Flow vs. Power for a Normally Closed valve at 20 psig supply pressure and a variety of ambient temperatures.

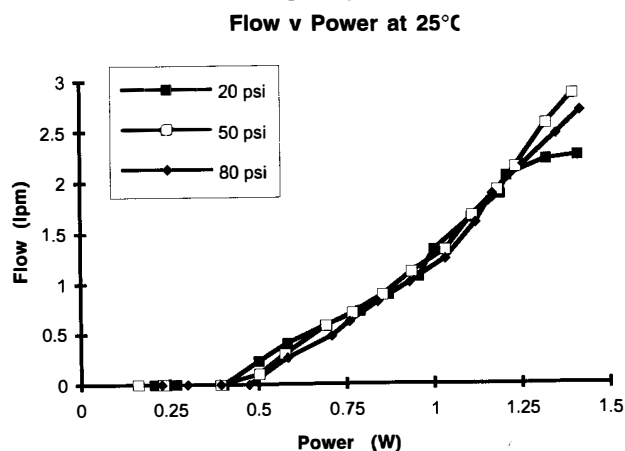


Figure 6b: Flow vs. Power for a Normally Closed valve at a variety of supply pressures and 20 °C ambient temperature.

the world, including electrophoresis separation, optical detectors, pH sensors, valves, and temperature controlled reaction chambers. Integrating them together will provide a compact chemical analysis system with tremendous flexibility and sensitivity.

### Conclusions

A microfabricated valve has been developed for operation on both gases and liquids. This device has enabled the development of Electro/Fluidic Multi-Chip-Modules. Already, this level of integration provides an architecture capable of perform complex functions in a small space. The next challenge will be to provide these chips in a monolithic construct, with multiple valves or sensors manufactured simultaneously on a common substrate — the first Electro-Fluidic Integrated Circuits. Mirroring the semiconductor industry, these chips will rapidly increase in capabilities, as their size and costs are reduced. The revolutionary impact on the instrumentation marketplace will be analogous to the impact of semiconductors on the computer marketplace. Today's instruments — the equivalent of yesterday's mainframe computers — will be replaced by the instrumentation equivalents of workstations, lap-tops, and field portable units.

**-TABLE 1-**  
Performance Benefits of E/F MCM Pressure Regulators

Performance Criteria	E/F MCM	Mechanical
Dynamic Range:	100,000:1	100:1
Supply Rejection:	> 100 dB	< 40 dB
Flow Rate Rejection: (percent of full scale pressure)	< 0.1%	0.5%
Temperature Insensitivity: (percent of full scale pressure/°C)	< 0.1%	1.0%
Long Term Stability: (percent pressure variation/year)	< 0.1%	1.0%
Programmability:	yes	no

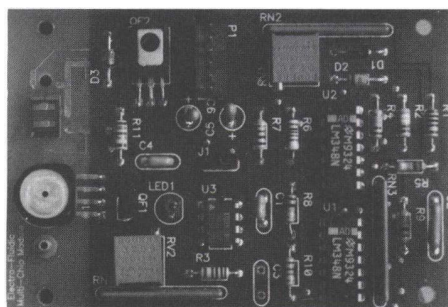


**Figure 7:** The size and cost benefits of E/F MCM products increase as product complexity increases. Custom manifolds and multiplexors — such as this pressure regulator for a protein synthesizing instrument — will replace larger, more expensive electro-mechanical systems.

- 1 Terry S C, Jerman J H and Angell J B, 1979, "A gas chromatographic air analyzer fabricated on a silicon wafer," *IEEE Trans. Electron Devices*, ED-26 1880-6.
- 2 Tuckerman D B and Pease R F W, 1981, "High performance heat sinking for VLSI," *IEEE Electron Device Letters*, ED-2 126-9.
- 3 Zdeblick M J, Barth J B and Angell J B, 1986, "Microminiature fluidic amplifier," *Tech. Digest IEEE Solid-State Sensor and Actuator Workshop (Hilton Head Island, SC, 1986)* (New York: IEEE)
- 4 Zdeblick M J, Barth J B and Angell J B, 1986, "A microminiature fluidic amplifier," *Sensors & Actuators*, 15 (1988) 427-433 (Elsevier Sequia/ The Netherlands)
- 5 Zdeblick M J and Angell J B, 1987, "A microminiature electric-to-fluidic valve," *Tech. digest IEEE Transducers 87 (Tokyo, 1987)* (New York: IEEE) pp 827-9
- 6 Zdeblick M J "A planar process for an electric-to-fluidic valve," PhD Thesis, Stanford University (Menlo Park, CA: Redwood Microsystems)
- 7 Zdeblick, M.J., "Electro-Fluidic Amplifiers and Actuators on Silicon," Seminar at the University of California at Berkeley, Berkeley, CA, 22 February 1987.
- 8 Shoji S, Esashi M and Matsuo T, 1988, "Prototype miniature blood gas analyser fabricated on a silicon wafer," *Sensors and Actuators* 14 101-7.
- 9 Nakagawa S, Shoji S and Esashi m, 1990, "A microchemical analyzing system integrated on a silicon wafer," *proc. IEEE Mems 90 (Napa Valley, CA, 1990)* (New York: IEEE) pp 89-94
- 10 Petersen K E, 1979, "Fabrication of an integrated planar silicon ink-jet structure," *IEEE Trans. Electron Devices*, ED-26 1918-20.
- 11 Smits J G, 1990, "A piezoelectric micropump with three valves working peristaltically," *Sensors and Actuators* 15 153-67
- 12 van Lintel H T C, van der Pol F C M and Bouwstra S, "A micro pump based on micromachining of silicon," *Proc. Eurosensor I (Cambridge, UK, 1987)* (New York: elsevier) pp 20-1.
- 13 Jerman J H, 1990, "Electrically-activated micromachined diaphragm valves," *Proc. Micro System Technologies 90 (Berlin 1990)* (Berlin: Springer) pp 806-11
- 14 TiNi paper
- 15 Huff M A and Schmidt m M A, 1992, "Fabrication, packaging and testing of a wafer-bonded microvalve," *Tech. Digest IEEE Solid-State Sensor and Actuator Workshop (Hilton Head Island, SC, 1992)* pp 194-7.
- 16 Petersen K E, Brown J and Renken W, 1985, "High-precision, high-performance mass flow sensor with integral laminar flow micro-channels," *Tech. digest IEEE Transducers 85 (Philadelphia, PA, 1985)* (New York: IEEE) pp 830-3
- 17 Mans A, Fettinger J C, Verpoorten E, Harrison D J, Ludi H, and Widmer H M, 1991, "Integrated electroosmotic pumps and flow manifolds for total chemical analysis," *Tech. Digest IEEE Transducers 91 (San Francisco, CA, 1991)* (New York: IEEE) pp 939-41.
- 18 Gravesen P, Branebjerg J, and Jensen O S, "Microfluidics — a review," *J. Micromech. Microeng.* 3 (1993) 168-182.

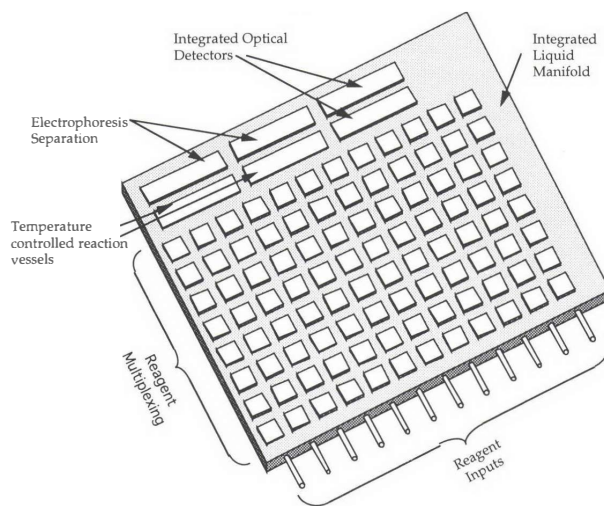


**Figure 8:** Universal chemical analysis manifold

# A MULTICHANNEL NEURAL PROBE FOR SELECTIVE CHEMICAL DELIVERY AT THE CELLULAR LEVEL

Jingkuang Chen and Kensall D. Wise

Center for Integrated Sensors and Circuits  
Department of Electrical Engineering and Computer Science  
The University of Michigan  
Ann Arbor, MI 48109-2122

## ABSTRACT

A bulk-micromachined multichannel silicon probe capable of selectively delivering chemicals at the cellular level as well as electrically recording from and stimulating neurons in-vivo has been developed. The probe allows detailed studies of neural responses to a variety of chemical stimuli for the first time and represents an important step toward improving our understanding of neural systems and treating a variety of neurophysiological disorders. The probe buries multiple flow channels in the probe substrate, resulting in a hollow-core device. This approach leaves the upper surface planar to accommodate existing thin-film electrode structures. Flow in these microtubes has been studied theoretically using analytical models as well as experimentally using fabricated devices. For an effective channel diameter of  $10\mu\text{m}$ , a channel length of 4mm, and a fluid flow equivalent to 100pl/sec, the flow velocity is about 1.3mm/sec and the measured drive pressure is 11Torr.

## INTRODUCTION

It is well known that complex biochemical reactions are the underlying mechanism on which the functionality of the nervous system is based. In order to better understand the behavior of biological neural networks at the circuit level, it is important to be able to deliver chemicals (drugs) to highly-localized areas of neural tissue in precise quantities while monitoring the neuronal responses in vivo. For example, specific caged molecules such as calcium can be delivered to influence cellular behavior, and NMDA (n-methyl-d-aspartate) can be delivered to modify synaptic activity. In these applications, it is important that the injecting device be very small so as not to disturb the neural system and that it be able to inject fluid volumes in the 10-1000pl range controllably. In the past, the most commonly used techniques for injecting chemicals into brain tissue have been microiontophoresis [1-4] and pressure ejection [2] using single- and multiple-barrel glass micropipettes. The responses of nearby neurons were measured using separately-positioned pipettes filled with electrolyte. These approaches typically suffer from relatively poor control in positioning the injecting pipette relative to the monitoring points. Moreover, the complicated procedures required for the assembly of multi-barrel pipette structures also prevent them from being widely used.

This paper describes the development of a neural drug-delivery probe which is able to selectively deliver chemicals at the cellular level as well as electrically record from and stimulate neurons in vivo. The probe allows detailed studies of the neural responses to a variety of chemical stimuli for the first time and represents an important step toward improving our understanding of neural systems and treating a variety of neurophysiological disorders. In contrast to a previously-reported probe based on surface micromachining [5], this probe is bulk-micromachined. It is also directly process compatible with the formation of thin-film electrode arrays for electrical recording and stimulation [6,7] on the same substrate. The electrode sites and outlet orifices on the probe are defined using photolithography, which results in reproducible precisely-controlled device dimensions. Separations as small as  $2.5\mu\text{m}$  between the electrode sites and the outlet orifices can be achieved. The technology also allows probes containing multiple flow channels to be realized. This permits multipoint injection and recording/stimulation using a single probe.

## DESIGN AND FABRICATION

Figure 1 shows the structure of the new probe, which buries multiple flow channels in the (formerly solid) probe substrate, resulting in a hollow-core device. This approach leaves the upper surface of the probe planar to accommodate existing electrode structures. The formation of the flow channels requires only one mask in addition to the five required for a normal multielectrode probe [6]. The fabrication of the microchannels begins with a shallow boron diffusion to form a  $3\mu\text{m}$ -thick highly-boron-doped layer on the surface of a p-type (100) silicon wafer. The intended channel area is then opened through this layer in the form of a chevron pattern using a reactive ion etch (RIE), and an anisotropic silicon etch (EDP) is used to undercut this chevron structure to form a flow tube aligned with the  $\langle 110 \rangle$  direction as shown in Figs. 2 and 3. A deep boron diffusion is now performed to define the probe shank as in the usual probe fabrication process. Sealing of the channel is accomplished using thermal oxidation, LPCVD deposited dielectrics, and an optional planarizing etch-back. Processing then continues as for a normal probe [6]. Figure 4 shows the cross-section of a sealed flow channel. Multichannel arrays with channel-to-channel separations as small as  $4\mu\text{m}$  can be achieved.

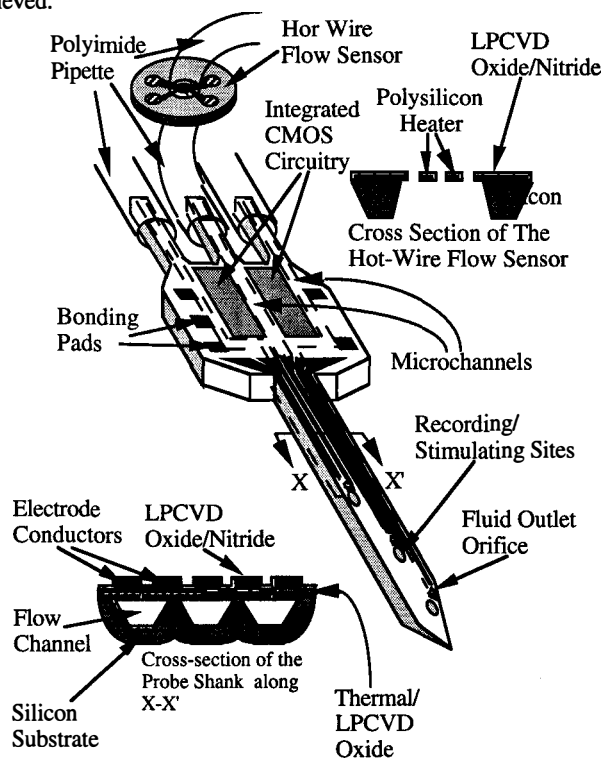


Fig. 1: Perspective view of a three-channel micromachined drug-delivery probe.

Micropubes with one to four flow channels have been designed and fabricated. The channel widths have been varied from  $10\mu\text{m}$  to  $32\mu\text{m}$  while the probe shank widths ranged from  $58\mu\text{m}$  to

74 $\mu\text{m}$ . The flow tubes do not increase the overall width of a typical probe structure as long as only a few are needed. All the probes to date have had a shank length of 4mm, consistent with the targeted cortical systems. The channel depths are controlled by etch time and by the lateral width of the channel opening, with depths of 10 $\mu\text{m}$  being typical. At the back of the probe, the flow channels protrude from the body of the substrate to allow flexible pipette tubing to be sealed around them. This tubing is 60 $\mu\text{m}$  in diameter with a 7 $\mu\text{m}$ -thick wall and connects to a thermally-based flow sensor and an external pump. The flow sensor is process compatible with the probe and is fabricated on the same wafer. A cross-section of this hot-wire flow sensor is shown as an inset in Fig. 1. A mesh structure is formed by a polysilicon heater supported by a dielectric membrane and is suspended across a hole in the substrate created by masking the boron doping used for shank definition from the area under the intended mesh. When fluid flows through the mesh, it cools the structure, changing the resistance of the polysilicon and providing an indication of the flow rate.

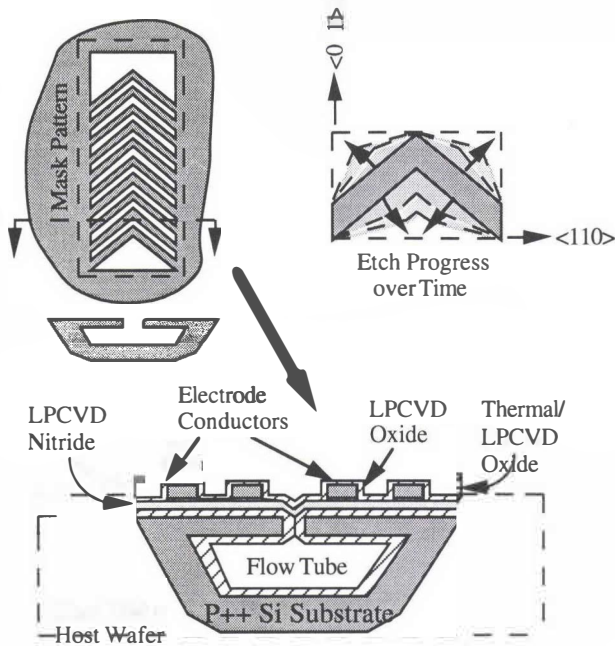


Fig. 2: An integrated flow channel structure. The channel is formed by undercutting a boron-doped silicon chevron structure, followed by a sealing process using thermal and LPCVD dielectrics.

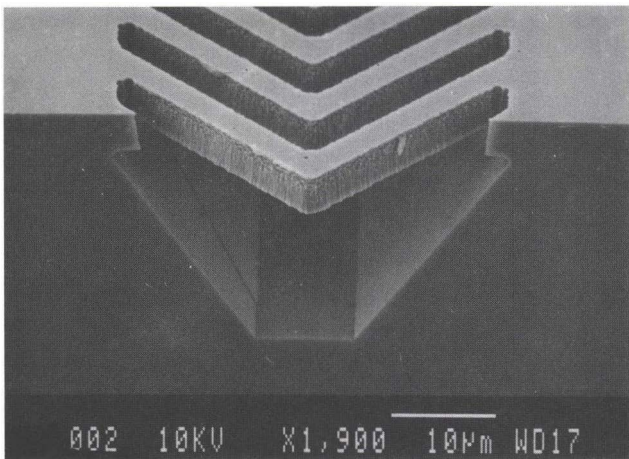


Fig. 3: Cross-section of an etched microtube after undercutting the silicon chevron pattern in EDP.

After sealing the microchannels, fabrication of the microprobe continues by depositing a polysilicon conductor layer and doping it with phosphorus. The polysilicon is then patterned by RIE, followed by LPCVD oxide/nitride/oxide triple-layer passivation. The areas for the recording/stimulating sites and bonding pads are next opened using RIE, and chromium/gold is deposited in the openings and patterned using liftoff. Finally, the dielectrics outside the intended device areas are removed, and the fluid ports for the channels are opened using a masked etch.

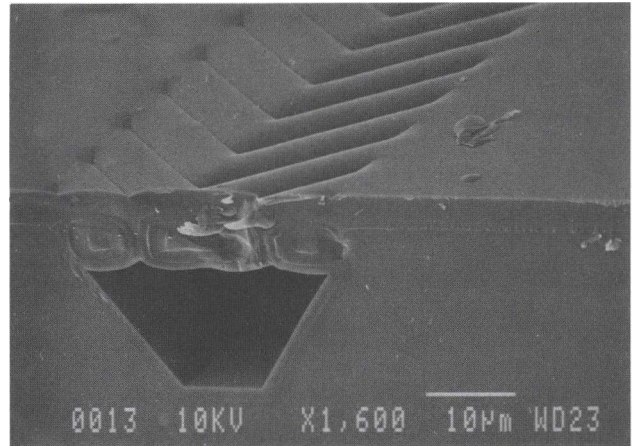


Fig. 4: Cross-section of a flow tube sealed by thermal oxide and by LPCVD oxide/nitride/oxide layers.

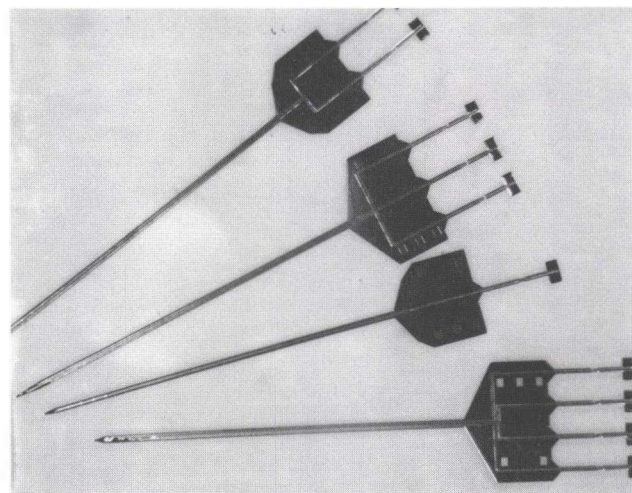


Fig. 5: Four different neural probe designs having one, two, three, and four microchannels for drug delivery.

The most critical step in this fabrication process is the sealing of the channels. Improper sealing will result in cracking of the channel during subsequent high-temperature processing. As described above, the sealing process begins with a thermal oxidation. The growth of thermal oxide on the silicon beams spanning the channel will reduce the width of the chevron-shaped openings. As a result, the thicker the oxide is grown, the thinner the LPCVD dielectrics that are required to seal the channel. However, as the width of the chevron-shaped silicon beams is reduced, the thermal oxidation time becomes critical in determining the robustness of the channel structure. For very narrow beams, over-oxidation will convert all of the beam into oxide, making the ceiling over the channel transparent. In this case, the membrane over the channel is prone to crack during subsequent high-temperature processing. This can be avoided by reducing the oxidation time to preserve silicon in the chevron bridge structure.

Figure 5 shows examples of neural drug-delivery probes containing one, two, three, and four barrels. At the back of each

probe, the flow channels protrude from the body of the substrate to allow flexible pipette tubing to be sealed around them. These protrusions are designed to be broken halfway back to fit into the tubing. The big rectangles at the ends of the protrusions are for ease in handling. Figure 6 shows the cross-section of a three-barrel probe; the polysilicon interconnect lines on top of the channels can be clearly seen. Figure 7 shows the tip of a four-barrel probe; each outlet orifice has a recording site beside it. The site at the tip of the probe has a larger area, designed so it can function for both electrical recording and stimulation. Figure 8 shows a closer view of an outlet orifice. The distance between the orifice and the recording site is 2.5 $\mu$ m.

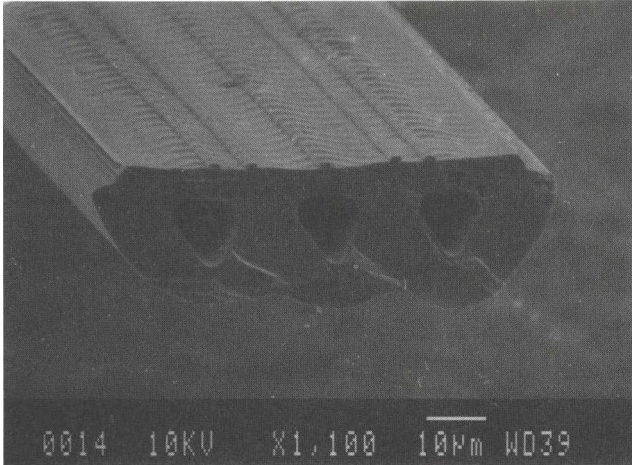


Fig. 6: Cross-section of a three barrel microprobe. The polysilicon interconnect for electrical recording and stimulating electrodes can be clearly seen on top of the flow channels.

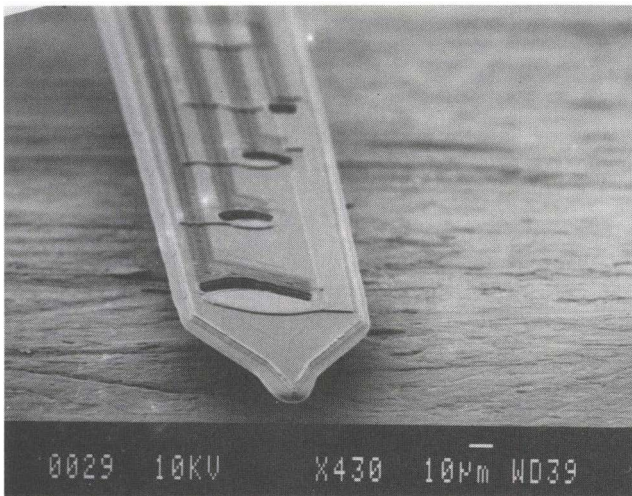


Fig. 7: Tip of a four-barrel probe. Each fluid outlet port has a recording site beside it. The site at the tip of the probe has a larger area and can serve both for recording and stimulation.

### FRICIONAL LOSSES IN MICROCHANNEL FLUID FLOW

In injecting chemicals using such microprobes, knowledge of the friction losses in the microchannels is important in determining how much pressure should be applied to achieve the desired flow rate. The friction losses associated with fluid flowing in a pipe depend on many factors, including the average velocity  $V$  of pipe flow, the pipe diameter  $D$ , the fluid density  $\rho$ , the fluid viscosity  $\mu$ , and the average pipe wall roughness [8]. From conventional fluid dynamics, for laminar flow, the product of Reynolds number  $R_e$  and the Darcy friction factor  $f$  is a constant  $C$ , which depends on the geometry of the pipe cross-section [9]. The

definitions of Reynolds number  $R_e$  and the Darcy friction factor  $f$  are

$$R_e = \rho V D / \mu$$

$$f = \frac{2D(\Delta p)}{\rho V^2 L}$$

where  $\rho$  is the fluid density (996 kg/m<sup>3</sup> for water at 23°C),  $V$  is the cross-sectional average velocity of fluid in the pipe,  $D$  is the hydraulic diameter of the channel (four times the cross-sectional area divided by the wetted perimeter length),  $\mu$  is the viscosity of the fluid (for water, 9.85x10<sup>-4</sup> kg/m·sec at 23°C),  $\Delta p$  is the pressure drop across the channel due to friction losses, and  $L$  is the length of the channel.

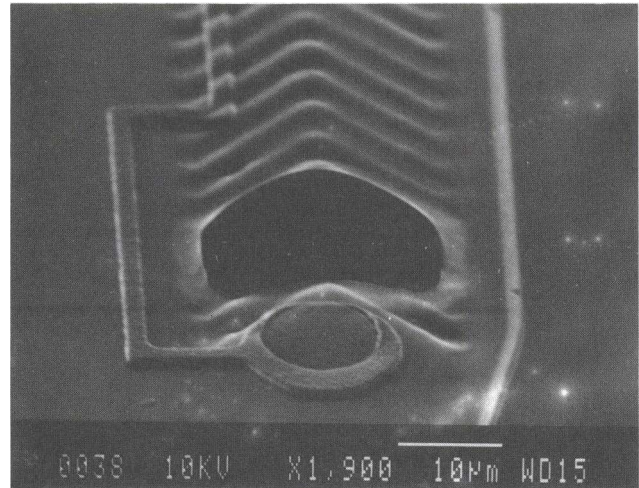


Fig. 8: Close-up of an outlet orifice. The distance between the orifice and the electrode site is 2.5 $\mu$ m.

In order to determine the friction loss for fluid flowing in the microchannels, silicon chips with 2.15cm long microchannels were fabricated. The upper width of the channels was kept at 40 $\mu$ m (defined by the etch mask), while the channel depths varied from 14 $\mu$ m to 17 $\mu$ m. These dimensions were measured under an optical microscope by cleaving the chips after the experiments. The hydraulic diameter  $D$  of the channel could then be calculated. Distilled water was used for the measurements. Regulated nitrogen was applied through a cylindrical accumulator to pressurize the distilled water. Before entering the microchannel, the water was passed through a 0.45 $\mu$ m filter to prevent any possibility of plugging of the microchannel. The pressure drop across the channel was measured using a differential pressure sensor. With the channel oriented horizontally and taking the water to be incompressible, this pressure drop resulted from friction losses. The volumetric flow rate was determined by monitoring the movement of the water meniscus in a transparent constant-cross-section micropipette. In order to minimize the influence of water evaporation on the measurement, a drop of vegetable oil was kept in the far end of the measuring pipette to form a buffer of air between the water meniscus and oil drop. In all measurements, the flow was assumed to be laminar and fully developed since  $R_e < 1$  and  $D/L < 10^{-5}$ . All the measurements were performed at 21-23°C.

With the volumetric flow rate  $V$  and the pressure drop  $\Delta p$  measured, the Reynolds number  $R_e$  and the Darcy friction factor  $f$  can be calculated. Figure 9 shows the product of  $R_e$  and  $f$  as a function of  $R_e$ . The minimum flow rate was about 300 $\mu$ m/sec, which is of the same order as the flow rates used with the chemical delivery probe. According to conventional fluid dynamics, for a normal-sized pipe of trapezoidal cross-section, the product of Reynolds number and the Darcy friction factor is about 60 [9,10].

From the experiment results here, this product is more typically about 55 for a microchannel with a hydraulic diameter of 18 $\mu$ m.

The above results can be used to determine the pressure needed in the chemical delivery system to achieve the desired flow. If we assume the volume of chemical to be injected is about 10% of the tissue volume normally monitored by a cortical recording electrode (about (100 $\mu$ m)<sup>3</sup>) and further assume that the chemical must be injected in one second, then for an effective channel diameter of 10 $\mu$ m and a channel length of 4mm, the required flow rate is 1.3mm/sec and the required drive pressure is 11Torr.

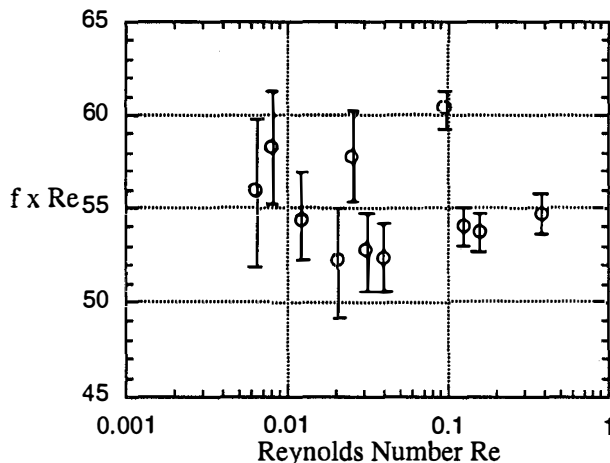


Fig. 9: Product of Reynolds number  $Re$  and the Darcy friction factor  $f$  as a function of  $Re$ . Each data point was measured more than five times, and the error bars represent the range of the measured results. The measurements were performed on different chips with channels of similar dimensions.

### INTERMIXING

Intermixing is a natural phenomenon occurring when two solutions are put in contact. When a drug-delivering neural probe is being inserted into tissue, even without applied pressure on the external port of the microchannel, the drug will intermix with tissue fluid in the vicinity of the outlet orifice through diffusion. Using the one-dimensional form of Fick's diffusion equation [11], the interdiffusion of ions or molecules in such a solution can be described and can be solved using finite difference methods. As an example, assume the chemical stored in the microchannel is acetylcholine, and the volume to be injected is 100 $\mu$ l. The diffusion coefficient of acetylcholine at 25°C is 6.11 $\times 10^{-6}$  cm<sup>2</sup>/sec [4]. Further assume that at time  $t=0$ , the acetylcholine and tissue fluid form an abrupt boundary at  $x=0$ ; from  $x=-\infty$  to  $x=0$  the channel is filled with acetylcholine, and from  $x=0$  to  $x=+\infty$  a 'virtual' channel is filled with tissue fluid. Figure 10 shows the calculated mixing as a function of time. The relative amount of acetylcholine diffused into tissue is normalized by dividing by the intended dose,  $Q_s$ . The result indicates that in 141 minutes, the amount of acetylcholine diffused into tissue fluid is about the same as that of the intended injection. Although in a real situation, mixing may be influenced by cell membranes and by the finite dimensions of the channel, these preliminary results indicate that the influence of intermixing can not be ignored, especially in chronic applications. For better control over drug injection, intermixing should be minimized by the use of microvalves at the outlet orifices. Such structures are currently being developed.

### CONCLUSIONS

A bulk-micromachined silicon probe has been developed that is capable of delivering chemicals to neural tissue with a spatial resolution at the cellular level. The probes bury microchannels in

the probe substrate and are compatible with the formation of active and passive electrode arrays for electrical recording and stimulation on the same chip. Four typical flow channels can be accommodated on a shank 75 $\mu$ m wide. Such structures can provide multi-point drug delivery along with multi-point recording and/or stimulation with minimal disruption to the tissue. The friction losses associated with fluid flow in these microtubes have been studied both theoretically and experimentally. The friction constant  $C (=Re \times f)$  is somewhat smaller than the values predicted by theory derived from normal-sized macrotubes. The influence of intermixing at the outlet orifice has also been evaluated. For acute experiments, the influence of intermixing may not be significant; however, for chronic operation of the probes, its effects can not be ignored, and microvalves or shutters should be used over the channel orifices.

### Acknowledgments

The authors would like to thank D. J. Anderson, S. C. Bledsoe, B. Casey, and J. F. Hetke for their contributions to this work. Research in this area has been supported in part by the Neural Prosthesis Program under contract NIH-NINDS-N01-NS-4-2303.

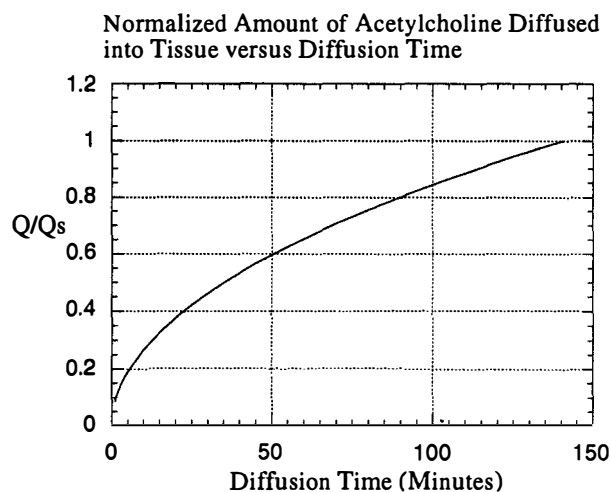


Fig. 10: Simulation of the amount of acetylcholine naturally diffusing into tissue versus diffusion time, normalized to a typical desired injection dose.

### REFERENCES

1. T. P. Hicks, "The History and Development of Microiontophoresis in Experimental Neurobiology," *Prog. Neurobiol.*, 22, (3), pp. 185-240, 1984.
2. G. A. Gerhardt, and M. R. Palmer, "Characterization of the Techniques of Pressure Ejection and Microiontophoresis using In-Vivo Electrochemistry," *J. Neurosci. Methods*, 22, (2), pp. 147-159, 1987.
3. M. O. West and D. J. Woodward, "A Technique for Microiontophoretic Study of Single Neurons in the Freely-moving Rat," *J. Neurosci. Methods*, 11, (3), pp. 179-186, 1984.
4. V. E. Dionne, "Characterization of Drug Iontophoresis with Fast Microassay Technique," *Biophys J.*, 16, (7), pp. 705-717, 1976.
5. L. Lin, A. P. Pisano, and R. S. Muller, "Silicon Processed Microneedles," *IEEE International Conference on Solid-State Sensors and Actuators*, Yokohama, pp. 237-240, June 1993.
6. K. Najafi, K. D. Wise, and T. Mochizuki, "A High-yield IC-compatible Multichannel Recording Array," *IEEE Transactions on Electron Devices*, 32, 7, pp. 1206-1211, July 1985.
7. S. J. Tanghe and K. D. Wise, "A 16-Channel CMOS Stimulating Array," *IEEE J. Solid-State Circuits*, 27, pp. 1819-1825, December 1992.
8. R. H. F. Pao, *Fluid Dynamics*. Columbus: Charles E. Merrill, 1966.
9. J. G. Knudsen and D. L. Katz, *Fluid Dynamics and Heat Transfer*. New York: McGraw-Hill, 1958.
10. R. K. Shah and A. L. London, *Laminar Flow Forced Convection in Ducts*. New York: Academic Press, 1978.
11. M. M. S. Lih, *Transport Phenomena in Medicine and Biology*. New York: Wiley Interscience, pp. 343-354, 1975.

# MICROFABRICATED FUSED SILICA FLOW CHAMBERS FOR FLOW CYTOMETRY

Daniel Sobek

Stephen. D. Senturia

Martha L. Gray

Microsystems Technology Laboratories and Laboratory for Electromagnetic and Electronic Systems  
Department of Electrical Engineering and Computer Science  
Massachusetts Institute of Technology  
Cambridge, MA 02139

## ABSTRACT

The long-term goal of our research effort is to develop a low-cost microfabricated flow cell with integrated optics and electronics for applications in flow cytometry, a method for high-throughput measurements of physical and chemical characteristics of microscopic biological particles. The goal of the work reported here was to fabricate a low-cost flow cell (\$10/cell) which supports hydrodynamic focusing and integration of optical fibers. A key feature of the device described here is that it is fabricated entirely from fused silica (quartz) wafers using two wafers, a single mask, standard etchants, and wafer-level alignment and bonding. Tests showed that the resulting devices easily allow hydrodynamic focusing and have flat, optically transparent surfaces. Integrated optical fibers provided illumination of the sample stream adequate for the detection of fluorescent particles. The use of quartz—which does not autofluoresce and is transparent over a broad range of wavelengths including the UV—suggests these flow cells will be useful for high sensitivity optical sensing applications.

## INTRODUCTION

Flow cytometers are instruments widely used for high throughput optically-based measurements of cells and other microscopic biological particles [1]. These devices have proved to be particularly useful in studies that require classification of subpopulations of biological particles or detection and investigation of rare subpopulations. Flow cytometry is used extensively in clinical hematology and oncology and is applied in a number of diverse research settings ranging from immunology to ecology.

The basis of flow cytometric analysis is that specific optical characteristics (e.g. light scatter, fluorescence) can provide a measure of specific physical or chemical properties of the particle (e.g. size, DNA content, membrane receptors). The optical measurements are made as particles flow through a "sensing region" delimited by the intersection of the illumination and collection regions provided by light source and optical detector assemblies. Typically particles are constrained to the centermost flow stream of two concentric fluid flows and are thereby made to pass single-file through the sensing region. The technique for achieving the concentric flows, referred to as hydrodynamic focusing, imposes an absolute requirement for laminar flow in all positions within the flow cell.

Existing commercial flow cytometers are relatively complicated instruments requiring frequent adjustment of optical components used to align the optics to the sample flow. In order to simplify the operation of such instruments, Shapiro et al. [2] introduced the use of optical fibers as an

alternative to lenses for sample illumination and light collection. In addition, they proposed combining a flow channel, integrated optical elements, laser diodes, detectors, and signal conditioning electronics to form a "flow cytometer on a chip." Simplified integrated flow cytometers could potentially be more accessible for routine clinical and research applications and require less expertise for their operation.

Several microfabricated sheath flow cells have been reported previously including a five-layer stainless steel/glass laminate described by Miyake et al. [3] and a four-wafer silicon micromachined flow chamber built by our group [4]. These reports were important in demonstrating the feasibility of fabricating devices capable of supporting hydrodynamic focusing; however, the fabrication schemes were relatively complex. The long-term goal of our research effort is to develop a low-cost device, possibly using a hybrid chip approach, which includes a flow cell with integrated optics, fluid handling, and electronics for applications including flow cytometry. This paper reports on the fabrication and testing of the first steps toward such a "flow cytometer on a chip": a quartz micromachined flow cell with provisions for hydrodynamic focusing and fiber optic illumination.

## FLOW CHAMBER DESCRIPTION

The flow cell (Fig. 1) has a sample injector used to introduce a dye or particle suspension into a flowing sheath liquid and a two-dimensional nozzle to focus the sample into a narrow stream. The sample and sheath flows pass through the capillary, and exit through ports in the outlet region. In some devices optical fibers are positioned perpendicular to the capillary axis to allow for illumination and (ultimately) scatter and fluorescence detection.

Our initial mask designs are conservative, allowing only 8 devices per 4 inch wafer. The final "chip" dimensions are roughly those of a microscope slide (30 mm  $\times$  15 mm  $\times$  1 mm) with a 1 cm-long capillary of oval cross-section (height 250  $\mu$ m and width 500  $\mu$ m) — dimensions which are comparable to the flow cells on commercially available flow cytometers. The sample injector has a nearly circular cross-section with a height of 250  $\mu$ m and width of 280  $\mu$ m. The sample fluid is introduced using a #32 stainless steel hypodermic needle. External connections to the sheath inlet and outlet ports are achieved by securing the chip in a custom-machined package with an intervening O-ring seal. The grooves for the optical fibers are slightly larger than the cladding diameter of the multimode optical fibers. The fibers used were selected for 442 nm excitation, have a 0.3 numerical aperture, and have core and cladding diameters of 100 and 140  $\mu$ m, respectively.

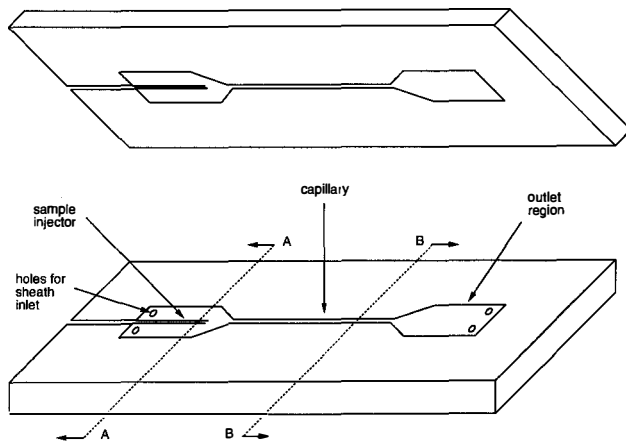


Figure 1: Exploded view of the fused silica flow chamber. The top and bottom plates have matching injection and outlet areas with a capillary joining them. Through-holes in the bottom plate are for sheath inflow and outflow. The sample is introduced through the injector into the center of the sheath flow.

### FLOW CELL FABRICATION

Fabrication of the flow cells involves using a single mask to create two fused silica wafers with matching isotropically-etched flow features and openings for optical fibers. After through-holes for fluid inlet and outlet are drilled in the bottom wafer, the two wafers are aligned and thermally bonded. Finally, the needle and optical fibers are secured in place.

As illustrated in Fig.2, the specific fabrication process starts with a LPCVD deposition of  $2.5\ \mu\text{m}$  of polysilicon onto HOYA T-4040 synthetic quartz (i.e., fused silica) wafers. This substrate material has low impurity levels making it compatible with CMOS production environments. Process characterization studies showed that such thick masking layers were necessary to ensure negligible pin hole formation during the wet etching. This use of polysilicon as a mask for etching of quartz was independently reported by Kaplan et al. at MEMS 94 [5]. The use of fine grained polysilicon masking layers may allow lower poly thicknesses. The openings for the optical fibers and the flow features are defined photolithographically, and established by plasma etching of the polysilicon masking film followed by an isotropic hot ( $50^\circ\text{C}$ ) 7:1 BOE etch of the fused silica substrate. Fused silica etch rates of  $23.0\ \mu\text{m}/\text{hr}$  were measured under these conditions. The inlet/outlet holes are drilled using electrochemical discharge machining [6]. (The precise position of the holes is not critical.) Finally, the polysilicon film is removed using 20 wt % KOH at  $60^\circ\text{C}$  and the wafers are cleaned, aligned using a customized attachment for a standard contact aligner[7], and bonded at  $1000^\circ\text{C}$ . Immediately prior to testing, the needle and fibers are secured into place using UV curable glue. After the fibers or needles are positioned in their corresponding grooves under microscopic observation, the glue is introduced by capillary action and its flow stopped with the exposure to UV illumination. This method assured precise filling and sealing of the fiber and needle grooves.

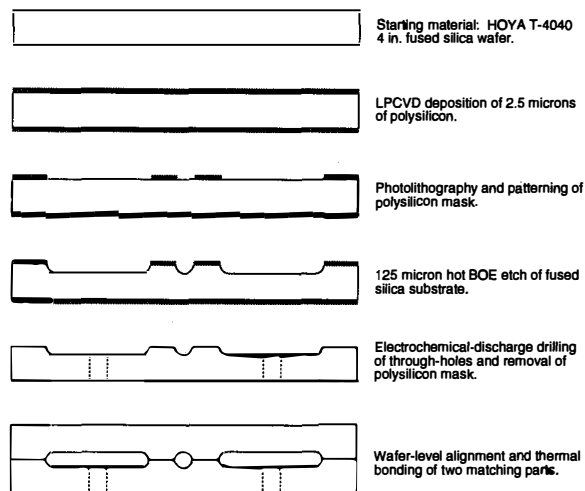


Figure 2: Fabrication sequence (shown along cross-section A-A of Fig. 1).

### RESULTS

The technical feasibility of the fabrication process has been validated with the fabrication of several prototypes. The circular and ovoid cross-sections of the injector and capillary are apparent from the SEM micrographs (Figs. 3 & 4). The smooth, flat surface of the capillary is consistent with the good optical properties observed in the tests described below. There was no obvious asymmetry between the top and bottom wafers; the slight offset observed in the capillary and injector resulted from a slight misalignment of roughly  $1\ \mu\text{m}$ . Preliminary data suggest that the fabrication sequence, including the etch characterization is reliable.

The hydrodynamic tests were performed after mounting the package on a microscope with either a video camera or photomultiplier tube connected to the video port. Sample and sheath flows were driven by a syringe pump and pressure vessel, respectively. A differential pressure sensor mounted between the inlet and outlet ports allowed us to relate flow rates to pressure drops. Hydrodynamic focusing in the horizontal plane was verified by microscopic visualization of a device operating with a water sheath and dye-containing sample (Fig. 5). The width of the sample stream changed in accordance with changes in the relative sample and sheath flow rates (Fig. 6). Focusing was maintained for mean velocities of up to at least  $10\ \text{m}/\text{s}$  (requiring an inlet to outlet pressure drop of 28 psi). Hydrodynamic focusing in the vertical plane was verified in two ways. First, for sample stream diameters smaller than  $10\ \mu\text{m}$ , conservative estimates based on measured sample and sheath flow rates indicate that the height of the sample stream must be less than  $160\ \mu\text{m}$ , far less than the  $250\ \mu\text{m}$  height of the capillary. Second, by adjusting the focal point along the vertical axis the dye did not appear to contact the capillary wall. It was not possible, however, to use this approach to reliably identify the vertical position of the interface between sheath and dye. Although the precise dimensions of the sample stream are not known, these results are significant in demonstrating that this comparatively simple device design provides hydrodynamic focusing in both the horizontal and vertical dimensions.

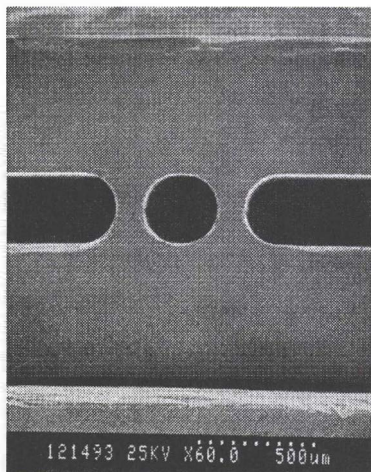


Figure 3: SEM micrograph showing a cross-section (section A-A of Fig. 1) of the sample injector and part of the passages for the surrounding sheath flow.

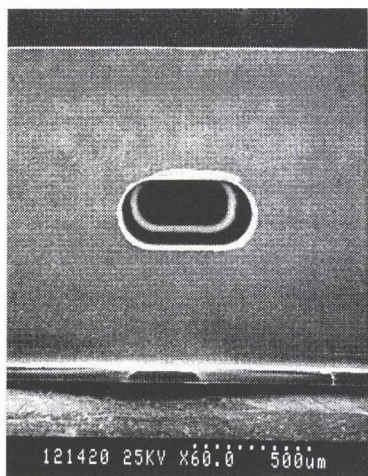


Figure 4: SEM micrograph showing a cross-section (section B-B of Fig. 1) of the capillary duct. The bottom and top surfaces are optically flat.

The good optical characteristics of the device suggested by the optical clarity of the hydrodynamically-focused dye stream were further illustrated by fiber optic illumination of a sample stream containing fluorescein isothiocyanate (FITC) (Fig. 7). These studies were done using a 60mW He-Cd laser beam (tuned to 442 nm), coupled to the multimode optical fiber using a lens and precision positioner. The adequacy of the coupling of the laser beam to the optical fiber was determined by measuring the power output at its end. This measurement was made using an optometer with a silicon photodiode head (calibrated at 442 nm) before placing the fiber in the flow cell. At optimal alignment, we measured a 30 mW power output.

The presence of the fiber *per se* did not appear to perturb the fluid flow (as long as the fiber did not protrude into the channel). In some cases the groove containing the fiber was not sealed so that through a venturi effect, air bubbles were periodically released into the flow stream, perturbing the flow. The normal flow patterns were subsequently reestablished. Fluorescence of the sample stream could be quantified using a PMT mounted in the video port of the microscope. The distribution of fluorescent intensity resulting from 2  $\mu\text{m}$  fluorescent particles illuminated with the optical fiber was determined by connecting the PMT output to standard flow cytometry amplifier and data acquisition system. This analysis resulted in distributions having coefficients of variation (CV; standard deviation/mean) on the order of 8% (Fig. 8) which compares well the the CV's obtained on commercially available cytometers. Improvements in the CV would presumably result from the use of a single mode rather than multimode optical fiber (both because of the gaussian intensity distribution and the smaller illumination volume) and from more substantial sample stream focusing in the vertical plane.

## CONCLUSIONS

In summary, the work described in this paper demonstrates the feasibility of microfabricating flow chambers from fused silica wafers using a comparatively simple two wafer, single mask process. Although the structure geometry directly imposes focusing in the horizontal plane, the resulting flows clearly show focusing in both the horizontal and vertical planes. Improved vertical focusing can probably be achieved by decreasing the vertical dimensions of the injector, a change which could be implemented with a second mask. Initial tests using the precision-positioned optical fibers are encouraging in that illumination of the sample stream and detection of fluorescence were demonstrated. Additional studies are necessary to determine the flow conditions for which the illumination volume includes the entire sample stream and whether integrated optical fibers can be used for detection of fluorescence or scatter.

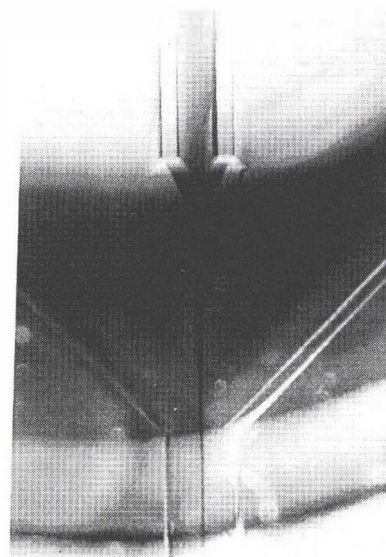


Figure 5: Demonstration of hydrodynamic focusing. The photograph shows dye being introduced through the injector into the nozzle. In this picture the dye stream at the entrance of the capillary is focused to a 10 micron width.

## ACKNOWLEDGEMENTS

This work was supported by grants from SEQ Ltd. and the National Science Foundation under grant # BCS 8808341. Additional support was provided by the J. W. Kieckhefer Foundation, and the Barton L. Weller Professorship. Special thanks to Dr. Kevin Ulmer and Dr. Sheila Frankel for their guidance and assistance. We gratefully acknowledge the assistance of the MTL staff in this work.

## References

- [1] M. R. Melamed, T. Lindmo, and M. L. Mendelsohn, (eds.), *Flow Cytometry and Sorting*, 2nd. Edition, John Wiley & Sons, 1991.
- [2] H. M. Shapiro and M. Hercher, "Flow Cytometers Using Optical Waveguides in Place of Lenses for Specimen Illumination and Light Collection," *Cytometry*, Vol. 7, pp. 221-223, 1986.
- [3] R. Miyake, H. Ohki, I. Yamazaki, and R. Yabe, "A Development of Micro Sheath Flow Chamber," in *Proceedings of the IEEE Micro Electro Mechanical Systems Workshop*, pp. 259-264, Nara, Japan, January 1991.
- [4] D. Sobek, A. M. Young, M. L. Gray, and S. D. Senturia, "A Microfabricated Flow Chamber for Optical Measurements in Fluids," in *Proceedings of the IEEE Micro Electro Mechanical Systems Workshop*, pp. 219-224, Fort Lauderdale, FL, February 1993.
- [5] W. Kaplan, H. Elderstig, and C. Vieider, "A Novel Microfabrication Method of Capillary Tubes on Quartz for Chemical Analysis Applications," in *Proceedings of the IEEE Micro Electro Mechanical Systems Workshop*, pp. 63-68, Oiso, Japan, January 1994.
- [6] S. Shoji, and M. Esashi, "Photoetching and Electrochemical Discharge Drilling of Pyrex Glass," in *Technical Digest of the 9th Sensor Symposium*, pp. 27-30, 1990.
- [7] A. M. Young, "Microfabricated Pressure Transducers Based on Anti-Resonant Reflecting Optical Waveguides," Ph. D. Thesis, Department of Electrical Engineering and Computer Science, MIT, 1994.

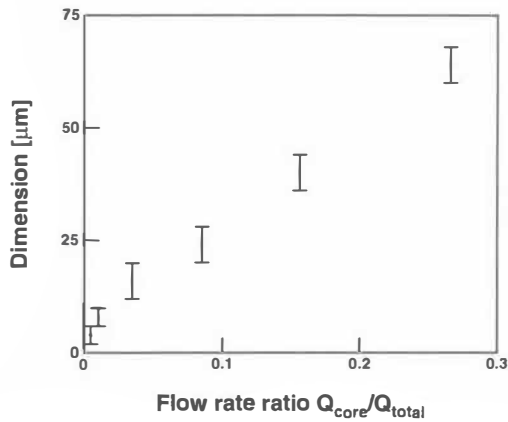


Figure 6: Width of the dye stream as a function of ratio between core flow rate ( $Q_{core}$ ) and total flow rate ( $Q_{total}$ ).

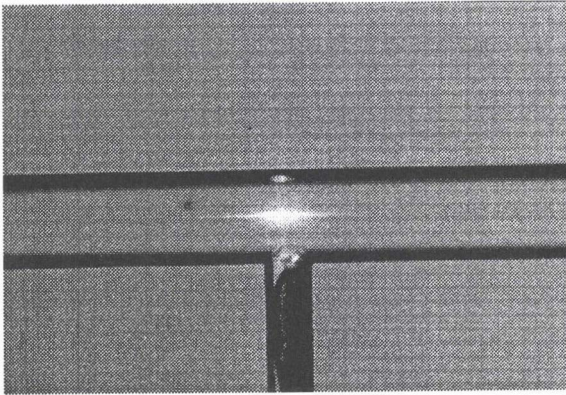


Figure 7: Fiberoptic illumination of the flow channel. Sample stream contains FITC.

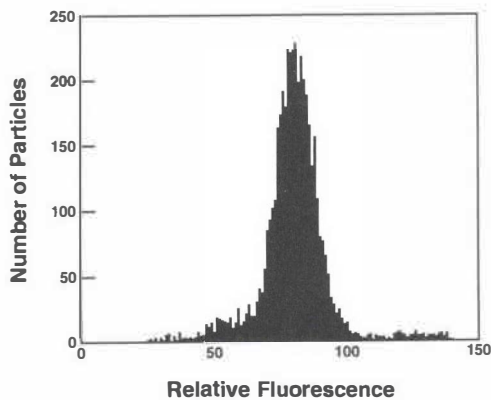


Figure 8: Fluorescence intensity distribution for 2 micron diameter fluorescent particles, illuminated at 442 nm through a multimode optical fiber, and detected using a PMT attached to the microscope.

# A Micromachined Polysilicon Hot-Wire Anemometer

Fukang Jiang, Yu-Chong Tai  
Chih-Ming Ho\*, Wen J. Li\*

EE 116-81, Caltech, CA 91125, USA  
\*MANE, UCLA, Los Angeles, CA 90024, USA

## ABSTRACT

Micromachined polysilicon hot-wire anemometers have been designed, fabricated and tested. In comparison to conventional hot-wire anemometers, the new designs feature a wire which is greatly reduced in size. The geometrical structure and material properties of the polysilicon wire have been investigated and optimized to improve the performance of the anemometers. Two types of polysilicon wires with different boron doping profiles were fabricated: centerly lightly doped and uniformly doped. The first type has faster response (2  $\mu$ s in constant current mode) and higher sensitivity, but the second type shows better stability. In extensive wind tunnel testing, both types have demonstrated faster frequency response, higher spatial resolution and greater sensitivity over conventional counterparts.

## 1. INTRODUCTION

A hot-wire anemometer is a thermal transducer which is capable of sensing point flow velocity through temperature variation using a heated resistive wire which has a non-zero temperature coefficient of resistance (TCR). When the electrically heated wire is placed in the flow of fluid, the heat is taken away by the flow-induced forced convection. Depending on the operation modes (constant current or constant temperature), either the resistance or the output voltage drop across the wire is a function of the flow velocity.

Conventional hot-wire anemometers have been used for flow velocity measurements for over 80 years. Fig 1(a) shows the structure of a typical hot-wire anemometer. A metal wire is welded or soldered to two metal needles which are molded to the probe body. The wire is usually made of platinum or tungsten and is typically 5  $\mu$ m in diameter and 1 mm in length. It has a resistance of 10 - 30 ohms at room temperature and needs 10 - 40 mA of current to operate[1-2]. These conventional anemometers have to be hand-assembled one by one, thus making it difficult to be arrayed for simultaneous velocity distribution measurement. Also, since the wire diameter is difficult to control with good repeatability, the anemometer probes are essentially not interchangeable without recalibrating the whole anemometer system.

Since the spatial resolution of the anemometers for flow velocity distribution measurement is determined by its dimensions, it is advantageous if the wire size can be further reduced. This would also decrease power consumption and thermal interference to the flow and increase frequency response. In fact, many anemometer designs have been demonstrated using either surface or bulk micromachining technologies[3-7]. Interestingly, however, they are either bulk-micromachined chip-sized devices or wires on top of chips. No one really simulates the real feature of a conventional hot-wire anemometer, i.e., a wire thermistor free-standing in space without anything nearby so that best thermal isolation is achieved. As a result, they can not be direct replacements for the conventional hot-wire anemometers. Here, we report our research on a new type of micromachined anemometers that emphasize the real simulation of a hot-wire anemometer but with greatly reduced wire size. This is made possible by combining surface and bulk micromachining technologies. Not only the spatial resolution and device sensitivity are better, the frequency response is also improved by at least one order of magnitude (confirmed from extensive wind tunnel calibration) over the conventional hot-wire anemometers. Optimization of the structural geometry and the material properties has resulted in anemometers with time constant of 2  $\mu$ s in the constant current mode (the current record of the time constant for thermal anemometers).

## 2. DESIGN

Our micromachined hot-wire anemometers have a structure similar to that of conventional hot-wire anemometers. It consists of a sensing wire, two parallel supports, a Si beam, and the thick Si handle, as shown in Fig. 1(b). The Si beam acts as a thermal and mechanical buffer between the supports (0.5  $\mu$ m thick) and the handle (500  $\mu$ m thick) to avoid interference with the flow. The sensing wires are about 0.5  $\mu$ m thick, 1  $\mu$ m wide, 10-160  $\mu$ m long, and are free standing to optimize the interaction with the flow and to minimize the thermal conduction to the handle. Polysili-

con, instead of platinum or tungsten, is used as the sensing and supporting material because of its compatibility with existing micromachining technologies and because of its controllable TCR in the range of  $-1\%/^{\circ}\text{C}$  to  $+0.2\%/^{\circ}\text{C}$ , depending on the doping concentration. The doping concentration of  $10^{18}\text{cm}^{-3}$  corresponds to a reproducible TCR of  $-1\%/^{\circ}\text{C}$  for our polysilicon, with which high thermal sensitivity can be achieved even at low operating temperature (shown later).

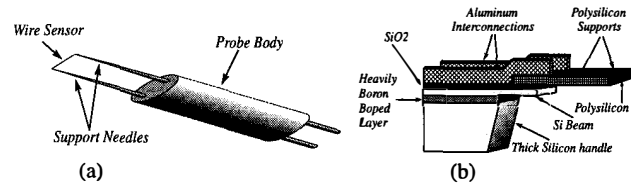


Fig 1. Structures of hot-wire anemometers: (a) Conventional. (b) Micromachined.

The polysilicon wires can be uniformly doped by high dose boron implantation (type I) or nonuniformly doped by a low dose implantation followed by a high dose implantation with the center part of about 2  $\mu$ m being masked (type II). Type I poly wires behavior similar to the platinum or tungsten wires, the resistance and the ohmic heating are concentrated at the 2  $\mu$ m lightly doped center region. The other part of the wire acts only as the electrical conductor and mechanical support[8]. It can be expected that anemometers with this type of wire should have improved frequency response and spatial resolution over the type I wires. However, the sensitivity of type II device is not necessarily higher than that of type I device even with a much larger TCR because the temperature change caused by the forced convection may not be as high as that of longer wires. Since the lightly doped part is very short, the total resistance of the anemometer is still within a reasonable range (<20kilo-ohms) which can be adequately handled by signal processing circuits.

## 3. FABRICATION

It has been reported that polysilicon, deposited in amorphous state and then crystallized has better controllable qualities than as-deposited polysilicon with the deposition temperature at 620 $^{\circ}\text{C}$ [9]. We chose to use the former polysilicon, of which the electrical properties were previously calibrated, in the fabrication of our anemometers. We found that its TCR is about 50% higher and the temperature behavior is more linear than the normal poly in the high doping range. Fig 2 shows the resistance changes with temperature for three different types of polysilicon. Moreover, the stress distribution in this polysilicon along the depth is much more uniform, as we will see from the SEM pictures in the late part of this paper. The calibration results show that  $2 \times 10^{20}\text{cm}^{-3}$  is the doping concentration which gives the lowest sheet resistivity (  $30\Omega/\square$  ) and highest positive TCR, and therefore, is the optimum doping concentration for the heavily doped leads in type II anemometers and for the whole wire of the type I anemometers. The doping of the center part ( $10^{18}\text{cm}^{-3}$ ) for type II wire is determined such that the resistance ratio between the center part and the leads is 10 ~ 20 near the operating point. This doping concentration also gives a satisfactory TCR of approximately  $-1\%/^{\circ}\text{C}$ . Another factor which needs to be considered for type II is how to avoid lateral diffusion of the boron dopants from the heavily doped leads to the center part during the annealing process which follows after the boron ion implantations. The annealing temperature must not be so high that it causes significant lateral diffusion in the standard 30 min. annealing, but it can not be so low that stable polysilicon resistors could not be made. Therefore, calibration of the lateral boron diffusivity in nonuniformly doped polysilicon was conducted in order to determine the annealing temperature. Fig 3 shows the diffusivity vs. temperature curve. The highest annealing temperature for type II wire is determined to be 900 $^{\circ}\text{C}$  from the diffusion model using these data.

Two generations of anemometers have been fabricated at the Caltech Micromachining Lab. The 1st generation has silicon nitride encapsulating the polysilicon probe wires. The poly wires of the 2nd generation are directly exposed to air and consequently the frequency response has improved by an order of magnitude. Fig 4 shows the fabrication process

flow of the 2nd generation.

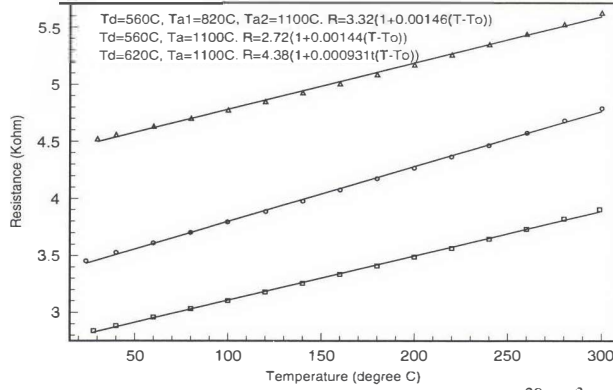


**Fig 2.** The temperature behavior of boron doped ( $2 \times 10^{20} \text{cm}^{-3}$ ) polysilicon resistors (50 squares) under different deposition and annealing conditions.

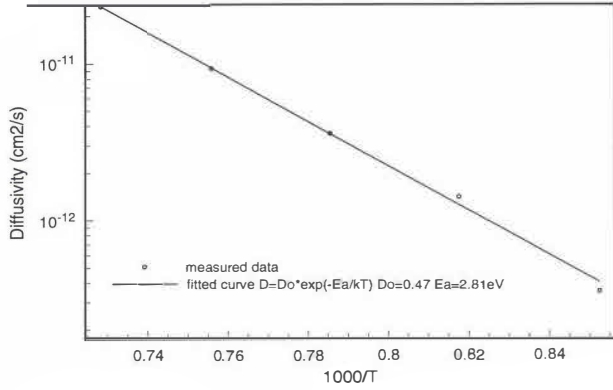


**Fig 3.** Lateral boron diffusivity at different temperatures in polysilicon deposited at  $560^\circ\text{C}$  and annealed at  $1100^\circ\text{C}$ .

Two generations of anemometers have been fabricated at the Caltech Micromachining Lab. The 1st generation has silicon nitride encapsulating the polysilicon probe wires. The poly wires of the 2nd generation are directly exposed to air and consequently the frequency response has improved by an order of magnitude. Fig 4 shows the fabrication process flow of the 2nd generation.

The fabrication starts with the oxidation of the (100) Si wafers which have a  $10 \mu\text{m}$  lightly doped epi layer on top of a  $8 \mu\text{m}$  heavily boron doped etch stop layer. A  $600 \text{nm}$  thick amorphous Si layer is deposited at  $560^\circ\text{C}$  and patterned by plasma etching. Photoresist implantation barriers are then formed on type II poly wires and this is followed by boron ion implantation with a dose of  $10^{16} \text{cm}^{-2}$  and an energy of  $80 \text{keV}$ . After stripping the PR barrier, low dose boron ions ( $10^{14} \text{cm}^{-2}$ ) are implanted to dope the center parts of type II wires. Annealing is done at  $1100^\circ\text{C}$  for type I wafers and at  $900^\circ\text{C}$  for type II wafers for 30 min.. After the aluminum metallization, a  $3 \mu\text{m}$  LTO is deposited at  $450^\circ\text{C}$  and the frontside and backside Si substrate windows are opened using both wet and dry etchings. A 10 hours EDP etching at  $95^\circ\text{C}$  removes the Si underneath the poly probe. Finally, HNA Si isotropic etchant and pad oxide etchant are used to strip the heavily doped boron layer and the LTO respectively. Fig 5 shows SEM pictures of some hot-wire anemometers fabricated using this process.

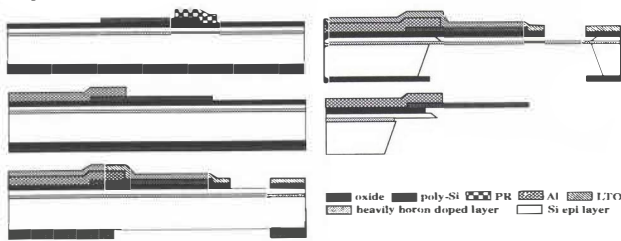


**Fig 4.** Process flow of polysilicon hot-wire anemometers using both surface and bulk micromachining technologies.

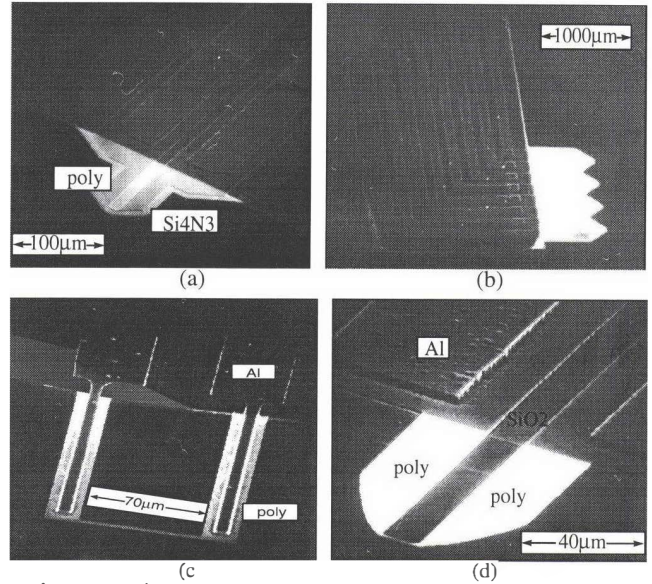


**Fig 5.** SEM pictures of (a) 1st generation "hot-point anemometer", (b) 1st generation anemometer array for simultaneous velocity distribution measurement, (c) 2nd generation heavily doped anemometer, (d) 2nd generation centerly lightly doped anemometer.

#### 4. THEORY AND EXPERIMENTAL RESULTS

Anemometers can operate either in constant current mode (without feedback) or in constant temperature mode (with feedback). Here, we only use the constant current mode in the early testing stages of our anemometers because of its simplicity. Currently, wind tunnel tests of anemometers in constant temperature mode are under way and will be reported later.

##### 4.1 Time constant

###### 4.1.1 Transient analysis

For a wire with length  $l$ , width  $w$  and thickness  $d$  at some time  $t$  and position  $x$  from one end, the sum of the heat absorbed by a unit length wire and the heat flowing into it through thermal conduction and convection in unit time must be equal to the ohmic power [10], i.e.,

$$w d c_p \frac{\partial T}{\partial t} - \kappa_{poly} w d \frac{\partial^2 T}{\partial x^2} + 2h(w+d)(T-T_a) = J^2 \rho_0 w d [1 + \alpha(T-T_a)] \quad (1)$$

where  $\rho = 2.32 \text{g/cm}^3$ ,  $c_p = 0.7 \text{J/g} \cdot ^\circ\text{C}$ ,  $\rho_0$ ,  $\kappa_{poly}$ ,  $\alpha = 0.0015/^\circ\text{C}$  are the density, specific heat, resistivity, thermal conductivity, temperature coefficient of the resistance for the polysilicon,  $J$  is the current density,  $T_a$  is the ambient temperature. The above differential equation can be solved with the boundary condition  $T(0,t) = T(l,t) = T_a$  and initial condition  $T(x,0) = T_a$ , assuming that the two supports are perfect heat sinks. The solution is a multi-mode response. The first mode determines the time constant,

$$\tau = \tau_1 \tau_2 / (\tau_1 + \tau_2) \quad (2)$$

$$\tau_1 = \frac{\rho c_p}{\left(-\alpha J^2 \rho_0 + \frac{\kappa_{air} Nu}{wd}\right)}, \tau_2 = \left(\frac{l}{\pi}\right)^2 \frac{\rho c_p}{\kappa_{poly}}$$

where  $\kappa_{air} = 2.5 \times 10^{-4} \text{W/cm} \cdot ^\circ\text{C}$  is the thermal conductivity of the air at room temperature.  $Nu$  is the Nusselt number of the wire. It can be seen from the above expressions that the time constant is due to two components: convection time constant  $\tau_1$ , which dominates for long wires, and conduction time constant  $\tau_2$ , which dominates for short wires.

For the centerly lightly doped probes,  $\tau \approx \tau_2$  with  $l$  being replaced by the effective length of the wire  $l_{eff}$ , which is longer than the length of the lightly doped part. However, it is still expected that type II anemometers have a much smaller time constant than type I anemometers since  $l_{eff} < L$ , which is the total wire length.

###### 4.1.2 Time constant measurement

The time constant is determined by passing a step current through the anemometer in still air and observing the voltage rise (for positive TCR) or fall (for negative TCR) in an oscilloscope. If a steady flow with certain velocity is applied, the time constant will be reduced. For a conventional hot-wire anemometer  $5 \mu\text{m}$  in diameter, the time constant is about  $0.5 \text{ms}$ .

Fig 7 shows the time constant in constant current mode of our anemometers for varying wire lengths. The solid line is the fitted curve of Eq. (2) for type I probes.  $Nu = 0.78$  and  $\kappa_{poly} = 0.26 \text{ W/cm}^2\text{C}$  ( $0.34 \text{ W/cm}^2\text{C}$  in [11]) are the fitting parameters. The fluctuations in the fitted curve are due to the scattering of  $w$  from fabrication. The effective width  $w$  is calculated from the measured wire resistances with the known sheet resistance of  $30 \Omega/\square$ . There is no curve fit for type II probes, but the measured  $\tau$  does not change that much for probes with different lengths. From the data we estimated  $t_{eff}$  and they range from  $15 \mu\text{m}$  to  $38 \mu\text{m}$ . This large  $t_{eff}$  is the result of the low resistivity of the lightly doped part, which was not controlled well in this batch. Note that the  $30 \mu\text{m}$  long probe of this type with a heating  $\tau$  of only  $2 \mu\text{s}$  and a cooling  $\tau$  of  $8 \mu\text{s}$  in constant current mode (Fig 7) is currently the fastest anemometer probe.

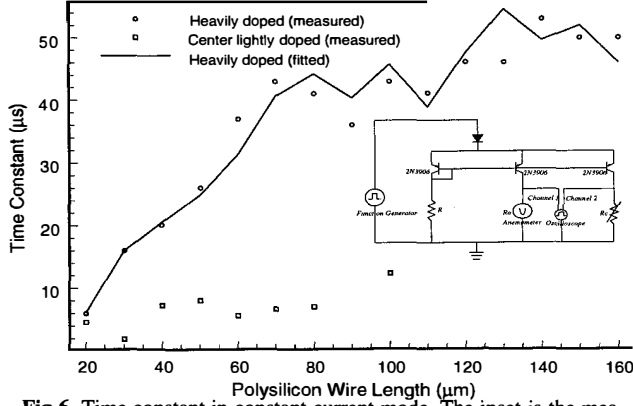
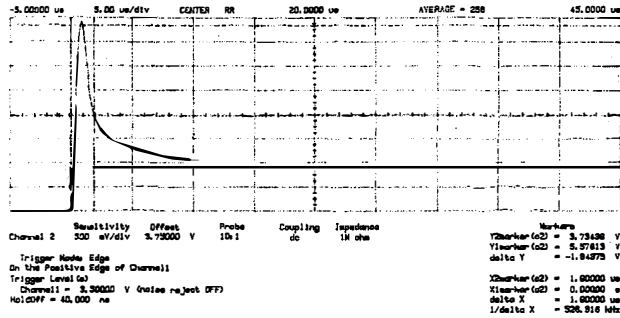
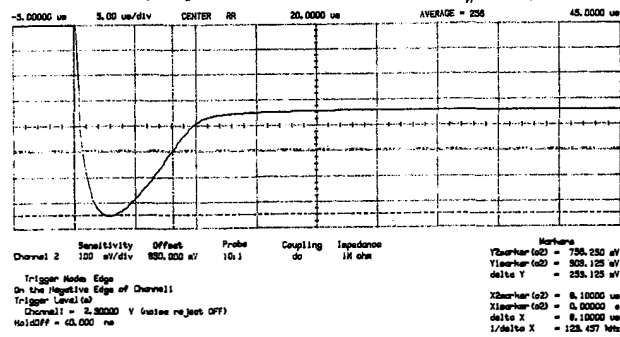


Fig 6. Time constant in constant current mode. The inset is the measurement setup, in which  $R_c$  is used to cancel the inherent time delay of the input signal and the circuit.



(a) Heating response:  $I = 0.4 \text{ mA}, \Delta V \approx 3 \text{ V}, \tau_h = 1.9 \mu\text{s}$



(b) Cooling response:  $I = 50 \mu\text{A}, \Delta V \approx 0.2 \text{ V}, \tau_c = 8.1 \mu\text{s}$

Fig 7. The time constant is determined by observing the rise or fall of the voltage waveform in oscilloscope when a step current is applied.

## 4.2 Steady state response

### 4.2.1 King's law

In steady state, power generation and heat dissipation is balanced, i.e.,

$$IV = K_{eff}(U)(T - T_a) \quad (3)$$

where  $T$  is the wire temperature,  $T_a$  is the ambient temperature,  $U$  is the flow velocity, and  $K_{eff}(U)$  is the effective heat transfer coefficient. In a laminar flow, King's law applies,

$$K_{eff}(U) = K_0 + K_1 U^n \quad (4)$$

where  $K_0$  is the heat transfer coefficient which takes into account of conduction, radiation and free convection and is not a function of  $U$ .  $K_1 U^n$  represents forced convection by the flow boundary layer. The power  $n$  depends on the structure and is around 0.5 for conventional hot-wire an-

emometers. In constant temperature mode, it can be derived from (3) and (4) that

$$V^2 = A_1 + B_1 U^n \quad (5)$$

In constant current mode,

$$T - T_a = \frac{(R - R_a)}{\alpha R_a} = \frac{(V - IR_a)}{\alpha IR_a} = \frac{a}{\alpha}$$

where  $R_a$  and  $\alpha$  are the resistance and TCR at the ambient temperature,  $a$  is the over heat ratio. It can be shown that

$$V = \frac{(A_2 + B_2 U^n)}{(1 + BU^n)} \quad (6)$$

where

$$A_2 = \frac{K_0 IR_a}{(K_0 - \alpha I^2 R_a)}, B_2 = \frac{K_1}{K_0} A_2, B = \frac{K_1}{(K_0 - \alpha I^2 R_a)}$$

Or

$$V_0 - V = \frac{AU^n}{(1 + BU^n)}$$

where  $V_0$  is the voltage at  $U = 0$ , and  $A = \frac{K_1 \alpha I^3 R_a^2}{(K_0 - \alpha I^2 R_a)^2}$ . If  $B$  is small, then

$$V \approx A_2 + B_2 U^n \quad (8)$$

### 4.2.2 Wind tunnel test

Fig. 8 shows the response of a  $70 \mu\text{m}$  long, heavily doped anemometer (SEM picture in Fig 5(c)) and of a conventional hot-wire anemometer in a wind tunnel at different over heat ratios without any electronic gain. The lines in Fig 8 are the fitted curves of Eq. (7). The sensitivity of our anemometer biased by 2-3 mW is higher than that of the conventional anemometer operating at 4-8 mW. This is due to the smaller size and the higher resistivity of polysilicon over platinum and tungsten. The power  $n$  of the velocity  $U$  for our anemometer and for the conventional anemometer are around 1.1 and 0.6 respectively. Thus, in comparison with the conventional anemometer, our anemometer has a more linear response and less degradation in sensitivity in the high velocity regime than the conventional anemometer. We believe that this is the result of conduction to the supports which in turn causes nonuniform temperature distribution, a situation which is usually avoided in conventional hot-wire anemometers with large  $ld$ . The directional dependence of the sensitivity has also been tested and the results are shown in Fig 9. The three sets of measured data points at three different angles almost completely overlap. Thus, it is nearly isotropic as long as the angle is not close to  $90$  degree. This is rather surprising because the theory [1] predicts that the directional dependence of sensitivity follows the cosine law, which is the case of conventional hot-wire anemometers. One possible reason for this might be that the supports have interfered with the flow in our devices.

Fig 10 shows the responses of a  $20 \mu\text{m}$  long type II anemometer at two different angles. It is almost isotropic, but not as much as the heavily doped probe. The near isotropic characteristic can be explained by its short length. Note that it has higher sensitivities than type I even at lower power. Since the I-V curve of type II anemometer is highly nonlinear, it is difficult to estimate the over heat ratio without doing more complicated calibration.

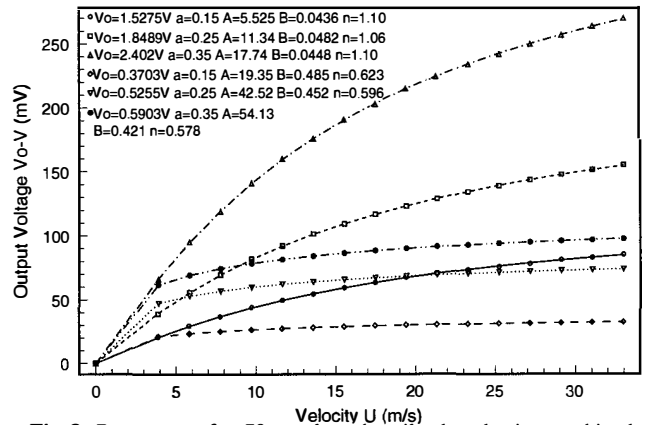
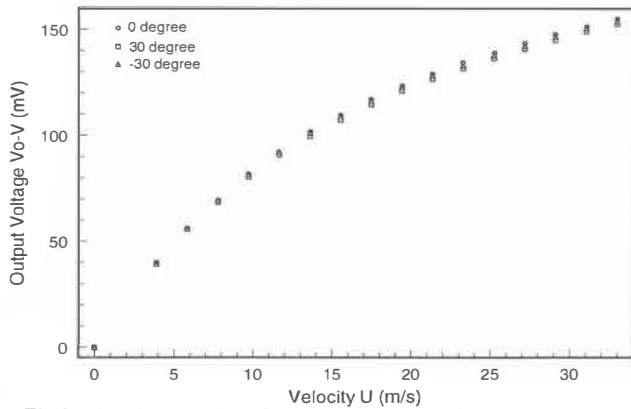
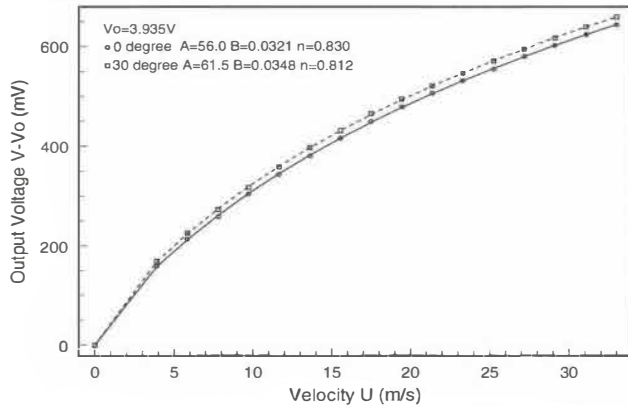


Fig 8. Responses of a  $70 \mu\text{m}$  long heavily doped micromachined (data points represented by circles, squares and triangles) and a conventional (data points represented by diamonds, upside-down triangles and bold dots) hot-wire anemometer in a wind tunnel operating at three different over heat ratios in constant current mode ( $I = 1.05, 1.22, 1.29 \text{ mA}$  for the micromachined, and  $10, 13, 14 \text{ mA}$  for the conventional, respectively).



**Fig 9.** Directional testing of the same 70  $\mu\text{m}$  heavily doped anemometer in constant current mode at  $I = 1.22 \text{ mA}$  with over heat ratio of 0.25. The angle is between the flow and the normal to the wire in the anemometer plane.



**Fig 10.** Response of a 20  $\mu\text{m}$  long type II anemometer at two different angles. The average sensitivity is 20  $\text{mV/m.s}$  at  $I = 0.5 \text{ mA}$ .

## 5. DISCUSSION

As previously mentioned in the design section, we found that the stress distribution along the depth of the polysilicon deposited at  $620^\circ\text{C}$  and annealed at  $1100^\circ\text{C}$  is not uniform. Sometimes, the tips of all the anemometer probes in a wafer made from this type of poly bend up about 50  $\mu\text{m}$ , as shown in Fig 11. However, this phenomenon is never observed in anemometers made from the polysilicon deposited at  $560^\circ\text{C}$  and annealed at  $1100^\circ\text{C}$ . The reason might be that the structure of as-deposited and as-implanted amorphous silicon films are uniform along the depth. During annealing, the grain growth is uniform, so the stress distribution is uniform too.

Fig 12 shows the temporal drift of a 70  $\mu\text{m}$  long heavily doped probe. The resistance increases slowly. Several factors contribute to the drift. First, the polysilicon is not protected and could be oxidized during high temperature operation. This can be avoided by a conformal anti-oxidation

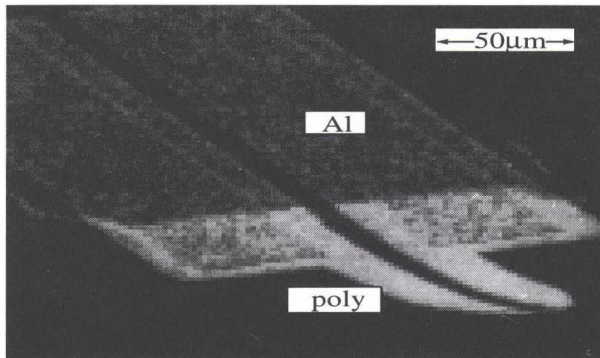


**Fig 11.** SEM picture of the intrinsically bent anemometer probe

layer coating over the free standing polysilicon structures which only increases the time constant a little. Second, since polysilicon has high dif-

fusivity, the temperature nonuniformity and the electric field across the wire at the operating temperature of a few hundred degrees may cause the slow diffusion of dopants. Amemiya *et al*[12] found that the resistivity of heavily doped polysilicon decreases under high current density. This contradicts our observation. Further study need to be done on the mechanism of this drift.

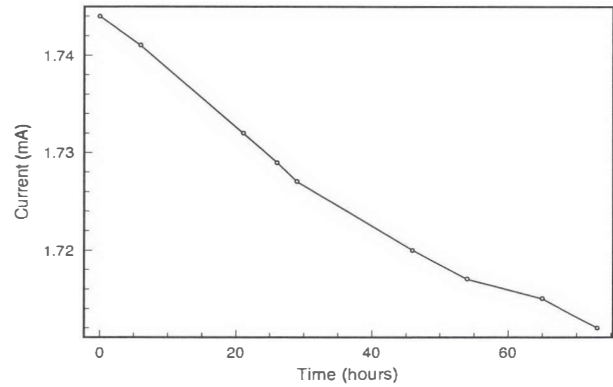


**Fig 12.** The temporal drift of a 70  $\mu\text{m}$  long heavily doped anemometer at  $V = 2.5\text{V}$  and  $\alpha = 0.35$ .

## 6. CONCLUSION

Two types of micromachined polysilicon anemometers have been developed. Both have demonstrated superior performance over conventional hot-wire anemometers. Reliability tests and design iterations still need to be done for practical wind tunnel use.

## ACKNOWLEDGMENT

This project is supported by AFOSR under Grant F49620-92-J-0424. The authors would like to thank Jianqiang Liu, Chang Liu, Ren Wu and Trevor Roper for many discussions and help in the designing and fabrication.

## REFERENCES

- [1] R. F. Blackwelder, *Methods of Experimental Physics: Fluid Dynamics*, Vol. 18, Part A, Academic Press, 1981, pp. 259-314.
- [2] A. E. Perry, *Hot-Wire Anemometry*, Clarendon Press, Oxford, 1982.
- [3] Y. C. Tai, and R. S. Muller, "Polysilicon Bridge for Anemometer Application", *Digest Tech Papers, Transducers '85*, Philadelphia, PA, June 4-7, 1985, pp. 354-357.
- [4] H. Rahnamai, and J. N. Zemel, "Pyroelectric Anemometers: Preparation and Velocity Measurements", *Sensors and Actuators*, Vol.2, 1981, pp. 3-16.
- [5] M. Stenberg, G. Stemme, G. Kittilsd, and K. Pedersen, "A Silicon Sensor for Measurement of Liquid Flow and Thickness of Fouling Biofilms", *Sensors and Actuators*, Vol.13, 1988, pp. 203-221.
- [6] B. W. van Oudheusden, and J. H. Huijsing, "Integrated Silicon Flow Direction Sensor", *Sensors and Actuators*, Vol.16, 1989, pp. 109-119.
- [7] R. Kersjes, J. Eichholz, A. Langerbein, Y. Manoli, W. Mokwa, "An Integrated Sensor for Invasive Blood-Velocity Measurement", *Sensors and Actuators*, Vol. 37-38, 1993, pp. 674-678.
- [8] Y. C. Tai, and R. S. Muller, "Lightly Doped Polysilicon Bridge as a Flow Meter", *Sensors and Actuators*, Vol. 15, No. 1, 1988, pp. 63-75.
- [9] G. Harbecke, L. Krausbauer, E. F. Steigmeier, A. E. Widmer, H. F. Kappert and G. Neugebauer, "Growth and Physical Properties of LPCVD Polycrystalline Silicon Films", *J. Electrochem. Soc.*, Vol.131(3), 1984, pp. 675-682.
- [10] C. H. Mastrangelo, *M.S. Thesis*, UC Berkeley, 1987.
- [11] Y. C. Tai, C. H. Mastrangelo, and R. S. Muller, "Thermal Conductivity of LPCVD Polycrystalline Silicon", *J. Appl. Physics*, Vol. 63, No. 5, 1988, pp. 1442-1447.
- [12] Y. Amemiya, T. Ono, and K. Kato, "Electrical Trimming of Heavily Doped Polycrystalline Silicon Resistors", *IEEE Trans. Electron Devices*, Vol. ED-26, No. 11, 1979, pp. 1738-1742.

## AUTHOR INDEX

- Allen, M. G. 90, 243  
Allred, R. E. 180  
Ananthasuresh, G. K. 189  
Anderson, J. 7  
Anderson, R. 251  
Apte, R. B. 1  
Aquilino, P. D. 86  
Baker, J. W. 248  
Banyai, W. C. 1  
Barth, P. W. 248  
Bartholomew, J. W. 180, 193  
Beatty, C. C. 248  
Beaudoin, K. 7  
Bernstein, J. 73  
Bloom, D. M. 1  
Bloomstein, T. M. 142  
Bonne, U. 78, 176  
Borkholder, D. A. 95  
Boyd, M. R. 123  
Breuer, K. S. 111  
Brewer, L. 176  
Brown, R. B. 25  
Burns, D. W. 221  
Bynum, O. W. 176  
Cavicchi, R. E. 53  
Cernosek, R. W. 229  
Chang, S.-C. 225  
Chaparala, P. 53  
Chen, J. 256  
Chen, L.-Y. 99  
Chen, P. Y. 239  
Christel, L. 251  
Christenson, T. R. 49  
Chu, W.-H. 107  
Coe, D. J. 243  
Cole, B. H. 7  
Crary, S. B. 123  
Crawforth, L. 38  
Crooks, R. M. 180  
Dadoo, R. 61  
Davidson, J. L. 172  
Deng, K. 234  
DeSouza, R. J. 13  
Dhuler, V. R. 234  
Earles, T. 49  
Eddy, D. S. 225  
Ehrlich, D. J. 142  
Fan, L. S. 17, 38  
Fan, Z. 21  
Fedder, G. K. 145  
Ferrari, M. 132  
Field, L. A. 248  
Fluri, K. 21  
Frazier, A. B. 90  
French, H. B. 197  
Frye, G. C. 193, 229  
Furukawa, S. 234  
Gaitan, M. 53  
Gianchandani, Y. 189, 116  
Gilbert, J. R. 184  
Giles, M. D. 123  
Glezer, A. 243  
Goldberg, H. D. 111  
Gordon, G. B. 248  
Gray, M. L. 260  
Guckel, H. 49, 221  
Gupta, R. K. 184  
Gurbuz, Y. 172  
Han, C.-J. 7  
Harrison, D. J. 21  
Herb, W. R. 221  
Hergenröder, R. 65  
Hicks, D. B. 225  
Higashi, R. E. 7  
Ho, C.-H. 264  
Hoen, S. 17, 209  
Hoffman, D. W. 176  
Holmen, J. 7  
Horning, R. D. 221  
Howe, R. T. 145  
Hower, R. W. 25  
Hsu, C. H. 151  
Hughes, R. C. 57  
Jacobsen, S. C. 65  
Jankowski, J. 251  
Jenkins, M. W. 57  
Jiang, F. 264  
Juan, W. H. 82  
Judy, J. W. 43  
Kang, W. P. 172  
Karnowski, M. 49  
Keller, C. 132

Kerns, D. V. 172  
 Klein, J. 49  
 Kline-Schoder, B. 251  
 Kota, S. 189  
 Kovacs, G. T. A. 61, 95  
 Kovalchuk, A. 176  
 Kreider, K. G. 53  
 Kubisiak, D. 78  
 Lee, S. S. 33  
 Lenz, J. E. 197  
 Li, W. J. 264  
 Liu, C. 103  
 Logothetis, E. M. 176  
 Lund, J. 29  
 Ma, K. J. 160  
 MacDonald, N. C. 99  
 Madou, M. 164  
 Maluf, N. I. 95  
 Mamim, H. J. 17, 209  
 Man, P. F. 156  
 Marsh, H. 7  
 Martin, S. J. 229  
 Mastrangelo, C. H. 156  
 McLaughlin, E. 73  
 Mehregany, M. 107, 234  
 Merit, F. L. 234  
 Miles, R. 251  
 Miyajima, H. 234  
 Moore, A. W. 65  
 Moore, R. C. 38  
 Moreno, D. J. 57  
 Moser, M. A. 38  
 Muller, R. S. 43, 239  
 Najafi, K. 82, 116, 138, 160, 201, 213  
 Nathan, A. 119  
 Newstrom, K. 7  
 Nielsen, D. 7  
 Ohnstein, T. 49  
 Olson, G. J. 197  
 Osbourn, G. C. 180, 193  
 Osterberg, P. M. 184  
 Pang, S. W. 82  
 Poplawski, M. E. 25  
 Powers, J. 73  
 Putty, M. W. 82, 213, 225  
 Ramsey, J. M. 65  
 Reay, R. J. 61  
 Reiley, T. C. 38  
 Ricco, A. J. 180, 193  
 Richard, M. A. 176  
 Ridley, J. 7  
 Ried, R. P. 33  
 Rimai, L. 176  
 Rodriguez, J. L. 57  
 Rouse, G. F. 197  
 Rugar, D. 17, 209  
 Sandejas, F. S. A. 1  
 Schmidt, M. A. 111, 127, 151  
 Seiler, K. 21  
 Selvakumar, A. 82, 138  
 Semancik, S. 53  
 Senturia, S. D. 229, 260, 184  
 Smith, R. B. 197  
 Smith, S. W. 234  
 Sobek, D. 260  
 Soltis, R. E. 176  
 Storment, C. W. 61, 95  
 Suehle, J. S. 53  
 Suh, J. W. 95  
 Swart, N. R. 119  
 Tai, Y.-C. 103  
 Tai, Y.-C. 264  
 Tito, F. 73  
 Trautman, M. A. 243  
 Visser, J. H. 176  
 Wago, K. 209  
 Warren, K. 69  
 Weber, W. 251  
 Weinberg, M. 73  
 Westerlind, V. A. 95  
 White, R. M. 33  
 Wilson, P. 7  
 Wise, K. D. 13, 29, 205, 256  
 Woodman, S. J. 38  
 Xu, C. 180  
 Yannoni, C. S. 209  
 Yazdi, N. 160  
 Yeh, C. 201  
 Zanini, M. 176  
 Zappe, H. H. 43  
 Zare, R. N. 61  
 Zavracky, P. M. 86  
 Zdeblick, M. J. 251  
 Zhang, Y. 205  
 Zins, C. , 7  
 Zook, J. D. 49, 221  
 Züger, O. 209

## KEYWORD INDEX

- Accelerometer - 69, 145, 151, 156, 160, 197, 225  
Aluminum - 90, 95  
Atomic Force Microscope - 17  
Calorimetric Sensor - 176  
Capacitive Resonator Drive/Sense - 221  
Capillary Electrophoresis - 21, 61, 65  
Catalytic Gate Hydrogen Sensor - 57  
Chemical Sensors - 164, 180  
Chemometric Cluster/Pattern Analysis - 180, 193  
CMOS - 7, 29, 53  
Compliant Micromechanisms - 189  
Copper - 38, 156  
Data Storage - 17  
Diamond - 172  
Display - 1  
Dissolved Wafer Process - 13, 160, 201, 205, 256  
Dry Etching of Polymers - 82, 95  
Electrochemical Detector - 61  
Electroformed Metals - 38, 43, 49, 73, 90, 213, 234  
Electromagnetic Microactuator - 49  
Electromechanical CAD - 184  
Electromechanical Modeling and Design - 123, 189  
Electron Cyclotron Resonance - 82  
Electronic Compass - 197  
Electroplating Molds - 82  
Electrostatic Microactuator - 38, 95, 138, 145, 234  
    *See also* Lateral Comb Drive - 38, 145, 239  
    Variable Capacitance Drive - 234  
    Vertical Comb Drive - 138  
    Vertical Parallel Plate - 95, 145  
Electrostatic Pull-In - 184  
Flip-chip Interconnect - 25  
Flow Cytometry - 260  
Force Detector - 209  
Gas Sensor - 53, 57, 172, 176  
Gold - 73  
Gyroscope/Tuning Fork - 151  
Gyroscope/Vibrating Ring - 213  
Hot-Wire Anemometer - 264  
Hydrophone - 73  
Implantable Sensor - 29  
Infrared Source - 7, 234  
Integrated Process - 7, 73, 145, 151  
Laser Micromachining - 142  
Lateral Comb Drive - 38, 145, 239  
LIGA - 49  
Magnetic Microactuator - 43  
Magnetic Resonance Force Microscopy - 209  
Mechanical Property Test Structures - 116, 184  
Microanalytical Equipment - 164  
Microelectrode - 29  
Microfluidic System - 21, 172, 256, 260  
Microlamp - 239  
Micromachined Jets - 243  
Micromotor - 234  
Microphone - 33  
Microspeaker - 33  
Multi-Level Microstructures - 99  
Neural Probe - 256  
Nickel - 234  
Nickel-Iron - 43, 49  
Optical - 1  
Optical Scanner - 234  
Packaging - 25, 29, 111  
Piezoelectric - 33, 225  
Piezoelectric Resonator Drive/Sense - 225  
Polyimide - 82, 90  
Polysilicon - 119, 132, 138, 145, 221, 234, 239, 264  
Polysilicon Resistance Stability - 119  
Pressure Sensor/Capacitive - 205  
Pressure Sensor/Resonant Microbeam - 221  
Pressure Sensor/Thermal - 78  
Pressure Sensor/Tunneling Tip - 201  
Pumping/Electroosmotic - 21, 65  
Quartz Resonant Density/Viscosity Sensors - 229  
Quartz Wafer Bonding - 260  
Resonant Bridge Microaccelerometer - 225  
SAW Chemical Sensors - 180, 193  
Scene Generator - 7  
Screen-printing - 25  
Sealed Microcavities - 103, 151  
Selective CVD Tungsten - 99  
Shear-Stress Sensor - 111  
Shock Sensor - 156  
Sigma-Delta Modulator Servo Control - 145  
Silicon Bulk Micromachining - 13, 107, 243, 248, 251  
Silicon Microvalve - 248, 251  
Silicon Nitride - 1, 7, 17, 209  
Silicon Wafer Bonding - 111, 127, 151  
Silicon-on-Insulator - 69, 86  
Tactile Imager - 13  
Tensile Testing Micromachine - 132  
Thermal Bimetallic Actuator - 107, 248  
Thermal Isolation Structure - 7, 53, 119, 176  
Thermopneumatic Actuation - 251  
Thin-Film Strain Sensor - 116  
Trench Refill Microstructures - 132, 138  
Variable Capacitance Drive - 234  
Vertical Comb Drive - 138  
Vertical Parallel Plate - 95, 145  
Zinc Oxide - 33, 225  
Zone-Melting-Recrystallization - 86